

Unveiling the Structure of the Circumgalactic Medium of High-Redshift Galaxies via Emission and Absorption Lines

Thesis by
Zhihui Li

In Partial Fulfillment of the Requirements for the
Degree of
Doctor of Philosophy

The logo for the California Institute of Technology (Caltech), featuring the word "Caltech" in a bold, orange, sans-serif font.

CALIFORNIA INSTITUTE OF TECHNOLOGY
Pasadena, California

2024
Defended May 21, 2024

© 2024

Zhihui Li

ORCID: 0000-0001-5113-7558

All rights reserved

ACKNOWLEDGEMENTS

As I approach the completion of this six-year journey, I am particularly grateful to my advisor, Chuck Steidel. His guidance has been invaluable, urging me to embrace independence in my research endeavors right from the outset, while encouraging me to collaborate with researchers globally. He has not only granted me the freedom to pursue projects that resonated with my passions, but has also demonstrated a profound understanding of the big picture, while meticulously attending to the intricate details and steering clear of biases and preconceived notions. I also wish to extend my heartfelt appreciation to my additional thesis committee members: Phil Hopkins, Lynne Hillenbrand, and Kareem El-Badry, for graciously agreeing to serve despite their demanding schedules, and for their illuminating discussions that have significantly enriched this journey.

I would like to express my gratitude to Max Gronke, who I have been collaborating closely with since my first year. He generously shared his Ly α radiative transfer code `tlac` with me, which eventually evolved into the cornerstone of my subsequent research. Despite his busy schedule, he consistently made time for our weekly meetings, accommodating the challenging nine-hour time zone difference between Pasadena and Garching. He shared countless ideas and insights with me throughout the years, and provided invaluable assistance during my postdoc application process, offering a unique perspective as a senior researcher in academia. I am also grateful to Phil Hopkins, with whom I embarked on my first research project in graduate school. Despite being primarily a theorist, he welcomed me regardless of my observational background and entrusted me with a fascinating simulation project on the circumgalactic medium to kickstart my graduate studies. He also generously let me use hundreds of thousands of hours of his computational time at no cost, a resource that was pivotal in maximizing my productivity throughout my PhD. In addition, I am deeply thankful to Dawn Erb, who trusted me and collaborated with me on a number of intriguing research projects. As an outstanding researcher and a patient, approachable instructor, she has been a significant source of inspiration for me. Her artistic approach to science and meticulous attention to detail have profoundly influenced my work. I truly appreciate her recommendation for my postdoc application, and her support throughout the years has been invaluable to me.

I extend my gratefulness to the senior graduate students in the astronomy depart-

ment whose guidance proved invaluable during my early years in grad school, including Yuguang Chen, Mia de los Reyes, and Dillon Dong. I offer special thanks to Michael Zhang, whose generous assistance throughout my grad school journey was instrumental. Amidst the pandemic, we initiated a daily routine of screen sharing to maintain our productivity, a practice that continues to this day. In addition, I wish to express appreciation to my fellow peers in our research group, including Nik Prusinski, Zhuyun Zhuang, and Evan Núñez, for their enriching discussions and unwavering emotional support.

I am also deeply grateful to my undergraduate research advisors, Luis Ho, Ann Zabludoff, and Matt Malkan, whose mentorship introduced me to the captivating world of astronomy research. Their guidance was indispensable in paving the path for my journey. I also thank my parents for their continuous support throughout the years. Lastly, I am profoundly indebted to my wife, Celestine, for her unwavering encouragement, steadfast support, and transformative influence, which have helped shape me into a more wholesome person throughout this incredible journey.

ABSTRACT

The circumgalactic medium (CGM), namely the gaseous matter beyond the stars and interstellar medium of a galaxy and within the virial radius of its dark matter halo, plays a pivotal role in governing crucial aspects of galaxy evolution. This thesis focuses on investigating the multiphase, clumpy structure of the CGM through the application of state-of-the-art numerical simulations, the development of novel semi-analytic models, and comprehensive analyses involving comparison with high-resolution, spatially resolved observational data obtained from the world's largest ground-based telescopes.

In this thesis, Chapter 2 represents a theoretical investigation into the fate of cool clouds within a hot ambient medium, which offers new insights into predicting the destiny of cool clouds based on observed CGM properties. Chapters 3 and 4 detail endeavors to model spatially resolved Ly α emission spectra obtained from SSA22 Ly α Blob 1 and 2 to constrain the cool gas properties, employing a multiphase, clumpy radiative transfer (RT) model for the CGM. Chapter 5 offers a theoretical exploration on extracting and interpreting physical parameters of cool gas in the CGM from Ly α spectra using physically realistic RT models. Chapter 6 introduces a novel method to self-consistently reproduce the spatially extended Ly α emission from the CGM of twelve extreme emission line galaxies at $z \sim 2$, marking the first successful attempt to model spatially varying Ly α emission within a physically realistic CGM framework. Chapter 7 introduces ALPACA, a new semi-analytic model for simulating low-ionization state (LIS) metal absorption lines in the clumpy CGM. Applying ALPACA to model C II, $\lambda 1334$ absorption line profiles in star-forming galaxies at $2 < z < 3$, the study reveals the intricate physical and kinematic structure of the CGM, and it underscores the necessity of integrating emission and absorption line modeling to effectively break the intrinsic degeneracy of complex CGM models. Concluding the thesis, Chapter 8 offers a brief summary and outlines potential applications of the newly developed CGM models in the James Webb Space Telescope (JWST) era.

PUBLISHED CONTENT AND CONTRIBUTIONS

- Li, Zhihui, Max Gronke, and Charles C. Steidel (Mar. 2024). “ALPACA: a new semi-analytical model for metal absorption lines emerging from clumpy galactic environments”. In: *MNRAS* 529.1, pp. 444–463. DOI: 10.1093/mnras/stae469. arXiv: 2306.11089 [astro-ph.GA].
Z.L. conceived the project, derived the analytic equations, conducted the numerical experiments, applied the model to observational data and wrote the manuscript.
- Erb, Dawn K., Zhihui Li, Charles C. Steidel, et al. (Aug. 2023). “The Circumgalactic Medium of Extreme Emission Line Galaxies at $z \sim 2$: Resolved Spectroscopy and Radiative Transfer Modeling of Spatially Extended Ly α Emission in the KBSS-KCWI Survey”. In: *ApJ* 953.1, 118, p. 118. DOI: 10.3847/1538-4357/acd849. arXiv: 2210.02465 [astro-ph.GA].
Z.L. conducted radiative transfer modeling and interpretation of the KCWI datacubes and contributed to the writing of the manuscript.
- Li, Zhihui and Max Gronke (July 2022a). “Deciphering the Lyman- α emission line: towards the understanding of galactic properties extracted from Ly α spectra via radiative transfer modelling”. In: *MNRAS* 513.4, pp. 5034–5051. DOI: 10.1093/mnras/stac1207. arXiv: 2111.03671 [astro-ph.GA].
Z.L. conceived the project, derived the analytic equations, conducted the numerical experiments, and wrote the manuscript.
- Li, Zhihui, Charles C. Steidel, Max Gronke, et al. (July 2022b). “Where outflows meet inflows: gas kinematics in SSA22 Ly α blob 2 decoded by advanced radiative transfer modelling”. In: *MNRAS* 513.3, pp. 3414–3428. DOI: 10.1093/mnras/stac958. arXiv: 2104.10682 [astro-ph.GA].
Z.L. conceived the project with input from collaborators, conducted modeling and interpretation of the data, and wrote the manuscript.
- Li, Zhihui, Charles C. Steidel, Max Gronke, and Yuguang Chen (Apr. 2021). “Revisiting the gas kinematics in SSA22 Lyman- α Blob 1 with radiative transfer modelling in a multiphase, clumpy medium”. In: *MNRAS* 502.2, pp. 2389–2408. DOI: 10.1093/mnras/staa3951. arXiv: 2008.09130 [astro-ph.GA].
Z.L. conceived the project with input from collaborators, conducted modeling and interpretation of the data, and wrote the manuscript.
- Li, Zhihui, Philip F. Hopkins, Jonathan Squire, et al. (Feb. 2020). “On the survival of cool clouds in the circumgalactic medium”. In: *MNRAS* 492.2, pp. 1841–1854. DOI: 10.1093/mnras/stz3567. arXiv: 1909.02632 [astro-ph.GA].
Z.L. conceived the project with input from collaborators, conducted analyses and interpretation of the numerical simulations, and wrote the manuscript.

TABLE OF CONTENTS

Acknowledgements	iii
Abstract	v
Published Content and Contributions	vi
Table of Contents	vi
List of Illustrations	ix
List of Tables	xxxv
Chapter I: Introduction	1
1.1 The Circumgalactic Medium	1
1.2 Thesis Outline	1
Chapter II: On the Survival of Cool Clouds in the Circumgalactic Medium	7
2.1 Introduction	7
2.2 Methods	9
2.3 Different Regimes of Dominant Physics	16
2.4 Conclusions	36
2.5 Appendix	39
Chapter III: Revisiting the Gas Kinematics in SSA22 Lyman- α Blob 1 with Radiative Transfer Modeling in a Multiphase, Clumpy Medium	41
3.1 Introduction	41
3.2 Observations and Data Reduction	44
3.3 The Gas Kinematic Structure of LAB1	46
3.4 Radiative Transfer Modeling Using The Multiphase Clumpy Model	57
3.5 Conclusions	66
3.6 Appendix	68
Chapter IV: Where Outflows Meet Inflows: Gas Kinematics in SSA22 Lyman- α Blob 2 Decoded by Advanced Radiative Transfer Modeling	73
4.1 Introduction	73
4.2 Observations and Data Reduction	75
4.3 Ly α Emission in LAB2	77
4.4 Non-Detection of Nebular Emission Lines	83
4.5 Radiative Transfer Modeling Using The Multiphase Clumpy Model	84
4.6 Previous Studies of LAB2	96
4.7 Conclusions	99
Chapter V: Deciphering the Lyman- α Emission Line: Towards the Understanding of Galactic Properties Extracted from Ly α Spectra via Radiative Transfer Modeling	103
5.1 Introduction	103
5.2 Methodology	107
5.3 Results I: Intrinsic Parameter Degeneracies of the Shell Model	108

5.4 Results II: Connecting the Shell Model to the Multiphase, Clumpy Model	112
5.5 Discussion	135
5.6 Conclusions	139
5.7 Appendix	141
Chapter VI: The Circumgalactic Medium of Extreme Emission Line Galaxies at $z \sim 2$: Resolved Spectroscopy and Radiative Transfer Modeling of Spatially Extended Ly α Emission in the KBSS-KCWI Survey	146
6.1 Introduction	146
6.2 Sample, Observations and Data Reduction	150
6.3 Global Ly α Measurements	154
6.4 Spatially Averaged Ly α Profiles	157
6.5 Modeling Ly α Emission and Low Ionization Interstellar Absorption Lines	163
6.6 Summary and Discussion	183
6.7 Appendix	189
Chapter VII: ALPACA: A New Semi-Analytic Model for Metal Absorption Lines Emerging from Clumpy Galactic Environments	197
7.1 Introduction	197
7.2 ALPACA: A Non-Sobolev Clumpy Model For Metal Absorption Lines	200
7.3 Model Validation	210
7.4 Effect of Individual Parameters	213
7.5 Application Example: Modeling the ISM and CGM of a Sample of Lyman Break Galaxies	214
7.6 Covering and Volume Filling Parameters of the Cool Gas	225
7.7 Sobolev vs. Non-Sobolev	229
7.8 Previous Work Modeling UV Absorption Lines	235
7.9 Caveats and Outlook	238
7.10 Conclusions	240
7.11 Appendix	242
Chapter VIII: Summary and Outlook	244
Bibliography	249

LIST OF ILLUSTRATIONS

<i>Number</i>	<i>Page</i>
2.1 Time evolution of the normalized cloud masses, $f_{\text{cl}}(t)$, for four clouds with initial conditions of $T_{\text{h}} = 10^6$ K, $v_{\text{cl}} = 100$ km s$^{-1}$, $n_{\text{h}} = 10^{-3}$ cm$^{-3}$ and $L_{\text{cl}} = 0.1$–100 pc. Here $f_{\text{cl}}(t)$ is defined as $m_{\text{cl},50}(t)/m_{\text{cl},50}(t = 0)$, where $m_{\text{cl},50}$ is the cloud mass with density $\rho > (\rho_{\text{cl}}^0 \rho_{\text{h}}^0)^{1/2}$, i.e., the geometric mean of the initial cloud and ambient medium densities. These clouds “disrupt” in a well-defined manner in our simulations. We therefore define a cloud “lifetime”, t_{life} , as the time when the cloud mass falls below 10% of its initial value for the first time, i.e., $f_{\text{cl}}(t = t_{\text{life}}) \leq 0.1$	15
2.2 Time evolution of the maximum density (n_{max}) in a cloud for two representative cases. <i>Upper:</i> If $N_{\text{H}} \lesssim N_{\text{H}}^{\text{grav}}$ (Eq. 2.14), i.e., the cloud is initially Jeans-stable, then turning on or off self-gravity or self-shielding makes little difference. <i>Lower:</i> If $N_{\text{H}} \gtrsim N_{\text{H}}^{\text{grav}}$ (the cloud is initially Jeans-unstable), turning on self-gravity leads to cloud collapse (n_{max} runs away) in a free-fall time, as expected.	19
2.3 Simulation tests of the criteria for separating different cloud behaviors discussed in § 2.3 and § 2.3. <i>Upper:</i> Cooling time of ambient hot gas ($t_{\text{cool,h}}$) vs. crossing time of that gas over the cloud (t_{cross}). When cooling is faster than cloud velocity/sound crossing times, the clouds cannot be meaningfully pressure-confined and simply expand (neglecting self-gravity). The green triangles denote simulations used to check this directly, which confirm the validity of the simple analytic criteria for this behavior in Eq. (2.16). <i>Lower:</i> Same, but comparing $t_{\text{cool,h}}$ to the cloud “destruction time” in the limit where cooling is <i>not</i> important ($t_{\text{life,pred}}$, given in § 2.3, Eq. 2.19). When cooling of the hot gas in the cloud front is faster than cloud disruption, the cloud accretes and grows: simulations confirm the simple analytic criterion derived in Eq. (2.17).	21

- 2.4 *Upper*: Sliced density maps of two clouds in the “classical cloud destruction” regime with initial conditions of $T_h = 10^6$ K, $v_{cl} = 100$ km s $^{-1}$, $n_h = 10^{-3}$ cm $^{-3}$, $L_{cl} = 1$ and 100 pc, respectively. *Lower left*: Sliced density map of a “growing” cloud ($N_H \gtrsim N_H^{grow}$, with $T_h = 10^6$ K, $v_{cl} = 100$ km s $^{-1}$, $n_h = 10^{-3}$ cm $^{-3}$, $L_{cl} = 1000$ pc). *Lower right*: Sliced density map of a “pressure unconfined” cloud ($N_H \gtrsim N_H^{confine}$, with $T_h = 10^5$ K, $v_{cl} = 100$ km s $^{-1}$, $n_h = 10^{-1}$ cm $^{-3}$, $L_{cl} = 100$ pc). 22
- 2.5 **The cloud column density ($N_{H,cl}$) vs. the temperature of the ambient medium (T_h).** Different regimes of dominant physics are shown: (1) The “conduction description fails” regime (§2.3, Eq. 2.13, shown in yellow); (2) The “self-shielding and self-gravity dominate” regime (§2.3, Eq. 2.14, 2.15, shown in green and orange); (3) The “CGM pressure confinement fails” regime (§2.3, Eq. 2.16, shown in pink); (4) The “cloud grows” regime (§2.3, Eq. 2.17, shown in blue); (5) The “classical cloud destruction” regime (§2.3, Eq. 2.18, shown in white). Typical values of certain parameters have been adopted ($v_{cl} = 100$ km s $^{-1}$, $n_h = 10^{-2}$ cm $^{-3}$, $\tilde{f} = 1$). 24
- 2.6 **Simulated cloud “lifetimes”, $t_{life,sim}$ (in units of ten cloud-crushing time, $10 t_{cc}$) vs. different initial conditions: cloud size L_{cl} , ambient density n_h , ambient temperature T_h and cloud velocity v_{cl} .** Dotted lines connect simulations that have one varying parameter but otherwise identical initial conditions. In units of t_{cc} , the cloud lifetime has a weak dependence on T_h , modestly increases with L_{cl} and n_h (i.e., cloud N_H), and a slightly stronger dependence on v_{cl} . These dependencies are captured in the scaling of $t_{life,pred}$ with \tilde{f} in Eq. 2.19. Note that we factor out t_{cc} because it is the dominant effect here: our most extreme cases differ by factors of $\sim 10^8$ in their absolute lifetimes or values of t_{cc} (see, e.g., Figure 2.3); the “residuals” here, while still large (~ 1 dex), are much smaller. 26
- 2.7 **Cloud lifetimes measured in simulations ($t_{life,sim}$) vs. the “predicted” lifetimes ($t_{life,pred}$) from a simple multi-variable power-law fit to t_{life} vs. L_{cl} , n_h , T_h , and v_{cl} , given in Eq. (2.19).** Given a dynamic range $\sim 10^8$ in absolute cloud lifetimes, the simulations can be remarkably well-fit by a power law of the form $t_{life,pred} \approx 10 t_{cc} \tilde{f}$ with $\tilde{f} \sim L_1^{0.3} n_{0.01}^{0.3} v_{100}^{0.6}$ (so \tilde{f} encompasses all deviations from the cloud-crushing scaling). 27

- 2.8 **Sliced density maps for a cloud in the “classical cloud destruction” regime** ($T_h = 10^6$ K, $v_{cl} = 100$ km s $^{-1}$, $n_h = 10^{-3}$ cm $^{-3}$, $L_{cl} = 1$ pc), with each panel from left to right showing a simulation that includes additional physical effects (at the same physical time, **0.3 Myr**). From left to right we show: Hydro = ideal hydrodynamics; Hydro + Cooling = ideal hydrodynamics + radiative cooling, etc. Our default physics set is MHD + Cooling + Conduction + Viscosity. The cloud mass evolution curves for the same set of simulations are shown in Figure 2.9. 28
- 2.9 **Evolution of the normalized cloud mass, f_{cl} (defined in Figure 2.1) vs. time, for the simulations shown in Figure 2.8** ($T_h = 10^6$ K, $v_{cl} = 100$ km s $^{-1}$, $n_h = 10^{-3}$ cm $^{-3}$, $L_{cl} = 1$ pc) with different physics included (labeled as in Figure 2.8). The cloud mass vs. time is remarkably similar across these runs, given the different physics and morphologies in Figure 2.8. 29
- 2.10 **Evolution of the normalized cloud mass, f_{cl} (defined in Figure 2.1) vs. time, for otherwise identical initial conditions** ($T_h = 10^6$ K, $v_{cl} = 100$ km s $^{-1}$, $n_h = 10^{-2}$ cm $^{-3}$, $L_{cl} = 1$ pc) with different magnetic field configurations. We can see that when the magnetic field is aligned with the relative velocity ($\mathbf{B} \parallel \mathbf{v}_{cl}$), the cloud mass decreases most rapidly. For the azimuthal configuration (looped magnetic fields inside the cloud plus $\mathbf{B} \perp \mathbf{v}_{cl}$ outside the cloud, which produces maximal shielding to conduction), the cloud mass decreases most slowly. In all other cases, the magnetic field configuration does not have a large effect on the mass evolution: the lifetimes are identical to within a factor of < 2 30

- 2.11 **The simulated cloud lifetimes in units of the cloud-crushing time, $t_{\text{lifc}}/t_{\text{cc}}$, vs. the saturation parameter, σ_0 (Eq. 2.21 in § 2.3, which quantifies the strength of conduction) for clouds in the “classical destruction” regime.** The simulations are color-coded from light yellow to dark blue with decreasing $t_{\text{evap}}/t_{\text{cc}}$, where t_{evap} is the cloud evaporation time for a non-moving cloud in a conducting medium (Eq. 2.25). Simulations with $t_{\text{evap}} \ll t_{\text{cc}}$ are evaporated before cloud-crushing, explaining why $t_{\text{lifc}} \ll t_{\text{cc}}$. These clouds almost exclusively have $\sigma_0 \gg 1$, i.e., are in the regime of saturated conduction, where $t_{\text{evap}} \propto t_{\text{cc}} v_{\text{cl}}$, explaining the strong dependence of \tilde{f} on v_{cl} . While for simulations with $t_{\text{evap}} \gg t_{\text{cc}}$, clouds are only weakly influenced by conduction, and therefore $t_{\text{lifc}} \propto t_{\text{cc}}$ 35
- 2.12 **Evolution of the normalized cloud mass, f_{cl} (defined in Figure 2.1) vs. time, for one representative initial condition in the “classical cloud destruction” regime ($T_{\text{h}} = 10^6 \text{ K}$, $v_{\text{cl}} = 100 \text{ km s}^{-1}$, $n_{\text{h}} = 10^{-3} \text{ cm}^{-3}$, $L_{\text{cl}} = 1 \text{ pc}$) with our default physics set simulated at seven different mass resolution (m_i) levels, as labeled.** The resulting cloud lifetime is remarkably robust to resolution, changing by $< 10\%$ from $m_i/M_{\text{cl}} \sim 10^{-5} - 10^{-7}$ and by a factor of < 2 (< 3) even at resolutions $m_i/M_{\text{cl}} \sim 10^{-4}$ ($\sim 10^{-3}$). Recall our default resolution in the main text is $m_i/M_{\text{cl}} \sim 10^{-6}$. The small change in behavior at early times and high resolution (with a longer “delay” until destruction begins) owes to better tracking of small, high-density “features” (e.g., Kelvin-Helmholtz whorls) which remain locally high density even as mixing begins. 40

- 3.1 **Ly α and continuum images of LAB1.** *Left:* The narrow band Ly α image, obtained by collapsing the original KCWI datacube over 4959 – 5009 Å, which contains the Ly α line (see Section 2). The UV continuum near the wavelength of Ly α has been subtracted. *Right:* The *HST*/STIS optical continuum image. The positions of four MOSFIRE slits (Slit 1–4), two Lyman-break galaxies (C11 and C15), three submillimeter sources (ALMA-a, b, and c), a *K*-band selected galaxy (K1) and three [O III]/Ly α serendipitous sources (c₁ to c₃) have been marked on each image (see Table 3.2). The Ly α isophotes with levels of $SB_{Ly\alpha} = [120, 80, 40, 15, 4] \times 10^{-19} \text{ erg s}^{-1} \text{ cm}^{-2} \text{ arcsec}^{-2}$ have also been overlaid. All images have been registered to the same world-coordinate system. 48
- 3.2 **$F_{Ly\alpha}/F_{H\beta}$ as a function of the H I gas temperature T_{HI} in the photoionization (red patch) and collisional excitation (orange curve) scenarios.** Also shown are the ranges of $F_{Ly\alpha}/F_{H\beta}$ measured along four MOSFIRE slits for both the restricted regions (shaded in blue slashes) and extended regions (shaded in green slashes) (see §3.3 for the definitions of restricted and extended regions). 50
- 3.3 **Surface brightness distributions of Ly α (blue), [O III] (red) and H β (green) along four MOSFIRE slits** (the leftmost panels, (a) – (d) correspond to slits 1 – 4, respectively). For reference, the smoothed 2D spectra of H β (the second column) and [O III] (the third and fourth columns, for 4960 Å and 5008 Å, respectively) are also shown. Both the observed wavelengths (λ_{obs}) and the rest-frame wavelengths (λ_{rest} , assuming $z = 3.1000$) are shown. The positions of known sources are indicated with black arrows. We calculate $F_{[OIII]}/F_{H\beta}$ (shown in red numbers) by integrating $SB_{H\beta}$ and $SB_{[OIII]}$ along the slits for each identified source. We also calculate $F_{Ly\alpha}/F_{H\beta}$ (shown in green numbers) in two ways, where $F_{Ly\alpha}$ is calculated either by integrating $SB_{Ly\alpha}$ over the same region as H β and [O III] (as indicated by solid arrows), or by integrating over the full extent of Ly α (as indicated by dashed arrows). Note that the blue regions in the 2D spectra are negative images due to dithering. 52

- 3.4 **The first ($v_{\text{Ly}\alpha}$) and second ($\sigma_{\text{Ly}\alpha}$) moment maps of LAB1.** The two major Ly α emitting regions have been delineated by rectangular boxes (dashed white lines), and their zooming-in views are shown in the right panels. For the northern region, the colorbar limits have been adjusted accordingly to account for the smaller value range. The positions of the identified continuum sources are indicated by circles with labels. The Ly α SB isophotes (solid white lines) with levels of $\text{SB}_{\text{Ly}\alpha} = [120, 80, 40, 15, 4] \times 10^{-19} \text{ erg s}^{-1} \text{ cm}^{-2} \text{ arcsec}^{-2}$ have also been overlaid onto each image for visual reference. . . . 56
- 3.5 **Eleven representative continuum-subtracted, spatially resolved Ly α profiles from the high SB regions in LAB1.** All the spectra have been smoothed by a 3 pixel \times 3 pixel boxcar (0.9'') spatially and Gaussian smoothed ($\sigma = 0.5 \text{ \AA}$) in the wavelength dimension. The multiphase clumpy model best-fits (red, with orange 1- σ Poisson errors) and the observed Ly α profiles (black, with grey 1- σ error bars) have both been normalized. The observed Ly α spectra have also been shifted by $-\Delta v$ to their local systemic redshifts. For each subpanel, the x -axis is the velocity (in km s^{-1}) with respect to the local systemic redshift, and the y -axis is the normalized line flux. The spectrum number of each spectrum has been marked on the SB map (the right panel). For visual reference, the horizontal and vertical black dashed lines in each subpanel indicate zero flux level and zero velocity with respect to the local systemic redshift, respectively. . . . 58

- 3.6 **The effects of each individual physical parameter in $[n_{\text{HI,ICM}}, F_V, \sigma_{\text{cl}}, v_{\text{cl}}, v_{\text{ICM}}, \Delta v]$ (taking spectrum 10 as an example).** From the top left to the bottom right panel, one parameter is varied at a time (as shown in lines and labeled with different colors) and others are fixed (to the best-fit parameter values of spectrum 10, see Table 3.4). The red line in each panel represents the best-fit model of spectrum 10. The x -axis is the velocity (in km s^{-1}) with respect to the local systemic redshift of spectrum 10, and the y -axis is the normalized line flux. It can be seen that different parameters affect the model spectra in different ways – $n_{\text{HI,ICM}}$ determines the overall shape and the trough depth of the spectrum; F_V and v_{cl} determine the shapes and strengths of the peak(s); σ_{cl} determines the width of the spectrum; v_{ICM} determines the location of the main peak and the trough; Δv shifts the spectrum in the velocity dimension. 60
- 3.7 **Single Gaussian fits to the observed [O III] profiles of two LBGs, C11 and C15.** The [O III] emission is spatially integrated over the ranges indicated by black solid arrows in Figure 3.3, which include all the significant [O III] emission of C11 and C15. The observed fluxes (shown in black) with $1\text{-}\sigma$ uncertainties (shaded in grey), the best-fit model (shown in red) and best-fit parameters (with $1\text{-}\sigma$ uncertainties) are shown in each panel. Note that skylines are present near the [O III] lines, as indicated by large flux uncertainties. 69
- 3.8 **Justification of using spatially integrated models to fit the spatially resolved $\text{Ly}\alpha$ profiles.** *Left:* Configuration of the multiphase, clumpy model and the way we construct our photon bins for the observer. *Right:* Comparison of integrated models and binned models for spectra 1 and 2. Assuming the largest impact parameter of all the photons is b_{max} , we made three photon bins within the 2σ range ($0.05 < b/b_{\text{max}} \leq 0.35$, $0.35 < b/b_{\text{max}} \leq 0.65$ and $0.65 < b/b_{\text{max}} \leq 0.95$) and constructed three binned model spectra with these photon bins respectively. It can be seen the binned models are qualitatively very similar to the integrated model. 72

- 4.1 **Ly α and continuum images of LAB2.** *Left:* The narrow band Ly α image, obtained by collapsing the original KCWI datacube over 4949 – 5009 Å, which encloses the Ly α line (see §4.3). The UV continuum near the wavelength of Ly α has been subtracted. The positions of the MOSFIRE slits are delineated by parallel yellow and orange lines (see §4.2), and the numbers (1–15, in black) indicate the positions of spectra that we sample for radiative transfer modeling in §4.5. *Right:* The *HST* WFC3-IR F160W rest-frame optical continuum image. The positions of a Lyman-break galaxy (M14, labeled as ‘M’), an X-ray source (labeled as ‘X’) with IR (‘b’) and submm (‘A’) counterparts, and an IR source (‘a’) have been marked on each image (see §4.3 and Table 4.2). The Ly α isophotes with levels of $\text{SB}_{\text{Ly}\alpha} = [150, 80, 40, 20, 10] \times 10^{-19} \text{ erg s}^{-1} \text{ cm}^{-2} \text{ arcsec}^{-2}$ have also been overlaid, and the dashed white ellipse indicates the PSF in the final datacube with $\text{FWHM} \simeq 0.90'' \times 1.08''$ (X and Y-direction, respectively). Both images have been registered to the same world-coordinate system. 79
- 4.2 **Fifteen representative continuum-subtracted, spatially resolved and normalized Ly α profiles (black, with grey 1- σ error bars) from the high SB regions in LAB2.** The spectrum number of each spectrum has been marked on the SB map in Figure 4.1. All the spectra have been smoothed by a 3 pixel \times 3 pixel boxcar (0.9'') spatially and Gaussian smoothed ($\sigma = 0.5 \text{ \AA}$) in the wavelength dimension. As we will detail in §4.5, the multiphase, clumpy model best-fits (red, with orange 1- σ Poisson errors) and the shell model best-fits (blue, with cyan 1- σ Poisson errors) are both shown in each subpanel. The observed Ly α spectra have also been shifted by $-\Delta v_{\text{clumpy}}$ to their local systemic redshifts (as determined by the best-fits), and the shell model best-fits are shifted correspondingly as well for direct comparison. For each subpanel, the x -axis is the velocity (in km s^{-1}) with respect to the local systemic redshift, and the y -axis is the normalized line flux. For visual reference, the horizontal and vertical black dashed lines in each subpanel indicate zero flux level and zero velocity with respect to the local systemic redshift, respectively. The vertical blue dashed lines indicate the initial guess for the systemic redshift ($z = 3.09$ for spectrum 1 and $z = 3.098$ for all other spectra). 80

- 4.3 **The spatial distribution of the blue-to-red flux ratio ($F_{\text{blue}}/F_{\text{red}}$) and its relation to SB.** *Left:* The map of $F_{\text{blue}}/F_{\text{red}}$ of LAB2 with Ly α SB contours overlaid (same as in Figure 4.1 but in yellow color) and spectrum numbers marked (same as in Figure 4.1 but in yellow color for spectra 3 and 14 for clarity). The black contour indicates where $F_{\text{blue}}/F_{\text{red}} = 1$. It can be seen that $F_{\text{blue}}/F_{\text{red}}$ is the lowest in the highest SB region, and increases outwards as the SB decreases. *Right:* The 2D density map of $F_{\text{blue}}/F_{\text{red}}$ vs. SB (on log scale) for all the individual pixels (as shown with grey points) with log SB > -18.0 (i.e., within the outermost yellow contour in the left panel). A simple power-law fit yields $F_{\text{blue}}/F_{\text{red}} \propto \text{SB}^{-0.4}$, as shown in the orange dashed line. Note the anti-correlation between $F_{\text{blue}}/F_{\text{red}}$ and Ly α SB, which may be due to the decline of the projected line-of-sight outflow velocity and the increase of inflow velocity towards the blob outskirts. Also shown on the right are the unweighted (blue curve) and SB-weighted (red curve) frequency distributions of $F_{\text{blue}}/F_{\text{red}}$. Both distributions peak at $F_{\text{blue}}/F_{\text{red}} < 1$, where the SB-weighted one leans more towards lower $F_{\text{blue}}/F_{\text{red}}$ 81
- 4.4 **Correlations between the multiphase, clumpy model parameters and the shell model parameters.** Only one significant ($\gtrsim 5\sigma$) positive correlation is observed between v_{cl} and v_{exp} . Interestingly, $\sigma_{\text{cl}} \leq \sigma_{\text{i}}$ and $|v_{\text{cl}}| \geq |v_{\text{exp}}|$ are almost always true. The Δv_{clumpy} vs. Δv_{shell} correlation is insignificant, but the data points are broadly consistent with a 1-to-1 relation within 2σ uncertainties. The color-coded points represent different Ly α spectra (see Figure 4.1 and 4.2). The $2\text{-}\sigma$ uncertainties of the data points are indicated by grey error bars. For the v_{cl} vs. v_{exp} correlation, the level of significance and the linear best-fit coefficients (slope m and intercept b , with $1\text{-}\sigma$ uncertainties) are shown at the lower right corner in the middle panel. The orange shaded region represent the range of twenty best-fits of the data points perturbed by their uncertainties. 85

- 4.5 **Results of fitting spatially resolved Ly α spectra (9, 10 and 11) at different impact parameters simultaneously.** *Left:* Illustration of how different photon bins are constructed in the multiphase, clumpy model. The ranges of impact parameters of three different Ly α photon bins are: $0.05 < b/b_{\max} \leq 0.35$, $0.35 < b/b_{\max} \leq 0.65$ and $0.65 < b/b_{\max} \leq 0.95$, where b_{\max} is the largest impact parameter of all the scattered Ly α photons. The solid red arrows represent an isotropic outflow of the cool clumps with velocity v_{iso} , and the dashed red arrow represents the observed clump outflow velocity projected along the line-of-sight, v_{LOS} . *Middle:* Three aligned and equally spaced Ly α spectra (black, with grey 1- σ error bars) and the corresponding binned best-fits (red, with orange 1- σ Poisson errors). The likelihoods of the binned fits are comparable to those of the individual fits. *Right:* The Ly α SB map, with the alignment of three modeled spectra indicated by a black arrow. 94
- 4.6 **The relation between the clump outflow velocity (v_{cl}) and the impact parameter (b).** The color-coded points represent v_{cl} values (with 1- σ error bars shown in grey) derived from individual fits of eight different Ly α spectra from the south high SB region, and the orange shaded region represent the range of twenty best-fits (using Eq. 4.4) of the data points perturbed by their 1- σ uncertainties. The best-fit parameters with 1- σ uncertainties are also shown in the lower left. The blue solid and dashed curves are reference v_{cl} vs. b curves generated by setting $v_{\text{iso}} = 193_{-15}^{+24}$ km s $^{-1}$ (derived from the combined fit) and $b_{\max} = 33$ kpc (calculated by mapping the geometric distances in the model to the actual physical distances in Eq. 4.4). The reference v_{cl} vs. b curve from the combined fit is fairly consistent with the v_{cl} values derived from individual fits (as well as the fitted v_{iso} and b_{\max} values) within 1- σ uncertainties, suggesting the variations in v_{cl} may be simply the projection of a radial outflow along the line-of-sight. 97

- 4.7 **Justification for using the multiphase, clumpy models to fit the spatially resolved Ly α profiles. four multiphase, clumpy models have $(\log n_{\text{ICM}} (\text{cm}^{-3}), F_{\text{V}}, \log N_{\text{HI,cl}} (\text{cm}^{-2}), \sigma_{\text{cl}} (\text{km s}^{-1})) = (-5.0, 0.2, 18.0, 400)$ and $v_{\text{cl}} (\text{km s}^{-1}) = (100, 107, 122, 163)$, respectively.** The photons from the following ranges of impact parameters are selected to construct the Ly α spectra for each of the four models: $b/b_{\text{max}} \in (0.1, 0.3], (0.3, 0.5], (0.5, 0.7],$ and $(0.7, 0.9]$, respectively. The line-of-sight v_{cl} for the $b/b_{\text{max}} \in (0.1, 0.3]$ photons (i.e., nearly "down the barrel") of the first model and for the other three bins of photons (i.e., "off the barrel") are basically the same. The Ly α model spectra constructed from these four bins of photons are consistent with each other within $1\text{-}\sigma$ uncertainties (about 10% assuming Poisson photon distribution). 102
- 5.1 **A schematic representation of the configuration of the shell model and the multiphase, clumpy model.** The four most important parameters in the shell model are: the shell expansion velocity (v_{exp}), the shell H I column density ($N_{\text{HI,shell}}$), the shell effective temperature (T_{shell}) or the Doppler parameter (b), and the intrinsic Ly α line width (σ_i). The multiphase, clumpy model has six most crucial parameters: (1) the cloud covering factor (f_{cl}), which is the mean number of clumps per line-of-sight; (2) the H I column density of the clumps ($N_{\text{HI,cl}}$); (3) the velocity dispersion of the clumps (σ_{cl}); (4) the radial outflow velocity of the clumps (v_{cl}); (5) the residual H I number density in the inter-clump medium (ICM, $n_{\text{HI,ICM}}$); (6) the radial outflow velocity of the ICM (v_{ICM}). The orange solar sign represents the central Ly α emitting source in each model. Two different geometries for the multiphase, clumpy model, slab and sphere, are explored in this work. 106
- 5.2 **Examples of degenerate static shell models with the same $N_{\text{HI}} T^{0.5}$.** Different colored curves represent two sets of shell models ($\sigma_i = 200$ and 400 km s^{-1} , respectively) with the same $N_{\text{HI}} T^{0.5}$. It can be seen that the normalized intensity distributions of each set of models are nearly identical. Note that this degeneracy only exists in the optically thick regime ($a\tau_0 \gtrsim 10^3$); at $a\tau_0 = 2.8 \times 10^{-13} (N_{\text{HI}}/T) \simeq 100$ the models start to deviate from the other degenerate models (the light lime and light pink curves). 109

- 5.3 **Examples of degenerate outflowing shell models.** Different colored curves represent two sets of outflowing shell models ($\sigma_i = 300$ and 400 km s^{-1} , respectively), each consisting of a series of models with increasing T_{shell} , with a step size of 0.5 dex. Accordingly, $N_{\text{HI,shell}}$ decreases by 0.25 dex and v_{exp} increases by a factor of $\sqrt{2}$. Each set of spectra appear essentially identical to each other, except for the one with the largest T_{shell} (the black curve), which is the only model in the series that does not satisfy $a\tau_0 \gtrsim 10^3$. We fit this model with our shell model grid by fixing $N_{\text{HI,shell}}$, T_{shell} and σ_i at the expected values and leaving v_{exp} and Δv free. A decent fit is achieved, albeit with the best-fit v_{exp} values (shown in bold) slightly lower than expected. 110
- 5.4 **Degeneracy shown in fitting the Ly α spectrum of a Green Pea galaxy, GP 0926+4427.** The observed spectrum is shown in black and two degenerate best-fit shell models are shown in red and blue, respectively. The χ^2 (per degree of freedom, DOF) values of these two best-fit models are very close to each other, but the shell expansion velocity of the high temperature model is about a factor of two higher than the low temperature model (as highlighted in bold), which consequently affects the fitted systemic redshift of the Ly α source. This result may explain the two major discrepancies reported in the literature (see §5.3 for details). 113
- 5.5 **Results of fitting static clumpy slab models with static shell models.** The blue and red points represent the parameter values derived from fitting with the customized, small shell model grid (with fixed $\sigma_i = 12.85 \text{ km s}^{-1}$) and the large shell model grid (with varying $\sigma_i \in [1, 800] \text{ km s}^{-1}$), respectively. *Upper:* The correlation between $N_{\text{HI,total}}$ and $N_{\text{HI,shell}}$. A very tight 1-to-1 correlation is present over three orders of magnitude. *Lower:* The distribution of the best-fit shell model temperatures T_{shell} . In all cases, T_{shell} values of 10^4 K (the clump temperature) are obtained within $1\text{-}\sigma$ uncertainties. . . . 115

- 5.6 **Examples of static shell model best-fits (obtained by using the shell model grid with fixed σ_i) to static clumpy slab models.** Two panels represent two different $[f_{\text{cl}}, N_{\text{HI,cl}}]$ cases. The black curves represent the static clumpy slab model spectra and the red curves represent the shell model best-fits. Both T_{shell} and $N_{\text{HI,shell}}$ have been obtained at the expected values. 117
- 5.7 **Results of fitting clumpy slab models with randomly moving clumps with shell models.** *Upper:* The yielded $N_{\text{HI,shell}}$ values are around the $N_{\text{HI,total}}$ values, but a noticeable deviation has emerged. *Middle:* The yielded shell temperatures (T_{shell}) are mostly at the effective temperatures of the clumpy slab model. *Lower:* The distribution of the derived line widths of the intrinsic Ly α emission (σ_i) of the best-fit shell models. The blue and red points represent the $\sigma_{\text{cl}} = 50$ and 100 km s^{-1} models, respectively. 118
- 5.8 **Examples of shell model best-fits to randomly moving clumpy slab models.** Four panels represent four different $(N_{\text{HI,total}}, \sigma_{\text{cl}})$ cases. The black curves represent the outflowing clumpy slab model spectra and the red curves represent the shell model best-fits. T_{shell} have been obtained at the expected values from Eq. (5.2) within uncertainties. 119
- 5.9 **Model examples showing the degeneracy between $N_{\text{HI,shell}}$ and T_{shell} .** The curves with different colors represent the clumpy slab model fitted (black) and the degenerate shell models with different $(\log N_{\text{HI,shell}}, \log T_{\text{shell}}, \chi^2)$, obtained by fitting within a certain parameter subspace. As shown in the inset, the models with higher T_{shell} have more extended troughs at line center and thus are less favored in the fitting to the clumpy slab models (the mock data), which have sharper troughs at high $N_{\text{HI,total}}$ 120

- 5.10 **Comparison between a clumpy slab model and two shell models with corresponding parameters and $\sigma_i = 12.85 / 600 \text{ km s}^{-1}$.** The black curve is an example clumpy slab model with $N_{\text{HI,total}}$ and σ_{cl} values labeled on the top of the plot; the red and blue curves are the shell models at the expected $N_{\text{HI,total}}$ and T_{shell} values with $\sigma_i = 12.85 \text{ km s}^{-1}$ and 600 km s^{-1} , respectively. It is clear that the clumpy slab model tends to have lower peaks and larger fluxes near the line center than the corresponding homogeneous shell model with a small σ_i ; such a mismatch is mitigated by the broadening effect of a large σ_i 121
- 5.11 **Results of fitting clumpy slab models with outflowing moving clumps with shell models.** *Upper:* The derived shell expansion velocities are mostly at the clump outflow velocities; *Upper Middle:* $N_{\text{HI,shell}}$ are reproduced mostly at $N_{\text{HI,total}}$, albeit with several outliers with $\Delta \log N_{\text{HI}} \gtrsim 0.3 \text{ dex}$; *Lower Middle:* The derived shell temperatures are mostly at the effective temperatures of the clumpy slab model; *Lower:* The distribution of the derived intrinsic Ly α line widths (σ_i) of the best-fit shell models, which increase as σ_{cl} or v_{cl} increases. The green, blue and red points represent the $\sigma_{\text{cl}} = 0, 50$ and 100 km s^{-1} models, respectively. 123
- 5.12 **Examples of outflowing shell model best-fits to outflowing clumpy slab models.** Four panels represent four different ($N_{\text{HI,total}}, \sigma_{\text{cl}}, v_{\text{cl}}$) cases. The black curves represent the outflowing clumpy slab model spectra and the red curves represent the shell model best-fits. v_{exp} have been obtained at the expected values within uncertainties. . . . 124
- 5.13 **Examples of clumpy slab models with linearly increasing outflow velocities, compared to those with constant outflow velocities.** The upper two rows are four models with linearly increasing outflow velocities, whereas the lower two rows are four models with constant outflow velocities. For the models with linearly increasing outflow velocities, the blue-to-red peak flux ratio is much higher. The peak separation is also larger, which boosts the fitted T_{shell} and σ_i values, but $N_{\text{HI,shell}} \simeq N_{\text{HI,total}}$ remains true. v_{exp} is roughly obtained at $\frac{1}{2}v_{\text{max}}$ 125

- 5.14 **Examples of momentum-driven radial velocity profiles given by Eq. (5.4).** Different colored curves represent five $v(r)$ profiles with different $(\sigma_{\text{cl}}, v_{\text{cl},\infty})$. Here σ_{cl} is fixed to 50 km s^{-1} and $v_{\text{cl},\infty}$ are adjusted to make the average radial velocity, $\overline{v(r)} = 60, 100, 200, 300$ and 400 km s^{-1} . The acceleration decreases with radius, and the velocity either flattens or drops at large r , depending on the actual values of σ_{cl} and $v_{\text{cl},\infty}$ 126
- 5.15 **Relation between the average radial velocity $\overline{v_{\text{cl}}(r)}$ of clumpy slab models and the derived v_{exp} from shell model fitting.** The red points represent the linearly increasing scenario, and the blue points represent the momentum driven scenario. For both scenarios, $\overline{v_{\text{cl}}(r)}$ and v_{exp} are basically consistent, suggesting that shell model fitting probes the average radial velocity of the clumps. 127
- 5.16 **Results of fitting clumpy slab models with static and outflowing ICM with shell models.** *Upper:* The derived shell expansion velocities are much smaller than the clump/ICM outflow velocities unless both components are co-outflowing, which yields $v_{\text{exp}} \simeq v_{\text{cl}} = v_{\text{ICM}}$; *Upper Middle:* $N_{\text{HI,shell}}$ are mostly at $N_{\text{HI,total}}$, albeit with several outliers with $\Delta \log N_{\text{HI}} \gtrsim 0.3$ dex; *Lower Middle:* The derived shell temperatures are boosted by the hot ICM to be higher than the effective temperatures of the clumpy slab model; *Lower:* The distribution of the derived intrinsic Ly α line widths (σ_i) of the best-fit shell models, which increase as σ_{cl} or v_{cl} increases. The green, blue and red points represent (1) $v_{\text{cl}} > 0, v_{\text{ICM}} = 0$ (2) $v_{\text{cl}} = 0, v_{\text{ICM}} > 0$ (3) $v_{\text{cl}} = v_{\text{ICM}} > 0$ models, respectively. 130
- 5.17 **Examples of shell model best-fits to outflowing clumpy slab models with and without ICM.** The first row represents three $v_{\text{cl}} > 0$ cases without ICM. The second row represents three $v_{\text{cl}} > 0$ cases with a static, $T = 10^6 \text{ K}$, $n_{\text{HI}} = 10^{-3} \text{ cm}^{-3}$ ICM. Adding this hot phase of static ICM tends to: (1) deepen the trough at line center; (2) increase the peak separation; (3) increase the blue-to-red peak flux ratio. The third row represents three $v_{\text{cl}} > 0$ cases with an outflowing ICM. A $v_{\text{ICM}} > 0$ ICM will further decrease the blue-to-red peak flux ratio and increase the v_{exp} of the shell model best-fit. In particular, the model with the same clump and ICM outflow velocity prefers a shell expansion velocity $v_{\text{exp}} \simeq v_{\text{cl}} = v_{\text{ICM}}$ 132

- 5.18 **Comparison between clumpy sphere models and clumpy slab models.** *Upper row:* The first two panels show that a non-outflowing ($v_{\text{cl}} = v_{\text{ICM}} = 0$) spherical model with $(\sigma_{\text{cl}}, \sqrt{3}N_{\text{HI,total}}, \sqrt{3}N_{\text{HI,ICM}})$ gives an identical spectrum to a slab model with $(\sigma_{\text{cl}}, N_{\text{HI,total}}, N_{\text{HI,ICM}})$, and hence yields the same shell model best-fit parameters. The factor $\sqrt{3}$ should arise from the geometrical difference a sphere and a slab (see §5.4 for details). The third panel shows that adding the same v_{cl} yields a mismatch between the two models, which should be a non-linear effect due to the geometrical difference. *Lower row:* The first panel shows the shell model best-fit to a clumpy slab model (with $v_{\text{exp}} \simeq v_{\text{cl}}$, $N_{\text{HI,shell}} \simeq N_{\text{HI,total}}$ and $T_{\text{shell}} \simeq T_{\text{eff,slab}}$), and the second panel shows the best-fit to the corresponding clumpy spherical model, where v_{exp} and T_{shell} are lower than expected and $N_{\text{HI,shell}}$ is higher than expected. The third panel shows that if we restrict T_{shell} to be $\geq 10^{5.5}$ K, the best-fit v_{exp} and $N_{\text{HI,shell}}$ become closer to the expected values, although the best-fit gives a higher χ^2 due to the mismatch in the red peak. 133
- 5.19 **Shell model fits to clumpy spherical models with decreasing $f_{\text{cl}}/f_{\text{cl,crit}}$.** The three panels correspond to three $(\sigma_{\text{cl}}, v_{\text{cl}}, \log N_{\text{HI,total}}) = (50, 0, 21.08)$ models with different $f_{\text{cl}}/f_{\text{cl,crit}}$ values: $\sim 60, 20,$ and $10,$ respectively. The blue curves are the clumpy spherical model spectra and the red curves are the shell model best-fits. As $f_{\text{cl}}/f_{\text{cl,crit}}$ decreases, in the beginning the shell model is still able to produce a decent fit with reasonable parameters (albeit with the mismatch at line center), but eventually the fit fails at $f_{\text{cl}}/f_{\text{cl,crit}} \simeq 10.$ 135

- 5.20 **Effect of ICM temperature on Ly α transmission function and Ly α model spectra.** Here we show one example: a two-phase scattering medium that consists of cool clumps with velocity dispersion $\sigma_{\text{cl}} = 50 \text{ km s}^{-1}$ (hence effective temperature $\log T_{\text{eff}}(\text{K}) = 5.2$) and total H I column density $\log N_{\text{HI, total, cool}} = 19.6$, and a hot ICM with total H I column density $\log N_{\text{HI, total, ICM}} = 17.2$. *Top:* The transmission function of the cool clumps (the orange curve) as compared to those of the ICM at different temperatures. *Bottom:* The model Ly α profile as a function of the ICM temperature. As inferred from Eq. (5.7), at $\log T_{\text{ICM}}(\text{K}) \sim 5.6$ (the black curves) the ICM starts to have an impact on both the transmission function and the model Ly α profile. 143
- 5.21 **Effect of ICM with different column densities on the critical clump covering factor, $f_{\text{cl, crit}}$.** Here we show one set of examples: a two-phase clumpy slab with $\log N_{\text{HI, total}} = 20.0$ in the static clumps, and a hot ICM with total H I column density $\log N_{\text{HI, ICM}} = 14.2 - 16.2$ (or equivalently, $n_{\text{HI, ICM}} = 10^{-6} - 10^{-4} \text{ cm}^{-3}$). With $\log N_{\text{HI, ICM}}$ varying by two orders of magnitudes, $f_{\text{cl, crit}}$ only changes by a factor of ~ 1.5 , suggesting that the hot ICM only has a minor effect on $f_{\text{cl, crit}}$ and the boundaries of different RT regimes. 144
- 6.1 **Continuum-subtracted Ly α profiles from spatially integrated spectra, with double asymmetric Gaussian fits shown in orange.** . . . 155
- 6.2 **Continuum-subtracted Ly α images.** White contours show the Ly α surface brightness, with the same levels in each panel: 1×10^{-18} (dotted), 5×10^{-18} (dashed), 1×10^{-17} (dash-dot), and 2×10^{-17} (solid) $\text{erg s}^{-1} \text{ cm}^{-2} \text{ arcsec}^{-2}$, and black contours indicate the adjacent UV continuum measured in a rest-frame 75 \AA window redward of the Ly α emission line. 156

- 6.3 **Normalized annular Ly α profiles, constructed by binning all spaxels that have S/N > 2 in the continuum-subtracted Ly α images in single spaxel (0.3) radial increments.** The spectra are color-coded by radius, with the inner portions of the halo in red and the outer portions in blue. The legend in each panel gives the median radius of each bin. For most of the sample, the blue-to-red peak ratio increases and the depth of the trough between the peaks decreases with increasing radius. In nearly all cases, the optimally extracted spectra shown in Figure 6.1 are statistically indistinguishable from the annular profiles at $r \approx 3$ kpc. 159
- 6.4 **Results of the line profile measurements of the annular spectra described in Section 6.4.** *Top row:* Ly α peak ratio vs. radius; Ly α peak separation vs. radius; and peak separation vs. ratio. *Middle row:* Ly α peak ratio vs. normalized Ly α surface brightness; Ly α peak separation vs. surface brightness; and surface brightness vs. radius. *Bottom row:* The fraction of total flux within ± 100 km s $^{-1}$ of the trough between the peaks f_{tr} vs. radius; f_{tr} vs. peak separation. . . 160
- 6.5 Top two rows: Blue-to-red Ly α flux ratios from radially binned spectra of the 60 $^\circ$ angular regions that maximize (dark blue circles) and minimize (light blue triangles) the gradient in peak ratio with radius. Second two rows: Same as first two rows, for measurements of the Ly α peak separation, with maximum gradients indicated by gold squares and minimum gradients by light yellow diamonds. The annular averages from Figure 6.4 are also shown as red stars in all panels. See Section 6.4 for details. 161

- 6.6 **Modeling results of the annular-averaged, spatially resolved Ly α spectra and of the average line profile of Si II λ 1260 and C II λ 1334 observed down the barrel for Q0207-BX144 (see Appendix 6.7 for the rest of the sample).** The top row shows the best-fit models (red) to the spatially resolved Ly α spectra (black, with 1- σ uncertainties shown in grey) from the inner to the outer halo. In each subpanel of the top row, the vertical and horizontal black dashed lines indicate the systemic redshift (determined from nebular emission lines) and zero flux density, respectively. The middle row and the first panel of the bottom row show a comparison between the radial trends of peak separation, blue-to-red flux ratio, trough flux fraction, and normalized SB vs. the normalized impact parameter predicted by the best-fit models (red squares) and measured from observation (black points, with 1- σ uncertainties). Note that the impact parameters may be slightly different for the model and the data: the models are binned consistently as $b/b_{\max} \in (0, \frac{1}{3}]$, $(\frac{1}{3}, \frac{2}{3}]$ and $(\frac{2}{3}, 1]$, and while the data are binned in the same way, the halos are asymmetric with the result that the median distance to the spaxels included in each bin varies from object to object. The rest of the bottom row shows the best-fit models (red) to the average line profile (black, with 1- σ uncertainties shown in grey) of Si II λ 1260 (blue) and C II λ 1334 (orange) profiles, as well as a comparison of clump radial outflow velocity profiles inferred from Ly α RT modeling (red) and metal absorption line fitting (blue hatched patch). The shaded regions represent the velocity ranges spanned by 50 points in the parameter space after convergence has been achieved for the fitting. 169

- 6.7 **Schematic of the escape of two Ly α photons at low and high impact parameters in the multiphase, clumpy model.** The large circle represents the boundary of the simulated spherical region, divided into shaded green, red hatched, and blue regions indicating the three ranges of impact parameters modeled. The location of the observer is indicated by the telescope dome at the bottom, and the dotted horizontal line indicates that photons in the blue peak arise from the near side of the halo while those in the red peak predominantly come from the far side. The gold sun symbol represents the Ly α emitting source at the center, the grey clouds represent HI clumps with random motions and radial outflows, and the small red circles represent the diffuse, hot ICM. The impact parameters b and b' are defined as the orthogonal distance from the center to the direction of the photon escape trajectories shown by the black solid and dashed lines. The photon that escapes at a higher $b > b'$ will experience several differences before it escapes: (1) it will scatter with lower HI column densities from the clumps, due to the decrease in the clump covering fraction at large radii; (2) it will experience (on average) a lower projected component of the clump outflow velocity along its traveling direction ($v_{\text{cl},\parallel} < v'_{\text{cl},\parallel}$, as indicated by the black arrows near the last clump that scatters each photon); (3) it will suffer from less absorption at line center from the ICM, due to its lower traveling distance at the outskirts of the halo. Also note that the photon escaping at b' passes through a clump on the near side of the halo unimpeded, because it is out of resonance with the clump due to its previous scattering. 172

- 6.8 **Experiments designed to test our hypotheses for the differences between Ly α photons that escape at low and high impact parameters.** In each of the four subpanels, three binned model Ly α spectra are shown according to their last-scattering impact parameters: $b/r_h \in (0, \frac{1}{3}]$ (green solid), $(\frac{1}{3}, \frac{2}{3}]$ (red dash-dotted) and $(\frac{2}{3}, 1]$ (blue dotted), where r_h is the radius of the modeled halo. *Left:* The fiducial model with $(F_V, \log N_{\text{HI,cl}}, \sigma_{\text{cl}}, v_{\text{cl},\infty}, \log n_{\text{HI,ICM}}) = (0.05, 18.5, 80, 500, -7.0)$. *Second from left:* Model I, in which more clumps are placed at large radii so that the number density of the clumps $n_{\text{cl}}(r) \simeq \text{constant}$. *Third from left:* Model II, in which the clump radial velocity is set to be tangential, so that the projected component of the clump outflow velocity along the traveling direction is no longer preferentially small for photons that escape at high impact parameters. *Right:* Model III, in which the number density of the ICM is increased by a factor of 20 in the outer 60% of the halo radius. In each of the three test models, the change in the model configuration offsets the corresponding spatial variation of the Ly α spectral morphology (i.e., peak separation, peak flux ratio and trough flux fraction), hence supporting our explanation. 175
- 6.9 **Examples of Ly α model spectra with different clump outflow velocities showing the pattern in the change of the blue-to-red peak flux ratio.** Five models with $(F_V, \log N_{\text{HI,cl}}, \log n_{\text{ICM}}, \sigma_{\text{cl}}) = (0.04, 17.5, -6.5, 125)$ and $v_{\text{cl},\infty} = (500, 600, 700, 800, 900)$ are shown with different colors and linestyles. *Left:* spatially integrated Ly α model spectra with different $v_{\text{cl},\infty}$ values. As $v_{\text{cl},\infty}$ increases, the average clump radial outflow velocity increases, and the blue-to-red peak flux ratio first decreases (comparing the black and green curves) and then increases (comparing the red, blue and orange curves). For visual convenience, we have normalized all the model spectra so that the maximum flux density of the red peak is one. *Right:* The corresponding clump radial velocity profiles for different $v_{\text{cl},\infty}$. Note that $v_{\text{cl}}(r)$ and $v_{\text{cl},\infty}$ are positively correlated, but $v_{\text{cl}}(r)$ is always smaller than (typically by several hundred km s^{-1}) $v_{\text{cl},\infty}$ due to the effect of gravitational deceleration. 177

6.10	Comparison of results from the radiative transfer models with properties of the spatially integrated spectra of the central regions of the galaxies shown in Figure 6.1. <i>Top row, left to right:</i> the Ly α blue-to-red flux ratio, peak separation, trough flux fraction f_{tr} and mean low-ionization absorption line equivalent width vs. the total HI column density. <i>Middle row:</i> the same four spectral quantities vs. the residual HI density in the ICM. <i>Bottom row, left to right:</i> Ly α blue-to-red flux ratio, peak separation, and f_{tr} vs. mean low-ionization absorption line equivalent width. In the top two rows the darker points show the results of our best-fit spatially resolved modeling, while the fainter points show the results of modeling the single, spatially integrated line profiles. The lower corner of each panel gives the p -value resulting from a Spearman correlation test using the spatially resolved models only. Values with $p < 0.1$ are highlighted in red.	182
6.11	Same as Figure 6.6, but for Q0142-BX165 and Q0142-BX186. . . .	190
6.12	Same as Figure 6.6, but for Q0207-BX87 and Q0449-BX110. . . .	191
6.13	Same as Figure 6.6, but for Q0449-BX115 and Q0821-MD36. . . .	192
6.14	Same as Figure 6.6, but for Q1549-BX102 and Q1700-BX729. . . .	193
6.15	Same as Figure 6.6, but for Q2206-BX151 and Q2343-BX418. . . .	194
6.16	Same as Figure 6.6, but for Q2343-BX660.	195
6.17	Posterior distribution of spatially resolved modeling for Q0207-BX144. The [2.5%, 50%, 97.5%] (i.e., $2\text{-}\sigma$ confidence intervals) quantiles of parameters are indicated by vertical black dashed lines, and the maximum likelihood point in the parameter space is indicated by vertical red dashed lines.	196

- 7.1 **Schematic for ALPACA, a non-Sobolev clumpy model for metal absorption lines.** For the DTB absorption line profile, it is assumed that a central source emits continuum photons isotropically and that all photons travel radially in a spherical halo that contains a number of absorbing clumps. For computational convenience, the halo is divided into a series of equally spaced, concentric shells. The probability of escape for a continuum photon observed at a particular velocity is determined by the product of transmission probabilities through all radial shells. In each shell, the transmission probability is the sum of the probabilities of propagating through “holes” that are not occupied by any clumps (given by $1 - C_f(r_i)$) and penetrating through clumps (given by $C_f(r_i)e^{-\tau_{\text{ion}}(v-v_i)}$). The EW vs. b profile can be similarly calculated at different impact parameters. We refer the readers to Section 7.2 for a detailed derivation. 201
- 7.2 **Schematic for calculating the geometric covering fraction of clumps at radius r .** The contribution of one clump (as shown in blue) to the geometric covering fraction at a shell midplane at r (as shown by the dotted black arc) is given by $\sim \pi[R_{\text{cl}}^2(r') - (r - r')^2]$, which, after being integrated over $r \pm d/2$, gives the total geometric covering fraction at r , $C_f(r)$ 203
- 7.3 **Clump radial outflow velocity profiles $v_{\text{cl, out}}(r)$ with different $\{M_{\text{vir}}, \mathcal{V}, \alpha\}$ values as given by Eq. (7.16).** In each panel, only one parameter is varied while the other two are fixed. The $v_{\text{cl, out}}(r)$ profiles derived from varying one of the parameters are shown in different colors. 207
- 7.4 **Comparison of the absorption line profiles predicted by ALPACA and t1ac.** The fiducial set of parameters are: $F_V = 0.005$, $\mathcal{V} = 700 \text{ km s}^{-1}$, $\alpha = 2.0$, $\sigma_{\text{cl, rand}} = 0 \text{ km s}^{-1}$, $\gamma = 2.0$, $\log N_{\text{HI, cl}} = 15$, $R_{\text{cl}} = 500 \text{ pc}$, and $b_D = 12.85 \text{ km s}^{-1}$. In each panel, only one parameter is varied (as indicated by three different colors) while the other parameters are fixed at their fiducial values. The model spectra predicted by ALPACA and t1ac are shown in thick and thin curves, respectively. The absorption line profiles predicted by the two models are highly consistent over a wide range of physical parameters, suggesting that the formalism that we introduced in Section 7.2 is remarkably successful. 210

- 7.5 **Results of joint modeling the composite DTB absorption line profile and the EW vs. b profile of C II λ 1334.** The posterior PDF is shown, along with the $1\text{-}\sigma$ confidence intervals of the fitted parameters. The location of the maximum likelihood point is indicated by red dashed lines. On the upper right, panel (a) shows the best-fit model to the DTB absorption line profile. The non-outflowing ISM component and the outflowing CGM component are shown in green and red colors, respectively. Panel (b) shows the best-fit model (red) to the observed EW vs. b profile (black) at three different impact parameters: $b/r_h \simeq [\frac{1}{3}, \frac{2}{3}, 1]$. Also shown are twenty models with the highest likelihoods (blue). Panel (c) shows the clump outflow velocity profiles of twenty models (blue) with the highest likelihoods in the parameter space, as well as the best-fit outflow velocity profile (red). The level of the clump radial velocity dispersion ($\sigma_{\text{cl,rand}} = 120 \text{ km s}^{-1}$) is shown by a horizontal black dashed line. . 215
- 7.6 **Probability density distribution of the normalized galactocentric radii of the clumps, r/r_{min} , weighted by the attenuation factor $C_f(r)(1 - e^{-\tau(r)})$ at three different observed velocities.** For $v_{\text{obs}} = -500 \text{ km s}^{-1}$, the probability density distribution decreases monotonically with radius, and the majority of absorption comes from $r/r_{\text{min}} \lesssim 40$. For $v_{\text{obs}} = -200 \text{ km s}^{-1}$, the contribution to the total absorption comes from all over the halo. For $v_{\text{obs}} = +100 \text{ km s}^{-1}$, the majority of absorption comes from $r/r_{\text{min}} \sim 1$ and $r/r_{\text{min}} \gtrsim 30$, whereas the contribution within $1 < r/r_{\text{min}} < 30$ is negligible. . . . 222

- 7.7 **Results of joint modeling using an alternative clump outflow velocity profile assuming gravitational deceleration is negligible (see Eq. 7.26).** Panel (a) shows the best-fit model to the DTB absorption line profile. The non-outflowing ISM component and the outflowing CGM component are shown in green and red colors, respectively. Panel (b) shows the best-fit model (red) to the observed EW vs. b profile (black) at three different impact parameters: $b/r_h \simeq [\frac{1}{3}, \frac{2}{3}, 1]$. Also shown are twenty models with the highest likelihoods (blue). Panel (c) shows the clump outflow velocity profiles of twenty models (blue) with the highest likelihoods in the parameter space, as well as the best-fit outflow velocity profile (red). The level of the clump radial velocity dispersion ($\sigma_{cl,rand} = 120 \text{ km s}^{-1}$) is shown by a horizontal black dashed line. 224
- 7.8 **Experiments designed to demonstrate the difference between the Sobolev and non-Sobolev modeling.** We consider a homogeneous medium vs. an extremely clumpy medium where the covering fraction $C_f(r) \simeq 1$ everywhere. *Left:* If the radial velocity gradient is large, the Sobolev models (thick curves) are consistent with the corresponding non-Sobolev models (thin curves), suggesting that the Sobolev approximation works in this regime. Two sets of models with two different number density profiles of the ions or clumps ($n(r) \propto r^{-1}$ and r^{-2}) are shown in green and blue, respectively. *Middle:* If the radial velocity gradient is small, the Sobolev models underpredict the amount of absorption on both the red and blue sides of the line center, suggesting that the Sobolev approximation starts to break down. *Right:* If the radial velocity gradient is large but there is a small random velocity ($\sigma = 20 \text{ km s}^{-1}$), the absorption line profiles predicted by the Sobolev approximation quickly become chaotic and noisy due to the stochasticity added to the velocity gradient, whereas the profiles predicted by non-Sobolev modeling remain basically unperturbed and stable. 228

7.9 **Same as Figure 7.8, but for a non-volume-filling clumpy medium.**

We consider a non-volume-filling clumpy medium that contains holes through which the photons can pass freely. *Left:* If the radial velocity gradient is large, the non-Sobolev models tend to converge to the Monte-Carlo simulations by `tlac` as the number of shells increases (or equivalently, as d/R_{cl} decreases). However, the amount of absorption predicted by the Sobolev models (shown by thick curves) decreases as the number of clumps that produce resonant absorption at each velocity has decreased. Note that the $d/R_{\text{cl}} = 1$ Sobolev model is coincidentally consistent with the non-Sobolev models (see discussion in Section 7.7). *Middle:* If the radial velocity gradient is small, the Sobolev models always underestimate the amount of the absorption, regardless of the choice of the number of shells. *Right:* If the radial velocity gradient is large but there is a small random velocity ($\sigma_{\text{cl,rand}} = 20 \text{ km s}^{-1}$), the Sobolev model exhibits a significant deviation from the non-Sobolev model and the `tlac` prediction, suggesting that the Sobolev approximation is breaking down. 232

7.10 **Testing the convergence of ALPACA by varying d/R_{cl} .** The fiducial model parameters are given in the text, and two sets of models with $\sigma_{\text{cl,rand}} = 50$ and 100 km s^{-1} are calculated (shown in dash-dotted and solid lines, respectively). In each model set, the number of shells is varied (hence the d/R_{cl} values) and the model spectra are shown in different colors. For both sets of models, the convergence is achieved at $d/R_{\text{cl}} \sim 0.1$ 243

LIST OF TABLES

<i>Number</i>	<i>Page</i>
2.1	10
2.2	13
3.1	46
3.2	47
3.3	53
3.4	59
4.1	77
4.2	78
4.3	86
4.4	87
4.5	95
5.1	116
6.1	151
6.2	164
6.3	170
7.1	217

Chapter 1

INTRODUCTION

1.1 The Circumgalactic Medium

During my PhD, my research has been focused on studying the “atmospheres” of galaxies, formally referred to as the circumgalactic medium (CGM). The CGM is a vast, diffuse region of gaseous matter beyond the stars and interstellar medium (ISM) of a galaxy and within the virial radius of its dark matter halo. It plays a pivotal role in governing crucial aspects of galaxy evolution. Serving as a reservoir of gas, the CGM facilitates the accretion of material necessary for the formation of new stars within galaxies. As these stars reach the end of their life cycles, they unleash powerful supernovae that propel energetic galactic outflows, which, in turn, inject energy, momentum, and heavy elements into the CGM. These processes intricately modulate the CGM’s physical and chemical properties and regulate star formation within the galaxy. In essence, the CGM functions as a dynamic interface, bridging galaxies with their surrounding environments, often referred to as a “cosmic ecosystem”. The profound scientific significance of understanding the CGM and these cosmic ecosystems places it among the three top priority research areas for the next decade, as recognized by national academies of sciences (National Academies of Sciences et al., 2021). However, despite extensive observational and theoretical efforts, our knowledge of the CGM is still limited by its intricate structure, kinematics, thermal conditions and chemical composition.

1.2 Thesis Outline

Thus far, it has been well-established that the CGM is a multi-phase medium, encompassing gas spanning temperatures from a thousand to a few million degrees Kelvin. Among these phases, the “cool” phase ($\sim 10^4$ K) typically dominates both in terms of mass and energetics of the CGM. My research has been primarily centered on elucidating the physical properties of the cool phase. To achieve this goal, I have utilized state-of-the-art numerical simulations, developed novel semi-analytic models, and conducted thorough analyses by comparing them with high-resolution, spatially resolved observational data acquired from the world’s largest ground-based telescopes.

Chapter 2 stems from my first-year project, representing a somewhat distinct en-

deavor compared to the subsequent chapters. It stands out as a purely theoretical exploration without any analysis of observational data. In this project, I explored the classic “cloud-crushing” problem in the context of the CGM, examining the fate of cool clouds within a hot ambient medium. I conducted an unprecedentedly extensive analysis of a comprehensive suite of idealized hydrodynamical simulations of the CGM, utilizing the GIZMO code (Hopkins, 2015). I explored a wide range of cloud parameters, including cloud size, velocity, ambient temperature, and density. I also identified five distinct physical regimes, each corresponding to different fates for the clouds, ranging from their destruction due to instabilities induced by the hot ambient medium to their survival and growth through the accretion of cooled material onto their surfaces. Furthermore, I derived and calibrated an empirical scaling relation between the cloud lifetime and various cloud physical parameters, which has been widely employed and extensively discussed in many follow-up studies (e.g., Kanjilal et al. 2021; Farber et al. 2022; Abruzzo et al. 2022; Abruzzo et al. 2024; Abruzzo et al. 2023). I concluded that radiative cooling and conduction are the most important physics that affect cloud survival, whereas magnetic fields, turbulence, and viscosity are likely to have a minor effect. This study represents one of the most comprehensive explorations of parameter space to date and serves as a valuable framework for predicting the destiny of cool clouds based on observed CGM properties.

Starting from Chapter 3, the overarching goal of my research has been to constrain the properties of the CGM of high-redshift galaxies through systematic modeling of its emission and absorption lines. One of the most powerful tools for studying the CGM properties is to use Ly α emission, which is one of the most luminous emission lines in the spectra of distant galaxies. Ly α photons undergo resonant scattering by neutral hydrogen (H I) atoms as they traverse the CGM, thereby imprinting crucial information about the properties of H I onto the observed Ly α spectra.

Currently, the majority of Ly α studies of the CGM either involve empirical analyses of Ly α spectral properties, or rely on overly simplistic radiative transfer (RT) models that are unable to adequately capture the complex structure of the CGM. As of now, the most widely used model for Ly α RT modeling is the “shell model” – a monolithic, spherical expanding or contracting shell of neutral hydrogen with a single column density and outflow velocity. It is motivated by the observational evidence that starburst-driven galactic winds can produce such H I shells. This simple shell model has been employed successfully to reproduce a variety of Ly α pro-

files. However, the shell model is known to be an unrealistic representation of the complex, multiphase, and clumpy CGM. Indeed, several discrepancies between the best-fit parameters derived from the shell model and complementary observations have been noted. For example, Orlitová et al. (2018) fit the Ly α profiles of a sample of low-redshift Green Pea galaxies with the shell model and found that the best-fit systemic redshifts, shell outflow velocities, and intrinsic Ly α line widths are all significantly inconsistent with additional observational constraints.

Alternatively, several studies have delved into the development of more physically realistic RT models that are capable of capturing the multiphase, clumpy nature of the CGM (Richling, 2003; Hansen et al., 2006; Dijkstra et al., 2012; Laursen et al., 2013; Duval et al., 2014; Gronke et al., 2016a). Particularly noteworthy is the work by Gronke et al. (2016a), which outlines the formalism of a multi-variable multiphase, clumpy RT model designed for the practical application in modeling observed Ly α emission line profiles.

Chapter 3 and 4 are a pair of papers where I pioneered the modeling of spatially resolved Ly α emission spectra obtained by the Keck Cosmic Web Imager (KCWI) with the multiphase, clumpy RT model for SSA22 Ly α Blob 1 and 2, two of the earliest discovered Ly α blobs (LABs). These enigmatic objects are giant gaseous nebulae with immense Ly α luminosities at high redshifts. The physical origins of LABs remain a subject of intense debate, with various hypotheses proposed, including photo-ionization by central energetic sources, starburst-driven galactic outflows, cooling radiation from the accretion of cold gas streams, among many others. The Ly α profiles observed in LAB1 and LAB2 vary spatially, suggesting a corresponding variation in the physical properties of the H I gas in the CGM. To extract the underlying CGM gas properties, I developed a pipeline leveraging the nested sampling algorithm, which utilizes the multiphase, clumpy model to fit the spatially resolved Ly α spectra observed for LAB1 and LAB2. My modeling revealed that for both LABs, the dominant powering mechanism involves central sources producing Ly α photons that are subsequently scattered outward by high-velocity galactic outflows. In particular, for LAB2, the observed blue-dominated Ly α profiles observed at the blob outskirts indicate the presence of infalling cool gas, but we found that its energy contribution is likely to be minor. These works represent the first attempts to model spatially resolved Ly α emission spectra acquired from integral field unit (IFU) spectrographs with a physically realistic RT model that captures the multiphase, clumpy nature of the CGM.

Drawing upon my experience gained from fitting the spatially resolved Ly α profiles observed in LABs, Chapter 5 delves into a theoretical examination of the proper extraction and interpretation of the physical parameters of the cool gas in the CGM from Ly α spectra using RT models. Through a systematic comparison between a suite of multiphase, clumpy models and the shell models, I investigated the connections and differences between the more physically realistic multiphase, clumpy model and the traditional shell model. I found that the multiphase, clumpy model effectively resolves the discrepancies present in the shell model. For instance, within the multiphase, clumpy framework, a large intrinsic line width is no longer necessary; instead, the random motion of clumps sufficiently broadens the line profile. Moreover, the overly small shell expansion velocity should be interpreted as a radial and phase-averaged outflow velocity of the multiphase gas. In short, I demonstrated how the best-fit parameters derived from shell model fitting should be interpreted as specific properties of a multiphase, clumpy medium, and emphasized the importance of utilizing information from additional observations to break the intrinsic model degeneracies. This study provides a viable solution to the major issues of the shell model reported in previous literature, marking a significant advancement in accurately translating Ly α observables into the physical characteristics of the cool gas in the CGM.

In Chapter 6, building on a deeper understanding of the multiphase, clumpy CGM model, I developed a new approach to *self-consistently* reproduce the spatially extended Ly α emission originating from the CGM of twelve extreme emission line galaxies at $z \sim 2$. Our deep KCWI observations unveiled a striking pattern among these objects – they typically exhibit double-peaked Ly α profiles that span their entire Ly α halos, characterized by three intriguing trends: as the distance from the galactic center increases, the flux ratio of the blue peak to the red peak increases, the separation in velocity between the two peaks decreases, and the flux at the line center increases. By separating all the scattered Ly α photons in the multiphase, clumpy model into three radial bins according to their escaping impact parameters and comparing them with their corresponding observed Ly α profiles, I managed to find the best-fit RT model that *simultaneously reproduces* the Ly α spectra observed at three different impact parameters and all three radial trends. Furthermore, I found that all three radial trends of spatially resolved Ly α emission can be explained by considering the different RT behaviors of photons in the inner and outer regions of the halo. Specifically, the radial variation in the peak flux ratio, peak separation, and flux at the line center can be explained by radial variations in the line-of-sight

component of the clump outflow velocity, the clump number density, and the residual neutral density in the inter-clump medium, respectively. This work stands as the first successful attempt to self-consistently reproduce spatially varying Ly α emission via comprehensive RT modeling within the framework of a physically realistic CGM model.

In addition to Ly α emission, low-ionization state (LIS) metal absorption lines such as Si II λ 1260 and C II λ 1334 also serve as valuable tracers of the cool gas in the CGM due to their similar ionization potential. In Chapter 7, I shifted focus from Ly α emission to the study of metal absorption lines. I developed a new semi-analytic model named ALPACA to simulate the LIS metal absorption line profiles originating from a clumpy CGM. One of the prevalent models for analyzing the LIS absorption lines is the “picket-fence” model, which assumes that the absorption line profile is shaped by the partial covering of the emitting photon source by intervening gas. While the picket-fence model has successfully reproduced many absorption line profiles, it remains somewhat phenomenological in nature. This is because it parameterizes the absorption at a particular velocity in terms of the effective gas covering fraction and optical depth, without delving into the intricate details of the interaction between the photons and the gas moving at different velocities. Moreover, the picket-fence model oversimplifies the absorption process by implicitly assuming that absorption observed at a particular velocity originates solely from gas moving at the corresponding velocity at a single radius. It does not account for the potential contribution of gas at different radii to absorption at a given velocity, nor does it account for non-resonant absorption due to the finite Doppler width of the clumps.

In contrast, ALPACA is a physically motivated model that properly accounts for the interaction between the photons and the turbulent, outflowing, and clumpy gas in the CGM. It establishes a direct connection between the absorption line profile and the physical properties of the clumps, including the clump number densities, clump radii, clump radial velocities and clump column densities. Therefore, through modeling the absorption line profile, ALPACA enables direct constraints to be placed on the clump properties in the CGM. In addition, ALPACA accommodates non-monotonic radial velocity profiles and incorporates the random motion of the clumps, reflecting the turbulent motion in the CGM induced by gravitational effects or various mixing and cooling processes. Previous models, including the picket-fence model, typically neglected clump random motion and assumed a continuous,

monotonic outflow velocity profile. Consequently, the absorption observed at a particular velocity would originate solely from a single radius, where the photons appear resonant in the clump’s reference frame. In ALPACA, however, the clumps at different radii may exhibit similar total radial velocities due to their random motion. Thus, the absorption observed at a specific velocity could result from contributions by clumps situated across a broad range of radii. I found that this scenario aligns more closely with additional observations of the cool gas in the CGM.

In Chapter 7, I presented the general framework of the ALPACA model and showcased its successful application in modeling the C II $\lambda 1334$ absorption line profiles of star-forming galaxies at $2 < z < 3$. My joint modeling of the “down the barrel” absorption line profile and “out of the barrel” absorption equivalent widths revealed an intriguing picture of the cool gas in the CGM: the absorption observed at a particular velocity stems from non-volume-filling clumps that simultaneously exhibit outflowing and random motion across a considerably broad range of radii. Meanwhile, I discovered that there remained some freedom in the clump radial velocity profile that was not entirely constrained in the joint modeling process, which underscores the importance of incorporating spatially resolved Ly α emission modeling. The synergistic combination of modeling spatially resolved Ly α emission and LIS metal absorption lines will be a powerful approach for effectively breaking parameter degeneracies and facilitating accurate determinations of critical properties of the cool gas in the CGM.

Finally, in Chapter 8, I provided some concluding thoughts and outlined several potential applications of the new models that I have developed in the James Webb Space Telescope (JWST) era.

Chapter 2

ON THE SURVIVAL OF COOL CLOUDS IN THE CIRUMGALACTIC MEDIUM

Li, Zhihui, Philip F. Hopkins, Jonathan Squire, et al. (Feb. 2020). “On the survival of cool clouds in the circumgalactic medium”. In: *MNRAS* 492.2, pp. 1841–1854. DOI: 10.1093/mnras/stz3567. arXiv:1909.02632 [astro-ph.GA].

2.1 Introduction

The circumgalactic medium (CGM) is the diffuse, multi-phase gas surrounding a galaxy inside its virial radius and outside its disk and interstellar medium. In recent years, observations and simulations have revealed that CGM plays a significant role in galaxy evolution, in the sense that it both supplies gas for the galaxy’s star formation and recycles the energy and metals produced by stellar and AGN feedback (Tumlinson et al., 2017).

Over the past twenty years, direct observations have revealed the complex multi-phase structure in the CGM, in its ionization structure and dynamics. It is customary to classify the CGM gas into three components in different physical states (Cen, 2013), namely: (a) the cool gas phase ($T < 10^5$ K), mainly composed of neutral hydrogen and low-ionization-potential ions like Mg II, Si II and C II (e.g., Churchill et al. 1996; Chen et al. 1998; Steidel et al. 2010; Prochaska et al. 2014; Johnson et al. 2017); (b) the warm-hot gas phase ($T \sim 10^5 - 10^6$ K), specifically the high ionization-potential ions like C III, C IV, O VI, and Ne VIII (e.g., Stocke et al. 2006; Savage et al. 2011; Werk et al. 2014); (c) the hot gas phase ($T > 10^6$ K), consisting even more highly ionized species, like O VII and O VIII (e.g., Richter et al. 2008; Yao et al. 2010). Different ions in different physical states also display varied kinematics, resulting in a variety of absorption line profiles (Werk et al., 2016).

The existence of multi-phase gas raises fundamental questions about how the “cool” phases can be maintained. While the CGM can be thermally unstable, it is well-known from ideal-hydrodynamic simulations that a cool cloud moving through a hot medium at any appreciable velocity will be rapidly “shredded” and destroyed (mixed into the hot medium) by a combination of shocks, Rayleigh-Taylor, Kelvin-

Helmholtz, and related instabilities (McKee et al., 1975). If clouds are “ejected” from the galaxy directly in a cool phase of galactic outflows, or form “in-situ” in outflow cooling shocks/shells, they are expected to have large (super-sonic) relative velocities to the ambient medium (Thompson et al., 2016). Even if they form in situ in a thermally-unstable hydrostatic CGM “halo” of hot gas around the galaxy, they are buoyantly unstable and will “sink” at trans-sonic velocities (McCourt et al., 2018).

The simple formulation of this problem – namely the survival of a cold cloud moving through a hot ambient medium – is the classical “cloud crushing” problem, and has been studied for several decades in the context of the interstellar medium (ISM), particularly for the case of giant molecular clouds (GMC) being hit by supernova shocks (e.g., Cowie et al. 1977; McKee et al. 1977; Klein et al. 1994). However, in the CGM, the dominant physics and their effects are expected to be very different from those in the ISM. For example, GMCs are marginally self-gravitating, highly supersonically-turbulent (turbulent Mach numbers $\sim 10 - 100$), molecular and self-shielding¹ (temperatures $\sim 10 - 1000$ K, column densities $\gtrsim 100 M_{\odot} \text{pc}^{-2} \sim 10^{22} \text{cm}^{-2}$), with ratios of thermal-to-magnetic pressure much less than one (plasma $\beta \ll 1$), and extremely short ion/electron mean-free-paths (negligible conduction/viscosity). CGM clouds, on the other hand, are generally not self-gravitating or Jeans-unstable, are ionized or atomic (non-molecular, non-self-shielded, with temperatures $\gtrsim 10^4$ K), exhibit weakly sub-sonic or (at most) trans-sonic turbulence (turbulent Mach numbers $\lesssim 1$), and have dynamically negligible magnetic field strengths ($\beta \gg 1$). Further, given their lower densities and higher temperatures, such clouds can be comparable in size to the mean-free-paths of hot electrons in the ambient medium, meaning that conduction and viscosity could be extremely important. Moreover, those conduction/viscosity effects will be very anisotropic, given the small ratio of the particles’ gyro radii to the system size, and could easily be in regimes where standard classical results break down.

All of this means that it is unclear how much, if any, intuition can be “borrowed” from the historical cloud-crushing studies in the ISM. As a result, there has been a recent resurgence of work on this idealized cloud-crushing problem but in the CGM context (e.g., Scannapieco et al. 2015; Brügger et al. 2016; Liang et al. 2016;

¹By “self-shielding” we mean the cloud column density is high enough to absorb all the incoming ionizing photons from the meta-galactic UV background and shield the inner neutral gas from being ionized.

Armillotta et al. 2017; Liang et al. 2018; Gronke et al. 2018; Gronke et al. 2020; Sparre et al. 2019). However, given the more recent nature of these studies and the computational expense of simulations including all of the physics above, this work has generally been limited in one of two ways: either (1) neglecting key physics (e.g., ignoring radiative cooling, magnetic fields, anisotropic conduction/viscosity, saturation effects, or considering only two-dimensional cases), or (2) considering only a very limited parameter space (i.e., a couple of example clouds). In this paper, we therefore seek to build an analytical picture on the insights of these recent works by surveying a large parameter space of relevance to CGM clouds (e.g., of cloud sizes, column densities, and velocities, as well as ambient temperatures, densities, and magnetic field properties). We include radiative cooling, magnetic fields, and fully anisotropic conduction and viscosity, as well as self-shielding and self-gravity, in three-dimensional high-resolution numerical simulations.

The structure of this paper is as follows. We describe the relevant physics equations, the simulation code and initial conditions, and the range of parameters surveyed, in § 2.2. Using our suite of simulations and analytic scalings, we then isolate various parameter regimes which give rise to *qualitatively* different behaviors in § 2.3. We focus on the “classical cloud destruction” regime in § 2.3: there we parameterize the dependence of the cloud lifetime on the different physical parameters described above, and discuss the effects of different physics. We summarize and conclude in § 2.4.

2.2 Methods

Overview and Equations Solved

We wish to study the problem of a cloud moving through the ambient CGM. Within the cloud (ignoring, for now, the boundary and shock layer with the hot medium), ideal MHD should be a good approximation but the cooling times are short compared to other macroscopic timescales ($t_{\text{cool}} \sim 6 \times 10^{-5}$ Myr), so we expect clouds to be approximately isothermal at $\sim 10^4$ K (if they are not self-shielding, in which case they might be colder). In the hot medium, on the other hand, radiative cooling is usually negligible over the timescales we consider, as is self-gravity, but the deflection lengths (mean free paths) of the electrons and ions are not negligible. Because the electron and ion gyro-radii are vastly smaller than all other scales in the system, the system can be reasonably described by including appropriate, anisotropic conductive and viscous diffusion coefficients (“Braginskii” conduction and viscosity; Braginskii, 1965), which can provide a reasonable description of the kinetic physics

Table 2.1: Definitions of variables used in this paper.

x_h	value of quantity x in the hot, ambient medium
x_{cl}	value of quantity x in the cool cloud
t_{cool}	cooling time = $(3/2)k_B T/n\Lambda$
Λ	cooling function
κ_{cond}	conduction coefficient (see Eq. 2.9)
ν_{visc}	viscosity coefficient (see Eq. 2.11)
$\ln \Lambda_D$	Coulomb logarithm ($\Lambda_D \sim n_e \lambda_D^3$)
n_e	electron number density
β	plasma $\beta \equiv P_{therm}/P_B$
P_{therm}	thermal pressure = $n k_B T$
P_B	magnetic pressure = $ \mathbf{B} ^2/8\pi$
χ	density contrast n_{cl}/n_h ($= T_h/T_{cl}$, in equilibrium)
c_s	thermal sound speed
\mathcal{M}_h	initial Mach number of the hot medium $\equiv v_{cl}/c_{s,h}$
t_{cc}	classical cloud-crushing time $\equiv \chi^{1/2} R_{cl}/v_{cl}$
$t_{life, pred}$	predicted cloud lifetime from power-law fit
$t_{life, sim}$	simulated cloud lifetime
P_{ram}	ram pressure of the ambient medium = $\mu m_p n_h v_{cl}^2$

at play (see, e.g., discussion in Squire et al. 2019). Indeed, for the regimes considered, transport coefficients perpendicular to the magnetic field are suppressed by factors of $\sim 10^{-8}$ compared to the parallel coefficients. Given the large ionization fractions – $f_{ion} \sim 0.01 - 1$ inside the cloud, and $f_{ion} \approx 1$ outside it – we can safely neglect the effect of ambipolar diffusion, the Hall effect, and Ohmic resistivity on the evolution of the magnetic field.

The system of fluid equations we solve is therefore given by:

$$\frac{\partial \rho}{\partial t} + \nabla \cdot (\rho \mathbf{v}) = 0 \quad (2.1)$$

$$\frac{\partial \mathbf{v}}{\partial t} + (\mathbf{v} \cdot \nabla) \mathbf{v} = \frac{1}{\rho} \nabla \cdot \mathbf{S} - \nabla \Phi \quad (2.2)$$

$$\frac{\partial e}{\partial t} + \nabla \cdot (e \mathbf{v}) = \nabla \cdot (\mathbf{S} \cdot \mathbf{v} + \mathbf{K} \cdot \nabla T) - \rho \mathbf{v} \cdot \nabla \Phi - n^2 \Lambda \quad (2.3)$$

$$\frac{\partial \mathbf{B}}{\partial t} = \nabla \times (\mathbf{v} \times \mathbf{B}) \quad (2.4)$$

$$\nabla^2 \Phi = 4\pi G \rho \quad (2.5)$$

$$\mathbf{S} \equiv \left(P + \frac{\mathbf{B} \cdot \mathbf{B}}{2} \right) \mathbf{I} - \mathbf{B} \otimes \mathbf{B} - \mathbf{\Pi} \quad (2.6)$$

$$e \equiv \frac{1}{(\gamma - 1)} P + \frac{1}{2} \rho \mathbf{v} \cdot \mathbf{v} + \frac{\mathbf{B} \cdot \mathbf{B}}{2} \quad (2.7)$$

These are the usual continuity, momentum, energy, induction, Poisson (self-gravity) equations, for the gas mass density ρ , velocity \mathbf{v} , energy e , gravitational potential ϕ , and magnetic field \mathbf{B}^2 . Here \mathbf{S} is the stress tensor, with $P = nk_B T$ the usual isotropic (thermal) pressure (T the temperature and $n = \rho/\mu$ the particle number density, with local adiabatic index $\gamma = 5/3$). The conductivity (\mathbf{K}) and the viscous part of the stress tensor ($\mathbf{\Pi}$) are given by Spitzer et al. (1953) and Braginskii (1965) as:

$$\mathbf{K} \equiv \kappa_{\text{cond}} \hat{\mathbf{B}} \otimes \hat{\mathbf{B}} \quad (2.8)$$

$$\kappa_{\text{cond}} = \frac{0.96 f_i (k_B T)^{5/2} k_B}{m_e^{1/2} e^4 \ln \Lambda_D} (1 + 4.2 \ell_e / \ell_T)^{-1} \quad (2.9)$$

$$\mathbf{\Pi} \equiv 3 \nu_{\text{visc}} \left(\hat{\mathbf{B}} \otimes \hat{\mathbf{B}} - \frac{1}{3} \mathbf{I} \right) \left[\left(\hat{\mathbf{B}} \otimes \hat{\mathbf{B}} - \frac{1}{3} \mathbf{I} \right) : (\nabla \otimes \mathbf{v}) \right] \quad (2.10)$$

$$\nu_{\text{visc}} = \frac{0.406 f_i m_i^{1/2} (k_B T)^{5/2}}{(Z_i e)^4 \ln \Lambda_D} (1 + 4.2 \ell_i / \ell_v)^{-1} \quad (2.11)$$

where \otimes denotes the outer product; \mathbf{I} is the identity matrix; “:” denotes the double-dot-product ($\mathbf{A} : \mathbf{B} \equiv \text{Trace}(\mathbf{A} \cdot \mathbf{B})$); $\ln \Lambda_D \approx 37.8$ from Sarazin (1988); m_e , e , m_i , $Z_i e = e$ are the electron mass and charge and ion mass and charge; f_i the ionized fraction (calculated self-consistently in our cooling routines); k_B the Boltzmann constant; $\ell_e \approx 0.73 (k_B T)^2 / (n_e e^4 \ln \Lambda_D)$ is the electron mean-free path and $\ell_T = T / |\nabla T|$ the temperature gradient scale length (ℓ_i and $\ell_v = |\mathbf{v}| / \|\nabla \otimes \mathbf{v}\|$ are the ion mean-free path and velocity gradient scale length). These additional terms

²To maintain $\nabla \cdot \mathbf{B} = 0$, we adopt the divergence cleaning scheme proposed in Dedner et al. (2002) and the constrained gradient scheme in Hopkins (2016).

account for saturation of κ or ν , although, due to the current uncertainty in the relevant physics, they neglect the effect of plasma “micro-instabilities”, which can act to limit the flux further in the high- β regime (e.g., Kunz et al., 2014; Komarov et al., 2016). At a sharp discontinuity – for example, the contact discontinuity at the edge of the cloud – the form of Eq. (2.9) ensures the conductive flux takes the saturated form from Cowie et al. (1977): $q_{\text{sat}} \approx 0.4(2k_B T / \pi m_e)^{1/2} n_e k_B T \cos \theta \hat{\mathbf{B}}$ (where θ is the angle between \mathbf{B} and ∇T). Note, however, that by solving a single set of fluid equations we are assuming that ions and electrons maintain similar temperatures, despite the species having different conductive heat fluxes. Finally, $\Lambda = \Lambda(T, n, Z, I_\nu, \dots)$ represents cooling *and* heating (so it can have either sign) via additional processes such as radiation, cosmic rays, dust collisions and photo-electric processes, etc. (details below).

Simulation Code

We solve the equations (2.1)–(2.11) in the code GIZMO (Hopkins, 2015)³, which uses a Lagrangian mesh-free finite-volume Godunov method, in its meshless finite-volume (finite-element) “MFV” mode. We have also compared simulations using GIZMO with its meshless finite-mass, or fixed-grid finite volume solvers, to verify that the choice of hydrodynamic solver in GIZMO has only small effects on our results. Hopkins (2015), Thompson et al. (2016), and Hopkins (2016) and Hopkins (2017) present details of these methods and extensive tests of their accuracy and convergence in good agreement with state-of-the-art grid codes (e.g., ATHENA). In particular the MFV method is manifestly conservative of mass, momentum, and energy, with sharp shock-capturing and accurate treatment of fluid-mixing instabilities (e.g., Kelvin-Helmholtz (KH) and Rayleigh-Taylor (RT) instabilities), and correctly captures MHD phenomena including the magneto-rotational instability (MRI), magnetic jet launching in disks, magnetic fluid-mixing instabilities, and sub-sonic and super-sonic MHD turbulent dynamos. In Hopkins (2017), we show that the numerical implementation of the anisotropic diffusion operators (\mathbf{K} and $\mathbf{\Pi}$) is accurate, able to handle arbitrarily large anisotropies, converges comparably to higher-order fixed-grid codes, and is able to correctly capture complicated non-linear instabilities sourced by anisotropic diffusion such as the magneto-thermal and heat-flux buoyancy instabilities; this has also been tested in fully non-linear simulations of galaxy and star formation (Su et al., 2017). GIZMO also includes full

³A public version of this code is available at <http://www.tapir.caltech.edu/~phopkins/Site/GIZMO.html>.

Table 2.2: Parameters varied.

Name	Description	Values considered
L_{cl}	initial cloud diameter ($=2R_{\text{cl}}$)	0.01, 0.1, 1, 10, 100, 1000 pc
v_{cl}	initial cloud velocity	10, 100, 1000 km s ⁻¹
T_{h}	ambient temperature	10 ⁵ , 10 ⁶ , 10 ⁷ K
n_{h}	ambient density	10 ⁻⁴ , 10 ⁻³ , 10 ⁻² , 10 ⁻¹ cm ⁻³

Notes. The description and parameter space of the main physical parameters varied in this paper.

self-gravity (ϕ) using an improved version of the Tree-PM solver from GADGET-3 (Springel, 2005), with fully-adaptive and conservative gravitational force softenings (so hydrodynamic and gravitational force resolution is self-consistently matched) following Price et al. (2007). Finally, GIZMO includes a detailed, fully-implicit solver for radiative heating and cooling (Λ). We use the cooling physics from the cosmological FIRE galaxy simulations, with all details given in Appendix B of Hopkins et al. (2018): cooling is tracked self-consistently from 10 – 10¹⁰ K, including free-free, photo-ionization/recombination, Compton, photoelectric and dust collisional, cosmic ray, molecular, and metal-line and fine-structure processes (tabulated from CLOUDY; Ferland et al. 1998) from each of 11 species, accounting for photo-heating by a meta-galactic UV background (using the $z = 0$ value from Faucher-Giguère et al. 2009), with self-shielding (as in Rahmati et al., 2013) and optically thick cooling. Additional details are provided in Hopkins et al. (2018); the cooling physics have been used extensively in simulations of star and galaxy formation in the FIRE project. Ionization states are calculated self-consistently accounting for both collisional and photo-ionization.

Initial Conditions and “Default” Problem Setup

Our simulations follow a standard “cloud crushing” problem setup, always in three dimensions. For simplicity, a spherical cloud of radius R_{cl} and mean density $n_{\text{cl}} \equiv M_{\text{cl}}/(4\pi/3 R_{\text{cl}}^3 m_p)$ is initialized at an equilibrium temperature $T_{\text{cl}} \sim 10^4$ K (with heating and cooling from the meta-galactic UV background), in pressure equilibrium with a homogeneous box filled with gas at electron density $n_e = n_{\text{h}}$, temperature T_{h} , and relative velocity $\mathbf{v} = v_{\text{cl}}\hat{y}$ to the cloud (we relax the cloud before turning on velocities to ensure equilibrium temperature and pressure⁴). The system is contained

⁴We confirm that the cloud expansion during the relaxation process is negligible and does not affect the subsequent cloud evolution.

in a periodic box with size-length $10R_{\text{cl}}$ in the \hat{x} and \hat{z} directions and $20R_{\text{cl}}$ in the \hat{y} direction, with an inflow boundary on the “upwind” \hat{y} side such that the upwind portion of the box is always filled with gas at the initial ambient properties (with outflow out of the opposite \hat{y} side). The box moves with the cloud meaning that we can follow the system over long evolution times⁵, as long as the cloud does not become sufficiently elongated that it exceeds the box size. We have run simulations with box sizes up to $\sim 100R_{\text{cl}}$ in length to verify that this does not affect our conclusions. One advantage of our Lagrangian code is that it makes no difference (to machine precision) whether we assign the velocity to the cloud or ambient medium.

In our “default” simulations, the box is populated with equal-mass resolution elements with $m_i \approx 10^{-6}M_{\text{cl}}$. Because the method is Lagrangian, our mass resolution is fixed but spatial resolution is automatically adaptive with $\Delta x_i \approx 0.01R_{\text{cl}}(n/n_{\text{cl}})^{-1/3}(m_i/10^{-6}M_{\text{cl}})^{1/3}$. In some of the simulations below we disable self-shielding⁶ and self-gravity: without self-shielding there is effectively a temperature floor of $\sim 10^4$ K set by the UV background, while with self-shielding gas can cool to ~ 10 K in principle. The default simulations initialize an intentionally weak uniform magnetic field with $\beta \equiv P_{\text{therm}}/P_B = 10^6$, oriented perpendicular to the cloud velocity vector, but we vary this below. A small subset of our simulations consider “turbulent” initial conditions, as described below. In Appendix 2.5, we show the effects of changing resolution ($m_i \sim 10^{-7} - 10^{-3}M_{\text{cl}}$) and verify that the predicted cloud lifetimes are robust to the choice of resolution.

Table 2.2 lists the key physical parameters that we vary between simulations. We survey a wide range of parameters, including L_{cl} from 0.01 to 1000 pc, v_{cl} from 10 to 1000 km s^{-1} , T_{h} from 10^5 to 10^7 K, and n_{h} from 10^{-4} to 10^{-1} cm^{-3} .

Definition of Cloud “Destruction” and “Lifetime”

Although it is often obvious “by-eye” when a cloud is being “destroyed” or “mixed”, there is no obvious rigorous definition. Following one common convention in the literature, we simply define the “cloud mass” as the mass above some density threshold relative to the background. Since we consider a range of clouds with different initial density contrasts, we specifically define the mass variable $m_{\text{cl},x}$ as the mass in the box with density $\log \rho > \log \rho_{\text{h}}^0 + (x/100)(\log \rho_{\text{cl}}^0 - \log \rho_{\text{h}}^0)$, where ρ_{h}^0

⁵Every time when the cloud material gets too close to the boundary of the box, we shift the entire box to accommodate the cloud again.

⁶We account for self-shielding following Faucher-Giguère et al. (2015) by locally attenuating the UV background. So to disable self-shielding we simply unattenuate the UV background.

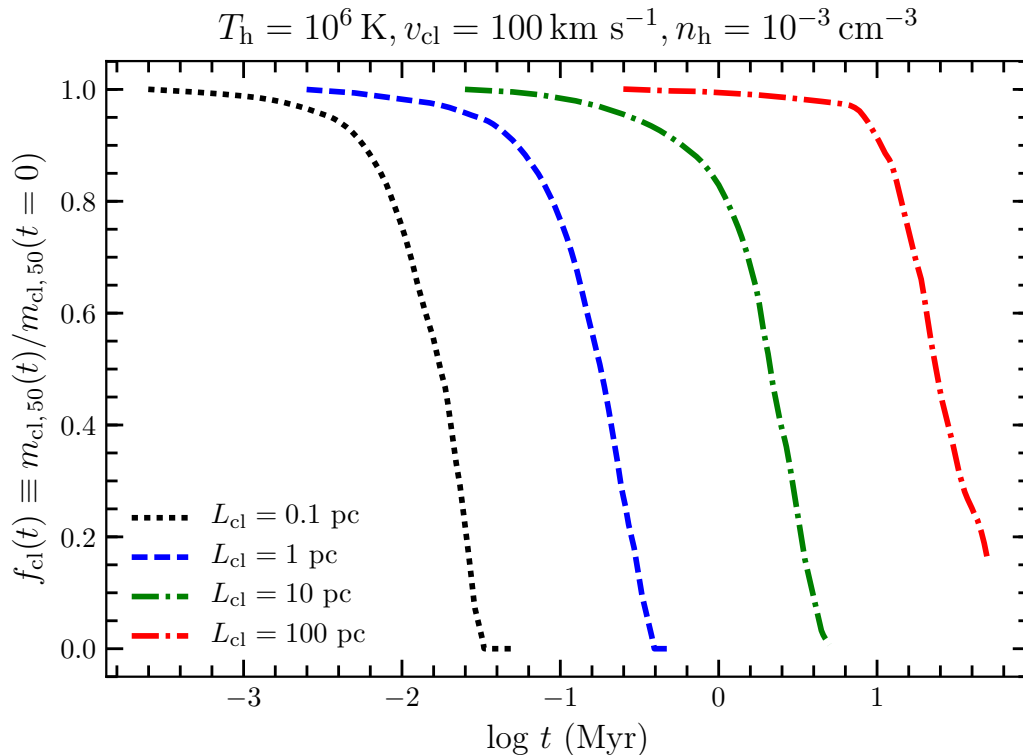


Figure 2.1: **Time evolution of the normalized cloud masses, $f_{\text{cl}}(t)$, for four clouds with initial conditions of $T_h = 10^6 \text{ K}$, $v_{\text{cl}} = 100 \text{ km s}^{-1}$, $n_h = 10^{-3} \text{ cm}^{-3}$ and $L_{\text{cl}} = 0.1\text{--}100 \text{ pc}$.** Here $f_{\text{cl}}(t)$ is defined as $m_{\text{cl},50}(t)/m_{\text{cl},50}(t=0)$, where $m_{\text{cl},50}$ is the cloud mass with density $\rho > (\rho_{\text{cl}}^0 \rho_h^0)^{1/2}$, i.e., the geometric mean of the initial cloud and ambient medium densities. These clouds “disrupt” in a well-defined manner in our simulations. We therefore define a cloud “lifetime”, t_{life} , as the time when the cloud mass falls below 10% of its initial value for the first time, i.e., $f_{\text{cl}}(t = t_{\text{life}}) \leq 0.1$.

and ρ_{cl}^0 are the initial ambient and cloud mean densities. So $m_{\text{cl},50}$ is the mass above a density threshold equal to $(\rho_{\text{cl}}^0 \rho_h^0)^{1/2}$, i.e., the geometric mean of the initial cloud and ambient medium densities. We have experimented with different values of x from $\sim 5 - 95$, as well as different functional forms for a density threshold and combined density-temperature thresholds. We find that $m_{\text{cl},50}$ defined in this manner gives the most robust estimate of the visually identified “cloud” material, so we will adopt this by default throughout.

Figure 2.1 shows several examples of the cloud mass estimator, $f_{\text{cl}}(t) \equiv m_{\text{cl},50}(t)/m_{\text{cl},50}(t=0)$ (cloud mass normalized to the initial cloud mass at time $t=0$), as a function of time. We see in many of the cases discussed below that the cloud mass (mass

remaining at high densities) declines steadily with time. In these cases, it is convenient to define a “lifetime” t_{life} of the cloud, although this is again somewhat arbitrary. We define this as the time when $f_{\text{cl}}(t = t_{\text{life}}) \leq 0.1$ for the first time – i.e., when the cloud mass as defined above falls below 10% of its initial value. We find this is more stable than fitting, e.g., an exponential or power-law decay timescale, because exponential or power-law decay is often not a good approximation to the simulation results. The choice of $\sim 10\%$ of the initial mass is arbitrary, but our results are qualitatively identical for choices in the range $\sim 1 - 50\%$ (above $\sim 50\%$, we find we often under-estimate the lifetimes of clouds, as they partially disrupt or evaporate but retain a long-lived “core”, and below $\sim 1 - 2\%$, resolution concerns begin to dominate).

Not all clouds decay in mass: as we will show below, some grow. For these, we can define a growth timescale as the approximate e -folding time.

2.3 Different Regimes of Dominant Physics

Guided by our simulation parameter survey, plus some basic analytic considerations, we now define different regimes of cloud behavior in the CGM and the most relevant physics in each.

The Smallest Clouds: Where Conduction Breaks Down

The thermal conductivity of the hot medium is defined by the transport of hot electrons, with $\kappa/k_B n_h \sim \lambda_{e,h} c_{s,e,h}$ where

$$\lambda_{e,h} \equiv 3 m_e^{1/2} (k_B T_e)^{3/2} c_{s,e,h} / (4\sqrt{2\pi} n_i e^4 \ln \Lambda_D) \approx 0.1 \text{ pc} \frac{T_6^2}{n_{h,0.01}} \quad (2.12)$$

(using $\ln \Lambda_D \approx 26$ for $T_h \sim 10^5 - 10^6$ K) is the electron Coulomb deflection length (along the magnetic field) and $c_{s,e,h}$ is the electron isothermal sound speed ($\equiv \sqrt{k_B T_h/m_e}$) defined in the hot medium. When the hot electrons encounter a cold cloud, they are able to penetrate to a skin depth $\lambda_{\text{skin}} = \lambda_{e,h} (n_h/n_{\text{cl}}) = \lambda_{e,h} (T_{\text{cl}}/T_h)$. If $\lambda_{\text{skin}} \gtrsim R_{\text{cl}}$, then our description of heat transport (conduction) via Eq. (2.3) breaks down (regardless of the accounting for saturated vs. unsaturated conduction). Using the values above, this occurs when

$$N_{\text{H}} \lesssim N_{\text{H}}^{\text{mfp}} \sim 10^{16} \text{ cm}^{-2} T_6^2 \quad (2.13)$$

where $T_6 \equiv T_h/10^6$ K, and $N_{\text{H}} \equiv R_{\text{cl}} \langle n_{\text{cl}} \rangle$ is the column density through the cloud⁷.

⁷It is sometimes stated that the “fluid approximation” breaks down on scales small compared to λ_{skin} or even the (much larger) $\lambda_{e,h}$, but this is not necessarily correct. So long as the gyro radii

We therefore intentionally avoid simulating systems below this scale. However, we can estimate what will occur. In this limit, the free e^- in the hot medium effectively do not “see” the cloud: the cloud will effectively be immersed in a sea of hot e^- with number density equal to the ambient hot e^- density, which contribute a uniform volumetric Coulomb heating rate. If the cloud is ionized, this is just $\dot{e} = 0.34 n_{e,h} (c_{s,e,h}/\lambda_{\text{skin}}) k_B T_h$ (Brüggen et al., 2016), and if $T_6^{3/2} \Lambda_{\text{cl},-23} \lesssim 0.14$, then the volumetric heating rate from hot e^- is larger than the cooling rate of gas in the cloud, and they should evaporate on a timescale short compared to their sound-crossing times. This process is analyzed in detail in Balbus et al. (1982).

Self-Gravity and Self-Shielding

At the other extreme, consider very large clouds. If a cloud is *initially* self-gravitating/Jeans-unstable, i.e., has $\lambda_J \equiv c_{s,\text{cl}}/\sqrt{G\rho_{\text{cl}}} \ll R_{\text{cl}}$, or $R_{\text{cl}} \gtrsim 1 \text{ kpc} (n_{\text{h},0.01} T_6)^{-1/2}$, or

$$\begin{aligned} N_{\text{H}} &\gtrsim N_{\text{H}}^{\text{grav}} \sim 0.5 \times 10^{22} \text{ cm}^{-2} (n_{\text{h},0.01} T_6)^{1/2} \\ &\sim 10^{22} \text{ cm}^{-2} P_{-12}^{1/2} \end{aligned} \quad (2.14)$$

where $P_{-12} \equiv P_{\text{h}}/10^{-12} \text{ erg cm}^{-3}$, then (a) the gravitational force per unit area is larger than the external (confining/stripping) pressure, and (b) its collapse/free-fall time is shorter than its sound-crossing time, itself shorter than the cloud destruction time (in the absence of gravity). Figure 2.2 shows that in our simulations with self-gravity on, we confirm that clouds which are initially Jeans-unstable ($N_{\text{H}} > N_{\text{H}}^{\text{grav}}$; Eq. 2.14) indeed fragment/collapse rapidly⁸, while clouds which are initially Jeans-stable ($N_{\text{H}} < N_{\text{H}}^{\text{grav}}$) behave essentially identically whether or not self-gravity is included. Thus, self-gravity is very much a “threshold” effect: it dominates in Jeans-unstable clouds, and is irrelevant in Jeans-stable clouds (at least on the spatial/time scales we simulate). There is only a very narrow, fine-tuned, and dynamically unstable parameter space where clouds are “just barely” Jeans-stable initially and can have sub-regions “pushed into” Jeans instability by their interactions with the ambient medium (we find just one such example in our entire parameter survey, with initial $N_{\text{H}} \sim 0.8 N_{\text{H}}^{\text{grav}}$)⁹. This should not be surprising: the same behavior has been

of the particles remain small compared to the relevant scales, equations with a similar form to the fluid MHD equations (the “kinetic MHD” equations of Kulsrud 1983) remain valid. However, our descriptions of parallel heat and momentum transport clearly become problematic below λ_{skin} , as does the assumption that the electrons and ions remain at the same temperature.

⁸Since we do not include star formation, we eventually stop the simulations when most of the gas in the initial cloud has collapsed to densities $> 10^5$ times larger than its initial mean density.

⁹This is expected: 1D compression (e.g., the initial “pancaking” of the cloud as it shocks) does not strongly enhance Jeans instability. Consider an initially Jeans-stable, isothermal cloud with

repeatedly demonstrated for clouds in the ISM (see, e.g., Mouschovias, 1976b; Mouschovias, 1976a; Li et al., 2014; Federrath et al., 2015; Körtgen et al., 2019).

Likewise, if the cloud can *initially* self-shield to molecular or fine-structure metal-line cooling to temperatures $T \sim 10 - 100 \text{ K} \ll 10^4 \text{ K}$, it will cool to those temperatures very quickly, which will remove its internal pressure support and render it immediately Jeans-unstable (even more so, given the rapid compression by the ambient medium which would follow). This is well-studied in the ISM context and requires a surface density $\gtrsim 10 M_\odot \text{ pc}^{-2} (Z_\odot/Z)$ (see Robertson et al., 2008; Krumholz et al., 2011, for extended discussion), or a column density

$$N_{\text{H}} \gtrsim N_{\text{H}}^{\text{shield}} \sim 1.5 \times 10^{22} \text{ cm}^{-2} Z_{0.1}^{-1} \quad (2.15)$$

where $Z_{0.1} \equiv Z/0.1 Z_\odot$. Like with self-gravity, we find this is a sharp “threshold” effect, not surprising since the self-shielding attenuation ($\propto e^{-\tau}$) is an extremely strong function of the N_{H} , which can vary by orders of magnitude. Usually, self-shielded clouds ($N_{\text{H}} > N_{\text{H}}^{\text{shield}}$; Eq. 2.15) are already self-gravitating, but it is largely irrelevant which occurs “first”. A self-shielded (but initially Jeans-stable) cloud rapidly becomes Jeans-unstable, while a Jeans-unstable (but non-shielded) cloud collapses isothermally (at $\sim 10^4 \text{ K}$) until it becomes self-shielded, then collapses more rapidly (see Robertson et al. 2008; Orr et al. 2018). Because the criterion here is a simple column-density threshold, it is also obvious that 1D compression of the cloud does not strongly alter its self-shielding. For the sake of completeness and testing our theory of cloud destruction, we have re-run all our simulations *without* self-gravity and self-shielding, so we can see whether and “how fast” they would be destroyed in the absence of these physics in our analysis below, but we stress that this is purely a counter-factual exercise.

Rapid Cooling of the Hot Medium: Failure of Pressure Confinement

If the hot gas cools faster than the time it takes to cross/envelop the cloud, it cannot maintain meaningful pressure confinement. Even if we add some global (spatially uniform) heating rate per unit volume or heat conduction in the hot medium, such that the ambient gas *equilibrium* temperature remains fixed at the “target” temperature, in this limit the hot gas is still thermally unstable and it cannot re-

(pre-shock) Jeans length $\lambda_{\text{J}}^0 > R_0$ (radius $R = R_0$), compressed or “pancaked” to width $H \ll R_0$ along the short axis (retaining $R = R_0$ along the long axis). Fragmentation along the short axis requires a Jeans-like criterion $\lambda_{\text{J}}^{\text{new}} < H$, but $\lambda_{\text{J}}^{\text{new}} = c_s / \sqrt{G \rho^{\text{new}}} \sim H (\lambda_{\text{J}}^0 / R_0) (R_0 / H)^{1/2} \gg H$. Along the long-axis, fragmentation must be treated two-dimensionally, and requires $\lambda_{\text{J}}^{2D} < R_0$ where $\lambda_{\text{J}}^{2D} \equiv c_s^2 / (\pi G \Sigma_{\text{cloud}}) \sim R_0 (\lambda_{\text{J}}^0 / R_0)^2 \gg R_0$. So an initially Jeans-stable cloud remains stable.

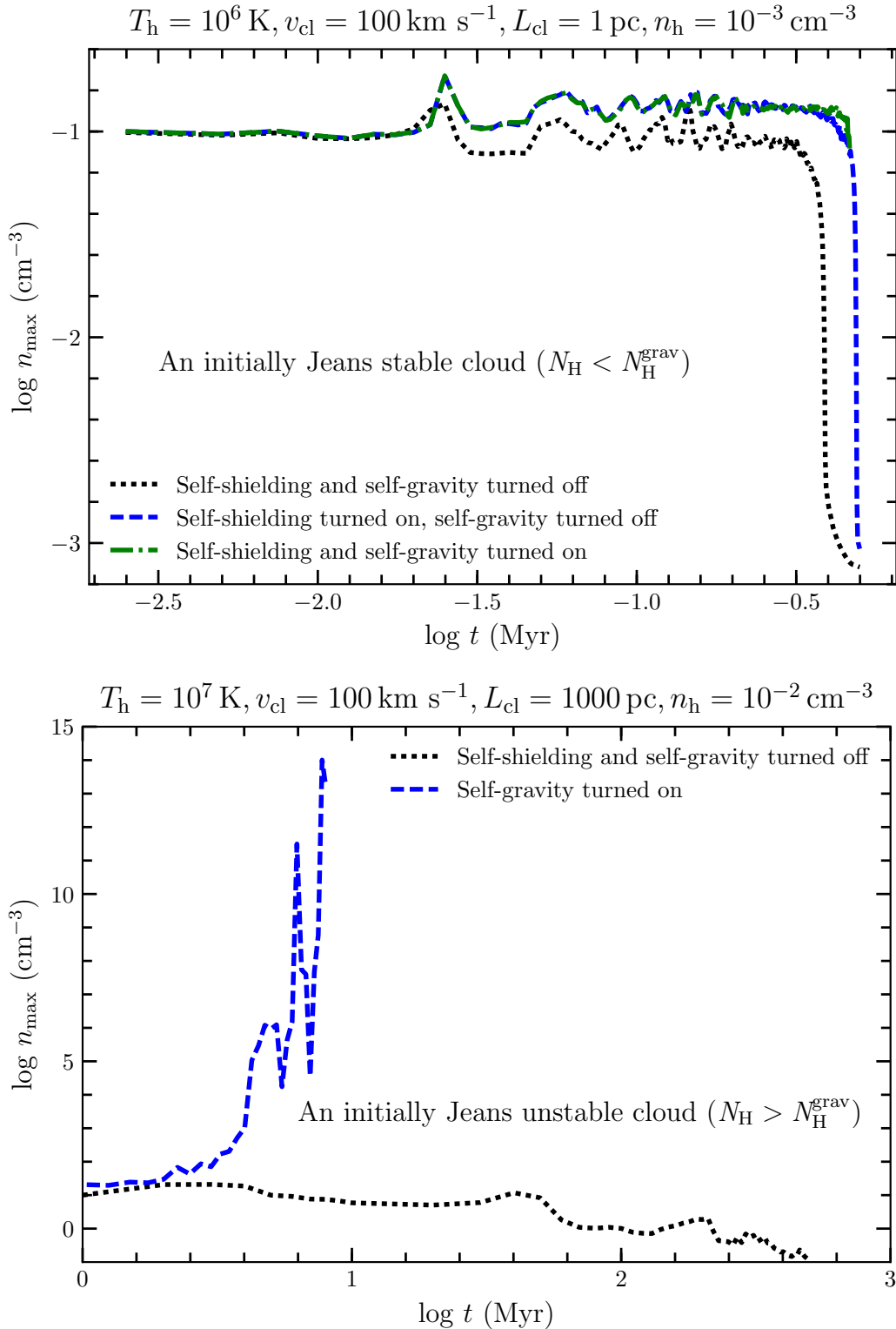


Figure 2.2: **Time evolution of the maximum density (n_{max}) in a cloud for two representative cases.** *Upper:* If $N_{\text{H}} \lesssim N_{\text{H}}^{\text{grav}}$ (Eq. 2.14), i.e., the cloud is initially Jeans-stable, then turning on or off self-gravity or self-shielding makes little difference. *Lower:* If $N_{\text{H}} \gtrsim N_{\text{H}}^{\text{grav}}$ (the cloud is initially Jeans-unstable), turning on self-gravity leads to cloud collapse (n_{max} runs away) in a free-fall time, as expected.

spond to perturbations of the cloud shape or expansion of the cloud, so the cloud will behave as if it is in an essentially pressure-free medium. This occurs when $t_{\text{cool,h}} \lesssim t_{\text{cross}} \sim R_{\text{cl}}/v_{\text{cl}}$ (or $R_{\text{cl}}/c_{\text{s,cl}}$ if $v_{\text{cl}} \lesssim c_{\text{s,cl}}$), giving:

$$N_{\text{H}} \gtrsim N_{\text{H}}^{\text{confine}} \sim 0.5 \times 10^{22} \text{ cm}^{-2} T_6^2 v_{100} \Lambda_{\text{h,-23}}^{-1} \quad (2.16)$$

where $v_{100} \equiv v_{\text{cl}}/100 \text{ km s}^{-1}$ and $\Lambda_{\text{h,x}} \equiv \Lambda(n_{\text{h}}, T_{\text{h}}, Z_{\text{h}})/10^x \text{ erg cm}^3$. For $T_{\text{h}} \gtrsim 10^6 \text{ K}$, this requires larger column densities than would already be self-gravitating or self-shielding, so this parameter regime becomes irrelevant. However, when the hot medium is cooler than $\sim 10^6 \text{ K}$, cooling becomes much more efficient, and the required N_{H} for this regime drops rapidly (to $\gtrsim 10^{18} \text{ cm}^{-2}$ at $T_{\text{h}} \sim 10^5 \text{ K}$). In the CGM, this naturally coincides with the virial temperatures below which “hot halos” that can maintain a stable virial shock and quasi-hydrostatic pressure-supported gas halo cease to exist.

In Figure 2.3 and 2.4, we confirm in our simulations that clouds with $N_{\text{H}} \gtrsim N_{\text{H}}^{\text{confine}}$ (Eq. 2.16) indeed behave as if there is negligible confining pressure. As shown in the lower right panel of Figure 2.4, they expand into the ambient, low-pressure medium, which does cause the cloud density to decrease, but ambient gas cooling/accretion also causes the cloud mass to grow, so this is clearly distinct from classical cloud “destruction”. If Eq. (2.16) is satisfied, the failure of pressure confinement occurs with or without the addition of an artificial spatially uniform heating rate Q (such that the heating+cooling rate per unit volume is $\dot{e} = Q - n^2 \Lambda$), with Q chosen so the hot gas evolved in isolation (no cold cloud) remains exactly at its initial temperature. While not surprising, this is important for application of our conclusions in the CGM, especially around dwarf galaxies, which are in the “cold mode” of accretion without “hot halos” (Kereš et al., 2009). In that regime, cold clouds from, e.g., galactic winds, may well have $N_{\text{H}} \gtrsim N_{\text{H}}^{\text{confine}}$, and thus could behave as if they are expanding into vacuum.

Clouds Grow: Accreting Ambient Hot Gas

As discussed in recent work by, e.g., Gronke et al. (2018) and Gronke et al. (2020), if clouds avoid destruction for a time longer than the cooling time of swept-up material, the front of the hot material entrained by the cloud (and mixing with the denser, cooler, cloud material) cools rapidly and effectively gets “accreted” onto the cloud. We can crudely estimate when this occurs by comparing our estimated cloud destruction time via “shredding” (in the absence of cooling), $t_{\text{life,pred}} \sim 10 t_{\text{cc}} \tilde{f}$

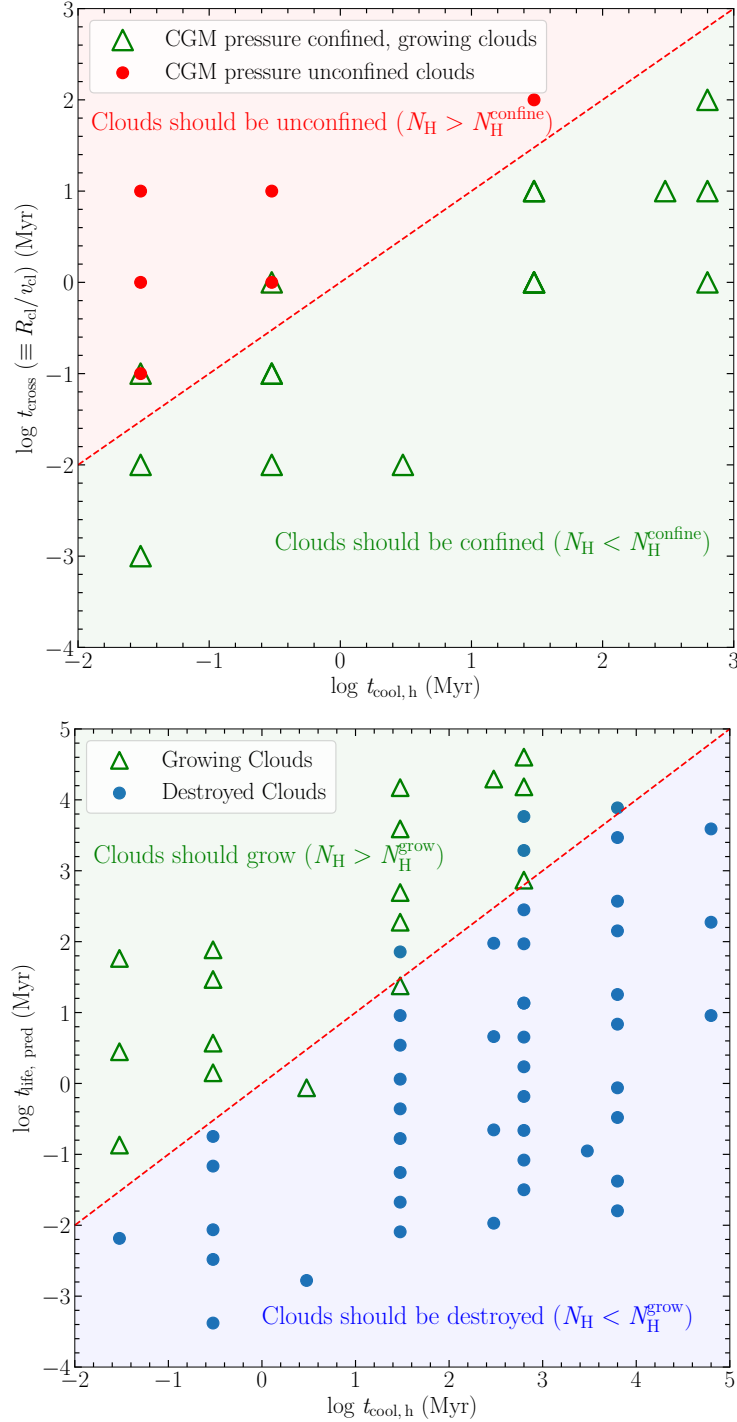


Figure 2.3: Simulation tests of the criteria for separating different cloud behaviors discussed in § 2.3 and § 2.3. *Upper:* Cooling time of ambient hot gas ($t_{\text{cool,h}}$) vs. crossing time of that gas over the cloud (t_{cross}). When cooling is faster than cloud velocity/sound crossing times, the clouds cannot be meaningfully pressure-confined and simply expand (neglecting self-gravity). The green triangles denote simulations used to check this directly, which confirm the validity of the simple analytic criteria for this behavior in Eq. (2.16). *Lower:* Same, but comparing $t_{\text{cool,h}}$ to the cloud “destruction time” in the limit where cooling is *not* important ($t_{\text{life,pred}}$, given in § 2.3, Eq. 2.19). When cooling of the hot gas in the cloud front is faster than cloud disruption, the cloud accretes and grows: simulations confirm the simple analytic criterion derived in Eq. (2.17).

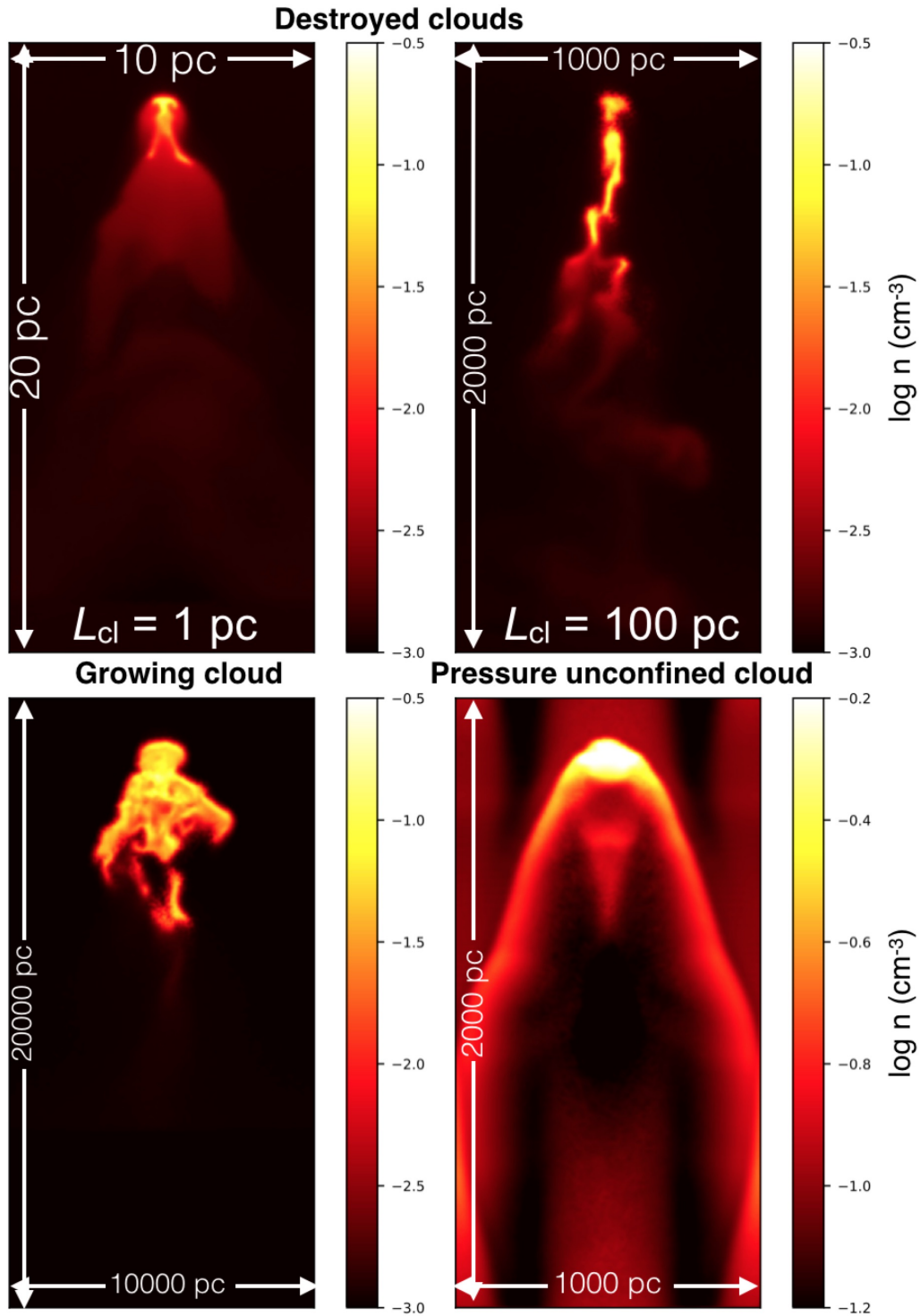


Figure 2.4: *Upper:* Sliced density maps of two clouds in the “classical cloud destruction” regime with initial conditions of $T_{\text{h}} = 10^6$ K, $v_{\text{cl}} = 100$ km s $^{-1}$, $n_{\text{h}} = 10^{-3}$ cm $^{-3}$, $L_{\text{cl}} = 1$ and 100 pc, respectively. *Lower left:* Sliced density map of a “growing” cloud ($N_{\text{H}} \gtrsim N_{\text{H}}^{\text{grow}}$, with $T_{\text{h}} = 10^6$ K, $v_{\text{cl}} = 100$ km s $^{-1}$, $n_{\text{h}} = 10^{-3}$ cm $^{-3}$, $L_{\text{cl}} = 1000$ pc). *Lower right:* Sliced density map of a “pressure unconfined” cloud ($N_{\text{H}} \gtrsim N_{\text{H}}^{\text{confine}}$, with $T_{\text{h}} = 10^5$ K, $v_{\text{cl}} = 100$ km s $^{-1}$, $n_{\text{h}} = 10^{-1}$ cm $^{-3}$, $L_{\text{cl}} = 100$ pc).

(defined in § 2.3 below) to the cooling time of the hot medium, $t_{\text{cool,h}}$. This gives:

$$N_{\text{H}} \gtrsim N_{\text{H}}^{\text{grow}} \sim 2 \times 10^{20} \text{ cm}^{-2} T_6^{3/2} v_{100} \tilde{f}^{-1} \Lambda_{\text{h},-23}^{-1} \quad (2.17)$$

(The material in the front has been heated modestly by compression and/or shocks, but also increased in density, and rapid conduction suppresses temperature variations; thus for the conditions simulated here the cooling time of the front material is order-unity similar to the cooling time in the ambient gas). For the range of parameters of interest in the CGM, this *almost always* occurs at lower N_{H} compared to the “failure of pressure confinement” above. So if a cloud “begins” life in-between ($N_{\text{H}}^{\text{grow}} \lesssim N_{\text{H}} \lesssim N_{\text{H}}^{\text{confine}}$), it will grow until it reaches that larger N_{H} threshold, at which point it will continue to “sweep up” any gas in its path, but also expand in the “backward” direction as the gas cools around it. Note that, however, if the cloud increases its N_{H} (mass) by an order-unity factor, momentum conservation requires it decelerate by a similar factor. So the cloud will slow down and stop, which in turn decreases v_{100} , making it even more above-threshold to survive. So we end up with essentially static, long-lived clouds in this limit.

Note that Gronke et al. (2020) derive a criterion for “cloud growth” that is slightly different from ours. They start from the same principle, comparing cloud lifetimes and cooling time in the mixing layer/front, but assume the cloud lifetime is t_{cc} and the cooling time of the ambient hot gas is $t_{\text{cool,h}}/\chi$ (this arises from assuming the “near-cloud” hot gas has geometric-mean temperature and density between cloud and ambient medium, and neglecting the dependence of Λ on T). Accounting for both efficient conduction and rapid “sweeping” of the hot gas past the cloud, we find that simply using $t_{\text{cool,h}}$ for the ambient gas, together with our more accurate cloud lifetime estimates, provides a more accurate and robust criterion for distinguishing between “growing” and “destroyed” cloud cases. This is especially true at high ambient temperatures ($T_{\text{h}} \gtrsim 10^6 \text{ K}$), as can be seen in the lower panel of Figure 2.3. One possible explanation is that efficient conduction heats up the gas in the front and makes it difficult for a mixing layer at intermediate temperature to exist. This effect is shown in the density maps we present in §2.3, where the cloud with conduction has sharper edges, indicating a sharper density and temperature contrast. Understanding the cause of this discrepancy in more detail will be left to future work.

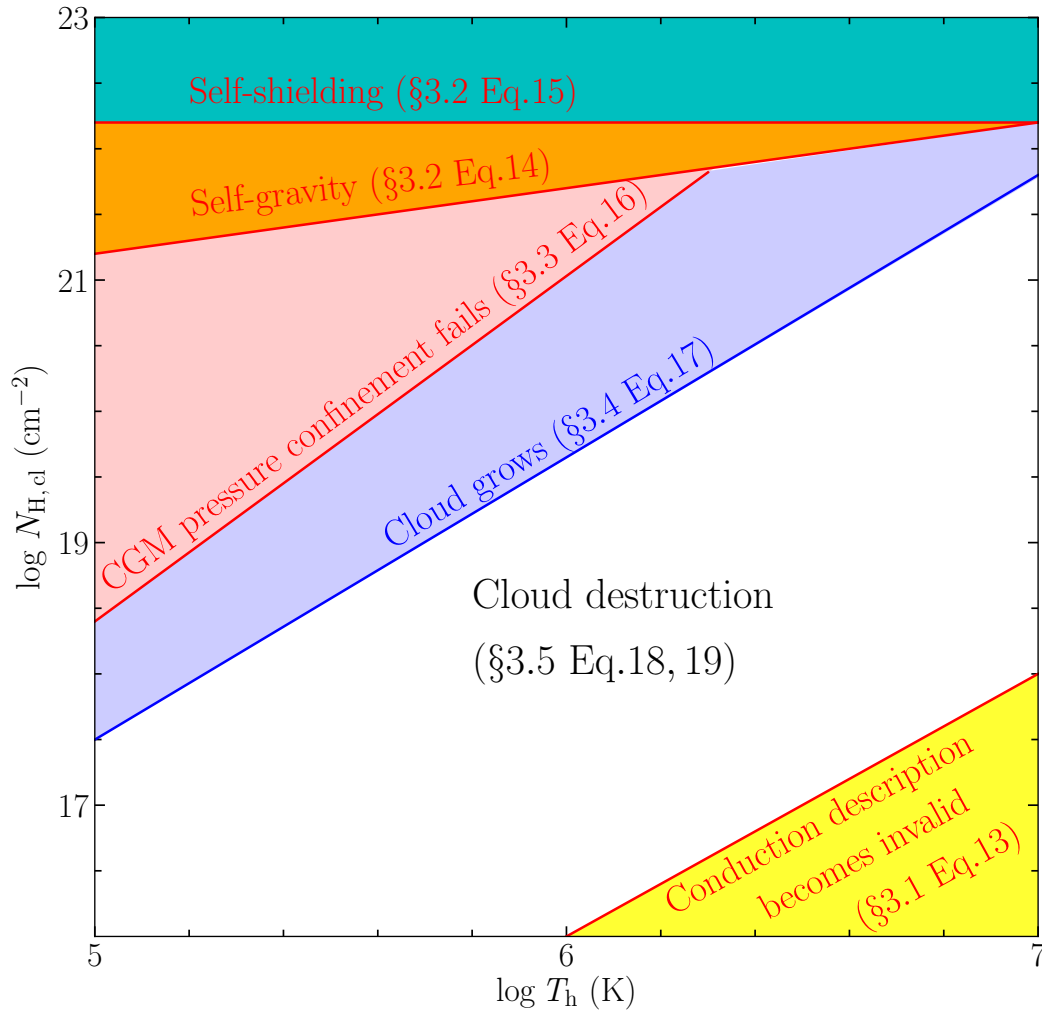


Figure 2.5: **The cloud column density ($N_{\text{H,cl}}$) vs. the temperature of the ambient medium (T_{h}).** Different regimes of dominant physics are shown: (1) The “conduction description fails” regime (§2.3, Eq. 2.13, shown in yellow); (2) The “self-shielding and self-gravity dominate” regime (§2.3, Eq. 2.14, 2.15, shown in green and orange); (3) The “CGM pressure confinement fails” regime (§2.3, Eq. 2.16, shown in pink); (4) The “cloud grows” regime (§2.3, Eq. 2.17, shown in blue); (5) The “classical cloud destruction” regime (§2.3, Eq. 2.18, shown in white). Typical values of certain parameters have been adopted ($v_{\text{cl}} = 100 \text{ km s}^{-1}$, $n_{\text{h}} = 10^{-2} \text{ cm}^{-3}$, $\tilde{f} = 1$).

In-Between: Classical Cloud “Destruction” (Shredding)

If we exclude all of the regimes above, i.e., consider only clouds with

$$N_{\text{H}}^{\text{mfp}} \ll N_{\text{H}} \ll \min \{ N_{\text{H}}^{\text{grow}}, N_{\text{H}}^{\text{confine}}, N_{\text{H}}^{\text{shield}}, N_{\text{H}}^{\text{grav}} \} \quad (2.18)$$

then we find that all the clouds we simulate are eventually destroyed/dissolved. The boundaries of this parameter space (where clouds are destroyed) are illustrated in a simple “contour” form in Figure 2.5. We find that all clouds in this regime can be at least order-of-magnitude described by traditional cloud-crushing arguments (Klein et al., 1994). This conclusion holds regardless of the specific physics included in a given simulation (e.g., conduction, or self gravity), with the classical cloud-crushing estimate $t_{\text{cc}} \sim \chi^{1/2} R_{\text{cl}}/v_{\text{cl}}$ providing a reasonable qualitative starting point to understand the actual cloud destruction times in the simulations. The majority of this section is dedicated to explaining why this is the case.

Before discussing physics, it is helpful to analyze our full simulation set to understand how the cloud lifetime varies with different parameters. Given the non-scale-free nature of the physical effects we include, there is not an obvious set of dimensionless parameters with which to fit the data, so we opt to simply use the physical parameters L_{cl} , n_{h} , T_{h} , and v_{cl} . Figure 2.6 shows that how the cloud lifetimes, normalized by classical cloud-destruction time t_{cc} , scale with each of these four parameters. We perform a multi-variable log-linear fitting to these four parameters, and find that predicted lifetime scales as approximately,

$$t_{\text{life,pred}} \approx 10 t_{\text{cc}} \tilde{f} \quad (2.19)$$

$$\tilde{f} \equiv (0.9 \pm 0.1) L_1^{0.3} n_{0.01}^{0.3} T_6^{0.0} v_{100}^{0.6}$$

where $L_1 \equiv L_{\text{cl}}/1 \text{ pc}$ and $n_{0.01} \equiv n_{\text{h}}/0.01 \text{ cm}^{-3}$. The $1\text{-}\sigma$ values of the power-law dependences on $[L_{\text{cl}}, n_{\text{h}}, T_{\text{h}}, v_{\text{cl}}]$ are $[0.3 \pm 0.1, 0.3 \pm 0.1, 0.0 \pm 0.1, 0.6 \pm 0.1]$. This fit is plotted in Figure 2.7. For clouds with $v_{\text{h}} > 10 \text{ km s}^{-1}$, and for clouds in a cooler ambient medium with $T_{\text{h}} = 10^5 \text{ K}$, the dependence of $t_{\text{life,pred}}/t_{\text{cc}}$ on v_{h} is much weaker. This is discussed further in §2.3 below.

Given the complex and non-scale-free physics involved in our default simulations, the fit (Eq. 2.19) is remarkably universal. In particular, it is rather surprising that by simply assuming a separable power law in each variable, we have almost directly reproduced the classical cloud-crushing time, aside from the small correction factor \tilde{f} . We now discuss the reason for this universality by discussing in turn the effects that different physics have on the cloud-crushing process. These effects are shown

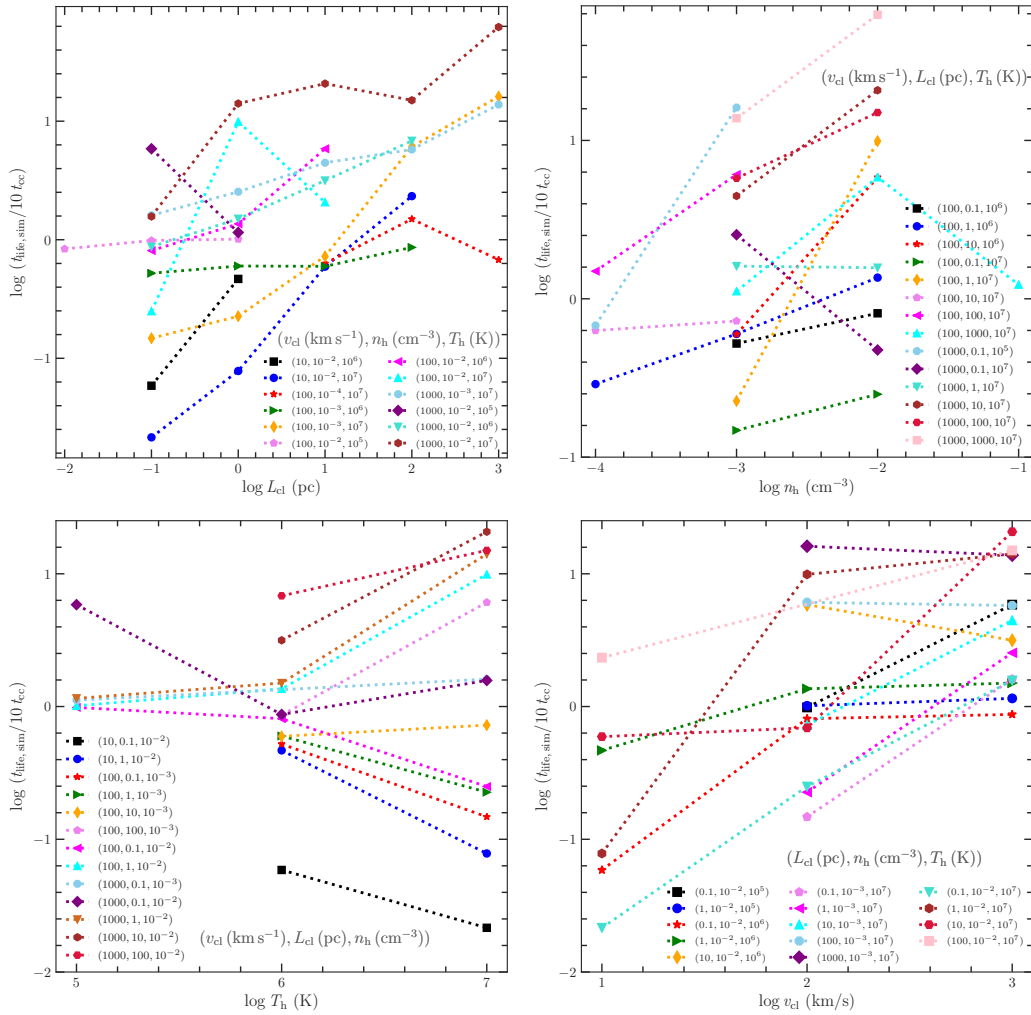


Figure 2.6: **Simulated cloud “lifetimes”, $t_{\text{lfe,sim}}$ (in units of ten cloud-crushing time, $10 t_{\text{cc}}$) vs. different initial conditions: cloud size L_{cl} , ambient density n_{h} , ambient temperature T_{h} and cloud velocity v_{cl} .** Dotted lines connect simulations that have one varying parameter but otherwise identical initial conditions. In units of t_{cc} , the cloud lifetime has a weak dependence on T_{h} , modestly increases with L_{cl} and n_{h} (i.e., cloud N_{H}), and a slightly stronger dependence on v_{cl} . These dependencies are captured in the scaling of $t_{\text{lfe,pred}}$ with \tilde{f} in Eq. 2.19. Note that we factor out t_{cc} because it is the dominant effect here: our most extreme cases differ by factors of $\sim 10^8$ in their absolute lifetimes or values of t_{cc} (see, e.g., Figure 2.3); the “residuals” here, while still large (~ 1 dex), are much smaller.

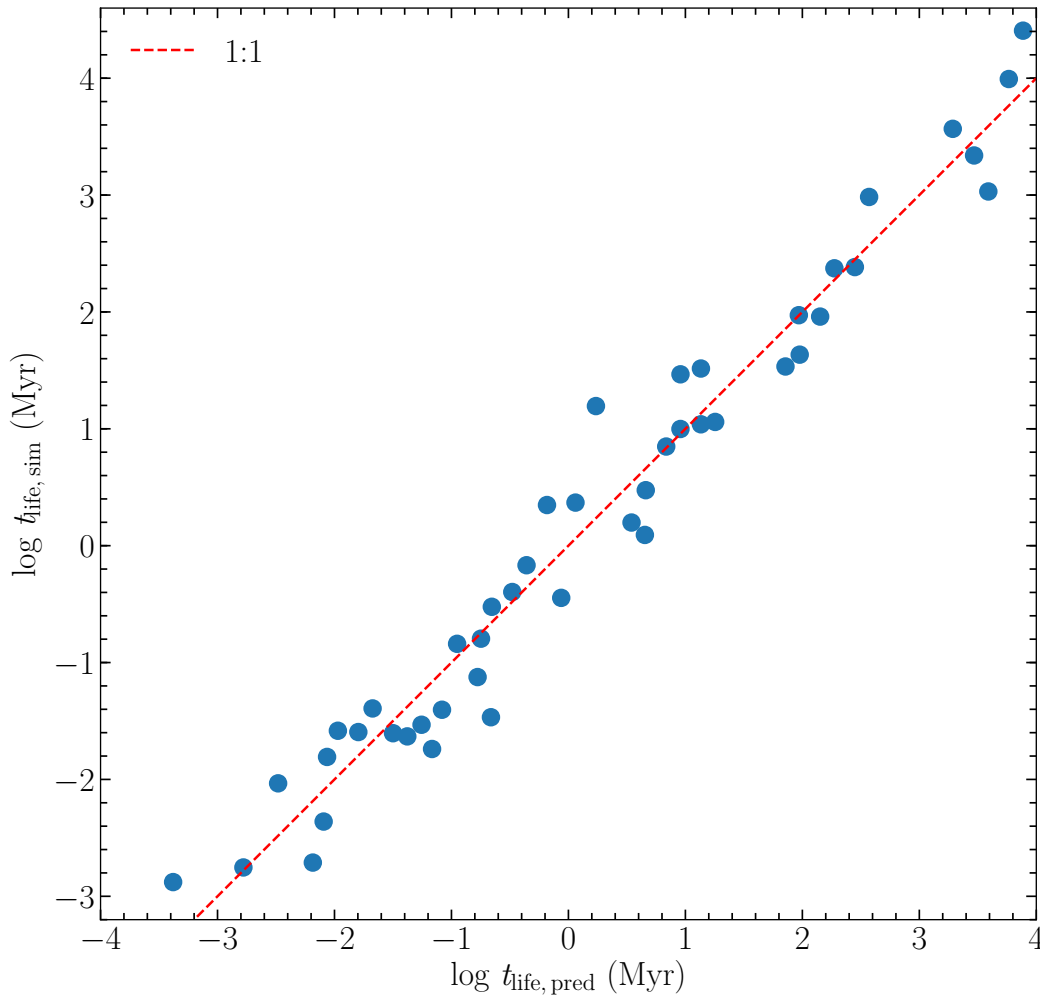


Figure 2.7: **Cloud lifetimes measured in simulations ($t_{\text{life,sim}}$) vs. the “predicted” lifetimes ($t_{\text{life,pred}}$) from a simple multi-variable power-law fit to t_{life} vs. L_{cl} , n_{h} , T_{h} , and v_{cl} , given in Eq. (2.19).** Given a dynamic range $\sim 10^8$ in absolute cloud lifetimes, the simulations can be remarkably well-fit by a power law of the form $t_{\text{life,pred}} \approx 10 t_{\text{cc}} \tilde{f}$ with $\tilde{f} \sim L_1^{0.3} n_{0.01}^{0.3} v_{100}^{0.6}$ (so \tilde{f} encompasses all deviations from the cloud-crushing scaling).

graphically in Figure 2.8, showing a cloud in the process of being crushed, as we successively add physics to the pure hydrodynamical simulation (far left) in the form of (from left to right) cooling, magnetic fields, conduction, viscosity, self-shielding, and self-gravity.

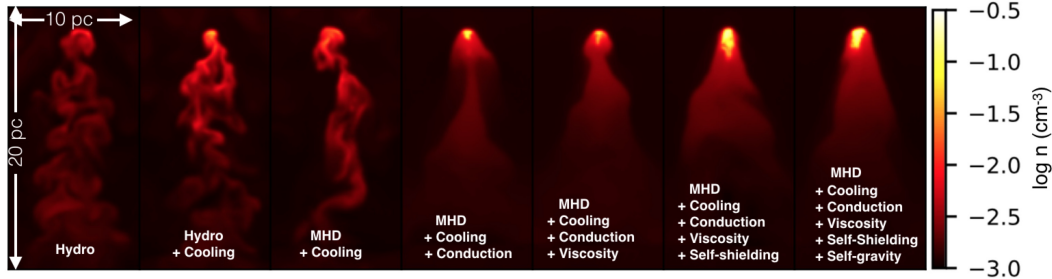


Figure 2.8: **Sliced density maps for a cloud in the “classical cloud destruction” regime** ($T_h = 10^6$ K, $v_{cl} = 100$ km s $^{-1}$, $n_h = 10^{-3}$ cm $^{-3}$, $L_{cl} = 1$ pc), with each panel from left to right showing a simulation that includes additional physical effects (at the same physical time, 0.3 Myr). From left to right we show: Hydro = ideal hydrodynamics; Hydro + Cooling = ideal hydrodynamics + radiative cooling, etc. Our default physics set is MHD + Cooling + Conduction + Viscosity. The cloud mass evolution curves for the same set of simulations are shown in Figure 2.9.

Effect of Radiative Cooling

Radiative cooling has a modestly significant effect on cloud lifetime, as discussed in previous works (see, e.g., Section 5.3 of Klein et al. 1994). The basic effect of cooling on gas is to soften its equation of state (lower γ), which effectively renders the cloud more compressible (Scannapieco et al., 2015). This makes the cloud more strongly crushed in the direction transverse to the flow, forming a thinner, denser filament with a smaller cross section. Although KH instabilities can grow more violently on this thinner cloud than for an adiabatic cloud because it moves faster with respect to the hot medium (due to its smaller drag), the net effect is for the cloud to survive modestly longer than an equivalent cloud with no cooling due to its higher density. This behavior is nicely illustrated by the comparison of the black and blue curves in Figure 2.9. Moreover, as shown in the left two panels of Figure 2.8, cooling can also enhance the formation of smaller, denser cloudlets in the wake (McCourt et al., 2018). This effect, however, can be suppressed by magnetic fields (Figure 2.8, see also Grønnow et al. 2018). Detailed analyses of the cloudlet properties have been carried out in several recent works (e.g., Sparre et al. 2019).

Effect of Magnetic Fields

Magnetic fields can modify cloud destruction in two qualitatively distinct ways: (1) dynamically (via magnetic pressure or tension), or (2) by suppressing conduc-

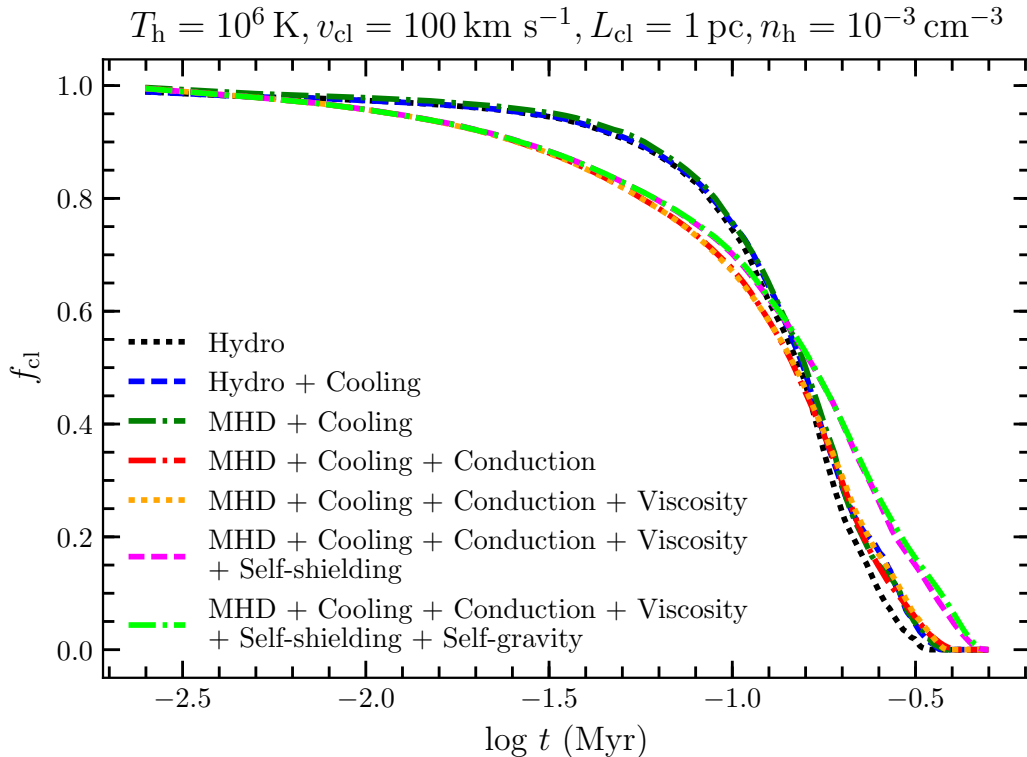


Figure 2.9: **Evolution of the normalized cloud mass, f_{cl} (defined in Figure 2.1) vs. time, for the simulations shown in Figure 2.8 ($T_h = 10^6 \text{ K}$, $v_{\text{cl}} = 100 \text{ km s}^{-1}$, $n_h = 10^{-3} \text{ cm}^{-3}$, $L_{\text{cl}} = 1 \text{ pc}$) with different physics included (labeled as in Figure 2.8).** The cloud mass vs. time is remarkably similar across these runs, given the different physics and morphologies in Figure 2.8.

tion/viscosity.

Regarding (1), the magnetized “cloud-crushing” problem without cooling, conduction, or viscosity is well-studied (see Mac Low et al., 1994; Jones et al., 1996; Shin et al., 2008, and references therein); for very strong fields within or surrounding the cloud such that magnetic pressure is comparable to ram pressure (i.e., $P_B \gtrsim P_{\text{ram}} \sim \rho v_{\text{cl}}^2$, or $\beta \lesssim \mathcal{M}_h^{-2}$), cloud destruction is strongly suppressed. While $\beta \lesssim 1$ is common in very cold (e.g., molecular) gas in the ISM, in the warm and hot CGM realistic estimates of β range from $\sim 10^2 - 10^9$ (see Su et al., 2017; Martin-Alvarez et al., 2018; Hopkins et al., 2019), viz., the direct dynamical effects of the fields are negligible. Alternatively, it has been proposed that a strong field could build up via “magnetic draping” (Markevitch et al., 2007), wherein the cloud “sweeps up” field lines oriented perpendicular to \mathbf{v}_{cl} , compressing the field lead-

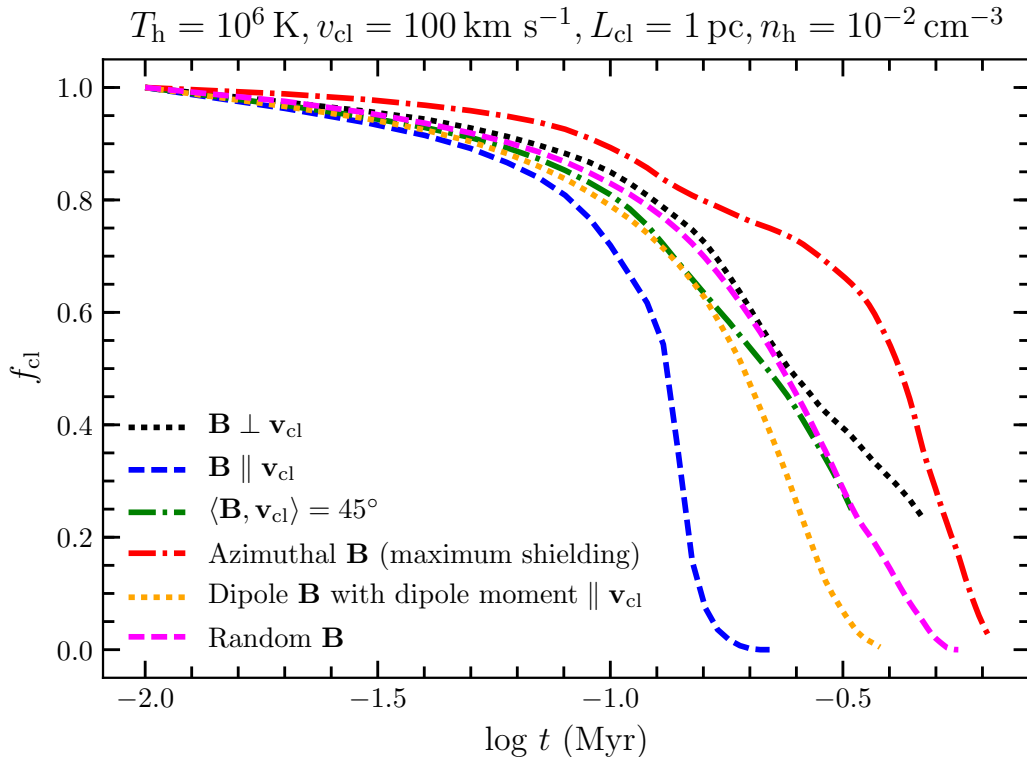


Figure 2.10: **Evolution of the normalized cloud mass, f_{cl} (defined in Figure 2.1) vs. time, for otherwise identical initial conditions ($T_h = 10^6 \text{ K}$, $v_{\text{cl}} = 100 \text{ km s}^{-1}$, $n_h = 10^{-2} \text{ cm}^{-3}$, $L_{\text{cl}} = 1 \text{ pc}$) with different magnetic field configurations.** We can see that when the magnetic field is aligned with the relative velocity ($\mathbf{B} \parallel \mathbf{v}_{\text{cl}}$), the cloud mass decreases most rapidly. For the azimuthal configuration (looped magnetic fields inside the cloud plus $\mathbf{B} \perp \mathbf{v}_{\text{cl}}$ outside the cloud, which produces maximal shielding to conduction), the cloud mass decreases most slowly. In all other cases, the magnetic field configuration does not have a large effect on the mass evolution: the lifetimes are identical to within a factor of < 2 .

ing the cloud and increasing $|\mathbf{B}|$. Miniati et al. (1999) define the “draping time,¹⁰” which we can turn into the equivalent length:

$$L_{\text{drape}} \sim \frac{\pi R_{\text{cl}} \chi^{2/3}}{50} \left(\frac{P_{\text{ram}} + P_{\text{therm}}}{P_{\text{B}}} \right)^{2/3} \approx 3 \text{ kpc } R_{\text{pc}} (\beta_{1000} T_6 v_{100}^2)^{2/3} \quad (2.20)$$

L_{drape} is the path length that a cloud must travel for the accumulated field to appreciably alter its destruction (assuming $P_{\text{therm}} \ll P_{\text{ram}}$ for supersonic clouds). However, L_{drape} is much longer than the length scale over which clouds are destroyed,

¹⁰We emphasize that the context in which draping was originally proposed referred to much larger structures, namely “bubbles” and jets emanating from AGN in the CGM of massive halos/clusters, which have physical size scales $\sim 10 - 100 \text{ kpc}$ and travel $\gtrsim 100 \text{ kpc}$, vastly different from what we model here.

$L_{cc} \approx t_{cc} v_{cl} \approx 9 \text{ pc } R_{pc} v_{100} \mathcal{M}_{cl}^{-1}$. In other words, CGM magnetic fields are nowhere near sufficiently strong to dynamically suppress cloud destruction. This can be seen visually by comparing the second and third panels of Figure 2.8 (or the relevant lines in Figure 2.9), which shows how MHD and hydrodynamic simulations remain very similar without the effects of conduction. We have also confirmed this conclusion by re-running a subset of our simulations with plasma β multiplied or divided by a factor of ~ 1000 , which makes no difference to the measured lifetimes (as expected, since they remain in the weak-field limit).

However, regarding (2), even a very weak field is sufficient to suppress perpendicular conduction, viscosity (typically the perpendicular transport coefficients are suppressed by $\sim \lambda_{e,\text{gyro}}/\lambda_{e,h} \sim 10^{-8}$) and hydrodynamic instabilities (Dursi et al., 2008; Banda-Barragán et al., 2016; Banda-Barragán et al., 2018). In this case the field *geometry* is what matters, while the field strength is irrelevant. In Figure 2.10, we therefore explore a series of simulations of one of our typical cloud-destruction cases, varying the initial field geometry. In general, the magnetic field configuration does not have a strong effect on the evolution of cloud mass. This is not surprising, as draping can rearrange the geometry of the magnetic field around the cloud to similar configurations and yield similar amount of suppression of conduction, viscosity and instabilities, regardless of the initial field geometry (note that the arguments of §2.3 below suggest that conduction plays only a secondary role anyway). However, in several extreme cases, such as when the magnetic field is aligned with the relative velocity ($\mathbf{B} \parallel \mathbf{v}_{cl}$), we do see a more rapid decrease in the cloud mass as there is essentially no draping. In contrast, with an azimuthal field configuration (looped magnetic fields inside the cloud plus $\mathbf{B} \perp \mathbf{v}_{cl}$ outside the cloud), the cloud mass decreases most slowly, indicating that the field can shield the cloud particularly efficiently in this case¹¹(see also Li et al. 2013; Banda-Barragán et al. 2016; Grønnow et al. 2017).

Effect of Conduction

The influence of conduction on isolated, undisturbed clouds (i.e., those without an impinging wind) has been studied by Cowie et al. (1977), McKee et al. (1977), and Balbus et al. (1982). For the range of temperatures relevant to our study ($10^5 \text{ K} \lesssim$

¹¹Note that in the “cloud growing” regime, transverse magnetic fields can shield the cloud via draping, reduce both mixing and warm gas mass loading and prevent condensation (see Grønnow et al. 2018). Also note that self-contained magnetic fields can enhance clumping and reduce cloud destruction (Li et al., 2013; McCourt et al., 2015; Banda-Barragán et al., 2018). We defer a detailed study of these effects to future work.

$T_h \lesssim 10^7$ K) the conclusion of these papers is that cloud evaporation/condensation is controlled by the saturation parameter¹²

$$\sigma_0 \approx 3.2 \frac{\lambda_{e,h}}{R_{cl}} \approx 0.4 \frac{T_6^3}{\langle n_{cl} \rangle R_{pc}} \approx T_6^3 \left(\frac{N_H}{1.2 \times 10^{18} \text{ cm}^{-2}} \right)^{-1} \quad (2.21)$$

For small values of $\sigma_0 \lesssim 0.01$ (large clouds), the cooling of the hot material onto the cloud is sufficiently rapid that the cloud condenses. The necessary size of such clouds ($N_H \gtrsim 1.2 \times 10^{20} T_6^3 \text{ cm}^{-2}$) corresponds, within an order of magnitude, to the “growing-cloud” regimes discussed in §2.3 (the cloud sizes required for growth in the crushed problem are slightly larger, which intuitively makes sense given they are being actively ripped apart by the wind). On the other side, large values of $\sigma_0 \gtrsim \chi$ correspond to the smallest clouds discussed in §2.3, which are immediately evaporated by hot electrons penetrating throughout the entire cloud (Balbus et al., 1982). Thus, effectively all of our clouds in the “classical cloud destruction” regime lie in the range $0.01 \lesssim \sigma_0 \lesssim \chi$, which, in the absence of the hot wind would slowly evaporate into the ambient medium. As shown by McKee et al. (1977), the conductive heat flux that evaporates the cloud is in the unsaturated regime for clouds with $\sigma_0 \lesssim 1$, while the heat flux is saturated for $\sigma_0 \gtrsim 1$.

To make further progress, let us compare the cloud evaporation timescale to the cloud-crushing time. In the $\sigma_0 \lesssim 1$ regime, Cowie et al. (1977) compute the mass-loss rate by solving the hydrodynamic equations in spherical geometry, deriving the evaporation time of the cloud as (setting $\ln \Lambda_D = 30$)

$$t_{\text{evap}} \approx 30 \text{ Myr} n_{0.01} R_{pc}^2 T_6^{-5/2} \quad (2.22)$$

In the $\sigma_0 \gtrsim 1$ regime, where the heat flux is saturated, one can derive the evaporation time by comparing the rate at which energy is transferred to the cold cloud due to the saturated heat flux,

$$\dot{E} = 4\pi R_{cl}^2 q_{\text{sat}} \approx 4\pi \alpha R_{cl}^2 n_h c_{s,e,h} k_B T_h \quad (2.23)$$

(here $\alpha \approx 0.3$ is chosen to match Eq. 2.9), to the total energy required to evaporate the cloud by heating it up to the hot-medium temperature,

$$E \approx \frac{4}{3} \pi R_{cl}^3 n_{cl} k_B T_h \quad (2.24)$$

¹²We define σ_0 to match the numerical value given of σ_0 in McKee et al. (1977), which leads to a slightly different definition in terms of $\lambda_{e,h}/R_{cl}$ compared to Cowie et al. (1977) because of a different definition of $\lambda_{e,h}$.

(A more complicated approach in Cowie et al. (1977) gives a similar estimate; see their Eq. 64). Because the heat flux is effectively given by the minimum of the unsaturated and saturated values (see Eq. 2.9), the time for the cloud to evaporate is the maximum of the unsaturated and saturated estimates, or

$$\frac{t_{\text{evap}}}{t_{\text{cc}}} \approx \max \left\{ 2\mathcal{M}_h n_{\text{cl}} L_{\text{pc}} T_6^{-5/2}, 0.3\mathcal{M}_h T_6^{1/2} \right\} \quad (2.25)$$

Note that the saturated (right-hand) expression is simply $\approx v_{\text{cl}}/(300 \text{ km s}^{-1})$.

We see that across the range of parameters surveyed, $t_{\text{evap}}/t_{\text{cc}}$ ranges from much larger than 1 for large clouds in fast winds, to somewhat less than 1 for smaller clouds. What will be the effect of this evaporation on the cloud-crushing process? For $t_{\text{evap}}/t_{\text{cc}} \ll 1$ we expect the cloud to behave effectively as it would in the absence of a wind, evaporating rapidly into the hot medium. On the other hand, when $t_{\text{evap}}/t_{\text{cc}} \gtrsim 1$ the evaporation has only a minor effect on the cloud lifetime, because it is crushed by the wind before the heat flux has much of an effect (the static approach of Cowie et al. 1977 also becomes highly questionable in such a strongly perturbed cloud). There does, however, seem to be a reasonably significant effect on the cloud morphology, which is evident in the change between the third and fourth panels of Figure 2.8 (see also Brüggem et al. 2016). This type of behavior, which occurs at $t_{\text{evap}}/t_{\text{cc}} \sim 1$, seems to be related to the fast creation of a conductive boundary layer, which causes an inwards pressure on the cloud due to the outflow of hot material from its outer edges. This compresses the cloud and increases its density, which sometimes has the effect of modestly increasing the cloud lifetime. Indeed, if we make the gross approximation that the mass is lost from the cloud with an outflow velocity that is approximately the ion sound speed (since the ions will be heated by the impinging hot electrons to approximately T_h), one finds that the ratio of the inwards pressure due to the outflow ($P_{\text{evap}} \approx \dot{m} v_{\text{out}}/(4\pi R^2) \approx m v_{\text{out}}/(4\pi R^2 t_{\text{evap}})$) to the thermal pressure of the cloud (P_{cl}) is approximately

$$\frac{P_{\text{evap}}}{P_{\text{cl}}} \approx \min \left\{ 2 \frac{T_6^3}{n_{\text{cl}} R_{\text{pc}}}, 10 \right\} \quad (2.26)$$

where the left-hand expression is that of the unsaturated ($\sigma_0 \lesssim 1$) regime, and the right-hand expression is that of the saturated ($\sigma_0 \gtrsim 1$) regime. We thus see that for smaller clouds, the pressure from evaporative outflow is modestly large compared to that of the cloud, and should thus be able to cause some compression, as seen in Figure 2.8.

The broad ideas of the previous paragraphs are confirmed in Figure 2.11, which plots $t_{\text{lif}}/t_{\text{cc}}$ vs. σ_0 for our full suite of simulations, with each point colored by

$t_{\text{evap}}/t_{\text{cc}}$ from Eq. 2.25. We see that, as expected, only those simulations with $t_{\text{evap}}/t_{\text{cc}} \ll 1$ are destroyed significantly faster than t_{cc} (these are all low-velocity clouds). The lifetime of simulations with $t_{\text{evap}}/t_{\text{cc}} \gtrsim 1$ is mostly independent of σ_0 , aside from a possible slight increase in lifetime for $\sigma_0 \gtrsim 1$, which may be indicative of cloud compression due to the evaporative outflow. Finally, we note that this general framework explains our measured empirical scaling of $t_{\text{life}}/t_{\text{cc}}$ with a positive power of v_{cl} (see Eq. 2.19), because the lowest velocity clouds are quickly destroyed by saturated conduction, i.e., their $t_{\text{life}} \sim t_{\text{evap}} \propto t_{\text{cc}} v_{\text{cl}}$ (Eq. 2.25), while those with higher velocities can live somewhat longer than t_{cc} due to the evaporative compression to higher densities. Meanwhile, for, e.g., $T_{\text{h}} = 10^5 \text{K}$, all clouds fall into the $\sigma_0 \lesssim 1$ regime (see Eq. 2.21), where $t_{\text{evap}}/t_{\text{cc}} > 1$ and the evaporative pressure (Eq. 2.26) is unimportant, so we simply obtain $t_{\text{life}} \propto t_{\text{cc}}$.

Effect of Viscosity

The effect of viscosity is in general sub-dominant to conduction. This is not surprising because conduction is controlled by the thermal velocity of hot electrons, while viscosity is controlled by the thermal velocity of ions, and the ratio of these thermal velocities (and thus the strength of conductivity and viscosity) is $(m_i/m_e)^{1/2} \sim 40$, assuming each has the same temperature. Nonetheless, viscosity does provide some non-zero insulating effects as a viscous “boundary layer” that forms around the cloud, which drags the co-moving boundary layer and can slightly increase the cloud lifetime for some clouds. This minor effect can be seen through the comparison of the fourth and fifth panels in Figure 2.8.

Effect of Turbulence in the Cloud or Ambient Medium

Some historical studies have argued that clouds which have initial “turbulence” (large density and velocity fluctuations) like GMCs in the ISM (e.g., Schneider et al., 2015, and references therein) might be much more rapidly disrupted. However, most of these studies have considered clouds with large internal turbulent Mach numbers $\mathcal{M}_{\text{cl}}^{\text{turb}} \equiv |\delta \mathbf{v}_{\text{turb}}|/c_{s,\text{cl}} \sim 10 - 100$, akin to GMCs (see § 2.1), e.g., Schneider et al. (2015) consider an internal 3D Mach number $\mathcal{M}_{\text{cl}}^{\text{turb}} \sim 9$ (or equivalently, 1D Mach number $\mathcal{M}_{\text{cl}}^{\text{turb}} \sim 5$), which produces nearly ~ 1 dex initial rms density fluctuations.

However, for realistic turbulent Mach numbers in the CGM, turbulence should produce much weaker effects. This is because the initial cloud temperature is 10^4K

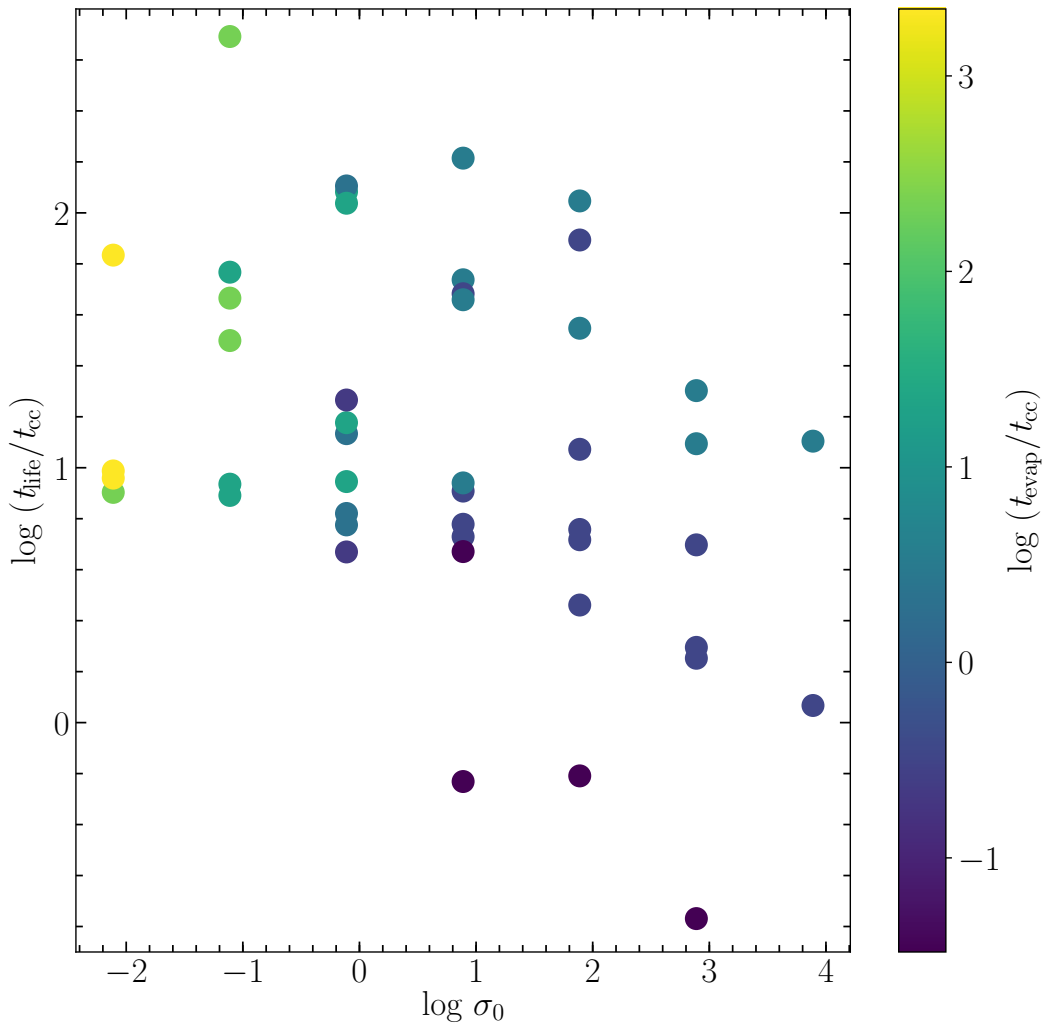


Figure 2.11: **The simulated cloud lifetimes in units of the cloud-crushing time, $t_{\text{life}}/t_{\text{cc}}$, vs. the saturation parameter, σ_0 (Eq. 2.21 in § 2.3, which quantifies the strength of conduction) for clouds in the “classical destruction” regime.** The simulations are color-coded from light yellow to dark blue with decreasing $t_{\text{evap}}/t_{\text{cc}}$, where t_{evap} is the cloud evaporation time for a non-moving cloud in a conducting medium (Eq. 2.25). Simulations with $t_{\text{evap}} \ll t_{\text{cc}}$ are evaporated before cloud-crushing, explaining why $t_{\text{life}} \ll t_{\text{cc}}$. These clouds almost exclusively have $\sigma_0 \gg 1$, i.e., are in the regime of saturated conduction, where $t_{\text{evap}} \propto t_{\text{cc}} \nu_{\text{cl}}$, explaining the strong dependence of \tilde{f} on ν_{cl} . While for simulations with $t_{\text{evap}} \gg t_{\text{cc}}$, clouds are only weakly influenced by conduction, and therefore $t_{\text{life}} \propto t_{\text{cc}}$.

($c_{s,cl} = 10 \text{ km s}^{-1}$), as compared to $\sim 10\text{K}$ in GMCs, and the density and temperature fluctuations only become very large for large turbulent Mach numbers ($\mathcal{M}_{cl}^{\text{turb}} \gg 1$), which are highly unrealistic in the CGM (e.g., clouds do not have internal velocity dispersions of $\sim 100\text{km s}^{-1}$). The turbulent Mach numbers should be even lower in the hot medium. Moreover, $\mathcal{M}_{cl}^{\text{turb}} \gg 1$ is not a self-consistent “cloud” under the conditions we consider, because it necessarily implies a turbulent ram pressure much larger than the confining gas pressure (the “cloud” would simply fly apart as soon as the simulation begins): in GMCs this is resolved by confinement via self-gravity, but we have already excluded this regime.

We therefore have considered a subset of simulations using initial conditions drawn from driven periodic box simulations of turbulence (taken from Colbrook et al., 2017), for the cloud itself, the ambient hot medium, or both, with Mach numbers in each medium of $\sim 0.1, 0.5, 1$. Not surprisingly, these have little effect on the supersonic cloud-crushing process (consistent with Banda-Barragán et al. 2018; Banda-Barragán et al. 2019). For example, for $\mathcal{M}_{cl} \sim 0.1$, the initial density and pressure fluctuations are only of the order of $\sim 1\%$, much smaller than those introduced almost immediately by the cloud-wind interaction. We therefore do not discuss these cases in more detail.

2.4 Conclusions

In this paper, we have systematically explored the survival of cool clouds traveling through hot gas – the so-called “cloud crushing” problem – for parameters relevant to the CGM. We present a comprehensive parameter survey, with cloud diameters from $\sim 0.01 - 1000\text{pc}$, relative velocities $\sim 10 - 1000\text{km s}^{-1}$, ambient temperatures $\sim 10^5 - 10^7\text{K}$ and ambient densities $\sim 10^{-4} - 10^{-1}\text{cm}^{-3}$. We study the effects of a range of physics, including radiative cooling, anisotropic conduction and viscosity, magnetic fields, self-shielding and self-gravity. We identify several unique regimes, which give rise to qualitatively different behaviors, including collapse, growth, expansion, shredding, and evaporation. For mid-sized clouds, those in the “classical cloud destruction” regime, we also quantify the cloud lifetime as a function of parameters across the broad range of initial conditions. We reach a number of important conclusions, including:

1. Clouds which are *initially* self-gravitating/J Jeans-unstable, or self-shielding to molecular/low-temperature metal-line fine-structure cooling and thus able to cool to temperatures $T \ll 1000\text{K}$, will fragment and form stars before they

are disrupted. For clouds that are initially Jeans-stable and non-shielding, these effects can be neglected. This transition occurs when the cloud exceeds large, DLA-like column densities (Eq. 2.14, 2.15).

2. In an ambient medium where the “diffuse” gas cooling time is shorter than the time for diffuse gas to cross the cloud ($\sim R_{\text{cl}}/v_{\text{cl}}$), pressure-confinement of the cloud cannot effectively operate and the cloud-crushing problem is ill-posed. In hotter medium ($T_{\text{h}} \gtrsim 10^6 \text{ K}$) this only occurs at high enough column densities such that the cloud would already be self-gravitating; while in cooler ambient halos ($T_{\text{h}} < 10^6 \text{ K}$), which are generally not able to sustain a “hot halo” in quasi-hydrostatic equilibrium, even clouds with more modest column densities $N_{\text{H}} \gtrsim 10^{18} \text{ cm}^{-2}$ can reach this regime (see Eq. 2.16).
3. If the expected destruction time of a cloud through shocks and fluid mixing (cloud crushing) is longer than the cooling time of the swept-up material in the shock front leading the cloud, the cloud can grow in time, rather than disrupt (Gronke et al., 2018). The cooling of the shock front material adds to the cloud mass (with the growth time simply being the timescale to “sweep up” new mass), faster than instabilities can disrupt the cloud, and the cloud acts more like a seed for the thermal instability. This can occur at column densities well below the self-gravity/shielding/ambient medium rapid cooling thresholds above (see Eq. 2.17).
4. If we restrict to clouds *below* the sizes/column densities of the above thresholds, and *above* the size/column density where they become smaller than the penetration length of hot electrons into the cloud ($N_{\text{H}} \gtrsim 10^{16} \text{ cm}^{-2} T_6^2$; Eq. 2.13), then we find that the clouds are indeed disrupted and mixed by a combination of instabilities, shocks, and conduction. Remarkably, the cloud lifetimes can be well fit by a single power law similar to the classical “cloud-crushing” scaling for the pure hydrodynamic problem, albeit with a larger normalization and a secondary dependence on the ambient temperature and velocity, which is introduced by the combination of cooling and conduction. We develop simple analytic scalings to understand how this modification to the scaling arises.
5. Braginskii viscosity, turbulent density/velocity fluctuations in the cloud, and magnetic field geometry and strength have relatively weak effects on cloud lifetimes and do not qualitatively alter our conclusions. Viscous effects tend

to be sub-dominant to conduction because of the relative scaling of ion and electron mean-free-paths in the CGM (although we caution that our model assumes equal ion and electron temperatures). Turbulent effects are weak for realistic initial cloud turbulence, because CGM clouds, unlike GMCs in the ISM, cannot be highly supersonic (this would require *internal* turbulent Mach numbers in the cloud $\gg 1$). This implies that the initial density fluctuations in the cloud are quite small. Magnetic field strength has little effect because the CGM plasma has $\beta \gg 1$ (i.e., magnetic pressure is much weaker than thermal pressure, which is yet smaller than the ram pressure) and the distance clouds would have to travel to acquire dynamically important fields via “draping” is much longer than the length over which they are destroyed. Field geometry has some effect, by suppressing thermal conduction in the directions perpendicular to the field. However, we show the net effect of the field geometry is minor for most plausible geometries ($\sim 10\%$ in t_{life}) and even the most extreme favorable/unfavorable field geometries produce only a factor of ~ 2 systematic change in cloud lifetimes.

We caution that there are still a number of caveats to this study. There remain a number of simplifications in the physics included in our model (Eqs. 2.2–2.7), which may be important for some regimes. The most important of these is likely the assumption of equal electron and ion temperatures, even in the presence of strong conduction and cooling on scales approaching the electron mean free path. Indeed, because the timescale for ions to collisionally equilibrate with electrons is $\sim m_i/m_e$ times the electron-electron collision timescale, regions with large (saturated) electron heat fluxes may also have $T_e \gg T_i$ or $T_i \gg T_e$. Unfortunately, tackling this issue in detail is difficult and computationally demanding even in simplified setups (see, e.g., Kawazura et al., 2019), and is well beyond current computational capabilities for a highly inhomogeneous problem such as cloud crushing. On fluid scales, there are also significant uncertainties that arise from our basic numerical setup, which we have intentionally restricted to be rather idealized. Potential complications that might be relevant and interesting to study in future work include lack of pressure equilibrium in the cool gas (as could arise from, e.g., supersonic turbulence, Banda-Barragán et al. 2018), the effect of stratification of the ambient medium, and the interaction with scales that are not resolved in our simulations here (see, e.g., McCourt et al., 2018). However, in view of the simple physical arguments that have supplemented most of the main conclusions of this paper (see above), it seems un-

likely that these effects would cause significant qualitative changes to our main results.

Acknowledgements

Support for ZL and co-authors was provided by an Alfred P. Sloan Research Fellowship, NSF Collaborative Research Grant #1715847 and CAREER grant #1455342, and NASA grants NNX15AT06G, JPL 1589742, 17-ATP17-0214. JS acknowledges the support of the Royal Society Te Apārangi through a Rutherford Discovery Fellowship RDF-U001804 and Marsden Fund grant UOO1727. Numerical calculations were run on the Caltech compute cluster “Wheeler”, allocations from XSEDE TG-AST130039 and PRAC NSF.1713353 supported by the NSF, and NASA HEC SMD-16-7592.

2.5 Appendix

Convergence Tests

We have verified that our results are robust to numerical resolution ($m_i \sim 10^{-7} - 10^{-3} M_{\text{cl}}$, or equivalently, $\sim 134 - 6$ cells per R_{cl}) via a variety of tests. For at least one cloud in every “regime” shown in Figure 2.5, we have re-run the same initial conditions at three resolution levels (our default, and one and two orders-of-magnitude lower resolution). In all cases we confirm that the measured cloud lifetime is robust to better than a factor of ~ 2 (although the cloud lifetimes do become systematically shorter at low resolution, as expected owing to numerical mixing). We have also randomly selected ten clouds in the “classical cloud destruction” regime to simulate at both lower and higher resolutions (a factor of ~ 8 change): we find the lifetimes change by a factor of < 1.5 in these cases. In Figure 2.12, we show one fiducial cloud, for which we simulate at seven different resolution levels. The agreement in cloud lifetime is excellent at order-of-magnitude higher and lower resolutions, compared to our default choice in the main text, which lends confidence to our conclusion that our key results are not strongly sensitive to numerical resolution.

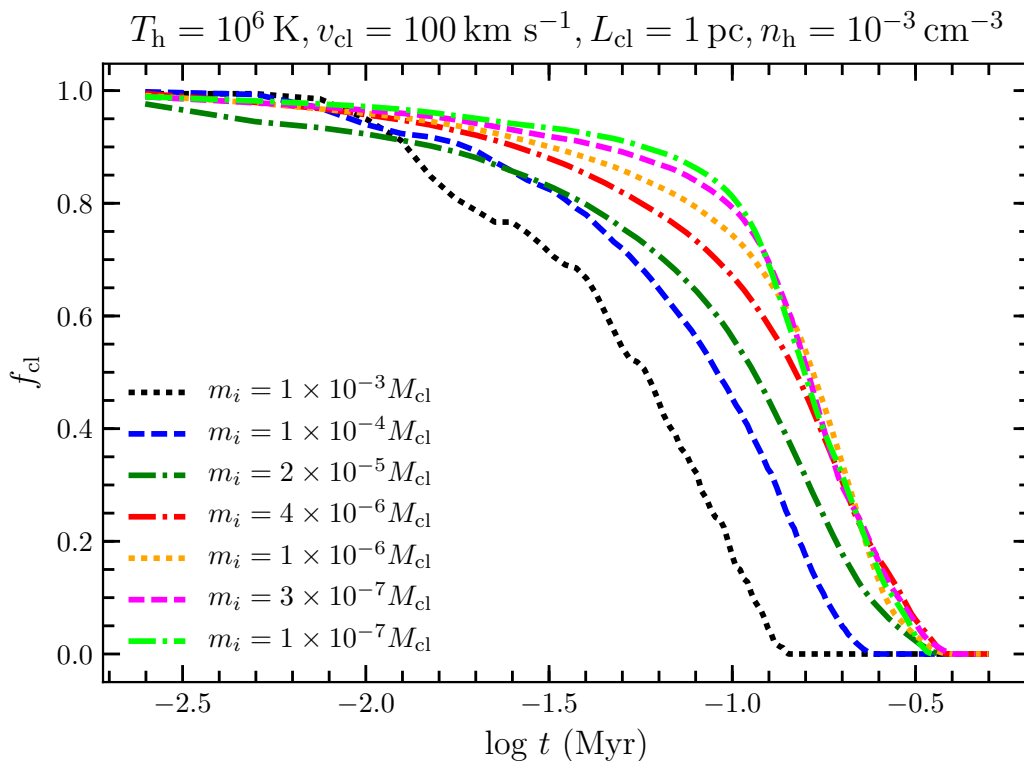


Figure 2.12: **Evolution of the normalized cloud mass, f_{cl} (defined in Figure 2.1) vs. time, for one representative initial condition in the “classical cloud destruction” regime ($T_h = 10^6 \text{ K}$, $v_{\text{cl}} = 100 \text{ km s}^{-1}$, $n_h = 10^{-3} \text{ cm}^{-3}$, $L_{\text{cl}} = 1 \text{ pc}$) with our default physics set simulated at seven different mass resolution (m_i) levels, as labeled.** The resulting cloud lifetime is remarkably robust to resolution, changing by $< 10\%$ from $m_i/M_{\text{cl}} \sim 10^{-5} - 10^{-7}$ and by a factor of < 2 (< 3) even at resolutions $m_i/M_{\text{cl}} \sim 10^{-4}$ ($\sim 10^{-3}$). Recall our default resolution in the main text is $m_i/M_{\text{cl}} \sim 10^{-6}$. The small change in behavior at early times and high resolution (with a longer “delay” until destruction begins) owes to better tracking of small, high-density “features” (e.g., Kelvin-Helmholtz whorls) which remain locally high density even as mixing begins.

REVISITING THE GAS KINEMATICS IN SSA22 LYMAN- α BLOB 1 WITH RADIATIVE TRANSFER MODELING IN A MULTIPHASE, CLUMPY MEDIUM

Li, Zhihui, Charles C. Steidel, Max Gronke, and Yuguang Chen (Apr. 2021). “Revisiting the gas kinematics in SSA22 Lyman- α Blob 1 with radiative transfer modelling in a multiphase, clumpy medium”. In: *MNRAS* 502.2, pp. 2389–2408. DOI: 10.1093/mnras/staa3951. arXiv: 2008.09130 [astro-ph.GA].

3.1 Introduction

Ly α Blobs (LABs) – spatially extended (projected sizes $\gtrsim 100$ kpc) gaseous nebulae at high redshift ($z \gtrsim 2$) with immense Ly α luminosities ($L_{\text{Ly}\alpha} \sim 10^{43-44}$ erg s $^{-1}$) – are among the most enigmatic and intriguing objects in the universe. To date, hundreds of LABs have been discovered (e.g., Francis et al. 1996; Fynbo et al. 1999; Keel et al. 1999; Steidel et al. 2000; Matsuda et al. 2004; Matsuda et al. 2011; Dey et al. 2005; Saito et al. 2006; Smith et al. 2007; Hennawi et al. 2009; Ouchi et al. 2009; Prescott et al. 2009; Prescott et al. 2012; Erb et al. 2011; Cai et al. 2017), yet their physical origin remains murky. Many of the LABs have been found in overdense regions associated with massive proto-clusters, which will presumably evolve into rich galaxy clusters observed today (e.g., Steidel et al. 1998; Prescott et al. 2008; Yang et al. 2009; Yang et al. 2010; Hine et al. 2016a). Hence, the study of LABs may elucidate the formation process of massive galaxies and the mechanisms of concurrent feedback events.

What are the possible energy sources that power the observed Ly α emission of LABs? Thus far, numerous attempts have been made to answer this fundamental question, but a consensus is yet to be reached. Among many proposed scenarios, one of the most plausible Ly α production mechanisms is photo-ionization via embedded energetic sources (e.g., starburst galaxies or AGNs) followed by subsequent recombination (Haiman et al., 2001; Cantalupo et al., 2005; Cantalupo et al., 2014). This scenario has been corroborated by the discovery of luminous galaxies and AGNs (Chapman et al., 2001; Dey et al., 2005; Geach et al., 2005; Geach et al., 2007; Geach et al., 2009; Colbert et al., 2006; Webb et al., 2009) inside some LABs via infrared and submillimeter observations. If the ionizing sources are star-

bursts, supernova-induced energetic winds may be triggered (Heckman et al., 1990; Taniguchi et al., 2000; Taniguchi et al., 2001; Mori et al., 2004), producing outflowing super-bubbles and additional Ly α emission via shock heating. Evidence for the existence of such ‘superwinds’ includes the observed double-peaked Ly α profiles (Ohyama et al., 2003) and bubble-like structures (Matsuda et al., 2004). Alternatively, Ly α emission can originate from cooling radiation via accretion of cold gas streams in dark matter halos onto protogalaxies (Haiman et al., 2000; Fardal et al., 2001; Furlanetto et al., 2005; Dijkstra et al., 2006a; Dijkstra et al., 2006b; Scarlata et al., 2009; Goerdt et al., 2010; Faucher-Giguère et al., 2010; Rosdahl et al., 2012). This explanation is especially favored for LABs with no or only weak associated energy sources identified even with deep multi-wavelength observations (Nilsson et al., 2006; Smith et al., 2007; Saito et al., 2008; Smith et al., 2008). In either case, a substantial fraction of the Ly α photons will be resonantly scattered multiple times before escape (Steidel et al., 2010; Steidel et al., 2011), although the ‘cold accretion’ scenario is supposed to induce a lower degree of polarization due to a lower chance of scattering from the inside out (Dijkstra et al., 2009; Hayes et al., 2011; Trebitsch et al., 2016; Eide et al., 2018).

In this paper, we present new observations and analyses of one of the first LABs ever discovered, SSA22-Blob1 (LAB1, Steidel et al. 2000). LAB1 is one of the brightest and largest LABs discovered to date, with a Ly α luminosity of $\sim 1.1 \times 10^{44}$ erg s $^{-1}$ (Weijmans et al., 2010) and a spatial extent of ~ 100 kpc (Matsuda et al., 2004). Since its discovery, LAB1 has been studied extensively, at wavelengths including X-ray (Geach et al., 2009), optical (Ohyama et al., 2003; Bower et al., 2004; Weijmans et al., 2010), infrared (IR, Uchimoto et al. 2008; Uchimoto et al. 2012; Webb et al. 2009) and submillimeter (submm, Geach et al. 2005; Matsuda et al. 2007; Geach et al. 2014; Hine et al. 2016a). Two Lyman-break galaxies (LBG), C11 and C15 (Steidel et al., 2000; Steidel et al., 2003; Matsuda et al., 2004), and multiple dust-obscured star-forming galaxies (Geach et al., 2007; Geach et al., 2014; Geach et al., 2016) have been identified within LAB1. However, X-ray observations yield non-detections, indicating the absence of (Compton-thin) AGNs (Geach et al., 2009).

To determine the principle energy source(s) powering LAB1, three main approaches have been adopted: the first is to infer the gas kinematics (e.g., inflows vs. outflows) from the observed properties of Ly α as well as other non-resonant emission lines (e.g., [O III], H α , H β). For example, Bower et al. (2004) and Weijmans et al. (2010)

measured a velocity shear of the Ly α emission from C11 and C15 using integral-field spectroscopy, which suggests the presence of outflows. On the other hand, McLinden et al. (2013) reported a nearly zero velocity offset between Ly α and [O III] in C11 and C15, which they interpreted as an absence of strong outflows. An alternative approach is to compare the available energy budget of possible energy sources with the observed Ly α emission. For example, Geach et al. (2016) deduced the IR luminosities and corresponding star formation rate (SFR, $\sim 150 M_{\odot} \text{ yr}^{-1}$) of the embedded sources from their 850 μm flux density measured with ALMA, and found that this energy budget is sufficient to power the observed Ly α luminosity. However, as it is difficult to independently constrain the fraction of Ly α photons that escape from the galaxy and scatter into our line of sight, additional energy sources (e.g., cold accretion) cannot be ruled out entirely (Geach et al., 2014; Hine et al., 2016a). Thirdly, Hayes et al. (2011) and Beck et al. (2016) have measured polarized Ly α emission using polarimetric imaging. Although they claimed that this result should be strongly supportive of a ‘central powering + scattering’ model, Trebitsch et al. (2016) pointed out that the scattering inside the cold filaments in the ‘cold accretion’ scenario could still account for the degree of polarization observed.

In this paper, we use an advanced kinematic approach to further test the feasibility of the ‘central powering + scattering’ scenario. The traditional kinematic approach – inferring the underlying gas velocity field from the observed peak shifts and line widths (e.g., McLinden et al. 2013) is worth scrutinizing, as resonant scattering may modify the line profiles in a very complex way. Instead, we model the Ly α profiles using Monte-Carlo radiative transfer (MCRT). Due to its computationally expensive nature, Ly α MCRT modeling normally assumes a simple, idealized geometry, e.g., a spherically symmetric expanding shell of H I gas surrounding a central Ly α emitting source (the ‘shell model’, Verhamme et al. 2006; Dijkstra et al. 2006b). This simple model has successfully reproduced many observed Ly α spectra (e.g., Schaerer et al. 2008; Verhamme et al. 2008; Dessauges-Zavadsky et al. 2010; Vanzella et al. 2010; Gronke 2017), although it has also encountered some challenges for those with multiple peaks (Verhamme et al. 2008; Kulas et al. 2012; Rivera-Thorsen et al. 2017) or very large line widths (Hashimoto et al. 2015; Yang et al. 2016; Yang et al. 2017; Orlitová et al. 2018). Moreover, recent observations have shown increasing evidence that the circumgalactic medium (CGM), just like the interstellar medium (ISM), is multiphase and clumpy (e.g., the Ly α emission and metal absorption line observations of high-redshift quasars (Cantalupo et al. 2014; Hennawi et al. 2015), which is further corroborated by simulations with in-

creased spatial resolution (e.g., Hummels et al. 2019). Therefore, a more realistic model that accounts for the multiphase nature and clumpy geometry of H I gas is needed to properly characterize the radiative transfer processes of Ly α photons.

Up to now, this multiphase ‘clumpy’ model has been explored theoretically via both semi-analytical calculations (Neufeld, 1991) and Monte-Carlo simulations (Hansen et al., 2006; Dijkstra et al., 2012; Laursen et al., 2013; Gronke et al., 2016a). However, due to its complex and multivariate nature, the multiphase ‘clumpy’ model has not been widely used in fitting real Ly α spectra (albeit the first attempt made in Forero-Romero et al. 2018). In this work, we use the framework proposed by Gronke et al. (2016a) to model the spatially resolved Ly α spectra in LAB1.

In addition to the Ly α observations in the optical (rest-frame UV) using the Keck Cosmic Web Imager (KCWI; Martin et al. 2010; Morrissey et al. 2012), we have carried out near-infrared (NIR, rest-frame optical) spectroscopic observations using the Keck Multi-object Spectrometer for Infrared Exploration (MOSFIRE; McLean et al. 2010; McLean et al. 2012). By comparing the spatial distribution of Ly α , [O III] and H β emission and fitting Ly α line profiles, we map the kinematic structure of H I in LAB1 and constrain its possible powering mechanism(s).

The structure of this paper is as follows. In §3.2, we describe our KCWI and MOSFIRE observations and data reduction procedures. In §3.3, we present our new observational results and analyses. In §3.4, we detail the methodology and present our results of radiative transfer modeling using the multiphase, clumpy model. In §3.5, we summarize and conclude. Throughout this paper we adopt a flat Λ CDM cosmology with $\Omega_m = 0.315$, $\Omega_\Lambda = 0.685$, and $H_0 = 67.4 \text{ km s}^{-1} \text{ Mpc}^{-1}$ (Planck Collaboration et al., 2020). We use the following vacuum wavelengths: 1215.67 Å for Ly α , 4862.683 Å for H β , and 4960.295/5008.240 Å for [O III] from the Atomic Line List v2.04¹.

3.2 Observations and Data Reduction

KCWI Observations

The KCWI observations of LAB1 were carried out on the night of 2018 June 16, with a seeing of $\sim 1.0''$ full width at half maximum (FWHM). We used the KCWI large slicer, which provides a contiguous field-of-view (FOV) of 20.4'' (slice length) \times 33'' (24 \times 1.35'' slice width). With the BM VPH grating set up for $\lambda_c = 4800 \text{ Å}$, the wavelength coverage is $\sim 4260 - 5330 \text{ Å}$, with spectral resolution $R \simeq 1800 -$

¹<http://www.pa.uky.edu/~peter/atomic/index.html>

2200. The data were obtained as 9 individual 1200 s exposures, with small telescope offsets in the direction perpendicular to slices applied between each, in an effort to recover some spatial resolution given the relatively large slice width. The total on-source exposure time was 3 hours.

Individual exposures were reduced using the KCWI Data Reduction Pipeline², which includes wavelength calibration, atmospheric refraction correction, background subtraction, and flux calibration. The individual datacubes were then spatially re-sampled onto a uniform astrometric grid with 0.3" by 0.3" spaxels, with a sampling of $0.5 \text{ \AA} \text{ pix}^{-1}$ (4.75 pixels per spectral resolution element) along the wavelength axis, using a variant of the ‘drizzle’ algorithm (with a drizzle factor of 0.9) in the MONTAGE³ package. The re-sampled cubes were then combined into a final stacked cube by averaging with exposure time weighting. Owing to the coarser spatial sampling in the long dimension of the spatial cube, the PSF in the final datacube is elongated along the N-S direction, with FWHM $\simeq 0.96'' \times 1.44''$ (X-direction and Y-direction, respectively).

The resampled final datacube covers a scientifically useful solid angle of $18.9'' \times 32.7''$ on the sky, and a wavelength range (vacuum, heliocentric) of 4214 – 5243 \AA . A variance image with the same dimensions was created by propagating errors based on a noise model throughout the data reduction.

MOSFIRE Observations

We observed selected regions of LAB1, chosen to include the highest Ly α surface brightness areas as determined from a very deep narrow-band Ly α image (see Steidel et al. 2011; Nestor et al. 2011) using MOSFIRE (McLean et al., 2010; McLean et al., 2012; Steidel et al., 2014) on the Keck I telescope. Spectra in the near-IR *K* band (1.95 – 2.40 μm) were obtained using four different slitmasks, each of which included a slit passing through part of LAB1 with a different RA, Dec, and position angle (PA). The four slits are labeled as ‘slit 1’ through ‘slit 4’ in Figure 3.1, and the observations are summarized in Table 3.1. Slits 1 – 3 were obtained using slits of width 0.7'', providing spectral resolving power of $R \simeq 3700$; slit 4 observations used a 1.0'' wide slit, yielding $R \simeq 2600$. The observations were obtained during four different observing runs between 2012 June and 2019 November, under clear skies with seeing in the range 0.43'' – 0.53'', as summarized in Table 3.1.

²<https://github.com/Keck-DataReductionPipelines/KcwiDRP>

³<http://montage.ipac.caltech.edu>

Table 3.1: MOSFIRE K -band observations of LAB1.

Name	Width	R	PA	Exp	Seeing	Date of Obs	Nod
(1)	(2)	(3)	(4)	(5)	(6)	(7)	(8)
Slit 1	0.7	3660	-68.0	4.0	0.50	2012 Sep15	3.0
Slit 2	0.7	3660	-3.5	1.5	0.43	2012 Jun30	3.0
Slit 3	0.7	3660	27.0	1.5	0.52	2012 Sep13	3.0
Slit 4	1.0	2560	-54.0	2.5	0.53	2019 Jun15	15.0

Notes. The details of the MOSFIRE K -band observations of LAB1. The columns are: (1) slit name; (2) slit width ("); (3) resolving power ($\lambda/\Delta\lambda$); (4) slit PA (degrees E of N); (5) exposure time in hours; (6) seeing FWHM ("); (7) UT date of observation; (8) nod amplitude between A and B positions (").

The MOSFIRE K band observations (slit 1 was also observed in H band) were all obtained using an ABAB nod pattern along the slit direction with nod amplitude of 3" between position A and position B for slits 1, 2, and 3, and 15" for slit 4. Total integration times were 1.5 – 4.0 hours, as listed in Table 3.1, composed of 30 – 80 individual 180 s exposures. The data for each observation sequence were reduced using the MOSFIRE data reduction pipeline⁴ to produce two-dimensional, rectified, background-subtracted vacuum wavelength calibrated spectrograms (see Steidel et al. 2014 for details). Observations obtained on different observing nights using the same slitmask were reduced independently; the 2-D spectrograms were shifted into the heliocentric rest frame and combined with inverse variance weighting using tasks in the MOSPEC (Strom et al., 2017) analysis package.

3.3 The Gas Kinematic Structure of LAB1

Spatial Distribution of $\text{Ly}\alpha$ Emission

To get an overview of the $\text{Ly}\alpha$ surface brightness (SB) distribution in LAB1, we first generate a $\text{Ly}\alpha$ narrow-band image by optimally summing all the $\text{Ly}\alpha$ fluxes over the relevant wavelength range. Here we follow the ‘matched filtering’ procedures for creating a narrow-band image (Herenz et al., 2020) using LSDCat (Herenz et al., 2017). Firstly, we apply spatial filtering to the continuum-subtracted KCWI datacube using a 2D Gaussian filter with a constant 1.2" FWHM, which equals the seeing point spread function (PSF) measured from a bright star in the SSA22 field. Secondly, we apply a 1D Gaussian spectral filter with $\text{FWHM} = 1000 \text{ km s}^{-1}$, which is the typical observed $\text{Ly}\alpha$ line width estimated via visual inspection. Thirdly, we

⁴<https://github.com/Keck-DataReductionPipelines/MosfireDRP>

Table 3.2: Continuum sources identified in LAB1.

Name	RA (J2000)	Dec (J2000)	z_{sys}	Type	Refs.
C11 ^a	22:17:25.70	+00:12:34.7	3.0980 ± 0.0001	[O III]	(1)(2)
C15 ^a	22:17:26.15	+00:12:54.7	3.0975 ± 0.0001	[O III]	(1)(2)
ALMA-a	22:17:25.94	+00:12:36.6	(3)
ALMA-b	22:17:26.01	+00:12:36.4	(3)
ALMA-c	22:17:26.11	+00:12:32.4	3.1000 ± 0.0003	[C II]	(5)
	22:17:26.10	+00:12:32.3	3.0993 ± 0.0004	[O III]	(3)
K1	22:17:25.70	+00:12:38.7	3.1007 ± 0.0002	[O III]	(4)
c ₁	22:17:25.94	+00:12:36.0	3.0988	[O III]	(1)
c ₂ /S1	22:17:26.08	+00:12:34.2	3.0968	[O III]	(1)(3)
c ₃	22:17:26.05	+00:12:38.7	2.7542	Ly α	(1)

^aOriginally defined in Steidel et al. (2000).

References. (1) This work; (2) McLinden et al. (2013); (3) Geach et al. (2016); (4) Kubo et al. (2015); (5) Umehata et al. (2017).

use this filtered datacube to generate a S/N cube. We can then choose appropriate S/N thresholds for the filtered datacube to produce SB and moment maps (see Section 3.3).

In the left panel of Figure 3.1, we present our narrow-band Ly α image. It is constructed by summing over all the voxels of the filtered datacube with $S/N \geq 4$ over $4959 - 5009 \text{ \AA}$, which should enclose all possible Ly α emission. To further examine whether the Ly α emission coincides with the identified sources, we also present the *HST*/STIS optical continuum image of LAB1⁵.

We have also marked the positions of previously identified sources on each image as references. Among these sources, C11 and C15 are both LBGs (Steidel et al., 2000); ALMA-a, b and c are three submillimeter galaxies (Geach et al., 2016); K1 is a *K*-band selected galaxy (Kubo et al., 2015); c₁ and c₂ (the same as S1 in Geach et al. 2016) are two [O III] serendipitous sources; c₃ is a Ly α serendipitous source at a lower redshift ($z = 2.7542$). The detailed information (especially spectroscopic redshifts, if available) of all the identified sources are presented in Table 3.2. The Ly α isophotes (contours with the same SB) with levels of $SB_{\text{Ly}\alpha} = [120, 80, 40, 15, 4] \times 10^{-19} \text{ erg s}^{-1} \text{ cm}^{-2} \text{ arcsec}^{-2}$ have also been overlaid onto each

⁵The KCWI and *HST*/STIS images have been registered to the same world-coordinate system using cross-correlation.

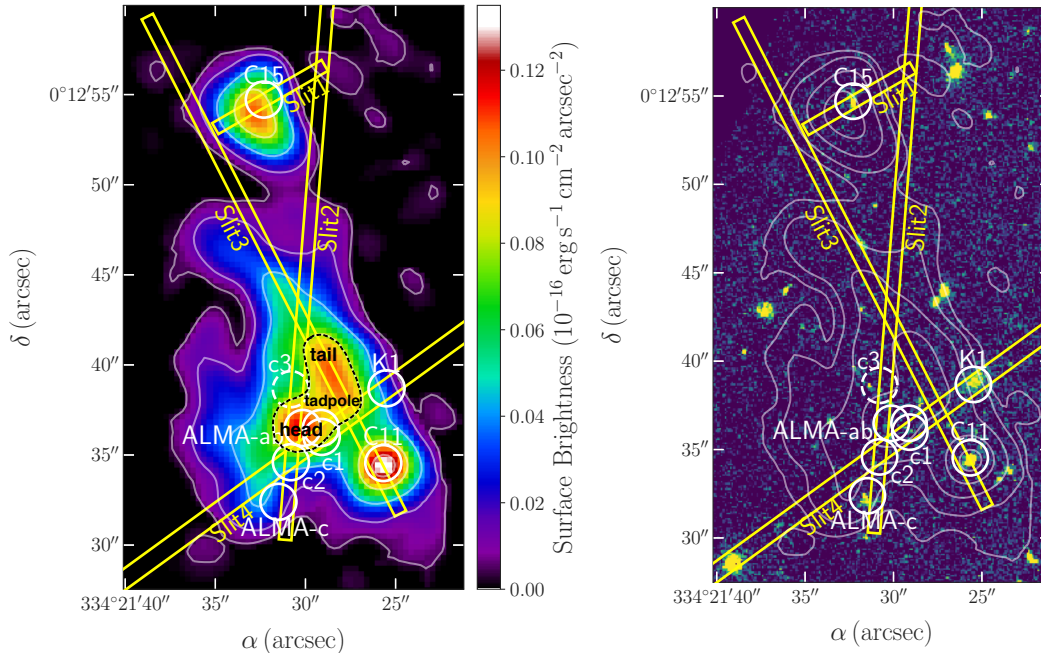


Figure 3.1: **Ly α and continuum images of LAB1.** *Left:* The narrow band Ly α image, obtained by collapsing the original KCWI datacube over 4959 – 5009 Å, which contains the Ly α line (see Section 2). The UV continuum near the wavelength of Ly α has been subtracted. *Right:* The *HST/STIS* optical continuum image. The positions of four MOSFIRE slits (Slit 1–4), two Lyman-break galaxies (C11 and C15), three submillimeter sources (ALMA-a, b, and c), a *K*-band selected galaxy (K1) and three [O III]/Ly α serendipitous sources (c_1 to c_3) have been marked on each image (see Table 3.2). The Ly α isophotes with levels of $SB_{\text{Ly}\alpha} = [120, 80, 40, 15, 4] \times 10^{-19} \text{ erg s}^{-1} \text{ cm}^{-2} \text{ arcsec}^{-2}$ have also been overlaid. All images have been registered to the same world-coordinate system.

image.

Several prominent features are evident in Figure 3.1: (1) In general, the regions with the highest SB are associated with identified sources (e.g., C11, C15 and ALMA-a), although the position of the maximum Ly α SB may be offset from the continuum source (e.g., C15); (2) An exception worth noting is a tadpole-shaped structure (marked in Figure 3.1), which starts from the ALMA-ab sources, wriggles towards the north-west first and then north-east. Interestingly, although the ‘head’ of the tadpole overlaps with ALMA-a, its ‘tail’ does not overlap with any source; (3) The regions with identified continuum sources do not necessarily have significant Ly α emission (e.g., ALMA-c, c_2 , K1).

Spatial Distribution of [O III] and H β Emission

To test whether the extended Ly α emission is produced ‘in situ’ or ‘ex situ’ (the latter requires scattering), we further use MOSFIRE to map the spatial distribution of two other non-resonant lines, [O III] and H β , and quantitatively compare them with Ly α emission at the same spatial position. The positions of the four MOSFIRE slits are also shown in Figure 3.1.

Theoretically, we consider two principal scenarios of Ly α production: (1) photoionization + recombination (e.g., due to star formation); (2) collisional excitation + radiative de-excitation (e.g., due to cold accretion). For scenario 1, assuming case B recombination, we use the `PYNeb` package (Luridiana et al., 2015) to calculate $F_{\text{Ly}\alpha}/F_{\text{H}\beta}$ for $T_{\text{HI}} \text{ (K)} \in [10^3, 10^5]$ and $n_e \text{ (cm}^{-3}\text{)} \in [1, 10^4]$, where T_{HI} and n_e are the kinetic temperature of the HI gas and electron number density, respectively. For scenario 2, assuming collisional ionization equilibrium, we use the `ChiantiPy` package (Dere et al., 1997; Dere, 2013; Dere et al., 2019) to calculate $F_{\text{Ly}\alpha}/F_{\text{H}\beta}$ for the same ranges of T_{HI} and n_e as above. The derived $F_{\text{Ly}\alpha}/F_{\text{H}\beta}$ as a function of T_{HI} for both scenarios are shown in Figure 3.2. It can be seen that as T_{HI} increases, the predicted $F_{\text{Ly}\alpha}/F_{\text{H}\beta}$ is roughly constant for scenario 1, but decreases for scenario 2, as Ly α emissivity drops more quickly than H β .

Now we compare our spectroscopic data to the theoretical predictions above. For each MOSFIRE slit in Figure 3.1, we construct a corresponding pseudo-slit to extract a 2D spectrum from the 3D KCWI datacube via a 3D datacube visualization tool `QFitsView` (Davies et al., 2010; Ott, 2012). We then integrate the flux density in the wavelength dimension for each line and convert it to a SB accounting for the slit width.

In Figure 3.3, we show the line SB for Ly α , [O III] and H β along each slit. Evidently, Ly α is not necessarily co-spatial with [O III] or H β , and is usually more extended along the slit. We further calculate $F_{\text{[O III]}}/F_{\text{H}\beta}$ (shown in red numbers) by integrating $SB_{\text{H}\beta}$ and $SB_{\text{[O III]}}$ along the slits for each identified source. We also calculate $F_{\text{Ly}\alpha}/F_{\text{H}\beta}$ in two ways, where $F_{\text{Ly}\alpha}$ is calculated either by integrating $SB_{\text{Ly}\alpha}$ over the same region as H β and [O III] (the ‘restricted’ region, as indicated by solid arrows), or by integrating over the full extent of Ly α (the ‘extended’ region, as indicated by dashed arrows). The results are shown next to the arrows (red for $F_{\text{[O III]}}/F_{\text{H}\beta}$ and green for $F_{\text{Ly}\alpha}/F_{\text{H}\beta}$).

The results in Figure 3.2 and 3.3 show that: (1) For slit 1 and 2, $F_{\text{Ly}\alpha}/F_{\text{H}\beta}$ are always smaller than the predicted value of scenario 1. Considering that Ly α is subject to

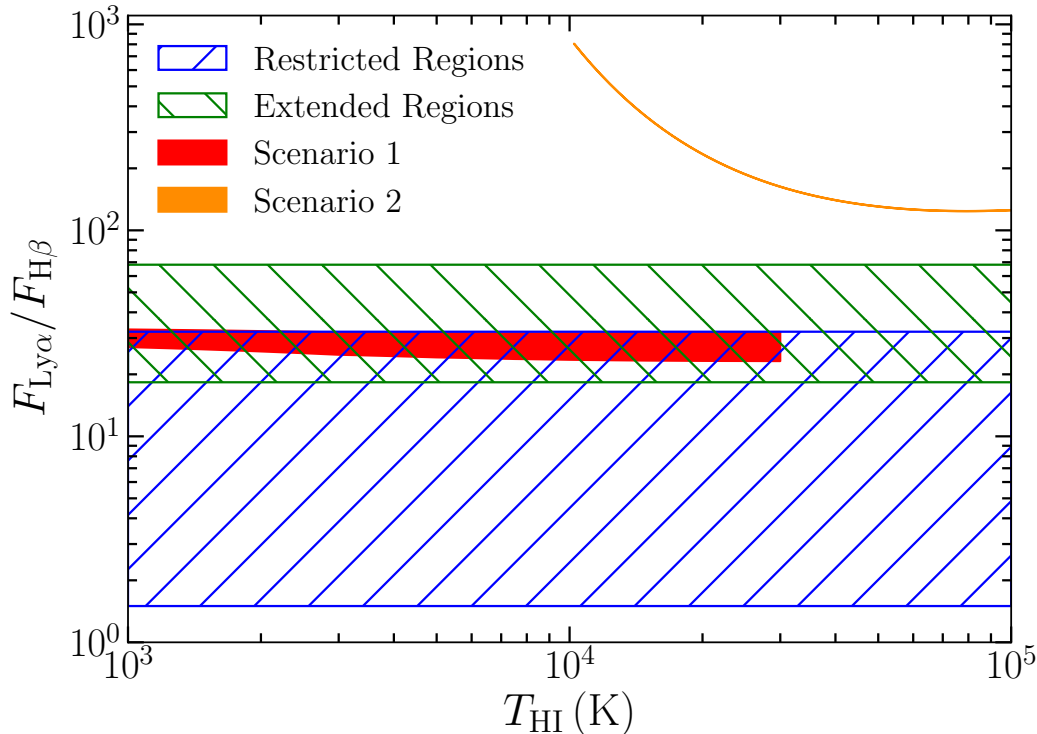
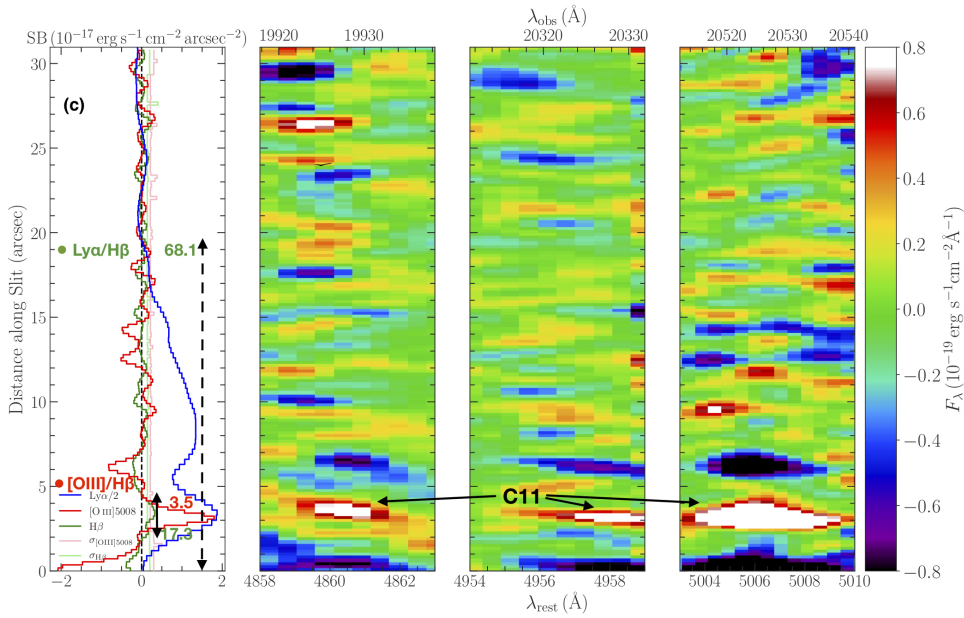
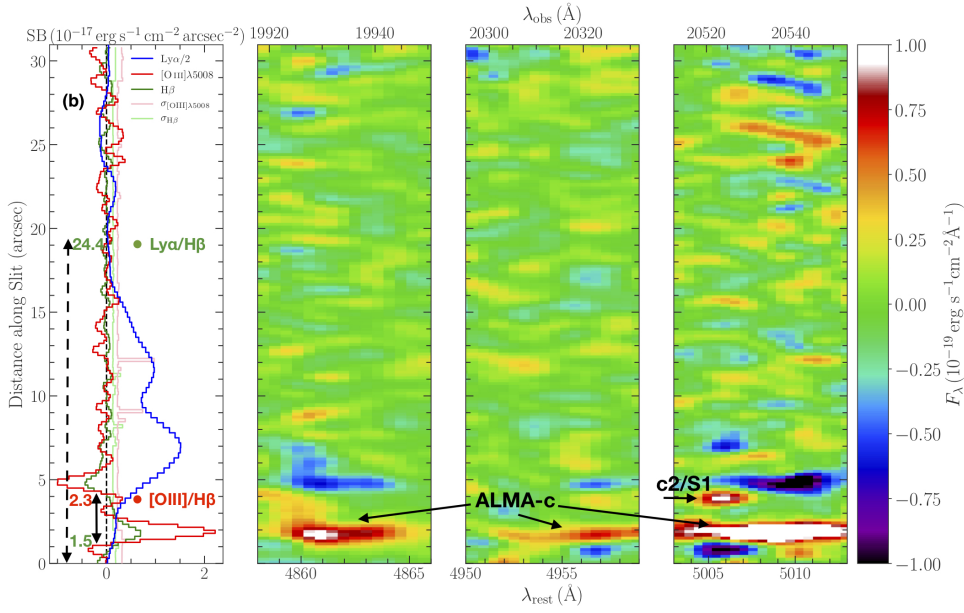
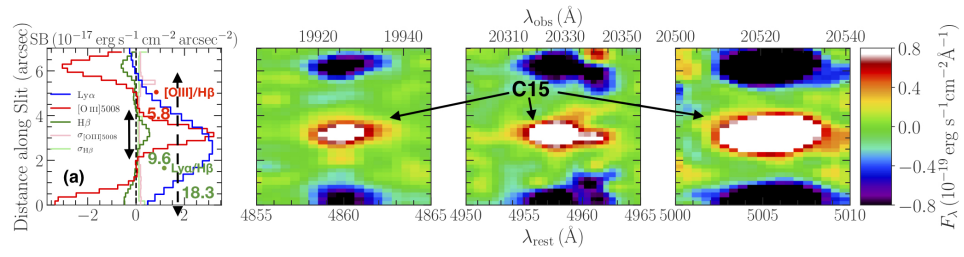


Figure 3.2: $F_{\text{Ly}\alpha}/F_{\text{H}\beta}$ as a function of the H I gas temperature T_{HI} in the photo-ionization (red patch) and collisional excitation (orange curve) scenarios. Also shown are the ranges of $F_{\text{Ly}\alpha}/F_{\text{H}\beta}$ measured along four MOSFIRE slits for both the restricted regions (shaded in blue slashes) and extended regions (shaded in green slashes) (see §3.3 for the definitions of restricted and extended regions).

heavier dust extinction⁶ than H β , this result suggests that scenario 1 itself is sufficient to explain the observed $F_{\text{Ly}\alpha}/F_{\text{H}\beta}$; (2) For slit 3 and 4, we do see $F_{\text{Ly}\alpha}/F_{\text{H}\beta}$ ratios ($\sim 50 - 70$, see Table 3.3) higher than that predicted by scenario 1, but still far lower than those predicted by scenario 2 (especially in the $T_{\text{HI}} \geq 10^4$ K region, where both Ly α and H β have been sufficiently excited). Simply scenario 1 and resonant scattering are sufficient to explain all the observed line ratios. Furthermore, we do not see a significant number of Ly α profiles that have a blue dominant peak (signature of cold accretion, see, e.g., Zheng et al. 2002; Dijkstra et al. 2006b; Faucher-Giguère et al. 2010) in these regions. Therefore, it is highly likely that photo-ionization + recombination is the main source of Ly α photons, and resonant scattering (as indicated by significant polarization detections from Hayes et al. 2011 and Beck et al. 2016) has substantially altered their spatial and kinematic distribution.

⁶Additionally, the scattering of Ly α photons out of the line-of-sight can also reduce the observed $F_{\text{Ly}\alpha}/F_{\text{H}\beta}$ ratio.



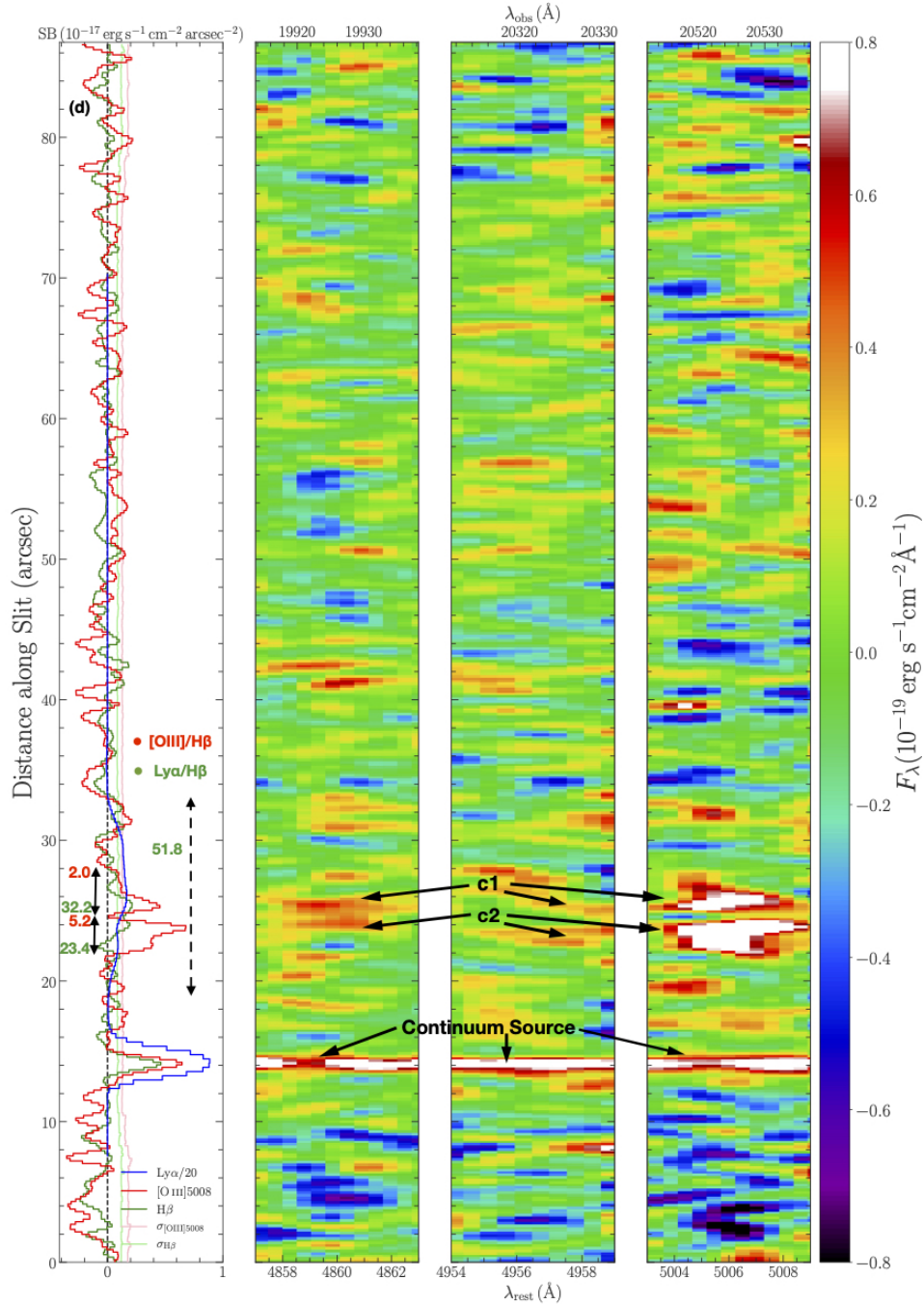


Figure 3.3: **Surface brightness distributions of Ly α (blue), [O III] (red) and H β (green) along four MOSFIRE slits** (the leftmost panels, (a) – (d) correspond to slits 1 – 4, respectively). For reference, the smoothed 2D spectra of H β (the second column) and [O III] (the third and fourth columns, for 4960 Å and 5008 Å, respectively) are also shown. Both the observed wavelengths (λ_{obs}) and the rest-frame wavelengths (λ_{rest} , assuming $z = 3.1000$) are shown. The positions of known sources are indicated with black arrows. We calculate $F_{[\text{O III}]} / F_{\text{H}\beta}$ (shown in red numbers) by integrating $SB_{\text{H}\beta}$ and $SB_{[\text{O III}]}$ along the slits for each identified source. We also calculate $F_{\text{Ly}\alpha} / F_{\text{H}\beta}$ (shown in green numbers) in two ways, where $F_{\text{Ly}\alpha}$ is calculated either by integrating $SB_{\text{Ly}\alpha}$ over the same region as H β and [O III] (as indicated by solid arrows), or by integrating over the full extent of Ly α (as indicated by dashed arrows). Note that the blue regions in the 2D spectra are negative images due to dithering.

Table 3.3: Ly α , [O III] and H β fluxes and line ratios measured along four MOSFIRE slits.

Slit No.	Restricted Regions					Extended Regions	
	Ly α	[O III]	H β	Ly α /H β	[O III]/H β	Ly α	Ly α /H β
(1)	(2)	(3)	(4)	(5)	(6)	(7)	(8)
1	4.8	2.3	0.4	9.6	5.8	9.3	18.3
2	1.3	1.5	0.7	1.5	2.3	20.9	24.4
3	7.5	1.2	0.3	17.3	3.5	29.3	68.1
4	9.2/4.3	0.6/1.1	0.3/0.2	32.2/23.4	2.0/5.2	24.3	51.8

Notes. Ly α , [O III] and H β fluxes measured by integrating along the four MOSFIRE slits (see Figure 3.1 and Table 3.1 for details) and the corresponding extracted pseudo-slits from the KCWI datacube and line ratios (Ly α /H β and [O III]/H β). The columns are: (1) the slit number (as marked in Figure 3.1); (2) the Ly α flux of the restricted regions (where $F_{\text{Ly}\alpha}$ is calculated over the same region as H β and [O III], as indicated by solid arrows in Figure 3.3); (3) the [O III] flux; (4) the H β flux; (5) the Ly α /H β ratio; (6) the [O III]/H β ratio; (7)(8) same as (2)(5), but for extended regions (where $F_{\text{Ly}\alpha}$ is calculated over the full extent of Ly α , as indicated by dashed arrows in Figure 3.3). All fluxes are in units of $10^{-17} \text{ erg s}^{-1} \text{ cm}^{-2}$.

Profiles of Ly α Emission

In this section, we investigate the variations of spatially resolved Ly α profiles in major emitting regions. Before proceeding, we first use [O III] to determine the systemic redshifts of three associated sources: C11, C15 and c_1 . Single Gaussian fits to the [O III] line profiles (see Appendix 3.6 for details) yield redshifts (after heliocentric corrections) $z(\text{C11}) = 3.0980$, $z(\text{C15}) = 3.0975^7$ and $z(c_1) = 3.0988$, which we adopt as fiducial redshifts in the following analysis.

We then visualize the spatial variations of Ly α peak position ($v_{\text{Ly}\alpha}$) and line width ($\sigma_{\text{Ly}\alpha}$) by making moment maps. The first and second flux-weighted moments are defined as:

$$v_{\text{Ly}\alpha,xy} = \frac{\sum_k v_{xyk} I_{xyk}}{\sum_k I_{xyk}} \quad (3.1)$$

⁷Compared to McLinden et al. (2013), our measurements for $z(\text{C15})$ are consistent but our $z(\text{C11})$ are slightly different. This may be due to: (1) the asymmetric nature of the [O III] profile of C11; (2) the misalignment between the MOSFIRE slit and the galaxy continuum emission.

$$\sigma_{\text{Ly}\alpha,xy} = \sqrt{\frac{\sum_k (v_{xyk} - v_{\text{Ly}\alpha,xy})^2 I_{xyk}}{\sum_k I_{xyk}}} \quad (3.2)$$

where I_{xyk} and v_{xyk} are the flux density and velocity (relative to a fiducial redshift) of the k th wavelength layer at position (x, y) . In our moment analysis we fix the fiducial redshift of LAB1 at $z = 3.1$, and all the summations are carried out over $4959 - 5009 \text{ \AA}$. Before applying Eqs. (3.1) and (3.2), we filter out all the voxels with $S/N < 6$ (for $v_{\text{Ly}\alpha}$) or 4 (for $\sigma_{\text{Ly}\alpha}$)⁸. The $\sigma_{\text{Ly}\alpha}$ map has been further corrected for the KCWI instrumental line spread function (LSF), $\sigma = 65 \text{ km s}^{-1}$.

The resulting moment maps are shown in Figure 3.4. The two major $\text{Ly}\alpha$ emitting regions have been delineated by rectangular boxes. We zoom in on these two regions in separate panels. By adjusting the dynamic range, we are able to discern more subtle structures, discussed in the following sections.

Northern Region

There is only one identified source (C15) in the northern $\text{Ly}\alpha$ emitting region. We first use a large aperture to measure the global properties of LBG C15. The global line widths of $\text{Ly}\alpha$ and [O III] of C15 are 250 and 64 km s^{-1} (corrected for LSF, $\sigma = 65 \text{ km s}^{-1}$ for KCWI and 35 km s^{-1} for MOSFIRE). The global velocity offset between $\text{Ly}\alpha$ and [O III] is $\Delta v_{\text{Ly}\alpha} = -22 \text{ km s}^{-1}$, although it varies at different locations. This $\Delta v_{\text{Ly}\alpha}$ is significantly smaller than the velocity offsets observed in LBGs (Steidel et al., 2010) and LAEs (McLinden et al., 2011), both of which are $\gtrsim 300 \text{ km s}^{-1}$ and are interpreted as signs of outflows. Therefore, it is tempting to conclude that this region should be lack of significant outflows. However, as we will show in Section 3.4, our multiphase, clumpy model predicts that significant outflow velocities can still be present in profiles with $\Delta v_{\text{Ly}\alpha} \simeq 0$ (e.g., in our spectra 1 and 2).

Most $\text{Ly}\alpha$ profiles in the northern region are considerably asymmetric and consist of a ‘main peak’ and a ‘red bump’ (see spectrum 1 in Figure 3.5 as an example). Moreover, the main peak is redshifted towards the eastern region, and blueshifted towards the west. The largest $v_{\text{Ly}\alpha}$ can be up to $\sim 500 \text{ km s}^{-1}$, which explains the evident east-west $v_{\text{Ly}\alpha}$ gradient in Figure 3.4. This shear in $v_{\text{Ly}\alpha}$ appears to be per-

⁸Our experiments show that these choices maximize the inclusion of real signal without introducing spurious detections.

pendicular to the major axis of C15, which is consistent with the suggestion by Weijmans et al. (2010) that outflow or rotation is indicated.

As for $\sigma_{\text{Ly}\alpha}$, its largest value ($\sim 400 \text{ km s}^{-1}$) is located slightly north-east of C15, beyond which $\sigma_{\text{Ly}\alpha}$ gradually decreases moving away from C15. In general, the $\sigma_{\text{Ly}\alpha}$ values in the northern region are much larger than the global $\sigma_{[\text{O III}]}$. This is unexpected if one were to assume that both $\text{Ly}\alpha$ and $[\text{O III}]$ photons are emitted by the same sources, unless the kinematics of $\text{Ly}\alpha$ have been altered by radiative transfer effects. We attempt to explain the broadening of $\text{Ly}\alpha$ in Section 3.4.

Southern Region

Multiple discrete continuum sources have been identified within the southern portion of LAB1, including the LBG C11, three ALMA submm sources, and several very faint objects with spectroscopic confirmation (K1, c_1 , c_2 and c_3). We first use a large aperture to measure the global properties of LBG C11. The LSF-corrected global line widths of $\text{Ly}\alpha$ and $[\text{O III}]$ of C11 are 178 and 78 km s^{-1} . The global velocity offset between $\text{Ly}\alpha$ and $[\text{O III}]$ is $\Delta v_{\text{Ly}\alpha} = +175 \text{ km s}^{-1}$ (i.e., redshifted with respect to systemic), and -197 km s^{-1} between the Si II 1526 absorption line (from LRIS observations) and $\text{Ly}\alpha$. Similar velocity offsets between $\text{Ly}\alpha$ and interstellar absorption features are commonly observed in ‘down the barrel’ spectra of LBGs, and are generally interpreted as signatures of outflow (Steidel et al., 2010). However, they are inconsistent with the non-detection of a significant offset between $\text{Ly}\alpha$ and $[\text{O III}]$ by McLinden et al. (2011). This may be due to the high asymmetry of the $[\text{O III}]$ profile of C11.

Most $\text{Ly}\alpha$ profiles from spatial locations near C11 exhibit double peaks – a red dominant peak + a blue ‘bump’ (see spectrum 10 in Figure 3.5 as an example). The position of the red dominant peak tends to move towards more blueshifted velocities along the northwest-southeast direction. The largest $v_{\text{Ly}\alpha}$ is $\sim 300 \text{ km s}^{-1}$, which gives rise to the $v_{\text{Ly}\alpha}$ northwest-southeast gradient in Figure 3.4. This shear in $v_{\text{Ly}\alpha}$ appears to be parallel to the major axis of C11, consistent with Weijmans et al. (2010).

As for $\sigma_{\text{Ly}\alpha}$, its largest value ($\sim 500 \text{ km s}^{-1}$) is located in the southwest corner, while the majority of the spectra around C11 have a rather homogeneous $\sigma_{\text{Ly}\alpha} \sim 400 \text{ km s}^{-1}$. Again, these values are much larger than $\sigma_{[\text{O III}]}$.

The $\text{Ly}\alpha$ profiles near the ALMA sources are more complex – most of them are

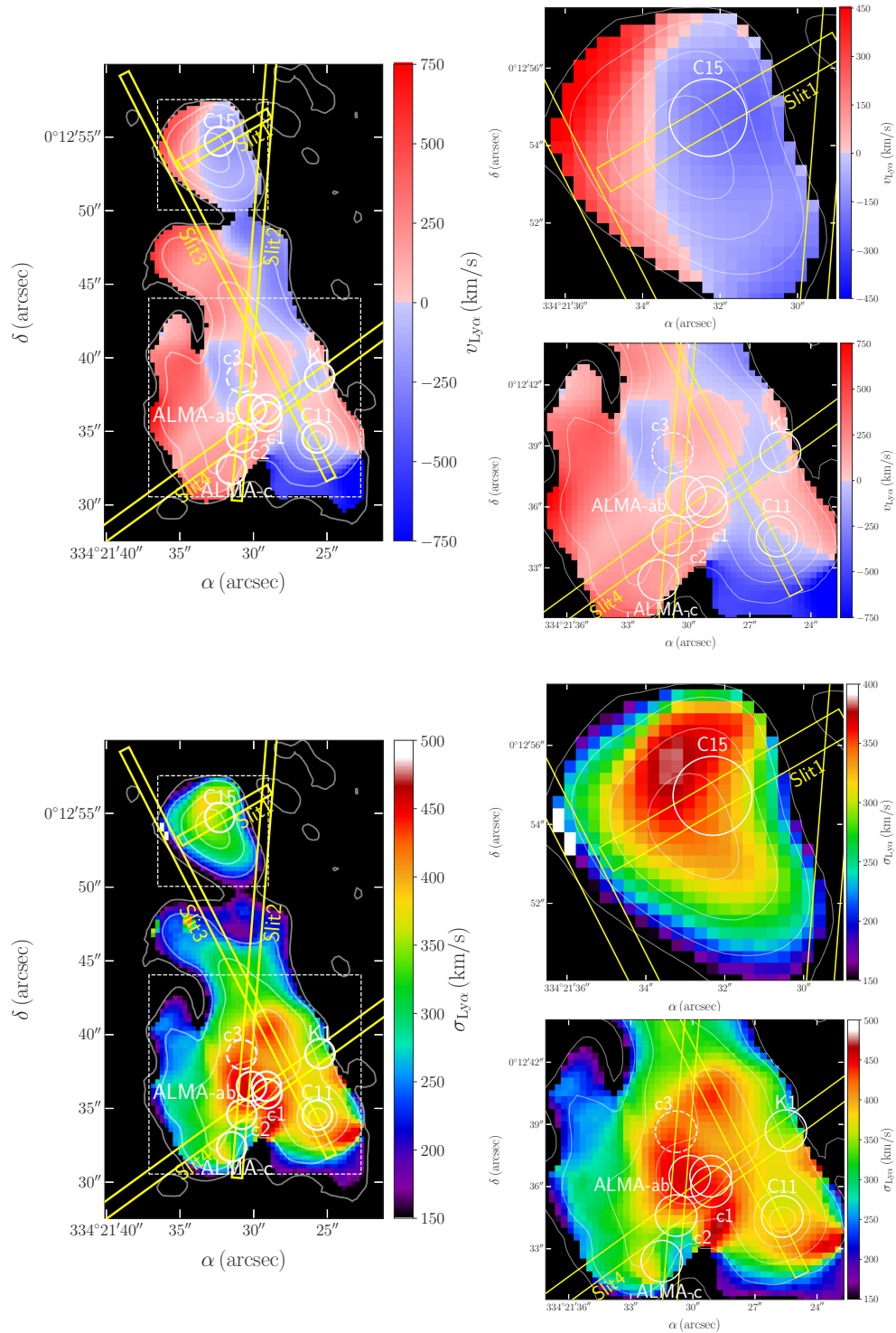


Figure 3.4: **The first ($v_{\text{Ly}\alpha}$) and second ($\sigma_{\text{Ly}\alpha}$) moment maps of LAB1.** The two major Ly α emitting regions have been delineated by rectangular boxes (dashed white lines), and their zooming-in views are shown in the right panels. For the northern region, the colorbar limits have been adjusted accordingly to account for the smaller value range. The positions of the identified continuum sources are indicated by circles with labels. The Ly α SB isophotes (solid white lines) with levels of $\text{SB}_{\text{Ly}\alpha} = [120, 80, 40, 15, 4] \times 10^{-19} \text{ erg s}^{-1} \text{ cm}^{-2} \text{ arcsec}^{-2}$ have also been overlaid onto each image for visual reference.

very broad, highly asymmetric, and have multiple peaks. Some of the profiles (e.g., the northeast corner) are even dominated by a ‘blue peak’, as shown in spectrum 4 in Figure 3.5.

On the $v_{\text{Ly}\alpha}$ map, there is an alternate pattern of positive and negative $v_{\text{Ly}\alpha}$ from the east to the west. Yet again, we see a similar coherent velocity structure that coincides with the high SB ‘tadpole’ structure (see Section 3.3). This structure is also seen on the $\sigma_{\text{Ly}\alpha}$ map, but with a slightly different trend – starting from the south, first going towards northeast, and then turning northwest. The largest $\sigma_{\text{Ly}\alpha}$ values ($\sim 500 \text{ km s}^{-1}$) still overlap with ALMA-a, which indicates that the ALMA source may be responsible for the Ly α line broadening (e.g., via starburst-driven outflows).

Our $v_{\text{Ly}\alpha}$ and $\sigma_{\text{Ly}\alpha}$ maps are qualitatively similar to the ones presented in a recent work by Herenz et al. (2020), albeit with slight differences in the extent of the Ly α emitting regions and the number of spaxels included, due to different FOVs of instruments and S/N threshold choices. The alternate pattern of positive and negative $v_{\text{Ly}\alpha}$ is consistent with the left panel in their Figure 7, and the large $\sigma_{\text{Ly}\alpha}$ values near ALMA-ab sources are consistent with the right panel in their Figure 7.

3.4 Radiative Transfer Modeling Using The Multiphase Clumpy Model

Methodology

Although the moment map analysis above provides a cursory overview of the apparent gas velocity field, it is purely phenomenological and could even be misleading, in the sense that if radiative transfer effects dominate, the observed $v_{\text{Ly}\alpha}$ would not necessarily be linked directly to the local gas kinematics. To gain more physical insight and to account for the possibly important radiative transfer effects, we generated a series of model spectra using MCRT and fit them to the observed Ly α spectra at different positions in LAB1.

Our first attempt was to fit the Ly α profiles using the widely used ‘shell model’ (Verhamme et al., 2006; Dijkstra et al., 2006b). However, as most line profiles are fairly broad and multi-peaked with significant flux close to line center, the fits either fail to reproduce the major features or have inexplicably large intrinsic line widths (see, e.g., Orlitová et al. 2018). Therefore, we adopt a more sophisticated and physically realistic multiphase ‘clumpy model’ instead. As described in Gronke et al. (2016a), the geometric setup of this ‘clumpy model’ is a number of spherical HI clumps moving within a hot ($T \sim 10^{5-7} \text{ K}$), ionized inter-clump medium (ICM)

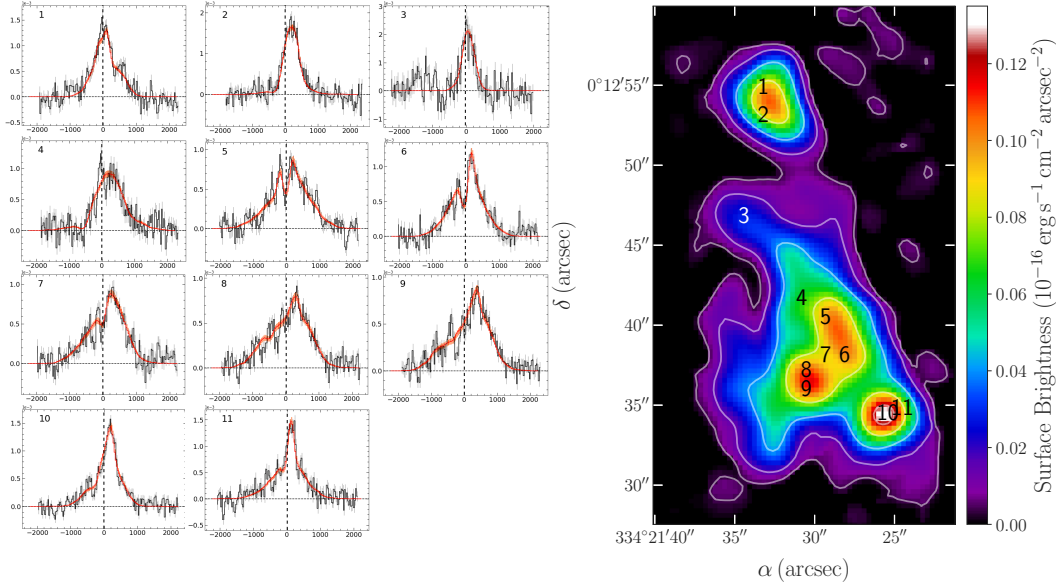


Figure 3.5: Eleven representative continuum-subtracted, spatially resolved Ly α profiles from the high SB regions in LAB1. All the spectra have been smoothed by a $3 \text{ pixel} \times 3 \text{ pixel}$ boxcar ($0.9''$) spatially and Gaussian smoothed ($\sigma = 0.5 \text{ \AA}$) in the wavelength dimension. The multiphase clumpy model best-fits (red, with orange $1\text{-}\sigma$ Poisson errors) and the observed Ly α profiles (black, with grey $1\text{-}\sigma$ error bars) have both been normalized. The observed Ly α spectra have also been shifted by $-\Delta v$ to their local systemic redshifts. For each subpanel, the x -axis is the velocity (in km s^{-1}) with respect to the local systemic redshift, and the y -axis is the normalized line flux. The spectrum number of each spectrum has been marked on the SB map (the right panel). For visual reference, the horizontal and vertical black dashed lines in each subpanel indicate zero flux level and zero velocity with respect to the local systemic redshift, respectively.

(see also Laursen et al., 2013). This model predicts the Ly α spectra produced by a central Ly α emitting source, accounting for the scattering by H I (both in the clumps and the ICM)⁹. It has 14 parameters in total (see the detailed formulation in Gronke et al. 2016a), among which the most important ones are the cloud covering factor (f_{cl}) that describes the mean number of clumps per line-of-sight from the center to the boundary of the simulation sphere, the H I number density in the ICM ($n_{\text{HI, ICM}}$), and kinematic parameters of the clumps and ICM. Specifically, the clump motion is assumed to be a superposition of an isotropic Gaussian random motion (characterized by σ_{cl} , the velocity dispersion of the clumps) and a radial uniform outflow with a constant velocity v_{cl} . In addition, we consider an outflow velocity of

⁹As we will show below, the scattering process washes out the information about the Ly α emitting source, i.e., the initial spatial or spectral shape of the source does not significantly affect the emergent spectra.

Table 3.4: Fitted parameters of the multiphase clumpy model and derived quantities.

No.	RA (J2000)	Dec (J2000)	Fitted Parameters						Derived Parameters		Moments	
			$\log n_{\text{HI,ICM}}$ (cm^{-3})	F_V	σ_{cl} (km s^{-1})	v_{cl} (km s^{-1})	v_{ICM} (km s^{-1})	Δv (km s^{-1})	$f_{\text{cl}}/f_{\text{cl,crit}}$	$\log \tau_{0,\text{ICM}}$	$v_{\text{Ly}\alpha}$ (km s^{-1})	$\sigma_{\text{Ly}\alpha}$ (km s^{-1})
(1)	(2)	(3)	(4)	(5)	(6)	(7)	(8)	(9)	(10)	(11)	(12)	(13)
1	22:17:26.214	+00:12:54.85	$-7.13^{+0.10}_{-0.13}$	$0.37^{+0.15}_{-0.16}$	131^{+167}_{-94}	773^{+26}_{-159}	8^{+19}_{-7}	-195^{+34}_{-49}	$12.8^{+17.2}_{-10.2}$	$0.8^{+0.1}_{-0.1}$	-98.2	373.9
2	22:17:26.214	+00:12:53.05	$-6.47^{+0.40}_{-0.80}$	$0.37^{+0.22}_{-0.25}$	242^{+112}_{-104}	497^{+217}_{-203}	444^{+131}_{-60}	-268^{+60}_{-88}	$0.8^{+1.8}_{-0.7}$	$-3.6^{+1.0}_{-0.8}$	-54.2	324.2
3	22:17:26.294	+00:12:46.75	$-7.01^{+0.88}_{-0.88}$	$0.32^{+0.26}_{-0.21}$	111^{+263}_{-102}	392^{+385}_{-259}	348^{+156}_{-96}	43^{+92}_{-129}	$0.1^{+6.9}_{-0.1}$	$-2.1^{+1.5}_{-2.8}$	193.4	254.1
4	22:17:26.054	+00:12:41.65	$-6.15^{+0.14}_{-0.31}$	$0.18^{+0.25}_{-0.07}$	705^{+91}_{-392}	689^{+108}_{-494}	653^{+123}_{-62}	-200^{+48}_{-90}	$0.7^{+0.7}_{-0.6}$	$-4.2^{+0.2}_{-0.3}$	20.6	339.2
5	22:17:25.954	+00:12:40.45	$-6.94^{+0.09}_{-0.57}$	$0.23^{+0.09}_{-0.03}$	534^{+53}_{-91}	474^{+205}_{-463}	7^{+58}_{-7}	-69^{+139}_{-27}	$2.0^{+1.4}_{-0.4}$	$1.0^{+0.1}_{-0.1}$	81.5	435.2
6	22:17:25.874	+00:12:38.05	$-6.90^{+0.10}_{-0.26}$	$0.18^{+0.04}_{-0.02}$	455^{+48}_{-47}	208^{+234}_{-196}	48^{+46}_{-28}	-66^{+58}_{-32}	$1.8^{+0.5}_{-0.3}$	$1.0^{+0.1}_{-0.4}$	6.2	394.9
7	22:17:25.954	+00:12:38.05	$-7.02^{+0.14}_{-0.90}$	$0.29^{+0.19}_{-0.06}$	437^{+48}_{-41}	376^{+127}_{-188}	16^{+391}_{-15}	-100^{+53}_{-44}	$3.0^{+1.6}_{-0.8}$	$0.9^{+0.1}_{-0.1}$	46.3	402.5
8	22:17:26.034	+00:12:37.15	$-7.90^{+0.53}_{-0.10}$	$0.51^{+0.04}_{-0.05}$	498^{+77}_{-39}	228^{+98}_{-76}	435^{+138}_{-112}	-162^{+61}_{-65}	$4.3^{+0.5}_{-0.8}$	$-4.8^{+2.2}_{-1.0}$	14.6	448.8
9	22:17:26.034	+00:12:35.95	$-7.83^{+0.72}_{-0.16}$	$0.56^{+0.03}_{-0.07}$	475^{+47}_{-31}	276^{+68}_{-123}	425^{+108}_{-108}	-181^{+89}_{-62}	$4.6^{+0.5}_{-0.6}$	$-4.6^{+2.5}_{-1.1}$	54.3	452.9
10	22:17:25.694	+00:12:34.45	$-7.49^{+0.33}_{-0.48}$	$0.28^{+0.15}_{-0.11}$	353^{+110}_{-32}	270^{+75}_{-246}	302^{+91}_{-70}	-135^{+109}_{-73}	$2.8^{+1.1}_{-1.0}$	$-1.9^{+1.1}_{-2.0}$	-19.6	377.1
11	22:17:25.634	+00:12:34.75	$-7.32^{+0.41}_{-0.64}$	$0.19^{+0.33}_{-0.05}$	453^{+95}_{-111}	268^{+309}_{-256}	151^{+260}_{-95}	-9^{+69}_{-180}	$1.9^{+2.6}_{-0.7}$	$0.0^{+0.9}_{-4.3}$	44.7	378.4

Notes. Fitted parameters (averages and 2.5% – 97.5% quantiles, i.e., 2- σ confidence intervals) of the multiphase clumpy model, derived quantities and spectral moments. The columns are: (1) the spectrum number (as marked in Figure 3.5); (2) the right ascension of the center of the extracted region; (3) the declination of the center of the extracted region; (4) the H I number density in the ICM; (5) the cloud volume filling factor; (6) the velocity dispersion of the clumps; (7) the radial outflow velocity of the clumps; (8) the H I outflow velocity in the ICM; (9) the velocity shift relative to $z = 3.1000$ (a negative/positive value means that the model spectrum has been blue/redshifted to match the data); (10) the clump covering fraction (defined as the number of clumps per line-of-sight) normalized by the critical clump covering fraction. In our case $f_{\text{cl}} = 75 F_V$. The critical clump covering fraction, $f_{\text{cl,crit}}$, determines different physical regimes and is calculated via Eq. (3.7) (see Appendix 3.6 for a detailed derivation); (11) the optical depth at the Ly α line center of the H I in the ICM; (12) the first moment of the center of the extracted region; (13) the second moment of the center of the extracted region (corrected for KCWI LSF).

the low density H I in the ICM, v_{ICM} , and a post-processed parameter, the velocity shift with respect to $z = 3.1000$, Δv . This Δv parameter represents the best-fit systemic redshift of the Ly α source function relative to $z = 3.1000$ (the initial guess for the systemic redshift).

Note that Ly α radiative transfer in such a multiphase medium exhibits two characteristic regimes defined by the values of f_{cl} . If f_{cl} is (much) greater than a critical value $f_{\text{cl,crit}}$ (which is a function of other model parameters, such as the kinematics and H I column density of the clumps), the photons would escape as if the medium is homogeneous and the emergent spectra are similar to the ones predicted by the aforementioned ‘shell model’ (Gronke et al., 2017). Otherwise, for fewer clumps per line-of-sight, the photons preferentially travel in the ionized ICM and escape closer to the line center of Ly α . As most of our observed Ly α spectra have consid-

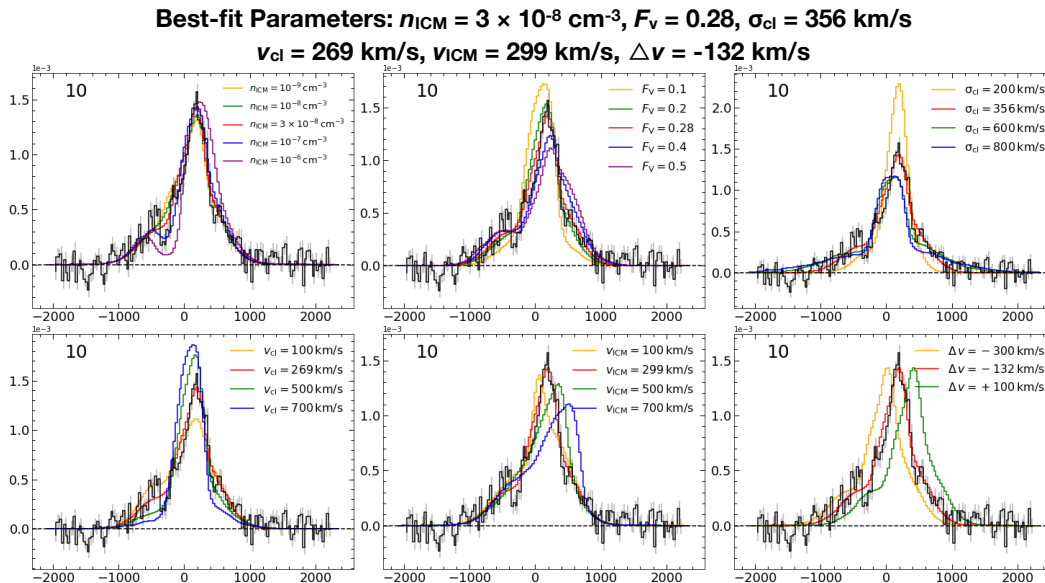


Figure 3.6: **The effects of each individual physical parameter in $[n_{\text{HI,ICM}}, F_V, \sigma_{\text{cl}}, v_{\text{cl}}, v_{\text{ICM}}, \Delta v]$ (taking spectrum 10 as an example).** From the top left to the bottom right panel, one parameter is varied at a time (as shown in lines and labeled with different colors) and others are fixed (to the best-fit parameter values of spectrum 10, see Table 3.4). The red line in each panel represents the best-fit model of spectrum 10. The x -axis is the velocity (in km s^{-1}) with respect to the local systemic redshift of spectrum 10, and the y -axis is the normalized line flux. It can be seen that different parameters affect the model spectra in different ways – $n_{\text{HI,ICM}}$ determines the overall shape and the trough depth of the spectrum; F_V and v_{cl} determine the shapes and strengths of the peak(s); σ_{cl} determines the width of the spectrum; v_{ICM} determines the location of the main peak and the trough; Δv shifts the spectrum in the velocity dimension.

erable flux near the line center, we expect $f_{\text{cl}} \lesssim f_{\text{cl,crit}}$ in our cases, and will focus on that regime¹⁰.

Based on these considerations, we further construct a five-dimensional hypercubic grid by varying five crucial physical parameters: $[\log n_{\text{HI,ICM}}, F_V, \sigma_{\text{cl}}, v_{\text{cl}}, v_{\text{ICM}}]$ ¹¹. The prior ranges of $\log n_{\text{HI,ICM}}$ (cm^{-3}), F_V and $[\sigma_{\text{cl}}, v_{\text{cl}}, v_{\text{ICM}}]$ (km s^{-1}) are $[-8, -6]$, $[0.1, 0.6]$ and $[0, 800]$ (with spacings of 0.4, 0.1 and 100), respectively. We fix the subdominant parameters, such as the ICM temperature T_{ICM} to 10^6 K, and the clump column density to 10^{17} cm^{-2} in order to reduce the dimensionality of the parameter

¹⁰Note that the model spectra are sensitive to $\sim f_{\text{cl}}/f_{\text{cl,crit}}$ but not to certain individual model parameters, such as the HI column density or the shape of the clumps (Hansen et al., 2006).

¹¹For convenience we vary F_V rather than f_{cl} when generating clumps, but they are directly related via $f_{\text{cl}} = 3r_{\text{gal}}/4r_{\text{cl}} F_V$, where $r_{\text{gal}} = 5 \text{ kpc}$ is the radius of the simulation sphere and $r_{\text{cl}} = 50 \text{ pc}$ is the clump radius (hence $f_{\text{cl}} = 75 F_V$ in our case).

space¹².

Such a configuration amounts to 26244 models in total. Each model is calculated via radiative transfer using 10000 Ly α photon packages generated from a Gaussian intrinsic spectrum $N(0, \sigma_{\text{cl}}^2)$, where $\sigma_{\text{cl}} = 12.85 \text{ km s}^{-1}$ is the canonical thermal velocity dispersion of $T = 10^4 \text{ K}$ gas¹³. The sixth parameter, Δv , is varied continuously in post-processing. To properly explore the multimodal posterior of the parameters, we further use a python nested sampling package `dynesty` (Skilling, 2004; Skilling, 2006; Speagle, 2020) to fit the Ly α spectra.

To demonstrate the feasibility of this fitting routine using clumpy models, we selected eleven representative Ly α spectra from the high SB regions, as shown in Figure 3.5. All of the spectra presented have been smoothed spatially by a 3 pixel \times 3 pixel boxcar and were extracted by using an $R = 3$ pixel (0.9'') aperture. For each spectrum, we used 1500 live points (the initial randomly drawn samples from the prior) to calculate a set of clumpy models via linear flux interpolation on the grid and convolved with the KCWI LSF before comparing them to the observed Ly α profiles. The best-fit spectra are also shown in Figure 3.5.

Results

In Figure 3.5, one can see that most of the model fits match the observations reasonably well. The values of the fitted parameters are presented in Table 3.4. We find that different parameters affect the model spectra in different ways – $n_{\text{HI,ICM}}$ determines the overall shape of the spectrum and the depth of the intensity minimum near the systemic velocity (the ‘trough’); F_V and v_{cl} determine the shapes and strengths of the peak(s); σ_{cl} determines the width of the spectrum; v_{ICM} determines the location of the main peak and the trough; Δv shifts the spectrum in the velocity dimension. In Figure 3.6, we illustrate the impact of each parameter on the emergent model spectrum. Each parameter was varied individually while others were kept fixed to the best-fit parameter values.

Specifically, spectra 1 and 2 (near the LBG C15) are clearly single-peaked, although spectrum 1 has a subdominant red bump. Interestingly, although spectrum 1 appears to be broader and has a larger $\sigma_{\text{Ly}\alpha}$ on the moment map, it actually requires

¹²Here we modeled each observed spectrum with a set of parameters of the scattering medium independently, whereas in reality the Ly α photons are likely to be scattered by a common medium with spatially varying parameters. The application of a more advanced, self-consistent model is beyond the scope of this work but will be explored in the future.

¹³Note that we did not employ the commonly used ‘core-skipping’ technique, as it may cause artifacts in a multiphase medium.

a smaller σ_{cl} ($\sim 150 \text{ km s}^{-1}$) than spectrum 2. The fit of spectrum 1 has a very large v_{cl} ($\sim 800 \text{ km s}^{-1}$) and a negligible v_{ICM} , whereas the fit of spectrum 2 has comparable v_{cl} and v_{ICM} (both $\sim 500 \text{ km s}^{-1}$). This is due to the fact that multiphase outflows increase the asymmetry as well as the width of the spectra, and this degeneracy is not captured by the moment analysis. In particular, for spectrum 1, the optical depth at the Ly α line center $\tau_{0,\text{ICM}}^{14} \sim 1$, so the Ly α photons likely interact with the ICM prior to the clumps (as opposed to spectrum 2 where $\tau_{0,\text{ICM}} \ll 1$). This implies that photons can then scatter approximately orthogonally off the clumps (see Appendix 3.6), which yields an additional broadening of the spectrum that is larger than σ_{cl} . The derived Δv ($\sim -200 \text{ km s}^{-1}$) is also consistent with the C15 systemic redshift ($z = 3.0975$) measured from [O III]. Also note that although spectrum 1 exhibits a blue dominant peak and a smaller red ‘hump’ (which is commonly interpreted as a signature of inflows), our outflow model has successfully reproduced the observed line profile.

Spectrum 3 has a fairly narrow main peak, which yields the lowest σ_{cl} ($\sim 100 \text{ km s}^{-1}$) of all eleven sampled spectra. The fit has comparable v_{cl} and v_{ICM} (both $\sim 350 \text{ km s}^{-1}$) and a small Δv ($\sim 50 \text{ km s}^{-1}$). It also has some dubious emission on the far blue side, which is not captured by the clumpy models. Increasing σ_{cl} in order to include both the red and blue peaks could potentially provide a better fit but would lack physical motivation.

Spectra 4 and 5 (the tail of the tadpole) both possess two comparable peaks and a trough in the middle. The best-fit of the former is single-peaked, while the latter is double-peaked and captured the trough. Both fits have very large σ_{cl} ($> 500 \text{ km s}^{-1}$) to account for the line widths. The fit of spectrum 4 has comparably large v_{cl} and v_{ICM} (both $\sim 700 \text{ km s}^{-1}$), whereas spectrum 5 has a v_{cl} of $\sim 500 \text{ km s}^{-1}$ and a negligible v_{ICM} .

Spectra 6 and 7 (the body of the tadpole) are both multi-peaked and dominated by a red peak. The best-fits both have $\sigma_{\text{cl}} \sim 450 \text{ km s}^{-1}$. They have moderate v_{cl} (~ 200 and 400 km s^{-1} , respectively) and small $v_{\text{ICM}} < 50 \text{ km s}^{-1}$ (dictated by the location of the absorption features).

Spectra 8 and 9 (the head of the tadpole, near ALMA-a) are both very broad ($\sigma_{\text{cl}} \sim 500 \text{ km s}^{-1}$) and red-dominant double-peaked with a deep trough between two

¹⁴Here $\tau_{0,\text{ICM}} = n_{\text{HI,ICM}} r_{\text{gal}} \sigma_{\text{HI}}(T_{\text{ICM}}, v_{\text{ICM}})$, where $\sigma_{\text{HI}}(T_{\text{ICM}}, v_{\text{ICM}})$ is the Ly α absorption cross-section at HI temperature T_{ICM} and velocity v_{ICM} .

peaks. They both have high F_V (~ 0.5) and moderate v_{cl} ($\sim 250 \text{ km s}^{-1}$) and v_{ICM} ($\sim 400 \text{ km s}^{-1}$).

Spectra 10 and 11 (near the LBG C11) are also red-dominant double-peaked, although with slightly narrower line widths ($\sigma_{\text{cl}} \sim 400 \text{ km s}^{-1}$). Compared with spectra 8 and 9, they have lower F_V (< 0.3), comparable v_{cl} ($\sim 250 \text{ km s}^{-1}$) and lower v_{ICM} ($< 300 \text{ km s}^{-1}$). The derived Δv of spectrum 10 ($\sim -150 \text{ km s}^{-1}$) is also consistent with the C11 systemic redshift ($z = 3.0980 \pm 0.0001$) measured from [O III]. Notably, the prominent double peak profiles in this region require a considerable outflow velocity for both the clumps and the ICM. This strongly suggests the presence of outflows, which is consistent with the indication of the large global velocity offsets between Ly α , [O III] and Si II.

It is noteworthy that although the observed $v_{\text{Ly}\alpha}$ is fairly small in many positions (e.g., spectra 4 – 9), large σ_{cl} , v_{cl} and non-zero v_{ICM} are still preferred by the broad, asymmetric Ly α profiles¹⁵. This concerns us that the first moment does not fully capture the gas kinematic information encoded in the Ly α profiles. Second moments may be helpful in quantifying the line widths, whose possible physical interpretation is the random velocity dispersion of H I clumps. Furthermore, the outflow velocity (parameterized as v_{cl} and v_{ICM} in the model) may be difficult to determine directly from the observed spectra (especially for complex Ly α profiles), but might be retrieved using realistic radiative transfer modeling.

In addition, we note that both the average and the standard deviation of all the derived Δv are fairly small ($\langle \Delta v \rangle = -122 \text{ km s}^{-1}$, $\sigma(\Delta v) = 87 \text{ km s}^{-1}$), despite the large outflow velocities indicated by many of the Ly α profiles. This corresponds to an average systemic redshift of LAB1, $\langle z_{\text{sys}} \rangle = 3.0983 \pm 0.0004$.

We caution that the effect of Ly α absorption from the intergalactic medium (IGM) is not modeled in this work. It is expected that at $z \sim 3$ this effect is in general non-negligible on the blue side of the spectrum (Dijkstra et al., 2007; Laursen et al., 2011). However, we do not expect the effect of the IGM to be significant here, as it would cause sharp absorption troughs and yield multiple peaks, which should be clearly visible given the widths of the observed spectra (see Byrohl et al., 2020 for a discussion of this effect) instead of simply attenuating the spectrum smoothly.

To recap, the main results of our analysis are:

¹⁵This is also notable in cases where an [O III] measurement is available and the velocity offset between Ly α and [O III] is close to zero (e.g., spectra 1 and 2).

1. The observed Ly α spectra require relatively few clumps per line-of-sight ($f_{\text{cl}} \lesssim f_{\text{cl,crit}}$) as they have significant fluxes at the line center. Therefore, they are very different from the spectra of most Ly α emitting *galaxies* at essentially all redshifts (e.g., Steidel et al. 2010; Erb et al. 2014; Trainor et al. 2015; Yang et al. 2016; Yang et al. 2017; Gronke 2017; Orlitová et al. 2018), which can usually be reproduced by a uniform medium (e.g., the ‘shell model’)¹⁶ or by a multiphase medium with a large number H I clumps ($f_{\text{cl}} \gg f_{\text{cl,crit}}$).
2. The velocity dispersion of the scattering clumps yields a broadening of the spectra from the intrinsic line width $\sigma_i \sim 13 \text{ km s}^{-1}$ to $\gg 100 \text{ km s}^{-1}$ as observed. This is possible when $f_{\text{cl}} \sim \alpha f_{\text{cl,crit}}$ with $\alpha \sim$ a few¹⁷. Such a process may be crucial in galaxies where the observed Ly α line is always broader, usually by at least a factor of two, than the corresponding non-resonant lines such as [O III], H α or H β (e.g., Orlitová et al., 2018).
3. While the widths of the spectra are set primarily by the velocity dispersion of the clumps, i.e., $\sigma_{\text{Ly}\alpha} \sim \sigma_{\text{cl}}$, we found that the clump bulk outflow can also cause additional broadening, as seen in spectrum 1. In this case, one might naively assume that the photons do not interact with the clumps due to their large velocity offsets ($v_{\text{cl}} \gg \sigma_{\text{cl}}$). However, if $\tau_{0,\text{ICM}} \gtrsim 1$, the photons may first interact with the ICM, which significantly reduces the parallel component of v_{cl} ($v_{\text{cl},\parallel}$) appearing to the photons, and hence greatly increases the optical depth. This result suggests that we may have interpreted our model too naively (e.g., using single-scattering approximation), especially considering that the kinematics of our model are clearly simplistic and not strictly hydrodynamically stable (we usually expect $v_{\text{cl}} \sim v_{\text{ICM}}$, i.e., the clouds are entrained by the local flow, see, e.g., Klein et al. 1994; Li et al. 2020)¹⁸. Moreover, although we found that significant outflow velocities ($\gtrsim 100 \text{ km s}^{-1}$) are required to reproduce the observed spectra, the exact values may still be subject to considerable uncertainties, due to the internal degeneracies and the presumably more complicated kinematics in reality (e.g., Steidel et al. 2010 show that gas outflows even within the same galaxy have a range of velocities that goes from 0 to 800 km s^{-1} with varying effective optical depths).

¹⁶The success of shell model fitting may no longer be achieved when the model parameters are further constrained by additional observations (e.g., optical emission lines or UV absorption lines, see Orlitová et al. 2018).

¹⁷Note that the scattering off the surface of the clumps broadens the spectrum as long as $\sigma_{\text{cl}} > \sigma_i$ (and $f_{\text{cl}} \sim f_{\text{cl,crit}}$). Hence, the emergent spectra are insensitive to the exact value of σ_i .

¹⁸We do see $v_{\text{cl}} \sim v_{\text{ICM}}$ in our fits of spectra 3, 4, 5, 10 and 11.

4. In our best-fit spectra, the H I in the ICM is responsible for the absorption feature close to the line center (cf. spectrum 5 or 6). However, several tentative absorption features can be present in a single spectrum (e.g., spectra 5, 6, 7 and 9), and they are not captured simultaneously by our model. These multiple features might be caused by the H I in the outer CGM / IGM, where the probability of back-scattering into the line-of-sight is negligible.

The derived values of our fitted parameters also fit into a broader picture in at least two ways:

1. The σ_{cl} values correspond to reasonable dark matter halo masses. The dynamical mass of the LAB1 halo can be estimated from the velocity dispersion and physical size (assuming spherical symmetry):

$$M_{\text{dyn}} = \frac{3\sigma_{\text{cl}}^2 R}{G} = 6.9 \times 10^9 \left(\frac{\sigma_{\text{cl}}}{100 \text{ km s}^{-1}} \right)^2 \left(\frac{R}{\text{kpc}} \right) M_{\odot}. \quad (3.3)$$

Taking $R \sim 100$ kpc, the highest σ_{cl} ($\sim 700 \text{ km s}^{-1}$) corresponds to $M_{\text{dyn}} \sim 10^{13.5} M_{\odot}$. This result is consistent with the predicted halo masses from the Millennium simulations at $z = 3.06$. As calculated by Kubo et al. (2016), the halo masses range from $10^{12.2}$ to $10^{14.0} M_{\odot}$ (with median $10^{13.2} M_{\odot}$) for the De Lucia et al. (2007) model, and from $10^{12.4}$ to $10^{14.1} M_{\odot}$ (with median $10^{13.2} M_{\odot}$) for the Guo et al. (2011) model.

2. The v_{cl} values correspond to reasonable survival times of the clumps. Here we consider two different criteria proposed by Li et al. (2020) and Gronke et al. (2018), respectively. Following Li et al. (2020), assuming the ionized medium has H II number density $n_{\text{hot}} = 0.01 \text{ cm}^{-3}$, an outflow velocity $v_{\text{cl}} \sim 500 \text{ km s}^{-1}$ corresponds to a cloud lifetime $t_{\text{life}} \sim 100 \text{ Myr}$. The cooling time of the hot medium, $t_{\text{cool,h}} \sim 30 \text{ Myr} \leq t_{\text{life}}$. Whereas following Gronke et al. (2018), the cooling time of the mixing layer $t_{\text{cool,mix}} \sim 3 \text{ Myr}$, and the cloud-crushing time $t_{\text{cc}} \sim 1 \text{ Myr} \simeq t_{\text{cool,mix}}$, which implies possible survival of the cold gas. So either criterion indicates that the clumps can survive for a fairly long time, and may even grow in mass as they accrete the cooling hot material from the ambient medium.

Recently, Herenz et al. (2020) have reported a significant detection of He II $\lambda 1640$ emission in three regions of LAB1 (which are close to C15, the tail of the tadpole

structure, and C11, respectively) as well as a non-detection of C IV $\lambda\lambda 1548, 1550$ doublet. They have carried out a detailed analysis and concluded that their observed He II/Ly α and C IV/Ly α ratios are consistent with cooling radiation, feedback-driven shocks, and/or photo-ionization from an embedded AGN. We examined our MOSFIRE spectra around these regions but did not find additional rest-UV collisionally excited emission lines near Ly α that are significant, although we do see significant outflow velocities in these three regions (cf. spectra 1, 2, 5, 10, and 11). More observations are needed to distinguish these different powering mechanisms.

In summary, the multiphase clumpy model is versatile enough to reproduce the diverse Ly α morphologies observed. The fitting results are still, not surprisingly, model dependent – different assumptions on the geometry and moving pattern of the H I gas may yield different results. Furthermore, our modeling with parameters of scattering medium varying independently at different locations can be handled in a more self-consistent manner, as in reality the Ly α photons are likely to be scattered by a common, spatially varying medium. Nonetheless, our analysis is a first attempt to model the spatially resolved Ly α profiles in LAB1 with more physically realistic clumpy models. It provides us with insights on the gas kinematics and will serve as the foundation of more advanced radiative transfer modeling in the future. One promising future direction is to use more elaborate clump velocity profiles (e.g., consistent with absorption line observations) which can alter $f_{\text{cl,crit}}$ (cf. Appendix 3.6). We will explore such new physical regimes in our future work.

3.5 Conclusions

We have carried out deep spectroscopic observations of SSA22-LAB1 at $z = 3.1$ using KCWI and MOSFIRE. The main conclusions of our analysis are:

1. By applying matched filtering to the KCWI datacube, we have created a narrow-band Ly α image of LAB1. The most prominent feature is a tadpole-shaped structure, whose ‘head’ overlaps with one of the ALMA sources yet whose ‘tail’ does not associate with any identified sources;
2. By comparing the spatial distributions and intensities of Ly α and H β , we find that recombination of photo-ionized H I gas followed by resonant scattering is sufficient to explain all the observed Ly α /H β ratios;
3. Using both moment map analysis and MCRT modeling, we have managed to extract physical information from the spatially resolved Ly α profiles. We

find that moment maps can be used as a crude indicator of the H I gas kinematics, but realistic MCRT modeling needs to be invoked to extract detailed kinematic information and make physical interpretations. By fitting a set of multiphase, ‘clumpy’ models to the observed Ly α profiles, we are able to reasonably constrain many physical parameters, namely the H I number density in the ICM, the cloud volume filling factor, the random velocity and outflow velocity of the clumps, the H I outflow velocity of the ICM and the local systemic redshift. Our model has successfully reproduced the diverse Ly α morphologies at different locations, and the main results are: (1) The observed Ly α spectra require relatively few clumps per line-of-sight ($f_{\text{cl}} \lesssim f_{\text{cl,crit}}$) as they have significant fluxes at the line center; (2) The velocity dispersion of the scattering clumps yields a significant broadening of the spectra as observed; (3) The clump bulk outflow can also cause additional broadening if $\tau_{0,\text{ICM}} \gtrsim 1$. In that case, the photons may first interact with the ICM, which significantly reduces the parallel component of clump outflow velocity appearing to the photons, and hence greatly increases the optical depth of the clumps; (4) The H I in the ICM is responsible for the absorption feature close to the Ly α line center.

We caution that there are still a number of caveats to this study. For example, our MCRT modeling is inherently model dependent, in particular on the specific assumptions about the kinematics of the cold clumps. A combination of results from hydrodynamical simulations and additional observations (e.g., absorption line studies) may help constrain the actual gas kinematics better. We intend to explore these possibilities in our future work.

Acknowledgements

ZL thanks Phil Hopkins for providing us with adequate computational resources. ZL acknowledges Michael Zhang, for his professional guidance and kind company during the excruciating debugging process. The data presented herein were obtained at the W. M. Keck Observatory, which is operated as a scientific partnership among the California Institute of Technology, the University of California and the National Aeronautics and Space Administration. The Observatory was made possible by the generous financial support of the W. M. Keck Foundation. We are also grateful to the dedicated staff of the W.M. Keck Observatory who keep the instruments and telescopes running effectively. MG was supported by NASA through the

NASA Hubble Fellowship grant HST-HF2-51409 awarded by the Space Telescope Science Institute, which is operated by the Association of Universities for Research in Astronomy, Inc., for NASA, under contract NAS5-26555. Numerical calculations were run on the Caltech compute cluster “Wheeler”, allocations from XSEDE TG-AST130039 and PRAC NSF.1713353 supported by the NSF, and NASA HEC SMD-16-7592. This research made use of Montage. It is funded by the National Science Foundation under Grant Number ACI-1440620, and was previously funded by the National Aeronautics and Space Administration’s Earth Science Technology Office, Computation Technologies Project, under Cooperative Agreement Number NCC5-626 between NASA and the California Institute of Technology.

3.6 Appendix

Gaussian Fits to the [O III] Profiles of LBGs C11 and C15

In order to determine the systemic redshifts of two LBGs, C11 and C15, we fitted the [O III] profiles (5008.24 Å) with single Gaussians. The [O III] emission is spatially integrated over the ranges indicated by black solid arrows in Figure 3.3, which include all the significant [O III] emission of C11 and C15.

We used the `PySpecKit` package (Ginsburg et al., 2011) to fit the [O III] profiles with a single Gaussian model:

$$F_\lambda = F_0 e^{-\frac{(\lambda-\lambda_0)^2}{2\sigma^2}} \quad (3.4)$$

The fitting results and derived values with 1- σ uncertainties of the free parameters (F_0 , λ_0 and σ) are shown in Figure 3.7. The systemic redshifts of C11 and C15 are therefore determined to be $z(\text{C11}) = 3.0980 \pm 0.0001$, $z(\text{C15}) = 3.0975 \pm 0.0001$ (accounting for the typical redshift precision achieved by MOSFIRE measurements reported in Steidel et al. 2014).

Derivation of the Critical Clump Covering Fraction

Here we analytically derive the critical clump covering fraction, $f_{\text{cl,crit}}$, for a multiphase medium whose kinematics have been defined earlier in this work, i.e., H I clumps with a constant outflow velocity v_{cl} and a velocity dispersion σ_{cl} , and an inter-clump medium (ICM) with a constant outflow velocity v_{ICM} . The optical depth of the H I in the ICM at the Ly α intrinsic frequency is approximated as $\tau_{0,\text{ICM}}$, i.e.,

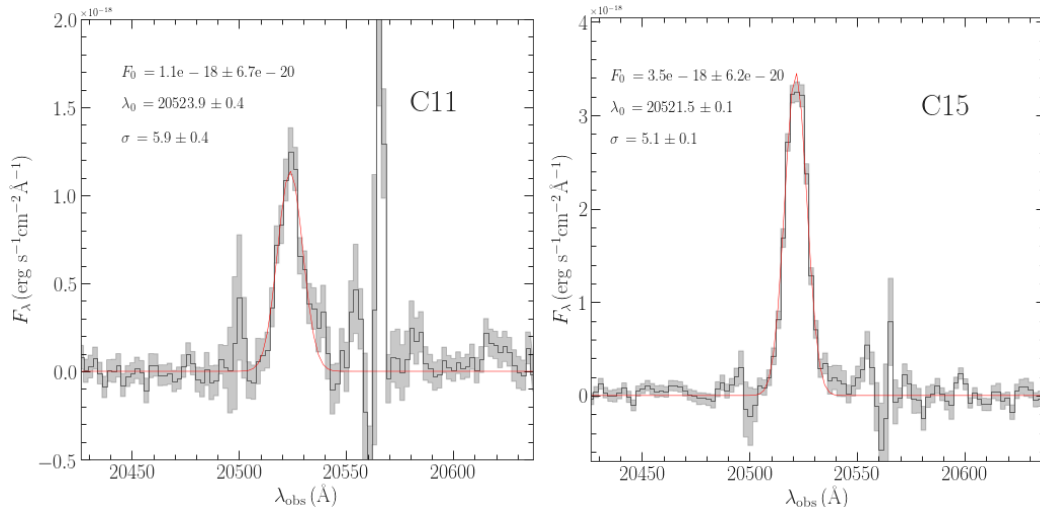


Figure 3.7: **Single Gaussian fits to the observed [O III] profiles of two LBGs, C11 and C15.** The [O III] emission is spatially integrated over the ranges indicated by black solid arrows in Figure 3.3, which include all the significant [O III] emission of C11 and C15. The observed fluxes (shown in black) with $1-\sigma$ uncertainties (shaded in grey), the best-fit model (shown in red) and best-fit parameters (with $1-\sigma$ uncertainties) are shown in each panel. Note that skylines are present near the [O III] lines, as indicated by large flux uncertainties.

the optical depth at the line center¹⁹.

The large widths of the observed spectra imply that photons escape in a single long flight, after they have been scattered off the surface of a fast moving clump (Gronke et al., 2017). It follows that $f_{\text{cl,crit}}$ is given by the condition that on average one clump interacts with a photon at its intrinsic frequency.

The width in velocity space of each clump, \tilde{v} , is determined by:

$$\tau_{\text{cl}}(\pm\tilde{v}/2) = \frac{4}{3} N_{\text{HI,cl}} \sigma_{\text{HI}}(\pm\tilde{v}/2) = 1 \quad (3.5)$$

where τ_{cl} is the optical depth of the clump, $N_{\text{HI,cl}}$ is the H I column density of the clump, and σ_{HI} is the Ly α cross section of the clump. The factor $4/3$ is simply due to the spherical geometry of the clump. Using the core approximation of the Ly α cross section ($\sigma_{\text{cl}}(v) \propto \exp(-v^2/v_{\text{th}}^2)$), the solution to Eq. (3.5) can be explicitly written as $\tilde{v} = 2v_{\text{th}}\sqrt{\ln \tau_{0,\text{cl}}}$, where $\tau_{0,\text{cl}} \equiv \tau_{\text{cl}}(v=0)$, and v_{th} is the thermal velocity dispersion of H I within the clumps. For the H I column density and temperature of the clumps used in this work, $\tilde{v} \simeq 78 \text{ km s}^{-1}$.

¹⁹Technically speaking, the optical depth of the H I in the ICM is expressed as $\int dv f_i(v) \tau_{\text{ICM}}(v)$ where $f_i(v)$ is the normalized intrinsic spectrum as a function of velocity. As our intrinsic spectrum is very narrow, this approximation holds.

Under the assumption that all photons are injected at the Ly α line center (which is a reasonable approximation for our setup since the width of the intrinsic spectrum $\sigma_i \ll \sigma_{cl}$), the average number of clumps per line-of-sight that intersect with $v = 0$ in velocity space is:

$$\tilde{f}_{cl} = f_{cl} \int_{-\tilde{v}}^{\tilde{v}} \mathcal{N}(v, \mu = v_{cl,||}, \sigma = \sigma_{cl}) dv \quad (3.6)$$

where \mathcal{N} denotes the normal distribution assumed for the velocity distribution of the clumps²⁰. Here $v_{cl,||}$ is a component of v_{cl} that is parallel to the trajectories of photons. The reason for considering $v_{cl,||}$ rather than v_{cl} is explained below.

Given the considerations above, demanding $\tilde{f}_{cl} = 1$ yields the critical number of clumps per line-of-sight (i.e., the clump covering fraction):

$$f_{cl,crit} = \frac{2}{\operatorname{erf}\left(\frac{-v_{cl,||} + 2v_{th}\sqrt{\ln \tau_{0,cl}}}{\sqrt{2}\sigma_{cl}}\right) + \operatorname{erf}\left(\frac{v_{cl,||} + 2v_{th}\sqrt{\ln \tau_{0,cl}}}{\sqrt{2}\sigma_{cl}}\right)}. \quad (3.7)$$

where $\operatorname{erf}(x)$ is the Gauss error function.

Note that this equation is a generalization of equation (12) in Gronke et al. (2017), where the radial velocity distribution of the clumps is approximated as a tophat profile. It converges to that equation when $v_{cl,||} \ll \sigma_{cl}$. For $v_{cl,||} \gg \sigma_{cl}$, this equation yields very large values of $f_{cl,crit}$.

Here we discuss $v_{cl,||}$ for two different cases: (1) If $\tau_{0,ICM} \ll 1$, initially the photons do not interact with the ICM. Therefore, $v_{cl,||} \approx v_{cl}$; (2) If $\tau_{0,ICM} \sim 1$ (up to a few), the photons can interact with the ICM prior to the clumps, and thus are likely to scatter orthogonally to the clump bulk outflow. Therefore, $v_{cl,||} \approx 0$ (with details depending on the exact value of $\tau_{0,ICM}$ and the clump distribution). We do not consider $\tau_{0,ICM} \gg 1$ cases, where the multiphase, clumpy medium converges to a homogeneous medium that would fail to reproduce the observed spectra presented in this work (cf. discussion in §3.4).

Justification of Using Spatially Integrated Models to Fit the Spatially Resolved Ly α Profiles

In this work, we have fitted spatially resolved Ly α profiles with spatially integrated models, which are derived from Ly α photons from the entire scattering region. Here

²⁰This choice is purely for practical purpose – in principle it can be replaced by any physically reasonable velocity distribution.

we emphasize that qualitatively, these spatially integrated models are very similar to the binned models, which are derived from Ly α photons within a certain impact parameter range.

We illustrate this in Figure 3.8. With spectra 1 and 2 as two examples, we binned all the scattered photons according to their impact parameters, b (the projected distance to the simulation center perpendicular to the line-of-sight). Assuming the largest impact parameter of all the photons is b_{\max} , we made three photon bins within the 2σ range ($0.05 < b/b_{\max} \leq 0.35$, $0.35 < b/b_{\max} \leq 0.65$ and $0.65 < b/b_{\max} \leq 0.95$) and constructed three binned model spectra with these photon bins respectively. It can be seen the binned models are qualitatively very similar to the integrated model. Therefore, it is approximately correct to model the spatially resolved profiles at positions away from the Ly α emitting sources with spatially integrated models.

The aim of our modeling in this work is to roughly extract the velocities and densities of HI that the Ly α photons ‘experience’ in-situ. In our following work, we plan to model the spatially resolved profiles in a more self-consistent way (e.g., modeling the spatially resolved Ly α profiles with a common scattering medium).

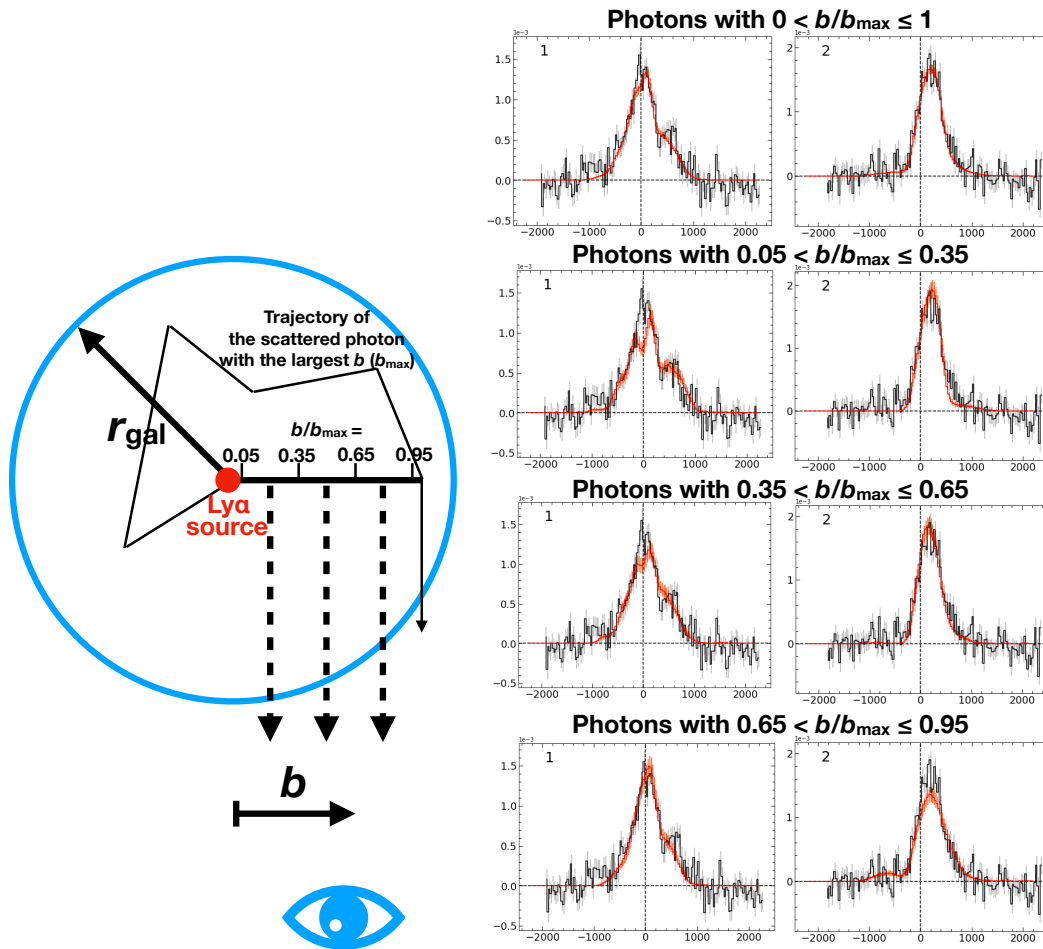


Figure 3.8: **Justification of using spatially integrated models to fit the spatially resolved $\text{Ly}\alpha$ profiles.** *Left:* Configuration of the multiphase, clumpy model and the way we construct our photon bins for the observer. *Right:* Comparison of integrated models and binned models for spectra 1 and 2. Assuming the largest impact parameter of all the photons is b_{\max} , we made three photon bins within the 2σ range ($0.05 < b/b_{\max} \leq 0.35$, $0.35 < b/b_{\max} \leq 0.65$ and $0.65 < b/b_{\max} \leq 0.95$) and constructed three binned model spectra with these photon bins respectively. It can be seen the binned models are qualitatively very similar to the integrated model.

Chapter 4

WHERE OUTFLOWS MEET INFLOWS: GAS KINEMATICS IN
SSA22 LYMAN- α BLOB 2 DECODED BY ADVANCED
RADIATIVE TRANSFER MODELING

Li, Zhihui, Charles C. Steidel, Max Gronke, et al. (July 2022). “Where outflows meet inflows: gas kinematics in SSA22 Ly α blob 2 decoded by advanced radiative transfer modelling”. In: *MNRAS* 513.3, pp. 3414–3428. DOI: 10.1093/mnras/stac958. arXiv: 2104.10682 [astro-ph.GA].

4.1 Introduction

Lyman- α blobs (LABs) – spatially extended (projected sizes $\gtrsim 100$ kpc) gaseous nebulae with tremendous Ly α luminosities ($L_{\text{Ly}\alpha} \sim 10^{43-44}$ erg s $^{-1}$) seen at high redshifts ($z \gtrsim 2$) – are among the most mysterious and intriguing objects in the universe. Thus far, numerous LABs have been discovered via narrow-band imaging or in galaxy surveys (e.g., Francis et al. 1996; Fynbo et al. 1999; Keel et al. 1999; Steidel et al. 2000; Matsuda et al. 2004; Matsuda et al. 2011; Dey et al. 2005; Saito et al. 2006; Smith et al. 2007; Hennawi et al. 2009; Ouchi et al. 2009; Prescott et al. 2009; Prescott et al. 2012; Erb et al. 2011; Cai et al. 2017), yet their physical origin remains obscure. It is found that LABs are preferentially located in overdense protocluster regions, which are expected to be the progenitors of the massive galaxy clusters observed today (e.g., Steidel et al. 1998; Prescott et al. 2008; Yang et al. 2009; Yang et al. 2010; Hine et al. 2016a). Therefore, the study of LABs may illuminate the formation and evolution of massive galaxies and the mechanisms of associated feedback events.

Up to now, many hypotheses about the powering mechanisms of LABs have been proposed, including: (1) Photo-ionization by central energetic sources (starburst galaxies or AGNs, see, e.g., Haiman et al. 2001; Cantalupo et al. 2005; Cantalupo et al. 2014). This scenario gained credence from infrared and submillimeter observations that discovered luminous galaxies and AGNs associated with some LABs (Chapman et al., 2001; Dey et al., 2005; Geach et al., 2005; Geach et al., 2007; Geach et al., 2009; Colbert et al., 2006; Webb et al., 2009). (2) Starburst-induced, shock-powered galactic-wide outflows (‘superwinds’, see, e.g., Heckman et al. 1990; Taniguchi et al. 2000; Taniguchi et al. 2001; Mori et al. 2004). This

scenario has been corroborated by the observed redward asymmetric Ly α profiles (Dawson et al., 2002; Ajiki et al., 2002) and shell-like or bubble-like structures (Matsuda et al., 2004; Wilman et al., 2005). (3) Gravitational cooling radiation from accretion of cold gas streams onto protogalaxies (e.g., Haiman et al. 2000; Fardal et al. 2001; Furlanetto et al. 2005; Dijkstra et al. 2006a; Dijkstra et al. 2006b; Goerdt et al. 2010; Faucher-Giguère et al. 2010; Rosdahl et al. 2012). This scenario may be preferred for LABs that appear to lack powerful sources despite deep multi-wavelength observations and exhibit blueward asymmetric Ly α profiles (Nilsson et al., 2006; Smith et al., 2007; Saito et al., 2008; Smith et al., 2008; Daddi et al., 2021). (4) Resonant scattering of Ly α photons (e.g., Dijkstra et al. 2008; Steidel et al. 2010; Steidel et al. 2011). As resonant scattering imposes polarization, recent polarimetric observations and simulations have provided evidence of scattering within LABs, albeit with remaining uncertainties (Dijkstra et al., 2009; Hayes et al., 2011; Beck et al., 2016; Trebitsch et al., 2016; Eide et al., 2018; Kim et al., 2020).

To further distinguish these different powering mechanisms, it is beneficial to study spatially resolved Ly α spectra, which are made possible by the outstanding capabilities of recently commissioned integral field unit (IFU) spectrographs, such as KCWI (Keck Cosmic Web Imager, Morrissey et al. 2018) and MUSE (Multi Unit Spectroscopic Explorer, Bacon et al. 2014). These instruments have revolutionized the study of extended Ly α nebulae by adding an additional spatial dimension with unprecedented sensitivity at rest-frame UV wavelengths (see, e.g., Wisotzki et al. 2016; Leclercq et al. 2017; Leclercq et al. 2020).

In this paper, we present new KCWI observations of one of the giant LABs discovered in the overdense proto-cluster region SSA22 at $z \sim 3.1$, SSA22-Blob2 (LAB2, Steidel et al. 1998; Steidel et al. 2000). LAB2 has an immense Ly α luminosity of $\sim 10^{44}$ erg s $^{-1}$ and a spatial extent of ~ 100 kpc. Ever since its discovery, LAB2 has become the target of many follow-up observations at multiple wavelengths, including X-ray (Basu-Zych et al., 2004; Geach et al., 2009; Lehmer et al., 2009a; Lehmer et al., 2009b), optical (Wilman et al., 2005; Martin et al., 2014), infrared (IR, Geach et al. 2007; Webb et al. 2009), and submillimeter (submm, Chapman et al. 2001; Hine et al. 2016b). A Lyman-break galaxy (LBG), M14 (Steidel et al., 2000), and an X-ray source (Basu-Zych et al., 2004) have been identified within LAB2.

To analyze the spatially resolved Ly α profiles obtained by KCWI, we carried out

Monte-Carlo radiative transfer (MCRT) modeling assuming a multiphase, clumpy H I gas model. As a presumably realistic description of the H I gas in the interstellar medium (ISM) and the circumgalactic medium (CGM), the multiphase, clumpy model has been explored by many theoretical studies (e.g., Neufeld 1991; Hansen et al. 2006; Dijkstra et al. 2012; Laursen et al. 2013; Gronke et al. 2016a). Observationally, Li et al. (2021) made the first successful attempt to systemically fit the spatially resolved Ly α profiles with the multiphase, clumpy model. The present work is a direct follow-up of Li et al. (2021), exploring a different parameter space with new physical interpretation of the derived parameters.

The structure of this paper is as follows. In §4.2, we describe our KCWI and MOSFIRE observations and data reduction procedures. In §4.3, we present the spatial distribution and spectral profiles of Ly α emission. In §4.4, we present the non-detection of nebular emission within LAB2 with MOSFIRE. In §4.5, we detail the methodology and present the results of radiative transfer modeling using the multiphase, clumpy model. In §4.6, we summarize previous studies of LAB2 and compare with this work. In §4.7, we summarize and conclude. Throughout this paper we adopt a flat Λ CDM cosmology with $\Omega_m = 0.315$, $\Omega_\Lambda = 0.685$, and $H_0 = 67.4$ km s $^{-1}$ Mpc $^{-1}$ (Planck Collaboration et al., 2020). We use the following vacuum wavelengths: 1215.67 Å for Ly α , 4862.683 Å for H β , and 4960.295/5008.240 Å for [O III] from the Atomic Line List v2.04¹.

4.2 Observations and Data Reduction

KCWI Observations

The KCWI observations of LAB2 were carried out on the night of 2019 September 27, with a seeing of $\sim 0.4 - 0.5''$ full width at half maximum (FWHM). We used the KCWI large slicer, which provides a contiguous field-of-view of $20.4''$ (slice length) \times $33''$ ($24 \times 1.35''$ slice width). With the BM VPH grating set up for $\lambda_c = 4800$ Å, the wavelength coverage is $\sim 4260 - 5330$ Å, with spectral resolution $R \simeq 1800 - 2200$. The data were obtained as 8 individual 1200 s exposures, with small telescope offsets in the direction perpendicular to slices applied between each, in an effort to recover some spatial resolution given the relatively large slice width. The total on-source exposure time was 2.7 hours, and the SB detection limit (1σ) is about 8×10^{-20} erg s $^{-1}$ cm $^{-2}$ arcsec $^{-2}$ per seeing element (1 arcsec 2) using an unresolved emission line near the Ly α emission wavelength at $z \sim 3.09$.

¹<http://www.pa.uky.edu/~peter/atomic/index.html>

Individual exposures were reduced using the KCWI Data Reduction Pipeline (DRP)², which includes wavelength calibration, atmospheric refraction correction, background subtraction, and flux calibration. The sky subtraction was conducted using both the DRP, which constructs a b-spline sky model, and a custom median filtering procedure to remove the low-order scattered light. Both the continuum and line emission sources were masked. For more details, we refer the readers to Chen et al. (2021), in which the data reduction procedures were adopted directly in this paper. The individual datacubes were then spatially re-sampled onto a uniform astrometric grid with 0.3" by 0.3" spaxels, with a sampling of 0.5 \AA pix^{-1} (4.75 pixels per spectral resolution element) along the wavelength axis, using a variant of the ‘drizzle’ algorithm (with a drizzle factor of 0.9) in the MONTAGE³ package. The re-sampled cubes were then combined into a final stacked cube by averaging with exposure time weighting. Owing to the coarser spatial sampling in the long dimension of the spatial cube, the PSF in the final datacube is elongated along the N-S direction, with FWHM $\simeq 0.90'' \times 1.08''$ (X-direction and Y-direction, respectively) measured from the most compact object in the field. We also conducted astrometry by cross-correlating the pseudo-white-light images from the KCWI datacubes to the existing wide-field astrometry-corrected images (e.g., the *HST* WFC3-IR F160W image in our Figure 4.1). This procedure is done for both individual exposures and the full stack of exposures, thus providing both relative and absolute astrometric information. An alignment with the *HST* image was done after drizzling and combining the individual KCWI exposures.

The resampled final datacube covers a scientifically useful solid angle of $22.6'' \times 33.6''$ on the sky. A variance image with the same dimensions was created by propagating errors based on a noise model throughout the data reduction.

MOSFIRE Observations

We observed selected regions of LAB2, chosen to include the highest Ly α surface brightness areas, using MOSFIRE (McLean et al., 2010; McLean et al., 2012; Steidel et al., 2014) on the Keck I telescope. Spectra in the near-IR *K* band (1.967 – 2.393 μm) were obtained using two slitmasks with the same sky PA, which cover two parallel regions of width 1" separated by 0.25" on the sky, as shown in Figure 4.1 and summarized in Table 4.1. Slit 1 passes through the region with the highest Ly α surface brightness (labeled 11 in Fig. 4.1), while Slit 2 abuts that region imme-

²<https://github.com/Keck-DataReductionPipelines/KcwiDRP>

³<http://montage.ipac.caltech.edu>

Table 4.1: MOSFIRE K -band observations of LAB2.

Name	Width	R	PA	Exp	Seeing	Date of Obs	Nod
(1)	(2)	(3)	(4)	(5)	(6)	(7)	(8)
Slit 1	1.0	2660	-54.0	2.0	0.71	2020 Nov 27	± 20.0
Slit 2	1.0	2660	-54.0	2.5	0.45	2019 Jun 15	± 15.0

Notes. The details of the MOSFIRE K -band observations of LAB2. The columns are: (1) slit name; (2) slit width ("); (3) resolving power ($\lambda/\Delta\lambda$); (4) slit PA (degrees E of N); (5) exposure time in hours; (6) seeing FWHM ("); (7) UT date of observation; (8) nod amplitude between A and B positions (").

diately to the south, and also includes a second high SB region (labeled 13) to the southeast.

The MOSFIRE observations of Slit 1 and Slit 2 were obtained on two separate observing runs (on 2020 November 27 and 2019 June 15, respectively), both under clear conditions with sub-arcsec seeing. With 1.0" slits in the K band, MOSFIRE achieves a spectral resolving power $R \sim 2660$. The data were taken with the MOSFIRE "masknod" mode, using two telescope positions separated by 30 – 40" along the slit direction, with individual exposures of 180 s between nods. The total integration times were 2.0 hours for Slit 1 and 2.5 hours for Slit 2. The data for each observation sequence were reduced using the MOSFIRE data reduction pipeline⁴ to produce two-dimensional, rectified, background-subtracted vacuum wavelength calibrated spectrograms (see Steidel et al. 2014 for details). Observations obtained on different observing nights using the same slitmask were reduced independently; the 2-D spectrograms were shifted into the heliocentric rest frame and combined with inverse variance weighting using tasks in the MOSPEC (Strom et al., 2017) analysis package.

4.3 $\text{Ly}\alpha$ Emission in LAB2

Spatial Distribution of $\text{Ly}\alpha$ Emission

In preparation for our following $\text{Ly}\alpha$ analyses, we first smoothed the KCWI datacube spatially with a 3 pixel \times 3 pixel boxcar, and spectrally with a $\sigma = 0.5 \text{ \AA}$ Gaussian function. Such a smoothed datacube will be used for all the following $\text{Ly}\alpha$ spectral analyses in this work. To provide an overview of the $\text{Ly}\alpha$ surface brightness (SB) distribution in LAB2, we generated a $\text{Ly}\alpha$ narrow-band image by summing all the $\text{Ly}\alpha$ fluxes over the relevant wavelength range. Similar to Li et al. (2021), we

⁴<https://github.com/Keck-DataReductionPipelines/MosfireDRP>

Table 4.2: Continuum sources identified in LAB2.

Name	RA (J2000)	Dec (J2000)	z_{sys}	Type	Refs.
M14 ^a	22:17:39.09	+00:13:29.8	3.091	Ly α	(1)(2)
LAB2-a	22:17:39.3	+00:13:22.0	...	IR	(3)
LAB2-b	22:17:39.1	+00:13:30.7	...	IR	(3)
LAB2-ALMA	22:17:39.079	+00:13:30.85	...	Submm	(4)
LAB2-X-ray	22:17:39.08	+00:13:30.7	...	X-ray	(5)

^aOriginally defined in Steidel et al. (2000).

Notes. Properties of the continuum sources identified in LAB2. The columns are: (1) name of the source; (2) right ascension; (3) declination; (4) systemic redshift; (5) type of observation; (6) references.

References. (1) Steidel et al. (2003); (2) Nestor et al. (2013); (3) Webb et al. (2009); (4) Ao et al. (2017); (5) Lehmer et al. (2009a).

followed the ‘matched filtering’ procedures using `LSDCat` (Herenz et al., 2017), specifically with three steps⁵: (1) applying spatial filtering to the aforementioned smoothed KCWI datacube using a 2D Gaussian filter with FWHM = 0.9” (the seeing point spread function (PSF) measured from a bright star in the SSA22 field); (2) applying a 1D Gaussian spectral filter with FWHM = 500 km s⁻¹ (a conservative lower limit on the observed Ly α line width estimated visually); (3) generating an S/N cube with the filtered datacube for thresholding.

We present the Ly α narrow-band image of LAB2 in the left panel of Figure 4.1. It is constructed by summing all the voxels of the continuum-subtracted filtered datacube with S/N ≥ 4 over 4949 – 5009 Å ($\sim -2000 - 1500$ km s⁻¹ at $z \sim 3.1$), which should enclose all possible Ly α emission. The level of the subtracted continuum is determined as the average of the two median UV flux densities bluewards (4849 – 4949 Å) and redwards (5009 – 5109 Å) of the Ly α emission. In the right panel, we present the *HST* WFC3-IR F160W rest-frame optical continuum image (Program 13844, PI: Bret Lehmer) of LAB2⁶ for comparison. The positions of previously identified sources are marked on each image as references. Thus far, multiple sources have been identified in LAB2: an LBG M14 (Steidel et al., 2000), an X-ray source (Basu-Zych et al., 2004; Lehmer et al., 2009a) with IR (LAB2-b, Webb et al. 2009) and submm (LAB2-ALMA, Ao et al. 2017)

⁵Note that the `LSDCat` procedures are only applied in this section for generating the Ly α narrow-band image.

⁶The KCWI and *HST* images have been registered to the same world-coordinate system using cross-correlation.

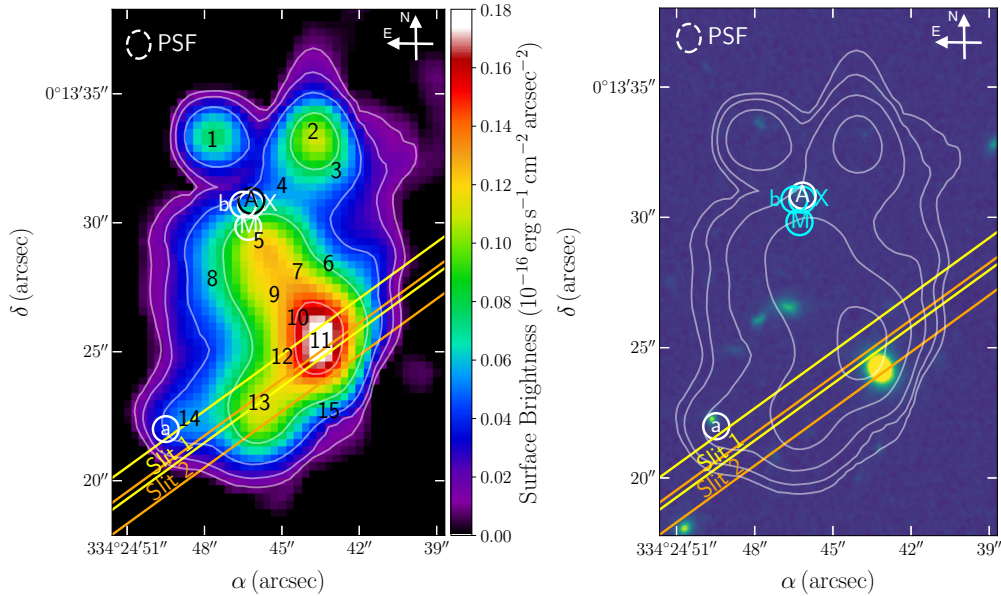


Figure 4.1: Ly α and continuum images of LAB2. *Left*: The narrow band Ly α image, obtained by collapsing the original KCWI datacube over 4949 – 5009 Å, which encloses the Ly α line (see §4.3). The UV continuum near the wavelength of Ly α has been subtracted. The positions of the MOSFIRE slits are delineated by parallel yellow and orange lines (see §4.2), and the numbers (1–15, in black) indicate the positions of spectra that we sample for radiative transfer modeling in §4.5. *Right*: The *HST* WFC3-IR F160W rest-frame optical continuum image. The positions of a Lyman-break galaxy (M14, labeled as ‘M’), an X-ray source (labeled as ‘X’) with IR (‘b’) and submm (‘A’) counterparts, and an IR source (‘a’) have been marked on each image (see §4.3 and Table 4.2). The Ly α isophotes with levels of $\text{SB}_{\text{Ly}\alpha} = [150, 80, 40, 20, 10] \times 10^{-19} \text{ erg s}^{-1} \text{ cm}^{-2} \text{ arcsec}^{-2}$ have also been overlaid, and the dashed white ellipse indicates the PSF in the final datacube with $\text{FWHM} \simeq 0.90'' \times 1.08''$ (X and Y-direction, respectively). Both images have been registered to the same world-coordinate system.

counterparts, and an IR source detected by *Spitzer* IRAC (LAB2-a, Webb et al. 2009). The detailed information for all the identified sources are presented in Table 4.2. The Ly α isophotes (contours with the same SB) with levels of $\text{SB}_{\text{Ly}\alpha} = [150, 80, 40, 20, 10] \times 10^{-19} \text{ erg s}^{-1} \text{ cm}^{-2} \text{ arcsec}^{-2}$ have also been overlaid onto each image.

In Figure 4.1, we see that the extended Ly α emission can be separated mainly in three distinct regions – the northeast (as indicated by a number ‘1’), the northwest (as indicated by a number ‘2’), and the south region. Among them, the south region has the largest extent. In this extended region there appears to be a high SB center (as indicated by a number ‘11’), yet neither M14 nor the X-ray source is close to

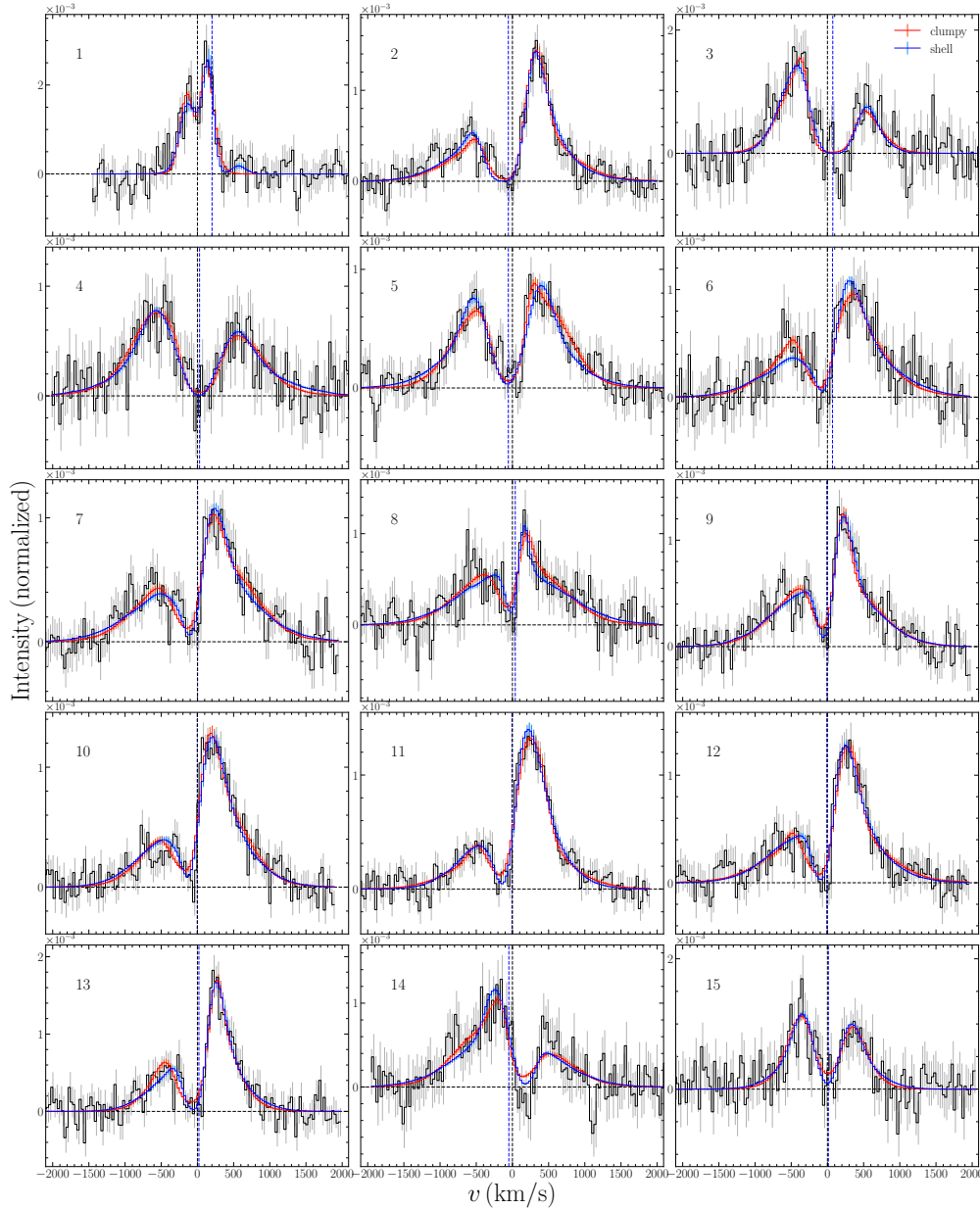


Figure 4.2: **Fifteen representative continuum-subtracted, spatially resolved and normalized Ly α profiles (black, with grey 1- σ error bars) from the high SB regions in LAB2.** The spectrum number of each spectrum has been marked on the SB map in Figure 4.1. All the spectra have been smoothed by a $3 \text{ pixel} \times 3 \text{ pixel}$ boxcar ($0.9''$) spatially and Gaussian smoothed ($\sigma = 0.5 \text{ \AA}$) in the wavelength dimension. As we will detail in §4.5, the multiphase, clumpy model best-fits (red, with orange 1- σ Poisson errors) and the shell model best-fits (blue, with cyan 1- σ Poisson errors) are both shown in each subpanel. The observed Ly α spectra have also been shifted by $-\Delta v_{\text{clumpy}}$ to their local systemic redshifts (as determined by the best-fits), and the shell model best-fits are shifted correspondingly as well for direct comparison. For each subpanel, the x -axis is the velocity (in km s^{-1}) with respect to the local systemic redshift, and the y -axis is the normalized line flux. For visual reference, the horizontal and vertical black dashed lines in each subpanel indicate zero flux level and zero velocity with respect to the local systemic redshift, respectively. The vertical blue dashed lines indicate the initial guess for the systemic redshift ($z = 3.09$ for spectrum 1 and $z = 3.098$ for all other spectra).

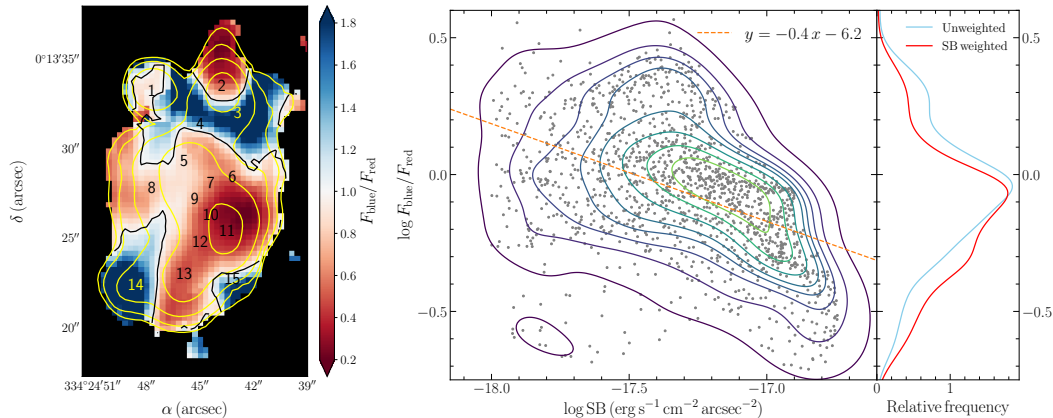


Figure 4.3: The spatial distribution of the blue-to-red flux ratio ($F_{\text{blue}}/F_{\text{red}}$) and its relation to SB. *Left:* The map of $F_{\text{blue}}/F_{\text{red}}$ of LAB2 with Ly α SB contours overlaid (same as in Figure 4.1 but in yellow color) and spectrum numbers marked (same as in Figure 4.1 but in yellow color for spectra 3 and 14 for clarity). The black contour indicates where $F_{\text{blue}}/F_{\text{red}} = 1$. It can be seen that $F_{\text{blue}}/F_{\text{red}}$ is the lowest in the highest SB region, and increases outwards as the SB decreases. *Right:* The 2D density map of $F_{\text{blue}}/F_{\text{red}}$ vs. SB (on log scale) for all the individual pixels (as shown with grey points) with $\log \text{SB} > -18.0$ (i.e., within the outermost yellow contour in the left panel). A simple power-law fit yields $F_{\text{blue}}/F_{\text{red}} \propto \text{SB}^{-0.4}$, as shown in the orange dashed line. Note the anti-correlation between $F_{\text{blue}}/F_{\text{red}}$ and Ly α SB, which may be due to the decline of the projected line-of-sight outflow velocity and the increase of inflow velocity towards the blob outskirts. Also shown on the right are the unweighted (blue curve) and SB-weighted (red curve) frequency distributions of $F_{\text{blue}}/F_{\text{red}}$. Both distributions peak at $F_{\text{blue}}/F_{\text{red}} < 1$, where the SB-weighted one leans more towards lower $F_{\text{blue}}/F_{\text{red}}$.

this position – instead, they are located in the northeast outskirts where the Ly α SB is relatively low. In addition, the variation of the Ly α SB with respect to the maximum value is highly direction-dependent. Two regions exhibiting monotonically declining Ly α SB towards the northeast and southeast directions are evident, the former of which is more elongated.

Profiles of Ly α Emission and Blue-to-Red Flux Ratio

The diverse Ly α profiles in three extended Ly α emitting regions as well as their outskirts are shown in Figure 4.2. All the profiles have been normalized such that the total flux (flux density integrated over the velocities) of the Ly α line is 1. The small northwest region exhibits a narrow double-peak profile with significant flux between the peaks. Both the northeast and the south region exhibit a similar pattern of an increase in the blue-to-red flux ratio ($F_{\text{blue}}/F_{\text{red}}$, the flux ratio of the blue peak

to the red peak) towards the outer, lower SB regions. We illustrate this quantitatively in Figure 4.3.

To calculate the blue-to-red flux ratio of the spectrum of each pixel, we first identified the local minimum (trough) between two peaks of the continuum-subtracted, spatially and spectrally smoothed spectrum, and then integrated both blueward and redward until the flux density goes to zero. The blue-to-red flux ratio is simply the ratio of the integrated fluxes of the blue peak (F_{blue} , the Ly α flux at negative velocities with respect to the local minimum) and the red peak (F_{red} , the Ly α flux at positive velocities with respect to the local minimum). In the left panel of Figure 4.3, we show the spatial distribution of $F_{\text{blue}}/F_{\text{red}}$ of LAB2 with SB contours overlaid. It can be seen that $F_{\text{blue}}/F_{\text{red}}$ is lowest in the highest SB region, and increases outwards as the SB decreases. Regions with $F_{\text{blue}}/F_{\text{red}} > 1$ are evident in the outskirts at three different directions: north, southeast and southwest, which is potentially a signature of accreting gas (see, e.g., Zheng et al. 2002; Dijkstra et al. 2006b; Faucher-Giguère et al. 2010).

In the right panel of Figure 4.3, we show in a 2D density map how $F_{\text{blue}}/F_{\text{red}}$ varies with SB for all the individual pixels with $\log \text{SB} > -18.0$ (i.e., within the outermost yellow contour in the left panel). We see that as SB increases, $F_{\text{blue}}/F_{\text{red}}$ (as shown with grey points) tends to decrease. A simple power-law fit yields $F_{\text{blue}}/F_{\text{red}} \propto \text{SB}^{-0.4}$ (as shown in the orange dashed line). This trend may be due to a combination of: (1) the decline of the projected line-of-sight outflow velocity towards the outskirts of the halo (where the SB is low), assuming a central, roughly symmetric outflow exists (we will quantitatively test this hypothesis in §4.5); (2) the increase of inflow velocity at the blob outskirts. Such a transition from outflow to inflow-domination has been observed at ~ 50 kpc for a large sample of star-forming galaxies at $z \sim 2$ (Chen et al., 2020). We also show the unweighted and SB-weighted pixel frequency distributions of $F_{\text{blue}}/F_{\text{red}}$. Both distributions peak at $F_{\text{blue}}/F_{\text{red}} < 1$, where the SB-weighted one leans more towards lower $F_{\text{blue}}/F_{\text{red}}$. It suggests that our spatially resolved (not SB-weighted) observations may be better at detecting blue-dominated Ly α profiles that would be otherwise missed in spatially integrated (SB-weighted) observations.

The anti-correlation between the median $F_{\text{blue}}/F_{\text{red}}$ and SB observed here is similar to the trend observed by Erb et al. (2018), who studied the Ly α halo of a low-mass star-forming galaxy at $z = 2.3$ and found that the red peak dominates in the central, high SB region, whereas $F_{\text{blue}}/F_{\text{red}} \gtrsim 1$ in the outskirts of the halo. They

also reported an anti-correlation between $F_{\text{blue}}/F_{\text{red}}$ and peak separation, which we do not observe in LAB2. Such a difference may reflect the intrinsic difference between Ly α halos illuminated by a single star-forming galaxy and by potentially multiple sources with various powering mechanisms (as in LAB2). We have also checked several other spectral properties, such as trough position, spectrum width and peak separation, but no significant trends have been found.

4.4 Non-Detection of Nebular Emission Lines

In this section, we summarize the results of our MOSFIRE observations. We have searched through both slits for nebular emission lines and found no significant detection of [O III] or H β emission at any location (especially where the Ly α SB is the highest) on either slit within the region covered by LAB2. For the [O III] λ 5008 line, we measured 2- σ flux upper limits of 2.8×10^{-18} and 2.5×10^{-18} erg s $^{-1}$ cm $^{-2}$ for Slit 1 and 2 respectively, using a window with spatial size of 3" and spectral width of $\sigma = 75$ km s $^{-1}$ assuming a systemic redshift of $z = 3.098$ (inferred from the following radiative transfer modeling in §4.5). We can then utilize these flux upper limits to infer the properties (e.g., star formation rate, SFR) of any possibly existing galaxies along the slits. Taking the observed range of [O III] λ 5008/H $\beta \sim 1 - 10$ for $z \sim 2 - 3$ star forming galaxies (Steidel et al., 2014) and assuming zero dust extinction and case B recombination (i.e., H α /H $\beta \simeq 2.86$), we get [O III] λ 5008/H $\alpha \sim 0.35 - 3.5$. Using the H α to SFR conversion factor derived by Kennicutt et al. (1994) and Madau et al. (1998), the [O III] λ 5008 2- σ upper limits correspond to SFR $\sim 0.6 - 6 M_{\odot} / \text{yr}$.

Although the non-detection of the nebular emission lines is puzzling, it is clear that the Ly α profiles near the high SB center are red-dominated and suggest the presence of outflows, which is most likely due to star formation or AGN-driven winds. It is therefore reasonable to hypothesize the existence of star-forming galaxies or AGNs hidden by dust extinction and/or contamination of a foreground source (see the right panel of Figure 4.1 for the location of a possible low- z interloper) near the Ly α SB peak. Our subsequent radiative transfer modeling analysis is also based on this assumed ‘central powering + scattering’ scenario⁷.

⁷One may speculate that the ‘cold accretion’ scenario can also produce red-dominated profiles if aided by IGM absorption preferentially on the blue side. However, such a scenario is likely to result in multiple (e.g., triple) peaks at $z \sim 3$, which we have not observed in LAB2 (Byrohl et al., 2020)

4.5 Radiative Transfer Modeling Using The Multiphase Clumpy Model

Methodology

To decode physical properties of the gas in LAB2 from the observational data, we used radiative transfer modeling to fit the spatially resolved Ly α profiles. Similar to Li et al. (2021), we adopted a multiphase, clumpy model, which assumes cool, spherical H I clumps moving within a hot, ionized inter-clump medium (ICM) (Laursen et al., 2013; Gronke et al., 2016a). The most crucial parameters of this model include: (1) the cloud covering factor (f_{cl}), which is the mean number of clumps per line-of-sight from the center to the boundary of the simulation sphere; (2) the residual⁸ H I number density in the ICM ($n_{\text{HI,ICM}}$), which determines the depth of the absorption trough; (3) the kinematics of the clumps, consisting of an isotropic Gaussian random motion (characterized by σ_{cl} , the velocity dispersion of the clumps) and a symmetric radial outflow with a constant velocity v_{cl} ; (4) the H I column density of the clumps.

Note that Ly α radiative transfer in such a multiphase, clumpy medium exhibits two characteristic regimes defined by the values of f_{cl} (Gronke et al., 2016b; Gronke et al., 2017). If f_{cl} is much larger than a critical value $f_{\text{cl,crit}}$ (which is a function of the H I column density and kinematics of the clumps, see Appendix B of Li et al. (2021) for a detailed derivation), the photons would escape as if the medium is homogeneous and the emergent spectra are similar to those predicted by the ‘shell model’ (Gronke et al., 2017). Otherwise, for a moderate number of clumps per line-of-sight, the photons preferentially travel in the hot ionized ICM and escape close to the Ly α line center.

We constructed a five-dimensional hypercubic grid of models by varying the aforementioned five crucial physical parameters: $[\log n_{\text{HI,ICM}}, F_V, \log N_{\text{HI,cl}}, \sigma_{\text{cl}}, v_{\text{cl}}]$ ⁹. The prior ranges of the parameters are summarized in Table 4.3. We fixed the subdominant parameters, such as the clump temperature T_{cl} to 10^4 K and the ICM temperature T_{ICM} to 10^6 K¹⁰. We varied an additional parameter, Δv_{clumpy} , continuously in

⁸Here we have assumed that the hydrogen in the hot ICM is highly ionized and only a very small fraction exists in the form of H I (i.e., $x_{\text{HI,ICM}} \ll 1$).

⁹For convenience we varied F_V rather than f_{cl} when generating clumps. These two parameters are proportionally related via the relation $f_{\text{cl}} = 3r_{\text{gal}}/4r_{\text{cl}} F_V$, where $r_{\text{gal}} = 5$ kpc is the radius of the simulation sphere and $r_{\text{cl}} = 50$ pc is the clump radius (hence $f_{\text{cl}} = 75 F_V$ in our case). Note that the physical sizes used in the simulation are unimportant to Ly α spectra; it is the H I column densities and corresponding optical depths that are important and can actually be constrained by the data.

¹⁰Different from Li et al. (2021), we set the ICM co-outflow with the clumps (i.e., $v_{\text{cl}} = v_{\text{ICM}}$), as both v_{cl} and v_{ICM} decrease the blue-to-red flux ratio, and in reality, a large velocity difference between two different phases would likely destroy the clumps via hydrodynamical instabilities on

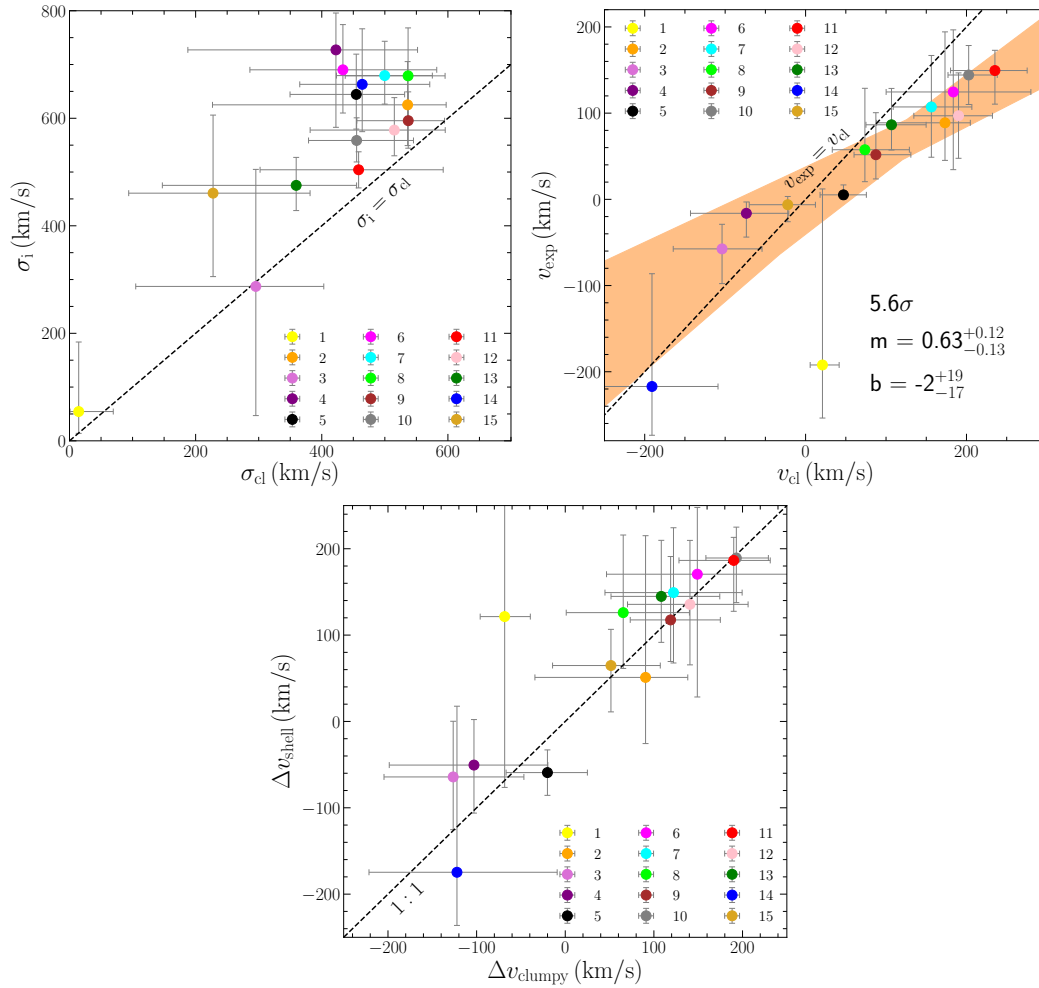


Figure 4.4: **Correlations between the multiphase, clumpy model parameters and the shell model parameters.** Only one significant ($\gtrsim 5\sigma$) positive correlation is observed between v_{cl} and v_{exp} . Interestingly, $\sigma_{cl} \leq \sigma_i$ and $|v_{cl}| \geq |v_{exp}|$ are almost always true. The Δv_{clumpy} vs. Δv_{shell} correlation is insignificant, but the data points are broadly consistent with a 1-to-1 relation within 2σ uncertainties. The color-coded points represent different Ly α spectra (see Figure 4.1 and 4.2). The 2σ uncertainties of the data points are indicated by grey error bars. For the v_{cl} vs. v_{exp} correlation, the level of significance and the linear best-fit coefficients (slope m and intercept b , with 1σ uncertainties) are shown at the lower right corner in the middle panel. The orange shaded region represent the range of twenty best-fits of the data points perturbed by their uncertainties.

Table 4.3: Parameter values of the grids of models.

Model (1)	Parameter (2)	Definition (3)	Values (4)
Clumpy	$\log n_{\text{HI,ICM}}$	ICM H I number density	(-7.5, -6.5, -5.5, -4.5) $\log \text{cm}^{-3}$
	F_V	Volume filling factor	(0.02, 0.1, 0.2, 0.3, 0.4, 0.5, 0.6)
	$\log N_{\text{HI,cl}}$	Clump H I column density	(17, 17.5, 18, 18.5, 19) $\log \text{cm}^{-2}$
	σ_{cl}	Clump velocity dispersion	(0, 100, ..., 600) km s^{-1}
	v_{cl}	Clump outflow velocity	(0, 100, 200, 300) km s^{-1}
	Δv_{clumpy}	Velocity shift	[-200, 200] km s^{-1}
Shell	v_{exp}	Shell expansion velocity	(0, 2, 5, 8, 10, 15, 20, 30, ..., 490) km s^{-1}
	$\log N_{\text{HI,shell}}$	Shell H I column density	(16.0, 16.2, ..., 21.8) $\log \text{cm}^{-2}$
	$\log T_{\text{shell}}$	Shell (effective) temperature	(4.0, 4.4, ..., 5.8) $\log \text{K}$
	σ_i	Intrinsic spectrum width	[1, 800] km s^{-1} (continuous)
	Δv_{shell}	Velocity shift	[-200, 200] km s^{-1} (continuous)

Notes. The parameter values of the model grids that we used for fitting the Ly α profiles. The columns are: (1) model type; (2) parameter name; (3) definition of the parameter; (4) parameter values on the grid. Note that negative values for v_{cl} and v_{exp} are also allowed in the fitting.

post-processing. This Δv_{clumpy} parameter represents the best-fit systemic redshift of the Ly α source function relative to $z = 3.098$ (the initial guess for the systemic redshift – it is where the trough of most Ly α spectra is located)¹¹. Furthermore, we considered *inflow* velocities (i.e., $v_{\text{cl}} < 0$) by mirroring the model spectra with respect to the line center.

Such a configuration amounts to 3920 models in total. Each model is calculated via radiative transfer using 10000 Ly α photon packages generated from a Gaussian intrinsic spectrum $N(0, \sigma_{i,\text{cl}}^2)$, where $\sigma_{i,\text{cl}} = 12.85 \text{ km s}^{-1}$ is the canonical thermal velocity dispersion of $T = 10^4 \text{ K}$ gas. To properly explore the multimodal posterior of the parameters, we used a python nested sampling package `dynesty` (Skilling, 2004; Skilling, 2006; Speagle, 2020) for our fitting pipeline.

Results

Fits and Derived Parameters

We selected fifteen representative Ly α spectra from the high SB regions in LAB2 for further model fitting. The positions of these spectra are shown in Figure 4.1, and the profiles are shown in Figure 4.2. All spectra were extracted from certain single spatial pixels of the boxcar-smoothed KCWI datacube, each representing the short timescales.

¹¹Note that the northeast Ly α emitting region is located at a lower redshift, $z = 3.09$, which we adopted as the initial guess for spectrum 1.

Table 4.4: Fitted parameters and derived quantities of the multiphase, clumpy model and the shell model.

No.	RA (J2000)	Dec (J2000)	Clumpy Model Parameters						Derived Quantities		Shell Model Parameters				
			$\log n_{\text{HI,ICM}}$ (cm^{-3})	F_V	$\log N_{\text{HI,cl}}$ (cm^{-2})	σ_{cl} (km s^{-1})	v_{cl} (km s^{-1})	Δv_{clumpy} (km s^{-1})	$f_{\text{cl}}/f_{\text{cl,crit}}$	$\log \tau_{0,\text{ICM}}$	v_{exp} (km s^{-1})	$\log N_{\text{HI,shell}}$ (cm^{-2})	$\log T_{\text{shell}}$ (K)	σ_1 (km s^{-1})	Δv_{shell} (km s^{-1})
(1)	(2)	(3)	(4)	(5)	(6)	(7)	(8)	(9)	(10)	(11)	(12)	(13)	(14)	(15)	(16)
1	22:17:39.179	+00:13:33.17	$-7.3^{+0.3}_{-0.2}$	$0.31^{+0.26}_{-0.23}$	$17.4^{+0.6}_{-0.4}$	14^{+54}_{-13}	20^{+20}_{-15}	-68^{+20}_{-23}	$23.3^{+20.0}_{-18.4}$	$0.7^{+0.3}_{-0.2}$	-192^{+204}_{-61}	$19.0^{+0.4}_{-2.7}$	$4.9^{+0.8}_{-0.8}$	54^{+129}_{-40}	121^{+44}_{-188}
2	22:17:38.919	+00:13:33.47	$-4.7^{+0.2}_{-0.6}$	$0.07^{+0.37}_{-0.04}$	$18.1^{+0.5}_{-0.9}$	536^{+61}_{-309}	173^{+31}_{-85}	90^{+35}_{-91}	$0.6^{+8.2}_{-0.3}$	$3.3^{+0.2}_{-0.6}$	88^{+105}_{-43}	$19.7^{+0.5}_{-1.6}$	$5.6^{+0.1}_{-1.4}$	624^{+80}_{-75}	50^{+125}_{-63}
3	22:17:38.859	+00:13:31.97	$-4.7^{+0.2}_{-0.6}$	$0.34^{+0.23}_{-0.24}$	$17.8^{+1.1}_{-0.7}$	295^{+107}_{-190}	-103^{+49}_{-60}	-126^{+62}_{-49}	$5.2^{+11.3}_{-3.6}$	$3.3^{+0.2}_{-0.6}$	-57^{+28}_{-40}	$20.3^{+0.4}_{-0.4}$	$5.6^{+0.2}_{-0.6}$	287^{+217}_{-240}	-64^{+57}_{-45}
4	22:17:38.999	+00:13:31.37	$-5.4^{+0.8}_{-1.4}$	$0.32^{+0.25}_{-0.21}$	$18.0^{+0.9}_{-0.9}$	422^{+129}_{-234}	-73^{+52}_{-69}	-102^{+64}_{-65}	$3.8^{+8.1}_{-2.5}$	$2.6^{+0.8}_{-1.4}$	-16^{+13}_{-27}	$20.8^{+0.5}_{-0.4}$	$5.0^{+0.6}_{-0.9}$	727^{+68}_{-144}	-50^{+51}_{-48}
5	22:17:39.059	+00:13:29.27	$-5.7^{+0.4}_{-0.4}$	$0.26^{+0.17}_{-0.16}$	$17.4^{+1.1}_{-0.4}$	454^{+76}_{-105}	47^{+28}_{-29}	-20^{+34}_{-36}	$2.6^{+2.0}_{-1.4}$	$2.3^{+0.4}_{-0.4}$	5^{+11}_{-5}	$20.6^{+0.4}_{-0.4}$	$4.8^{+0.6}_{-0.7}$	644^{+74}_{-64}	-59^{+23}_{-25}
6	22:17:38.879	+00:13:28.37	$-5.9^{+1.1}_{-0.7}$	$0.10^{+0.33}_{-0.08}$	$18.5^{+0.5}_{-1.4}$	433^{+148}_{-147}	183^{+96}_{-83}	148^{+45}_{-59}	$1.3^{+3.7}_{-1.1}$	$2.0^{+1.1}_{-0.7}$	124^{+72}_{-90}	$19.5^{+0.8}_{-0.3}$	$4.6^{+0.5}_{-0.6}$	690^{+84}_{-80}	170^{+128}_{-109}
7	22:17:38.959	+00:13:28.07	$-5.9^{+0.6}_{-0.4}$	$0.23^{+0.17}_{-0.17}$	$17.6^{+1.1}_{-0.5}$	499^{+75}_{-76}	156^{+50}_{-47}	122^{+58}_{-60}	$2.1^{+1.5}_{-1.5}$	$2.1^{+0.6}_{-0.4}$	107^{+59}_{-58}	$19.4^{+0.4}_{-0.3}$	$4.6^{+0.4}_{-0.5}$	679^{+63}_{-53}	149^{+45}_{-56}
8	22:17:39.179	+00:13:27.77	$-6.4^{+0.4}_{-0.3}$	$0.18^{+0.13}_{-0.12}$	$17.5^{+1.1}_{-0.4}$	536^{+58}_{-99}	73^{+55}_{-40}	65^{+50}_{-49}	$1.6^{+1.1}_{-0.9}$	$1.5^{+0.4}_{-0.3}$	57^{+71}_{-37}	$17.7^{+1.4}_{-1.5}$	$4.9^{+0.5}_{-0.7}$	678^{+89}_{-51}	126^{+54}_{-52}
9	22:17:39.019	+00:13:27.17	$-6.2^{+0.3}_{-0.3}$	$0.14^{+0.08}_{-0.06}$	$17.5^{+0.7}_{-0.4}$	537^{+57}_{-81}	87^{+43}_{-27}	118^{+35}_{-36}	$1.2^{+0.7}_{-0.5}$	$1.7^{+0.3}_{-0.3}$	51^{+48}_{-28}	$19.4^{+0.5}_{-0.6}$	$4.7^{+0.3}_{-0.7}$	595^{+53}_{-51}	117^{+54}_{-39}
10	22:17:38.959	+00:13:26.27	$-6.2^{+0.3}_{-0.3}$	$0.14^{+0.12}_{-0.06}$	$17.8^{+0.4}_{-0.7}$	455^{+90}_{-76}	202^{+35}_{-25}	193^{+6}_{-22}	$1.4^{+1.0}_{-0.7}$	$1.8^{+0.3}_{-0.3}$	144^{+34}_{-34}	$19.3^{+0.2}_{-0.6}$	$4.7^{+0.3}_{-0.6}$	558^{+42}_{-39}	189^{+10}_{-38}
11	22:17:38.899	+00:13:25.37	$-5.7^{+0.5}_{-0.6}$	$0.07^{+0.16}_{-0.03}$	$17.9^{+0.3}_{-0.5}$	458^{+134}_{-156}	235^{+40}_{-55}	190^{+9}_{-27}	$0.6^{+1.9}_{-0.4}$	$2.3^{+0.5}_{-0.8}$	149^{+23}_{-38}	$19.4^{+0.3}_{-0.1}$	$4.8^{+0.2}_{-0.6}$	504^{+33}_{-33}	186^{+12}_{-44}
12	22:17:38.999	+00:13:24.77	$-5.5^{+0.7}_{-0.4}$	$0.07^{+0.17}_{-0.04}$	$18.1^{+0.4}_{-1.0}$	515^{+80}_{-133}	190^{+42}_{-55}	140^{+50}_{-43}	$0.7^{+1.7}_{-0.4}$	$2.4^{+0.7}_{-0.6}$	96^{+49}_{-47}	$19.6^{+0.4}_{-0.4}$	$4.9^{+0.4}_{-0.8}$	578^{+60}_{-47}	135^{+54}_{-49}
13	22:17:39.059	+00:13:22.97	$-5.8^{+0.4}_{-0.4}$	$0.14^{+0.20}_{-0.07}$	$17.4^{+0.9}_{-0.4}$	359^{+95}_{-212}	106^{+43}_{-31}	108^{+49}_{-47}	$1.8^{+7.4}_{-0.9}$	$2.2^{+0.4}_{-0.4}$	86^{+42}_{-29}	$19.3^{+0.4}_{-0.8}$	$5.2^{+0.3}_{-0.4}$	475^{+52}_{-44}	144^{+49}_{-44}
14	22:17:39.239	+00:13:22.37	$-6.2^{+0.9}_{-0.5}$	$0.23^{+0.21}_{-0.19}$	$17.6^{+1.2}_{-0.6}$	464^{+107}_{-99}	-190^{+82}_{-77}	-122^{+77}_{-62}	$2.2^{+2.0}_{-1.8}$	$1.8^{+0.9}_{-0.5}$	-217^{+130}_{-56}	$18.5^{+1.2}_{-2.3}$	$5.1^{+0.4}_{-0.8}$	663^{+103}_{-88}	-174^{+140}_{-24}
15	22:17:38.879	+00:13:22.67	$-6.5^{+0.8}_{-0.9}$	$0.28^{+0.28}_{-0.23}$	$17.9^{+1.0}_{-0.8}$	227^{+153}_{-133}	-22^{+34}_{-47}	51^{+43}_{-45}	$6.3^{+13.5}_{-5.4}$	$1.4^{+0.8}_{-0.9}$	-6^{+9}_{-19}	$20.3^{+0.4}_{-1.1}$	$4.7^{+0.7}_{-0.7}$	460^{+145}_{-155}	64^{+40}_{-49}

Notes. Fitted parameters (averages and 2.5% – 97.5% quantiles, i.e., 2- σ confidence intervals) of the multiphase clumpy model and shell model, and derived quantities. The columns are: (1) the spectrum number (as marked in Figure 4.2); (2) the right ascension of the center of the extracted region; (3) the declination of the center of the extracted region; (4) the HI number density in the ICM; (5) the cloud volume filling factor; (6) the clump HI column density; (7) the velocity dispersion of the clumps; (8) the radial outflow velocity of the clumps; (9) the velocity shift relative to the initial guess for the systemic redshift ($z = 3.09$ for spectrum 1 and $z = 3.098$ for all other spectra; a negative/positive value means that the best-fit model spectrum has been blue/redshifted to match the data); (10) the clump covering fraction (defined as the number of clumps per line-of-sight) normalized by the critical clump covering fraction. In our case $f_{\text{cl}} = 75 F_V$. The critical clump covering fraction, $f_{\text{cl,crit}}$, determines different physical regimes and is calculated via Eq. (B3) in Li et al. (2021); (11) the optical depth at the Ly α line center of the HI in the ICM; (12) the expansion velocity of the shell; (13) the HI column density of the shell; (14) the HI temperature of the shell; (15) the required intrinsic line width; (16) the velocity shift relative to the initial guess for the systemic redshift.

average spectrum of a corresponding $3 \text{ pixel} \times 3 \text{ pixel}$ boxcar-smoothed region.

In addition to using the multiphase, clumpy models to fit the $\text{Ly}\alpha$ spectra, we also adopted the widely used ‘shell model’ (e.g., Ahn et al. 2003; Verhamme et al. 2006; Dijkstra et al. 2006b). A similar three-dimensional cubic grid of shell models was constructed by varying three parameters: the shell expansion velocity v_{exp} , the shell HI column density $\log N_{\text{HI,shell}}$, and the effective temperature of HI in the shell, $\log T_{\text{shell}}$. Two more parameters, namely the intrinsic line width σ_i and the velocity shift with respect to the initial guess for the systemic redshift ($z = 3.09$ for spectrum 1 and $z = 3.098$ for all other spectra), Δv_{shell} , are varied continuously in post-processing¹².

During the fitting procedure, each model spectrum is calculated via linear flux interpolation on the model grid¹³ and is convolved with the KCWI line-spread function (LSF, a Gaussian with $\sigma = 65 \text{ km s}^{-1}$) before being compared to the observed $\text{Ly}\alpha$ profiles. To better reproduce the profiles dominated by a blue peak (e.g., spectra 3, 4, 14 and 15), we have also incorporated model spectra with negative v_{cl} or v_{exp} that have been ‘mirrored’ in the velocity space from their positive $v_{\text{cl}}/v_{\text{exp}}$ counterparts into our calculation. The best-fit model spectra are also shown in Figure 4.2.

In Figure 4.2, one can see that, in most cases, both the multiphase, clumpy model fits and shell model fits match the observed $\text{Ly}\alpha$ profiles reasonably well. The values of the fitted parameters are presented in Table 4.4. The best-fit parameters are determined as the highest likelihood point in the sampled parameter space, and the uncertainties in the fitted parameters are determined as certain quantiles (e.g., 2.5% – 97.5%, or $2\text{-}\sigma$ confidence intervals) of the samples in the marginalized posterior probability distributions. Note that the best-fit parameters of the multiphase, clumpy model derived here should be interpreted as the local gas properties – e.g., HI column densities, clump velocity dispersions, and in particular, clump outflow velocities *along the line-of-sight* relative to the local systemic redshift. Such a practice provides the distribution of gas kinematics and HI column densities without relying on the assumption of the location of the $\text{Ly}\alpha$ source (see Appendix 4.7).

¹²The detailed configuration of the shell model is presented in Gronke et al. (2015), and an example of fitting $\text{Ly}\alpha$ spectra with a grid of shell models is presented, for instance, in Gronke (2017).

¹³Interpolation is necessary here because it is too computationally expensive if in the nested sampling process we calculate the model spectrum at each point in the parameter space “on the fly” (i.e., performing RT at that point). So instead, we used a pre-calculated and saved grid of models to calculate each model spectrum via a linear flux interpolation of the adjacent grid models, which is accurate enough for our purpose.

Motivated by the fact that certain parameters from both models should control similar Ly α spectral properties, we further attempted to find the link between the two models by correlating parameter pairs. As a result, we have only observed one significant ($\gtrsim 5\sigma$) positive correlation between v_{cl} and v_{exp} . We have also performed linear regressions to this correlation and estimated the uncertainties in the coefficients (slope m and intercept b) by perturbing the data points with asymmetric Gaussian noise with amplitude proportional to the error bars. The results are shown in Figure 4.4.

The existence of the significant correlation between v_{cl} and v_{exp} can be easily understood since this parameter pair controls the same spectral property, namely the blue-to-red flux ratio. Interestingly, we see that $\sigma_{\text{cl}} \leq \sigma_i$ and $|v_{\text{cl}}| \geq |v_{\text{exp}}|$ are almost always true. These results naturally alleviated the tension between the fitted shell model parameters and the observational constraints reported in, e.g., Orlitová et al. (2018), namely: (1) the required σ_i are on average three times broader than the observed non-resonant Balmer lines; (2) the derived v_{exp} are smaller than the outflow velocities determined from UV absorption lines. This suggests that the photon scattering between randomly moving clumps may be an efficient way of broadening Ly α profiles and circumventing overlarge σ_i (see also Hashimoto et al. 2015), and that v_{cl} in the clumpy medium is less efficient at increasing the spectrum asymmetry than v_{exp} . Such distinctions reflect the intrinsic differences between two models: in the shell model, all the photons have to traverse the shell and thus are shaped by the same shell outflow/inflow velocity; whereas in the multiphase, clumpy model, the photons can randomly walk between the clumps or even diffuse outwards with their frequencies unaffected¹⁴ (Neufeld, 1991; Gronke et al., 2016a). This means that the effective outflow velocity ‘experienced’ by the photons in the multiphase, clumpy model is smaller than that in the shell model, which needs to be compensated by a larger v_{cl} . Furthermore, as scattering orthogonally off the flowing clumps may yield additional broadening to the spectra (Li et al., 2021), the σ_{cl} values required to achieve the large observed widths of Ly α profiles are lower.

By the same token, correlations between (1) $n_{\text{HI,ICM}}$ (and $F_V N_{\text{HI,cl}}$ ¹⁵) and $N_{\text{HI,shell}}$; (2) Δv_{clumpy} and Δv_{shell} may exist, as they control the peak separation and the systemic redshift of the Ly α source, respectively. However, we found that the former correlation is insignificant, as the best-fits from two models prefer different peak

¹⁴Note that we focused on the $f_{\text{cl}}/f_{\text{cl,crit}} \simeq 1 - 10$ regime in this work.

¹⁵Both $n_{\text{HI,ICM}}$ and $F_V N_{\text{HI,cl}}$ (or $f_{\text{cl}} N_{\text{HI,cl}}$) contribute to the effective column density in the multiphase, clumpy model (see Eq. (1) in Gronke et al. 2016a).

separations in many cases (see, e.g., spectra 7, 8, 9 and 13). The latter correlation is also insignificant ($\lesssim 2\sigma$) with one apparent outlier – for spectrum 1, the multiphase, clumpy model prefers outflow, whereas the shell model prefers inflow. However, all 15 data points are broadly consistent with a 1-to-1 relation within 2σ uncertainties. Such a correspondence between Δv_{clumpy} and Δv_{shell} suggests that the inconsistency reported in Orlitová et al. (2018), i.e., the best-fit systemic redshifts inferred from the shell model are larger by $10 - 250 \text{ km s}^{-1}$ than those determined from optical emission lines, also exists in the multiphase, clumpy model. Further observations of non-resonant lines that are available for other objects are necessary to solve this issue.

We have not found any straightforward analytic mapping functions that can directly convert the best-fit parameters from one model to the other. In our future work, we will explore whether such analytic mapping functions exist between certain parameters first in the $f_{\text{cl}} \gg f_{\text{cl,crit}}$ regime, and then in the regime that we have explored in this work, i.e., f_{cl} is higher than $f_{\text{cl,crit}}$ but mostly within one order of magnitude, where only qualitative trends between parameter pairs have been observed.

Although the shell model fits have comparable likelihoods to the multiphase, clumpy model fits, they are less likely to be informative of the actual physical conditions in the circumgalactic medium (CGM), because (1) the shell model only has a single phase of H I with low-to-medium effective temperature ($T_{\text{shell}} \sim 10^{4-5} \text{ K}$); (2) the aforementioned v_{exp}, σ_i and Δv_{shell} values that are inconsistent with the observational constraints (e.g., Orlitová et al. 2018). Whereas the multiphase, clumpy model is not only likely a more realistic description of the CGM (Tumlinson et al., 2017), but it also yields more reasonable physical parameters (as we will elaborate below). Therefore, we will focus on the multiphase, clumpy model in the rest of this paper.

Interpretation of Fitted Parameters

In this section, we discuss how realistic the fitted parameters of the multiphase, clumpy model are compared to other studies.

1. *Covering fraction of the cool clumps*: The derived volume filling factors (F_V) range from $\sim 0.1 - 0.5$, which convert to covering factors (f_{cl}) of $\sim 7 - 40$ for clumps with $N_{\text{HI,cl}} \gtrsim 10^{17} \text{ cm}^{-2}$. Such high covering factors effectively

correspond to covering *fractions* of unity¹⁶ (Laursen et al., 2013). This result is consistent with the recent findings in Wisotzki et al. (2018), where they observed low SB Ly α emission surrounding high- z faint galaxies with MUSE and claimed that the H I covering fractions around galaxies should be sufficiently close to unity at $z > 3$, assuming the spatial distribution of circumgalactic H I is similar to the Ly α -emitting gas. Additionally, high H I covering fractions around galaxies have also been observed at lower redshifts ($z < 3$, see, e.g., Chen et al. 2001; Adelberger et al. 2003; Prochaska et al. 2011b; Rudie et al. 2012; Tumlinson et al. 2013), suggesting that large H I covering fractions should be universally present across different cosmic epochs.

2. *Velocity of the cool clumps:* The derived clump velocity dispersions (σ_{cl}) range from $\sim 300 - 600 \text{ km s}^{-1}$, which correspond to a dynamical halo mass of $M_{\text{dyn}} \sim 10^{13} M_{\odot}$, consistent with the predicted halo masses from the Millennium simulations (see Eq. 3 in Li et al. 2021 and discussions therein). The clump outflow velocities (v_{cl}) range from $\sim 100 - 250 \text{ km s}^{-1}$, which yield considerable cloud lifetimes (or even cloud growth) in the hot ICM (Gronke et al., 2018; Li et al., 2020; Li et al., 2021). Future observations may provide additional constraints on the relative velocities between the cool clumps and the ICM derived from simplistic configurations in this work.

In terms of the survival of cool clumps, it is also helpful to consider the thermal sound speed of the hot ICM, $c_{s,\text{ICM}} \sim \sqrt{k_B T_{\text{ICM}}/m_p} \sim 100 \text{ km s}^{-1}$. Therefore, the Mach numbers of the cool clumps $\mathcal{M}_{\text{cl}} \equiv v_{\text{cl}}/c_{s,\text{ICM}}$ or $\sigma_{\text{cl}}/c_{s,\text{ICM}} \sim 1 - 2.5$, which are transonic or mildly supersonic. These Mach numbers are realistic for circumgalactic gas, and may slightly affect the dynamics of the cool clumps in the hot medium (see, e.g., Scannapieco et al. 2015; Sparre et al. 2020).

3. *Energy contribution from the inflowing gas:* We have observed signatures of gas inflow at the blob outskirts (see the blue-peak dominated spectra 3, 4, 14 and 15 and the inferred negative ‘outflow’ velocities), and it is possible to estimate the associated cooling luminosity. As the blue-dominated profiles

¹⁶This is true especially in the central region; in the outskirts the covering fraction may decrease even for a homogeneous clump distribution (as assumed in this work). Technically, the effective covering factor to an external observer is $\tilde{f}_{\text{cl}} = f_{\text{cl}} \frac{2\sqrt{R^2 - b^2}}{R}$, which corresponds to an (area) covering fraction of $f_A(b) = 1 - \exp(-\tilde{f}_{\text{cl}})$, i.e., one minus the Poisson probability of photons intersecting with zero clumps. Here R is the radius of the studied region, and b is the projected distance from the center of the region relative to the line-of-sight.

encompass most of the blob (see Figure 4.3), we assume that the clumps inflow in a semi-isotropic manner. The mass flow rate of the inflowing H I gas is given by:

$$\dot{M}_{\text{HI}} = 4\pi R_{\text{h}}^2 \rho_{\text{HI}} \frac{dr}{dt} = 4\pi R_{\text{h}}^2 \rho_{\text{HI}} v_{\text{inflow}} \quad (4.1)$$

where R_{h} is the halo radius and v_{inflow} is the gas inflow velocity. The H I mass density, ρ_{HI} , is given by:

$$\rho_{\text{HI}} = \frac{M_{\text{HI}}}{V_{\text{h}}} = \frac{n_{\text{HI,cl}} m_{\text{H}} r_{\text{cl}}^3 N_{\text{cl}}}{R_{\text{h}}^3} \quad (4.2)$$

where $n_{\text{HI,cl}}$ is the clump H I number density, m_{H} is the mass of a hydrogen atom, and r_{cl} is the clump radius. The total number of clumps in the halo, N_{cl} , is related to the volume filling factor:

$$F_{\text{V}} = \frac{N_{\text{cl}} r_{\text{cl}}^3}{R_{\text{h}}^3} \quad (4.3)$$

With all these relations, the cooling luminosity generated from the released gravitational energy by gas infalling is:

$$\begin{aligned} L_{\text{cool}} &= \frac{GM_{\text{h}} \dot{M}_{\text{HI}}}{R_{\text{h}}} = 4\pi GM_{\text{h}} F_{\text{V}} f N_{\text{HI,cl}} m_{\text{H}} v_{\text{inflow}} \\ &= 1.4 \times 10^{42} F_{\text{V}} \left(\frac{N_{\text{HI,cl}}}{10^{17} \text{cm}^{-2}} \right) \left(\frac{M_{\text{h}}}{10^{13} M_{\odot}} \right) \left(\frac{v_{\text{inflow}}}{100 \text{km s}^{-1}} \right) \text{erg s}^{-1} \end{aligned}$$

Note that f is the radius ratio of the halo and the clumps (100 in our radiative transfer calculations). Taking $N_{\text{HI,cl}} \sim 10^{18} \text{cm}^{-2}$, and $F_{\text{V}} \sim 0.3$, $M_{\text{h}} \sim 10^{13} M_{\odot}$ and $v_{\text{inflow}} \sim 100 \text{km s}^{-1}$ (the mean of the derived inflow velocities), we get $L_{\text{cool}} \sim 4 \times 10^{42} \text{erg s}^{-1}$. This value is still more than one order of magnitude lower than the observed Ly α luminosity of LAB2, even if all the cooling luminosity is emitted in Ly α . Therefore, we conclude that the infalling of cool gas (cold accretion) plays a minor role in powering LAB2. This conclusion is consistent with the recent result of Ao et al. (2020), where they also found for a $z \sim 2.3$ LAB that cool gas infalling helps produce blue-peak dominated Ly α profiles, but is a subdominant powering mechanism compared to the photo-ionization process by embedded star-forming galaxies and/or AGNs¹⁷.

¹⁷We have assumed that all the observed Ly α emission comes from either photoionization by star-forming galaxies and/or AGN or accretion of infalling gas, because we were unable to identify any features that are suggestive of other powering mechanisms (e.g., shocks). The required SFR of ionizing sources inferred from the observed Ly α luminosity is $\sim 80 M_{\odot} / \text{yr}$ (Kennicutt et al., 1994).

4. *Residual HI density in the ICM*: The derived HI number densities correspond to column densities of $n_{\text{HI,ICM}} r_{\text{gal}} \sim 10^{15} - 10^{18} \text{ cm}^{-2}$ (recall that $r_{\text{gal}} = 5 \text{ kpc}$ is the radius of the simulation sphere) and Ly α optical depths at line center of $\tau_{0,\text{ICM}} \sim 10 - 10^3$. Such column densities are high enough to contribute to the broadening of Ly α spectra and produce (unsaturated) absorption at the line center. Taking the LAB2 halo radius as $R_{\text{h}} \sim 50 \text{ kpc}$, the derived $n_{\text{HI,ICM}}$ values correspond to actual residual HI number densities of $\sim 10^{-8} - 10^{-5} \text{ cm}^{-3}$. These values are moderately higher than the expected values assuming collisional ionization equilibrium, i.e., hydrogen number density $n_{\text{H,ICM}} \sim 10^{-3} - 10^{-2} \text{ cm}^{-3}$ and HI fraction $x_{\text{HI,ICM}} \sim 10^{-6}$ at $T_{\text{ICM}} = 10^6 \text{ K}$ (Dopita et al., 2003), but the difference is not significant especially considering that the highest $n_{\text{HI,ICM}}$ values (e.g., spectra 2 – 5) appear close to the X-ray/submm continuum sources, which may be due to galactic feedback (see, e.g., §2.2 of McQuinn 2016).

Fitting Spectra at Different Spatial Positions Simultaneously

In this section, we attempt to fit multiple spatially resolved Ly α profiles with multiphase, clumpy models in a more self-consistent way. We demonstrate that we can fit Ly α spectra at different distances from a high SB center (i.e., at different impact parameters) simultaneously in one fitting run¹⁸.

As illustrated in Figure 4.5, we chose spectra from three equally spaced regions along a line (in projection) with respect to the high SB center (spectra 9, 10 and 11¹⁹) to perform our fit. For each model calculated in the fitting procedure, the Ly α photon packages (10000 in total) are separated into three different bins, according to the impact parameter²⁰ of their last-scattering locations: $0.05 < b/b_{\text{max}} \leq 0.35$, $0.35 < b/b_{\text{max}} \leq 0.65$ and $0.65 < b/b_{\text{max}} \leq 0.95$, where b_{max} is the largest impact parameter of all the scattered Ly α photons. In this way, the representative photons included in each bin are numerous enough to construct a meaningful model spec-

¹⁸We have also attempted to fit spectra at different spatial positions assuming an identified continuum source (e.g., M14 or the X-ray source) as the central Ly α emitting source, but these attempts turned out to be unsuccessful. This is because in an outflow model the inner photons tend to be more red-dominated than the outer photons, which is opposite to the observed trend away from any continuum source (cf. §4.3)

¹⁹These three spectra are located at $b/b_{\text{max}} = 0$ (i.e., down the barrel), 0.3 and 0.6, respectively (see §4.5).

²⁰Here we define impact parameter b as the projected distance from the highest SB center relative to the line-of-sight. In the model, the impact parameter is determined as the distance from the center of the simulated region to the trajectory of the photon after the last scattering.

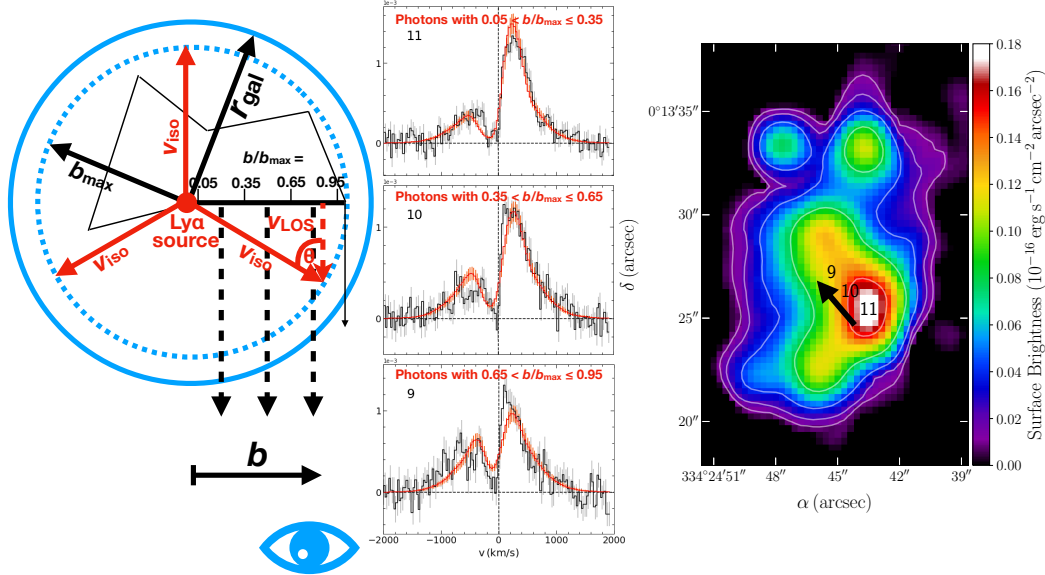


Figure 4.5: **Results of fitting spatially resolved Ly α spectra (9, 10 and 11) at different impact parameters simultaneously.** *Left:* Illustration of how different photon bins are constructed in the multiphase, clumpy model. The ranges of impact parameters of three different Ly α photon bins are: $0.05 < b/b_{\max} \leq 0.35$, $0.35 < b/b_{\max} \leq 0.65$ and $0.65 < b/b_{\max} \leq 0.95$, where b_{\max} is the largest impact parameter of all the scattered Ly α photons. The solid red arrows represent an isotropic outflow of the cool clumps with velocity v_{iso} , and the dashed red arrow represents the observed clump outflow velocity projected along the line-of-sight, v_{LOS} . *Middle:* Three aligned and equally spaced Ly α spectra (black, with grey 1- σ error bars) and the corresponding binned best-fits (red, with orange 1- σ Poisson errors). The likelihoods of the binned fits are comparable to those of the individual fits. *Right:* The Ly α SB map, with the alignment of three modeled spectra indicated by a black arrow.

trum. At every likelihood evaluation call, each observed Ly α spectrum is compared to the corresponding ‘binned’ model spectrum, and the likelihood is simply the sum of the likelihoods of three binned models.

The fitting results are shown in Figure 4.5. We found that the likelihoods of the binned fits are comparable to those of the individual fits (which were obtained by fitting spectra at each location independently). Moreover, the derived v_{cl} of this ‘combined fit’ is fully consistent with the value of the individual fit of spectrum 11. One notable discrepancy is that the outermost binned model ($0.65 < b/b_{\max} \leq 0.95$) failed to fully reproduce the Ly α flux density minimum near the systemic velocity of spectrum 9, which may be due to the assumption that $n_{\text{HI,ICM}}$ is constant over the whole simulated region, whereas in reality the residual H I density in the ICM

Table 4.5: Best-fit parameters of fitting spectra 9, 10 and 11 simultaneously with the multiphase, clumpy model.

$\log n_{\text{HI,ICM}}$	F_V	$\log N_{\text{HI,cl}}$	σ_{cl}	v_{cl}	Δv_{clumpy}
(cm^{-3})		(cm^{-2})	(km s^{-1})	(km s^{-1})	(km s^{-1})
(1)	(2)	(3)	(4)	(5)	(6)
$-6.0^{+0.2}_{-0.2}$	$0.07^{+0.01}_{-0.01}$	$18.2^{+0.1}_{-0.1}$	463^{+78}_{-33}	193^{+24}_{-15}	176^{+10}_{-10}

Notes. Results of fitting spectra 9, 10 and 11 simultaneously with the multiphase, clumpy model, as described in §4.5. The columns are: (1) the H I number density in the ICM; (2) the cloud volume filling factor; (3) the clump H I column density; (4) the velocity dispersion of the clumps; (5) the radial outflow velocity of the clumps; (6) the velocity shift relative to the initial guess for the systemic redshift ($z = 3.098$). The fitted parameters are given as averages and 16% – 84% quantiles, i.e., 1- σ confidence intervals.

may vary spatially or extend beyond the multiphase medium. It is therefore possible to remedy this mismatch by considering models with radially varying $n_{\text{HI,ICM}}$. Nevertheless, we have demonstrated the possibility of fitting spectra with different impact parameters simultaneously in a self-consistent manner. Further applications and extensions to the model are left to future work.

v_{cl} vs. b : A Simple Projection?

As presented in Table 4.4, the inferred outflow velocities of the cool clumps, v_{cl} , vary significantly at different positions. Here we test whether this variation can be consistent with being a projection effect, i.e., the derived v_{cl} values from the multiphase, clumpy models are simply the projected line-of-sight components of an isotropic outflow velocity.

The line-of-sight component of an isotropic outflow velocity is given by (as illustrated in the left panel of Figure 4.6):

$$\begin{aligned}
 v_{\text{LOS}} &= v_{\text{iso}} \cos\theta \\
 &= v_{\text{iso}} \sqrt{1 - (b/b_{\text{max}})^2}
 \end{aligned}
 \tag{4.4}$$

where v_{LOS} is the observed line-of-sight outflow velocity, v_{iso} is the isotropic outflow velocity, θ is the angle between the line-of-sight and the isotropic outflow velocity, b is the impact parameter of the observed location, and b_{max} is the maximum impact parameter of the observed region (or the radius if the region is spherically symmetric). We further examined Eq. (4.4) by plotting the v_{cl} values derived from individual fits²¹ along with the range of fitted v_{cl} vs. b curves in the right panel of Figure 4.6. A reference v_{cl} vs. b curve from the combined fit of spectra 9, 10 and 11 is also plotted for comparison, which is generated by setting $v_{\text{iso}} = 193_{-15}^{+24} \text{ km s}^{-1}$ (the v_{cl} of the combined fit of spectra 9, 10 and 11) and $b_{\text{max}} = 33 \text{ kpc}$ (calculated by mapping the geometric distances in the model to the actual physical distances²²) in Eq. (4.4).

As can be seen in Figure 4.6, the reference v_{cl} vs. b curve from the combined fit (blue solid and dashed lines) is fairly consistent with the v_{cl} values derived from individual fits (as well as the fitted v_{iso} and b_{max} values) within $1\text{-}\sigma$ uncertainties, suggesting the variations in v_{cl} may be simply the projection of a radial outflow along the line-of-sight. Therefore, we conclude that the observed variation in v_{cl} with respect to b can be reasonably accounted for by a simple line-of-sight projection effect. This would also naturally explain the observed increase in $F_{\text{blue}}/F_{\text{red}}$ ratio towards the blob outskirts, as $F_{\text{blue}}/F_{\text{red}}$ is inversely correlated with v_{cl} (see §4.3), although the blue-dominated spectra at the very largest distances require inflows.

4.6 Previous Studies of LAB2

Here we summarize the results of previous studies of LAB2 and compare with the present work. We classify different studies according to the wavelengths of their observations:

Optical: Steidel et al. (2000) first discovered LAB2 using narrow-band imaging and provided its angular size ($\sim 15''$), Ly α luminosity ($\sim 9.0 \times 10^{43} \text{ erg s}^{-1}$) and limits on the rest-frame equivalent width ($\gtrsim 370 \text{ \AA}$). They also identified a velocity shear of $\sim 2000 \text{ km s}^{-1}$ with respect to the LBG, M14.

Wilman et al. (2005) carried out IFU observations using SAURON on the 4.2 m William Herschel Telescope (WHT) on La Palma. They observed the ubiquitous ‘double-peak + central trough’ feature of most Ly α profiles in LAB2, and mod-

²¹Here we selected eight red-peak dominated spectra that are close to the Ly α SB center (i.e., spectrum 11) from the south high SB region: spectra 5, 6, 7, 9, 10, 11, 12, 13.

²²Specifically, the geometric distance between spectra 9 and 10 in the model is $0.3 b_{\text{max}}$, and the actual physical distance between these two locations are 9.9 kpc. Hence $b_{\text{max}} = 33 \text{ kpc}$.

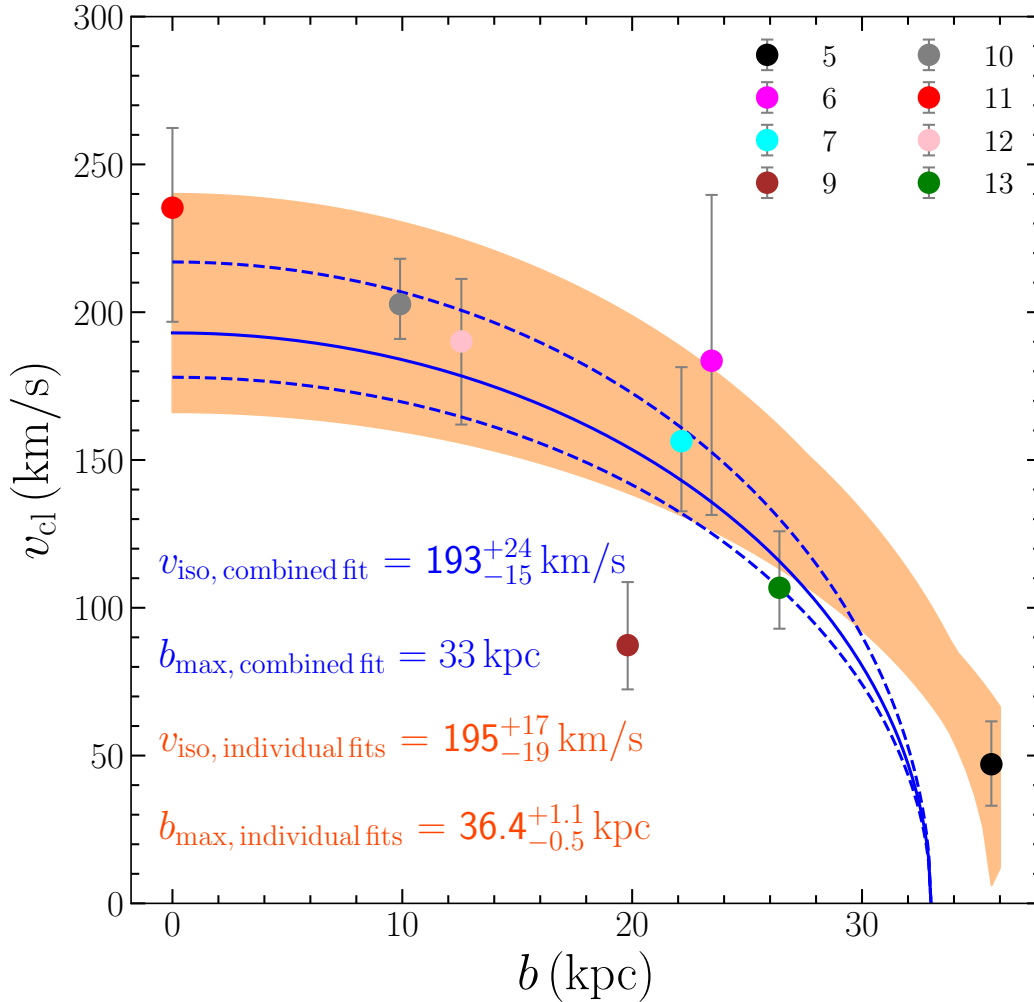


Figure 4.6: **The relation between the clump outflow velocity (v_{cl}) and the impact parameter (b).** The color-coded points represent v_{cl} values (with $1-\sigma$ error bars shown in grey) derived from individual fits of eight different Ly α spectra from the south high SB region, and the orange shaded region represent the range of twenty best-fits (using Eq. 4.4) of the data points perturbed by their $1-\sigma$ uncertainties. The best-fit parameters with $1-\sigma$ uncertainties are also shown in the lower left. The blue solid and dashed curves are reference v_{cl} vs. b curves generated by setting $v_{iso} = 193^{+24}_{-15}$ km s $^{-1}$ (derived from the combined fit) and $b_{\text{max}} = 33$ kpc (calculated by mapping the geometric distances in the model to the actual physical distances in Eq. 4.4). The reference v_{cl} vs. b curve from the combined fit is fairly consistent with the v_{cl} values derived from individual fits (as well as the fitted v_{iso} and b_{max} values) within $1-\sigma$ uncertainties, suggesting the variations in v_{cl} may be simply the projection of a radial outflow along the line-of-sight.

eled the profiles with a Gaussian emission line and a superimposed Voigt profile absorber. They claimed that the profiles can be explained by an ‘intrinsic Ly α emission + H I shell absorption’ model, where the shell is the cool material swept-up by starburst-driven outflows (‘superwinds’). They also noted that a large foreground absorber that covers the whole blob is unlikely, as the absorber would have an unreasonably large size.

Martin et al. (2014) made further IFU observations using the Palomar Cosmic Web Imager (PCWI). They proposed that the Ly α emission could be produced by either AGN fluorescence or gravitational cooling radiation. They also claimed that there is evidence of both inflows and outflows at different viewing angles, which is consistent with our findings that both blue-dominated and red-dominated Ly α profiles exist in LAB2.

X-Ray: Basu-Zych et al. (2004) first detected an obscured hard X-ray source in the *Chandra* 2 – 8 keV band. They claimed that the unabsorbed X-ray luminosity ($\sim 10^{44}$ erg s $^{-1}$) is consistent with an AGN. Deeper *Chandra* observations have been carried out in Lehmer et al. (2009a) and Lehmer et al. (2009b), based on which Geach et al. (2009) claimed that the UV luminosity of the AGN alone is sufficient to power the whole blob via photoionization. However, as we have shown in Figure 4.1 and subsequent analyses, the location of the AGN with respect to the Ly α emission is difficult to reconcile with the Ly α morphology.

IR: Geach et al. (2007) carried out *Spitzer* observations at IRAC (3.6 – 8 μ m) and MIPS (24 μ m). They reported detections at three positions in LAB2 (named a, b and c), where b is likely the counterpart of the X-ray source, and c is a foreground source at lower redshift²³. Webb et al. (2009) further confirmed the detection of a and b in the IRAC bands, and we have marked their positions in Figure 4.1.

Submm: Chapman et al. (2001) first reported a 3.3 ± 1.2 mJy detection at 850 μ m within the $\sim 15''$ beam of SCUBA. Geach et al. (2005) studied the relation between the Ly α luminosity and the bolometric luminosity of 23 LABs and noted that LAB2 is an outlier of the relation, which could be due to the effect of AGN and other environmental factors. However, a recent study by Hine et al. (2016b) reported a non-detection at 850 μ m using SCUBA-2. Another recent study by Ao et al. (2017)

²³We found that detection c is close to the position where the Ly α SB is the highest (see the left panel of Figure 4.1). Unfortunately, its mid-IR colors suggest that it should be a foreground galaxy at $z < 1$ (Geach et al., 2007; Webb et al., 2009). In our KCWI datacube, the location of its Ca II H and K lines suggests a redshift of $z = 0.213$.

reported a significant 0.91 ± 0.10 mJy detection at $850 \mu\text{m}$ using ALMA, which coincides with the X-ray detection from Lehmer et al. (2009a).

Previous studies on LAB2 focused mainly on qualitatively studying the continuum sources (e.g., the LBG M14 and the X-ray source) in terms of their energy budgets and/or analyzing the observed Ly α profiles with empirical tools without carrying out radiative transfer calculations. In contrast, the present work carefully examines the spatially resolved Ly α profiles (such as mapping their blue-to-red flux ratios, see §4.3) and decodes them using radiative transfer calculations with multiphase, clumpy models (see §4.5). In our modeling, we assumed that a central powering source exists near the highest Ly α SB regions, although it is still puzzling that there is no viable continuum source coincident with the Ly α SB peak (see §4.4). Not only have we successfully reproduced fifteen representative Ly α profiles with realistic physical parameters, but we also managed to fit Ly α profiles at different impact parameters consistently, and explained the observed spatial variation in the $F_{\text{blue}}/F_{\text{red}}$ ratio and outflow velocity. These results support the ‘central powering + scattering’ scenario, i.e., the Ly α photons are generated by central powering source(s) and then scatter with outflowing, multiphase H I gas while propagating outwards. We have also observed signatures of accretion of infalling cool gas at the blob outskirts. As we have shown in §4.5, although the infalling of cool gas is responsible for shaping the observed blue-dominated Ly α profiles, its energy contribution is likely to be minor compared to the photo-ionization by central (as yet unidentified) sources.

4.7 Conclusions

We present new deep spectroscopic observations of SSA22-LAB2 at $z = 3.1$ using KCWI and MOSFIRE. The main conclusions of our analysis are:

1. By creating a narrow-band Ly α image, we observed extended Ly α emission in three distinct regions, among which the south region is the largest and has a high Ly α SB center that is far away from known continuum sources;
2. We found that the Ly α profiles are dominated by a red peak in regions of high Ly α SB, but tend to be more symmetric and even blue-peak dominated in the low SB outskirts. The median blue-to-red flux ratio is anti-correlated with Ly α SB, which may be due to the decrease of the projected line-of-sight outflow velocity in the periphery of the halo;

3. We searched through the two MOSFIRE slits that had been observed near to the highest Ly α SB regions, and found no significant detection of nebular emission within the region of Ly α emission;
4. To decode the spatially resolved Ly α profiles using Monte-Carlo radiative transfer (MCRT) modeling, we used both multiphase, clumpy models and shell models, both of which successfully reproduced the diverse Ly α morphologies. We found a significant correlation between parameters of the two different models, and our derived parameters may alleviate the previously reported discrepancies between the shell model parameters and data;
5. We have managed to fit Ly α spectra at different impact parameters simultaneously assuming a common central source. We also found that the variation of the clump outflow velocity with respect to impact parameter can be approximately explained as a simple line-of-sight projection effect of a radial outflow;
6. We conclude that our results support the ‘central powering +scattering’ scenario, i.e., the Ly α photons are generated by a central powering source and then scatter with outflowing, multiphase H I gas while propagating outwards. The infalling of cool gas is responsible for shaping the observed blue-dominated Ly α profiles, but the energy contribution of infalling material to the total Ly α luminosity is less than 10%, i.e., minor compared to the photo-ionization by star-forming galaxies and/or AGNs.

Acknowledgements

We thank Phil Hopkins for providing computational resources. ZL, CCS and YC acknowledge financial support by NSF grant AST-2009278. YM acknowledges support from JSPS KAKENHI Grant (17H04831, 17KK0098, 19H00697 and 20H01953). The data presented herein were obtained at the W. M. Keck Observatory, which is operated as a scientific partnership among the California Institute of Technology, the University of California and the National Aeronautics and Space Administration. The Observatory was made possible by the generous financial support of the W. M. Keck Foundation. We are also grateful to the dedicated staff of the W.M. Keck Observatory who keep the instruments and telescopes running effectively. MG was supported by NASA through the NASA Hubble Fellowship grant HST-HF2-51409 awarded by the Space Telescope Science Institute, which is operated by the Association of Universities for Research in Astronomy, Inc.,

for NASA, under contract NAS5-26555. Numerical calculations were run on the Caltech compute cluster “Wheeler”, allocations from XSEDE TG-AST130039 and PRAC NSF.1713353 supported by the NSF, and NASA HEC SMD-16-7592. This research made use of Montage. It is funded by the National Science Foundation under Grant Number ACI-1440620, and was previously funded by the National Aeronautics and Space Administration’s Earth Science Technology Office, Computation Technologies Project, under Cooperative Agreement Number NCC5-626 between NASA and the California Institute of Technology. We also acknowledge the use of the following software packages: Astropy (Astropy Collaboration et al., 2018), the SciPy and NumPy system (Virtanen et al., 2020; Harris et al., 2020), seaborn (Waskom, 2021) and QFitsView²⁴.

Appendix

Note on The Usage of RT Models and Interpretation of Fitting Results

In this work, we have used the multiphase, clumpy model to fit spatially resolved Ly α spectra. Although the multiphase, clumpy model adopted in this work assumes a central Ly α source surrounded by an ensemble of gas clouds distributed isotropically, we emphasize that such an assumption does not affect our attempt to fit these models to the observed individual spatially resolved spectra as an approximate way to extract the local gas properties – e.g., HI column densities, clump velocity dispersions, and particularly, clump outflow velocities *along the line-of-sight* relative to the local systemic redshift.

To corroborate our point, we design an experiment where we run a set of four multiphase, clumpy models with different v_{cl} but otherwise the same parameters. We then plot the Ly α spectra in the “down the barrel” spatial bin of the first model and $\cos\theta$ ($= \sqrt{1 - (b/b_{\text{max}})^2}$, see Eq. 4.4) = $v_{\text{cl},1}/v_{\text{cl},i}$ spatial bin of the i th model ($i = 2, 3, 4$), so that the outflow velocities along the line-of-sight for all four models are the same. We show below that these four binned Ly α spectra are consistent.

We hereby illustrate our point with a specific example (whose parameters are typical in our fitting) in Figure 4.7: four multiphase, clumpy models have $(\log n_{\text{ICM}} (\text{cm}^{-3}), F_V, \log N_{\text{HI,cl}} (\text{cm}^{-2}), \sigma_{\text{cl}} (\text{km s}^{-1})) = (-5.0, 0.2, 18.0, 400)$ and $v_{\text{cl}} (\text{km s}^{-1}) = (100, 107, 122, 163)$, respectively. The photons from the following ranges of impact parameters are selected to construct the Ly α spectra for each of the four models: $b/b_{\text{max}} \in (0.1, 0.3], (0.3, 0.5], (0.5, 0.7],$ and $(0.7, 0.9]$, respectively. The line-of-

²⁴<https://www.mpe.mpg.de/ott/QFitsView/>

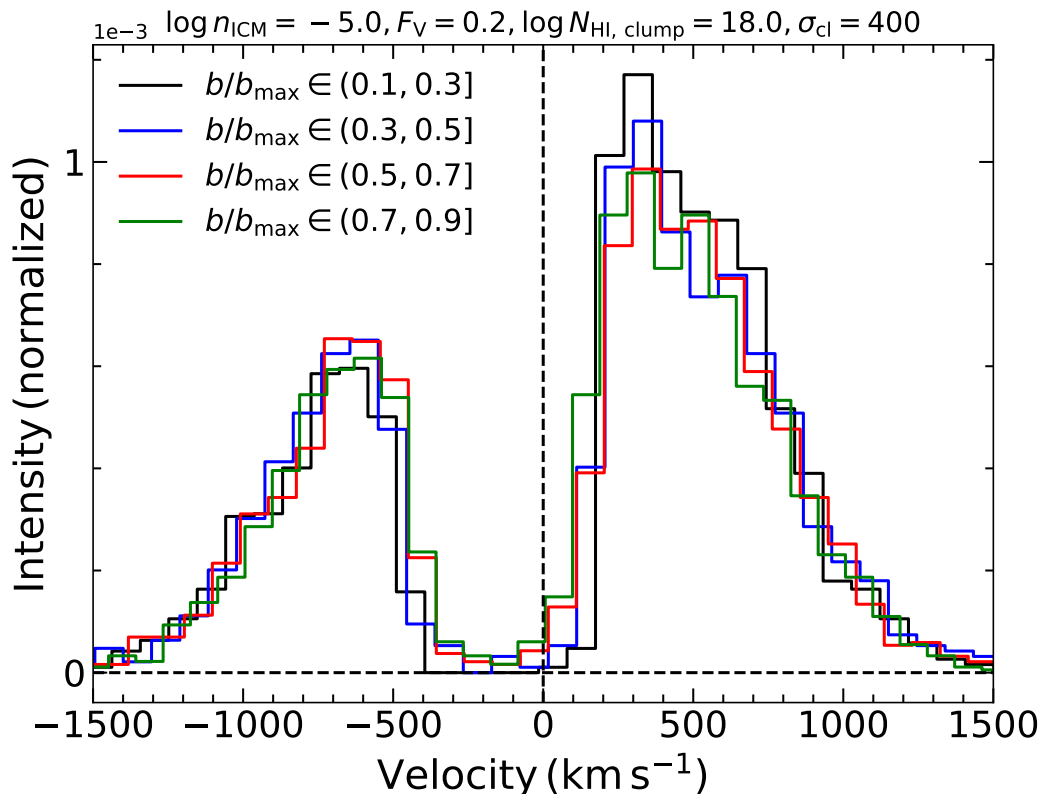


Figure 4.7: **Justification for using the multiphase, clumpy models to fit the spatially resolved Ly α profiles.** four multiphase, clumpy models have $(\log n_{\text{ICM}}(\text{cm}^{-3}), F_V, \log N_{\text{HI,cl}}(\text{cm}^{-2}), \sigma_{\text{cl}}(\text{km s}^{-1})) = (-5.0, 0.2, 18.0, 400)$ and $v_{\text{cl}}(\text{km s}^{-1}) = (100, 107, 122, 163)$, respectively. The photons from the following ranges of impact parameters are selected to construct the Ly α spectra for each of the four models: $b/b_{\text{max}} \in (0.1, 0.3]$, $(0.3, 0.5]$, $(0.5, 0.7]$, and $(0.7, 0.9]$, respectively. The line-of-sight v_{cl} for the $b/b_{\text{max}} \in (0.1, 0.3]$ photons (i.e., nearly "down the barrel") of the first model and for the other three bins of photons (i.e., "off the barrel") are basically the same. The Ly α model spectra constructed from these four bins of photons are consistent with each other within $1\text{-}\sigma$ uncertainties (about 10% assuming Poisson photon distribution).

sight v_{cl} for the $b/b_{\text{max}} \in (0.1, 0.3]$ photons (i.e., nearly "down the barrel") of the first model and for the other three bins of photons (i.e., "off the barrel") are basically the same (using Eq. 4.4). It can be seen that the Ly α model spectra constructed from these four different bins of photons are consistent. Therefore, it is reasonable to extract local gas properties by fitting Ly α spectra observed away from continuum sources, as long as we interpret the output clump outflow velocity as a projected, line-of-sight velocity with respect to the local systemic redshift.

DECIPHERING THE LYMAN- α EMISSION LINE: TOWARDS
THE UNDERSTANDING OF GALACTIC PROPERTIES
EXTRACTED FROM Ly α SPECTRA VIA RADIATIVE
TRANSFER MODELING

Li, Zhihui and Max Gronke (July 2022). “Deciphering the Lyman- α emission line: towards the understanding of galactic properties extracted from Ly α spectra via radiative transfer modelling”. In: *MNRAS* 513.4, pp. 5034–5051. DOI: 10.1093/mnras/stac1207. arXiv: 2111.03671 [astro-ph.GA].

5.1 Introduction

Owing to its luminous nature, Lyman- α (Ly α) is one of the best emission lines to explore the high-redshift universe, including identifying and studying the formation of distant galaxies as well as probing the reionization era (see a recent review by Ouchi et al., 2020). Despite all its advantages, the Ly α line is a resonant transition with a large cross-section, making its radiative transfer (RT) process notoriously difficult to model. Initially, the Ly α radiative transfer problem was studied analytically for several simple cases, e.g., static plane-parallel slabs (Harrington, 1973; Neufeld, 1990), a two-phase ISM (Neufeld, 1991), static uniform spherical shells (Dijkstra et al., 2006a), and a uniform neutral IGM with pure Hubble expansion (Loeb et al., 1999). Later on, more and more studies started to employ numerical (mostly Monte Carlo) methods in more sophisticated configurations, e.g., flattened, axially symmetric, rotating clouds (Zheng et al., 2002), expanding/contracting spherical shells (Zheng et al., 2002; Ahn et al., 2003; Ahn, 2004; Dijkstra et al., 2006a; Dijkstra et al., 2006b; Verhamme et al., 2006; Gronke et al., 2015; Song et al., 2020), (moving) multiphase, clumpy medium (Richling, 2003; Hansen et al., 2006; Dijkstra et al., 2012; Laursen et al., 2013; Duval et al., 2014; Gronke et al., 2016a), anisotropic gas distributions (Behrens et al., 2014; Zheng et al., 2014), and gas with power-law density profiles (Lao et al., 2020), as well as in the context of cosmological simulations (Cantalupo et al., 2005; Tasitsiomi, 2006; Laursen et al., 2007; Verhamme et al., 2012; Smith et al., 2019; Smith et al., 2021).

With the significant advancements on the theoretical side, many attempts have been made to bridge the gap between the simulations and observations, one of which is to

match the Ly α spectra derived from the RT models with the observed Ly α profiles. The most widely used RT model for this endeavor is the ‘shell model’, i.e., a spherical, expanding/contracting H I shell. Thus far, the shell model has managed to reproduce a wide variety of Ly α profiles, including typical single and double-peaked profiles from Lyman break galaxies (LBGs), Ly α emitters (LAEs), damped Ly α systems (DLAs) and Green Pea galaxies (e.g., Verhamme et al., 2008; Dessauges-Zavadsky et al., 2010; Vanzella et al., 2010; Krogager et al., 2013; Hashimoto et al., 2015; Yang et al., 2016; Yang et al., 2017), along with the P-Cygni profiles and damped absorption features in nearby starburst galaxies (e.g. Atek et al., 2009; Martin et al., 2015). Nevertheless, a number of discrepancies between the fitted parameters of the shell model and observational constraints have been observed (e.g. Kulas et al., 2012; Hashimoto et al., 2015; Yang et al., 2016; Yang et al., 2017). Most recently, Orlitová et al. (2018) reported three major discrepancies emerged from shell modeling of the observed Ly α profiles of twelve Green Pea galaxies, namely: (1) the required intrinsic Ly α line widths are on average three times broader than the observed Balmer lines; (2) the inferred outflow velocities of the shell ($\lesssim 150 \text{ km s}^{-1}$) are significantly lower than the characteristic outflow velocities ($\sim 300 \text{ km s}^{-1}$) indicated by the observed ultraviolet (UV) absorption lines of low-ionization-state elements; (3) the best-fit systemic redshifts are larger (by 10 – 250 km s^{-1}) than those derived from optical emission lines. Such inconsistencies suggest the limitations of the shell model and necessitate the development of more realistic RT models.

In addition, it is unclear whether the derived values of the shell model can be directly used to infer other physical properties of the Ly α -emitting object. For example, Verhamme et al. (2015) proposed that low H I column densities ($\lesssim 10^{18} \text{ cm}^{-2}$) inferred from observed Ly α profiles should indicate Lyman-continuum (LyC) leakage. However, it has not been verified quantitatively that a tight correlation does exist between the H I column density inferred from Ly α and the LyC escape fraction as expected theoretically (see Eq. (4) in Verhamme et al. 2017). The situation is even more complicated when more physics (e.g., turbulence) is considered, e.g., Kakiichi et al. (2021) find that a high average H I column density still allows high LyC leakage, as LyC photons can escape through narrow photoionized channels with a large fraction of hydrogen remaining neutral (see their Section 4.2; see also Kimm et al. 2019).

The shell model is known as being unrealistically monolithic as it consists of only

one phase of H I at $\sim 10^4$ K (the ‘cool’ phase). Alternatively, Ly α radiative transfer has been studied in multiphase, clumpy models (e.g., Neufeld 1991; Hansen et al. 2006; Dijkstra et al. 2012; Laursen et al. 2013; Duval et al. 2014; Gronke et al. 2016a), as numerous observations have revealed the multiphase nature of the interstellar/circumgalactic/intergalactic medium (ISM/CGM/IGM, respectively; see reviews by Cox 2005; Tumlinson et al. 2017; McQuinn 2016). This multiphase, clumpy model consists of two different phases of gas: cool clumps of H I ($\sim 10^4$ K) embedded in a hot, highly ionized medium ($\sim 10^6$ K). Using the framework in Gronke et al. (2016a), Li et al. (2021) and Li et al. (2022b) successfully reproduced the spatially resolved Ly α profiles in Ly α blobs 1 and 2 with the multiphase, clumpy model. These results have not only demonstrated the feasibility of the multiphase, clumpy model, but also motivated us to gain a deeper understanding of the physical meaning of the derived model parameters.

The primary goal of this work is to figure out the links between the parameters of the relatively newly developed, more physically realistic multiphase, clumpy model and the commonly adopted shell model, as well as what physical information can be extracted from observed Ly α spectra. A schematic representation of the configuration of these two models is shown in Figure 5.1. The shell model only has four most important parameters¹: the shell expansion velocity (v_{exp}), the shell H I column density ($N_{\text{HI,shell}}$), the shell effective temperature (T_{shell}) or the Doppler parameter (b), and the intrinsic Ly α line width (σ_i) (Verhamme et al., 2006; Gronke et al., 2015). The multiphase, clumpy model has six most crucial parameters: (1) the cloud covering factor (f_{cl}), which is the mean number of clumps per line-of-sight; (2) the H I column density of the clumps ($N_{\text{HI,cl}}$); (3) the velocity dispersion of the clumps (σ_{cl}); (4) the radial outflow velocity of the clumps (v_{cl}); (5) the residual H I number density in the inter-clump medium (ICM, $n_{\text{HI,ICM}}$); (6) the radial outflow velocity of the ICM (v_{ICM}). For both models, an additional post-processed parameter, Δv , is used to determine the systemic redshift of the Ly α emitting source. The shell model parameters capture different properties of the Ly α spectra: v_{exp} determines the blue-to-red peak flux ratio, and sets the position of the absorption trough between two peaks (as $-v_{\text{exp}}$ corresponds to the largest optical depth); $N_{\text{HI,shell}}$ dictates the amount of peak separation and the depth of the absorption trough; T_{shell} or b describes the internal kinematics of the shell (including thermal and turbulent velocities) and controls the width of the Ly α profile, but is usually poorly constrained

¹Here we assume that the shell model is dust-free, as the dust content is usually poorly constrained by the observed Ly α spectra (Gronke et al., 2015).

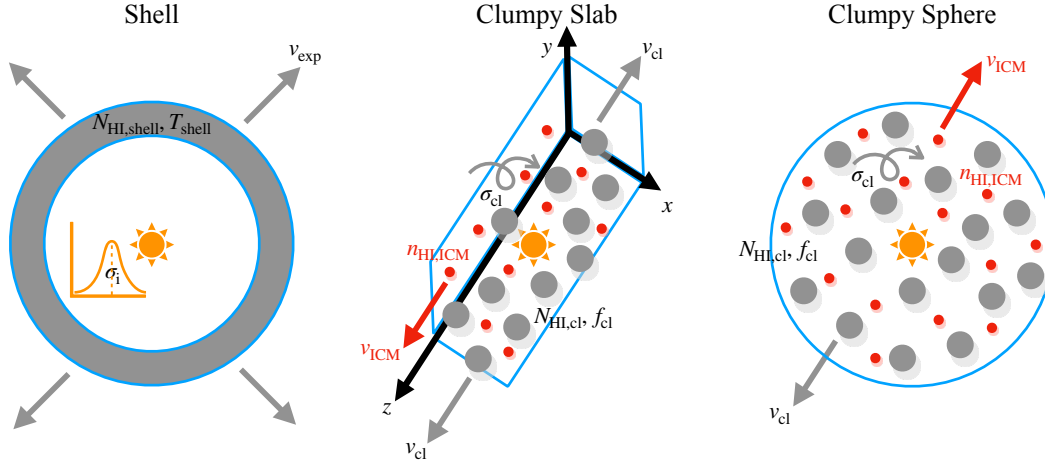


Figure 5.1: **A schematic representation of the configuration of the shell model and the multiphase, clumpy model.** The four most important parameters in the shell model are: the shell expansion velocity (v_{exp}), the shell HI column density ($N_{\text{HI,shell}}$), the shell effective temperature (T_{shell}) or the Doppler parameter (b), and the intrinsic Ly α line width (σ_i). The multiphase, clumpy model has six most crucial parameters: (1) the cloud covering factor (f_{cl}), which is the mean number of clumps per line-of-sight; (2) the HI column density of the clumps ($N_{\text{HI,cl}}$); (3) the velocity dispersion of the clumps (σ_{cl}); (4) the radial outflow velocity of the clumps (v_{cl}); (5) the residual HI number density in the inter-clump medium (ICM, $n_{\text{HI,ICM}}$); (6) the radial outflow velocity of the ICM (v_{ICM}). The orange solar sign represents the central Ly α emitting source in each model. Two different geometries for the multiphase, clumpy model, slab and sphere, are explored in this work.

by the data (Gronke et al., 2015); σ_i (if large enough) sets the extent of the wings of the spectrum. The multiphase, clumpy model parameters capture similar spectral properties but in different ways: v_{cl} and v_{ICM} determines the blue-to-red peak flux ratio²; $n_{\text{HI,ICM}}$ and $f_{\text{cl}}N_{\text{HI,cl}}$ together dictate the amount of peak separation and the depth of the absorption trough, as both of them contribute to the total HI column density; σ_{cl} sets the width of the spectrum.

Li et al. (2022b) have observed significant correlations between certain pair of model parameters (namely $v_{\text{exp}} - v_{\text{cl}}$) derived by fitting fifteen observed Ly α spectra. These results are enlightening yet not rigorous and may suffer from parameter degeneracy due to their empirical nature. Motivated by the fact that the multiphase, clumpy model may converge to the shell model in the limit of very high f_{cl} (Gronke

²In the multiphase, clumpy model, the absorption trough is not necessarily set by $-v_{\text{cl}}$ unless the total column density of the clumps is high enough to be optically thick (i.e., the flux density at line center is close to zero) and the clumps and ICM are co-outflowing at the same velocity (see §5.4).

et al., 2017), in this work we attempt to find quantitative correlations between the parameters of two models, with the aim of better understanding the physical meaning of model parameters and their relation to Ly α spectral properties.

The structure of this paper is as follows. In §5.2, we describe the methodology of this work. In §5.3, we present the intrinsic parameter degeneracies of the shell model. In §5.4, we explore the connection between the shell model and the multiphase, clumpy model. In §5.5, we discuss on how to interpret the physical parameters extracted from Ly α spectra. In §5.6, we summarize and conclude. The physical units used throughout this paper are km s $^{-1}$ for velocity, cm $^{-2}$ for column density, and K for temperature, unless otherwise specified.

5.2 Methodology

In this work, we extract physical parameters from Ly α spectra by fitting them with a grid of shell models. The fitted Ly α spectra can be one of the following: (1) a shell model spectrum; (2) a (multiphase) clumpy model spectrum; (3) an observed Ly α spectrum. The grid of shell models that we use was previously described in Gronke et al. (2015). This shell model grid consists of 12960 discrete RT models, with $[v_{\text{exp}}, \log N_{\text{HI, shell}}, \log T_{\text{shell}}]$ varying between $[0, 490]$ km s $^{-1}$, $[16.0, 21.8]$ cm $^{-2}$ and $[3, 5.8]$ K, respectively. Each shell model is calculated via Monte-Carlo RT using 20000 Ly α photon packages generated from an a priori Gaussian intrinsic spectrum $N(0, \sigma^2)$, where $\sigma = 800$ km s $^{-1}$. The intrinsic Ly α line width, $\sigma_i \in [1, 800]$ km s $^{-1}$, is accounted for in the form of a weighting function in post-processing. We do not consider the effect of dust in this work as it is usually a poorly constrained parameter³ (Gronke et al., 2015).

To properly explore the possibly multimodal posterior of the shell model parameters, we use a python package `dynesty` (Skilling, 2004; Skilling, 2006; Speagle, 2020) that implements the nested sampling algorithm for our fitting pipeline. The model spectrum of each sampled point in the parameter space is calculated via linear flux interpolation on the model grid rather than running the computationally expensive RT “on the fly”. When fitting the Ly α spectra, we manually add a constant 1- σ uncertainty of about 10% of the maximum flux density to the normalized (mock) data to reflect the typical observational uncertainties. The uncertainties in

³Note that dust plays a similar role in both the shell model and the multiphase, clumpy model (especially in the limit of many clumps per sightline, see, e.g. Neufeld, 1991; Gronke, 2017), which are both assumed to be homogeneous in this work. The effect of dust could be potentially important in an inhomogeneous medium (e.g., where the dust-to-gas ratio is inhomogeneous), but is beyond the scope of this work.

the fitted parameters are determined as certain quantiles (e.g., 16% – 84%, or 1- σ confidence intervals) of the samples in the marginalized posterior probability distributions.

5.3 Results I: Intrinsic Parameter Degeneracies of the Shell Model

In this section, we show the existence of intrinsic parameter degeneracies in the shell model revealed by fitting, in preparation for our subsequent discussion. We consider the two following cases: static shell and outflowing shell, respectively.

Static Shells: Degeneracy Between $N_{\text{HI, shell}}$ and T_{shell}

Here we show that for static shells in the optically thick regime, models with the same $N_{\text{HI, shell}} T_{\text{shell}}^{0.5}$ exhibit identical Ly α spectra. Theoretically, the angular-averaged Ly α spectral intensity $J(x)$ emerging from a static, uniform H I sphere is given analytically as (Adams, 1972; Harrington, 1973; Neufeld, 1990; Dijkstra et al., 2006a):

$$J(x) = \frac{\sqrt{\pi}}{\sqrt{24}a\tau_0} \left(\frac{x^2}{1 + \cosh \left[\sqrt{\frac{2\pi^3}{27}} \frac{|x^3|}{a\tau_0} \right]} \right) \quad (5.1)$$

where $x \equiv (\nu - \nu_0)/\Delta\nu_D$ is the unitless frequency, and the Doppler parameter $\Delta\nu_D = v_{\text{th}}\nu_0/c = \sqrt{2k_{\text{B}}T/m_{\text{H}}}\nu_0/c$, with T being the H I gas temperature. Here ν is the Ly α photon frequency and $\nu_0 = 2.47 \times 10^{15}$ Hz is the Ly α central frequency. Moreover, $a = \Delta\nu_{\text{L}}/2\Delta\nu_D \propto T^{-0.5}$ is the Voigt parameter, where $\Delta\nu_{\text{L}}$ is the natural line broadening; τ_0 is the H I optical depth at the line center and $\tau_0 \propto N_{\text{HI}} T^{-0.5}$. The complete expressions for a and τ_0 can be found, e.g., in Dijkstra et al. (2006a).

One can then switch from the frequency space to the velocity space by converting $J(x)$ to $J(v)$ via $(\nu - \nu_0)/\nu_0 = xv_{\text{th}}/c$. Then it is evident that with proper normalization, $J(v)$ would be identical for different combinations of (N_{HI}, T) that give the same $a\tau_0 v_{\text{th}}^3$, which is $\propto N_{\text{HI}} T^{0.5}$. Alternatively, one can derive this $N_{\text{HI}} T^{0.5}$ degeneracy by estimating the most likely escape frequency of Ly α photons (see, e.g., Eq. (5) in Gronke et al. 2017, which originally comes from Adams 1972).

We show this degeneracy in Figure 5.2 for two sets of static shell models ($\sigma_i = 200$ and 400 km s^{-1} , respectively) with the same $N_{\text{HI}} T^{0.5}$. It can be seen that the normalized intensity distributions of each set of models are nearly identical (modulo numerical noise). Note that this degeneracy only exists in the optically thick regime (i.e., $a\tau_0 \gtrsim 10^3$) where Eq. (5.1) holds (Harrington, 1973; Neufeld, 1990). As

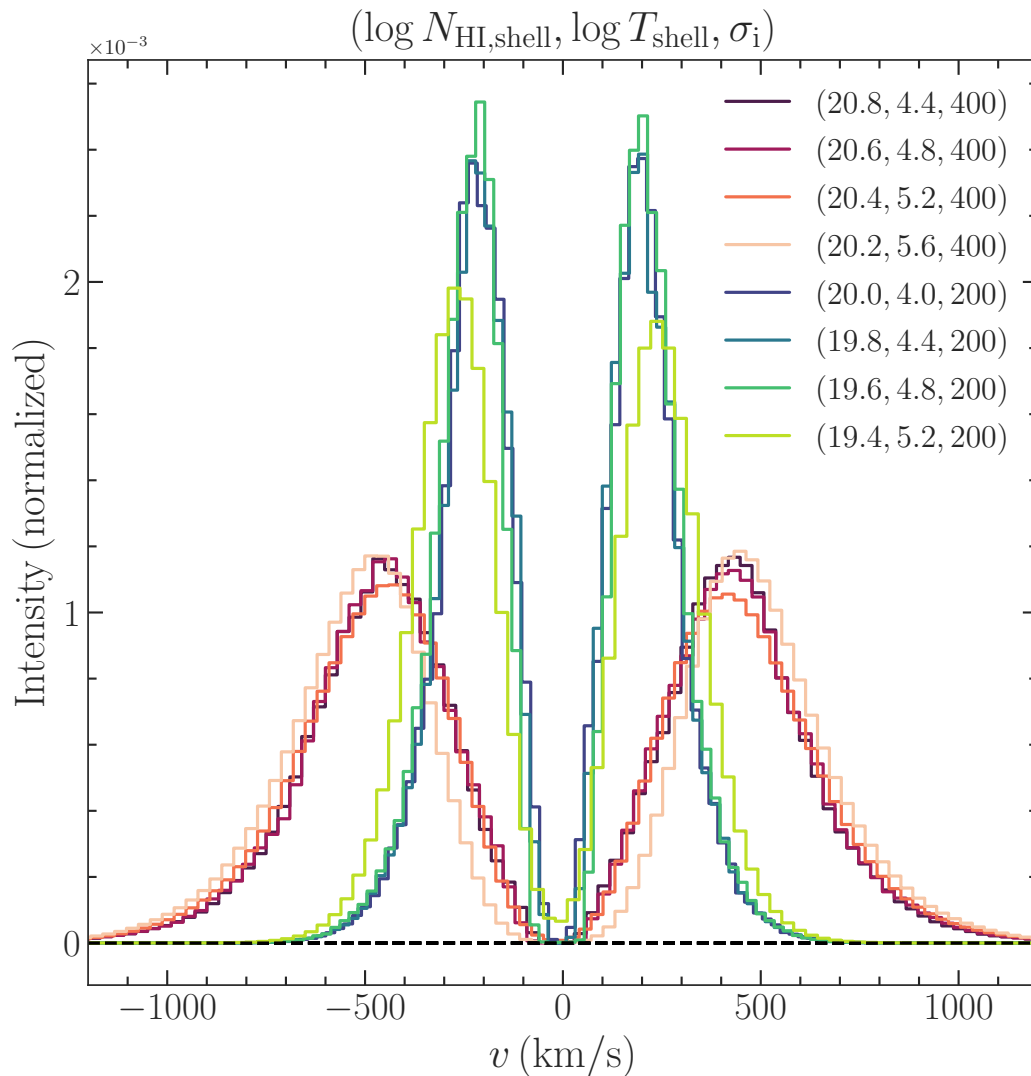


Figure 5.2: **Examples of degenerate static shell models with the same $N_{\text{HI}} T^{0.5}$.** Different colored curves represent two sets of shell models ($\sigma_i = 200$ and 400 km s^{-1} , respectively) with the same $N_{\text{HI}} T^{0.5}$. It can be seen that the normalized intensity distributions of each set of models are nearly identical. Note that this degeneracy only exists in the optically thick regime ($a\tau_0 \gtrsim 10^3$); at $a\tau_0 = 2.8 \times 10^{-13}(N_{\text{HI}}/T) \simeq 100$ the models start to deviate from the other degenerate models (the light lime and light pink curves).

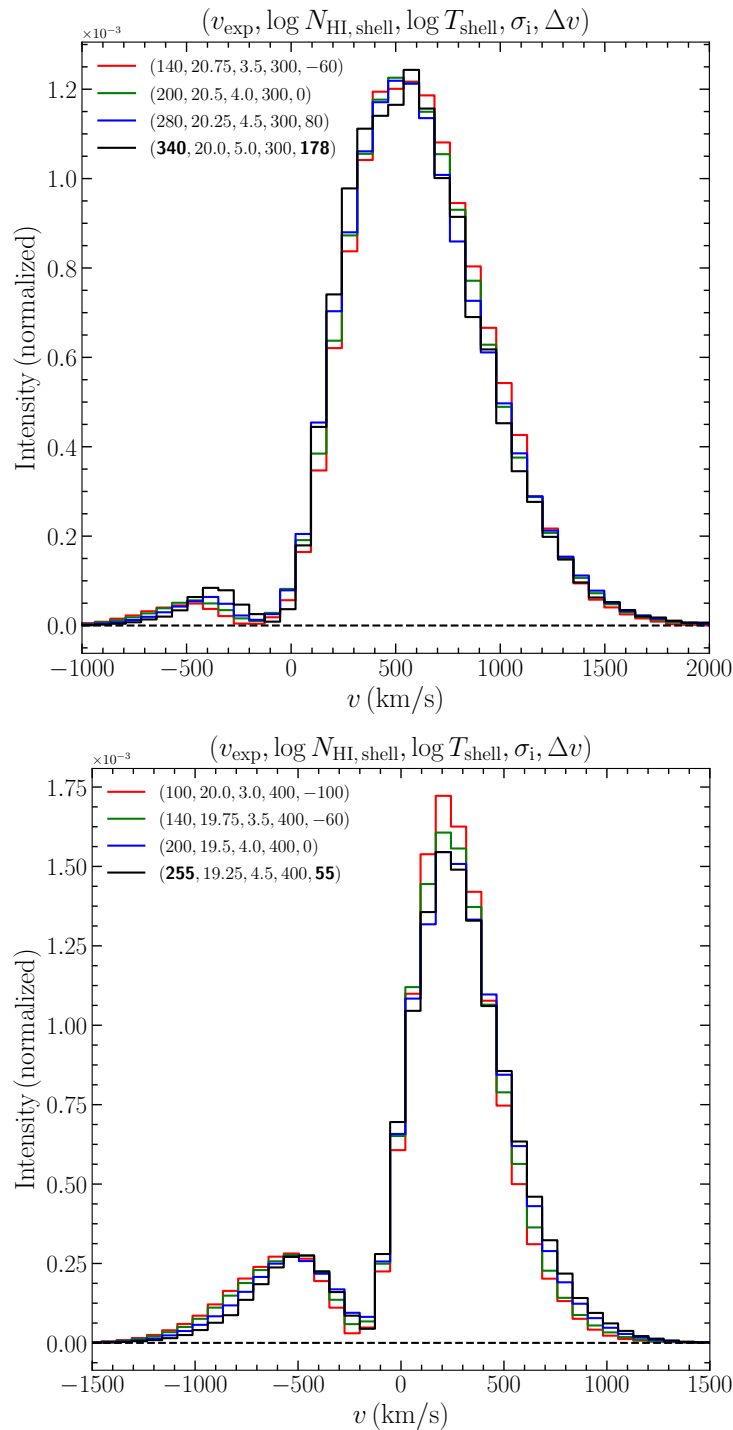


Figure 5.3: **Examples of degenerate outflowing shell models.** Different colored curves represent two sets of outflowing shell models ($\sigma_i = 300$ and 400 km s^{-1} , respectively), each consisting of a series of models with increasing T_{shell} , with a step size of 0.5 dex. Accordingly, $N_{\text{HI,shell}}$ decreases by 0.25 dex and v_{exp} increases by a factor of $\sqrt{2}$. Each set of spectra appear essentially identical to each other, except for the one with the largest T_{shell} (the black curve), which is the only model in the series that does not satisfy $a\tau_0 \gtrsim 10^3$. We fit this model with our shell model grid by fixing $N_{\text{HI,shell}}$, T_{shell} and σ_i at the expected values and leaving v_{exp} and Δv free. A decent fit is achieved, albeit with the best-fit v_{exp} values (shown in bold) slightly lower than expected.

shown in Figure 5.2, models with the same $N_{\text{HI}} T^{0.5}$ but $a\tau_0 = 2.8 \times 10^{-13} (N_{\text{HI}}/T) \simeq 100$ start to deviate from the other degenerate models, as Eq. (5.1) is no longer applicable.

Outflowing Shells: Degeneracy Among $(v_{\text{exp}}, N_{\text{HI,shell}}, T_{\text{shell}}, \Delta v)$

If the shell is outflowing, the $N_{\text{HI}} T^{0.5}$ degeneracy starts to be broken – in fact, the models with higher N_{HI} will have fewer flux in the blue peak, as it is more difficult for the blue photons to escape from the shell. However, such a larger level of asymmetry can be compensated by a lower shell expansion velocity. Heuristically, we find that if we allow the Ly α spectra to shift along the velocity axis (i.e., the systemic velocity of Ly α source is not necessarily at zero; this is often the case for fitting real observed Ly α spectra, where the systemic redshift of the Ly α source has considerable uncertainties), two shell models with $(v_{\text{exp}}, \log N_{\text{HI,shell}}, \log T_{\text{shell}})$ and $\sim (2v_{\text{exp}}, \log N_{\text{HI,shell}} - 0.5 \text{ dex}, \log T_{\text{shell}} + 1 \text{ dex}, \Delta v)$ are degenerate with each other, where Δv is the difference in systemic velocity of the two Ly α sources. We have not been able to analytically derive such a quadruple parameter degeneracy rigorously, but we verify its existence numerically in this section.

We show this degeneracy with two sets of examples in Figure 5.3. Each set contains a series of models with increasing T_{shell} , with a step size of 0.5 dex. Accordingly, $N_{\text{HI,shell}}$ decreases by 0.25 dex and v_{exp} increases by a factor of $\sqrt{2}$. As can be seen in Figure 5.3, each set of spectra appear essentially identical to each other, except for the one with the largest T_{shell} (the black curve), which is the only model in the series that does not satisfy $a\tau_0 \gtrsim 10^3$. We fit this model with our shell model grid by fixing $N_{\text{HI,shell}}$, T_{shell} and σ_i at the expected values and leaving v_{exp} and Δv free. It turns out that a decent fit can be achieved, with the best-fit v_{exp} values (shown in bold) slightly lower than expected. In other words, this quadruple degeneracy is broken quantitatively but still holds qualitatively.

Such a quadruple degeneracy reminds us of the limitation of shell models in fitting observed Ly α spectra, as v_{exp} , $N_{\text{HI,shell}}$, T_{shell} and Δv cannot be determined independently by merely fitting. Additional constraints (e.g., a very accurate measurement of the systemic redshift of the Ly α emitting source) have to be introduced break the parameter degeneracy.

A Real-World Example: Fitting the Ly α Spectrum of a Green Pea Galaxy, GP 0926+4427

Here we further show the quadruple degeneracy with a practical example. We fit an observed Ly α spectrum of a Green Pea galaxy, GP 0926+4427 ($z = 0.1807$; Henry et al. 2015) with our shell model grid. The spectrum is obtained from the Ly α Spectral Database (LASD⁴; Runnholm et al. 2021). Following Orlitová et al. (2018), we account for the spectral resolution of the HST Cosmic Origins Spectrograph (COS) by convolving the shell model spectra with a FWHM = 100 km s⁻¹ Gaussian before comparing them to the observed Ly α spectrum⁵.

We present two degenerate best-fit shell models in Figure 5.4. These two best-fit models, whose χ^2 per degree of freedom are very close to each other, have the parameter degeneracy as described in §5.3 – the shell expansion velocity of the high temperature model is about a factor of two higher than the low temperature model, which consequently affects the fitted systemic redshift of the Ly α source. This result may explain the two major discrepancies reported in Orlitová et al. (2018): (1) the inferred shell outflow velocities are significantly lower than the characteristic outflow velocities indicated by the observed UV absorption lines; (2) the best-fit systemic redshifts are larger than those derived from optical emission lines. When fitting observed Ly α spectra, the best-fit model with a low v_{exp} may happen to provide the best match for the data, but another degenerate model (or a series of degenerate models) with much higher v_{exp} values can actually fit the data similarly well and hence should also be considered as reasonable solutions.

5.4 Results II: Connecting the Shell Model to the Multiphase, Clumpy Model

In this section, we attempt to connect the shell model parameters to the multiphase, clumpy model parameters. We generate a series of clumpy models as our “mock data” for fitting. We first consider a three-dimensional semi-infinite slab geometry and later we will consider a finite spherical geometry (§5.4). This is because for a semi-infinite clumpy slab, it is numerically easier to achieve a very high clump covering factor ($f_{\text{cl}} \gtrsim 1000$, i.e., the average number of clumps per line-of-sight is large enough to be in the “very clumpy” regime, where the clumpy medium is expected to behave like a homogeneous medium in terms of the emergent Ly α

⁴<http://lasd.lyman-alpha.com>

⁵Note that different from Orlitová et al. (2018), we do not consider the effect of dust, as the dust optical depth is usually a poorly constrained parameter and may introduce additional degeneracy (Gronke et al., 2015).

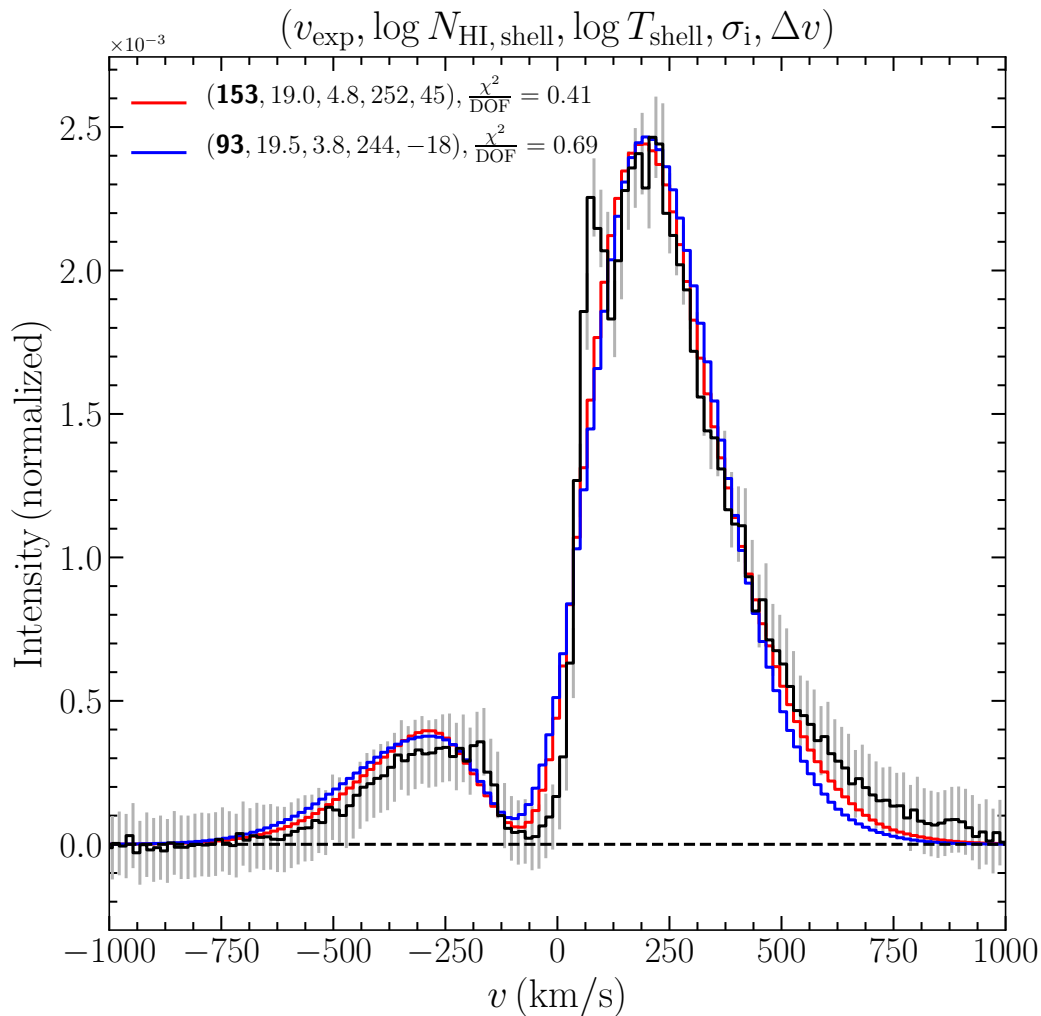


Figure 5.4: **Degeneracy shown in fitting the Ly α spectrum of a Green Pea galaxy, GP 0926+4427.** The observed spectrum is shown in black and two degenerate best-fit shell models are shown in red and blue, respectively. The χ^2 (per degree of freedom, DOF) values of these two best-fit models are very close to each other, but the shell expansion velocity of the high temperature model is about a factor of two higher than the low temperature model (as highlighted in bold), which consequently affects the fitted systemic redshift of the Ly α source. This result may explain the two major discrepancies reported in the literature (see §5.3 for details).

spectrum, Gronke 2017), which is prohibitively computationally expensive for a finite clumpy sphere. The clumpy slab models are periodic in the x and y directions with a half-height B of 50 pc⁶ in the z direction. The clumps within the slab are spherical with radius of $r_{\text{cl}} = 10^{-3}$ pc filled with H I of a column density $N_{\text{HI,cl}}$. The clump covering factor is directly proportional to the volume filling factor of the clumps F_V via $f_{\text{cl}} = 3F_V B / 4r_{\text{cl}}$ (Dijkstra et al., 2012; Gronke et al., 2017).

Each clumpy model is calculated via Monte-Carlo RT using 10000 Ly α photon packages assuming a Gaussian intrinsic spectrum $N(0, \sigma_i^2)$, where $\sigma_i = 12.85 \text{ km s}^{-1}$ is the canonical thermal velocity dispersion of $T = 10^4 \text{ K}$ H I gas in the clumps⁷. Each model spectrum is normalized to a total flux of one before being fitted with the shell model grid.

Clumpy Slab with Static Clumps

We start by correlating the H I column density of the shell model with the equivalent average total column density of the single-phase, clumpy slab model, which is given by $N_{\text{HI,total}} = \frac{4}{3} f_{\text{cl}} N_{\text{HI,cl}}$, where the factor 4/3 comes from the spherical geometry of the clumps (Gronke et al., 2017). We first generate a series of static, single-phase, clumpy slab models by varying $N_{\text{HI,cl}}$ of the clumps with a very high covering factor f_{cl} (i.e., in the “very clumpy” regime) as the mock data. The clumps are fixed to a temperature of $T_{\text{cl}} = 10^4 \text{ K}$ and do not have any motions (neither random nor outflow velocities). The parameter values that we use are given in the first row of Table 5.1.

We first attempt to fit the clumpy slab model spectra with the large grid of shell models that we have described in §5.2. We find that the best-fit shell models are usually noisy and unsatisfactory due to the low number of effective photon packages – i.e., in order to match the relatively narrow widths of the clumpy slab model spectra (especially the ones with low $N_{\text{HI,total}}$), a weighting function with a small σ_i ($\lesssim 100 \text{ km s}^{-1}$, the actual intrinsic Ly α line width needed) is required, which effectively only includes only a small fraction of modeled photons⁸. Therefore, we build a customized grid of shell models to fit the clumpy slab model spectra. Such a grid is smaller but similar to the large shell model grid, with two major

⁶We emphasize that it is the H I column density that actually matters in the radiative transfer instead of the physical scales of the models.

⁷In the clumpy model, σ_i is fixed to be small and the clump velocity dispersion is responsible for the broadening of the spectrum. σ_i will not affect Ly α model spectra as long as it is smaller than the clump velocity dispersion (which is almost always the case, see §5.4).

⁸This problem is mitigated when the clumps have a considerable random velocity dispersion, which broadens the spectrum significantly (see §5.4 and the subsequent sections).

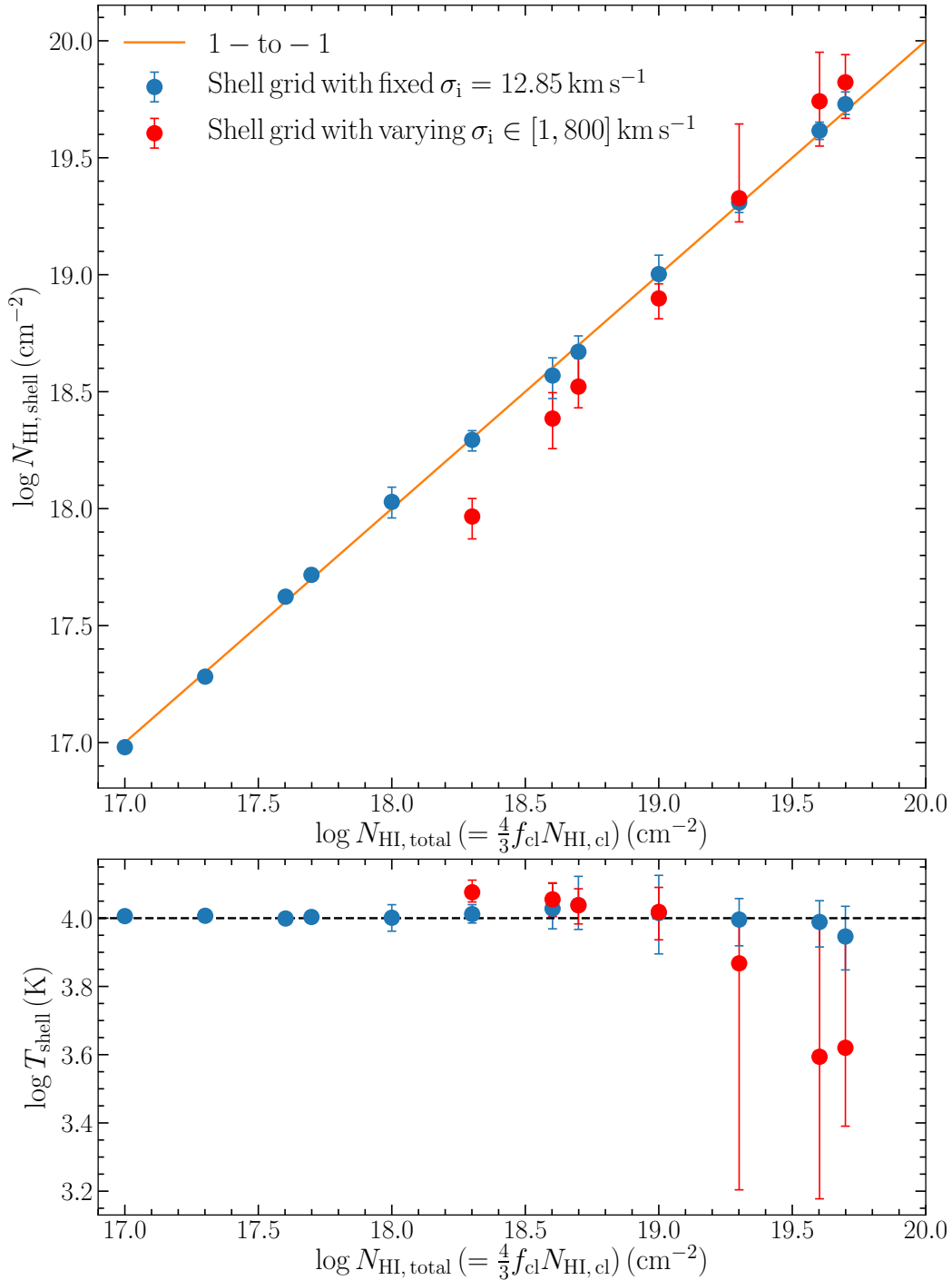


Figure 5.5: **Results of fitting static clumpy slab models with static shell models.** The blue and red points represent the parameter values derived from fitting with the customized, small shell model grid (with fixed $\sigma_i = 12.85 \text{ km s}^{-1}$) and the large shell model grid (with varying $\sigma_i \in [1, 800] \text{ km s}^{-1}$), respectively. *Upper:* The correlation between $N_{\text{HI, total}}$ and $N_{\text{HI, shell}}$. A very tight 1-to-1 correlation is present over three orders of magnitude. *Lower:* The distribution of the best-fit shell model temperatures T_{shell} . In all cases, T_{shell} values of 10^4 K (the clump temperature) are obtained within $1\text{-}\sigma$ uncertainties.

Table 5.1: Parameter values of the clumpy slab models (the mock data).

Model Parameter	F_V	f_{cl}	$\log N_{HI,cl}$	σ_{cl}	v_{cl}
Definition	Volume filling factor	Clump covering factor	Clump H I column density	Clump random velocity	Clump outflow velocity
(1)	(2)	(3)	(4)	(5)	(6)
Static Clumps	0.1	375	14.3 – 17.0 cm^{-2}	0	0
Randomly Moving Clumps	0.02 – 0.12	750 – 4500	15.7 – 17.6 cm^{-2}	(50, 100) km s^{-1}	0
Outflowing Clumps	0.08 – 0.12	3000 – 4500	15.7 – 17.0 cm^{-2}	(0, 50, 100) km s^{-1}	50 – 400 km s^{-1}

differences: (1) the shell expansion velocity is fixed to zero; (2) the photon packages are generated from a Gaussian intrinsic spectrum $N(0, \sigma_i^2)$ with $\sigma_i = 12.85 \text{ km s}^{-1}$, i.e., the same as the fitted clumpy slab models. In other words, the intrinsic Ly α spectrum has a fixed small line width that is also used to generate the mock data. We find that such a customized grid with only two varying parameters [$\log N_{HI,shell}$, $\log T_{shell}$] can yield better fits (as all the modeled photons contribute to the model spectra) and is significantly faster at fitting the mock data.

As shown in Figure 5.5, there is a tight, 1-to-1 correlation between $N_{HI,total}$ and $N_{HI,shell}$ over three orders of magnitude. Moreover, all of the T_{shell} values are consistent with 10^4 K (the clump temperature) within $1\text{-}\sigma$ uncertainties. Therefore, we conclude that the equivalent H I column density of a static, very clumpy slab can be exactly reproduced by a shell model with the same H I column density and the same temperature of the clumps. We show two examples of static shell model best-fits to static clumpy slab models in Figure 5.6.

Despite the shortcomings mentioned above, the large shell model grid is used to fit several static clumpy slab models to verify our results. Several examples⁹ are shown in Figure 5.5 with red points. We find that $N_{HI,shell}$ and T_{shell} can still be roughly obtained at their expected values, albeit with small deviations and larger uncertainties. The required intrinsic line widths range from ~ 50 to $\sim 100 \text{ km s}^{-1}$, depending on the width of the mock data. These intrinsic line width values should not have any physical meaning but just ensure that the extent of the wings is proper to yield a good fit.

Clumpy Slab with Randomly Moving Clumps

We further add a random velocity dispersion (a Gaussian with standard deviation of σ_{cl} for all three dimensions) to the clumps and attempt to correlate it with certain shell model parameters, such as the internal random motion (or the effective temperature of the shell, T_{shell}) of the shell model and the line width of the intrinsic Ly α

⁹These examples have $N_{HI,total}$ high enough to yield $\sigma_i \gtrsim 50 \text{ km s}^{-1}$, below which the fraction of photons included is too low to yield a decent fit.

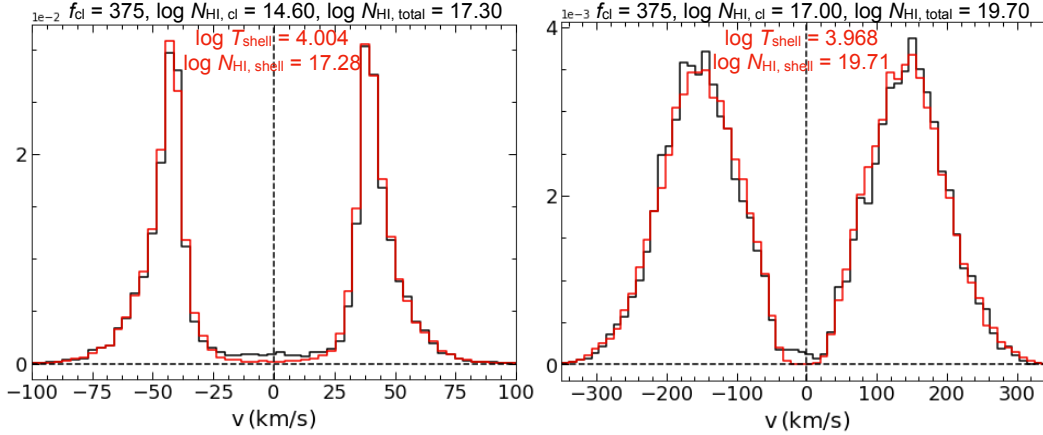


Figure 5.6: **Examples of static shell model best-fits (obtained by using the shell model grid with fixed σ_i) to static clumpy slab models.** Two panels represent two different $[f_{\text{cl}}, N_{\text{HI,cl}}]$ cases. The black curves represent the static clumpy slab model spectra and the red curves represent the shell model best-fits. Both T_{shell} and $N_{\text{HI,shell}}$ have been obtained at the expected values.

emission. We fit the clumpy slab model spectra with the large shell model grid, and the parameter values of the mock data are given in Table 5.1.

As shown in Figure 5.7, we find that:

1. The derived $N_{\text{HI,shell}}$ values are around the $N_{\text{HI,total}}$ values, but a noticeable deviation has emerged. On average, $N_{\text{HI,shell}}$ tends to be systemically higher than $N_{\text{HI,total}}$ by ~ 0.15 dex (a factor of 1.5), especially at $N_{\text{HI,total}} > 10^{20} \text{ cm}^{-2}$;
2. The shell effective temperatures (T_{shell}) are obtained at the effective temperatures of the clumpy slab model, defined as:

$$T_{\text{eff,slab}} = T_{\text{cl}} + \frac{\sigma_{\text{cl}}^2 m_{\text{H}}}{2k_{\text{B}}} \quad (5.2)$$

where T_{cl} is the kinematic temperature of one clump (fixed to 10^4 K), m_{H} is the hydrogen atom mass and k_{B} is the Boltzmann constant. As the maximum T_{shell} of our large shell model grid is set to be $10^{5.8}$ K, we only explore σ_{cl} up to $\sim 100 \text{ km s}^{-1}$, but we have verified that a larger σ_{cl} would still correspond to a T_{shell} value given by Eq. (5.2);

3. Large σ_i values (several times of σ_{cl}) are required to reproduce the wings of the clumpy slab models. These σ_i values are also positively correlated with σ_{cl} and $N_{\text{HI,total}}$, as shown in the bottom panel of Figure 5.7.

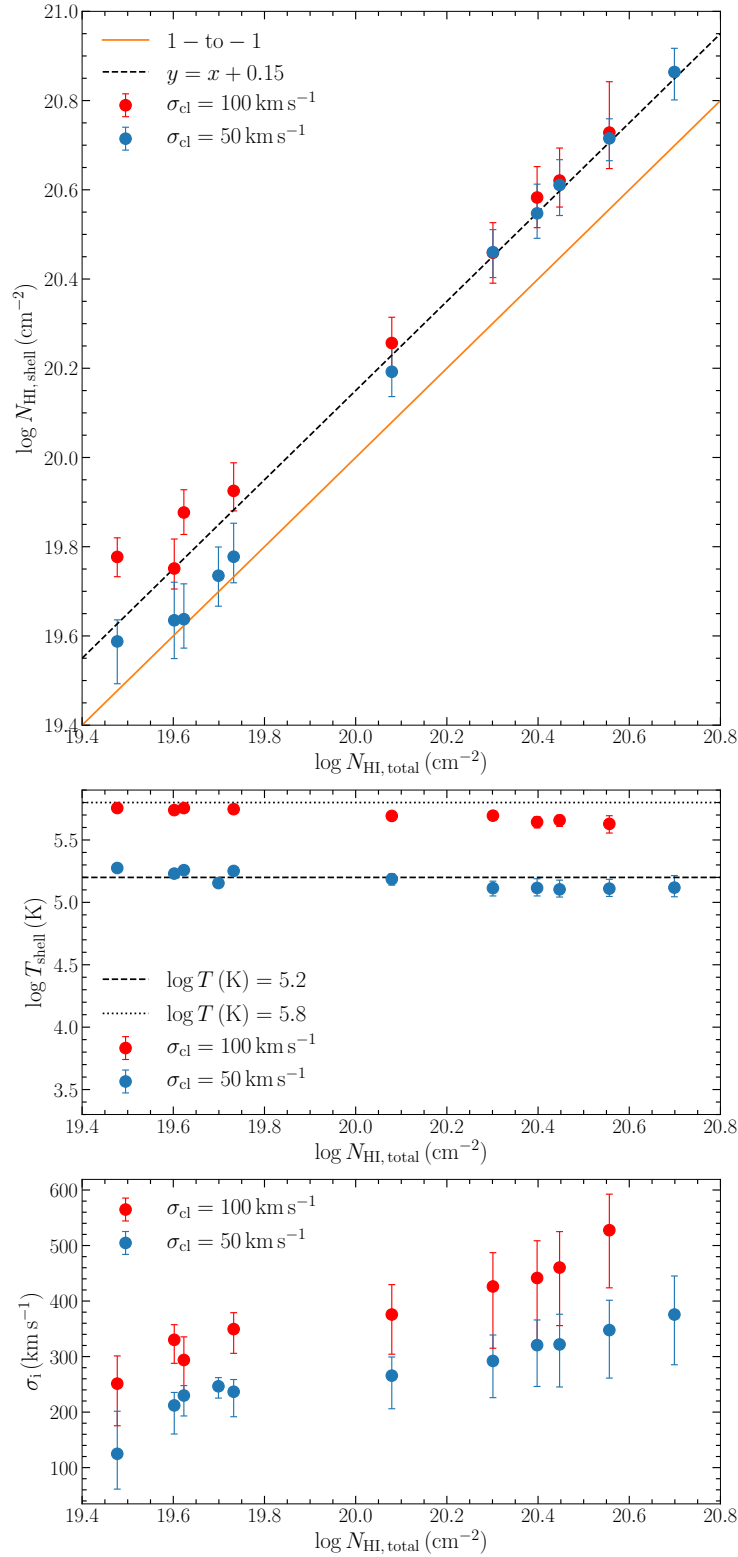


Figure 5.7: Results of fitting clumpy slab models with randomly moving clumps with shell models. *Upper:* The yielded $N_{\text{HI, shell}}$ values are around the $N_{\text{HI, total}}$ values, but a noticeable deviation has emerged. *Middle:* The yielded shell temperatures (T_{shell}) are mostly at the effective temperatures of the clumpy slab model. *Lower:* The distribution of the derived line widths of the intrinsic Ly α emission (σ_i) of the best-fit shell models. The blue and red points represent the $\sigma_{\text{cl}} = 50$ and 100 km s^{-1} models, respectively.

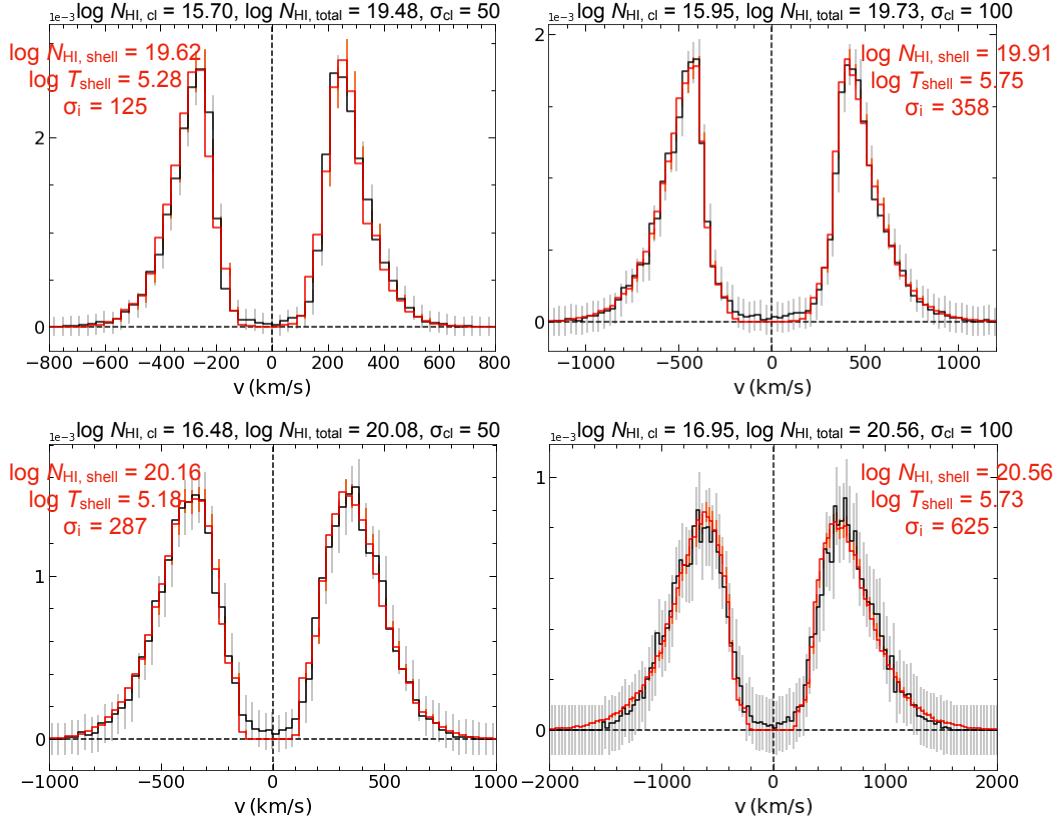


Figure 5.8: **Examples of shell model best-fits to randomly moving clumpy slab models.** Four panels represent four different $(N_{\text{HI,total}}, \sigma_{\text{cl}})$ cases. The black curves represent the outflowing clumpy slab model spectra and the red curves represent the shell model best-fits. T_{shell} have been obtained at the expected values from Eq. (5.2) within uncertainties.

We show four examples of shell model best-fits to the clumpy slab models in Figure 5.8. We find that (i) is due to the $N_{\text{HI,shell}} \propto T_{\text{shell}}^{-0.5}$ degeneracy. As we have detailed in Section 5.3, in the optically thick regime where $a\tau_0 = 2.8 \times 10^{-13} (N_{\text{HI,shell}}/T_{\text{shell}}) \gtrsim 10^3$, shell models with the same $N_{\text{HI,shell}} T_{\text{shell}}^{0.5}$ have almost identical line profiles, except that the ones with higher T_{shell} have slightly more extended troughs at the line center¹⁰. This explains the deviation of $N_{\text{HI,shell}}$ towards higher values at high HI column densities, where the trough of the clumpy slab model becomes “sharper” as the flux density at line center approaches zero, and is better fitted at a slightly lower T_{shell} (and hence higher $N_{\text{HI,shell}}$). We illustrate this effect in Figure 5.9. In other words, $N_{\text{HI,shell}}$ is still consistent with $N_{\text{HI,total}}$ if we account for this $N_{\text{HI,shell}} \propto T_{\text{shell}}^{-0.5}$ degeneracy.

¹⁰This is because the cross section function of a higher T_{shell} is more extended near the line center (see Eq. (54) and (55) in Dijkstra 2017).

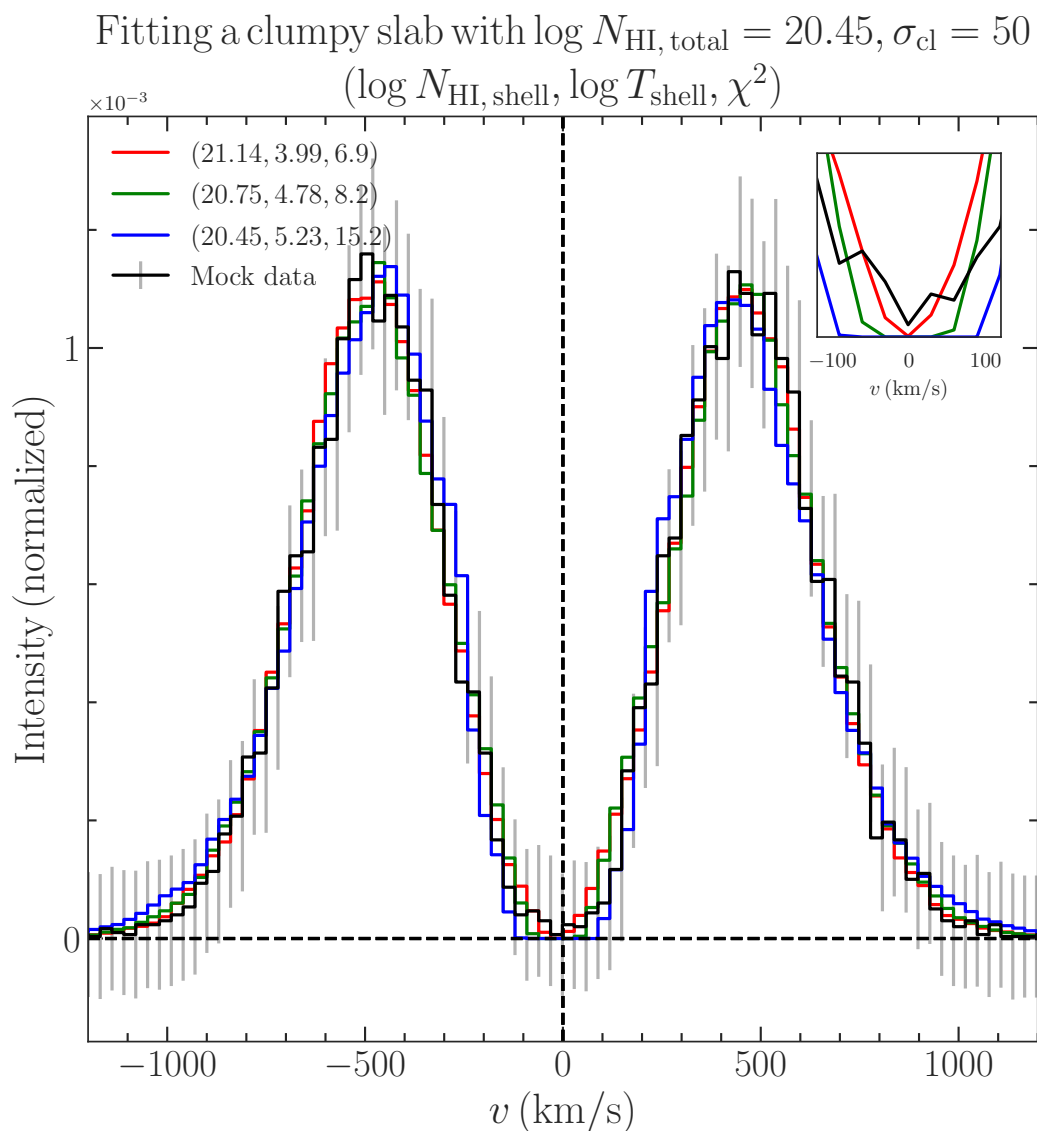


Figure 5.9: **Model examples showing the degeneracy between $N_{\text{HI, shell}}$ and T_{shell} .** The curves with different colors represent the clumpy slab model fitted (black) and the degenerate shell models with different $(\log N_{\text{HI, shell}}, \log T_{\text{shell}}, \chi^2)$, obtained by fitting within a certain parameter subspace. As shown in the inset, the models with higher T_{shell} have more extended troughs at line center and thus are less favored in the fitting to the clumpy slab models (the mock data), which have sharper troughs at high $N_{\text{HI, total}}$.

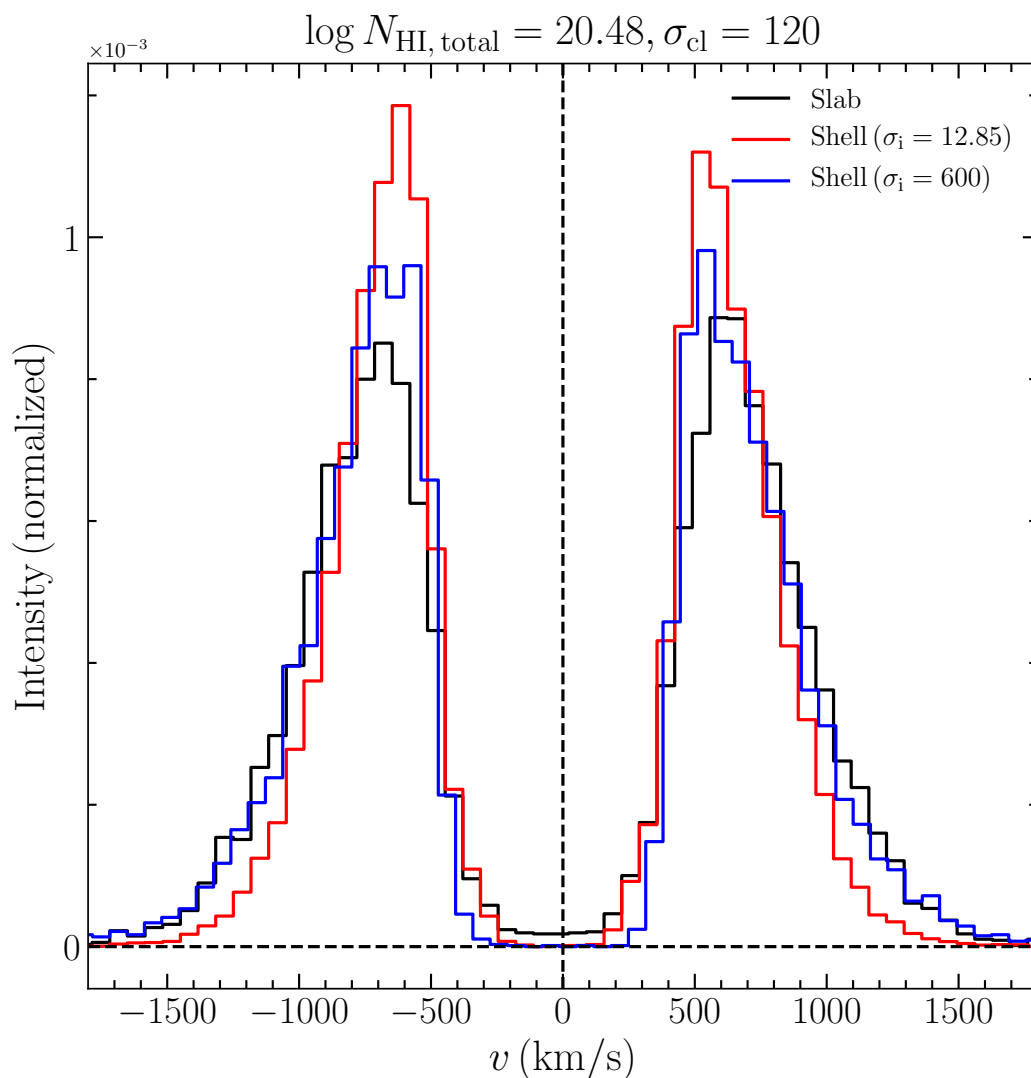


Figure 5.10: **Comparison between a clumpy slab model and two shell models with corresponding parameters and $\sigma_i = 12.85 / 600 \text{ km s}^{-1}$.** The black curve is an example clumpy slab model with $N_{\text{HI, total}}$ and σ_{cl} values labeled on the top of the plot; the red and blue curves are the shell models at the expected $N_{\text{HI, total}}$ and T_{shell} values with $\sigma_i = 12.85 \text{ km s}^{-1}$ and 600 km s^{-1} , respectively. It is clear that the clumpy slab model tends to have lower peaks and larger fluxes near the line center than the corresponding homogeneous shell model with a small σ_i ; such a mismatch is mitigated by the broadening effect of a large σ_i .

Moreover, (iii) is due to the intrinsic differences between the clumpy slab model and the shell model. As shown in Figure 5.10 (cf. Figure 5 in Gronke et al. 2017), for $\sigma_{\text{cl}} > 0$, the clumpy slab model (black curve) tends to have lower peaks and larger fluxes near the line center, as compared to the corresponding homogeneous shell model (red curve). Therefore, in order to obtain a good fit, a large σ_i is required to flatten the peaks and spread the fluxes out into the wings (blue curve). As σ_{cl} or $N_{\text{HI, total}}$ increases, the difference between the peak fluxes of two different models becomes larger, which requires a larger σ_i . If we force σ_i to be small, the shell models would fail to fit the clumpy slab model, as a much higher HI column density than $N_{\text{HI, total}}$ is required to fit the broad wings and it will inevitably yield a significant mismatch in the peaks.

As large σ_i values have been shown to be inconsistent with the observed nebular emission line widths (e.g., H α or H β , Orlitova et al. 2018), it is reasonable to postulate that the clumpy model is a more realistic description of the actual gas distribution in ISM/CGM, as it naturally alleviates such discrepancies with moderate velocity dispersions of the clumps (see also Li et al. 2022b). We will further discuss this point in §5.5.

Clumpy Slab with Outflowing Clumps

We further attempt to add a uniform outflow velocity (v_{cl}) to the clumps and correlate it with the shell expansion velocity (v_{exp}). We consider two different cases: (1) $v_{\text{cl}} > 0$, $\sigma_{\text{cl}} = 0$; (2) $v_{\text{cl}} > 0$, $\sigma_{\text{cl}} > 0$, i.e., outflowing clumps without and with clump random motion, respectively. We find that in both cases, a considerably large σ_i is still required to achieve decent fits, otherwise the shell model best-fit would have a dip between two peaks on the red side, whereas the clumpy slab model has only one smooth red peak.

As shown in Figure 5.11, we find that:

1. The fitted v_{exp} values are mostly consistent with v_{cl} within uncertainties;
2. $N_{\text{HI, shell}}$ are mostly reproduced at $N_{\text{HI, total}}$, albeit with several outliers with $\Delta \log N_{\text{HI}} \gtrsim 0.3$ dex in the large σ_{cl} cases;
3. T_{shell} are mostly reproduced at $T_{\text{eff, slab}}$ within uncertainties;
4. Large σ_i values are still required and they increase as σ_{cl} or v_{cl} increases.

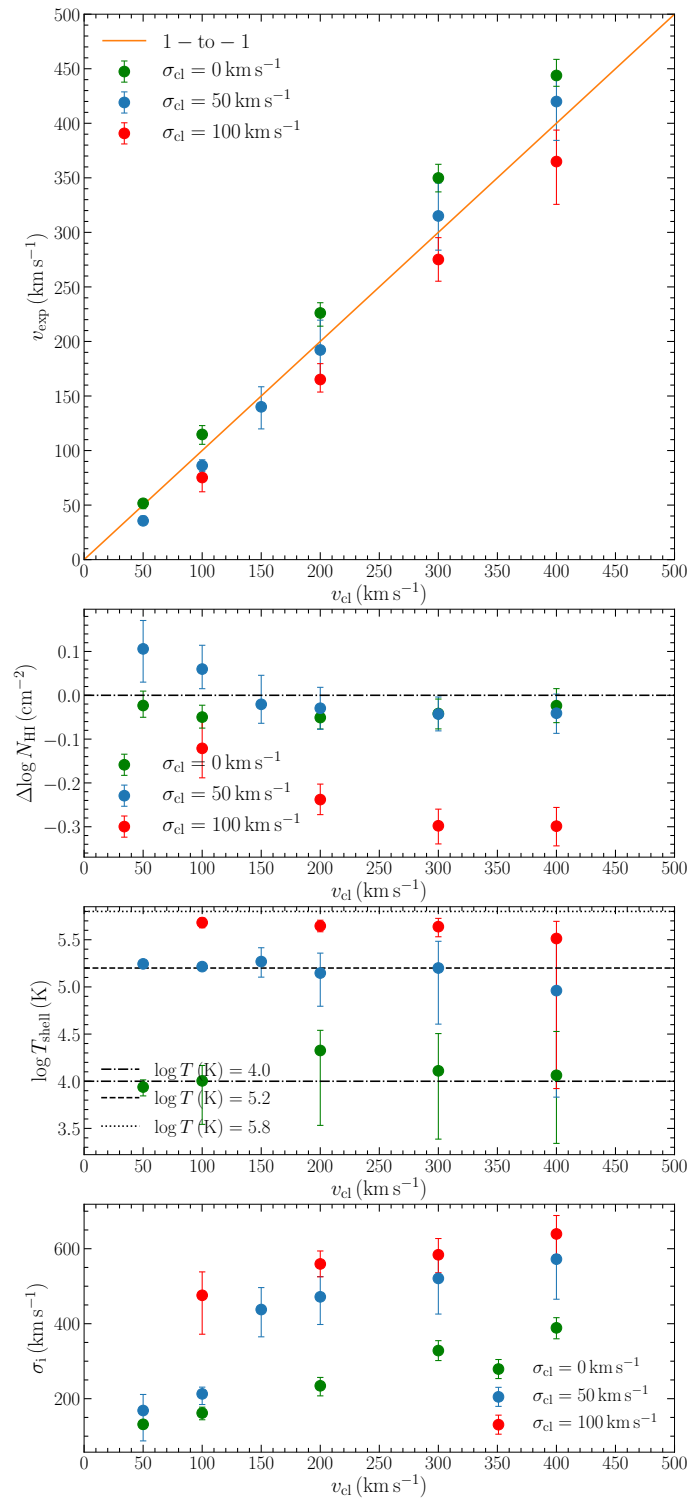


Figure 5.11: **Results of fitting clumpy slab models with outflowing moving clumps with shell models.** *Upper:* The derived shell expansion velocities are mostly at the clump outflow velocities; *Upper Middle:* $N_{\text{HI,shell}}$ are reproduced mostly at $N_{\text{HI,total}}$, albeit with several outliers with $\Delta \log N_{\text{HI}} \gtrsim 0.3$ dex; *Lower Middle:* The derived shell temperatures are mostly at the effective temperatures of the clumpy slab model; *Lower:* The distribution of the derived intrinsic Ly α line widths (σ_i) of the best-fit shell models, which increase as σ_{cl} or v_{cl} increases. The green, blue and red points represent the $\sigma_{\text{cl}} = 0, 50$ and 100 km s⁻¹ models, respectively.

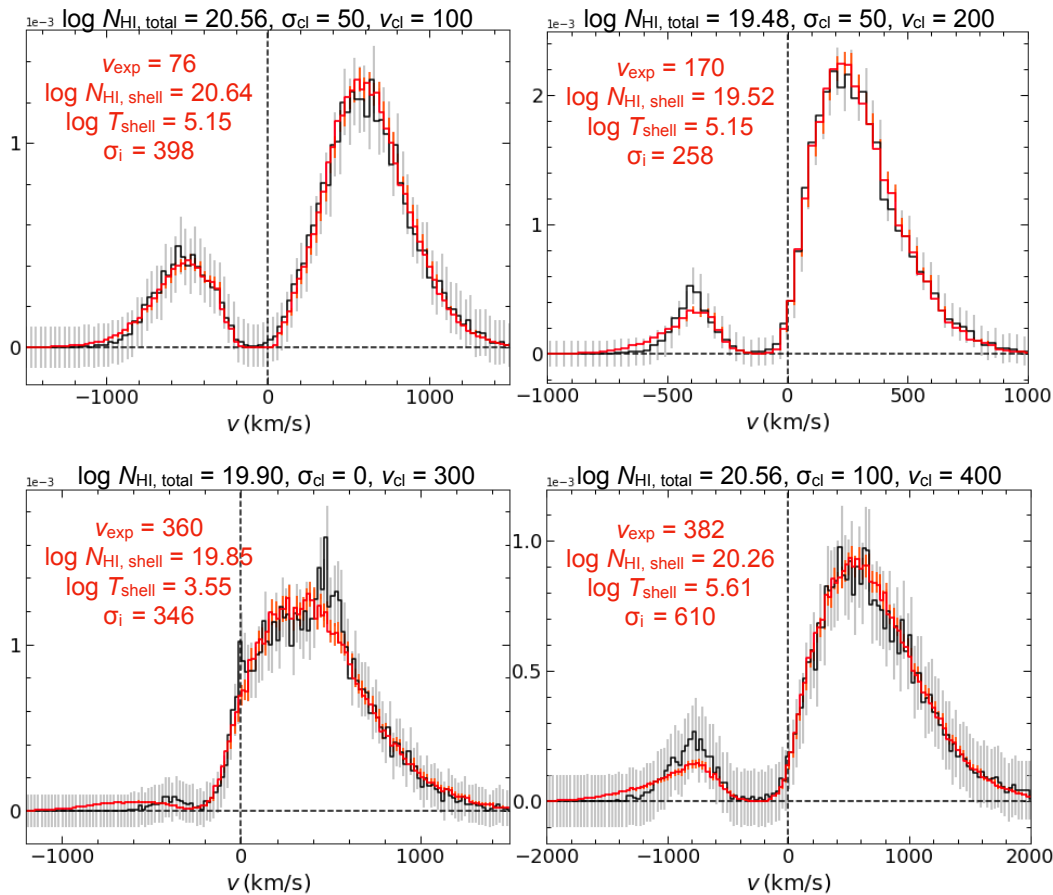


Figure 5.12: **Examples of outflowing shell model best-fits to outflowing clumpy slab models.** Four panels represent four different $(N_{\text{HI, total}}, \sigma_{\text{cl}}, v_{\text{cl}})$ cases. The black curves represent the outflowing clumpy slab model spectra and the red curves represent the shell model best-fits. v_{exp} have been obtained at the expected values within uncertainties.

We show four examples of outflowing shell model best-fits to outflowing clumpy slab models in Figure 5.12 to illustrate the quality of the fits.

In addition to adding a uniform clump outflow velocity, we have also experimented with two more sophisticated velocity profiles. Firstly, we add a Hubble flow-like outflow velocity increasing linearly from 0 (at the center of the simulation region) to v_{max} (at the boundary of the simulation region) to the clumps and fit the Ly α model spectra. The results are shown in Figure 5.13. The four panels in the first two rows represent four models with linearly increasing outflow velocities, as compared to the lower four panels with constant outflow velocities. It can be seen from the line profiles that for the models with linear increasing outflow velocities: (1) the blue-to-red peak flux ratio is much higher than that of the corresponding uniform outflow

$$\log N_{\text{HI, total}} = 20.56, \sigma_{\text{cl}} = 50$$

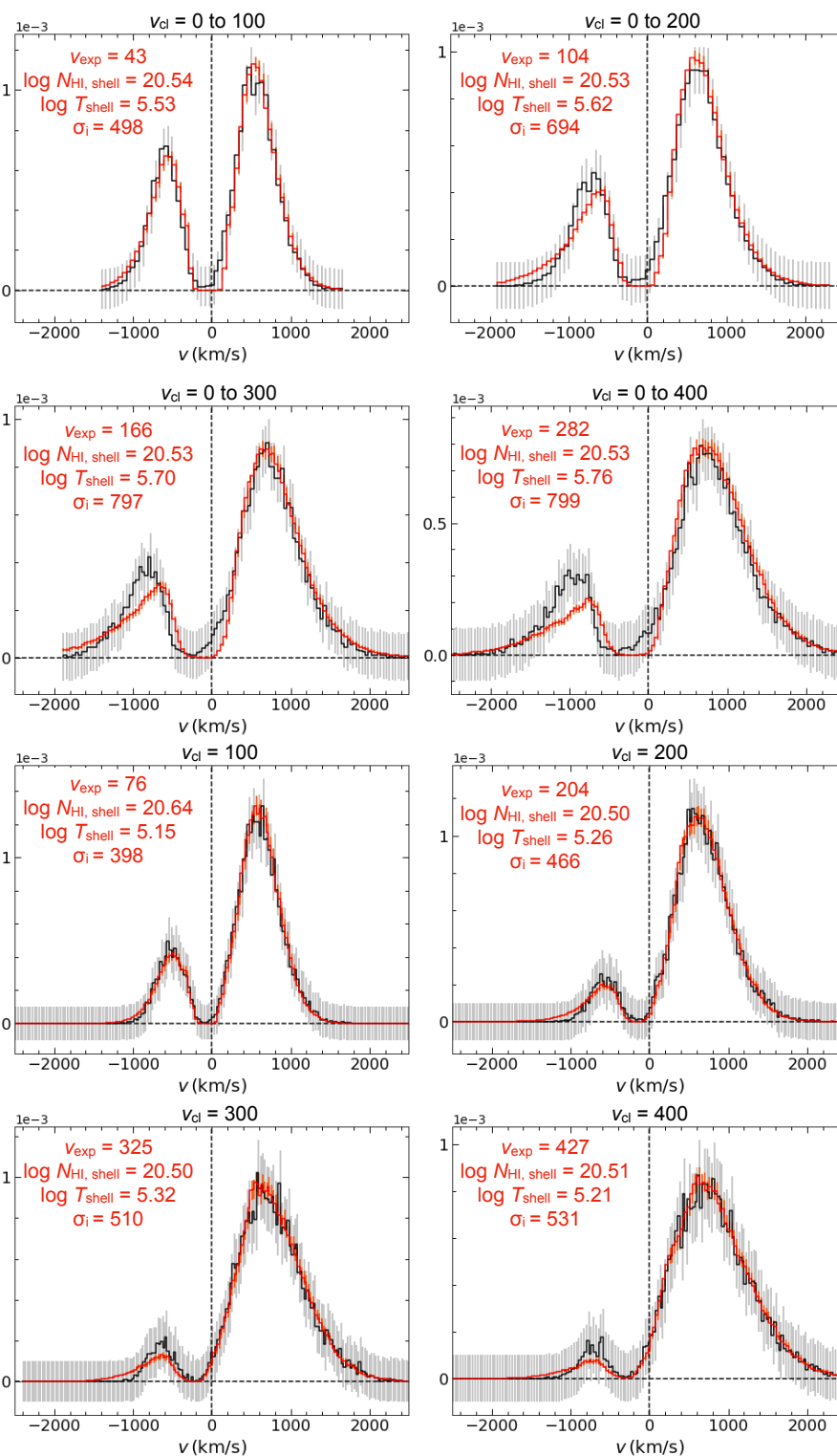


Figure 5.13: **Examples of clumpy slab models with linearly increasing outflow velocities, compared to those with constant outflow velocities.** The upper two rows are four models with linearly increasing outflow velocities, whereas the lower two rows are four models with constant outflow velocities. For the models with linearly increasing outflow velocities, the blue-to-red peak flux ratio is much higher. The peak separation is also larger, which boosts the fitted T_{shell} and σ_i values, but $N_{\text{HI, shell}} \simeq N_{\text{HI, total}}$ remains true. v_{exp} is roughly obtained at $\frac{1}{2} v_{\text{max}}$.

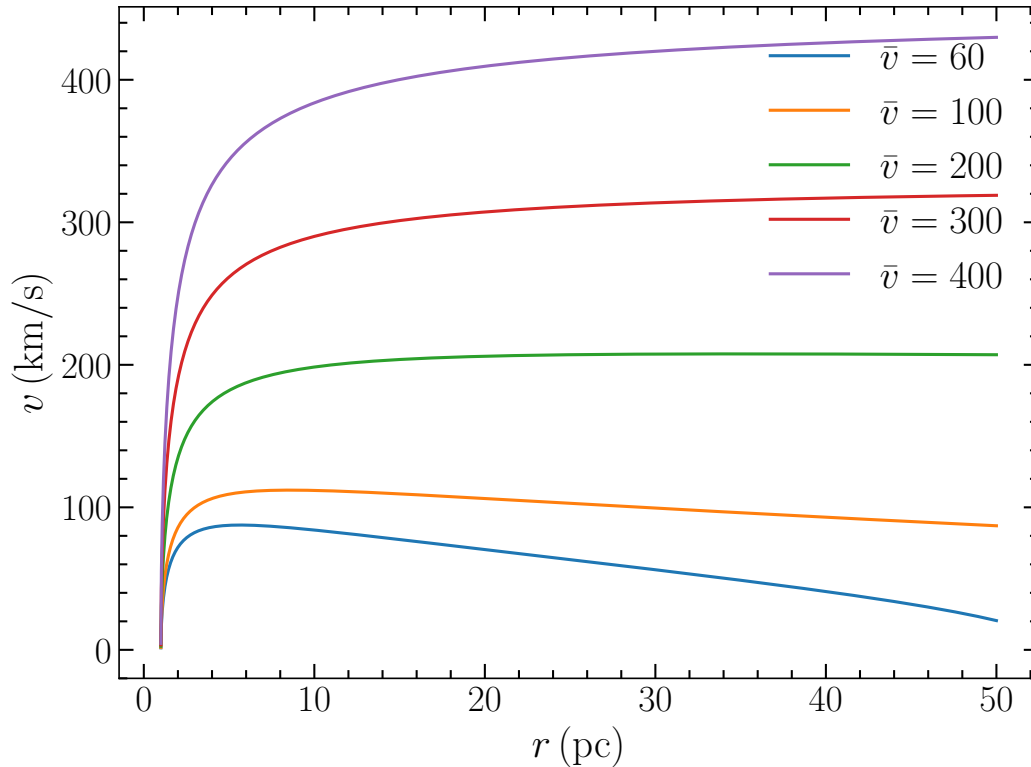


Figure 5.14: **Examples of momentum-driven radial velocity profiles given by Eq. (5.4).** Different colored curves represent five $v(r)$ profiles with different $(\sigma_{\text{cl}}, v_{\text{cl},\infty})$. Here σ_{cl} is fixed to 50 km s^{-1} and $v_{\text{cl},\infty}$ are adjusted to make the average radial velocity, $\bar{v}(r) = 60, 100, 200, 300$ and 400 km s^{-1} . The acceleration decreases with radius, and the velocity either flattens or drops at large r , depending on the actual values of σ_{cl} and $v_{\text{cl},\infty}$.

model (either with $v_{\text{cl}} = \frac{1}{2}v_{\text{max}}$ or v_{max}), which is not well captured by the best-fit shell model, especially at high outflow velocities; (2) the peak separation is also larger than that of the corresponding uniform outflow model. As a result, the fitted T_{shell} and σ_i values have been boosted due to (2), but $N_{\text{HI, shell}} \simeq N_{\text{HI, total}}$ remains true. v_{exp} is roughly obtained at $\frac{1}{2}v_{\text{max}}$, but should be considered as an upper limit as it actually yields a best-fit spectrum with a blue-to-red peak flux ratio lower than that of the fitted clumpy model.

Secondly, we consider a scenario where the clumps are accelerated in a momentum-driven manner and in the meantime, decelerated by a gravitational force. This is motivated by the fact that in real galactic environments, the cool clouds can be accelerated by radiation pressure or ram pressure of the hot wind as they break out of the ISM, as they are decelerating within the gravitational well of the dark matter

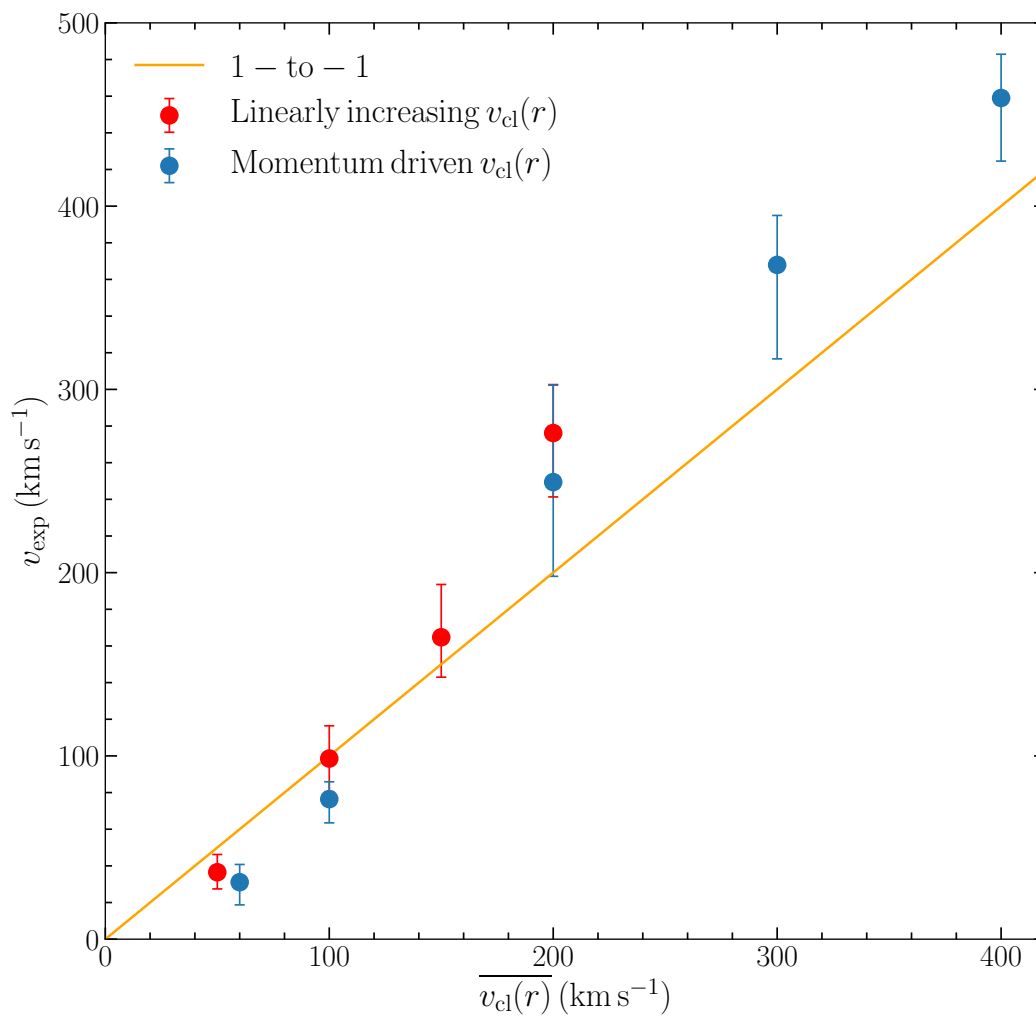


Figure 5.15: **Relation between the average radial velocity $\overline{v_{cl}(r)}$ of clumpy slab models and the derived v_{exp} from shell model fitting.** The red points represent the linearly increasing scenario, and the blue points represent the momentum driven scenario. For both scenarios, $\overline{v_{cl}(r)}$ and v_{exp} are basically consistent, suggesting that shell model fitting probes the average radial velocity of the clumps.

halo. The momentum equation of a clump can be then written as (Murray et al., 2005; Dijkstra et al., 2012):

$$\frac{dv(r)}{dt} = -\frac{GM(r)}{r^2} + Ar^{-\alpha} \quad (5.3)$$

where r is the clump radial position, $v(r)$ is the clump radial outflow velocity, and $M(r)$ is the total mass within r . Here the clump acceleration is determined by two competing terms on the right hand side, the first of which is due to gravitational deceleration and the second of which is an empirical power-law acceleration term (Steidel et al., 2010). Assuming the gravitational potential is of an isothermal sphere, then $M(r) = 2\sigma_{\text{cl}}^2 r/G$, where σ_{cl} is the velocity dispersion of the clumps. Eq. (5.3) can then be analytically solved as:

$$v(r) = \sqrt{4\sigma_{\text{cl}}^2 \ln\left(\frac{r_{\text{min}}}{r}\right) + v_{\text{cl},\infty}^2 \left(1 - \left(\frac{r}{r_{\text{min}}}\right)^{1-\alpha}\right)} \quad (5.4)$$

where r_{min} is the inner cutoff radius that satisfies $v(r_{\text{min}}) = 0$, and $v_{\text{cl},\infty} = \sqrt{2Ar_{\text{min}}^{1-\alpha}/(\alpha-1)}$ is the asymptotic maximum outflow velocity if there were no gravitational deceleration. Following Dijkstra et al. (2012), we have fixed $r_{\text{min}} = 1$ pc (note the clumpy slab model has a half height of 50 pc and the model is re-scalable by design) and $\alpha = 1.4$ ¹¹ and left σ_{cl} and $v_{\text{cl},\infty}$ as free parameters.

We show five examples of $v(r)$ with different $(\sigma_{\text{cl}}, v_{\text{cl},\infty})$ in Figure 5.14. It can be seen that the acceleration decreases with radius, and the velocity either flattens or drops at large r , depending on the actual values of σ_{cl} and $v_{\text{cl},\infty}$. We fix $\sigma_{\text{cl}} = 50 \text{ km s}^{-1}$ and adjust $v_{\text{cl},\infty}$ to achieve average radial velocities of $\overline{v_{\text{cl}}(r)} = 60, 100, 200, 300$ and 400 km s^{-1} . We then assign these radial velocity profiles to the clumps and fit their model spectra with shell models. We find that $N_{\text{HI,shell}}$ and T_{shell} are reproduced at the expected values, and v_{exp} is roughly obtained at the average radial velocity, $\overline{v_{\text{cl}}(r)}$.

We show that the derived v_{exp} is consistent with the average radial velocity $\overline{v_{\text{cl}}(r)}$ for these two scenarios, as shown in Figure 5.15. In reality, if the velocity distribution of the Ly α scattering clumps is semi-linear or similar to the ‘‘momentum-driven + gravitational deceleration’’ scenario, the shell model fitting will probe the average outflow velocity of the clumps. Assuming the same clumps are responsible

¹¹These choices come from the clump radial velocity models that provide good fits to the observed Ly α surface brightness profiles (Dijkstra et al., 2012).

for producing metal absorption (and ignoring effects due to an anisotropic gas distribution), the clump velocity distribution can be constrained by observations on UV absorption lines. One should then expect the outflow velocity v_{exp} output from shell model fitting to be consistent with the average of the absorption velocities. If the clump velocity distribution is non-linear, v_{exp} may no longer be an average outflow velocity, but should still lie between the minimum and maximum absorption velocities.

Clumpy Slab with an Inter-Clump Medium (ICM)

Motivated by the fact that in real astrophysical environments (e.g., in the CGM; Tumlinson et al., 2017), a hot, highly ionized gas phase with residual HI exists and affects Ly α RT (Laursen et al., 2013), we further add another hot phase of gas between the clumps to the clumpy slab model as the inter-clump medium (ICM). Although the total column density of the low-density ICM ($\sim n_{\text{HI,ICM}} r_{\text{gal}} \lesssim 10^{-4} \text{ cm}^{-3} \times \text{kpc} \sim 10^{17} \text{ cm}^{-2}$) is supposed to be several orders of magnitude lower than the typical values of $N_{\text{HI,total}}$ from the cool clumps, it has several non-negligible effects on the Ly α spectra. We find that adding another hot phase of gas at 10^6 K (the typical temperature of diffuse gas in a dark matter halo) will: (1) deepen the trough at line center; (2) increase the peak separation; (3) modify the blue-to-red peak flux ratio of the model Ly α spectrum¹².

Here we consider two different scenarios: static ICM and outflowing ICM. For both scenarios, we generate two sets of multiphase, clumpy slab models with $n_{\text{HI,ICM}} = 10^{-4}$ and 10^{-3} cm^{-3} (or equivalently, $N_{\text{HI,ICM}} = 10^{16.2}$ and $10^{17.2} \text{ cm}^{-2}$) and fit them using the large shell model grid. The values of the input and output parameters are shown in Figure 5.16. We hereby discuss two scenarios respectively:

Static Hot ICM: $T_{\text{ICM}} = 10^6 \text{ K}$, $v_{\text{ICM}} = 0$

We find that adding a static hot ICM increases the peak separation and increases the blue-to-red peak flux ratio of the model Ly α spectrum. These two effects can be seen by comparing the first and second rows of Figure 5.17. In terms of the shell model best-fit parameters, the former effect increases T_{shell} but does not boost $N_{\text{HI,total}}$ significantly, and the latter effect decreases v_{exp} to $\ll v_{\text{cl}}$. These effects are shown in Figure 5.16 by green circles and open squares (which correspond to two different ICM HI column densities).

¹²Regarding the effects of ICM with different temperatures and column densities, we refer the readers to Appendix 5.7 and 5.7.

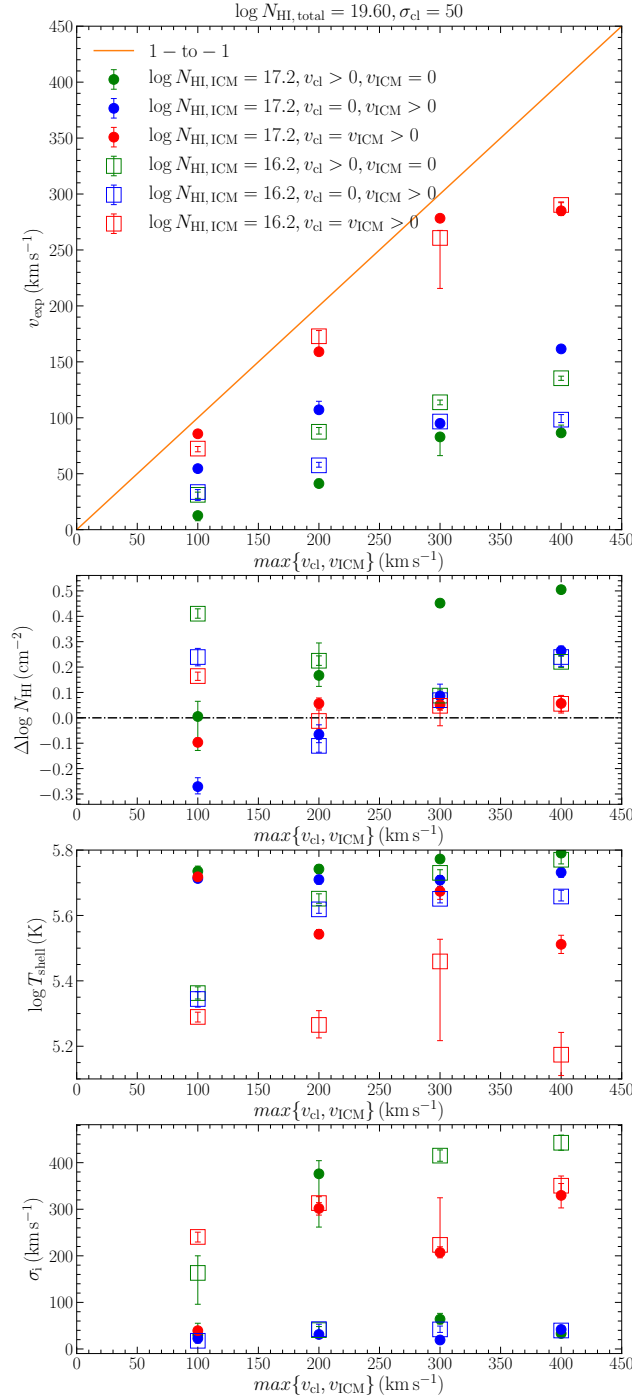


Figure 5.16: **Results of fitting clumpy slab models with static and outflowing ICM with shell models.** *Upper:* The derived shell expansion velocities are much smaller than the clump/ICM outflow velocities unless both components are co-outflowing, which yields $v_{\text{exp}} \simeq v_{\text{cl}} = v_{\text{ICM}}$; *Upper Middle:* $N_{\text{HI, shell}}$ are mostly at $N_{\text{HI, total}}$, albeit with several outliers with $\Delta \log N_{\text{HI}} \gtrsim 0.3$ dex; *Lower Middle:* The derived shell temperatures are boosted by the hot ICM to be higher than the effective temperatures of the clumpy slab model; *Lower:* The distribution of the derived intrinsic Ly α line widths (σ_i) of the best-fit shell models, which increase as σ_{cl} or v_{cl} increases. The green, blue and red points represent (1) $v_{\text{cl}} > 0, v_{\text{ICM}} = 0$ (2) $v_{\text{cl}} = 0, v_{\text{ICM}} > 0$ (3) $v_{\text{cl}} = v_{\text{ICM}} > 0$ models, respectively.

Outflowing Hot ICM: $T_{\text{ICM}} = 10^6 \text{ K}$, $v_{\text{ICM}} > 0$

As shown in the third row of Figure 5.17, adding an outflow velocity to the ICM will decrease the blue-to-red peak flux ratio. The first two panels have $v_{\text{cl}} = 0$ and $v_{\text{ICM}} > 0$, whereas the third panel has $v_{\text{cl}} = v_{\text{ICM}} > 0$. Notably, the quality of the best-fits has become worse, suggesting the non-linear effect of a hot ICM on the Ly α model spectra. The T_{shell} and $N_{\text{HI, total}}$ values are similar to the static ICM case. Interestingly, in the first two panels where $v_{\text{cl}} = 0$ and $v_{\text{ICM}} > 0$, we have $v_{\text{exp}} \simeq \frac{1}{2}v_{\text{ICM}}$; whereas in the third panel where $v_{\text{cl}} = v_{\text{ICM}} > 0$, the blue-to-red peak flux ratio becomes similar to the no-ICM case (the third panel in the first row), and $v_{\text{exp}} \simeq v_{\text{cl}} = v_{\text{ICM}}$ is obtained¹³.

It is therefore evident that if a multiphase, clumpy slab model with $(v_{\text{cl}}, v_{\text{ICM}})$ and a shell model with v_{exp} give the same Ly α spectrum (especially the same blue-to-red peak flux ratio), then v_{exp} should lie between v_{cl} and v_{ICM} . In particular, if $v_{\text{cl}} = v_{\text{ICM}}$, i.e., the cool clumps and the hot ICM are co-outflowing at the same speed, we would expect $v_{\text{exp}} = v_{\text{cl}} = v_{\text{ICM}}$. In reality, we expect the cool clumps to be entrained by the local flow of hot gas (i.e., $v_{\text{cl}} \simeq v_{\text{ICM}}$), as a large velocity difference between two phases of gas may destroy the cool clumps quickly via hydrodynamic instabilities¹⁴ (see, e.g., Klein et al. 1994). Therefore, we conclude that the gas outflow velocities extracted from fitting Ly α spectra should be consistent between the shell model and the multiphase, clumpy model.

Multiphase Clumpy Sphere

We further consider a more physically realistic gas geometric distribution, i.e., a multiphase clumpy sphere, which we have adopted in fitting observed spatially resolved Ly α spectra in Li et al. (2021) and Li et al. (2022b). As a multiphase sphere model has an upper limit for the clump volume filling factor F_V ($\lesssim 0.7$ for numerical reasons) and hence for the covering factor $f_{\text{cl}} (= 3r_{\text{gal}}/4r_{\text{cl}} F_V = 150 F_V)$, it cannot have an as high covering factor as the multiphase clumpy slab model (i.e., ‘less clumpy’). However, as long as f_{cl} is much larger than a critical value $f_{\text{cl, crit}}$, the clumpy model would be sufficiently similar to a homogeneous model (Gronke et al., 2017). If the condition $f_{\text{cl}} \gg f_{\text{cl, crit}}$ is not satisfied, a considerable number of Ly α photons would escape near the line center and yields residual fluxes at line

¹³Here “ \simeq ” refers to a difference within a factor of four.

¹⁴Note that in a relatively rare scenario (e.g., very close to the launching radius of a galactic wind), the hot phase may be moving faster than the cool clumps, i.e., $v_{\text{ICM}} > v_{\text{cl}}$, and the shell model fitting would obtain $v_{\text{ICM}} > v_{\text{exp}} > v_{\text{cl}}$.

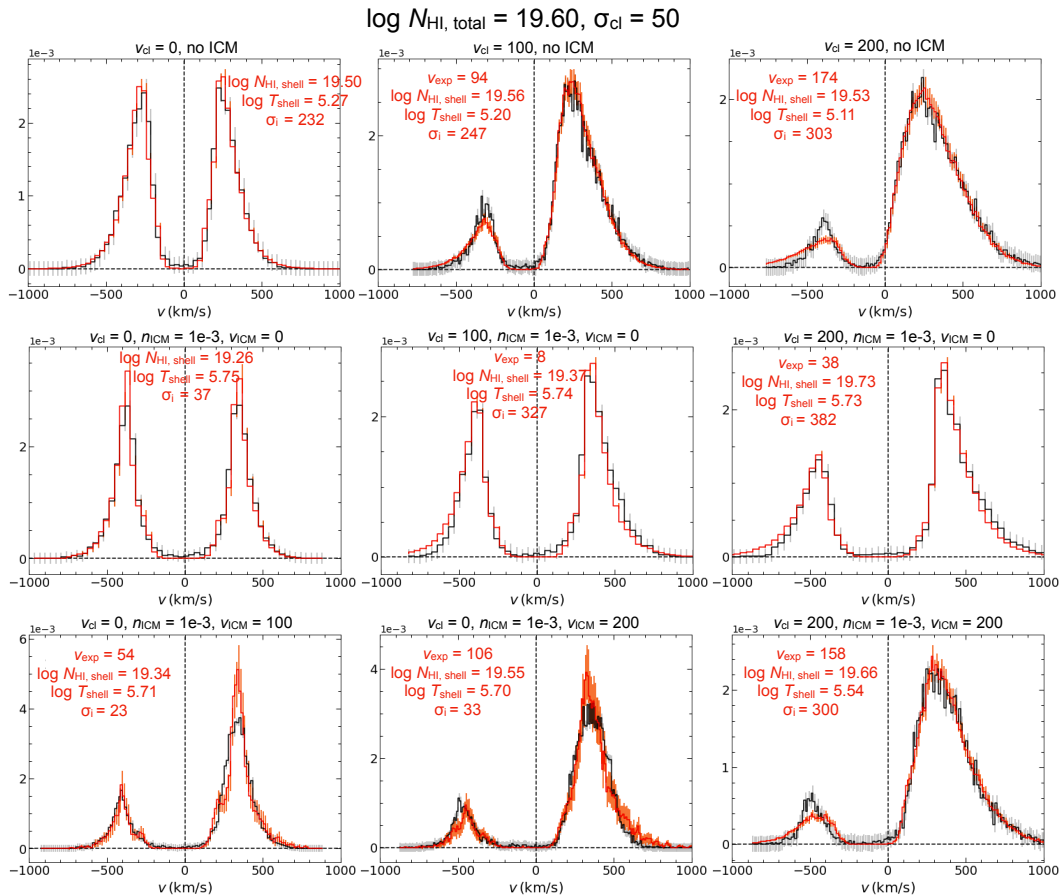


Figure 5.17: Examples of shell model best-fits to outflowing clumpy slab models with and without ICM. The first row represents three $v_{\text{cl}} > 0$ cases without ICM. The second row represents three $v_{\text{cl}} > 0$ cases with a static, $T = 10^6$ K, $n_{\text{HI}} = 10^{-3} \text{ cm}^{-3}$ ICM. Adding this hot phase of static ICM tends to: (1) deepen the trough at line center; (2) increase the peak separation; (3) increase the blue-to-red peak flux ratio. The third row represents three $v_{\text{cl}} > 0$ cases with an outflowing ICM. A $v_{\text{ICM}} > 0$ ICM will further decrease the blue-to-red peak flux ratio and increase the v_{exp} of the shell model best-fit. In particular, the model with the same clump and ICM outflow velocity prefers a shell expansion velocity $v_{\text{exp}} \simeq v_{\text{cl}} = v_{\text{ICM}}$.

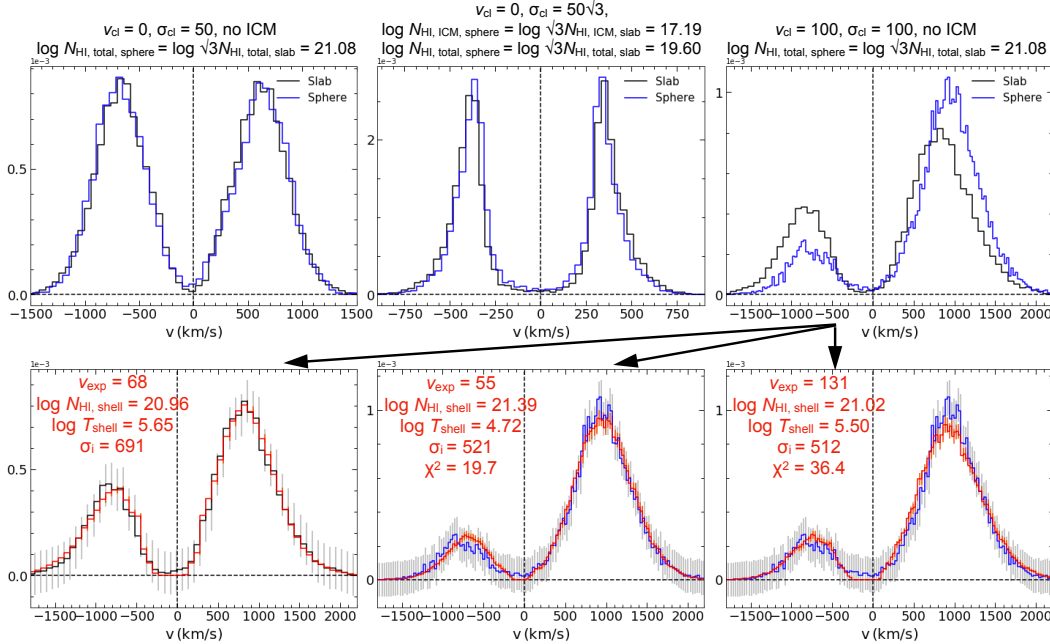


Figure 5.18: Comparison between clumpy sphere models and clumpy slab models. *Upper row:* The first two panels show that a non-outflowing ($v_{\text{cl}} = v_{\text{ICM}} = 0$) spherical model with $(\sigma_{\text{cl}}, \sqrt{3}N_{\text{HI,total}}, \sqrt{3}N_{\text{HI,ICM}})$ gives an identical spectrum to a slab model with $(\sigma_{\text{cl}}, N_{\text{HI,total}}, N_{\text{HI,ICM}})$, and hence yields the same shell model best-fit parameters. The factor $\sqrt{3}$ should arise from the geometrical difference a sphere and a slab (see §5.4 for details). The third panel shows that adding the same v_{cl} yields a mismatch between the two models, which should be a non-linear effect due to the geometrical difference. *Lower row:* The first panel shows the shell model best-fit to a clumpy slab model (with $v_{\text{exp}} \simeq v_{\text{cl}}$, $N_{\text{HI,shell}} \simeq N_{\text{HI,total}}$ and $T_{\text{shell}} \simeq T_{\text{eff,slab}}$), and the second panel shows the best-fit to the corresponding clumpy spherical model, where v_{exp} and T_{shell} are lower than expected and $N_{\text{HI,shell}}$ is higher than expected. The third panel shows that if we restrict T_{shell} to be $\geq 10^{5.5}$ K, the best-fit v_{exp} and $N_{\text{HI,shell}}$ become closer to the expected values, although the best-fit gives a higher χ^2 due to the mismatch in the red peak.

center in the emergent spectrum. Here we explore the connection between multiphase, clumpy spherical models and shell models in these two physical regimes respectively: $f_{\text{cl}} \gg f_{\text{cl,crit}}$ and $f_{\text{cl}} \simeq f_{\text{cl,crit}}$.

Very Clumpy Sphere: $f_{\text{cl}} \gg f_{\text{cl,crit}}$

For a very clumpy spherical model, i.e., $f_{\text{cl}} \gg f_{\text{cl,crit}}$, we find that a non-outflowing ($v_{\text{cl}} = v_{\text{ICM}} = 0$) spherical model with $(\sigma_{\text{cl}}, \sqrt{3}N_{\text{HI,total}}, \sqrt{3}N_{\text{HI,ICM}})$ gives an identical spectrum to a slab model with $(\sigma_{\text{cl}}, N_{\text{HI,total}}, N_{\text{HI,ICM}})$, and hence yields the same shell model best-fit parameters. This is shown in the first two panels in the first row of

Figure 5.18. The factor $\sqrt{3}$ should arise from the geometrical difference a sphere and a slab. Specifically, in the optically thick and $f_{\text{cl}} \gg f_{\text{cl,crit}}$ regime, the mean path length of Ly α photons is $\sqrt{3}B$ for a slab and R for a sphere, where B is the slab half-height and R is the sphere radius (Adams, 1975).

However, adding two different models the same outflow velocity to either the clumps or the ICM yields a mismatch, as shown in the third panel in the first row of Figure 5.18. Such a mismatch should be due to the geometrical difference as well, yet we are unable to relate the two models with a scale factor in their outflow velocities (e.g., a spherical model with $(\sigma_{\text{cl}}, \sqrt{3}N_{\text{HI,total}}, \sqrt{3}v_{\text{cl}})$ is still different from a slab model with $(\sigma_{\text{cl}}, N_{\text{HI,total}}, v_{\text{cl}})$). Therefore, we speculate that the geometrical difference has a non-linear effect on the propagation of the Ly α photons through the outflowing H I gas.

Nevertheless, we attempt to fit an outflowing clumpy spherical model with the shell model grid. The results are shown in the second row of Figure 5.18. The first panel shows the shell model best-fit to a clumpy slab model (with $v_{\text{exp}} \simeq v_{\text{cl}}$, $N_{\text{HI,shell}} \simeq N_{\text{HI,total}}$ and $T_{\text{shell}} \simeq T_{\text{eff,slab}}$ as expected), and the second panel shows the best-fit to the corresponding clumpy spherical model, where v_{exp} and T_{shell} are lower than expected and $N_{\text{HI,shell}}$ is higher than expected. However, we find that such a mismatch is due to the intrinsic parameter degeneracy of the shell model (see §5.3). If we restrict T_{shell} to be $\geq 10^{5.5}$ K, the best-fit v_{exp} and $N_{\text{HI,shell}}$ become consistent with the expected values, although the best-fit gives a higher χ^2 due to a larger mismatch in the trough and red peak (as shown in the third panel). We therefore speculate that the correspondence between shell models and clumpy slab models still roughly holds for clumpy spherical models, with slightly larger uncertainties due to the inessential geometrical difference.

Moderately Clumpy Sphere: $f_{\text{cl}} \simeq f_{\text{cl,crit}}$

If the spherical model is only moderately clumpy, i.e., $f_{\text{cl}} \simeq f_{\text{cl,crit}}$, the Ly α optical depth at line center will be low enough for photons to escape, which yields a significant non-zero residual flux density at line center¹⁵. We find that as $f_{\text{cl}}/f_{\text{cl,crit}}$ decreases, in the beginning the shell model is still able to produce a decent fit with reasonable parameters (albeit with the mismatch at line center), but eventually the fit fails at $f_{\text{cl}}/f_{\text{cl,crit}} \simeq 10$. We illustrate this result in Figure 5.19. In general, in

¹⁵Note that even in the $f_{\text{cl}} \gg f_{\text{cl,crit}}$ regime, residual flux density at line center still exists, although to a lesser extent (see, e.g., Figure 5.6 and 5.8).

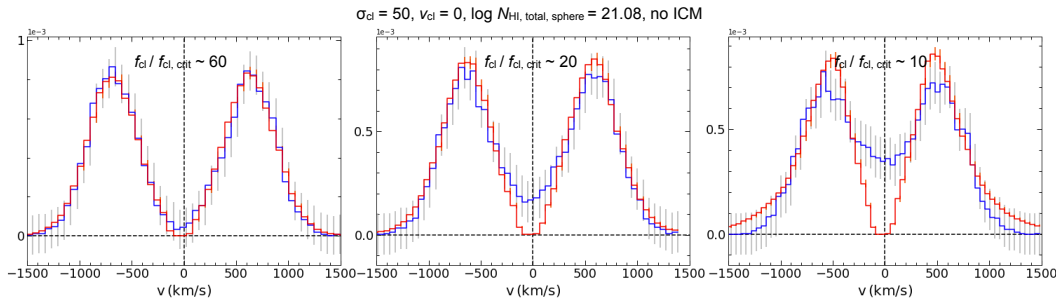


Figure 5.19: **Shell model fits to clumpy spherical models with decreasing $f_{\text{cl}}/f_{\text{cl,crit}}$.** The three panels correspond to three $(\sigma_{\text{cl}}, v_{\text{cl}}, \log N_{\text{HI, total}}) = (50, 0, 21.08)$ models with different $f_{\text{cl}}/f_{\text{cl,crit}}$ values: ~ 60 , 20 , and 10 , respectively. The blue curves are the clumpy spherical model spectra and the red curves are the shell model best-fits. As $f_{\text{cl}}/f_{\text{cl,crit}}$ decreases, in the beginning the shell model is still able to produce a decent fit with reasonable parameters (albeit with the mismatch at line center), but eventually the fit fails at $f_{\text{cl}}/f_{\text{cl,crit}} \simeq 10$.

the $f_{\text{cl}} \simeq f_{\text{cl,crit}}$ regime, no direct correlation has been found between the shell and clumpy model parameters due to the efficient escape of $\text{Ly}\alpha$ photons at line center in the clumpy model (Gronke et al., 2016a).

5.5 Discussion

Interpretation of Model Parameters

Assuming that the degeneracy we present in §5.3 can be somehow broken (see possible examples in the following §5.5), it is of great interest to decipher the crucial physical properties (kinematics, column density, etc.) of the $\text{Ly}\alpha$ scattering gaseous medium encoded in observed $\text{Ly}\alpha$ spectra, which exist ubiquitously in the Universe and often exhibit a diversity of morphology, e.g., different numbers and shapes of peaks, peak flux ratios, and peak separations. In this section, we summarize our findings on how one should interpret the parameters of the shell or clumpy model derived from fitting observed $\text{Ly}\alpha$ profiles. We will focus on the “very clumpy” regime ($f_{\text{cl}} \gg f_{\text{cl,crit}}$) unless otherwise noted.

1. **H I column density:** This parameter can be constrained by the peak separation and the extent of the wings of the $\text{Ly}\alpha$ profile. The best-fit shell model gives the H I column density of the shell $N_{\text{HI, shell}}$, whereas the best-fit clumpy model gives the *total* H I column density within the clumps¹⁶, given

¹⁶The total H I column density in the ICM is usually negligible compared to that within the clumps, as the ICM is usually much hotter ($\gtrsim 10^6$ K) and has a much lower H I number density.

by $N_{\text{HI, total}} = \frac{4}{3} f_{\text{cl}} N_{\text{HI, cl}}$. As we have shown in previous sections, $N_{\text{HI, shell}} \simeq N_{\text{HI, total}}$ usually holds for the clumpy model and the best-fit shell model, suggesting that the H I column density can be robustly determined from fitting.

However, this parameter should be treated with at least two caveats: (1) As we have shown in §5.3 and 5.4, in the optically thick regime, the (total) H I column density is degenerate with the shell effective temperature (or the random velocity of the clumps). Therefore, in order to get a well-constrained H I column density by fitting observed Ly α spectra, additional constraints are needed to break the degeneracy; (2) As both the shell model and the clumpy model assume an isotropic H I gas distribution, whereas in actual astrophysical environments the gas distribution is more likely to be anisotropic, the derived N_{HI} value should be regarded only as an average value along the paths of escape of the Ly α photons (which is actually not necessarily the average column density either along the line-of-sight or of all angles).

2. **Shell effective temperature (or Doppler parameter) / Clump velocity dispersion:** This parameter can be constrained by the width of the Ly α profile, i.e., the FWHM of the peak(s). As we have shown, the shell effective temperature is usually equal to the effective temperature of the clumpy model with velocity dispersion σ_{cl} (see Eq. 5.2). In other words, the turbulent velocity term in the Doppler parameter of the shell model (see Eq. 3 in Verhamme et al. 2006) is equivalent to σ_{cl} of the clumpy model for the same Ly α profile. We hereby highlight a scenario where the fitted T_{eff} of the shell model cannot be interpreted literally. If a Ly α spectrum is very broad and has very extended wings, it may require a high $T_{\text{eff}} \gtrsim 10^6 \text{ K}$ ¹⁷, or equivalently, Doppler parameter $b \gtrsim 100 \text{ km s}^{-1}$. Such a high Doppler parameter already corresponds to a very high internal turbulent Mach number $\mathcal{M}_{\text{cl}}^{\text{turb}} \sim 10$, which is enough to disintegrate the H I shell or shock-ionize the H I gas. Alternatively, we should interpret this as a clump velocity dispersion $\sigma_{\text{cl}} \gtrsim 100 \text{ km s}^{-1}$ of the clumpy model, which is physically reasonable in a strong gravitational field and/or in the presence of feedback.

3. **Shell expansion / Clump outflow velocity:** This parameter can be constrained by the blue-to-red peak flux ratio of the Ly α profile. As we have

¹⁷The FWHM of a Ly α profile is positively correlated with $N_{\text{HI, shell}}$ and T_{eff} ; for a static sphere, $\text{FWHM} \simeq 320 \left(\frac{N_{\text{HI, shell}}}{10^{20} \text{ cm}^{-2}} \right)^{1/3} \left(\frac{T_{\text{eff}}}{10^4 \text{ K}} \right)^{1/6} \text{ km s}^{-1}$ (see Eq. (87) from Dijkstra 2017).

shown, $v_{\text{exp}} \simeq v_{\text{cl}}$ usually holds for the clumpy model and the best-fit shell model, suggesting that this parameter can also be robustly determined from fitting. However, the fitted shell expansion velocity (v_{exp}) should not be interpreted literally as the bulk outflowing velocity of the H I gas in at least two cases: (1) The actual velocity field of the H I gas varies spatially. For example, in §5.4 we find that the best-fit shell model to a clumpy slab model with either a linearly increasing outflow or a “momentum-driven + gravitational deceleration” velocity profile has $v_{\text{exp}} \simeq \overline{v_{\text{cl}}(r)}$. Moreover, if the UV absorption lines suggest a series of outflow velocities, v_{exp} is expected to lie between the minimum and maximum absorption velocities; (2) The fitted Ly α spectrum emerges from a multiphase scattering medium. For example, in §5.4 we show that the best-fit shell model to a multiphase clumpy slab model with cool clumps outflowing at v_{cl} and a hot ICM outflowing at v_{ICM} has $v_{\text{exp}} < \max\{v_{\text{cl}}, v_{\text{ICM}}\}$ unless $v_{\text{cl}} = v_{\text{ICM}}$. Therefore, the fitted v_{exp} should be interpreted as an average outflow velocity – both space-wise and phase-wise.

4. **Intrinsic Line Width:** This parameter can be constrained by the extent of the wings of the Ly α profile (for the shell model only; in the clumpy model, the intrinsic line width is fixed to be small and σ_{cl} is responsible for the broadening of the wings). It is well known that the fitted intrinsic line width σ_{i} of the shell model is usually overly large compared to the widths of the observed Balmer lines (Orlitová et al., 2018). In this work, we have shown in §5.4 that a large intrinsic line width σ_{i} is always required for a shell model to fit a clumpy slab model with randomly moving clumps, and (1) σ_{i} increases as σ_{cl} increases; (2) $\sigma_{\text{i}} > \sigma_{\text{cl}}$ always holds (see Figure 5.7). This is due to the intrinsic difference between a shell model and a clumpy model with corresponding parameters: compared to the shell model, the clumpy model naturally has more extended wings and lower but more extended peaks (see Figure 5.10), and is better suited for fitting broad Ly α spectra with extended wings. This $\sigma_{\text{cl}} < \sigma_{\text{i}}$ trend, together with the quadruple degeneracy that we have discussed in §5.3, provides a viable solution to the three major discrepancies emerged from shell model fitting as reported by Orlitová et al. (2018). It also suggests that the large σ_{i} values required in shell model fitting may simply imply a clumpy gas distribution (with a considerable velocity dispersion).
5. **Systemic Redshift:** When fitting an observed Ly α profile, a parameter that dictates the systemic redshift of the modeled Ly α source is usually introduced

in post-processing. As Ly α profile fitting is usually done in velocity space, this parameter can be specified as Δv , which is the difference between the systemic velocity of the modeled Ly α source and the zero velocity of the observed Ly α profile. For a typical double-peak Ly α profile with a central trough between two peaks, the Δv of the best-fit shell model is correlated with v_{exp} , as the optical depth is maximum at $\sim -v_{\text{exp}}$ (i.e., the trough location; see Orlitová et al. 2018). In other words, Δv and v_{exp} are intrinsically degenerate with each other.

Now the clumpy model offers us more possibilities to solve this issue with more flexibility. Although a single-phase slab with a very high clump covering factor ($f_{\text{cl}} \gg f_{\text{cl,crit}}$) basically converges to the shell model, a multiphase clumpy medium can produce many different trough shapes: for example, for $f_{\text{cl}} \gg f_{\text{cl,crit}}$ with a static or outflowing ICM, the trough can extend to both sides of the zero velocity (see Figure 5.17); for $f_{\text{cl}} \simeq f_{\text{cl,crit}}$ with a static ICM, the trough has residual flux and is always located at the line center. More modeling of observed Ly α profiles is needed to examine whether these possibilities are physically reasonable.

Breaking the Degeneracy

The intrinsic parameter degeneracy of the shell model (and the clumpy model as well, at least in the “very clumpy” regime) that we have described in §5.3 concerns us that how much meaningful physical information, if any, can be extracted from Ly α spectra via RT modeling. In this section, we speculate several scenarios where the intrinsic parameter degeneracy can be broken and the physical properties of the Ly α scattering medium can actually be constrained.

1. **An accurate measurement of the systemic redshift of the Ly α source:** Assuming that all the Ly α photons are generated from recombination and nebular emission line(s) are clearly detected (e.g., H α , H β , or [O III]), the systemic redshift (i.e., the Δv parameter) of the Ly α source can be constrained reasonably well, and hence breaks the degeneracy. However, this requires that: (1) the observed Ly α spectrum has a clear trough between the double peaks so that v_{exp} can be constrained; (2) the asymmetry of the observed Ly α spectrum is significant enough so that the corresponding v_{exp} is much higher than the uncertainty of Δv .
2. **Additional observational constraints on the gas outflow velocity / velocity**

dispersion / H I column density: If additional information is available from other observations, it may also help break the parameter degeneracy. Nevertheless, as such quantities are derived rather than directly observed (e.g., the gas outflow velocity can be deduced from UV absorption lines, and the gas velocity dispersion can be inferred from the widths of nebular emission lines), it is more reasonable to treat them as priors that confine the parameter space. Therefore, unless these additional constraints are reasonably stringent, the output parameters will still suffer from the degeneracy (which actually exists continuously across the parameter space).

3. **The Ly α profile corresponds to an optically thin regime:** As we have only found the parameter degeneracy in the optically thick regime, it is anticipated that if the Ly α profile does not belong to this regime, it may not be heavily affected by the parameter degeneracy. Ly α spectra emerged from H I with very low column densities ($\lesssim 10^{18} \text{ cm}^{-2}$) will be naturally in the optically thin regime – they often exhibit narrow peak separations and/or residual flux at line center. However, objects that produce such Ly α profiles are presumably LyC leakers and are rare in the Universe (Cooke et al., 2014; Verhamme et al., 2015).

In short, one should be cautious when interpreting the extracted parameters from fitting observed Ly α spectra with idealized RT models. Additional observations on other lines may help break the intrinsic parameter degeneracy and better constrain the properties of the gaseous medium, although sometimes different types of constraints may contradict each other and yield unsuccessful fits (see, e.g., Section 4.1 in Orlitová et al. 2018). In that case, development of more advanced RT models that are more physically realistic and flexible may help solve this issue in the future.

5.6 Conclusions

In this work, we have explored what physical properties can be extracted from Ly α spectra via radiative transfer modeling. The main conclusions of this work are:

1. Intrinsic parameter degeneracies exist in the widely used shell model in the optically thick regime. For static shells, models with the same $N_{\text{HI,shell}} T_{\text{shell}}^{0.5}$ exhibit nearly identical Ly α spectra. For outflowing shells, a quadruple degeneracy exists among $(v_{\text{exp}}, N_{\text{HI,shell}}, T_{\text{shell}}, \Delta v)$. This finding reveals the limitations of the shell model and cautions against making any reasonable state-

ments about the physical properties of the Ly α scattering medium with only shell model fitting (cf. §5.3);

2. The parameters of a “very clumpy” slab model have a close correspondence to the parameters of the shell model. Specifically, (1) the *total* column density of the clumpy slab model, $N_{\text{HI, total}} = \frac{4}{3}f_{\text{cl}}N_{\text{HI, cl}}$ is equal to the H I column density of the shell model, $N_{\text{HI, shell}}$; (2) the effective temperature of the clumpy slab model, $T_{\text{eff, slab}} = T_{\text{cl}} + \frac{\sigma_{\text{cl}}^2 m_{\text{H}}}{2k_{\text{B}}}$, where σ_{cl} is the 1D velocity dispersion of the clumps, is equal to the effective temperature of the shell model, T_{shell} ; (3) the average radial clump outflow velocity, $\overline{v_{\text{cl}}(r)}$, is equal to the shell expansion velocity, v_{exp} . This reminds us that the shell model parameters should be interpreted in a more physically realistic context rather than literally;
3. In the shell model, large intrinsic line widths (several times of σ_{cl}) are required to reproduce the wings of the clumpy slab models, reflecting the intrinsic difference between two different models. This $\sigma_{\text{cl}} < \sigma_{\text{i}}$ trend, together with the quadruple degeneracy, provides a viable solution to the three major discrepancies emerged from shell model fitting as reported by Orlitová et al. (2018);
4. Adding another phase of hot inter-clump medium to the clumpy slab model will increase peak separation and boost T_{shell} , but keeps $N_{\text{HI, shell}} \simeq N_{\text{HI, total}}$. The fitted v_{exp} lies between v_{cl} and v_{ICM} . In particular, if $v_{\text{cl}} = v_{\text{ICM}}$, i.e., the cool clumps and the hot ICM are co-outflowing at the same speed, we get $v_{\text{exp}} \simeq v_{\text{cl}} = v_{\text{ICM}}$;
5. For multiphase, clumpy spherical models, if f_{cl} is much larger than a critical value $f_{\text{cl, crit}}$, the parameter correspondence still holds, albeit with larger uncertainties due to the geometrical difference; whereas if $f_{\text{cl}} \simeq f_{\text{cl, crit}}$, no direct correlation has been found between the shell and clumpy model parameters.

In general, in order to obtain meaningful constraints on the physical properties of the Ly α scattering gaseous medium, one should try to break the intrinsic parameter degeneracies revealed in this work with extra information from additional observations, rather than merely rely on fitting observed Ly α spectra with idealized RT models. Moreover, the model parameters derived from Ly α spectra fitting should not be understood literally – instead, they should be interpreted in a more physically realistic context, e.g., in a multiphase, clumpy medium that we have explored

in this work. Efforts in building more advanced RT models (e.g., with more realistic geometries) will also be helpful in the future.

Acknowledgements

We thank Phil Hopkins for providing computational resources. MG was supported by NASA through the NASA Hubble Fellowship grant HST-HF2-51409 awarded by the Space Telescope Science Institute, which is operated by the Association of Universities for Research in Astronomy, Inc., for NASA, under contract NAS5-26555. MG thanks the Max Planck Society for support through the Max Planck Research Group. Numerical calculations were run on the Caltech compute cluster “Wheeler”, allocations from XSEDE TG-AST130039 and PRAC NSF.1713353 supported by the NSF, and NASA HEC SMD-16-7592. We also acknowledge the use of the following software packages: Astropy (Astropy Collaboration et al., 2018), the SciPy and NumPy system (Virtanen et al., 2020; Harris et al., 2020).

5.7 Appendix

Effect of ICM Temperature on Ly α Model Spectra

Here we show that adding a hot phase of ICM does not necessarily affect the Ly α model spectrum unless it satisfies a certain condition. Specifically, the transmission function $\mathcal{T}(x) = e^{-\tau(x)} = e^{-\sigma_{\text{HI}}(x,T)N_{\text{HI}}}$ needs to be wider for the hot phase than the cool phase.

In the core of the Ly α line, the H I cross section, $\sigma_{\text{HI}} = \sigma_0 H(a_v, x) \sim \sigma_0 e^{-x^2}$, where $H(a_v, x)$ is the Voigt function, and $\sigma_0 \approx 5.895 \times 10^{-14} (T/10^4 \text{ K})^{-1/2} \text{ cm}^{-2}$ is the H I cross section at line center. Assuming that at a certain optical depth τ , $\mathcal{T}(x)$ becomes sufficiently small and reaches a threshold \mathcal{T}_0 (e.g., for $\tau(x) \gtrsim 7$, $\mathcal{T}(x) \lesssim 10^{-3}$), and denoting $C_1 = 5.895 \times 10^{-12} \text{ cm}^{-2}$ so that $\sigma_0 = C_1/\sqrt{T}$, we have:

$$e^{-\frac{C_1}{\sqrt{T}} e^{-x^2} N_{\text{HI}}} = \mathcal{T}_0 \quad (5.5)$$

so the threshold frequency can be solved as:

$$x_0 = \sqrt{-\ln \left(-\frac{\sqrt{T}}{C_1 N_{\text{HI}}} \ln \mathcal{T}_0 \right)} \quad (5.6)$$

which corresponds to a threshold velocity:

$$v_0 = x_0 v_{\text{th}} = \sqrt{-\ln \left(-\frac{\sqrt{T}}{C_1 N_{\text{HI}}} \ln \mathcal{T}_0 \right)} \sqrt{\frac{2k_{\text{B}}T}{m_{\text{H}}}} \quad (5.7)$$

In order to have an impact on the Ly α profile, the hot phase of ICM needs to have a threshold velocity larger than that of the cool phase, i.e., $v_{0,\text{ICM}} > v_{0,\text{cool}}$. We hereby consider the following example: a two-phase scattering medium that consists of cool clumps with velocity dispersion $\sigma_{\text{cl}} = 50 \text{ km s}^{-1}$ (hence effective temperature $\log T_{\text{eff}}(\text{K}) = 5.2$) and total H I column density $\log N_{\text{HI},\text{total,cool}} = 19.6$, and a hot ICM with total H I column density $\log N_{\text{HI},\text{total,ICM}} = 17.2$. Using Eq. (5.7) and demanding $v_{0,\text{ICM}} > v_{0,\text{cool}}$ yields that $\log T_{\text{ICM}}(\text{K}) \gtrsim 5.6$ is required for the ICM to have a wider transmission function than the cool clumps, and hence have a visible impact on the Ly α profile. We illustrate this result in Figure 5.20 by showing a series of ICM transmission functions and model Ly α profiles with different T_{ICM} values. It can be clearly seen that at $\log T_{\text{ICM}}(\text{K}) \sim 5.6$ the ICM starts to have an impact on both the transmission function and the model Ly α profile.

Effect of ICM on the Critical Covering Factor

In Gronke et al. (2017), an important physical quantity is defined – the critical covering factor of the clumps, $f_{\text{cl,crit}}$. It is the critical average number of clumps per line-of-sight, above which the clumpy scattering medium will behave like a homogeneous medium (i.e., a homogeneously filled shell or slab), and below which a significant number of Ly α photons will escape near the line center. In this section, we test how much impact the hot ICM component has on $f_{\text{cl,crit}}$, and hence on the boundaries of different RT regimes.

The value of $f_{\text{cl,crit}}$ sets the transition between two physical regimes of Ly α resonant scattering. Assuming that the ensemble of the clumps is optically thick at the Ly α line center (which is always true throughout this work), if $f_{\text{cl}} \lesssim f_{\text{cl,crit}}$, photons scatter off the clumps in a random-walk manner, and the number of clumps a photon intercepts scales as $N_{\text{cl}} \propto f_{\text{cl}}^2$; whereas if $f_{\text{cl}} \gtrsim f_{\text{cl,crit}}$, photons escape via a frequency excursion (i.e., a series of wing scatterings), and the number of clumps a photon intercepts scales as $N_{\text{cl}} \propto f_{\text{cl}}$. Therefore, $f_{\text{cl,crit}}$ can be estimated by determining the turning point of the scaling relation between N_{cl} and f_{cl} (see Figures 2, 4 and 6 from Gronke et al. 2017).

Here we show one set of examples in Figure 5.21: a two-phase clumpy slab with $\log N_{\text{HI},\text{total}} = 20.0$ in the clumps (which are static), and a hot ICM with total H I column density $\log N_{\text{HI},\text{ICM}} = 14.2 - 16.2$ (or equivalently, $n_{\text{HI},\text{ICM}} = 10^{-6} - 10^{-4} \text{ cm}^{-3}$). It can be seen that with $\log N_{\text{HI},\text{ICM}}$ varying by two orders of magnitudes, $f_{\text{cl,crit}}$ only changes by a factor of ~ 1.5 . This result suggests that although under certain con-

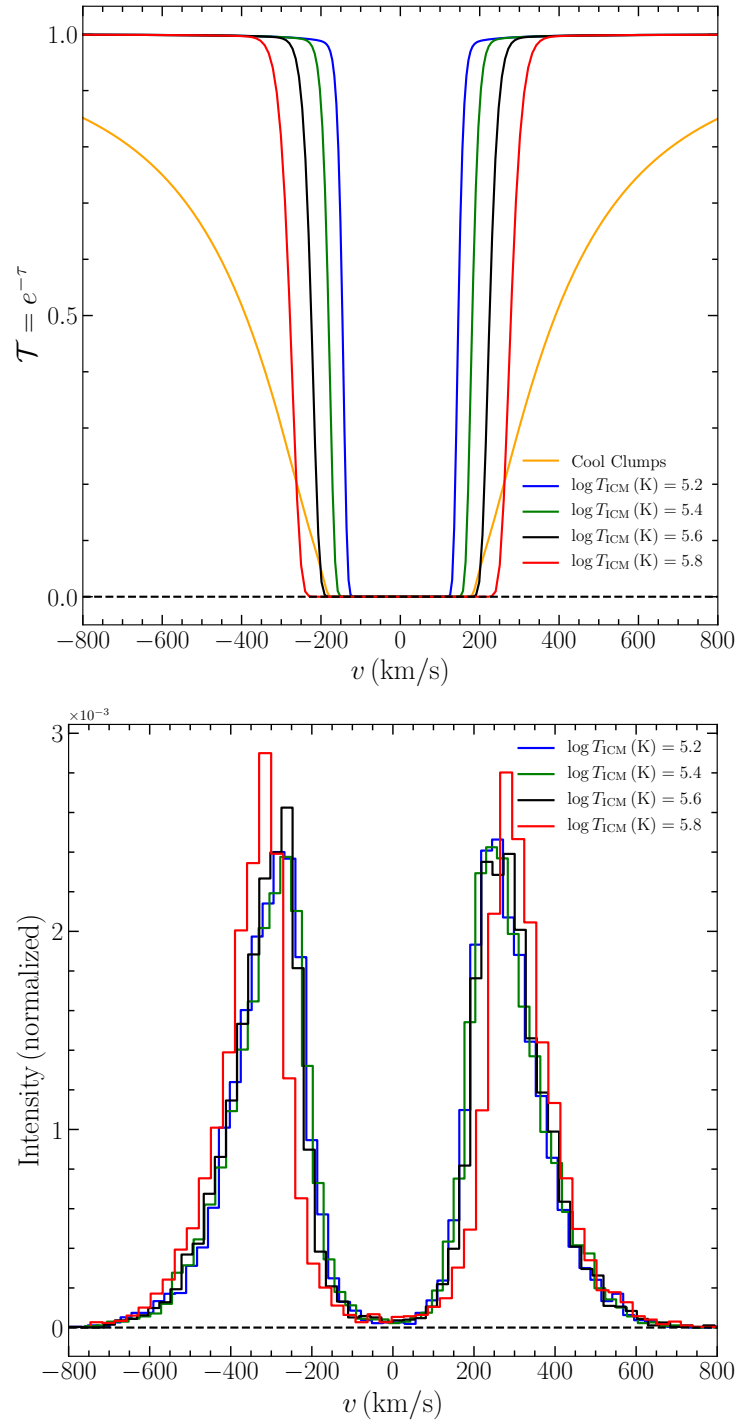


Figure 5.20: **Effect of ICM temperature on $\text{Ly}\alpha$ transmission function and $\text{Ly}\alpha$ model spectra.** Here we show one example: a two-phase scattering medium that consists of cool clumps with velocity dispersion $\sigma_{\text{cl}} = 50 \text{ km s}^{-1}$ (hence effective temperature $\log T_{\text{eff}}(\text{K}) = 5.2$) and total HI column density $\log N_{\text{HI, total, cool}} = 19.6$, and a hot ICM with total HI column density $\log N_{\text{HI, total, ICM}} = 17.2$. *Top:* The transmission function of the cool clumps (the orange curve) as compared to those of the ICM at different temperatures. *Bottom:* The model $\text{Ly}\alpha$ profile as a function of the ICM temperature. As inferred from Eq. (5.7), at $\log T_{\text{ICM}}(\text{K}) \sim 5.6$ (the black curves) the ICM starts to have an impact on both the transmission function and the model $\text{Ly}\alpha$ profile.

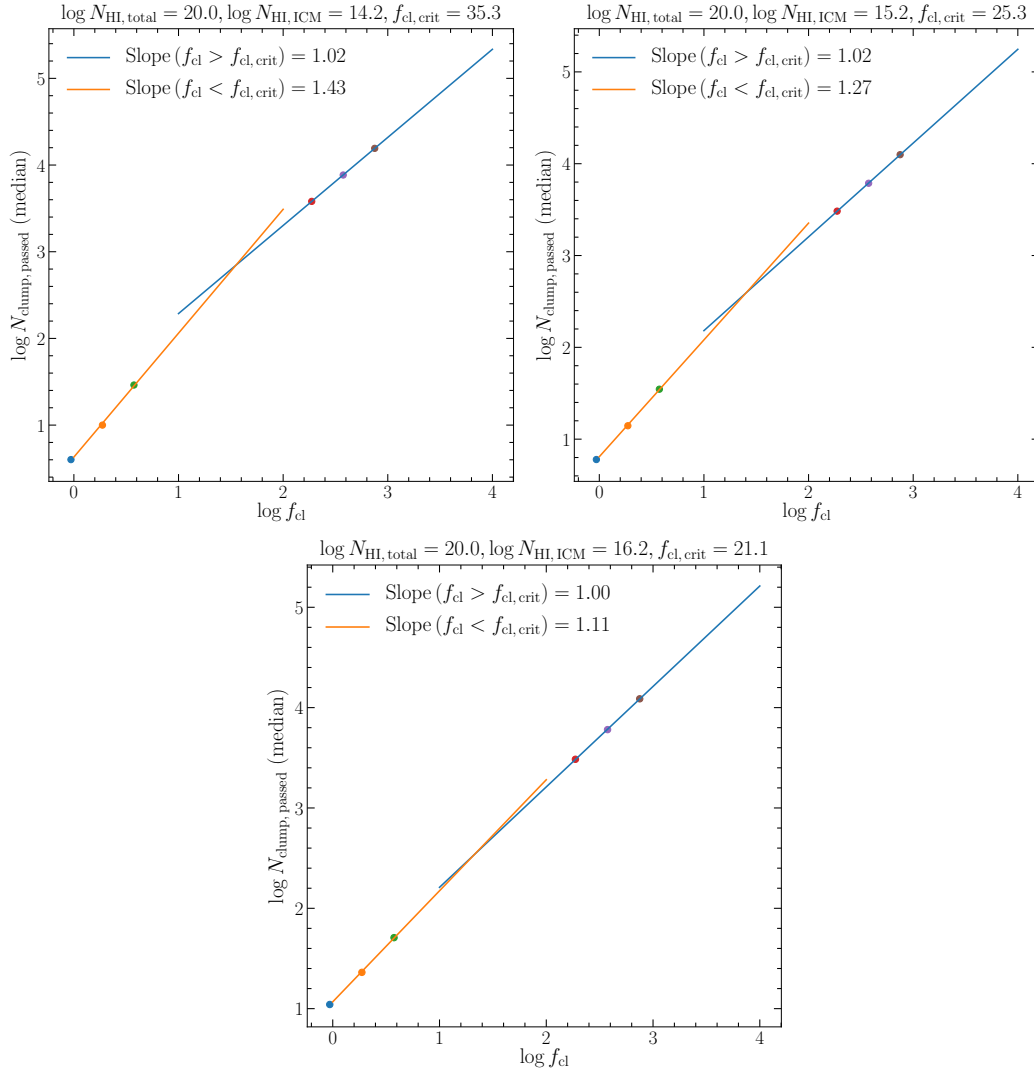


Figure 5.21: **Effect of ICM with different column densities on the critical clump covering factor, $f_{\text{cl,crit}}$.** Here we show one set of examples: a two-phase clumpy slab with $\log N_{\text{HI,total}} = 20.0$ in the static clumps, and a hot ICM with total HI column density $\log N_{\text{HI,ICM}} = 14.2 - 16.2$ (or equivalently, $n_{\text{HI,ICM}} = 10^{-6} - 10^{-4} \text{ cm}^{-3}$). With $\log N_{\text{HI,ICM}}$ varying by two orders of magnitudes, $f_{\text{cl,crit}}$ only changes by a factor of ~ 1.5 , suggesting that the hot ICM only has a minor effect on $f_{\text{cl,crit}}$ and the boundaries of different RT regimes.

ditions, the hot ICM can have a significant impact on the model Ly α spectrum (see §5.4 and §5.4), it only has a minor effect on $f_{\text{cl,crit}}$ and the boundaries of different RT regimes.

THE CIRCUMGALACTIC MEDIUM OF EXTREME EMISSION
LINE GALAXIES AT $z \sim 2$: RESOLVED SPECTROSCOPY AND
RADIATIVE TRANSFER MODELING OF SPATIALLY
EXTENDED $\text{Ly}\alpha$ EMISSION IN THE KBSS-KCWI SURVEY

Erb, Dawn K., Zhihui Li, Charles C. Steidel, et al. (Aug. 2023). “The Circumgalactic Medium of Extreme Emission Line Galaxies at $z \sim 2$: Resolved Spectroscopy and Radiative Transfer Modeling of Spatially Extended $\text{Ly}\alpha$ Emission in the KBSS-KCWI Survey”. In: *ApJ* 953.1, 118, p. 118. DOI: 10.3847/1538-4357/acd849. arXiv: 2210.02465 [astro-ph.GA].

This chapter contains excerpts from Erb et al. (2023) with permission from the corresponding author, Dawn K. Erb.

6.1 Introduction

A star-forming galaxy in the early universe is the nexus of a complex interchange of gas between stars and a nested series of gaseous reservoirs: the interstellar medium (ISM), consisting of the gas among the stars, the circumgalactic medium (CGM), and finally the intergalactic medium (IGM). As the transition region between the stars and the IGM, most of the key processes of galaxy evolution are modulated through the CGM (see Tumlinson et al. 2017 for a recent review). Outflows powered by star formation drive gas out of the galaxy and into the CGM, where it may be reaccreted onto the galaxy or continue on to leave the galaxy entirely (e.g., Veilleux et al. 2020). New fuel for star formation is accreted through the CGM, likely via dense, cold streams of gas (Kereš et al., 2005; Dekel et al., 2006). Ionizing photons that make their way out of the galaxy must also traverse the neutral hydrogen in the CGM (Rudie et al., 2013; Steidel et al., 2018).

The strongest emission line arising from gas in the CGM is due to the $\text{Ly}\alpha$ transition of hydrogen, and deep observations have now revealed that the diffuse, distant universe is aglow with $\text{Ly}\alpha$ emission (Wisotzki et al., 2018; Ouchi et al., 2020). This emission arises primarily from faint halos extending to tens of kpc around galaxies, but is also seen in the form of larger nebulae (“blobs”, e.g., Fynbo et al. 1999; Steidel et al. 2000) and filaments (e.g., Cantalupo et al. 2014; Umehata et al. 2019;

Daddi et al. 2021). The initial detections of spatially extended Ly α emission surrounding typical star-forming galaxies at high redshifts came from stacked, narrow-band images (Steidel et al., 2011; Momose et al., 2014; Momose et al., 2016; Xue et al., 2017), but more recently the Multi-Unit Spectroscopic Explorer (MUSE, Bacon et al. 2010) at the ESO-VLT and the Keck Cosmic Web Imager (KCWI, Martin et al. 2010; Morrissey et al. 2012) have enabled the study of individual halos around galaxies from $2 \lesssim z \lesssim 6$ (Wisotzki et al., 2016; Leclercq et al., 2017; Wisotzki et al., 2018; Erb et al., 2018; Leclercq et al., 2020; Chen et al., 2021).

A number of different mechanisms have been proposed to account for this extended Ly α emission. Perhaps the most straightforward of these is the resonant scattering of Ly α photons produced in galaxies by neutral hydrogen in the CGM (Zheng et al., 2011; Kusakabe et al., 2019; Byrohl et al., 2021), with the Ly α profile then reflecting the kinematics and geometry of the CGM gas. Other possible sources of the Ly α halo emission include *in situ* photoionization (fluorescence), either by ionizing radiation escaping from the galaxy or by an external radiation field (Kollmeier et al., 2010; Cantalupo et al., 2012; Mas-Ribas et al., 2016); cooling radiation from infalling gas (Haiman et al., 2000; Dijkstra et al., 2009; Faucher-Giguère et al., 2010; Lake et al., 2015); or Ly α emission from faint satellite galaxies (Mas-Ribas et al., 2017). Multiple mechanisms may contribute in a given halo, with their relative importance varying with radius (Mitchell et al., 2021). Recent theoretical results suggest that the Ly α properties of gaseous halos are primarily influenced by galactic outflows within ~ 50 kpc, while cold accretion flows dominate at larger radii (Chung et al., 2019); this result is in agreement with observations that find a transition between outflow and inflow-dominated kinematics at similar radius (Chen et al., 2020).

While most studies of Ly α halos to date have focused on the spatial distribution of the emission via imaging (either from narrowband filters or reconstructed from integral field unit [IFU] data cubes), a number of recent IFU studies have analyzed spectral variations in the extended emission, using small samples of gravitationally lensed (Patrício et al., 2016; Claeysens et al., 2019; Solimano et al., 2022) and unlensed (Erb et al., 2018; Leclercq et al., 2020) galaxies at $z > 2$. The inclusion of spectroscopic information has the potential to be a powerful discriminant among the proposed emission mechanisms, although the resonant nature of Ly α emission has made the extraction of physical quantities from observed spectra difficult, even in the case of single, spatially integrated line profiles. Due to multiple scatterings,

the emergent profile depends on the kinematics, geometry and density of neutral hydrogen and on the dust content (see Dijkstra 2014 for a review). The strongest peak of the observed Ly α profile is almost always redshifted relative to the systemic redshift of the galaxy due to backscattering from a receding galactic outflow, and when the opacity to Ly α photons in the outflow is relatively low (usually seen in lower mass, highly ionized galaxies) a secondary, blueshifted peak may be visible as well. In the local universe the separation between the two peaks has been observed to correlate with the escape of ionizing Lyman continuum radiation, with objects with narrower peak separations having higher escape fractions (Verhamme et al., 2017; Izotov et al., 2018).

Spatially resolved spectroscopic studies of individual Ly α halos have so far mostly been based on MUSE data, and have therefore necessarily focused on galaxies at $z > 3$. These MUSE studies have analyzed the spectral properties of Ly α emitters with a single peak, finding that the velocity shift of the line is generally smaller for higher surface brightness regions and that there is a correlation between the width and velocity shift of the line, with broader emission often tending to come from the outer halo (Claeyssens et al., 2019; Leclercq et al., 2020; Solimano et al., 2022). At $z = 2.3$, Erb et al. (2018) studied a single low-mass galaxy with KCWI, measuring variations in the peak ratio and separation of the double-peaked Ly α profile across the extended halo and finding that higher blue-to-red peak ratios and narrower separations tended to be found at larger radii. These spectroscopic studies have been broadly interpreted in the context of the resonant scattering of Ly α photons in a galactic outflow, but definitive models for the observed trends have yet to be constructed.

A number of radiative transfer (RT) codes have successfully reproduced the Ly α profiles of large numbers of spatially integrated spectra, generally by modeling the outflow as a spherical, expanding shell (e.g., Verhamme et al. 2008; Verhamme et al. 2015; Hashimoto et al. 2015; Yang et al. 2017; Gronke 2017). These models have provided constraints on the properties of the scattering medium, while also indicating that even within the simplified regime of the shell model the interpretation of the Ly α profile is complex. In general, the separation between the two peaks of the line increases with increasing H I column density, while the relative strength of the blue peak decreases with increasing velocity of the shell (e.g., Verhamme et al. 2015). However, the physical parameters inferred from shell models do not always match constraints on the gas obtained from interstellar absorption and nebular

emission lines (e.g., Kulas et al. 2012; Leitherer et al. 2013; Orlitová et al. 2018), with the models predicting lower outflow velocities and higher intrinsic line widths. More generally, the outflowing gas in real galaxies is multiphase and spans a wide range in velocity, in contrast to the single value assumed by the shell models (e.g., Steidel et al. 2010).

Alternatively, Ly α RT has been studied in a more realistic multiphase, clumpy medium, where cool, H I clumps are embedded in a hot, highly ionized interclump medium (ICM) (e.g., Neufeld 1991; Hansen et al. 2006; Dijkstra et al. 2012; Laursen et al. 2013; Duval et al. 2014; Gronke et al. 2016a). In this multiphase, clumpy model, the kinematics, covering factor, and column density of the clumps, along with the residual H I number density in the ICM, act together to shape the morphology of the Ly α profile. Such a clumpy model converges to the monolithic shell model in the limit of being “very clumpy” (i.e., having ~ 1000 clumps on average per line of sight), but its unique flexibility offers the possibility of obtaining more physically reasonable parameters of the gaseous medium that are consistent with other observations (Li et al., 2022a).

These models were first applied to fitting the KCWI-observed Ly α profiles of several regions in the $z = 3.1$ Ly α blob SSA22-LAB1 (Steidel et al., 2000) by Li et al. (2021), who managed to reproduce the diverse morphologies of the observed profiles with reasonable physical parameters of the gaseous medium. Notably, they found that many of the observed Ly α profiles have significant residual fluxes at the line center, which correspond to relatively few clumps per line-of-sight and low residual H I density in the ICM. In addition, the very broad Ly α wings can be reproduced by large random velocity dispersions of the clumps, but are hard to explain in the context of shell models without requiring unphysically large widths of the *intrinsic* profiles of the Ly α emission.

Follow-up work by Li et al. (2022b) modeled the Ly α profiles of another $z = 3.1$ Ly α blob, SSA22-LAB2, with both the multiphase, clumpy models and shell models. They identified a significant correlation between the shell expansion velocity and the clump outflow velocity, and found that the multiphase, clumpy model may alleviate the inconsistencies between the shell model parameters and the observational data. Moreover, for the first time, they attempted to use radially binned models to fit the spatially resolved Ly α profiles. They found that the Ly α profiles at different impact parameters can be reproduced self-consistently assuming a common central source, and that the variation of the clump outflow velocity with

respect to impact parameter can be explained by a line-of-sight projection effect of a radial outflow. In this paper, we build on the methodology of Li et al. (2022b) and continue to model spatially resolved Ly α spectra with the multiphase, clumpy model.

We analyze the spectral properties of spatially extended Ly α emission for a sample of 12 relatively low-mass, low-metallicity galaxies at $z \sim 2$, using integral field spectroscopy from KCWI. Our focus on low-mass galaxies with extreme nebular line emission is motivated by the likely importance of faint galaxies to reionization (e.g., Kuhlen et al. 2012; Robertson et al. 2015) and by the observed and expected connections between the Ly α profile and Lyman continuum escape (Dijkstra et al., 2016; Verhamme et al., 2017; Izotov et al., 2018; Steidel et al., 2018). Escaping ionizing radiation must travel through the CGM, and spatially resolved models of extended Ly α emission offer the possibility of obtaining constraints on the physical conditions in the multiphase CGM gas. The double-peaked nature of Ly α emission from highly ionized sources also provides additional constraints on the models; all 12 of our targets have double-peaked profiles, which we quantify in both individual spaxels and binned regions before modeling the results with state-of-the-art radiative transfer codes.

We describe our sample selection, observations, and data reduction in Section 6.2, and measure the global properties of the Ly α emission in Section 6.3. We bin the data with larger regions in Section 6.4, to measure both average properties and maximum and minimum gradients in peak ratio and separation. In Section 6.5 we apply new models to the both the spatially resolved Ly α emission and the rest-frame UV interstellar absorption lines, and we summarize our results and discuss their implications in Section 6.6. We assume the Planck Collaboration et al. (2020) values of the cosmological parameters, $H_0 = 67.7 \text{ km s}^{-1} \text{ Mpc}^{-1}$, $\Omega_m = 0.31$, and $\Omega_\Lambda = 0.69$; with these values, 1 arcsec subtends a distance of 8.4 proper kpc at $z = 2.3$, the median redshift of our sample.

6.2 Sample, Observations and Data Reduction

Sample Selection and Properties

Target selection for this study was motivated by the simultaneous goals of characterizing the CGM in relatively low-mass, extreme emission line galaxies and improving our ability to extract physical information from double-peaked Ly α emission. Because low-mass, low-metallicity, and highly ionized galaxies tend to ex-

Table 6.1: Targets Observed

ID	RA (J2000)	Dec (J2000)	\mathcal{R} (AB mag)	M_{UV} (AB mag)	β	z_{neb}	$\log(M_*/M_\odot)$	SFR ($M_\odot \text{ yr}^{-1}$)	sSFR (Gyr^{-1})	t_{exp} (hr)
(1)	(2)	(3)	(4)	(5)	(6)	(7)	(8)	(9)	(10)	(11)
Q0142-BX165	01:45:16.867	-09:46:03.47	23.51	-21.62	-1.90	2.3577	9.13	24.4	18.1	5.0
Q0142-BX186	01:45:17.484	-09:45:07.99	25.32	-19.81	-1.24	2.3569	8.59	12.2	31.3	5.0
Q0207-BX87	02:09:44.234	-00:04:13.51	23.84	-21.15	-1.72	2.1924	9.48	8.3	2.8	4.7
Q0207-BX144	02:09:49.209	-00:05:31.67	23.75	-21.22	-2.03	2.1682	9.22	18.9	11.4	4.5
Q0449-BX110	04:52:17.201	-16:39:40.64	23.94	-21.17	-1.72	2.3355	9.29	18.2	9.3	5.0
Q0449-BX115	04:52:17.861	-16:39:45.36	24.88	-20.23	-2.28	2.3348	8.90	2.1	2.6	5.0
Q0821-MD36	08:21:11.410	+31:08:29.44	24.48	-20.82	-1.62	2.5830	9.12	24.1	18.3	5.1
Q1549-BX102	15:51:55.982	+19:12:44.20	24.32	-20.67	-1.64	2.1934	9.64	6.0	1.4	5.0
Q1700-BX729	17:01:27.773	+64:12:29.48	24.02	-21.14	-1.87	2.3993	10.10	24.5	1.9	4.3
Q2206-BX151	22:08:48.674	-19:42:25.42	23.91	-21.09	-2.10	2.1974	9.97	5.5	0.6	4.9
Q2343-BX418	23:46:18.571	+12:47:47.36	23.99	-21.10	-2.05	2.3054	8.68	14.4	30.0	4.8
Q2343-BX660	23:46:29.433	+12:49:45.55	24.17	-20.81	-1.87	2.1742	8.73	13.9	25.8	5.0

Notes. Columns: (1) Galaxy ID; (2) Right ascension in hours, minutes and seconds; (3) Declination in degrees, minutes and seconds; (4) Observed \mathcal{R} -band AB magnitude; (5) Absolute UV magnitude at $\sim 2100 \text{ \AA}$; (6) Rest-frame UV slope β measured from $G - \mathcal{R}$ color; (7) Systemic redshift from rest-frame optical nebular emission lines; (8) Stellar mass from SED fit; (9) Star formation rate from $H\alpha$ luminosity (see Section 6.2); (10) Specific star formation rate SFR/M_* ; (11) Total KCWI integration time.

hibit strong, double-peaked $\text{Ly}\alpha$ emission (e.g., Henry et al. 2015; Erb et al. 2016; Trainor et al. 2016; Verhamme et al. 2017; Matthee et al. 2021), these objectives largely lead to the same targets.

Our targets are drawn from the Keck Baryonic Structure Survey (KBSS; Rudie et al. 2012; Steidel et al. 2014; Strom et al. 2017) of star-forming galaxies at $z \sim 2$. Selection is primarily based on nebular emission line measurements from KBSS-MOSFIRE (Steidel et al., 2014; Strom et al., 2017): five of our 12 targets are drawn from the sample of Erb et al. (2016), who studied the $\text{Ly}\alpha$ properties of $z \sim 2$ galaxies with extreme nebular emission line ratios placing them in the upper left corner of the $[\text{N II}]/H\alpha$ vs. $[\text{O III}]/H\beta$ “BPT” diagnostic diagram (Baldwin et al., 1981), with $\log([\text{N II}]/H\alpha) \leq -1.1$ and $\log([\text{O III}]/H\beta) \geq 0.75$. Galaxies in this region of the diagram lie at the low metallicity, high ionization end of the star-forming sequence, and the $z \sim 2$ galaxies in our sample have typical metallicities $12 + \log(\text{O}/\text{H}) \approx 8.0$ (see Erb et al. 2016 for discussion).

Four additional targets (Q0142-BX186, Q0449-BX110, Q0821-MD36, and Q1700-BX729) meet the nebular line ratio criteria used for the Erb et al. (2016) paper but were identified later, and the remaining three objects, Q0449-BX115, Q1549-BX102 and Q2206-BX151, were selected from among the strongest $\text{Ly}\alpha$ -emitters (LAEs) in the $z \sim 2$ KBSS sample. Q1549-BX102 lies just outside the emission line selection region, and Q0449-BX115 and Q2206-BX151 cannot be placed on the

diagram due to insufficient data (Q0449-BX115 is detected in [O III] but not $H\alpha$, and Q2206-BX151 has only $H\alpha$ observations). The median redshift of the sample is $z_{\text{med}} = 2.32$, and all of the targets fall above the canonical LAE threshold, with rest-frame equivalent width $W_{\text{Ly}\alpha} > 20 \text{ \AA}$ measured from long-slit spectroscopy.

The sample galaxies also have very high equivalent width [O III] $\lambda 5008$ emission, with $W_{[\text{O III}]}$ = 870 \AA measured from a composite H -band spectrum (we do not measure individual equivalent widths because the continuum is noisy in many of the individual spectra); this value is comparable to that of $z \sim 1\text{--}2$ reionization-era analogs selected for extreme [O III] emission (Tang et al., 2019).

Global properties of the galaxies are given in Table 6.1. The sample is largely blue and bright, with 75% of the objects brighter than $M_{\text{UV}}^* = -20.70$ at $z \sim 2.3$ (Reddy et al., 2009) and median UV slope $\beta_{\text{med}} = -1.87$. The median stellar mass of the sample is $1.5 \times 10^9 M_{\odot}$, from modeling the spectral energy distributions with the BPASSv2.2 stellar population synthesis models (Stanway et al., 2018) and assuming the SMC extinction law (Gordon et al., 2003) and an initial mass function with slope -2.35 over the range $0.5\text{--}100 M_{\odot}$ and -1.35 between $0.1\text{--}0.5 M_{\odot}$. This median stellar mass implies a halo mass of $\sim 3 \times 10^{11} M_{\odot}$ (Girelli et al., 2020), roughly three times lower than the typical halo mass of the KBSS parent sample (Adelberger et al., 2005; Conroy et al., 2008; Trainor et al., 2012); the corresponding virial radius is ~ 60 kpc. The SED modeling also indicates that the galaxies are young and relatively unreddened, with median age 100 Myr and median $E(B - V)_{\text{cont}} = 0.05$.

We use the $H\alpha/H\beta$ ratio and the SMC extinction law to correct the nebular emission lines for internal reddening, finding median $E(B - V)_{\text{neb}} = 0.14$. Two galaxies in the sample (Q0207-BX87 and Q2343-BX660) have $H\alpha/H\beta$ less than the theoretical value, here assumed to be 2.79 corresponding to Case B recombination at an electron temperature of 15,000 K. These galaxies are assigned $E(B - V)_{\text{neb}} = 0$. For the two objects that do not have measurements of the Balmer decrement we instead use reddening measurements from the SED fitting, $E(B - V)_{\text{cont}} = 0.0$ for both Q0449-BX115 and Q2206-BX151.

Star formation rates are computed from the dust-corrected $H\alpha$ luminosity using the calibration of Theios et al. (2019), who calculate the conversion between SFR and $H\alpha$ luminosity for the BPASSv2.2 stellar models used for the SED fitting described above. The resulting SFRs range from 2 to 25 $M_{\odot} \text{ yr}^{-1}$, with a median of 14 $M_{\odot} \text{ yr}^{-1}$. The galaxies with the two lowest SFRs in the sample, Q0449-BX115 and Q2206-BX151, are also the two for which we have determined the reddening using

results from the SED fitting; $E(B - V)_{\text{cont}}$ is typically smaller than $E(B - V)_{\text{neb}}$, so for these two objects we have potentially underestimated the extinction correction and therefore also the SFR (in fact $E(B - V)_{\text{cont}} = 0$ for both, so no extinction corrections were applied). In addition, Q2206-BX151 is the only object that has not been observed with MOSFIRE. The $H\alpha$ flux measurement from Keck-NIRSPEC is reported by Kulas et al. (2012), and has significant systematic uncertainties due to slit losses and the difficulties of accurate flux calibration (Erb et al. 2006 estimated a typical factor of ~ 2 slit loss correction for NIRSPEC observations of $H\alpha$ emission at $z \sim 2$).

From the stellar masses and SFRs we calculate the specific star formation rate, $\text{sSFR} \equiv \text{SFR}/M_*$, finding a sample median of 10.4 Gyr^{-1} , more than a factor of four larger than the KBSS-MOSFIRE sample median of 2.4 Gyr^{-1} (Strom et al., 2017). In other words, most of the galaxies in this sample lie significantly above the $z \sim 2$ SFR-stellar mass relation (Reddy et al. 2012; Whitaker et al. 2014, but note that samples remain incomplete at the low masses characteristic of our targets).

In summary, the galaxies studied here are relatively low-mass, highly star-forming, and luminous, with high specific star formation rates and nebular line ratios that place them at the upper end of their parent sample in ionization and electron density. They are not typical of star-forming galaxies at $z \sim 2$, but may more closely resemble galaxies observed in the reionization era (e.g., Stark et al. 2017).

Observations

The 12 targets were observed with KCWI over the course of a number of observing runs between September 2018 and August 2020. We used the Medium IFU with the BL grating, which provides a field of view of $16''.5 \times 20''.4$ and spectral resolution $R \approx 1800$. As detailed in Table 6.1, total integration times were approximately five hours per target, divided into individual 1200 s exposures between which we rotated the field by $10\text{--}90^\circ$.

Data Reduction

The KCWI data were reduced using procedures described in detail by Chen et al. (2021), but we give an overview of the method here. Each KCWI exposure was reduced using the official data reduction pipeline (DRP) written in IDL.¹ The DRP conducts overscan and bias subtraction, cosmic-ray removal, flat-fielding, sky subtraction, differential atmospheric refraction correction, and flux calibration, and as-

¹<https://github.com/Keck-DataReductionPipelines/KcwiDRP>

sembles 2D spectra of the slices into a 3D data cube. A median-filtered cube was constructed for each data cube using a running boxcar filter of size $0''.69 \times 4''.6 \times 100 \text{ \AA}$. This median-filtered cube was subtracted from the original cube to remove low-frequency scattered light in both the spatial and spectral dimensions.

The world coordinate system (WCS) of the post-DRP data cubes was corrected by cross-correlating the pseudo-white-light images of the data cubes with each other. Data cubes of multiple exposures for the same target were rotated to the north-up direction and resampled onto a common 3D grid of $0''.3 \times 0''.3 \times 1 \text{ \AA}$. The resampling was conducted using the “drizzle” method in the *Montage* package,² with a drizzle factor of 0.7. Finally, individually resampled data cubes were weighted by exposure time and averaged, creating the final data cube for each target.

6.3 Global Ly α Measurements

In this section we describe the global properties of the Ly α emission measured by KCWI. We begin with one-dimensional spectra designed to optimize the continuum S/N, for comparison with single slit studies. We define isophotal apertures by running SExtractor (Bertin et al., 1996) in detection mode on the collapsed, white-light images, and then extract spectra from these apertures, weighting by $(S/N)^2$. The resulting spectra are then rescaled to match the total aperture flux. Circularized radii of the apertures range from $0''.9$ to $2''.2$, with all but three within $0''.3$ of the sample median of $1''.6$. At the median redshift of the sample, these spectra cover rest-frame wavelengths $\sim 1060\text{--}1660 \text{ \AA}$, and include a number of interstellar absorption lines which we model along with the Ly α emission in Section 6.5.

We show the continuum-subtracted Ly α profiles from these spectra in Figure 6.1, which demonstrates that all objects in the sample have double-peaked profiles with a dominant red peak. The Ly α -adjacent continuum is defined as the median flux density in two windows on either side of the line, spanning $1199\text{--}1210 \text{ \AA}$ (-4000 to -1400 km s^{-1}) on the blue side and $1225\text{--}1236 \text{ \AA}$ ($+2300$ to $+5000 \text{ km s}^{-1}$) on the red side. Given the generally high continuum S/N of the optimally extracted spectra and the lack of underlying absorption, these relatively narrow windows provide an effective measurement of the continuum around the line, as can be seen by assessing the continuum subtraction in Figure 6.1.

In order to measure equivalent widths, we integrate the line between the limits at which it reaches the continuum and divide the resulting flux by the continuum level

²<http://montage.ipac.caltech.edu/>

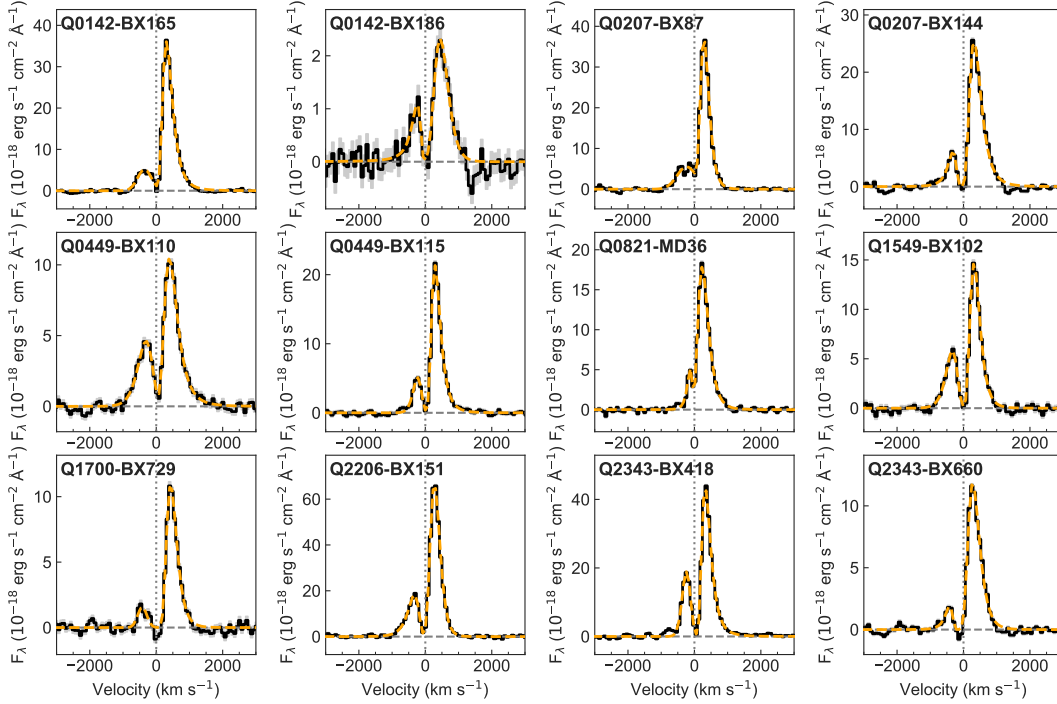


Figure 6.1: **Continuum-subtracted Ly α profiles from spatially integrated spectra, with double asymmetric Gaussian fits shown in orange.**

determined above. As previously known and by design, all are above the canonical Ly α -emitter threshold of $W_{\text{Ly}\alpha} > 20 \text{ \AA}$.

We next create pseudo-narrowband continuum-subtracted Ly α surface brightness images for each object in the sample. We first identify the spatial peak of the Ly α emission in each data cube, and then extract the summed one-dimensional Ly α profile of a large ($2''.4$ in diameter) region centered on this peak. We measure the wavelengths at which the Ly α emission from this large region meets the continuum on either side of the line, typically ~ -900 to $+1200 \text{ km s}^{-1}$, and use these as the wavelength limits of a $10''.5 \times 10''.5$ (i.e., $35 \times 35 0''.3$ pixels) subcube centered on the Ly α peak. We also extract blue and red subcubes with the same spatial size and spectral widths of 20 \AA in the rest frame from either side of the Ly α emission, from which we measure the continuum level (because we are here measuring the continuum of individual spaxels rather than a spatially integrated region as we did above, we use slightly wider windows to increase the S/N of the measurement). The median of the blue and red subcubes along the wavelength axis results in a continuum image, which we subtract from the Ly α subcube to create an emission-only cube. Finally, this cube is integrated along the wavelength axis to construct

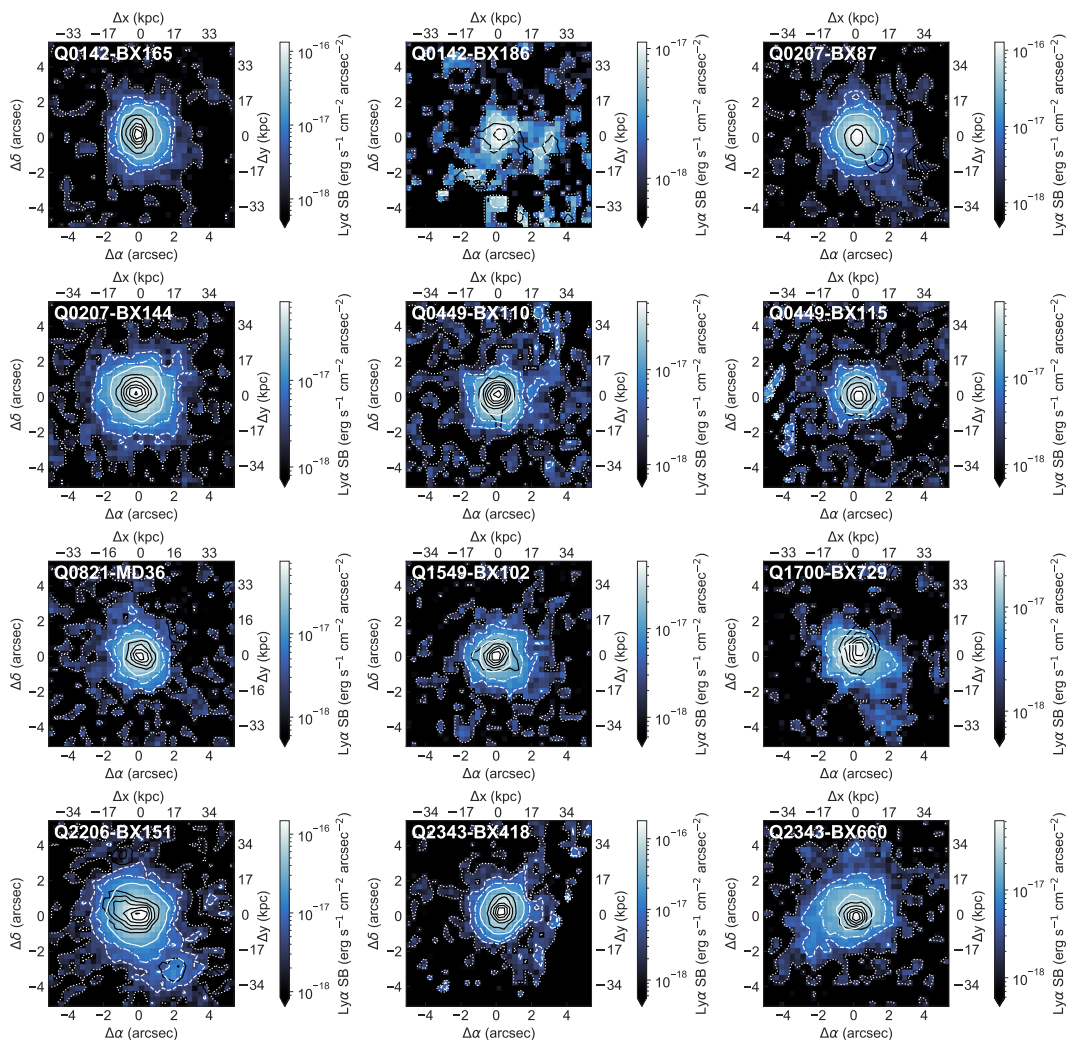


Figure 6.2: **Continuum-subtracted Ly α images.** White contours show the Ly α surface brightness, with the same levels in each panel: 1×10^{-18} (dotted), 5×10^{-18} (dashed), 1×10^{-17} (dash-dot), and 2×10^{-17} (solid) $\text{erg s}^{-1} \text{cm}^{-2} \text{arcsec}^{-2}$, and black contours indicate the adjacent UV continuum measured in a rest-frame 75 \AA window redward of the Ly α emission line.

the continuum-subtracted Ly α surface brightness images shown in Figure 6.2. We note that, in general, accurate modeling and subtraction of the continuum underlying Ly α emission can be challenging due to the complex nature of the line profiles, which often display a superposition of emission and absorption (e.g., Shapley et al. 2003; Kornei et al. 2010). However, the targets in the current sample have simpler profiles with strong emission and no detectable absorption, enabling effective continuum subtraction with the simple method described here.

The Ly α emission shown in Figure 6.2 is significantly more extended than the underlying UV continuum in all cases, as can be seen by comparing the white (Ly α) and black (continuum) contours in Figure 6.2. This comparison also shows that in most cases the Ly α and continuum peaks are spatially coincident. We measure the total Ly α flux of each extended halo by summing the largest connected region with $S/N > 1$ (corresponding to a surface brightness of $\sim 1\text{--}2 \times 10^{-18}$ erg s $^{-1}$ cm $^{-2}$ arcsec $^{-2}$ for targets with approximately 5 hrs of integration), and calculate an effective circular radius $r_{\text{Ly}\alpha}^{\text{eff}} = (A/\pi)^{1/2}$, where A is the area of the region. The total Ly α fluxes range from 0.4 to 7×10^{-16} erg s $^{-1}$ cm $^{-2}$, corresponding to Ly α luminosities ranging from 1.6×10^{42} to 2.6×10^{43} erg s $^{-1}$ with median 10^{43} erg s $^{-1}$, while the radii vary between 16 and 30 kpc.

6.4 Spatially Averaged Ly α Profiles

In order to determine general trends and study the spectral properties of the Ly α halos to larger radii than can be measured with individual spaxels and the small Voronoi bins, we also construct binned spectra of larger regions, using both the entire halo and smaller regions chosen based on their spectral properties.

Annular Ly α Profiles

We first study the average variation of the Ly α profile as a function of radius by making annular spectra binned by radius for all objects in the sample. Beginning with the central, highest surface brightness spaxel and including all spaxels with $S/N > 2$ in the continuum-subtracted Ly α images, we bin each halo in single spaxel ($0''.3$) radial increments. The spectra of all the spaxels in each bin are then summed, and the resulting Ly α profile is normalized to a total flux of 1. This normalization enables a straightforward visual examination of changes in the shape of the profile with radius, and is also used to format the spectra for the radiative transfer modeling discussed in Section 6.5. The normalized spectra are shown in Figure 6.3, color-coded by radius with the central portions of each halo in red and the outer portions

in blue.

The increasing strength of the blue peak relative to the red peak with increasing radius is clearly apparent for most of the objects in the sample. It is also clear that the depth of the trough between the two peaks decreases with increasing radius for most of the sample. Although generally less obvious to the eye, the trend of decreasing peak separation with increasing radius is also apparent in many of the sources. We quantify these trends by fitting double asymmetric Gaussian profiles to the binned annular spectra as described above, measuring the average peak ratio and separation as a function of both radius and average surface brightness. We also quantify the depth of the trough between the peaks by measuring f_{tr} , defined as the fraction of the total emission within $\pm 100 \text{ km s}^{-1}$ of the trough.³

The results are shown for all objects in Figure 6.4, and generally confirm expectations from visual inspection of the spectra. Central blue-to-red flux ratios are $\sim 0.2 \pm 0.2$, and the average ratio increases consistently with radius for most of the galaxies in the sample; all objects that can be measured at a radius beyond $\sim 16 \text{ kpc}$ have flux ratios > 0.6 at that radius. The trough flux fraction f_{tr} ranges from < 0 to ~ 0.1 at the center of the halos, and rises consistently with radius for most objects. The largest measured values are $f_{\text{tr}} \sim 0.2$, found in the outer halos of Q0207-BX87 and Q2343-BX418.

Trends with the average peak separation are somewhat more complicated. Most (10/12) of the halos have a central peak separation of $\sim 500\text{--}700 \text{ km s}^{-1}$, with the exceptions of Q0821-MD36 (365 km s^{-1}) and Q1700-BX729 (835 km s^{-1}). In most cases the average peak separation decreases with radius, with a typical change of $\sim -100 \text{ km s}^{-1}$ such that peak separations in the outer halo are $\sim 400\text{--}600 \text{ km s}^{-1}$; however, a few objects (e.g., Q0142-BX165 and Q2343-BX418) show steeper gradients. Two galaxies in the sample (Q2206-BX151 and Q2343-BX660) also show an *increase* in the peak separation at the largest radius; in both cases these increases are due to small regions with large separations at large radius. Unsurprisingly, however, the peak separation is closely related to the trough depth f_{tr} , decreasing as f_{tr} increases.

³ f_{tr} differs slightly from the quantity f_{cen} defined by Naidu et al. (2022), who measure the fraction of flux escaping within $\pm 100 \text{ km s}^{-1}$ of the systemic velocity; we instead measure the flux on either side of the trough to account for the fact that the trough is occasionally slightly offset from zero velocity (e.g., Q2343-BX660).

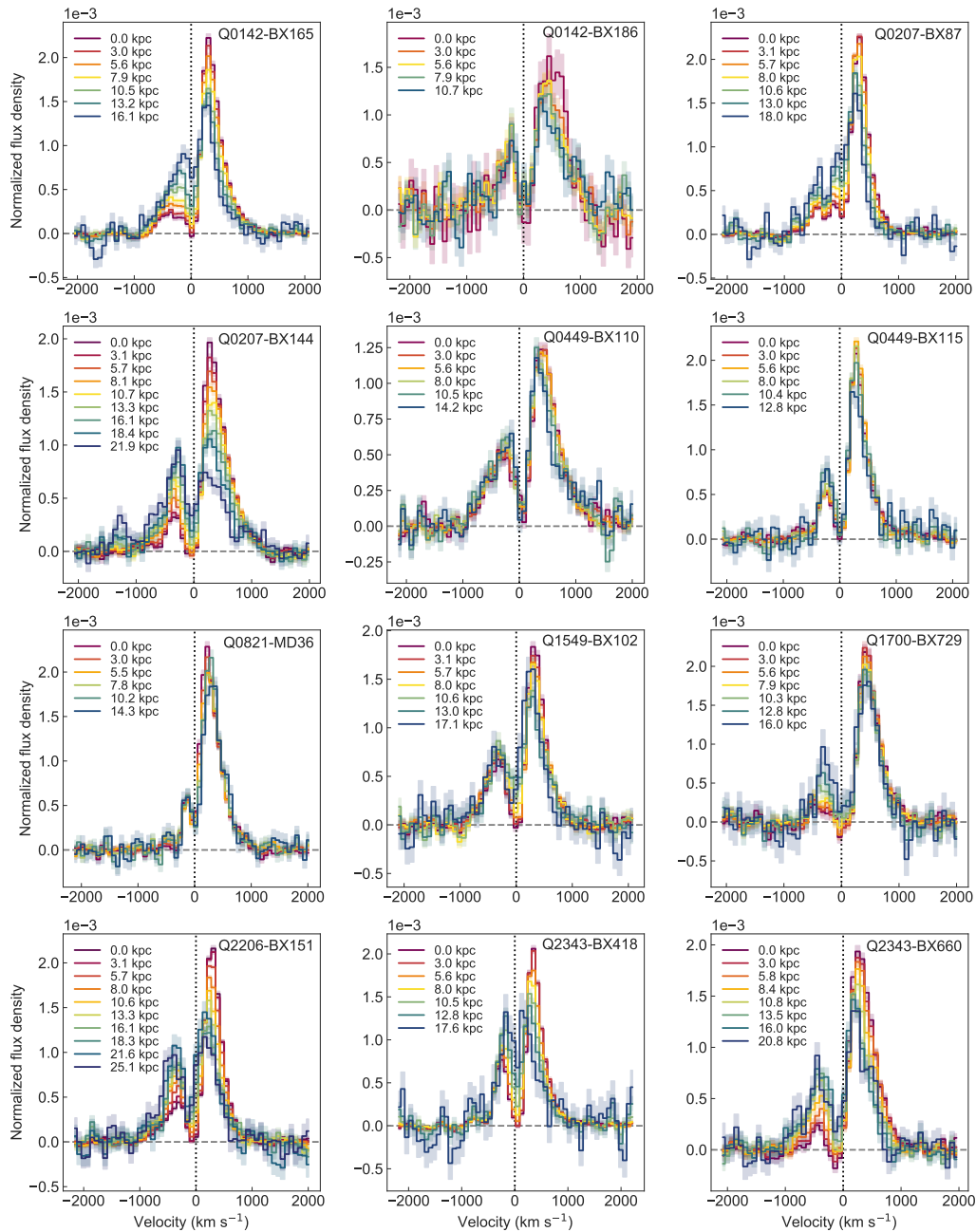


Figure 6.3: **Normalized annular Ly α profiles, constructed by binning all spaxels that have $S/N > 2$ in the continuum-subtracted Ly α images in single spaxel (0/3) radial increments.** The spectra are color-coded by radius, with the inner portions of the halo in red and the outer portions in blue. The legend in each panel gives the median radius of each bin. For most of the sample, the blue-to-red peak ratio increases and the depth of the trough between the peaks decreases with increasing radius. In nearly all cases, the optimally extracted spectra shown in Figure 6.1 are statistically indistinguishable from the annular profiles at $r \approx 3$ kpc.

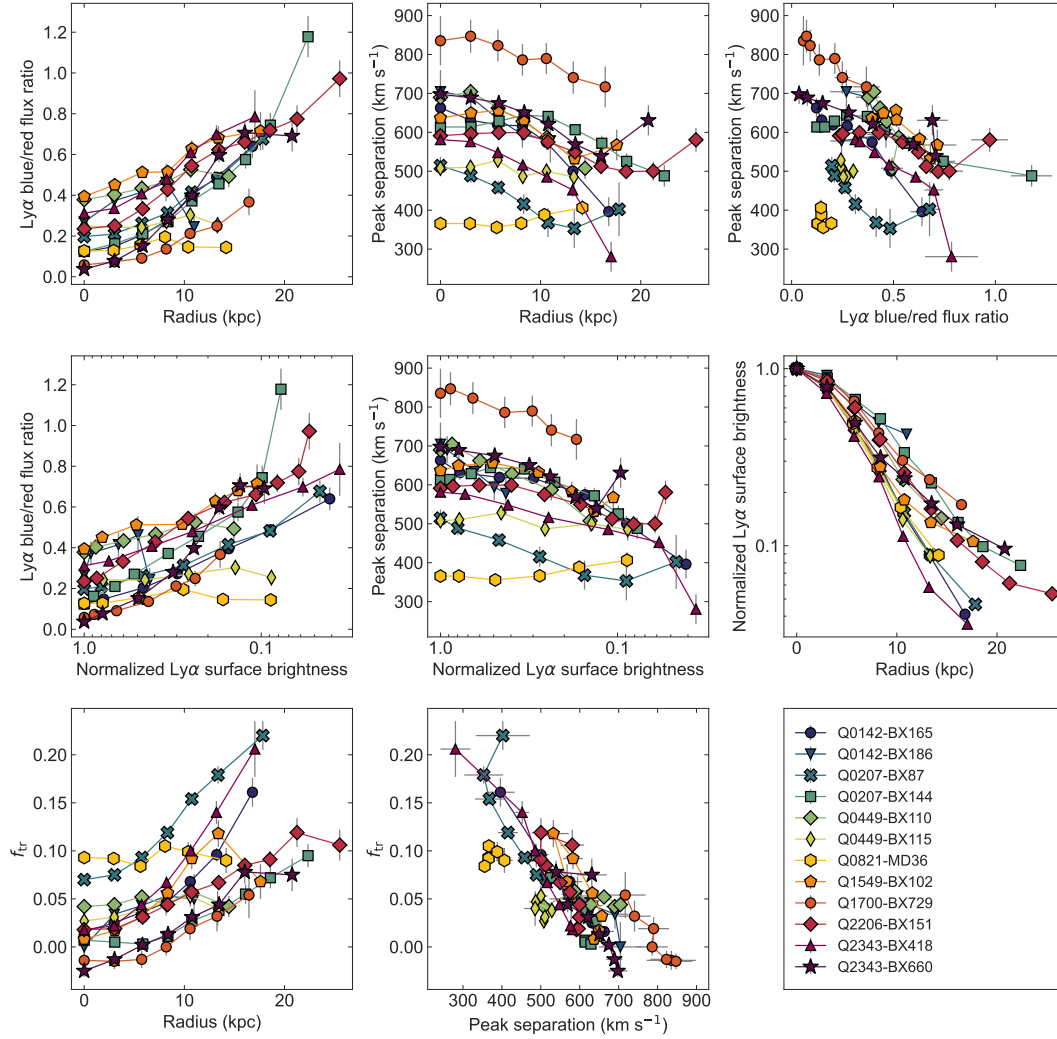


Figure 6.4: **Results of the line profile measurements of the annular spectra described in Section 6.4.** *Top row:* Ly α peak ratio vs. radius; Ly α peak separation vs. radius; and peak separation vs. ratio. *Middle row:* Ly α peak ratio vs. normalized Ly α surface brightness; Ly α peak separation vs. surface brightness; and surface brightness vs. radius. *Bottom row:* The fraction of total flux within ± 100 km s $^{-1}$ of the trough between the peaks f_{tr} vs. radius; f_{tr} vs. peak separation.

Gradients in Ly α Peak Ratio and Separation

While the binned, annular profiles described above are useful to characterize general trends in the extended Ly α emission, they also wash out the spectral variations seen in different parts of individual halos. The Ly α profiles across the halos are not radially symmetric, and there are significant differences in both peak ratio and separation at different position angles in a given halo. We therefore characterize the variations in the Ly α profile within individual halos by binning smaller regions,

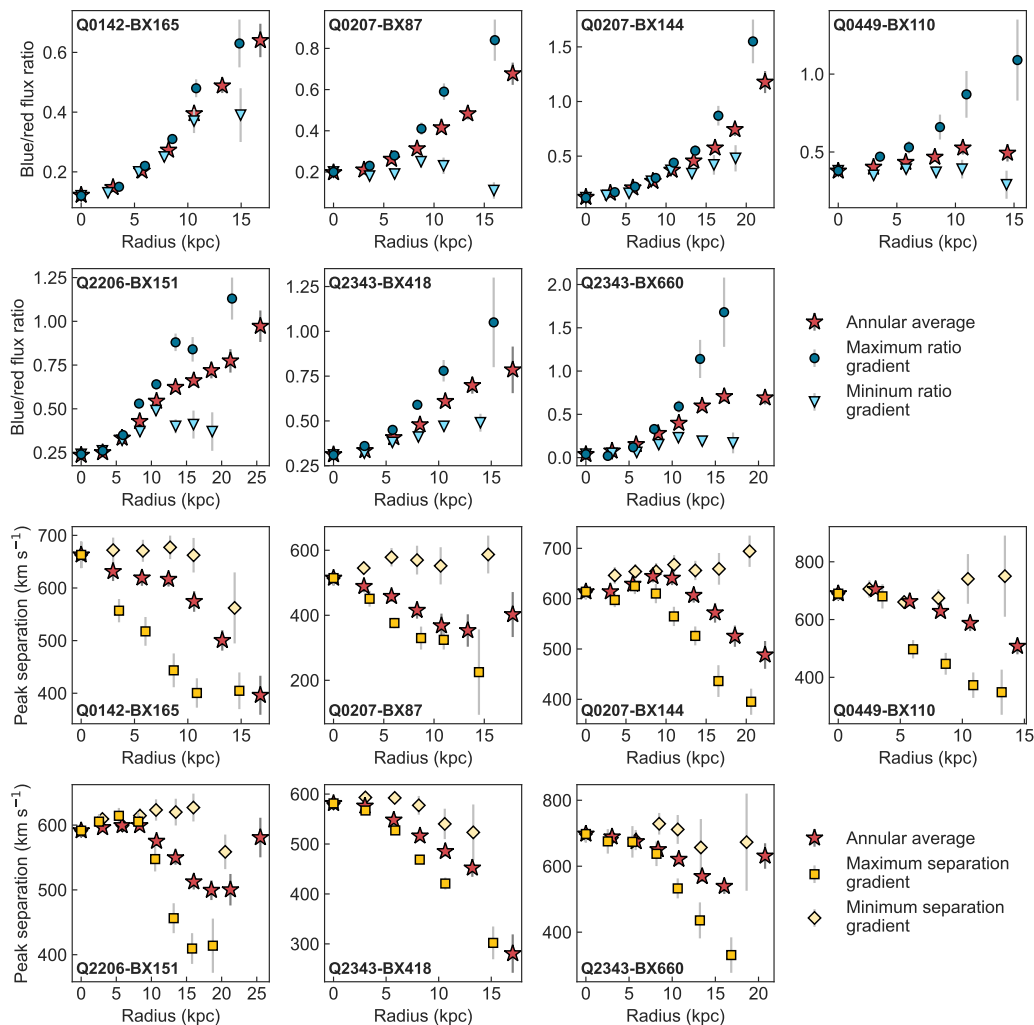


Figure 6.5: Top two rows: Blue-to-red Ly α flux ratios from radially binned spectra of the 60 $^\circ$ angular regions that maximize (dark blue circles) and minimize (light blue triangles) the gradient in peak ratio with radius. Second two rows: Same as first two rows, for measurements of the Ly α peak separation, with maximum gradients indicated by gold squares and minimum gradients by light yellow diamonds. The annular averages from Figure 6.4 are also shown as red stars in all panels. See Section 6.4 for details.

using seven of the eight brightest sources in the sample (we do not include Q0821-MD36, for which the blue peak is too weak to obtain useful measurements from binning smaller regions).

Our goal is to construct a series of binned spectra that maximize or minimize the gradients in peak ratio or separation from the center to the outskirts of the halo. Again beginning with all spaxels with S/N > 2 in the Ly α images, we then take a

subset of each halo corresponding to a 60° angular region (chosen to encompass a large enough region to increase the S/N by binning while still isolating different parts of the halos). As with the annular spectra, we radially bin the datacube in this region in single spaxel annular increments and measure the peak ratio and separation of each of the resulting Ly α profiles. We then rotate the 60° region by 10° and repeat the process until the entire halo has been covered.

We next measure the peak ratio and separation for each of the resulting 36 spectra, and locate the regions of maximum and minimum gradients in peak ratio and separation by identifying the two regions for which the difference in peak ratio with radius is maximized, and the two regions for which the difference in separation is maximized. For the peak ratio, the maximum gradient corresponds to the largest *increase* from the center to the outskirts, while for the separation it is the largest *decrease*. In other words, the steepest peak ratio gradient is found in the direction of the highest blue-to-red flux ratio, and the steepest peak separation gradient is found in the direction of the narrowest peak separation.

The results of this process are shown in Figure 6.5, in which we plot the maximum and minimum ratio gradients in the top two rows and the maximum and minimum separation gradients in the bottom two rows, along with the annular averages from Figure 6.4. Although the sample for which these measurements are feasible is small, this exercise shows that all of the halos have a region for which the peak ratio increases with radius, and a region for which the separation decreases with radius. Notably, however, in all cases the angular regions corresponding to these two maximum gradients do not overlap; this result is consistent with the finding that the correlation between peak ratio and separation is largely due to the underlying relationship of both with radius.

Turning to the minimum gradients, most of the halos also have at least one sightline for which the increase in peak ratio with radius is small or nonexistent, and at least one sightline for which the peak separation is relatively flat with radius (or even rising, in the case of Q0207-BX144). Unlike the maximum gradients, there is some overlap between the regions of minimum gradient; for four of the seven objects, the minimum gradient regions overlap by $10\text{--}30^\circ$. The minimum gradients show that most halos have regions for which the Ly α line profile does not follow the average trends. We discuss the implications of this observation further in Section 6.6, informed by the results of spatially resolved modeling of the Ly α emission.

6.5 Modeling Ly α Emission and Low Ionization Interstellar Absorption Lines

In the previous sections we have shown that the spectral morphology of Ly α emission changes significantly across the extended halos. On average, the blue-to-red peak flux ratio increases, the peak separation decreases, and the fraction of the total flux emerging between the two peaks increases with increasing radius; there are, however, variations in these patterns with azimuthal angle within a given halo. In this section we further examine both the spatially resolved Ly α profiles and the “down-the-barrel” rest-frame UV low-ionization interstellar metal absorption lines using physical models. This analysis will help us construct a consistent picture of the ISM and CGM of the galaxies in our sample.

Ly α Radiative Transfer Modeling

To extract physical properties of the gas in the halos from the observed Ly α profiles, we perform Monte Carlo radiative transfer (MCRT) modeling of the Ly α line. In contrast to the majority of previous studies in which spatially integrated Ly α spectra are modeled, in this work we attempt to fully leverage the power of KCWI and reproduce the spatially varying trends of the observed Ly α profiles.

Following a similar methodology to Li et al. (2022b), we model the spatially resolved Ly α profiles using the multiphase, clumpy model. Each model is a 3D spherically symmetric region that emulates a galactic halo with a Ly α emitting source located at its center and two phases of gas: cool ($\sim 10^4$ K) H I clumps and a hot ($\sim 10^6$ K), highly ionized inter-clump medium (ICM). As we will show below, such a hot, diffuse, low-density H I component is necessary to reproduce the observed Ly α profiles, primarily by producing additional absorption near the Ly α line center.⁴ In reality, such a component may correspond to the low column density absorbers ($\log N_{\text{HI}} \lesssim 10^{17} \text{cm}^{-2}$) that provide additional Ly α scatterings in a galactic outflow (see, e.g., Section 7.3 of Dijkstra et al. 2012). After interacting with these two phases of gas, Ly α photons that escape from different impact parameters can be separated into different spatial bins and the emergent spectra can then be compared to the corresponding observed spatially resolved Ly α profiles.

In practice, we construct a grid of multiphase, clumpy models for fitting the Ly α spectra by varying the five most important physical parameters: F_V , the volume filling factor of the clumps; $\log N_{\text{HI,cl}}$, the H I column density of the clumps; σ_{cl} ,

⁴In the multiphase, clumpy model, the flux at line center of the emergent Ly α spectra is predominantly controlled by the residual H I number density in the static ICM component. Without the ICM, a significant number of photons will escape at the line center.

Table 6.2: Parameter values of the multiphase, clumpy model grid.

Parameter (1)	Definition (2)	Values (3)
F_V	Clump volume filling factor	(0.01, 0.04, 0.08, 0.16)
$\log N_{\text{HI,cl}}$	Clump H I column density	(17, 17.5, 18, 18.5, 19) $\log \text{cm}^{-2}$
σ_{cl}	Clump velocity dispersion	(0, 25, 50, ..., 150) km s^{-1}
$v_{\text{cl},\infty}$	Clump asymptotic outflow velocity	(500, 600, 700, 800, 900) km s^{-1}
$\log n_{\text{HI,ICM}}$	ICM H I number density	(-8, -7.5, -7, -6.5) $\log \text{cm}^{-3}$
Δv	Velocity shift relative to systemic z	[-120, 120] km s^{-1}

Notes. The parameter values of the model grid that we used for fitting the Ly α profiles. The columns are: (1) parameter name; (2) parameter definition; (3) parameter values on the grid.

the random velocity dispersion of the clumps; v_{cl} , the radial outflow velocity of the clumps; and $\log n_{\text{HI,ICM}}$, the residual H I number density in the ICM.⁵ An additional parameter, Δv , is used in post-processing to determine the deviation between the best-fit systemic redshift of the Ly α emitting source and the observed systemic redshift inferred from non-resonant nebular emission lines. The parameter values of the model grid are summarized in Table 6.2. Note that the range of F_V corresponds to a cloud covering factor $f_c^{\text{Ly}\alpha}$ (the average number of clumps per line of sight) of $\sim 1 - 10$, which is similar to or moderately larger than the critical threshold $f_{c,\text{crit}}^{\text{Ly}\alpha}$. Here $f_{c,\text{crit}}^{\text{Ly}\alpha}$ denotes the critical average number of clumps per line of sight, above which the clumpy medium starts to transition to a homogeneous medium. In other words, we are exploring a unique physical regime ($f_c^{\text{Ly}\alpha} \simeq f_{c,\text{crit}}^{\text{Ly}\alpha}$) where the Ly α RT in a multiphase, clumpy medium does not fully converge to the homogeneous shell model (Gronke et al., 2016b; Gronke, 2017; Li et al., 2022a).

Previous work (Li et al., 2022b) assumed constant radial outflow velocities, but here we adopt a more physically realistic radially varying clump outflow velocity profile. Our choice is inspired by Dijkstra et al. (2012), who find that a radially varying velocity profile is able to better reproduce the surface brightness (SB) profiles of Ly α halos. Specifically, the momentum equation of an H I clump can be written as

⁵We have also experimented with a varying v_{ICM} (the radial outflow velocity of the ICM), but found that in almost all cases $v_{\text{ICM}} \simeq 0$ is preferred by the fitting. This is due to the prominent trough in most of the Ly α profiles that requires significant absorption at the line center. Therefore, we have fixed v_{ICM} to zero to reduce the dimensionality of our model grid. Similarly, varying the ICM temperature may have a minor effect on the emergent Ly α spectra, but we chose to fix it to 10^6K to keep the computational cost affordable.

(Murray et al., 2005; Martin, 2005):

$$\frac{dv(r)}{dt} = -\frac{GM(r)}{r^2} + Ar^{-\alpha} \quad (6.1)$$

where r is the clump's radial position, $v(r)$ is the clump radial outflow velocity at r , $M(r)$ is the total gravitational mass within r , and A is a constant that characterizes the amplitude of the power-law acceleration $r^{-\alpha}$. The acceleration of the clump is determined by two competing terms on the right hand side, the first of which is due to gravitational deceleration and the second of which is an empirical power-law acceleration term (Steidel et al., 2010). Major acceleration mechanisms for the cool clumps may include radiation pressure, ram pressure from a hot wind, and shock-accelerated cosmic rays, which all may correspond to an r^{-2} force (see Chisholm et al. 2016, and note that the radiation pressure should be in the optically thin regime). However, in reality, the clumps may suffer from extra deceleration (and acceleration, see Gronke et al., 2020) due to their interaction with other phases of gas, which yields an effective α less than 2.

Assuming the gravitational potential is an isothermal sphere, we have $M(r) = 2\sigma_{\text{cl}}^2 r/G$, where σ_{cl} is the velocity dispersion of the clumps. Equation 6.1 can then be analytically solved as:

$$v(r) = \sqrt{4\sigma_{\text{cl}}^2 \ln\left(\frac{r_{\text{min}}}{r}\right) + v_{\text{cl},\infty}^2 \left(1 - \left(\frac{r}{r_{\text{min}}}\right)^{1-\alpha}\right)} \quad (6.2)$$

where r_{min} is the inner cutoff (or “launching”) radius that satisfies $v(r_{\text{min}}) = 0$, and $v_{\text{cl},\infty} = \sqrt{2Ar_{\text{min}}^{1-\alpha}/(\alpha-1)}$ is the asymptotic maximum outflow velocity if there were no gravitational deceleration. Note that in general the actual $v(r)$ does not reach $v_{\text{cl},\infty}$ due to the gravitational deceleration term; even the maximum radial $v(r)$ is usually several hundred km s^{-1} smaller than $v_{\text{cl},\infty}$. Following Dijkstra et al. (2012), we have fixed $\alpha = 1.4$ and left σ_{cl} and $v_{\text{cl},\infty}$ as the free parameters in this model. We set r_{min} to be 1% of the simulated halo radius r_{h} , so that $\frac{r}{r_{\text{min}}} \in [1, 100]$. The model is intrinsically rescalable (i.e., increasing the size of every component in the model by any factor with all column densities unchanged would yield an identical model) and constrains only the ratio $\frac{r}{r_{\text{min}}}$, so the following analysis applies to $\text{Ly}\alpha$ halos of varying physical sizes.

For each multiphase, clumpy model on the grid, MCRT has been performed on 10^4 $\text{Ly}\alpha$ photon packages emitted at the center of the simulation sphere in the form of a normalized Gaussian intrinsic spectrum $\mathcal{N}(v, \mu = 0, \sigma = \sigma_{\text{i,cl}})$, where $\sigma_{\text{i,cl}} = 12.85 \text{ km s}^{-1}$ is the canonical thermal velocity dispersion of the H I gas in the

clumps at $T = 10^4$ K.⁶ The H I clumps with a constant column density $N_{\text{HI,cl}}$ are placed uniformly radially, so that their number density $n_{\text{cl}} \propto r^{-2}$ (i.e., mass conserving if the radial outflow velocity is constant).

Each model on the grid is further used to generate three spatially binned Ly α profiles by separating all the photons into three spatial bins according to their last-scattering impact parameters: $b/b_{\text{max}} \in (0, 0.25]$, $(0.25, 0.50]$ and $(0.50, 0.75]$, where b_{max} is the largest impact parameter of the scattered Ly α photons (see Figure 5 of Li et al. (2022b) for an illustrative schematic), and the impact parameter b is measured orthogonal to the direction of the photon’s escape trajectory. The difference between b_{max} and the halo radius r_{h} is negligible, and we simply fix $b_{\text{max}} = r_{\text{h}}$.

We only include the photons within 75% of b_{max} (or equivalently, within the inner $\sim 56\%$ of the total area) in our fitting in order to ensure a direct comparison between the model and the data, because the $S/N > 2$ regions of the halos used for the spectra (see Section 6.4) contain on average 58% of the total halo area. The spectra to be modeled are constructed in the same way as the annular spectra described in Section 6.4, except that the spaxels are divided into three radial bins with $0 < r \leq 0.33r_{\text{max}}$, $0.33r_{\text{max}} < r \leq 0.67r_{\text{max}}$, and $0.67r_{\text{max}} < r \leq r_{\text{max}}$, where r_{max} is the radius of the most distant spaxel in the modeled area. When we present our modeling results later in §6.5, we consider only the photons included in the modeling and renormalize the halo to $0.75 b_{\text{max}}$, so that $b/b_{\text{max}} \in (0, \frac{1}{3}]$, $(\frac{1}{3}, \frac{2}{3}]$ and $(\frac{2}{3}, 1]$.

Our fitting pipeline employs the python nested sampling package `dynesty` (Skilling, 2004; Skilling, 2006; Speagle, 2020). At each visited point of the parameter space, the pipeline executes the following three steps:

(1) calculate three binned Ly α model spectra via linear flux interpolation on the model grid (to circumvent doing computationally expensive RT “on the fly”), where the flux density of the model spectrum at each wavelength is calculated by a parameter-weighted multidimensional linear interpolation⁷ of the flux densities of the adjacent grid model spectra at the corresponding wavelength. The three binned Ly α model spectra are then convolved with a Gaussian function with $\sigma = 65 \text{ km s}^{-1}$ (the KCWI line spread function [LSF]) to mimic the finite instrumental resolution;

⁶In the multiphase, clumpy model, the width of the intrinsic spectrum is always assumed to be small and the clump velocity dispersion is responsible for broadening the spectrum. Such a choice has the advantage of avoiding obtaining unphysically large intrinsic line widths from fitting the spectrum (e.g., using the shell models, see Li et al., 2022a).

⁷Such an interpolation is carried out based on the distance between the visited point in the parameter space and its adjacent points on the grid (realized by the PYTHON function `scipy.interpolate.interpn`).

- (2) compare each binned model spectrum to an observed Ly α spectrum at the corresponding impact parameter range and calculate the likelihood;
- (3) sum the likelihoods of these three binned models as the likelihood of the current set of parameters.

Each fitting run yields a posterior probability distribution (PDF) of the model parameters. The parameter uncertainties can be further determined as certain quantiles (e.g., 16%–84%, or 1σ confidence intervals) of the samples in the marginalized PDF.

Metal Absorption Line Modeling

In addition to the Ly α profiles observed at both $b = 0$ and $b > 0$, the rest-UV, low-ionization metal absorption lines observed “down-the-barrel” (i.e., at $b = 0$) also encode rich information on the physical properties of the cool gas. These metal absorption line profiles are typically “sawtooth” shaped (e.g., Weiner et al. 2009), where the part blueward of the absorption trough (the location of the minimum flux density) gradually decreases with velocity while the part redward of the absorption trough increases with velocity relatively rapidly. The blueshifted absorption at negative velocities is produced by gas clumps with radially varying outflow velocities along the line-of-sight, whereas the red part is mainly produced by a group of non-outflowing, randomly moving clumps. In this work, we focus on modeling the portion blueward of the absorption trough for the average line profile of the Si II $\lambda 1260$ and C II $\lambda 1334$ transitions,⁸ as we are most interested in constraining the clump outflow kinematics. Our model is similar to the kinematic model used by Steidel et al. (2010), but with a different clump radial velocity profile.

In our model, we first assume that the clump radial outflow velocity is described by the same model we use for the Ly α emission, i.e., Equations 6.1 and 6.2 with two free parameters: the clump velocity dispersion σ_{cl} and the asymptotic maximum clump outflow velocity $v_{\text{cl},\infty}$. Assuming that the absorption lines are saturated⁹ (i.e., the column densities of the absorbing gas are so high that the depth of absorption simply reflects the gas covering fraction), the down-the-barrel absorption line profile $I(v)$ (the normalized, residual flux density as a function of velocity) is

⁸We did not fit Si II $\lambda 1260$ and C II $\lambda 1334$ separately as many of the individual lines have fairly low S/N ratios.

⁹The assumption of saturation comes from the fact that in our sample, Si II $\lambda 1260$ and Si II $\lambda 1526$ have similar equivalent widths (see, e.g., footnote 27 of Steidel et al. 2018).

simply given by

$$I(v) = 1 - f_c(v) \quad (6.3)$$

where $f_c(v)$ is the (clumpy) gas geometric covering fraction as a function of velocity, which is the fraction of the total lines of sight of the rest-UV emission that are intercepted by the absorbing gas. We further assume that the gas covering fraction decreases as a function of radius, in the form of a power law:

$$f_c(r) = f_{c,\max} \left(\frac{r}{r_{\min}} \right)^{-\gamma} \quad (6.4)$$

where r_{\min} is the launching radius and $f_{c,\max}$ is the maximum gas covering fraction that corresponds to the deepest part of the absorption trough. $f_c(r)$ can then be translated into $f_c(v)$ using the $v(r)$ dictated by Equation 6.2. Note that the gas geometric covering fraction in the Ly α RT models, which is a function of the number density and the physical size of the clumps (both of which may vary as a function of velocity or radius; see Equation 2 in Dijkstra et al. 2012), may not be fully consistent with the power law $f_c(r)$ assumed here. One may match them by using clumps with radially varying sizes in the RT model; we plan to explore this option in future work.

To be consistent with the Ly α modeling in §6.5, we fix $\alpha = 1.4$ in the clump radial velocity profile and set $r_{\min} = 0.1$ kpc with $\frac{r}{r_{\min}} \in [1, 100]$. Note again that only the ratio $\frac{r}{r_{\min}}$ (rather than r or r_{\min} individually) is constrained by the absorption line modeling. We then fit the observed absorption line profiles with `dynesty` to determine the PDF of the four parameters in this model: σ_{cl} , $v_{\text{cl},\infty}$, $f_{c,\max}$ and γ . We use flat priors for the fitted parameters (which can vary continuously): $\sigma_{\text{cl}} \in [0, 120]$ km s⁻¹, $v_{\text{cl},\infty} \in [100, 1500]$ km s⁻¹, $f_{c,\max} \in [0, 1]$, and $\gamma \in [0.1, 2.0]$. We restrict γ to be no larger than 2, as otherwise it suggests that the clumps are destroyed rapidly as they move outwards, contradictory to the observation of metal absorption at large impact parameters ($b \sim 100$ kpc, see Figure 21 of Steidel et al. 2010 and Rudie et al. 2019).

Modeling Results and Interpretation

Our modeling of both the spatially resolved Ly α emission and the UV absorption lines has achieved the following principal results:

- (1) reproducing the radially varying, spatially resolved Ly α profiles;

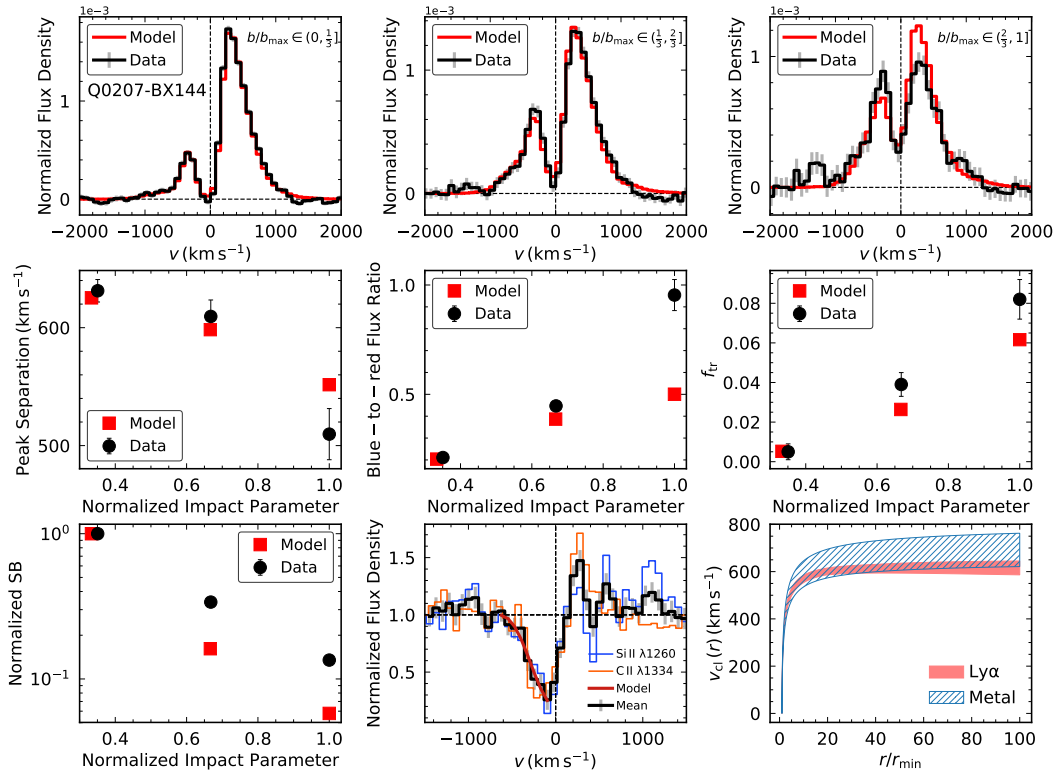


Figure 6.6: **Modeling results of the annular-averaged, spatially resolved $\text{Ly}\alpha$ spectra and of the average line profile of $\text{Si II } \lambda 1260$ and $\text{C II } \lambda 1334$ observed down the barrel for Q0207-BX144 (see Appendix 6.7 for the rest of the sample).** The top row shows the best-fit models (red) to the spatially resolved $\text{Ly}\alpha$ spectra (black, with $1\text{-}\sigma$ uncertainties shown in grey) from the inner to the outer halo. In each subpanel of the top row, the vertical and horizontal black dashed lines indicate the systemic redshift (determined from nebular emission lines) and zero flux density, respectively. The middle row and the first panel of the bottom row show a comparison between the radial trends of peak separation, blue-to-red flux ratio, trough flux fraction, and normalized SB vs. the normalized impact parameter predicted by the best-fit models (red squares) and measured from observation (black points, with $1\text{-}\sigma$ uncertainties). Note that the impact parameters may be slightly different for the model and the data: the models are binned consistently as $b/b_{\text{max}} \in (0, \frac{1}{3}]$, $(\frac{1}{3}, \frac{2}{3}]$ and $(\frac{2}{3}, 1]$, and while the data are binned in the same way, the halos are asymmetric with the result that the median distance to the spaxels included in each bin varies from object to object. The rest of the bottom row shows the best-fit models (red) to the average line profile (black, with $1\text{-}\sigma$ uncertainties shown in grey) of $\text{Si II } \lambda 1260$ (blue) and $\text{C II } \lambda 1334$ (orange) profiles, as well as a comparison of clump radial outflow velocity profiles inferred from $\text{Ly}\alpha$ RT modeling (red) and metal absorption line fitting (blue hatched patch). The shaded regions represent the velocity ranges spanned by 50 points in the parameter space after convergence has been achieved for the fitting.

Table 6.3: Best-fit parameters from modeling Ly α emission and the rest-UV low-ionization metal absorption lines

ID	Best-fit Parameters (Ly α)							Best-fit Parameters (Absorption)				
	F_V	$\log N_{\text{HI,cl}}$	σ_{cl}	$v_{\text{cl},\infty}$	$v_{\text{cl,max}}$	$\log n_{\text{HI,ICM}}$	Δv	$\sigma_{\text{cl,abs}}$	$v_{\text{cl},\infty,\text{abs}}$	$v_{\text{cl,max,abs}}$	$f_{\text{c,max}}$	γ
(1)	(2)	(3)	(4)	(5)	(6)	(7)	(8)	(9)	(10)	(11)	(12)	(13)
Q0142-BX165	$0.06^{+0.01}_{-0.01}$	$18.3^{+0.1}_{-0.1}$	142^{+4}_{-6}	748^{+24}_{-25}	392^{+26}_{-27}	$-7.13^{+0.05}_{-0.07}$	9^{+4}_{-4}	58^{+36}_{-33}	835^{+69}_{-69}	707^{+63}_{-46}	$0.8^{+0.1}_{-0.1}$	$1.7^{+0.2}_{-0.3}$
Q0142-BX186	$0.12^{+0.02}_{-0.02}$	$18.8^{+0.1}_{-0.1}$	117^{+14}_{-4}	533^{+48}_{-23}	235^{+17}_{-4}	$-7.28^{+0.16}_{-0.13}$	55^{+10}_{-10}	72^{+32}_{-41}	429^{+400}_{-205}	423^{+432}_{-157}	$0.6^{+0.3}_{-0.3}$	$1.2^{+0.6}_{-0.7}$
Q0207-BX87	$0.08^{+0.01}_{-0.00}$	$18.0^{+0.0}_{-0.0}$	98^{+0}_{-1}	617^{+11}_{-10}	389^{+13}_{-12}	$-7.14^{+0.02}_{-0.02}$	-4^{+5}_{-4}	61^{+40}_{-34}	1029^{+311}_{-264}	891^{+292}_{-262}	$0.2^{+0.1}_{-0.1}$	$1.1^{+0.6}_{-0.6}$
Q0207-BX144	$0.08^{+0.01}_{-0.01}$	$18.4^{+0.1}_{-0.1}$	106^{+17}_{-21}	842^{+40}_{-47}	622^{+17}_{-17}	$-6.69^{+0.04}_{-0.04}$	-47^{+3}_{-3}	53^{+37}_{-29}	807^{+79}_{-76}	684^{+50}_{-50}	$0.8^{+0.1}_{-0.1}$	$1.7^{+0.2}_{-0.3}$
Q0449-BX110	$0.09^{+0.02}_{-0.01}$	$18.3^{+0.1}_{-0.1}$	9^{+11}_{-6}	892^{+5}_{-9}	815^{+5}_{-9}	$-6.89^{+0.04}_{-0.04}$	33^{+5}_{-5}	62^{+36}_{-37}	1051^{+130}_{-102}	913^{+121}_{-84}	$0.8^{+0.1}_{-0.1}$	$1.6^{+0.3}_{-0.4}$
Q0449-BX115	$0.13^{+0.02}_{-0.02}$	$18.1^{+0.1}_{-0.1}$	18^{+20}_{-13}	550^{+19}_{-14}	495^{+9}_{-9}	$-6.93^{+0.04}_{-0.04}$	1^{+3}_{-3}	58^{+39}_{-35}	636^{+307}_{-155}	502^{+319}_{-131}	$0.7^{+0.2}_{-0.2}$	$1.3^{+0.5}_{-0.6}$
Q0821-MD36	$0.15^{+0.01}_{-0.01}$	$18.1^{+0.0}_{-0.0}$	60^{+4}_{-3}	506^{+10}_{-4}	386^{+9}_{-10}	$-7.47^{+0.03}_{-0.02}$	6^{+4}_{-7}	61^{+36}_{-37}	870^{+383}_{-269}	735^{+373}_{-100}	$0.3^{+0.3}_{-0.2}$	$1.2^{+0.5}_{-0.7}$
Q1549-BX102	$0.07^{+0.01}_{-0.01}$	$17.7^{+0.1}_{-0.1}$	134^{+6}_{-11}	882^{+11}_{-16}	578^{+24}_{-19}	$-6.67^{+0.03}_{-0.04}$	-15^{+4}_{-4}	58^{+40}_{-33}	633^{+170}_{-125}	497^{+166}_{-100}	$0.7^{+0.1}_{-0.2}$	$1.4^{+0.4}_{-0.6}$
Q1700-BX729	$0.16^{+0.00}_{-0.00}$	$18.5^{+0.0}_{-0.0}$	123^{+1}_{-3}	606^{+13}_{-6}	287^{+16}_{-11}	$-6.60^{+0.07}_{-0.09}$	67^{+7}_{-5}	44^{+35}_{-24}	563^{+74}_{-65}	468^{+44}_{-60}	$0.9^{+0.1}_{-0.1}$	$1.7^{+0.2}_{-0.3}$
Q2206-BX151	$0.10^{+0.02}_{-0.02}$	$17.6^{+0.1}_{-0.1}$	142^{+5}_{-8}	864^{+17}_{-23}	530^{+14}_{-15}	$-6.73^{+0.03}_{-0.03}$	-73^{+3}_{-3}	57^{+39}_{-33}	743^{+258}_{-137}	612^{+251}_{-127}	$0.5^{+0.1}_{-0.1}$	$1.4^{+0.4}_{-0.6}$
Q2343-BX418	$0.07^{+0.01}_{-0.01}$	$18.0^{+0.0}_{-0.1}$	6^{+14}_{-4}	606^{+19}_{-14}	553^{+11}_{-12}	$-6.99^{+0.03}_{-0.02}$	34^{+2}_{-2}	59^{+39}_{-35}	857^{+165}_{-107}	725^{+154}_{-96}	$0.6^{+0.2}_{-0.2}$	$1.4^{+0.5}_{-0.5}$
Q2343-BX660	$0.07^{+0.01}_{-0.01}$	$18.4^{+0.1}_{-0.1}$	134^{+8}_{-19}	876^{+17}_{-47}	571^{+21}_{-20}	$-6.62^{+0.04}_{-0.05}$	-112^{+5}_{-5}	55^{+37}_{-32}	697^{+78}_{-78}	569^{+69}_{-44}	$0.9^{+0.1}_{-0.1}$	$1.5^{+0.3}_{-0.3}$

Notes. Best-fit parameters (averages and 16% – 84% quantiles, i.e., 1σ confidence intervals) from the Ly α and low-ionization metal absorption line (the average of Si II λ 1260 and C II λ 1334) modeling. The columns are: (1) the object ID; (2) the clump volume filling factor; (3) the clump H I column density; (4) the clump velocity dispersion; (5) the clump asymptotic outflow velocity; (6) the actual maximum clump radial outflow velocity; (7) the residual H I number density of the ICM; (8) the velocity shift relative to the systemic redshift of the source. (9) – (13) are determined from the average metal absorption line profile. (9) the clump velocity dispersion; (10) the clump asymptotic outflow velocity; (11) the actual maximum clump radial outflow velocity; (12) the maximum clump covering fraction; (13) the power-law index of the clump covering fraction function.

(2) reproducing the radial trends of several important physical quantities of the Ly α profiles, including the peak separation, peak flux ratio, trough flux fraction, and SB vs. the impact parameter;

(3) reconciling the clump outflow velocities inferred from Ly α emission and metal absorption lines.

We present the modeling results for the spatially resolved Ly α spectra and the average line profile of Si II λ 1260 and C II λ 1334 for our sample in Figure 6.6 (using Q0207-BX144 as an example) and Appendix 6.7. In each panel, the top row shows the best-fit RT models (red) to the spatially resolved Ly α spectra (black); the middle row and the first panel of the bottom row show a comparison between the radial trends of peak separation, peak flux ratio, trough flux fraction, and SB predicted by

the best-fit models and measured from observations; and the rest of the bottom row shows the best-fit models (red) to the average metal absorption line profile (black), as well as a comparison of clump radial outflow velocity profiles inferred from Ly α emission and the average metal absorption line. The best-fit parameters are summarized in Table 6.3, and we present the posterior distribution of Q0207-BX144 as an example in Appendix 6.7. In Section 6.5 below we describe the relationships between impact parameter, the properties of the model Ly α profiles, and the parameters of the model, and in Section 6.5 we further discuss the best-fit parameters and relationships between them. Section 6.5 provides a comparison of spatially integrated vs. spatially resolved Ly α modeling, and we discuss caveats to the models in Section 6.5.

Radial Trends

The modeling results show that our multiphase, clumpy model is able to reproduce the spatially resolved Ly α spectra fairly well, especially for the innermost two spatial bins. In a number of cases (e.g., Q0142-BX165, Q0207-BX87, Q0207-BX144, Q1549-BX102 and Q2343-BX660) there is a noticeable mismatch between the model and data in the outermost bin, which may be because the gas in the outer halo does not fully follow the outflowing kinematics of the gas in the inner halo (e.g., due to external forces). In general, as the impact parameter increases, the best-fit Ly α RT model predicts a decrease in the peak separation, an increase in the blue-to-red peak flux ratio, and an increase in the trough flux fraction. These predicted radial trends of peak separation and peak flux ratio are broadly consistent with the observational data, although the exact values differ in some cases. The increase in the trough flux fraction is also evident in almost all objects, especially from a comparison between the innermost two spatial bins.

From a Ly α RT perspective, the peak separation, which reflects the most likely frequencies at which the Ly α photons escape, is directly related to the Ly α optical depth of the system. The optical depth, which is the product of the Ly α cross-section¹⁰ and the H I column density of the absorber, can therefore be expressed as a function of the temperature and column density of the absorber.¹¹ The blue-to-red peak flux ratio, however, is negatively correlated with the H I gas outflow velocity

¹⁰Strictly speaking, the peak separation is also related to the gas outflow velocity, since the Ly α cross section depends on the photons' apparent frequencies in the gas frame. However, our tests have shown that such an effect is minor compared to the one that the H I column density has on peak separation.

¹¹For example, the peak separation of Ly α photons that escape from an opaque, static H I sphere

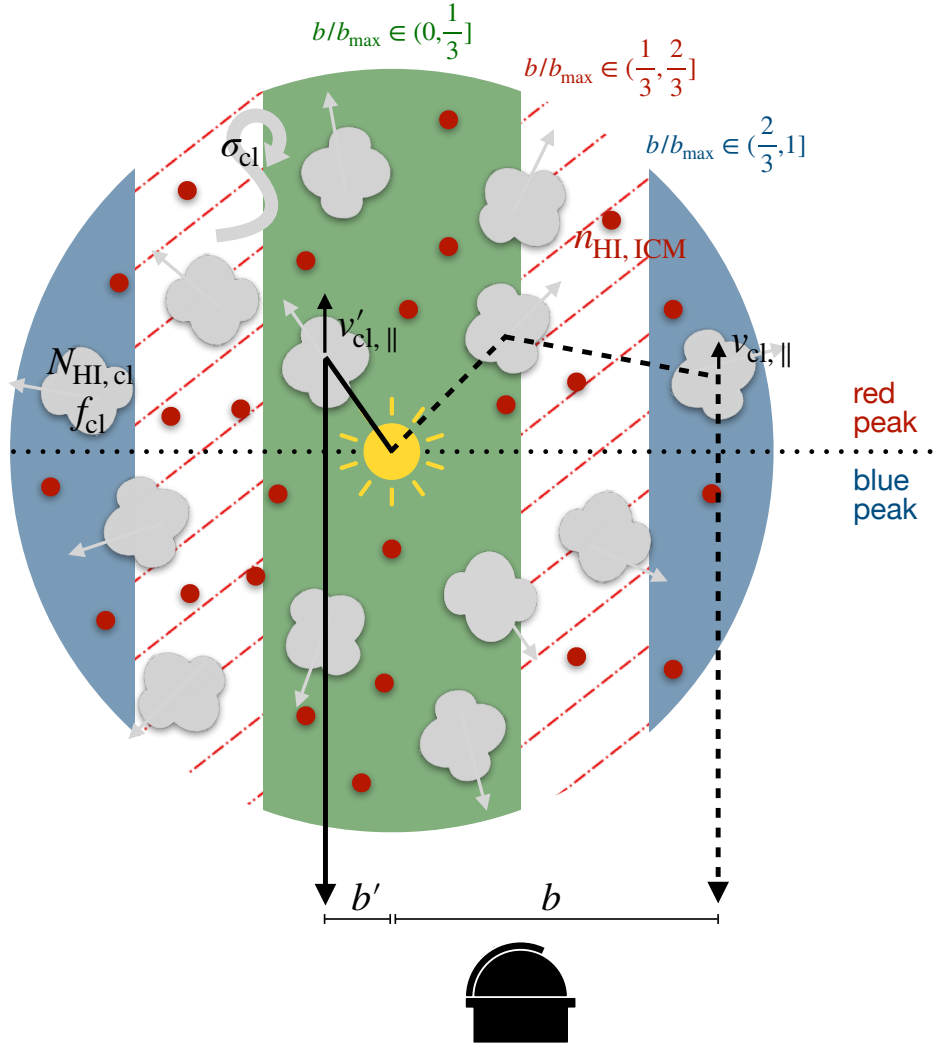


Figure 6.7: **Schematic of the escape of two Ly α photons at low and high impact parameters in the multiphase, clumpy model.** The large circle represents the boundary of the simulated spherical region, divided into shaded green, red hatched, and blue regions indicating the three ranges of impact parameters modeled. The location of the observer is indicated by the telescope dome at the bottom, and the dotted horizontal line indicates that photons in the blue peak arise from the near side of the halo while those in the red peak predominantly come from the far side. The gold sun symbol represents the Ly α emitting source at the center, the grey clouds represent HI clumps with random motions and radial outflows, and the small red circles represent the diffuse, hot ICM. The impact parameters b and b' are defined as the orthogonal distance from the center to the direction of the photon escape trajectories shown by the black solid and dashed lines. The photon that escapes at a higher $b > b'$ will experience several differences before it escapes: (1) it will scatter with lower HI column densities from the clumps, due to the decrease in the clump covering fraction at large radii; (2) it will experience (on average) a lower projected component of the clump outflow velocity along its traveling direction ($v_{\text{cl, ||}} < v'_{\text{cl, ||}}$, as indicated by the black arrows near the last clump that scatters each photon); (3) it will suffer from less absorption at line center from the ICM, due to its lower traveling distance at the outskirts of the halo. Also note that the photon escaping at b' passes through a clump on the near side of the halo unimpeded, because it is out of resonance with the clump due to its previous scattering.

as seen by the Ly α photons, as the blue photons are less likely to escape since they appear closer to resonance in the reference frame of the outflowing gas. Finally, as the absorption at the line center is mainly produced by the ICM, the trough flux fraction is mostly set by the ICM column density.

One can then imagine that the Ly α photons that escape at large impact parameters (i.e., the directions of their escape trajectories are almost orthogonal to the radial direction) will experience the following differences relative to photons from smaller impact parameters before they escape: (1) experience lower HI column densities from the clumps, as the area covering fraction of the clumps decreases at large radii due to the increase of the physical volume of the halo; (2) encounter (on average) a lower projected component of the clump outflow velocity along their traveling directions in the portion of the outer halo that they pass through before they escape;¹² (3) suffer from lower absorption (or equivalently, “see” a lower optical depth) at line center from the ICM in the outer halo, as on average the distance a photon travels within the halo before it escapes at large impact parameters is smaller than that at small impact parameters.¹³ These three effects are presumably responsible for the observed radial variation of the spatially binned Ly α profiles, and we illustrate them in Figure 6.7.

To test these hypotheses, we have designed several experiments and present them in Figure 6.8. We first generate our fiducial model by setting $(F_V, \log N_{\text{HI,cl}}, \sigma_{\text{cl}}, v_{\text{cl},\infty}, \log n_{\text{HI,ICM}}, \Delta v) = (0.05, 18.5, 80, 500, -7.0, 0)$. Such a choice roughly corresponds to the median parameter values of the model grid and proves to clearly demonstrate the radial variation of the peak separation, peak flux ratio, and the trough flux fraction of the radially binned Ly α spectra. We then generate three test models for comparison by modifying the configuration of the fiducial model in specific ways. In Model I, we adjust the spatial distribution of the clumps: instead of placing the clumps radially uniformly, we place more clumps at large radii so that the number density of the clumps $n_{\text{cl}}(r) \simeq \text{constant}$. In Model II, we change the direction of the clumps’ outflow velocity from radial to tangential by rotating the clumps’ velocity vector by 90 degrees, so that the projected component of the clump outflow veloc-

is $\Delta v_{\text{peak}} \simeq 320 \left(\frac{N_{\text{HI}}}{10^{20} \text{cm}^{-2}} \right)^{1/3} \left(\frac{T_{\text{HI}}}{10^4 \text{K}} \right)^{1/6} \text{ km s}^{-1}$ (Dijkstra, 2014).

¹²This is a purely geometrical effect; assuming the clump outflow is nearly isotropic, at high impact parameters ($b \simeq b_{\text{max}}$) the maximum projected component of the clump outflow velocity along the traveling direction of a photon goes as $v_{\text{cl},\parallel,\text{max}}(r) = \sqrt{1 - (b/b_{\text{max}})^2} v_{\text{cl}}(r) \simeq 0$ (Li et al., 2022b).

¹³Considering the spherical geometry of the halo, the largest distance that a photon can travel through without changing direction at impact parameter b is $\sim 2\sqrt{R^2 - b^2}$.

ity along the traveling direction is no longer preferentially small for photons that escape at high impact parameters. In Model III, we increase the number density of the ICM by a factor of 20 in the outer 60% of the halo radius in order to offset the shorter photon traveling distance at large radii. As shown in Figure 6.8, in Model I, the peak separation of the three binned Ly α model spectra is now roughly constant; in Model II, the significant increase in the blue-to-red peak flux ratio is no longer present, yet a slight decrease towards the outskirts is seen; and in Model III, the trough flux fractions are all much closer to zero. Therefore, we conclude that these experiments strongly support our above explanation for the radial trends of the peak separation, peak flux ratio and trough flux fraction.

Incidentally, our model has also reproduced the decreasing trend of Ly α SB vs. impact parameter, with only a few exceptions (e.g., Q0142-BX186 and Q1700-BX729). These two objects, which have a more gradual decline in SB, are the faintest objects in the sample, with the smallest fraction of the total halo area used for the spatially resolved Ly α modeling. This overall consistency adds further credence to our multiphase, clumpy RT model.

Best-Fit Parameters

One of the most interesting discoveries from our modeling is that the clump outflow velocities inferred from Ly α emission and the low-ionization metal absorption lines can be mutually consistent, with typical values of $\sim 400 - 600 \text{ km s}^{-1}$ obtained for both (see Table 6.3). The mismatch between the gas outflow velocities inferred from Ly α and from metal absorption lines has been a long-standing problem. For example, it is reported that the $\lesssim 150 \text{ km s}^{-1}$ outflow velocities of the shell model required to match the Ly α profiles of local starburst and green pea galaxies are *much lower* than the $\gtrsim 300 \text{ km s}^{-1}$ characteristic velocities of the metal absorption lines (e.g., Leitherer et al. 2013; Orlitová et al. 2018). The high outflow velocity regime of Ly α RT models has been little explored, possibly due to the belief that the Ly α photons will be seen as out of resonance by the fast moving gas and will therefore not scatter (e.g., Verhamme et al. 2015). However, we observe an interesting pattern in our multiphase, clumpy model: for a typical double-peaked Ly α profile, as the clump outflow velocity increases, the blue-to-red peak flux ratio (or the “level of symmetry”) first decreases and then increases, until the clump outflow velocity is so large that all the photons are completely shifted out of resonance as seen by the gas. This pattern, as shown by an example in Figure 6.9, suggests the possibility of

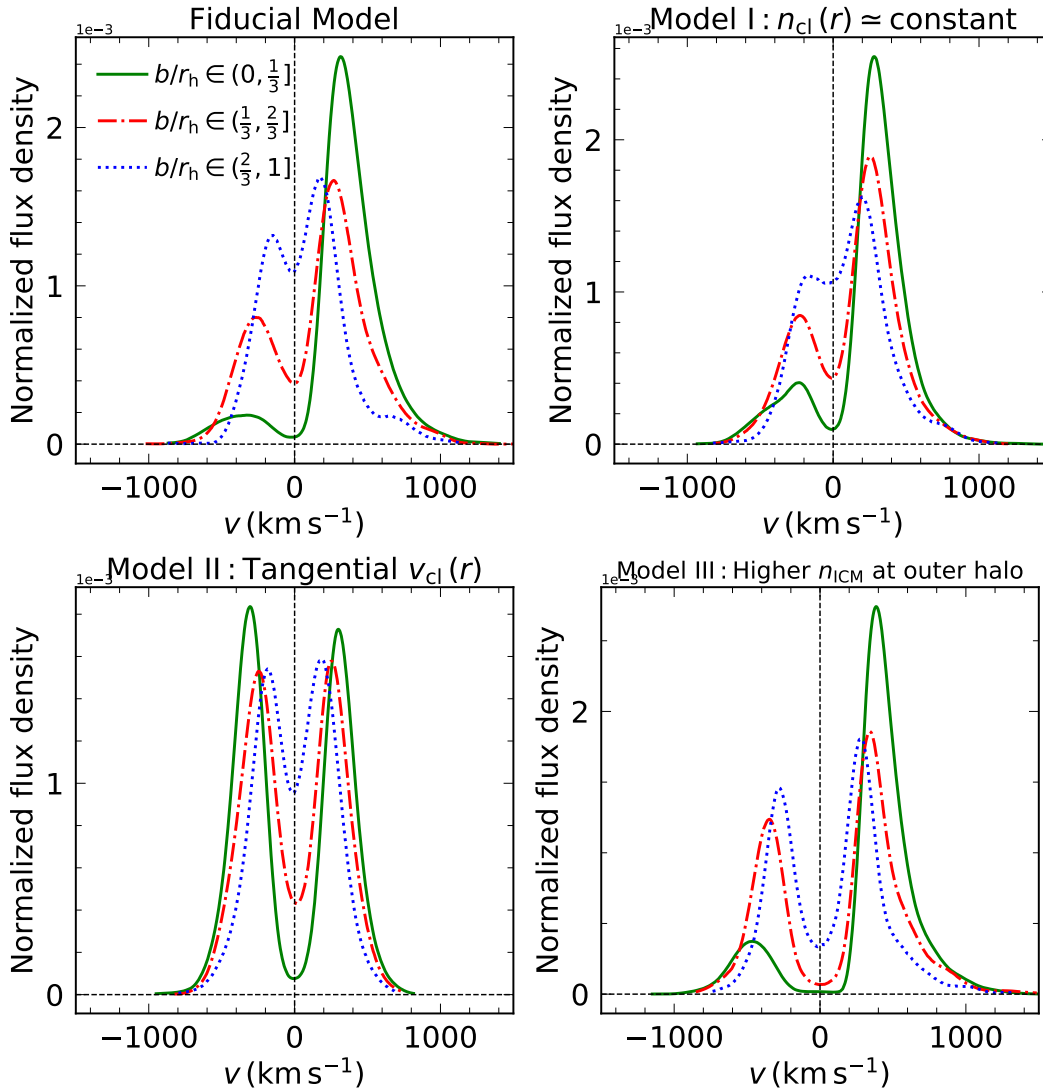


Figure 6.8: **Experiments designed to test our hypotheses for the differences between Ly α photons that escape at low and high impact parameters.** In each of the four subpanels, three binned model Ly α spectra are shown according to their last-scattering impact parameters: $b/r_h \in (0, \frac{1}{3}]$ (green solid), $(\frac{1}{3}, \frac{2}{3}]$ (red dash-dotted) and $(\frac{2}{3}, 1]$ (blue dotted), where r_h is the radius of the modeled halo. *Left:* The fiducial model with $(F_V, \log N_{\text{HI,cl}}, \sigma_{\text{cl}}, v_{\text{cl},\infty}, \log n_{\text{HI,ICM}}) = (0.05, 18.5, 80, 500, -7.0)$. *Second from left:* Model I, in which more clumps are placed at large radii so that the number density of the clumps $n_{\text{cl}}(r) \simeq \text{constant}$. *Third from left:* Model II, in which the clump radial velocity is set to be tangential, so that the projected component of the clump outflow velocity along the traveling direction is no longer preferentially small for photons that escape at high impact parameters. *Right:* Model III, in which the number density of the ICM is increased by a factor of 20 in the outer 60% of the halo radius. In each of the three test models, the change in the model configuration offsets the corresponding spatial variation of the Ly α spectral morphology (i.e., peak separation, peak flux ratio and trough flux fraction), hence supporting our explanation.

matching the observed asymmetric Ly α profiles in the high outflow velocity regime ($v_{\text{cl,max}} \gtrsim 400 - 600 \text{ km s}^{-1}$).

In our sample, consistency (accounting for uncertainties) between the clump outflow velocities inferred from Ly α and metal absorption lines is achieved in 8 / 12 objects.¹⁴ Such a high success rate demonstrates the feasibility of matching both the observed Ly α and metal absorption line profiles simultaneously with one clump radial velocity profile. Among the four inconsistent cases, two (Q0207-BX87 and Q2343-BX418) have relatively irregular and noisy absorption line profiles that yield a broad range of velocities, whereas in the other two cases (Q0142-BX165 and Q1700-BX729), the inconsistency may come from the unusual asymmetry of either their Ly α halo or stellar continuum: Chen et al. (2021) found that Q0142-BX165 is a significant outlier that has particularly asymmetric Ly α emission as a function of azimuthal angle, whereas Q1700-BX729 is one of the 5 galaxies in their sample of 40 that requires more than one source for a successful Sérsic profile fit to its stellar continuum. We also note that exact matches between the Ly α and absorption-line-inferred outflow velocities are not necessarily expected because the transitions probe somewhat different gas: the absorption lines are purely a line-of-sight measurement that probes the gas only on the near side of the halo, while the Ly α results incorporate gas on the far side of the galaxy and at large impact parameters that is not seen in absorption. An exact match between the velocities would therefore be seen only in the case of perfect angular symmetry.

The best-fit radial velocity profile of the clumps in the multiphase, clumpy model typically exhibits a rapid acceleration phase to $v_{\text{cl}} = v_{\text{cl,max}}$ within $1 \lesssim \frac{r}{r_{\text{min}}} \lesssim 10$ followed by a gradual deceleration¹⁵ (or $v_{\text{cl}} \simeq \text{constant}$) phase at $\frac{r}{r_{\text{min}}} \gtrsim 10$. The decline in the outflow velocity and possible transition to an inflow are physically expected due to the increasing importance of gravitational deceleration at large radii, and have been explored in previous works (e.g., Chen et al. 2020); however, the exact location of the transition is model-dependent and may need additional observational constraints.

We also note that there is a significant velocity difference between the outflowing cool clumps and the static hot ICM in the best-fit models, which is at odds with

¹⁴We define two velocity profiles as being consistent if they have a non-negligible overlap at $r > r_{\text{min}}$.

¹⁵Note, however, that such a deceleration phase is not preferred by the absorption line modeling as it will break the one-to-one relation between r and v_{cl} and yield a pathological absorption line profile $I(v)$.

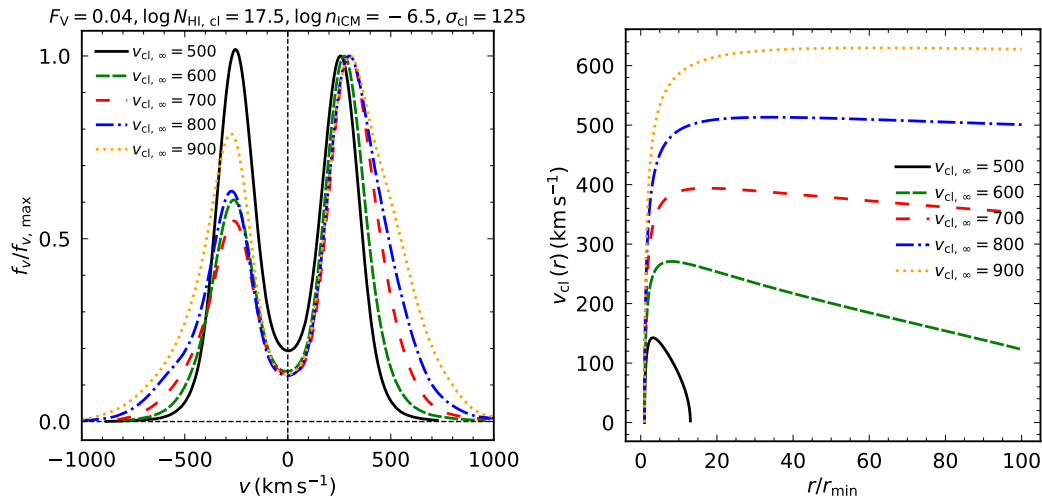


Figure 6.9: **Examples of Ly α model spectra with different clump outflow velocities showing the pattern in the change of the blue-to-red peak flux ratio.** Five models with $(F_V, \log N_{\text{HI, cl}}, \log n_{\text{ICM}}, \sigma_{\text{cl}}) = (0.04, 17.5, -6.5, 125)$ and $v_{\text{cl}, \infty} = (500, 600, 700, 800, 900)$ are shown with different colors and linestyles. *Left*: spatially integrated Ly α model spectra with different $v_{\text{cl}, \infty}$ values. As $v_{\text{cl}, \infty}$ increases, the average clump radial outflow velocity increases, and the blue-to-red peak flux ratio first decreases (comparing the black and green curves) and then increases (comparing the red, blue and orange curves). For visual convenience, we have normalized all the model spectra so that the maximum flux density of the red peak is one. *Right*: The corresponding clump radial velocity profiles for different $v_{\text{cl}, \infty}$. Note that $v_{\text{cl}}(r)$ and $v_{\text{cl}, \infty}$ are positively correlated, but $v_{\text{cl}}(r)$ is always smaller than (typically by several hundred km s^{-1}) $v_{\text{cl}, \infty}$ due to the effect of gravitational deceleration.

the traditional “hot wind entrains (and co-outflows with) the cold gas” paradigm (see, e.g., Gronke et al. 2018; Gronke et al. 2020, and references therein). It is possible, however, that the interaction between the hot phase and the Ly α photons is dominated by the decelerated, semi-static hot gas, as suggested by the deep troughs at line center in the observed Ly α profiles. A larger sample with more diverse Ly α morphologies will be helpful in assessing the impact of an outflowing hot gas component in the future.

We next turn to the other best-fit parameters of the models. For the Ly α modeling, the best-fit clump volume filling factors (F_V) range from 0.06 to 0.16 (corresponding to $\sim 5 - 10$ clumps on average per line-of-sight¹⁶), and the best-fit clump column

¹⁶Note that the number of clumps per line-of-sight and the associated gas covering fraction both decrease with r due to the increase of the halo volume at large r (cf. Figures 15 and 16 of Rudie et al. 2012).

densities ($N_{\text{HI,cl}}$) range from $\sim 10^{17.6}$ to $10^{18.8} \text{ cm}^{-2}$. The total H I column densities ($N_{\text{HI,total}} \simeq \frac{4}{3} f_{\text{cl}} N_{\text{HI,cl}} = (r_{\text{h}}/r_{\text{cl}}) F_{\text{V}} N_{\text{HI,cl}}$, Gronke et al. 2016b) of the best-fit models range from $\sim 10^{18.5}$ to $10^{19.9} \text{ cm}^{-2}$. Here $N_{\text{HI,total}}$ represents the inferred total H I column density of the modeled halo that a Ly α photon typically interacts with, either via scattering or free-streaming; the scattered, out-of-resonance Ly α photons may stream through the high-velocity, outflowing clumps without scattering (Gronke, 2017).

The residual H I column densities of the hot, diffuse ICM ($N_{\text{HI,ICM}} \simeq n_{\text{HI,ICM}} r_{\text{h}}$) range from $\sim 10^{15}$ to 10^{16} cm^{-2} . Such column densities are much smaller than those within the clumps, but are necessary to produce the absorption trough at line center, and may serve as optically thin channels for LyC escape along lines of sight that have relatively few H I clumps. The best-fit systemic redshifts of the Ly α sources are mostly consistent with the systemic redshifts determined from nebular emission lines ($|\Delta v| < 50 \text{ km s}^{-1}$ for 8 / 12 objects). The best-fit clump velocity dispersions (σ_{cl}) are all smaller than 150 km s^{-1} and span a similar range to the observed nebular emission line widths ($\sim 50 - 120 \text{ km s}^{-1}$). We compared the best-fit σ_{cl} values with the MOSFIRE *H*-band ([O III] and H β) and *K*-band (H α) nebular emission line widths (corrected for instrumental LSF), but did not find any significant correlation.

For the metal absorption line modeling, the best-fit clump velocity dispersions¹⁷ are all smaller than 75 km s^{-1} , suggesting that the gravitational deceleration only plays a minor role compared to the acceleration forces. The clump outflow velocities are high, mostly $\gtrsim 500 \text{ km s}^{-1}$, and generally correspond to the velocity where the blue side of the absorption line profile meets the continuum. The maximum clump covering fractions $f_{\text{c,max}}$ range from ~ 0.2 to 0.9 , depending on the minimum flux density of the absorption line profile. The power-law indices of the clump covering fraction function (γ) range from ~ 1.1 to 1.7 , corresponding to a mass-conserving-like (or more gradual) decrease in the number density of the clumps. A γ smaller than 2 may suggest that the clumps expand as they move outwards (e.g., due to the decrease of thermal/radiation pressure at large radii), because if the clumps are uniformly distributed radially and their sizes remain constant at different radii, γ will be exactly 2 due to the geometric volume increase at large radii ($dV \propto 4\pi r^2 dr$).

We have also checked if any correlations exist between the best-fit clump outflow velocities and the host galaxy properties such as stellar mass and SFR, as these

¹⁷Note that here the velocity dispersions are determined independently from the Ly α modeling. In fact, they are not very well constrained (i.e., flat posterior) by the absorption line data, as the acceleration term is preferred to be dominant.

are expected to be correlated due to the causal relation between stellar feedback and galactic outflows (e.g., Martin 2005; Rupke et al. 2005; Weiner et al. 2009; Chen et al. 2010; Martin et al. 2012; Rubin et al. 2014; Chisholm et al. 2015; Heckman et al. 2015; Trainor et al. 2015). Specifically, we tested for correlations between the *actual* maximum clump radial velocities $v_{\text{cl,max}}$ inferred from the Ly α and absorption line modeling vs. the stellar masses, SFRs and sSFRs of the host galaxies. We find that all three correlations are insignificant and have considerable scatter. Such a null result is unsurprising, however, as our sample is intentionally restricted to low-mass galaxies with high SFR and sSFR values and therefore has a limited dynamic range by design. We will revisit these correlations with larger and more well-rounded samples in future work.

Advantages of Spatially Resolved Ly α Modeling

In this section, we demonstrate the advantages of spatially resolved Ly α modeling by comparing it to the spatially integrated Ly α modeling that has typically been carried out in previous works. Assuming that for a Ly α -emitting source of interest, only a spatially integrated Ly α spectrum within a certain aperture can be obtained (e.g., due to the unavailability of IFU observations), we consider the following two scenarios: (1) the spatially integrated spectrum corresponds to the Ly α emission from only the central region, typical of observations using a slit or other small aperture (the spectra we extracted in Section 6.3 and showed in Figure 6.1 belong to this category); (2) the spatially integrated spectrum is extracted from a larger aperture that also includes the Ly α emission from a significant portion of the extended halo. For exploratory purposes, we model scenario (1) with spatially integrated multiphase, clumpy models in which all the emitted photons are included in the emergent spectra, assuming that we are completely unaware of any spatial variation of the Ly α emission. We model scenario (2) with spatially integrated models that include the photons with $b/r_h \lesssim 75\%$, assuming that we are aware that the data only represent part of the extended halo and should be compared to a corresponding fraction of the modeled halo. This is equivalent to merging the 3-bin spectra for both the data and the models in the spatially resolved modeling routine that we described in Section 6.5.

For scenario (1), we find that the best-fit clump outflow kinematics (namely the σ_{cl} and $v_{\text{cl},\infty}$ values) are similar in both the spatially integrated and resolved modeling, but the required clump volume filling factors (and hence the covering factor)

and ICM column densities are higher, on average, in the spatially integrated Ly α modeling. This is mainly because in the observed spatially integrated spectra, the trough depth at line center is similar to that of the innermost binned spectra used in the spatially resolved modeling, as they correspond to similar regions of the halos. In contrast, the trough depth at the line center of a spatially integrated Ly α model spectrum lies between that of its corresponding innermost and outermost binned model spectra due to the radial variation of the profile (see Section 6.5). Therefore, larger clump volume filling factors (which contribute to the total H I column densities) and ICM column densities are required to reproduce the deep troughs in the spatially integrated Ly α profiles.

A quantitative comparison of the best-fit total H I column densities from the clumps and the H I densities in the ICM for the spatially resolved and scenario (1) models is shown in Figure 6.10, with the darker and fainter points indicating the resolved and spatially integrated models from scenario (1) respectively. We plot the total N_{HI} and $n_{\text{HI,ICM}}$ vs. properties measured from the integrated spectra, and discuss the comparison further in Section 6.6 below. We find that values of total N_{HI} from spatially integrated modeling of the central region are larger on average by a factor of 1.5, while $n_{\text{HI,ICM}}$ is larger by at least a factor of 1.9, and likely significantly more because more than half of the sample requires values of $n_{\text{HI,ICM}}$ higher than the maximum value allowed by the model grid. The overestimation of $n_{\text{HI,ICM}}$ in the spatially integrated models manifests as an overestimation of the depth of the trough between the peaks, which is due to the omission of spatial information on the outer halo.

For scenario (2), we find that the best-fit parameters of the spatially resolved and integrated modeling are fully consistent with each other. This result is probably unsurprising, as a reasonable match between all three bins of model and data should still hold if the bins are merged for both the models and the data. The tightness of the constraints on the model parameters is also similar in both cases due to the similar average S/N ratio of the observational data. However, we stress that this result does not indicate that the spatially resolved modeling is no longer necessary, as we would not have found that the radial trends of peak separation, peak ratio, trough flux ratio, and SB can all be reasonably well-matched by the same best-fit model if we had not separated the photons into different spatial bins and modeled the Ly α profiles in a spatially resolved manner.

In short, our experiments in this section suggest that although spatially integrated

modeling may be used to crudely extract certain global properties of the CGM, it tends to either lose information about the outer regions of the halos and overestimate the neutral hydrogen content encountered by Ly α photons, or fail to account for the radial variation of the Ly α morphological properties. In comparison, spatially resolved Ly α modeling has the advantage of fully leveraging the spatial variation in the Ly α halo as observed by integral field unit spectrographs such as KCWI and quantifying the corresponding spatial changes of the physical parameters of the CGM. The overall good match in radial trends between the spatially resolved data and models provides a reassuring check on the validity of the multiphase, clumpy model.

Caveats

There are several important caveats to this work. First, we did not include the effect of dust (but note that the dust extinction of our sample is typically small), which means that all of the emitted Ly α photons will eventually escape from the simulation region and contribute to the emergent model spectra. Considering that the actual Ly α escape fraction is always smaller than one, we essentially assumed that the observed frequency distribution of Ly α photons is representative of the Ly α photons that escape in all directions. The validity of such an assumption requires further scrutiny.

Second, we used spherically symmetric RT models to model the angularly averaged Ly α profiles of asymmetric halos, so the results should be interpreted as average parameters within the modeled region. We have also experimented with modeling the spatially resolved Ly α profiles along the directions of maximum and minimum peak ratio and peak separation gradients (see Section 6.4), but did not find any significant dependence of the model parameters on these higher order spatial variations. This is mainly because the best-fit model is primarily constrained by the spectra of the two innermost bins, which have higher S/N, whereas the spectrum of the outermost bin may contribute strongly to the measured gradients but does not put strong constraints on the model parameters. Development of anisotropic RT models may shed light on this problem, as future observational facilities will likely improve the S/N of the spectra of the outer halo, and eventually the higher-order spatial variations should be able to put extra constraints on the model parameters.

Last but not least, some of the assumptions in our models are inevitably oversimplified. For example, we assumed a two-component model with temperatures

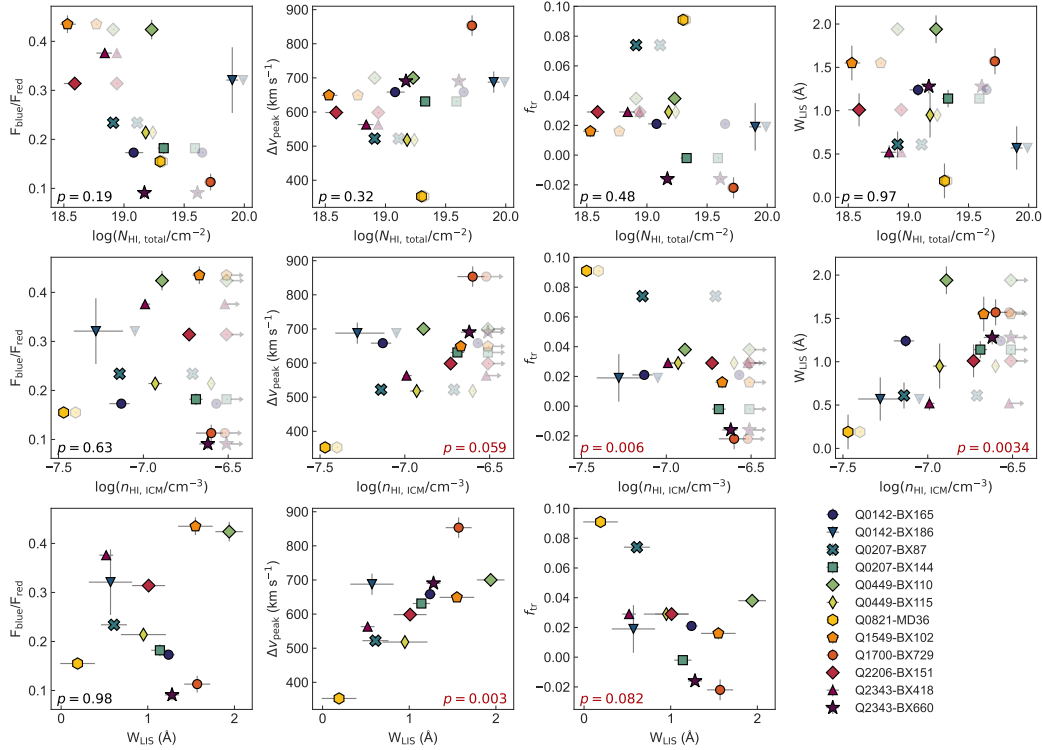


Figure 6.10: **Comparison of results from the radiative transfer models with properties of the spatially integrated spectra of the central regions of the galaxies shown in Figure 6.1.** *Top row, left to right:* the Ly α blue-to-red flux ratio, peak separation, trough flux fraction f_{tr} and mean low-ionization absorption line equivalent width vs. the total HI column density. *Middle row:* the same four spectral quantities vs. the residual HI density in the ICM. *Bottom row, left to right:* Ly α blue-to-red flux ratio, peak separation, and f_{tr} vs. mean low-ionization absorption line equivalent width. In the top two rows the darker points show the results of our best-fit spatially resolved modeling, while the fainter points show the results of modeling the single, spatially integrated line profiles. The lower corner of each panel gives the p -value resulting from a Spearman correlation test using the spatially resolved models only. Values with $p < 0.1$ are highlighted in red.

of 10^4 K and 10^6 K, whereas in reality HI absorbers at intermediate temperatures should exist (Rudie et al., 2019). The HI column densities and the physical sizes of the clumps are also simplistically assumed to be constant in the multiphase, clumpy model. Moreover, the actual motion of the clumps in the CGM may be more complicated than the idealistic kinematic model we employed (see, e.g., Fielding et al. 2022). We plan to upgrade our models in future work.

6.6 Summary and Discussion

We have presented KCWI integral field spectroscopy and radiative transfer modeling of spatially extended Ly α emission in a sample of 12 relatively low mass ($M_\star \sim 10^9 M_\odot$), extreme emission line galaxies at median redshift $z = 2.3$. As described in Section 6.2, the targets are primarily selected based on nebular emission line ratios indicating high ionization and low metallicity, and all are previously known Ly α -emitters. The sample galaxies have specific star formation rates ~ 4 times larger than that of their $z \sim 2$ parent sample, and may more closely resemble galaxies at earlier epochs of cosmic history. Our primary results are as follows:

1. All of the galaxies show strong, double-peaked Ly α emission (see Section 6.3 and Figure 6.1) and spatially extended Ly α halos, with luminosities ranging from 3×10^{42} to 3×10^{43} erg s $^{-1}$ and radii between 16 and 30 kpc (Figure 6.2).
2. We construct spatially averaged Ly α profiles, in order to identify general trends and measure the profiles to larger radii. We first construct azimuthally averaged spectra binned as a function of radius (Section 6.4 and Figure 6.3), and again measure the peak ratio and separation in each annular region as well as f_{tr} , the fraction of total flux escaping within ± 100 km s $^{-1}$ of the trough between the peaks (Figure 6.4). The blue-to-red flux ratio increases consistently with radius for most objects in the sample, with a typical central value of ~ 0.2 ; all objects that can be measured at a radius $\gtrsim 16$ kpc have peak flux ratios > 0.6 at that radius. f_{tr} also increases with radius for most of the sample. Trends with peak separation are more complex, but the typical central peak separation is ~ 600 km s $^{-1}$, with a moderate decrease toward the outer halo.
3. Because the annular binned spectra wash out the significant azimuthal variations in the line profiles, we also construct binned spectra of 60° angular

regions designed to maximize the gradients in peak ratio and separation from the center to the outer halo, using seven of the brightest galaxies in the sample (Section 6.4 and Figure 6.5). These spectra show that all of the halos have sightlines for which the peak ratio increases (typically from ~ 0.2 to ~ 1) or the peak separation decreases (typically from $\sim 600 - 700$ to $\sim 300 - 400$ km s^{-1}) with radius. In all cases, however, the regions of maximum peak ratio increase and maximum peak separation decrease do not overlap. We also construct spectra designed to minimize the gradients in peak ratio and separation, finding that most halos also have regions for which the changes in peak ratio and separation with radius are relatively small.

4. Using a new suite of $\text{Ly}\alpha$ radiative transfer simulations, we model the spatially resolved $\text{Ly}\alpha$ profiles in three radial bins with multiphase, clumpy models with radially varying outflow velocities (Section 6.5). These models are broadly successful in reproducing the observed line profiles, as well as the radial trends of peak flux ratio, peak separation, and trough flux fraction (Figures 6.6 and 6.11–6.16). The clumps reach a typical maximum velocity of ~ 500 km s^{-1} and have HI column densities of $\sim 10^{17.6}$ to $10^{18.8}$ cm^{-2} , while the total N_{HI} of the best-fit models ranges from $\sim 10^{18.5}$ to $10^{19.9}$ cm^{-2} . The clumps are embedded in a hot inter-clump medium with residual $N_{\text{HI,ICM}} \sim 10^{15} - 10^{16}$ cm^{-2} . Best-fit parameters of the models are given in Table 6.3.
5. We find that the trend in $\text{Ly}\alpha$ peak separation with radius is primarily governed by the HI column density, as photons that escape at larger radii are able to do so with a smaller velocity shift because they experience lower HI column densities from the clumps before they escape due to the decrease in clump covering fraction with radius. The $\text{Ly}\alpha$ peak ratio depends on the line-of-sight velocity, with the result that the variation in peak ratio with radius is largely a geometric effect as the projected component of the outflow velocity along the line of sight decreases with increasing impact parameter (Figure 6.7). The depth of the trough (or the trough flux fraction, f_{tr}) between the two peaks primarily depends on the residual neutral HI density of the ICM. We show the results of experiments designed to test these conclusions in Figure 6.8, and further explore the relationship between outflow velocity and peak ratio in Figure 6.9.

6. We self-consistently model the mean low-ionization absorption line profile of each object, employing the same radially varying velocity model used for the Ly α emission and a radially decreasing gas covering fraction (Section 6.5 and Figures 6.6 and 6.11–6.16). Typical clump maximum outflow velocities inferred from the absorption line profiles are $\gtrsim 500 \text{ km s}^{-1}$, in broad agreement with the velocities inferred from Ly α ; exact matches may not be expected because the down-the-barrel UV spectra and the radially binned Ly α emission are not probing entirely the same regions of the halos. This agreement alleviates a long-standing discrepancy between outflow velocities inferred from Ly α shell models and the UV absorption lines.
7. Finally, we compare the results of the spatially resolved Ly α modeling with those obtained from applying the same model to single, spatially integrated Ly α profiles, using both a small aperture capturing only the brightest region (scenario 1) and a larger aperture encompassing most of the halo (scenario 2). We find that modeling the integrated central profile (scenario 1) results in higher inferred values for both the total H I column density and the neutral component of the ICM, largely because the spatially integrated modeling does not account for the decrease in the depth of the trough between the peaks at larger radii; this decrease in depth reflects the lower neutral hydrogen content experienced by photons that escape from larger radii and indicates that some photons may escape at line center in the outer halo. The best-fit parameters obtained from modeling a larger aperture in scenario (2) are consistent with those from the spatially resolved modeling, but fail to capture the trends in the Ly α profile with radius and the physical insights these variations provide.

Our observations and modeling suggest a self-consistent physical picture of the CGM of this sample of $z \sim 2$ star-forming galaxies: a multiphase, clumpy medium in which cool ($\sim 10^4 \text{ K}$), outflowing gas clumps are embedded in a hot ($\sim 10^6 \text{ K}$), highly ionized, diffuse medium with low-density residual H I. The clumps typically have H I column densities of $\sim 10^{18} \text{ cm}^{-2}$ and provide a total column density of $\sim 10^{19} \text{ cm}^{-2}$, and the Ly α photons “solve the maze” by being resonantly scattered by and free-streaming through the clumps until they escape. The cool clumps also have random velocity dispersions of $\sim 100 \text{ km s}^{-1}$, and are accelerated to high radial outflow velocities of $\gtrsim 500 \text{ km s}^{-1}$ at large impact parameters, which give rise to both the asymmetric Ly α profiles and broad low-ionization metal absorption lines. The hot ICM is nearly static and has a low total H I column density ($\sim 10^{15} -$

10^{16} cm^{-2}), but is essential to shaping the emergent double-peaked Ly α profiles as it provides additional scattering that produces the absorption trough at line center.

Central Ly α Profiles and LyC Escape

With this physical model of the CGM in mind, we revisit the spatially integrated central Ly α profiles shown in Figure 6.1 and assess how (or if) quantities measured from these profiles relate to the properties of the CGM inferred from the spatially resolved modeling; such a comparison may aid in the interpretation of Ly α profiles when information from the outer halo is unavailable. In Figure 6.10 we compare the total N_{HI} and $n_{\text{HI,ICM}}$ from the models with the peak ratio, peak separation and trough flux fraction f_{tr} and the mean low-ionization absorption equivalent width W_{LIS} measured from the spatially integrated one-dimensional spectra, as well as the equivalent width vs. the Ly α profile properties in the bottom row. Darker points indicate the results of the spatially resolved Ly α modeling, while the fainter points are the result of modeling the central spatially integrated profiles (scenario 1 in Section 6.5). The lower corner of each panel gives the p -value resulting from a Spearman correlation test, with values of $p < 0.1$ highlighted in red. While none of the correlations are formally ($> 3\sigma$) significant, the strongest trends (~ 2.75 – 3σ) relate to the HI density in the ICM, which tends to be higher for larger peak separations, lower f_{tr} , and larger low-ionization equivalent width. We also find that smaller peak separations and higher values of f_{tr} tend to be associated with lower W_{LIS} . All correlations involving the total N_{HI} or the blue-to-red peak ratio have significance levels $\leq 1.3\sigma$.

These results broadly support our conclusion in Section 6.5 that the trough flux fraction can be understood as an indication of low N_{HI} in the ICM. Note, however, that the potential relationship between the central f_{tr} and modeled $n_{\text{HI,ICM}}$ relies on the results inferred from spatially resolved modeling of the extended halo; modeling the central profiles alone results in significantly higher values of $n_{\text{HI,ICM}}$, half of which are higher than the upper limit of the current model grid.

Previous work has suggested that significant Ly α flux at the systemic velocity may be an indication of LyC escape (e.g., Rivera-Thorsen et al. 2019; Naidu et al. 2022); if ionizing photons emerge through optically thin channels between clumps, then the transparency of the ICM is a key property governing LyC escape. A low covering fraction of neutral gas and significant residual intensity in the low-ionization absorption lines are also likely related to LyC escape (e.g., Heckman et al. 2011;

Reddy et al. 2016; Chisholm et al. 2018), so the potential relationship between $n_{\text{HI,ICM}}$ and W_{LIS} is also unsurprising.

Given the results of the spatially resolved Ly α modeling, we expect the peak separation to be most closely related to the total H I column density; however, there is no significant correlation between the central peak separation and $N_{\text{HI,total}}$ from the spatially resolved models. This lack of correlation may be due to the small sample size and the lack of dynamic range in peak separation, as 10 of the 12 objects in the sample have central peak separations between 500 and 700 km s $^{-1}$. These peak separations are also larger than the $\sim 200\text{--}500$ km s $^{-1}$ range over which Δv_{peak} is observed to correlate with the LyC escape fraction in local galaxies (Izotov et al., 2021). We do observe potential relationships between the peak separation and both $n_{\text{HI,ICM}}$ and W_{LIS} ; these may be due to the strong correlation between the peak separation and f_{tr} . Modeling of a larger sample with a wider range of central peak separations will clarify the relationship between Δv_{peak} and $N_{\text{HI,total}}$.

There are no observations covering wavelengths below the Lyman break for the galaxies in our sample, so we have no constraints on their LyC emission. However, based on the criteria discussed above involving the peak separation or central flux fraction, we would not expect most of the galaxies in the sample to have significant LyC emission. Possible exceptions are the two most likely LyC candidates, Q0821-MD36 and Q0207-BX87, which have the highest trough flux fractions $f_{\text{tr}} \sim 0.1$, relatively narrow peak separations, and the second and third highest Ly α equivalent widths in the sample (after Q2206-BX151).

Future Prospects

Although the inclusion of spatially resolved information increases the power of the radiative transfer modeling, we are still limited by the assumption of symmetry: we fit radially binned spectra with spherically symmetric models, but as we have shown, real halos show significant azimuthal variation (Figure 6.5). However, insights obtained from the modeling can aid in the interpretation of the variations across a given halo, at least qualitatively. Because the increase in blue-to-red peak ratio with radius is largely a geometric effect due to the decrease in the line-of-sight component of the outflow velocity, portions of the halos for which there is little change in the peak ratio with radius likely correspond to regions for which the velocity still has a significant component along the observer’s line of sight even in the outskirts of the halo. More broadly, azimuthal variations in the peak ratio

are indicative of velocity asymmetries and non-radial gas motions at large radii. Similarly, variations in the peak separation in the outer halo suggest varying HI column densities in the CGM, with regions for which Δv_{peak} does not decrease with radius likely having higher N_{HI} . Future modeling that does not assume azimuthal symmetry is needed in order to quantify these conclusions.

Finally, while the objects in this sample are likely to be more typical of galaxies at higher redshifts than of the general $z \sim 2$ population, extending the analysis of double-peaked Ly α profiles to more distant galaxies will be challenging. For example, the median redshift of the MUSE sample studied by Leclercq et al. (2020) is $z = 3.8$, while that of our KCWI sample is $z = 2.3$, and this difference in redshift results in a median decrease in surface brightness of a factor of 4.5 for the higher redshift sample. In addition, the blue-to-red Ly α peak ratio decreases with increasing redshift due to Ly α absorption by the IGM (Laursen et al., 2011; Hayes et al., 2021), and the mean IGM transmission of Ly α drops strongly from $\gtrsim 80\%$ at $z \approx 2.3$ to $\sim 45\%$ at $z \approx 3.8$ (Rudie et al., 2013; Inoue et al., 2014). The combination of these effects results in a typical factor of $\gtrsim 6$ decrease in the surface brightness of the blue peak at $z = 3.8$ relative to $z = 2.3$. These effects will, of course, be even more significant at $z > 4$.

Given the power of the double-peaked Ly α profile for constraining the kinematics and column density of the CGM, we therefore expect that integral field observations of galaxies at $z \sim 2$ will only grow in importance. As new observations from the James Webb Space Telescope precisely measure the properties of galaxies at both $z \sim 2$ and in the reionization era, it will be increasingly possible to robustly identify $z \sim 2$ analogs of reionization-era sources and quantify their CGM via spatially extended Ly α emission.

Acknowledgements

The authors thank Crystal Martin, Peng Oh and Tim Heckman for helpful discussions. D.K.E. is supported by the US National Science Foundation (NSF) through Astronomy and Astrophysics grant AST-1909198. C.C.S, Z.L. and Y.C. are supported in part by NSF grant AST-2009278. R.F.T. is a Cottrell Scholar receiving support from the Research Corporation for Science Advancement under grant ID 28289 and from the Pittsburgh Foundation under grant ID UN2021-121482. Some data presented herein were obtained at the W. M. Keck Observatory from telescope time allocated to the National Aeronautics and Space Administration through the

agency’s scientific partnership with the California Institute of Technology and the University of California. The Observatory was made possible by the generous financial support of the W. M. Keck Foundation. The authors wish to recognize and acknowledge the very significant cultural role and reverence that the summit of Maunakea has always had within the indigenous Hawaiian community. We are most fortunate to have the opportunity to conduct observations from this mountain. D.K.E. acknowledges in Milwaukee that we are on traditional Potawatomi, Ho-Chunk and Menominee homeland along the southwest shores of Michigami, North America’s largest system of freshwater lakes, where the Milwaukee, Menominee and Kinnickinnic rivers meet and the people of Wisconsin’s sovereign Anishinaabe, Ho-Chunk, Menominee, Oneida and Mohican nations remain present.

6.7 Appendix

Modeling Results of the Full Sample

In Figures 6.11 to 6.16 below we present the results of $\text{Ly}\alpha$ and metal absorption line modeling for all objects except Q0207-BX144 (already shown in Figure 6.6). In each panel, the top row shows the best-fit RT models (red) to the spatially resolved $\text{Ly}\alpha$ spectra (black); the middle row and the first panel of the bottom row show a comparison between the radial trends of peak separation, peak flux ratio, trough flux fraction, and SB predicted by the best-fit models and measured from observations; and the rest of the bottom row shows the best-fit models (red) to the average metal absorption line profile (black), as well as a comparison of clump radial outflow velocity profiles inferred from $\text{Ly}\alpha$ emission and the average metal absorption line.

Posterior Distribution Example: Q0207-BX144

As an example of constraints on the model parameters, we present the posterior distribution of the spatially resolved $\text{Ly}\alpha$ modeling of Q0207-BX144 in Figure 6.17.

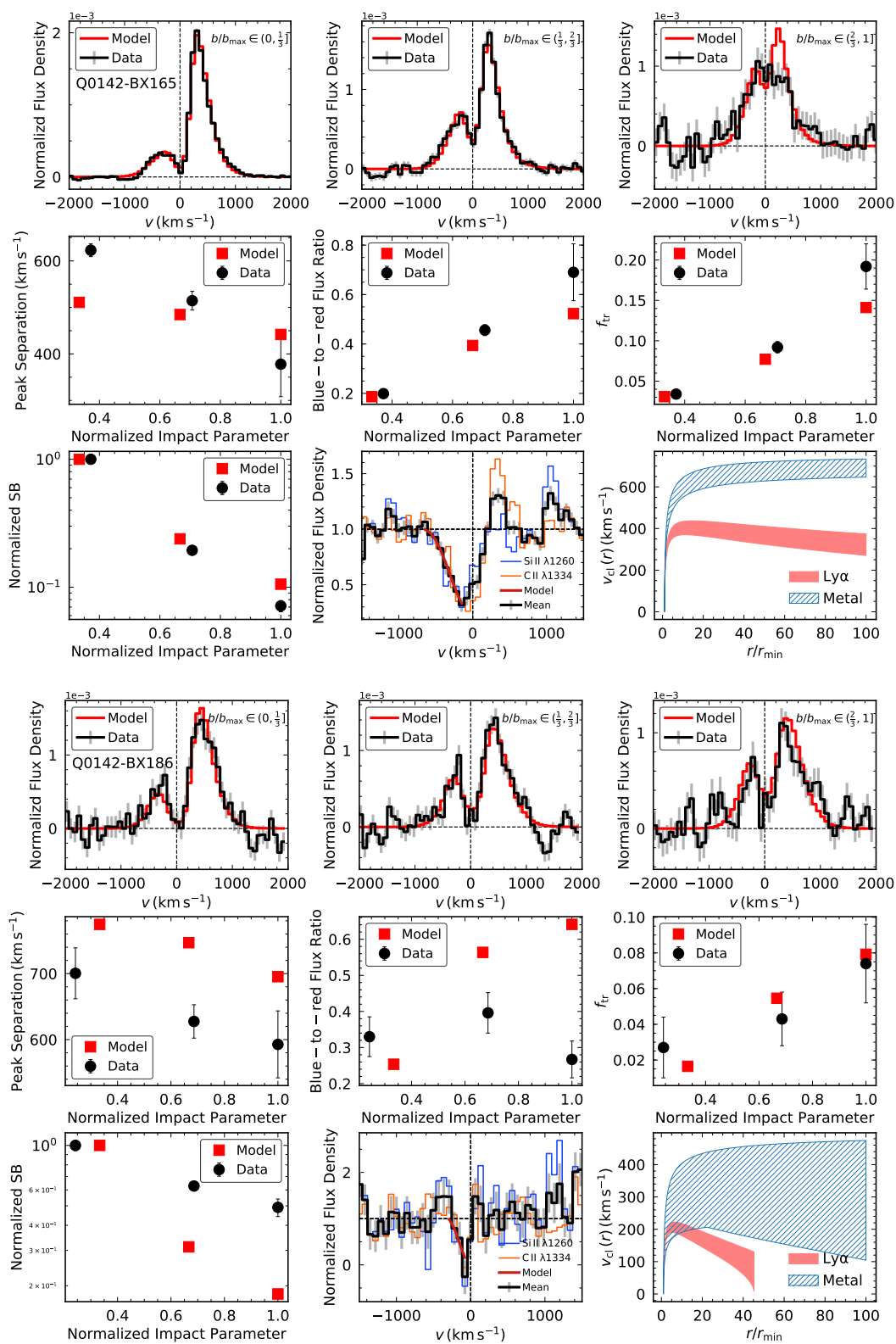


Figure 6.11: Same as Figure 6.6, but for Q0142-BX165 and Q0142-BX186.

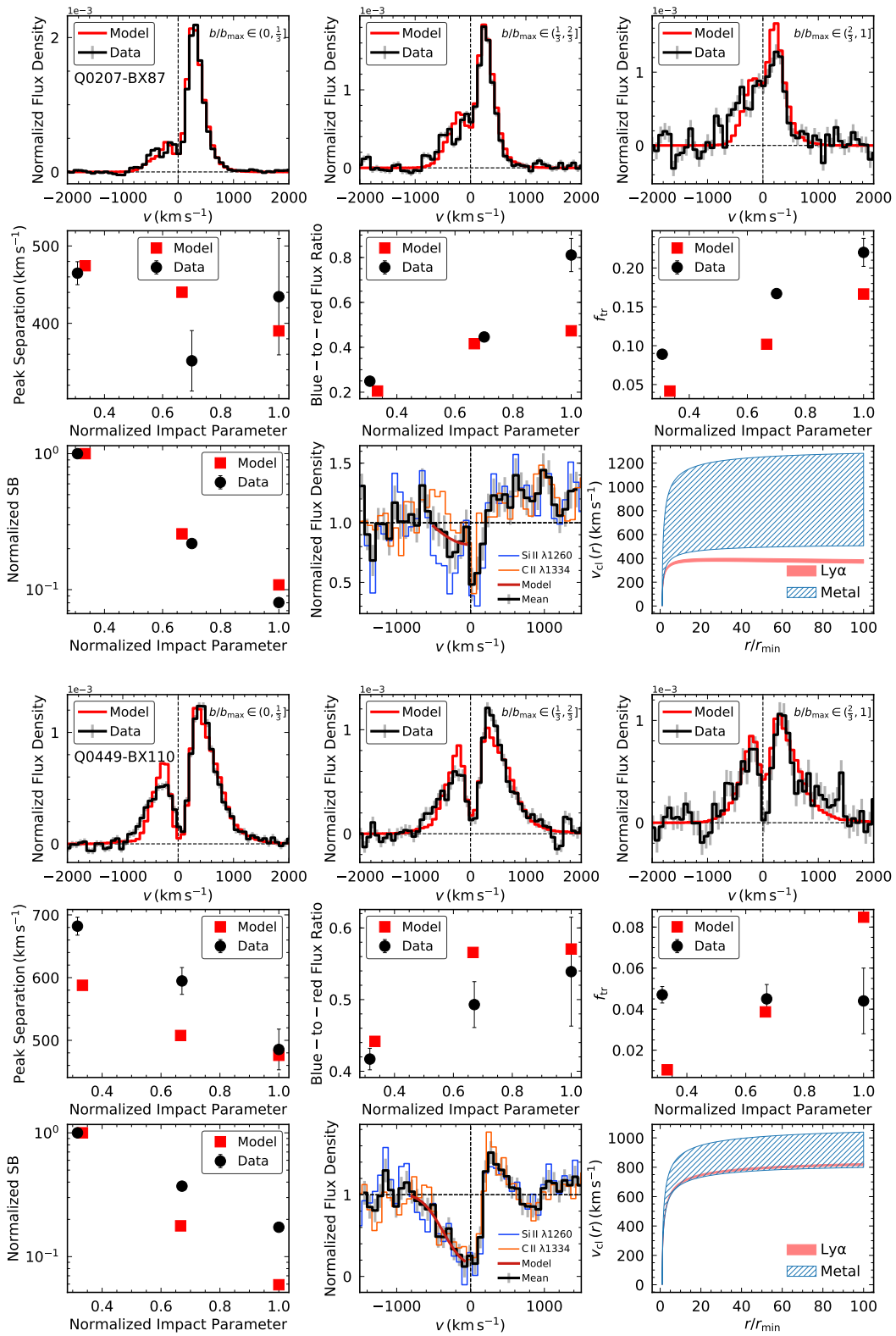


Figure 6.12: Same as Figure 6.6, but for Q0207-BX87 and Q0449-BX110.

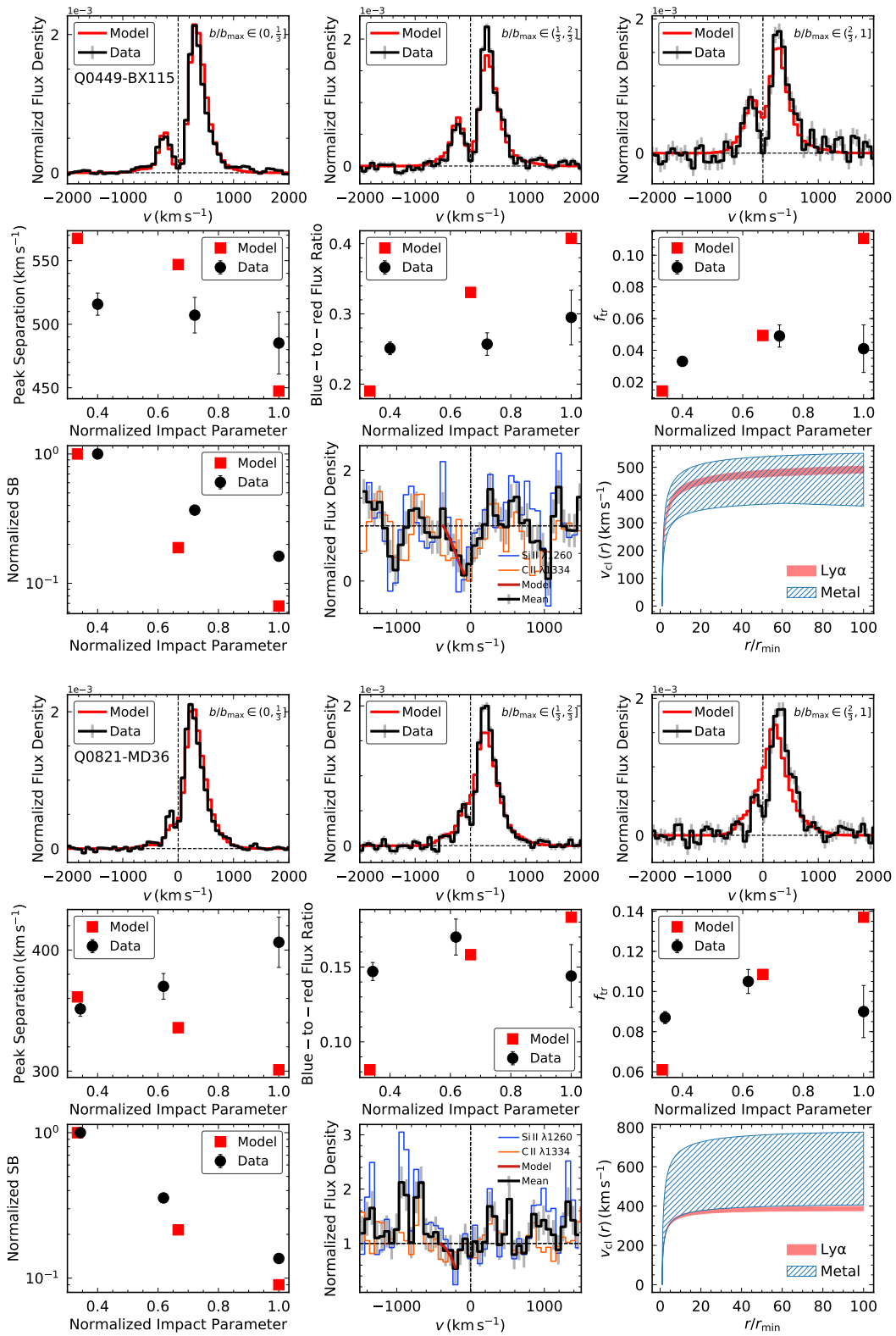


Figure 6.13: Same as Figure 6.6, but for Q0449-BX115 and Q0821-MD36.

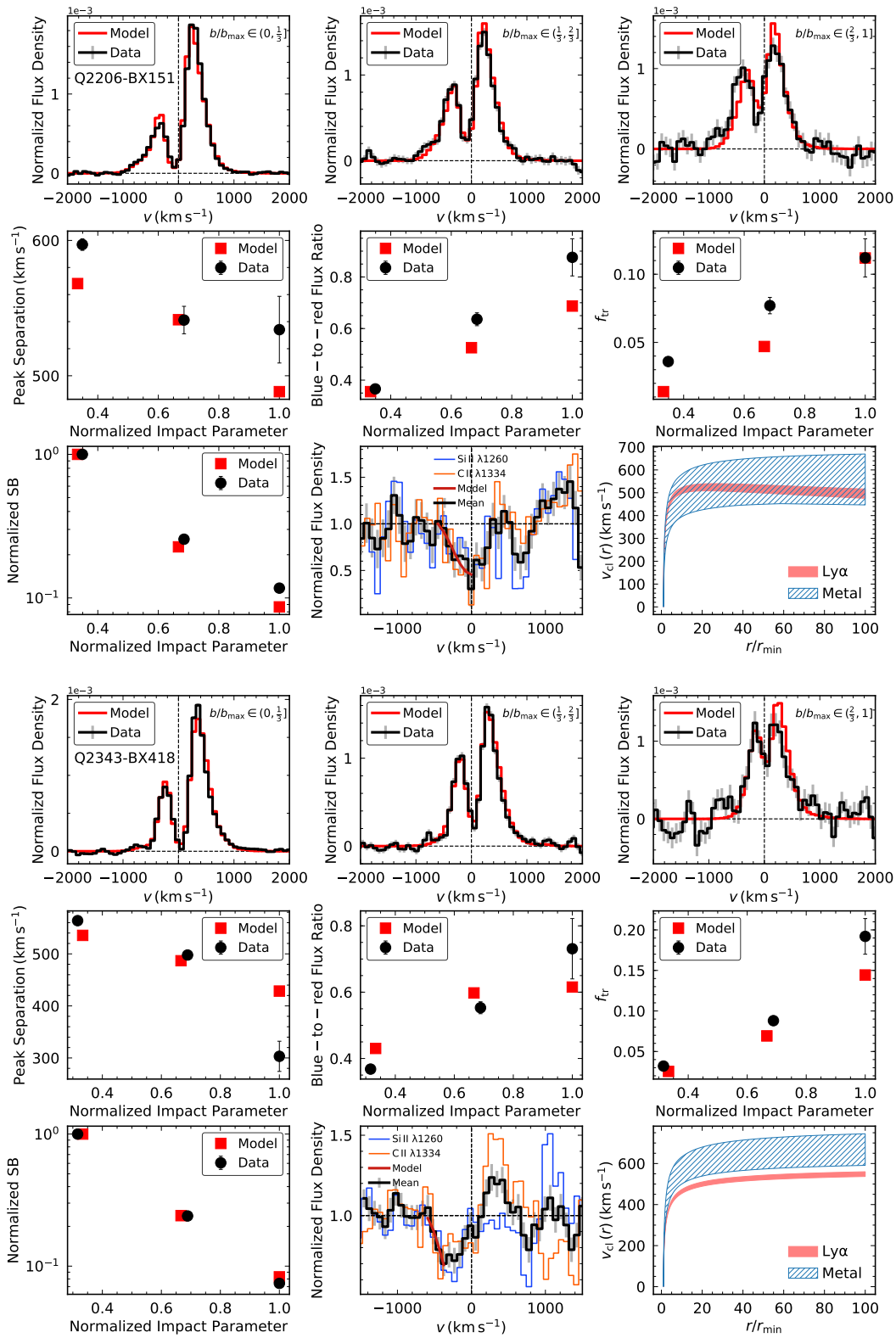


Figure 6.15: Same as Figure 6.6, but for Q2206-BX151 and Q2343-BX418.

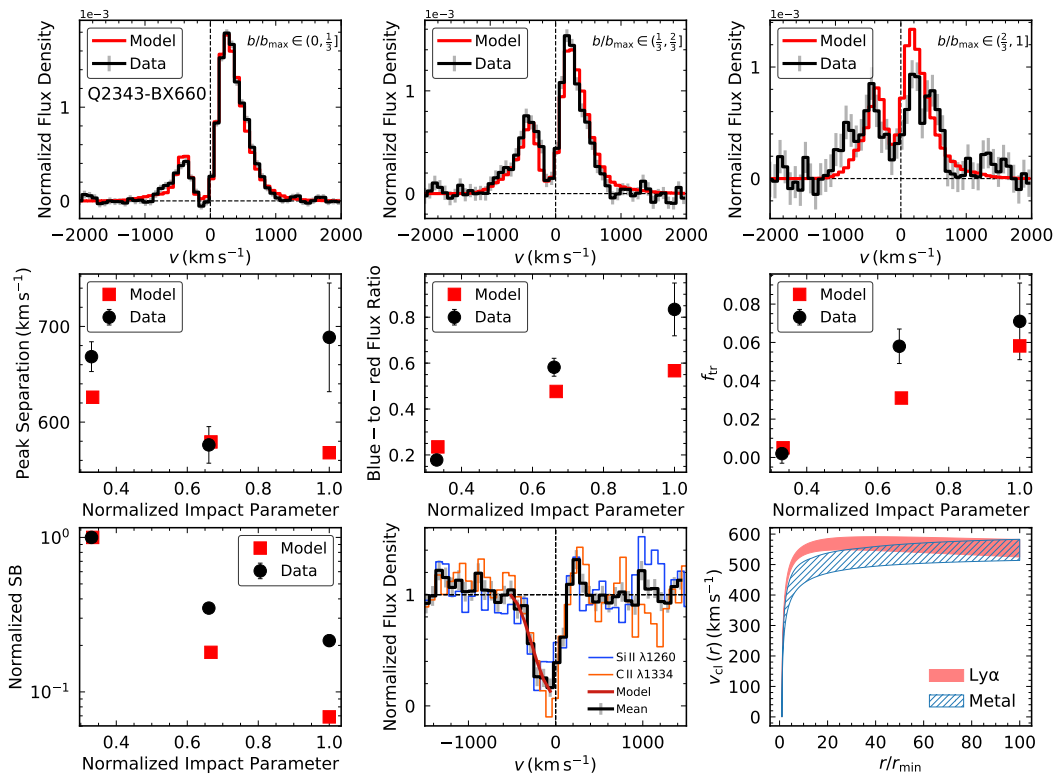


Figure 6.16: Same as Figure 6.6, but for Q2343-BX660.

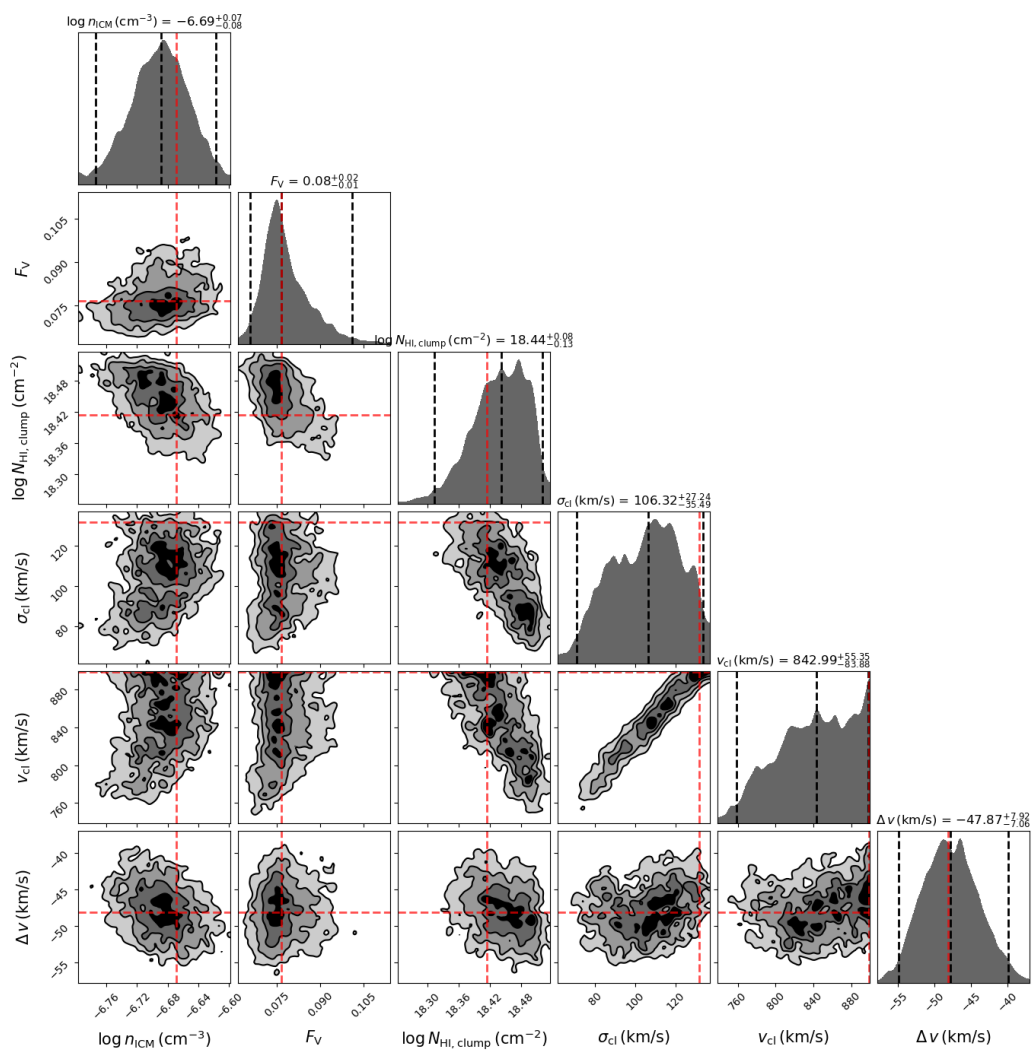


Figure 6.17: **Posterior distribution of spatially resolved modeling for Q0207-BX144.** The [2.5%, 50%, 97.5%] (i.e., 2- σ confidence intervals) quantiles of parameters are indicated by vertical black dashed lines, and the maximum likelihood point in the parameter space is indicated by vertical red dashed lines.

Chapter 7

ALPACA: A NEW SEMI-ANALYTIC MODEL FOR METAL ABSORPTION LINES EMERGING FROM CLUMPY GALACTIC ENVIRONMENTS

Li, Zhihui, Max Gronke, and Charles C. Steidel (Mar. 2024). “ALPACA: a new semi-analytical model for metal absorption lines emerging from clumpy galactic environments”. In: *MNRAS* 529.1, pp. 444–463. DOI: 10.1093/mnras/stae469. arXiv: 2306.11089 [astro-ph.GA].

7.1 Introduction

Metal absorption lines observed in the rest-frame ultraviolet (UV) encode abundant information about the physical properties of the gaseous matter in a galactic environment – from the interstellar medium (ISM; Tacconi et al. 2020) to the circumgalactic medium (CGM; Tumlinson et al. 2017; Faucher-Giguère et al. 2023) to the intergalactic medium (IGM; McQuinn 2016). Such absorption lines are typically produced via the transition of an atom or ion from the ground state to an excited state by absorbing the energetic UV continuum photons produced in star-forming regions. Depending on whether the ground state is further split into fine-structure levels, such transitions can be either resonant (e.g., Ly α and Mg II $\lambda\lambda$ 2796, 2803) or non-resonant (e.g., Si II λ 1260 and C II λ 1334), the latter of which is considered to have “fluorescent” channels through which the photons at the resonant wavelength can be emitted at a slightly lower energy.

A typical metal absorption line observed against a galaxy’s own starlight (namely “down-the-barrel”; DTB) is “sawtooth” shaped (e.g., Weiner et al. 2009; Rubin et al. 2010; Martin et al. 2012), although in reality it exhibits a wide variety of spectral morphologies. Specifically, the minimum flux density (the “trough”) is often located at a few hundred km s⁻¹ blueward (or even redward in rare cases; see, e.g., Rubin et al. 2012; Martin et al. 2012; Bouché et al. 2013; Ford et al. 2014; Kacprzak et al. 2014; Zabl et al. 2019; Afruni et al. 2022; Weldon et al. 2023) of the systemic velocity. On both sides of the trough, the flux density gradually rises to meet the continuum, yet in general, it rises significantly more steeply on the red side than the blue side. The spectral features of the metal absorption lines can then be used to infer the physical properties of the absorbing gas. For example,

the velocity range of the absorption line profile traces the gas outflow velocities, and the depth of the absorption probes the gas column density or covering fraction. In particular, the absorption lines from low-ionization states (LIS), such as Si II, C II and O I, closely trace neutral hydrogen due to their similar ionization potential. The derived gas properties from the LIS lines can therefore be utilized to constrain several important galactic properties, such as the mass outflow rates, the escape fraction of ionizing photons, etc. (e.g., Rupke et al. 2005; Martin 2005; Weiner et al. 2009; Martin et al. 2009; Rubin et al. 2014; Erb 2015; Chisholm et al. 2016; Chisholm et al. 2018; Steidel et al. 2018; Gazagnes et al. 2018; Gazagnes et al. 2020; Mauerhofer et al. 2021; Xu et al. 2022).

Thus far, a number of attempts have been made to model the metal absorption lines in DTB galaxy spectra. Most have adopted a “picket-fence” model (e.g., Steidel et al. 2010; Heckman et al. 2011; Zackrisson et al. 2013; Jones et al. 2013; Borthakur et al. 2014; Rivera-Thorsen et al. 2015; Reddy et al. 2016; Rivera-Thorsen et al. 2017; Steidel et al. 2018; Gazagnes et al. 2018; Gazagnes et al. 2020; Xu et al. 2022), which assumes that the stellar continuum is partially covered by optically thick absorbing gaseous material. Some have further accounted for radial variation of the gas outflow velocity to reproduce the line profiles of particular transitions (e.g., Steidel et al. 2010; Chisholm et al. 2016). Other work has explored, using semi-analytic models or Monte Carlo simulations, the absorption line profile resulting from transmission through a homogeneous, expanding wind (e.g., Prochaska et al. 2011a; Scarlata et al. 2015; Carr et al. 2021), while others have used cosmological simulations to predict the absorption line profiles emerging from realistic galactic environments (e.g., Kimm et al. 2011; Mauerhofer et al. 2021; Gazagnes et al. 2023). Many of the models have successfully produced absorption line profiles that closely resemble observations. Nevertheless, the majority of the models proposed in previous works rely on simplifying assumptions, e.g., that the gas column density is always high enough to result in saturated absorption so that the depth of absorption relative to the continuum directly traces the gas covering fraction; that continuum photons will be absorbed by the outflowing gas with a large velocity gradient only if they appear resonant in the reference frame of the gas (namely the Sobolev approximation), or that the absorbing gaseous medium is homogeneous without any holes or clumps. These assumptions may be (at least in part) unphysical or in tension with the most recent observations. For example, theoretical models, simulations and observations have revealed that galactic winds may reach a “plateau” phase at large radii where the wind velocity remains approximately constant (e.g., Chevalier

et al. 1985; Veilleux et al. 2005; Dorfi et al. 2012; Zhang 2018). Recent work also highlighted the importance of accounting for the multiphase, turbulent and kinematically complex structure of galactic winds (Schneider et al., 2020; Kim et al., 2020; Fielding et al., 2022; Steinwandel et al., 2022b; Steinwandel et al., 2022a; Rathjen et al., 2023). As these recent findings have posed significant challenges to the aforementioned simplifying assumptions, the models that depend on them should benefit from re-examination.

On the other hand, the properties of the absorbing gas surrounding galaxies can be constrained by measuring the strength of absorption at different galactocentric impact parameters. Specifically, one can plot the observed absorption equivalent width (EW) as a function of impact parameter (b) (e.g., Steidel et al. 2010; Prochaska et al. 2011b; Werk et al. 2013; Liang et al. 2014; Borthakur et al. 2015; Bordoloi et al. 2018; Méndez-Hernández et al. 2022). The relationship between EW and b not only captures the radial distribution of the absorbers but also encapsulates the spatial variations in the kinematics and column densities of the absorbers.

In this work, we build on previous models and present a new semi-analytic model for the UV metal absorption lines. Thus far, the clumpy nature of the “cool” ($T \sim 10^4$ K) gas in the ISM / CGM has been supported by abundant observational evidence (e.g., Rauch et al. 1999; Rauch et al. 2001a; Rauch et al. 2001b; Rauch et al. 2002; Ellison et al. 2004; Schaye et al. 2007; Rogerson et al. 2012; Crighton et al. 2015; Arrigoni Battaia et al. 2015; Rubin et al. 2018; Kulkarni et al. 2019; Zahedy et al. 2019; Zahedy et al. 2021). More specifically, the cool gas (which is responsible for producing the LIS lines) is likely to exist in the form of a clumpy mist or fog of cloudlets with a large area covering fraction but a small volume filling factor (McCourt et al., 2018; Fielding et al., 2020; Gronke et al., 2020; Nelson et al., 2020). In light of this physical picture, we explore the formation of metal absorption lines from a clumpy galactic outflow. We perform simultaneous modeling of the observed DTB absorption line profile and the strength of absorption as a function of impact parameter. The ultimate goal of this work is to develop a simple, usable model for the community to fit and interpret the observed metal absorption lines fast and robustly.

The structure of this paper is as follows. In §7.2, we describe the general formalism and a practical implementation of the analytic model. In §7.3, we validate the analytic model by comparing it to Monte-Carlo numerical simulations. In §7.4, we discuss the effect of each individual parameter of the analytic model. In §7.5,

we show an example of applying the analytic model to the composite C II $\lambda 1334$ spectrum of a sample of $z \sim 3$ Lyman break galaxies (LBG) observed for the Keck Lyman Continuum Spectroscopic Survey (KLCS; Steidel et al. 2018) and the EW vs. b profile observed for a sample of $z \sim 2$ star-forming galaxy-galaxy pairs. In §7.6, we discuss the definition and relationship between the gas covering and volume filling parameters. In §7.7, we compare the models that use or not use the Sobolev approximation. In §7.8, we discuss previous work modeling the UV absorption lines in comparison with our model. In §7.9, we discuss the limitations of our model and possible developments in the future. In §7.10, we summarize and conclude.

7.2 ALPACA: A Non-Sobolev Clumpy Model For Metal Absorption Lines

We introduce the semi-analytic model that we use in this work, ALPACA (Absorption Line Profiles Arising from Clumpy Absorbers)¹.

General Formalism

Down the Barrel Absorption

As illustrated in Figure 7.1, we consider the escape of photons from an idealized, spherical halo filled by an ensemble of spherical clumps that contain the corresponding metal ions (e.g., Si⁺ or C⁺) that produce the absorption. For the sake of computational convenience, we assume a spherical halo with inner and outer boundaries defined by the clump launch radius r_{\min} and the halo extent r_h , respectively; we then divide the halo into a series of concentric shells, equally spaced in radius. The absorption contributed by all concentric shells constitutes the total absorption of the model. The interval between the midplanes of two adjacent radial shells is $d = (r_h - r_{\min})/N_{\text{shell}}$, where N_{shell} is the total number of shells. The optimal way of choosing N_{shell} will be discussed later in this paper.

The ALPACA model accounts for the non-zero width of the absorption cross section in the velocity space and does not use the commonly adopted Sobolev approximation, which assumes that absorption occurs only when a photon appears exactly at the line center in the reference frame of the absorbing gas. Instead, in ALPACA, each outgoing photon will suffer from absorption by clumps with a range of velocities, even if it is not at the line center (i.e., out of resonance) in the reference frame of a clump. As we will demonstrate later in Section 7.7, this is particularly

¹The code for ALPACA is publicly available at: <https://github.com/astro-zhihuili/ALPACA>.

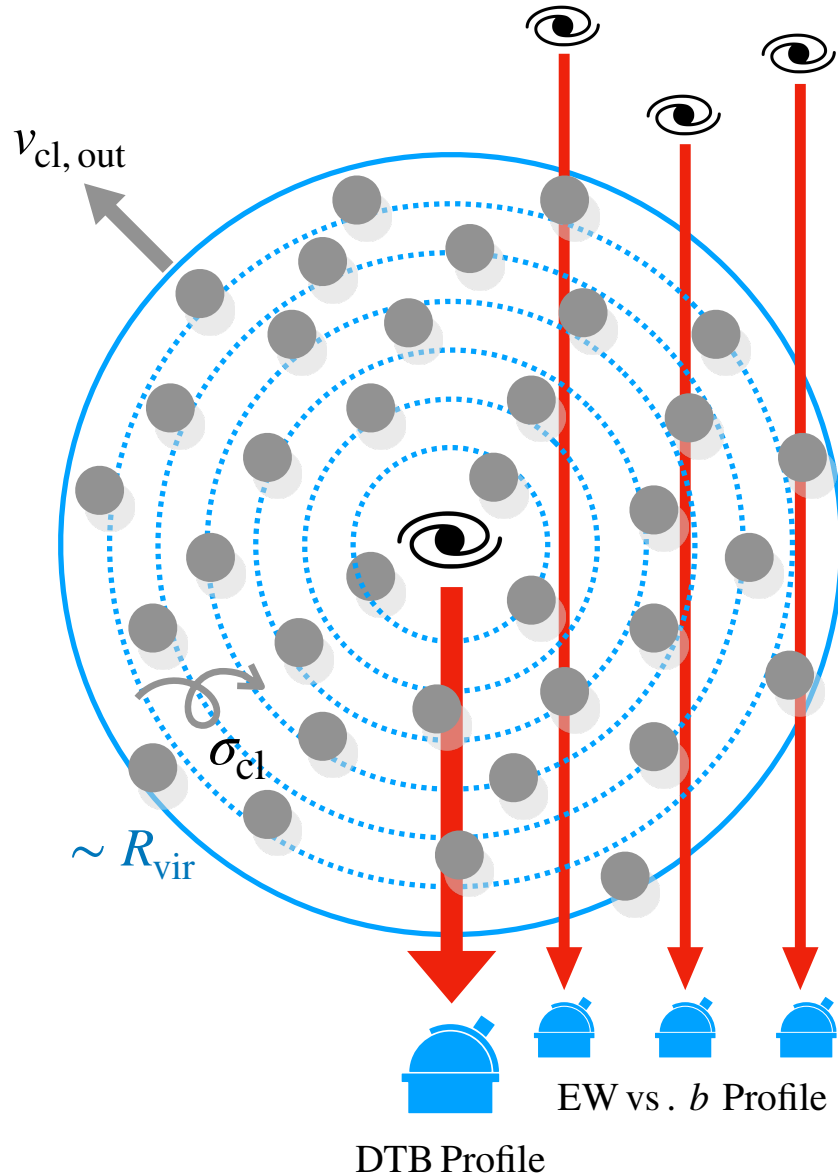


Figure 7.1: **Schematic for ALPACA, a non-Sobolev clumpy model for metal absorption lines.** For the DTB absorption line profile, it is assumed that a central source emits continuum photons isotropically and that all photons travel radially in a spherical halo that contains a number of absorbing clumps. For computational convenience, the halo is divided into a series of equally spaced, concentric shells. The probability of escape for a continuum photon observed at a particular velocity is determined by the product of transmission probabilities through all radial shells. In each shell, the transmission probability is the sum of the probabilities of propagating through “holes” that are not occupied by any clumps (given by $1 - C_f(r_i)$) and penetrating through clumps (given by $C_f(r_i)e^{-\tau_{\text{ion}}(v-v_i)}$). The EW vs. b profile can be similarly calculated at different impact parameters. We refer the readers to Section 7.2 for a detailed derivation.

important when the velocity gradient of the clumps is small or the clump random motion is non-negligible. To escape, each photon must pass through every shell consecutively. In each shell, a photon may either pass freely through “holes” where no clump exists (with a probability of $1 - C_f$, where C_f is the geometric covering fraction of the clumps), or penetrate through a clump (with a probability of $C_f e^{-\tau_{\text{ion}}}$, where τ_{ion} is the optical depth of one clump of the relevant transition). Therefore, the probability of escape for a photon originating from the ISM of a galaxy can be expressed as:

$$P_{\text{esc}}(-v) = \prod_{i=1}^{N_{\text{shell}}} (1 - C_f(r_i) + C_f(r_i) e^{-\tau_{\text{ion}}(v-v_i)}) \quad (7.1)$$

Here $-v$ represents the location in the rest-frame velocity space. This implies, e.g., if the clumps are outflowing with $v > 0$, absorption on the blue side at $-v < 0$ will be observed. v_i is the (average) clump velocity in the i -th shell, determined by the clump radial velocity profile:

$$v_i = v_{\text{cl}}(r)|_{r=r_i} \quad (7.2)$$

where r_i ($i = 1, 2, \dots, N_{\text{shell}}$) are the radial locations of the midplanes of all the shells where absorption will be calculated. $C_f(r_i)$ is the clump geometric covering fraction at r_i , and $\tau_{\text{ion}}(v - v_i)$ is the clump optical depth of the relevant transition evaluated at $v - v_i$, which is the photon’s apparent frequency in velocity space in the reference frame of the clumps outflowing at v_i .

The geometric gas covering fraction C_f , which is the fraction of the halo area covered by clumps at radius r , is given by (see also Dijkstra et al. 2012):

$$C_f(r) \approx \pi \int_{r-\frac{d}{2}}^{r+\frac{d}{2}} dr' n_{\text{cl}}(r') [R_{\text{cl}}^2(r') - (r - r')^2] \approx \pi n_{\text{cl}}(r) [R_{\text{cl}}^2(r) d - \frac{d^3}{12}] \quad (7.3)$$

where $n_{\text{cl}}(r)$ and $R_{\text{cl}}(r)$ are the number density² and radius of the clumps at r , respectively. Eq. (7.3) comes from the operation that each clump is assigned to a shell (with a thickness of d) within which its center is located and will only contribute to

²Here the “clump number density” refers to the volumetric number density of the clumps, defined as the number of clumps per physical volume. Not to be confused with the number density of ions *within* the clumps, which we do not use in the model (we consider the ion column density within the clumps instead).

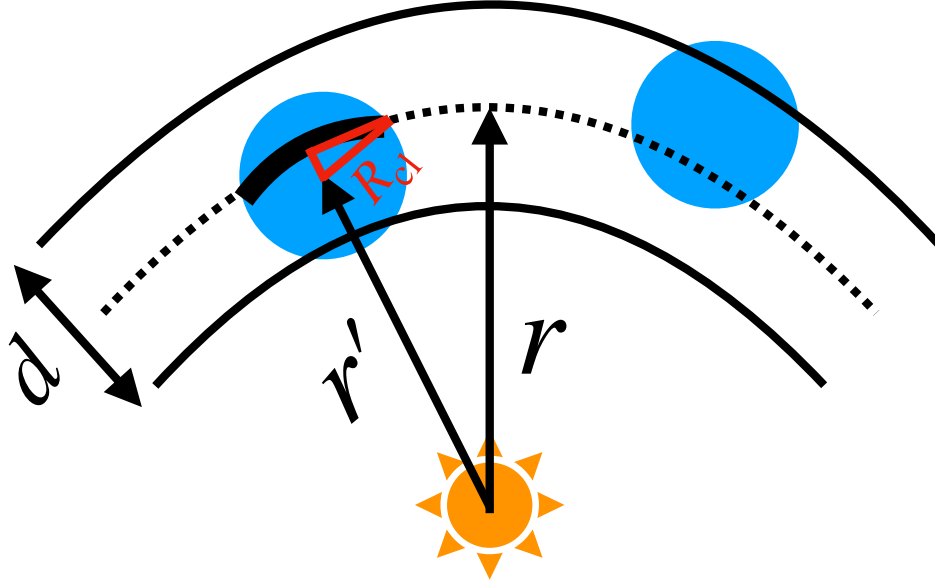


Figure 7.2: **Schematic for calculating the geometric covering fraction of clumps at radius r .** The contribution of one clump (as shown in blue) to the geometric covering fraction at a shell midplane at r (as shown by the dotted black arc) is given by $\sim \pi[R_{\text{cl}}^2(r') - (r - r')^2]$, which, after being integrated over $r \pm d/2$, gives the total geometric covering fraction at r , $C_f(r)$.

the absorption of this shell. Therefore, the clumps that contribute to the absorption of a particular shell must have their centers located within $r \pm d/2$. The way of calculating the contribution to $C_f(r)$ for each clump is illustrated in Figure 7.2.

Recall that the clump optical depth can be written as:

$$\tau_{\text{ion}}(\nu - \nu_i) = N_{\text{ion,cl}}(r_i) \sigma_{\text{ion}}(\nu - \nu_i) \quad (7.4)$$

where $N_{\text{ion,cl}}(r_i)$ is the clump's ion column density³ at r_i , and $\sigma_{\text{ion}}(\nu)$ is the cross section of the ion (both as a function of velocity), given by:

$$\sigma_{\text{ion}}(\nu) = \frac{\sqrt{\pi} e^2 f_{\text{line}}}{m_e c \Delta \nu_{\text{D}}} H(a, x) \quad (7.5)$$

where e is the electron charge, m_e is the electron mass, f_{line} is the oscillator strength of the line transition, $\Delta \nu_{\text{D}} = b_{\text{D}} \nu_0 / c$ is the Doppler width, b_{D} is the Doppler parameter within a single clump, $a = A / (4\pi \Delta \nu_{\text{D}})$ is the normalized natural line width (where A is the summation of the Einstein coefficients A_{line} of all the transitions from

³For a spherical clump, $N_{\text{ion,cl}} = \frac{4}{3} n_{\text{ion,cl}} R_{\text{cl}}$, where $n_{\text{ion,cl}}$ is the ion number density within the clump (Gronke et al., 2017).

the upper level, typically dominated by the resonant transition), $x = (\nu - \nu_0)/\Delta\nu_D = -v/b_D$ is the unitless photon frequency, and $H(a, x)$ is the Voigt function:

$$H(a, x) = \frac{a}{\pi} \int_{-\infty}^{+\infty} \frac{e^{-y^2}}{(y-x)^2 + a^2} dy \quad (7.6)$$

Next, specific radial profiles can be assumed for clump outflow velocity, clump number density, clump ion column density and clump radius as a function of the clumps' galactocentric radius r , namely $v_{\text{cl}}(r)$, $n_{\text{cl}}(r)$, $N_{\text{ion,cl}}(r)$ and $R_{\text{cl}}(r)$, respectively. The values of $n_{\text{cl}}(r)$ and $R_{\text{cl}}(r)$ can be used to calculate $C_f(r)$ using Eq. (7.3), whereas $v_{\text{cl}}(r)$ and $N_{\text{ion,cl}}(r)$ can be used to calculate $\tau_{\text{ion}}(v)$ using Eq. (7.4) – (7.6).

Finally, with Eq. (7.1) to (7.6), one can derive a (normalized) model absorption line profile, whose intensity is proportional to the photons' escape probability:

$$\frac{I(v)}{I_{\text{cont}}} = P_{\text{esc}}(v) \quad (7.7)$$

where I_{cont} is the intensity level of the continuum.

Absorption at Different Impact Parameters

ALPACA can also model the absorption of photons that are emitted from a background source at a particular impact parameter (i.e., along transverse sightlines), which is suitable for studying quasar-quasar/quasar-galaxy/galaxy-galaxy pairs (see, e.g., Hennawi et al. 2006; Hennawi et al. 2007; Prochaska et al. 2009; Steidel et al. 2010; Hennawi et al. 2013; Prochaska et al. 2013). For example, the equivalent width (EW) of the absorption as a function of impact parameter can be predicted in a manner similar to the derivation above (see also Dijkstra et al. 2012, which focused on Ly α absorption).

The EW at a particular impact parameter b is given by:

$$\text{EW}(b) = \int_{\lambda_{\text{min}}(b)}^{\lambda_{\text{max}}(b)} d\lambda (1 - e^{-\tau(\lambda)}) = \frac{1}{\nu_0} \int_{v_{\text{min}}(b)}^{v_{\text{max}}(b)} dv (1 - e^{-\tau(v)}) \quad (7.8)$$

where ν_0 is the line center frequency of the transition, and the integral is performed over the range of observed velocities v where absorption is seen at impact parameter b . The transmission at a particular velocity, $e^{-\tau(v)}$, comes from the contribution of

individual clumps along the transverse sightline at b . It can be calculated by separating the sightline into a number of line segments (which is analogous to separating the spherical halo into different shells):

$$e^{-\tau(v)} = \prod_{i=1}^{N_{\text{seg}}} (1 - C_{f,\parallel}(r_i) + C_{f,\parallel}(r_i)e^{-\tau_{\text{ion}}(v-v_{i,\parallel})}) \quad (7.9)$$

where the product is evaluated over all N_{seg} line segments. The galactocentric radii of the centers of the line segments constitute an array of r_i where the clump quantities are evaluated. Assuming that the angle between the vector $-\vec{r}_i$ and the line of sight towards the observer is θ ($\in [\arcsin(b/r_h), \pi/2]$), the clump covering fraction and the clump radial velocity projected along the line of sight at r_i , $C_{f,\parallel}(r_i)$ and $v_{i,\parallel}$, are given by:

$$C_{f,\parallel}(r_i) = f_c(r_i)\Delta l \quad (7.10)$$

$$v_{i,\parallel} = v_{\text{cl}}(r_i)\cos\theta \quad (7.11)$$

where $f_c(r_i) = \pi n_{\text{cl}}(r_i)R_{\text{cl}}^2(r_i)$ is the clump covering *factor* at r_i (see Eq. 7.28 below in Section 7.6), $\Delta l = 2\sqrt{r_h^2 - b^2}/N_{\text{seg}}$ is the length of each line segment, and $v_{\text{cl}}(r_i)$ is the clump radial velocity at r_i . Combined with Eq. (7.4) – (7.6), the equations presented above can be used to derive the EW of a particular transition as a function of the impact parameter b .

A Practical Implementation

In practice, the solution to the ALPACA model can be further simplified by assuming specific functional forms (e.g., power-laws) for the radial profiles of clump parameters. In this section, we explore a practical implementation of the model, so that it can be conveniently applied to model observational data.

Clump Outflow Kinematics

The cool clumps in a galactic outflow can be accelerated via a number of different mechanisms, including radiation pressure (e.g., Murray et al. 2005; Thompson et al. 2005; Martin 2005), ram pressure (e.g., Murray et al. 2005; Fujita et al. 2009; Martin et al. 2009; Sharma et al. 2012; Thompson et al. 2016) from the hot wind, and cosmic rays (e.g., Socrates et al. 2008; Everett et al. 2008; Dorfi et al. 2012;

Recchia et al. 2016; Zweibel 2017; Mao et al. 2018; Jacob et al. 2018; Chan et al. 2019; Quataert et al. 2022a; Quataert et al. 2022b). Since these mechanisms are often dependent on multiple physical parameters and the clumps are likely to be accelerated by several mechanisms at the same time, the actual scaling of the acceleration force with radius is uncertain and difficult to determine observationally. For simplicity, we explore an $r^{-\alpha}$ acceleration force, where the power-law index α describes how fast the acceleration force drops with the galactocentric radius. For example, $\alpha = 2$ is an approximate scaling expected for acceleration due to optically thin radiation pressure, ram pressure, or cosmic rays⁴ (Murray et al., 2005; Socrates et al., 2008; Martin et al., 2009; Chisholm et al., 2016). We stress that the formalism of the ALPACA model is general and applicable to other radial scalings of the acceleration force.

In addition to acceleration, the outflowing clumps will inevitably suffer from gravitational deceleration from the mass of the dark matter halo. Therefore, the kinematic equation of an outflowing clump, is given by:

$$\frac{dv_{\text{cl,out}}(r)}{dt} = -\frac{GM(r)}{r^2} + Ar^{-\alpha} \quad (7.12)$$

Assuming a Navarro–Frenk–White (NFW, Navarro et al. 1995) profile for the dark matter halo, the mass within radius r , is given by:

$$M(r) = 4\pi\rho_0r_s^3 \left[\ln(1 + r/r_s) - \frac{r/r_s}{1 + r/r_s} \right] \quad (7.13)$$

where ρ_0 is the central density, given by:

$$\rho_0 = \frac{M_{\text{vir}}}{4\pi r_s^3 \left[\ln(1 + r_{\text{vir}}/r_s) - \frac{r_{\text{vir}}/r_s}{1 + r_{\text{vir}}/r_s} \right]} \quad (7.14)$$

where M_{vir} and r_{vir} are the halo virial mass and virial radius, respectively. $r_s = r_{\text{vir}}/c$ is the scale radius, where c is the concentration parameter of the halo. In this context, Eq. (7.12) can be further simplified as:

$$\frac{d(\frac{1}{2}v_{\text{cl,out}}^2(r))}{dr} = -\frac{4\pi G\rho_0r_s^3}{r^2} \left[\ln(1 + r/r_s) - \frac{r/r_s}{1 + r/r_s} \right] + \frac{A}{r_s^\alpha} \left(\frac{r_s}{r} \right)^\alpha \quad (7.15)$$

⁴Such a scaling is derived for the acceleration force per unit area; for cool clumps that are in pressure equilibrium with a hot wind, one might expect $\alpha = 4/3$ (Steidel et al., 2010).

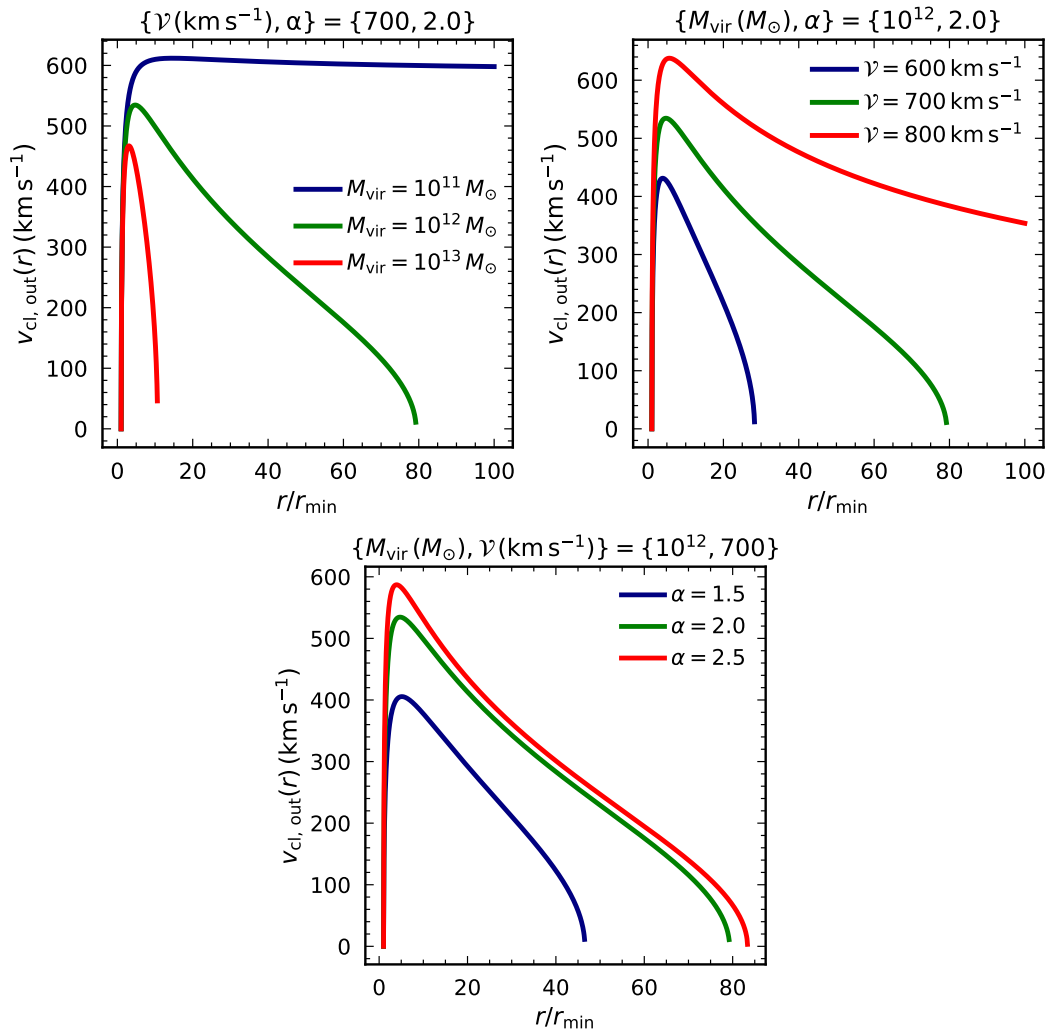


Figure 7.3: **Clump radial outflow velocity profiles $v_{cl,out}(r)$ with different $\{M_{vir}, \mathcal{V}, \alpha\}$ values as given by Eq. (7.16).** In each panel, only one parameter is varied while the other two are fixed. The $v_{cl,out}(r)$ profiles derived from varying one of the parameters are shown in different colors.

Integrating the equation above from the clump launch radius r_{\min} to r yields the following solution:

$$v_{\text{cl,out}}(r) = \left\{ \frac{2GM_{\text{vir}}}{\ln(1+c) - c/(1+c)} \left[\frac{\ln(1+r/r_s)}{r} - \frac{\ln(1+r_{\min}/r_s)}{r_{\min}} \right] + \mathcal{V}^2 \left[1 - \left(\frac{r}{r_{\min}} \right)^{1-\alpha} \right] \right\}^{1/2} \quad (7.16)$$

where we have replaced A with $\mathcal{V} (\equiv \sqrt{2Ar_{\min}^{1-\alpha}/(\alpha-1)})$, which is the asymptotic outflow velocity if there were no gravitational deceleration.

Eq. (7.16) shows that $v_{\text{cl,out}}(r)$ can be fully determined by six parameters in total: the virial mass M_{vir} , the virial radius r_{vir} , the concentration parameter c , the clump launch radius r_{\min} , the asymptotic velocity \mathcal{V} , and the power-law index α . Among these parameters, M_{vir} and r_{vir} can be inferred via the stellar mass-halo mass relation (e.g., Tasitsiomi et al. 2004; Moster et al. 2010; Moster et al. 2013; Behroozi et al. 2010; Behroozi et al. 2013; Rodríguez-Puebla et al. 2015; Rodríguez-Puebla et al. 2017; Kravtsov et al. 2018; Girelli et al. 2020) if the galaxy's stellar mass is known (e.g., from SED fitting), and c can be inferred via the concentration-halo mass relation (e.g., Wechsler et al. 2002; Prada et al. 2012; Dutton et al. 2014; Ludlow et al. 2014; Diemer et al. 2015; Child et al. 2018; Diemer et al. 2019). Therefore, for a given galaxy, this kinematic model has only three free parameters: \mathcal{V} , r_{\min} and α . In our following modeling, we simply fix r_{\min} to 1 kpc as its effect on $v_{\text{cl,out}}(r)$ is relatively minor. In Figure 7.3, we show several example $v_{\text{cl,out}}(r)$ profiles by varying M_{vir} , \mathcal{V} and α individually (assuming $r_{\min} = 1$ kpc).

Clump Number Density and Radius

Heuristically, the clump number density $n_{\text{cl}}(r)$ and the clump radius $R_{\text{cl}}(r)$, can be assumed to vary radially in the form of a power-law:

$$n_{\text{cl}}(r) = n_{\text{cl},0} \left(\frac{r}{r_{\min}} \right)^{-\gamma} \quad (7.17)$$

$$R_{\text{cl}}(r) = R_{\text{cl},0} \left(\frac{r}{r_{\min}} \right)^{\delta} \quad (7.18)$$

where $n_{\text{cl},0} = n_{\text{cl}}(r = r_{\min})$ and $R_{\text{cl},0} = R_{\text{cl}}(r = r_{\min})$. Although it is reasonable to assume that $\gamma \geq 0$ and $\delta \geq 0$ due to the increase in the volume of the halo and the decrease in ambient pressure at large r , we allow γ and δ to be negative as

other physical mechanisms may be at play in clump destruction, fragmentation and (re)formation.

Next, we normalize n_{cl} properly by introducing the total volume factor of the halo, F_V , which is the fraction of the halo volume occupied by the clumps. The total volume of the clumps in the halo, is given by:

$$\begin{aligned} V_{\text{cl,total}} &= \int_{r_{\text{min}}}^{r_{\text{h}}} 4\pi r^2 n_{\text{cl}}(r) V_{\text{cl}}(r) dr \\ &= \frac{16\pi^2 n_{\text{cl},0} R_{\text{cl},0}^3 r_{\text{min}}^3}{3(3\delta + 3 - \gamma)} \left[\left(\frac{r_{\text{h}}}{r_{\text{min}}} \right)^{3\delta+3-\gamma} - 1 \right] \end{aligned} \quad (7.19)$$

On the other hand,

$$V_{\text{cl,total}} = F_V V_{\text{h}} = F_V \frac{4}{3} \pi (r_{\text{h}}^3 - r_{\text{min}}^3) \quad (7.20)$$

Eq. (7.19) and (7.20) can be used to further simplify the expression for $C_{\text{f}}(r)$ (Eq. 7.3) to:

$$\begin{aligned} C_{\text{f}}(r) &\approx \pi n_{\text{cl}}(r) R_{\text{cl}}^2(r) d \\ &= \frac{(3\delta + 3 - \gamma) F_V \left[\left(\frac{r_{\text{h}}}{r_{\text{min}}} \right)^3 - 1 \right]}{4R_{\text{cl},0} \left[\left(\frac{r_{\text{h}}}{r_{\text{min}}} \right)^{3\delta+3-\gamma} - 1 \right]} \left(\frac{r}{r_{\text{min}}} \right)^{2\delta-\gamma} d \end{aligned} \quad (7.21)$$

Eq. (7.21) implies that there is a triple degeneracy among F_V , δ and γ – specifically, a parameter set $\{F_V, \gamma, \delta\}$ gives an identical $C_{\text{f}}(r)$ profile to the following parameter set (where Δ represents a particular variation in γ):

$$\left\{ \frac{\left[\left(\frac{r_{\text{h}}}{r_{\text{min}}} \right)^{3\delta+3-\gamma+\Delta/2} - 1 \right] (3\delta + 3 - \gamma)}{\left[\left(\frac{r_{\text{h}}}{r_{\text{min}}} \right)^{3\delta+3-\gamma} - 1 \right] (3\delta + 3 - \gamma + \Delta/2)} F_V, \gamma + \Delta, \delta + \frac{1}{2} \Delta \right\} \quad (7.22)$$

As the model absorption lines are only sensitive to the $C_{\text{f}}(r)$ profiles rather than the individual values of F_V , γ or δ , in the following modeling, we simply fix $\delta = 0$ while keeping F_V and γ as free parameters in order to reduce the parameter degeneracies and computational cost. The readers should keep in mind that in reality, it is likely that the clump radius varies with the galactocentric radius; nevertheless, such an effect is indistinguishable from a change in the radial distribution of the clumps under the current formalism of ALPACA.

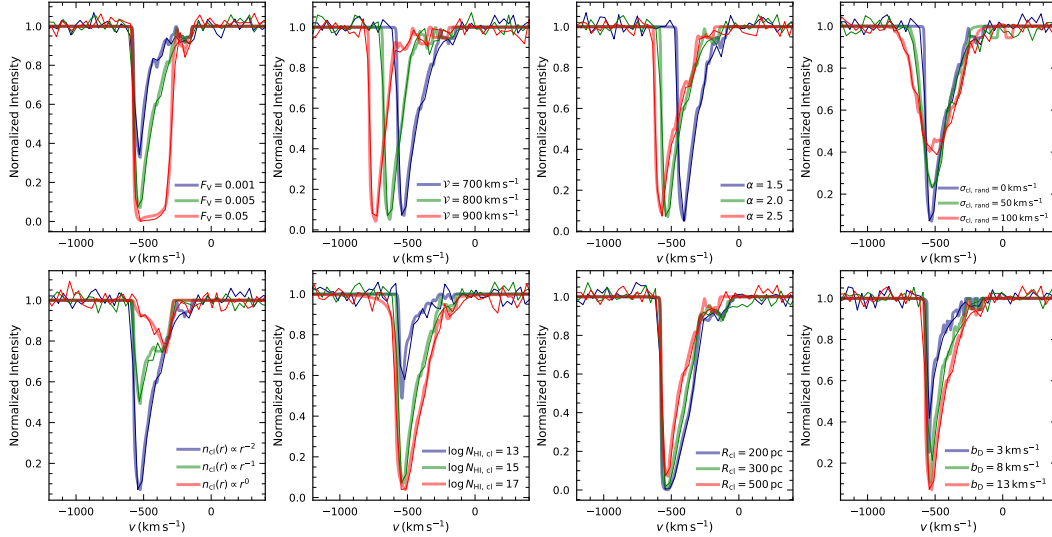


Figure 7.4: **Comparison of the absorption line profiles predicted by ALPACA and t1ac.** The fiducial set of parameters are: $F_V = 0.005$, $v = 700 \text{ km s}^{-1}$, $\alpha = 2.0$, $\sigma_{\text{cl,rand}} = 0 \text{ km s}^{-1}$, $\gamma = 2.0$, $\log N_{\text{HI,cl}} = 15$, $R_{\text{cl}} = 500 \text{ pc}$, and $b_D = 12.85 \text{ km s}^{-1}$. In each panel, only one parameter is varied (as indicated by three different colors) while the other parameters are fixed at their fiducial values. The model spectra predicted by ALPACA and t1ac are shown in thick and thin curves, respectively. The absorption line profiles predicted by the two models are highly consistent over a wide range of physical parameters, suggesting that the formalism that we introduced in Section 7.2 is remarkably successful.

Number of Shells

Although in principle, the choice of the spacing between two adjacent shells d is arbitrary, it is advantageous to choose a relatively small d to better sample the radial velocity profile and improve the accuracy of the model. In Appendix 7.11, we show that for $\sigma_{\text{cl,rand}} \lesssim 100 \text{ km s}^{-1}$, the model converges at $d/R_{\text{cl}} \sim 0.1$. Therefore, in the next section, we adopt $d/R_{\text{cl}} \sim 0.1$ as it achieves sufficient accuracy with reasonable computational cost.

7.3 Model Validation

In this section, we test the validity of the ALPACA model with a Monte-Carlo radiative transfer (RT) code, t1ac (Gronke et al., 2014; Gronke et al., 2015). t1ac is specifically designed for simulating the RT process of Ly α photons with idealized configurations. Nevertheless, the RT processes of Ly α and metal lines (e.g., Si II $\lambda 1260$ and C II $\lambda 1334$) are very similar in nature, despite the following two subtle differences:

(1) The line cross section is different for different transitions. Such a difference can be easily accounted for by replacing the relevant coefficients and physical constants used in calculating the line cross section, namely the oscillator strength of the line transition f_{line} , the Einstein coefficient of the transition A_{line} , the wavelength of the transition λ_{line} , and the ion mass m_{ion} ;

(2) Unlike $\text{Ly}\alpha$, the metal lines often have nearby non-resonant transitions (as the ground state is split into $^2P_{1/2}$ and $^2P_{3/2}$), so that a significant portion of the absorbed resonant photons can be re-emitted as non-resonant emission (e.g., $\text{Si II}^* \lambda 1265$). We neglect such fluorescent emission for the moment as we are mostly focused on the absorption line profile in this work.

With those in mind, we can test whether the ALPACA model gives the correct absorption line profile with different clump radial velocity profiles, clump number density profiles, clump radii and clump ion column densities as inputs, by comparing with the Monte-Carlo RT simulations performed by `tlac` using the $\text{Ly}\alpha$ $\lambda 1216$ line. Once the model is validated, we can use it to predict other metal (e.g., Si and C) absorption line profiles by simply switching to a different transition.

In order to perform Monte-Carlo RT simulations, `tlac` requires several input parameters / radial profiles, namely the total clump volume filling factor F_V , the radial distribution of the clumps, the clump radial velocity (including outflow and random motion), the clump column densities, and the clump radii. After the parameters of the clumps are fully specified, in each model, a UV continuum source is placed at the center of a spherically symmetric halo that emits 10^5 photons in the form of a flat continuum within $\pm 1500 \text{ km s}^{-1}$ of the rest-frame wavelength of the $\text{Ly}\alpha$ transition (1215.67 \AA). All the photons will eventually escape from the halo (as we only consider a dust-free medium in this work), whereas a fraction of the emitted photons will be resonantly scattered by the clumps by one or more times before they escape.

For each Monte-Carlo RT simulation, all the photons that are scattered by the clumps at least once are filtered out and only the photons that have zero scatterings are used to construct the model absorption line profile⁵. In this way, the output absorption line profile from `tlac`, which does not account for the contribution of re-emission from scattered photons (see Section 6.5 for a discussion of such re-

⁵This is essentially assuming all the scattered photons will not re-enter the line of sight of the observer in a real observation.

emission and the associated “infilling” effect), can be directly compared to that of ALPACA.

Our tests are based on the practical implementation described in Section 7.2, and are performed by varying the following key parameters or radial profiles, one at a time, with respect to the fiducial set of parameters ($F_V = 0.005$, $\mathcal{V} = 700 \text{ km s}^{-1}$, $\alpha = 2.0$, $\sigma_{\text{cl,rand}} = 0 \text{ km s}^{-1}$, $\gamma = 2.0$, $\log N_{\text{HI,cl}} = 15$, $R_{\text{cl}} = 500 \text{ pc}$, $b_D = 12.85 \text{ km s}^{-1}$):

1. the total clump volume filling factor F_V ;
2. the clump radial velocity profile, including the clump outflow velocity $v_{\text{cl,out}}(r)$ (which is a function of \mathcal{V} and α) and random velocity $v_{\text{cl,rand}}(r)$. The total clump radial velocity $v_{\text{cl}}(r)$, is given by:

$$v_{\text{cl}}(r) = v_{\text{cl,out}}(r) + v_{\text{cl,rand}}(r) \quad (7.23)$$

where

$$v_{\text{cl,rand}}(r) \sim \mathcal{N}(v, \mu = 0, \sigma = \sigma_{\text{cl,rand}}) \quad (7.24)$$

is a random velocity field in the form of a normalized Gaussian distribution that is characterized by $\sigma_{\text{cl,rand}}$, the 1D macroscopic velocity dispersion among the clumps;

3. the shape of the clump number density profile, namely the power-law index γ in Eq. (7.17);
4. the clump H I column density $N_{\text{HI,cl}}$;
5. the clump radius R_{cl} ;
6. the Doppler parameter within a single clump b_D .

These tests are designed to verify the consistency of the absorption line profiles predicted by `tlac` and ALPACA over a wide range of physical parameters. We note that at present, `tlac` only supports radially varying $v_{\text{cl}}(r)$ and $n_{\text{cl}}(r)$, but not $N_{\text{HI,cl}}(r)$ or $R_{\text{cl}}(r)$, i.e., the clump column density and radius cannot yet be varied continuously as a function of radius. These tests are therefore our first attempt to validate the ALPACA model with the currently available capabilities of `tlac`. In Section 7.5 where we apply ALPACA to observational data, we fix the clump radius to be constant (see the justification for such a choice in Section 7.2 above)

and restrict ourselves to using constant clump ion column densities. We therefore consider the tests described above sufficient for the validation and application of ALPACA in this work.

The results of these validation tests are presented in Figure 7.4. In each test, we consider a $z \sim 3$ galaxy with a halo mass of $M_{\text{vir}} \sim 10^{11.8} M_{\odot}$ and assume that the clump launch radius $r_{\text{min}} = 1$ kpc, the halo radius $r_{\text{h}} = 100$ kpc. It can be seen that the ALPACA model is highly consistent with the `tlac` model over a wide range of physical parameters, suggesting that the simple formalism that we introduced in Section 7.2 is remarkably successful at describing the absorption of photons.

7.4 Effect of Individual Parameters

Figure 7.4 also illustrates the effects of different physical parameters in the ALPACA model, and we summarize them as follows:

- Clump volume filling factor F_V : Increasing F_V will increase the depth of and broaden the width of the flux minimum (“trough”) while keeping the location of the trough and the velocity range of the absorption profile roughly constant. This is because the clump covering fraction $C_f(r)$ has increased proportionally at each radius (cf. Eq. 7.21).
- Clump asymptotic outflow velocity \mathcal{V} : Modifying \mathcal{V} simply shifts the overall spectrum horizontally without changing the shape of the profile. Note that the location of the trough corresponds to the maximum of $|v_{\text{cl}}(r)|$, which is always smaller than \mathcal{V} due to gravitational deceleration (cf. Eq. 7.16).
- Power-law index in the clump acceleration force profile α : Similar to \mathcal{V} , changing α also shifts the spectrum horizontally, although in a rather non-linear way. As α increases, the maximum clump outflow velocity increases (see Figure 7.3), and the location of the trough shifts bluewards correspondingly.
- Clump radial velocity dispersion $\sigma_{\text{cl,rand}}$: Increasing $\sigma_{\text{cl,rand}}$ tends to reduce the depth of the trough and broaden the “wings” of the absorption line profile. This can be understood as an effective broadening in the range of the clump velocities that produces the absorption (cf. Eq. 7.23).
- Power-law index in the clump number density profile γ : Decreasing γ , which yields a flatter radial declining profile for the number density of the clumps,

tends to decrease the depth of the trough and shift the location of the trough nearer to the line center. This is because decreasing γ essentially moves the clumps, on average, to larger galactocentric radii where the clumps have decelerated to lower velocities. Consequently, this leads to a decrease in the overall geometric covering fraction of the clumps.

- Clump H I column density $N_{\text{HI,cl}}$: Increasing $N_{\text{HI,cl}}$ deepens the trough and broadens the wings of the absorption by increasing the clump optical depth at all velocities (cf. Eq. 7.4).
- Clump radius R_{cl} : Increasing R_{cl} tends to decrease the depth of the trough, as it also changes $n_{\text{cl}}(r)$ at a fixed F_V and the net effect is to decrease $C_f(r)$ and produce less absorption (cf. Eq. 7.21).
- Clump Doppler parameter b_D : Increasing b_D yields more absorption at different velocities without increasing the observed velocity range of absorption, because the clump velocity distribution remains unchanged, yet there is more non-resonant absorption at each observed velocity.

7.5 Application Example: Modeling the ISM and CGM of a Sample of Lyman Break Galaxies

Now that we have verified that the absorption line profiles predicted by the ALPACA model are reasonable by comparing them to the Monte-Carlo simulations carried out by `tlac`, next we apply ALPACA to the low-ionization, metal absorption lines observed in the rest-frame UV wavelengths.

Fitting the Composite DTB Spectrum and the EW vs. b Relation Simultaneously

To tightly constrain the properties of the ISM and CGM of high- z galaxies, we utilize both the DTB absorption line spectrum and the observed EW vs. b relation and model them simultaneously with ALPACA.

The Composite DTB Absorption Line Profile

We use the stacked DTB C II $\lambda 1334$ spectrum of a sample of 55 (out of 124 in total) $z \sim 3$ LBGs that are observed as part of the Keck Lyman Continuum Spectroscopic Survey (KLCS; Steidel et al. 2018). This subsample of 55 galaxies has detected nebular emission lines by MOSFIRE and precisely determined systemic

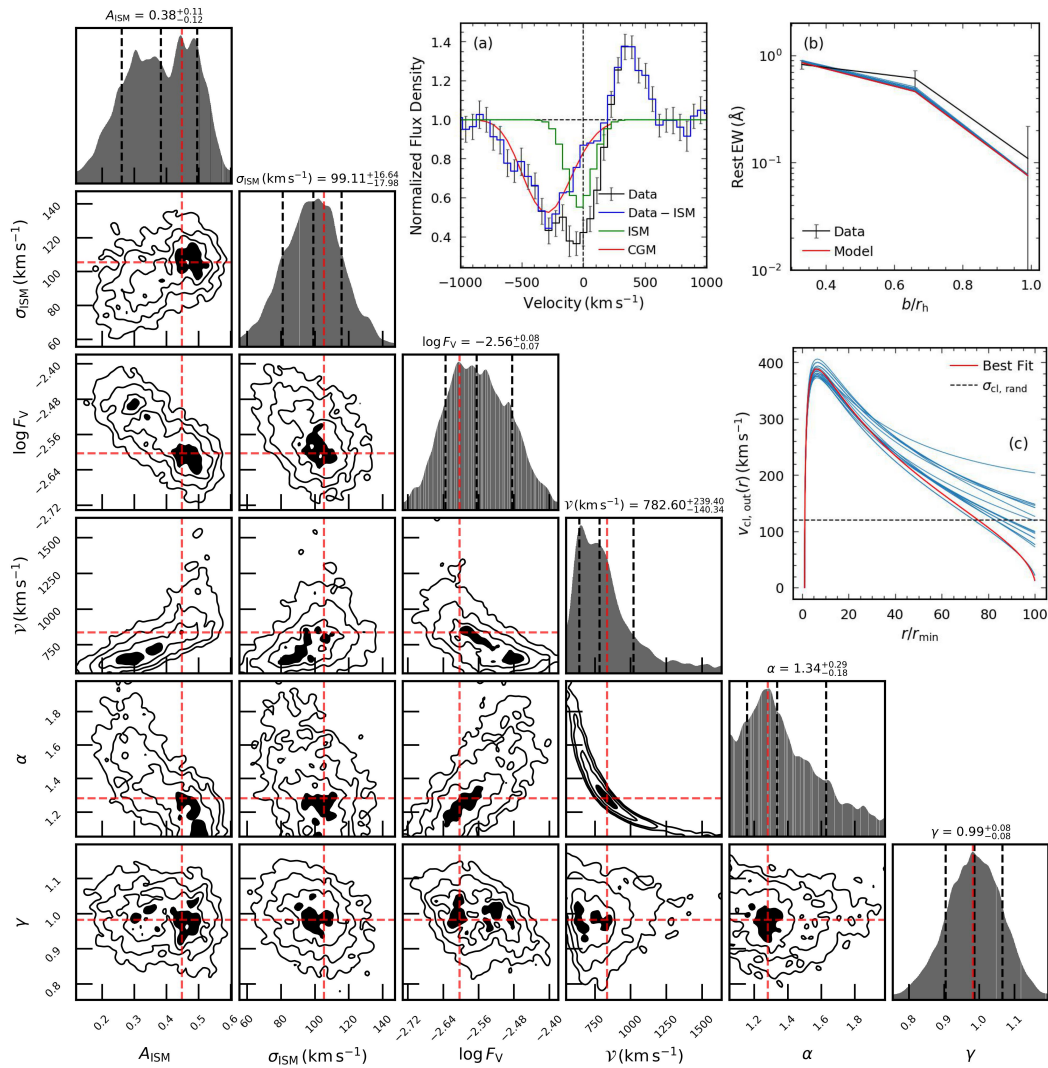


Figure 7.5: Results of joint modeling the composite DTB absorption line profile and the EW vs. b profile of $\text{C II } \lambda 1334$. The posterior PDF is shown, along with the 1- σ confidence intervals of the fitted parameters. The location of the maximum likelihood point is indicated by red dashed lines. On the upper right, panel (a) shows the best-fit model to the DTB absorption line profile. The non-outflowing ISM component and the outflowing CGM component are shown in green and red colors, respectively. Panel (b) shows the best-fit model (red) to the observed EW vs. b profile (black) at three different impact parameters: $b/r_h \simeq [\frac{1}{3}, \frac{2}{3}, 1]$. Also shown are twenty models with the highest likelihoods (blue). Panel (c) shows the clump outflow velocity profiles of twenty models (blue) with the highest likelihoods in the parameter space, as well as the best-fit outflow velocity profile (red). The level of the clump radial velocity dispersion ($\sigma_{\text{cl, rand}} = 120 \text{ km s}^{-1}$) is shown by a horizontal black dashed line.

redshifts (with uncertainties $< 20 \text{ km s}^{-1}$), which allows for the stacking of their absorption line profiles. The rest-UV spectra are obtained by the Low Resolution Imaging Spectrometer (LRIS) spectrograph on the Keck I telescope. The composite UV spectrum is constructed by stacking 55 individual spectra, which minimizes the effect of stochastic line-of-sight variation in the CGM and IGM attenuation compared to the spectrum of any single galaxy. The spectral resolution achieved at the wavelength of C II $\lambda 1334$ is $R \sim 1300$, or equivalently, $\text{FWHM} \sim 230 \text{ km s}^{-1}$ or $\sigma \sim 98 \text{ km s}^{-1}$. Before performing spectrum modeling, we have corrected the observed composite spectrum for CGM and IGM attenuation using the average transmission curve at $z \sim 3.05$ (Steidel et al., 2018).

The EW vs. b Profile

We use the observed EW vs. b relation⁶ of a sample of $z \sim 2$ star-forming galaxy-galaxy pairs obtained by LRIS (Steidel et al., 2010). The rest-frame EWs at three different impact parameters $\langle b \rangle = 31, 63, \text{ and } 103 \text{ kpc}$ are obtained by integrating over the corresponding stacked spectra of 42, 164, and 306 background galaxies, respectively. In addition, the EW at $b \sim 0$ is also estimated from the DTB spectra of all the foreground galaxies. We adopt the values given in Table 4 of Steidel et al. (2010) for C II $\lambda 1334$ for our modeling.

Joint Modeling of Two Datasets

To self-consistently model the DTB spectrum and the EW vs. b profile from two samples at different redshifts, we first check whether any correction needs to be applied to the datasets. We integrate the composite DTB C II $\lambda 1334$ absorption line profile of the $z \sim 3$ LBG sample to derive a rest-frame EW ($1.57 \pm 0.03 \text{ \AA}$) and compare with the average rest-frame EW at $b \sim 0$ measured from the foreground galaxies of the $z \sim 2$ star-forming galaxy sample ($1.72 \pm 0.02 \text{ \AA}$). We then apply a correction factor $f_{\text{corr}} = 1.57/1.72 = 0.91$ to the three EWs measured at $b > 0$. In this way, we can model the two different datasets jointly as if they were both obtained at $z \sim 3$. We note that the joint modeling we perform here is somewhat expedient; ideally one should do joint modeling on a sample with both $b = 0$ and $b > 0$ observations self-consistently.

⁶Ideally, one could also model the stacked absorption line profiles observed at different impact parameters. Nevertheless, we find that the uncertainties of such stacked line profiles in Steidel et al. (2010) are too large to yield any significant constraints on the model parameters. We are currently working on obtaining high-quality absorption line profiles at different impact parameters for our future modeling.

Table 7.1: Definitions and priors of the free parameters of ALPACA used to perform joint fitting.

Parameter (1)	Definition (2)	Prior Range (3)
A_{ISM}	Amplitude of the ISM absorption component	[0, 1]
σ_{ISM} (km s ⁻¹)	Standard deviation of the ISM absorption component	[50, 200]
$\log F_{\text{V}}$	Clump total volume filling factor	[-4.0, -0.5]
\mathcal{V} (km s ⁻¹)	Clump asymptotic outflow velocity	[300, 2000]
α	Power-law index in the clump acceleration force profile	[1.05, 2]
γ	Power-law index in the clump number density / covering fraction profile	[-5, 5]

Notes. The definitions and prior ranges of the free parameters of ALPACA used to fit the composite DTB C II $\lambda 1334$ spectrum and the EW vs. b profile jointly. The columns are: (1) parameter name; (2) parameter definition; (3) prior range of the parameter.

In addition, we assume that there is a non-outflowing ISM component that also contributes to absorption on top of the clumpy, outflowing CGM component described above (Steidel et al., 2010). The ISM absorption component is assumed to be a Gaussian centered at $v = 0$: $I_{\text{abs,ISM}} = A_{\text{ISM}}e^{-v^2/2\sigma_{\text{ISM}}^2}$, where A_{ISM} and σ_{ISM} are the amplitude⁷ and standard deviation of the absorption, respectively. Note that σ_{ISM} and $\sigma_{\text{cl,rand}}$ are two independent parameters that characterize the gas velocity dispersion in the ISM and CGM, respectively.

To reduce the dimensionality of the parameter space, we take into account that the typical stellar mass of the $z \sim 3$ LBG sample is $M_{\star} \sim 10^{9.7} M_{\odot}$ (Pahl et al., 2022). Using the stellar mass-halo mass relation from Moster et al. (2010) and the concentration-halo mass relation from Dutton et al. (2014), such a stellar mass corresponds to⁸ a virial mass of the halo $M_{\text{vir}} \sim 10^{12} M_{\odot}$, a virial radius $r_{\text{vir}} \sim 76$ kpc, and a concentration parameter $c \sim 8.3$. For simplicity, in the model, we assume the halo radius $r_{\text{h}} = 100$ kpc and the clump launch radius $r_{\text{min}} = 1$ kpc. We remind the readers that the results are not sensitive to these choices.

We further assume that the clump radius $R_{\text{cl}} = 100$ pc (Zahedy et al., 2019), clump C+ column density⁹ $N_{\text{C+,cl}} = 10^{15} \text{ cm}^{-2}$ (Gatkin et al., 2022), clump Doppler parameter $b_{\text{D}} = 15 \text{ km s}^{-1}$ (i.e., moderate internal turbulence), clump radial velocity

⁷More specifically, A_{ISM} denotes the fraction of continuum flux density attenuated by the ISM at $v = 0$.

⁸We have adopted $H_0 = 70 \text{ km s}^{-1} \text{ Mpc}^{-1}$, $\Omega_{\text{m},0} = 0.3$ and $\Omega_{\Lambda,0} = 0.7$.

⁹We stress that fixing $N_{\text{C+,cl}} = 10^{15} \text{ cm}^{-2}$ a pragmatic choice – due to the high dimensionality of the parameter space, we are currently unable to explore the potential degeneracy between $N_{\text{C+,cl}}$ and other parameters by adding the clump column density as an additional free parameter in our fitting. Such a choice yields a satisfactory fit to the data, but it may not be the only solution.

dispersion¹⁰ $\sigma_{\text{cl,rand}} = 120 \text{ km s}^{-1}$, which is close to the largest observed nebular emission line widths but slightly smaller than $1/\sqrt{3}$ of the circular velocity of the halo that we consider¹¹. As a result, the ALPACA model used to jointly fit the composite DTB C II $\lambda 1334$ spectrum and the EW vs. b profile contains six parameters in total: the amplitude of the ISM absorption component A_{ISM} , the standard deviation of the ISM absorption component σ_{ISM} , the total clump volume filling factor F_V (Eq. 7.21), the clump asymptotic outflow velocity \mathcal{V} (Eq. 7.16), the power-law index in the clump acceleration force profile¹² α (Eq. 7.16), and the power-law index in the clump number density (or covering fraction) γ (Eq. 7.21).

We use the nested sampling package `dynesty` (Skilling, 2004; Skilling, 2006; Speagle, 2020) in our fitting pipeline to map the posterior in such a multi-dimensional parameter space and find the best-fit parameters. At each sampled point in the parameter space, a model spectrum is calculated semi-analytically on-the-fly and convolved with the LRIS line spread function (LSF) with $\sigma \simeq 100 \text{ km s}^{-1}$ before being compared to the input observed spectrum, and three EWs at $b = 33, 66, \text{ and } 99$ kpc are also calculated to be compared with the three observed EWs at $b > 0$ correspondingly. The likelihood of each sampled point is the product of the likelihoods of the model for the DTB spectrum and the EW vs. b profile:

$$\begin{aligned} \mathcal{L}(A_{\text{ISM}}, \sigma_{\text{ISM}}, F_V, \mathcal{V}, \alpha, \gamma) &= \prod_{i=1}^{\mathcal{N}} \ell_{i,\text{DTB}}(A_{\text{ISM}}, \sigma_{\text{ISM}}, F_V, \mathcal{V}, \alpha, \gamma) \\ &\times \prod_{j=1}^3 \ell_{j,\text{EW}}(A_{\text{ISM}}, \sigma_{\text{ISM}}, F_V, \mathcal{V}, \alpha, \gamma) \end{aligned} \quad (7.25)$$

where $\ell_{i,\text{DTB}}$ ($\ell_{j,\text{EW}}$) is the probability that the i -th (j -th) predicted DTB flux density (EW) is drawn from the posterior distribution given by the observed value and its uncertainty. Upper limit measurements are treated as $1\text{-}\sigma$ detections. Each fitting run yields a posterior probability distribution function (PDF) of the six free model parameters. The uncertainties in the fitted parameters are determined as cer-

¹⁰Note that here $\sigma_{\text{cl,rand}}$ is the 1D macroscopic velocity dispersion among the clumps, rather than the velocity dispersion within an individual clump (which is characterized by the Doppler parameter b_D).

¹¹Note that in addition to gravitationally induced turbulence, the differential acceleration of the clumps can also contribute to the velocity dispersion (Nikolis and Gronke, in preparation).

¹²Owing to the functional form of the radial outflow velocity profile, we enforce a lower bound larger than 1 for α . We have verified that choosing a smaller $\alpha > 1$ value for the lower bound does not affect the results. Setting the lower bound to less than 1 will change the functional form of $v_{\text{cl,out}}(r)$ and is beyond the scope of this work; we plan to explore such possibilities in our future work.

tain quantiles (e.g., 16% – 84%, or 1- σ confidence intervals) of the samples in the marginalized PDF.

The priors of the parameters used for fitting are listed in Table 7.1. In Figure 7.5, we present the best-fit parameters of the fitting run and the posterior PDF. We also present the best-fit DTB model absorption line profile, EW vs. b profile, and the clump radial outflow velocity profiles in three subpanels.

Interpreting the Modeling Results

We hereby examine the best-fit parameters of the model to understand the corresponding physical scenario. In the best-fit model, the ISM component is preferred to contribute significantly to the absorption near the line center, with a standard deviation of $\sigma_{\text{ISM}} \sim 100 \text{ km s}^{-1}$. Such a value is consistent with the nebular emission line widths convolved with the instrumental LSF. As for the CGM component, the clumps are preferred to be highly non-volume-filling ($F_V \simeq 3 \times 10^{-3} \ll 1$), which corresponds to $f_c = \frac{3}{2} F_V \frac{r_h - r_{\text{min}}}{R_{\text{cl}}} \simeq 4$ clumps with $R_{\text{cl}} \sim 100 \text{ pc}$ along each radial sightline. Such an f_c value implies that the halo is essentially fully covered by clumps to an external observer, as the likelihood for a radial sightline to contain zero clumps is $\sim e^{-4} < 2\%$. (see Eq. 7.34 and 7.35 in Section 7.6).

As shown in Figure 7.5, the clump radial velocities are preferred to be a superposition of outflow and velocity dispersion. The outflowing component has a rapid acceleration phase ($r/r_{\text{min}} \lesssim 5$) towards a maximum outflow velocity of $v_{\text{out,max}} \sim 400 \text{ km s}^{-1}$ and then gradually decelerates until $r/r_{\text{min}} \sim 100$. The location of the absorption trough basically corresponds to $-v_{\text{out,max}}$, because the velocity gradient near $v = v_{\text{out,max}}$ is close to zero and the number of clumps that provide resonant or nearly resonant absorption at this velocity is the largest. The broad wings of the CGM absorption profile (especially on the blue side of the trough), however, are due to the perturbation on the clump outflow by a velocity dispersion of $\sigma_{\text{cl,rand}} = 120 \text{ km s}^{-1}$. The total clump radial velocities range from $\sim -250 \text{ km s}^{-1}$ to $\sim +700 \text{ km s}^{-1}$, which is slightly narrower than the velocity range where significant absorption is seen ($v_{\text{obs}} \sim -800 - 300 \text{ km s}^{-1}$), because (1) the non-resonant absorption of clumps with $b_D = 15 \text{ km s}^{-1}$ is accounted for; (2) the model spectrum is smoothed with $\sigma \simeq 100 \text{ km s}^{-1}$.

The best-fit power-law index in the clump acceleration force profile, $\alpha \simeq 1.3$, is consistent with the expected scaling ($\alpha = 4/3$) for cool clumps of constant mass that are in pressure equilibrium with a hot wind (Steidel et al., 2010). The power-

law index in the clump number density or covering fraction, γ , is preferred to be $\simeq 1$, which corresponds to a relatively steep decrease with radius. In general, at large r , the clump number density is expected to decrease due to the increase of the halo volume and the destruction of cold gas. On the other hand, the clumps are expected to expand in size due to the decrease in the pressure of the confining hot medium in the outer halo or grow due to various mixing and cooling processes. Our modeling suggests that the effect of the former physical process is more dominant over the latter.

Finally, we performed a fitting run by only fitting the DTB spectrum without using the EW measurements at $b > 0$. We find that in this case, γ becomes poorly constrained, yet the values of the other five free parameters remain basically the same. Such an experiment emphasizes the importance of incorporating the information about the absorption at $b > 0$, which is to help constrain the radial profile of the clump number density and covering fraction.

Parameter Degeneracies

As is shown in the posterior distribution in Figure 7.5, there are a number of significant degeneracies between the parameters of the ALPACA model. Here we discuss them as follows:

- A_{ISM} and F_{V} : These two parameters are anti-correlated, as they contribute to the total absorption by modulating the amplitude of the ISM component and the clump covering fraction of the CGM component, respectively.
- A_{ISM} and \mathcal{V} : These two parameters are positively correlated, as increasing A_{ISM} effectively adds more absorption around the line center and shifts the trough towards less negative velocities, whereas increasing \mathcal{V} shifts the trough towards more negative velocities (see Figure 7.4 in Section 7.4).
- \mathcal{V} and α : These two parameters are anti-correlated, as a larger \mathcal{V} increases the maximum clump outflow velocity, whereas a smaller α decreases the maximum clump outflow velocity (assuming \mathcal{V} is fixed; see Figure 7.3 in Section 7.2). Such a degeneracy also translates to an anti-correlation between A_{ISM} and α .
- F_{V} and γ : These two parameters are anti-correlated, as increasing F_{V} or decreasing γ while keeping other parameters fixed results in an increase in the

clump covering fraction and hence the total amount of absorption (see Eq. 7.21 and Figure 7.4).

The parameter degeneracies of the ALPACA model may be broken with additional modeling or observations. For example, Ly α emission modeling can be used to further constrain \mathcal{V} and α and help break corresponding degeneracies, as the clump kinematic parameters are strongly correlated with particular Ly α spectral features, e.g., the location of the double peaks and the blue-to-red peak ratio (Li et al. 2022b; Li et al. 2021; Li et al. 2022a; Erb et al. 2023).

Model Anatomy: Where Does the Absorption Come from in the CGM?

In ALPACA, since significant clump velocity dispersion is accounted for and there is no simple one-to-one mapping between the velocity space and the real space, it is not straightforward to describe where the majority of the absorption originates from. Therefore, here we zoom in on the internal structure of the model and reveal the relative contributions to the total absorption from the clumps located at different radii in the CGM. We examine three observed velocities in the DTB absorption line profile: $v_{\text{obs}} = +100, -200, \text{ and } -500 \text{ km s}^{-1}$.

As shown by Eq. (7.1), the ‘‘attenuation’’ factor of each shell, namely the fraction of flux density absorbed by the clumps, is given by $C_f(r)(1 - e^{-\tau(r)})$, where $C_f(r)$ and $\tau(r)$ are the clump covering fraction and optical depth at r , respectively. In Figure 7.6, we plot the probability density distributions of the normalized galactocentric radii of the clumps, r/r_{min} , weighted by the attenuation factor $C_f(r)(1 - e^{-\tau(r)})$ at three observed velocities. In this way, we can clearly see where the clumps contribute most to the total absorption in the CGM.

In Figure 7.6, we see that at all three different velocities, the largest contribution to the total absorption comes from $r/r_{\text{min}} \sim 1$. This is because in the best-fit model, $C_f(r) \propto n_{\text{cl}}(r) \propto r^{-1}$, i.e., the clump number density or covering fraction peaks at $r/r_{\text{min}} \sim 1$ and decreases fairly significantly with radius. For $v_{\text{obs}} = -500 \text{ km s}^{-1}$, the probability density distribution decreases monotonically with radius, and the majority of absorption comes from $r/r_{\text{min}} \lesssim 40$, within which the total velocity of the clumps is able to reach the corresponding resonant velocity $v_{\text{cl}} = 500 \text{ km s}^{-1}$. For $v_{\text{obs}} = -200 \text{ km s}^{-1}$, the contribution to the total absorption comes from all over the halo. For $v_{\text{obs}} = +100 \text{ km s}^{-1}$, the majority of absorption comes from $r/r_{\text{min}} \sim 1$ and $r/r_{\text{min}} \gtrsim 30$, whereas the contribution within $1 < r/r_{\text{min}} < 30$ is negligible, although the clump number density is high. This is because the only location for the

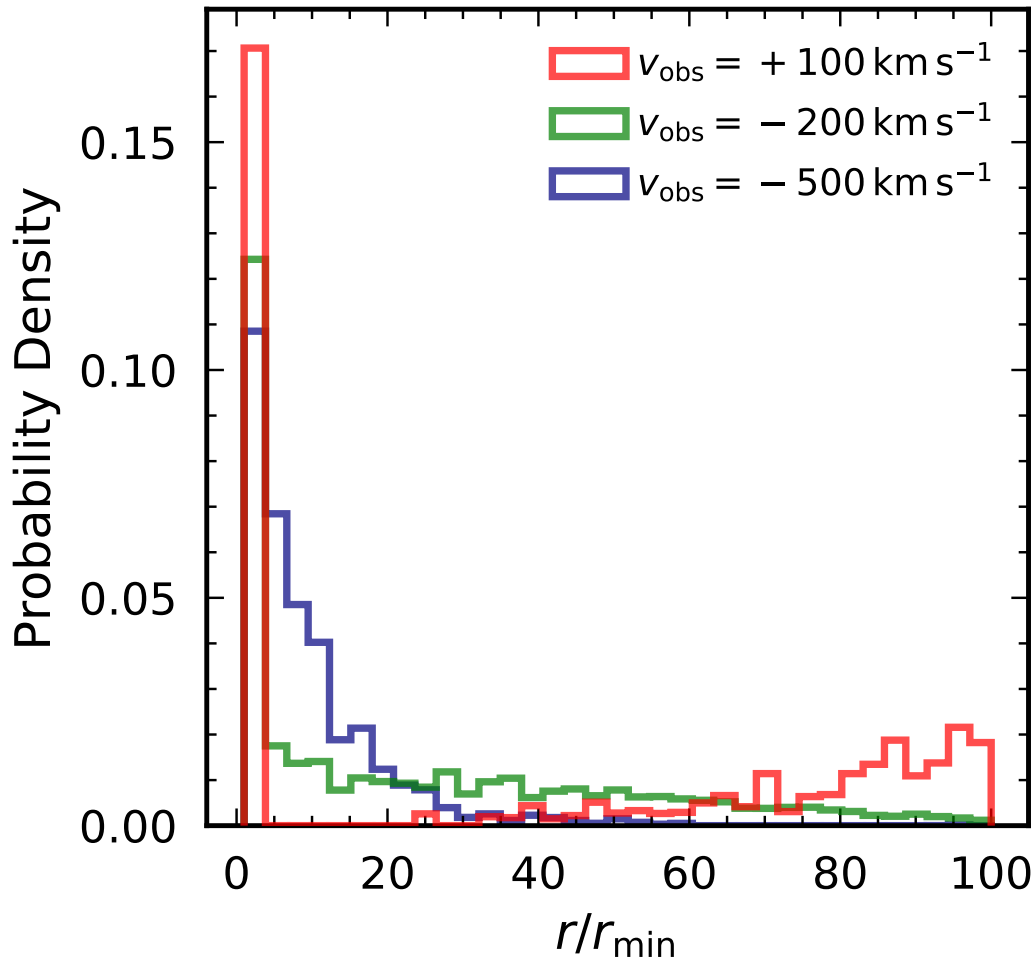


Figure 7.6: **Probability density distribution of the normalized galactocentric radii of the clumps, r/r_{\min} , weighted by the attenuation factor $C_f(r)(1 - e^{-\tau(r)})$ at three different observed velocities.** For $v_{\text{obs}} = -500 \text{ km s}^{-1}$, the probability density distribution decreases monotonically with radius, and the majority of absorption comes from $r/r_{\min} \lesssim 40$. For $v_{\text{obs}} = -200 \text{ km s}^{-1}$, the contribution to the total absorption comes from all over the halo. For $v_{\text{obs}} = +100 \text{ km s}^{-1}$, the majority of absorption comes from $r/r_{\min} \sim 1$ and $r/r_{\min} \gtrsim 30$, whereas the contribution within $1 < r/r_{\min} < 30$ is negligible.

clumps to have a net negative total velocity $v_{\text{tot}} = -100 \text{ km s}^{-1}$ is where the clump kinematics are random velocity-dominated; i.e., $v_{\text{out}} \simeq 0$ and $\sigma_{\text{cl,rand}} \simeq 120 \text{ km s}^{-1}$, which is best satisfied at $r/r_{\text{min}} \sim 1$ and ~ 100 .

The fact that the attenuation factor is highly velocity-dependent suggests that the clump optical depth $\tau(r)$ is still the dominant contributor to the total absorption, rather than the clump covering fraction $C_f(r)$. Overall, compared to the models that do not account for significant clump random motion, ALPACA reveals a physical scenario where the absorption observed at a particular velocity is contributed by the clumps from a fairly broad range of radii, rather than from a single point of resonance. We will investigate these differences further in Section 7.7.

Alternative Clump Radial Outflow Velocity Profiles

Although the formalism of the ALPACA model is general, any practical implementation for the purpose of application of the model will inevitably restrict the model to particular physical regimes. For example, the kinematic model of the clump outflow that we explored in Section 7.2 (Eq. 7.12) is highly simplistic and model-dependent, and will not capture all possible radial profiles of clump outflows. Therefore, here we explore a different type of radial profile for clump outflow velocities and see whether it can also provide a reasonable fit to the observational data.

We consider a scenario where the gravitational deceleration force is weak and negligible compared to the power-law acceleration force. In this case, the kinematic equation of an outflowing clump, is simply given by:

$$\frac{dv_{\text{cl,out}}(r)}{dt} = Ar^{-\alpha} \quad (7.26)$$

which can be solved as:

$$v_{\text{cl,out}}(r) = \mathcal{V} \left(1 - \left(\frac{r}{r_{\text{min}}} \right)^{1-\alpha} \right)^{1/2} \quad (7.27)$$

where we have replaced A with $\mathcal{V} (\equiv \sqrt{2Ar_{\text{min}}^{1-\alpha}/(\alpha-1)})$, the asymptotic clump outflow velocity at $r \rightarrow +\infty$. Eq. (7.27) is exactly the radial velocity profile used by Steidel et al. (2010). We find that such a monotonically increasing radial outflow velocity profile is also able to yield a reasonable fit to the composite C II $\lambda 1334$ DTB spectrum and the EW vs. b profile modeled in Section 7.5 with the following best-fit parameters: $A_{\text{ISM}} = 0.46_{-0.06}^{+0.05}$, $\sigma_{\text{ISM}} = 103_{-12}^{+14} \text{ km s}^{-1}$, $\log F_V = -2.66_{-0.04}^{+0.04}$, $\mathcal{V} =$

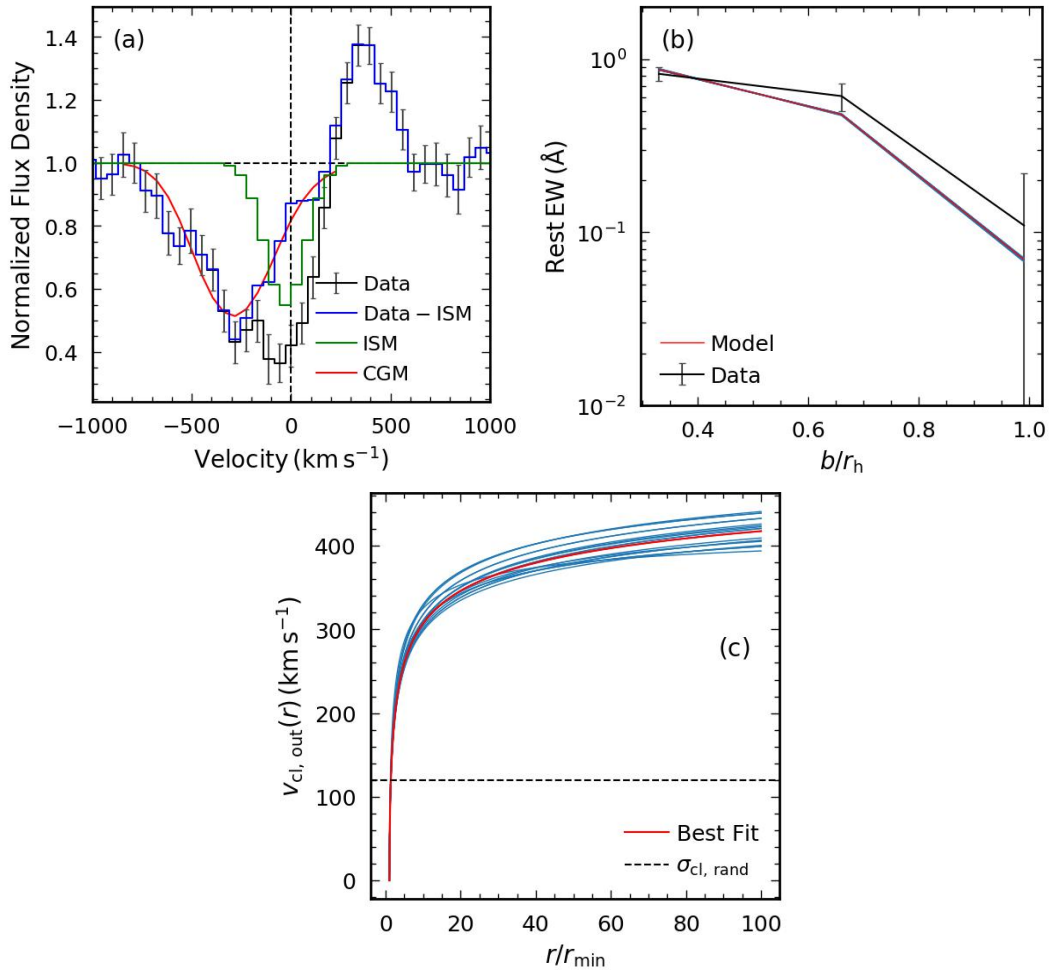


Figure 7.7: **Results of joint modeling using an alternative clump outflow velocity profile assuming gravitational deceleration is negligible (see Eq. 7.26).** Panel (a) shows the best-fit model to the DTB absorption line profile. The non-outflowing ISM component and the outflowing CGM component are shown in green and red colors, respectively. Panel (b) shows the best-fit model (red) to the observed EW vs. b profile (black) at three different impact parameters: $b/r_h \simeq [\frac{1}{3}, \frac{2}{3}, 1]$. Also shown are twenty models with the highest likelihoods (blue). Panel (c) shows the clump outflow velocity profiles of twenty models (blue) with the highest likelihoods in the parameter space, as well as the best-fit outflow velocity profile (red). The level of the clump radial velocity dispersion ($\sigma_{cl, rand} = 120 \text{ km s}^{-1}$) is shown by a horizontal black dashed line.

$452_{-90}^{+239} \text{ km s}^{-1}$, $\alpha = 1.30_{-0.20}^{+0.40}$, $\gamma = 1.05_{-0.09}^{+0.08}$, $\log N_{\text{C}^+, \text{cl}} = 15$, $\sigma_{\text{cl, rand}} = 120 \text{ km s}^{-1}$. In Figure 7.7, we show the best-fit models and the $v_{\text{cl, out}}(r)$ profiles of this joint fitting run.

Such an experiment reminds us that there is still some freedom in the clump radial velocity distribution that may not be fully constrained by the joint fitting of the DTB spectrum and the EW vs. b profile. Nonetheless, these different radial velocity distributions do share one thing in common: they can all be decomposed into two velocity components – a velocity dispersion and a radially varying outflow, the latter of which is smaller by several hundred km s^{-1} than the maximum velocity of absorption. One promising way to further constrain the clump radial velocity profile is to incorporate spatially resolved $\text{Ly}\alpha$ emission modeling, assuming that the gas that produces LIS absorption lines is also responsible for producing extended $\text{Ly}\alpha$ emission via resonant scattering. As the $\text{Ly}\alpha$ blue-to-red peak flux ratio is sensitive to the local clump outflow velocity, one can distinguish whether the clump outflow has decelerated significantly or remains at a high speed at large radii by modeling the $\text{Ly}\alpha$ profiles observed at the halo outskirts (Erb et al., 2023). Recently work on mapping the 2D line-of-sight kinematics via $\text{Ly}\alpha$ absorption may also help break the degeneracy (Chen et al., 2020). Future endeavors focused on statistically mapping the spatial variation of $\text{Ly}\alpha$ and LIS absorption lines using galaxy-QSO or galaxy-galaxy pairs across various redshifts will also be beneficial.

7.6 Covering and Volume Filling Parameters of the Cool Gas

The physical properties of the “cool” ($T \sim 10^4 \text{K}$) gas in a galactic environment, which is responsible for producing the UV absorption lines of the low ions, have been studied extensively in recent years, both theoretically and observationally. Notably, McCourt et al. (2018) first carried out a comprehensive analysis by combining hydrodynamic simulations with observations and summarized with the following physical picture for the cool gas: a mist or fog of cloudlets with a large area covering factor¹³ $f_c \gg 1$ but a small total volume filling factor $F_V \ll 1$ (see also Liang et al. 2020). This physical picture is supported by a number of observational studies, e.g., Stocke et al. (2013) report the volume filling factor of the cool clouds in the CGM of a sample of low- z galaxies is on average a few percent (see also Keeney

¹³Note that we have used a different terminology from McCourt et al. (2018). In this paper, we use the area covering *factor* to refer to the average number of cloudlets intercepted per line of sight, and the covering *fraction* to refer to the fraction of area covered by the clumpy gas. The volume filling fraction defined in McCourt et al. (2018) has the same meaning as the volume filling factor defined in this work.

et al. 2017), and Zahedy et al. (2019) find that the mean volume filling factor of the cool gas is about 10^{-3} for massive ellipticals at $z \sim 0.4$ ¹⁴. On the other hand, a close-to-unity coverage by the cool gas has been observed for the CGM halos of both galaxies and luminous quasars (e.g., Prochaska et al. 2013; Cantalupo et al. 2014; Hennawi et al. 2015; Borisova et al. 2016; Cai et al. 2017; Zahedy et al. 2019; Rudie et al. 2019).

Before we move on, it is instructive to clarify the definition of the covering fraction C_f , the covering factor f_c , and the volume filling factor F_V of the cool gas. All these three parameters can be evaluated as either a global quantity of a halo or a radially varying profile as a function of radius or velocity.

The expression for the covering fraction C_f as a function of radius has been derived in Eq. (7.3). As for f_c and F_V , considering the case of an idealized clumpy medium that only consists of spherical clumps and derived a relation between the covering factor and the volume filling factor. Specifically, the covering factor *at a particular radius*, $f_c(r)$, is given by (Dijkstra et al., 2012):

$$f_c(r) = n_{\text{cl}}(r)\sigma_{\text{cl}}(r) = n_{\text{cl}}(r)\pi R_{\text{cl}}^2(r) \quad (7.28)$$

where r is the radial location of the clumps, $n_{\text{cl}}(r)$ is the number density of the clumps and $\sigma_{\text{cl}}(r) = \pi R_{\text{cl}}^2(r)$ is the geometric cross-section of a clump of radius $R_{\text{cl}}(r)$. $f_c(r)$ has the units of length^{-1} and is analogous to the opacity $\kappa(r)$ in a homogeneous medium.

The volume filling factor *at a particular radius*, $F_V(r)$, is given by:

$$F_V(r) = n_{\text{cl}}(r)V_{\text{cl}}(r) = n_{\text{cl}}(r)\frac{4}{3}\pi R_{\text{cl}}^3(r) \quad (7.29)$$

where $V_{\text{cl}}(r) = \frac{4}{3}\pi R_{\text{cl}}^3(r)$ is the geometric volume of a clump with radius $R_{\text{cl}}(r)$. Comparing with Eq. (7.3) and (7.28), we have:

$$F_V(r) = \frac{4}{3}R_{\text{cl}}(r)f_c(r) \quad (7.30)$$

Note that although the above relation is derived under the assumption of spherical clumps, it also holds (modulo a geometric correction factor) for a more general

¹⁴See also Prochaska et al. (2019), who use FRB constraints and derive that the volume filling factor of the clumpy cool gas is $< 10^{-4}$ for a massive galaxy at $z \sim 0.4$.

geometric configuration of the clumpy gas. This is because $F_V(r)$ and $f_c(r)$ will always be proportional and different by a factor of $V_{cl}(r)/\sigma_{cl}(r)$, the clump volume-to-cross-section ratio.

One can further consider the following corresponding spatially integrated quantities:

- The *total* volume filling factor of the halo, F_V , is given by:

$$F_V = \frac{1}{V_h} \int_{r_{\min}}^{r_h} F_V(r) dV(r) \quad (7.31)$$

- The *integrated* gas covering factor, f_c , i.e., the mean number of clumps along a line of sight at impact parameter b , is given by:

$$f_c(b) = 2 \int_b^{r_h} \frac{r dr}{\sqrt{r^2 - b^2}} f_c(r) \quad (7.32)$$

In particular, at $b = 0$ (“down the barrel”), f_c is given by:

$$f_c(0) = 2 \int_{r_{\min}}^{r_h} f_c(r) dr = \frac{3}{2} \int_{r_{\min}}^{r_h} \frac{F_V(r)}{R_{cl}(r)} dr \quad (7.33)$$

which, in the special case where both $F_V(r)$ and $R_{cl}(r)$ are constant, can be simplified to:

$$f_c(0) = \frac{3}{2} F_V \frac{r_h - r_{\min}}{R_{cl}} \quad (7.34)$$

It can be seen that in the limit of $r_h/R_{cl} \gg 1$, even a small $F_V \ll 1$ can yield a large $f_c(0) \gg 1$ (McCourt et al., 2018).

- The *integrated* gas covering fraction of the halo, C_f , has the physical meaning of the fraction of sightlines at a particular impact parameter intercepted by at least one clump to an external observer. The Poisson probability of having sightlines at impact parameter b that contain zero clumps is:

$$P(N_{\text{clump}} = 0 | f_c(b)) = e^{-f_c(b)} \quad (7.35)$$

hence $C_f(b) = 1 - P(N_{\text{clump}} = 0 | f_c(b)) = 1 - e^{-f_c(b)}$.

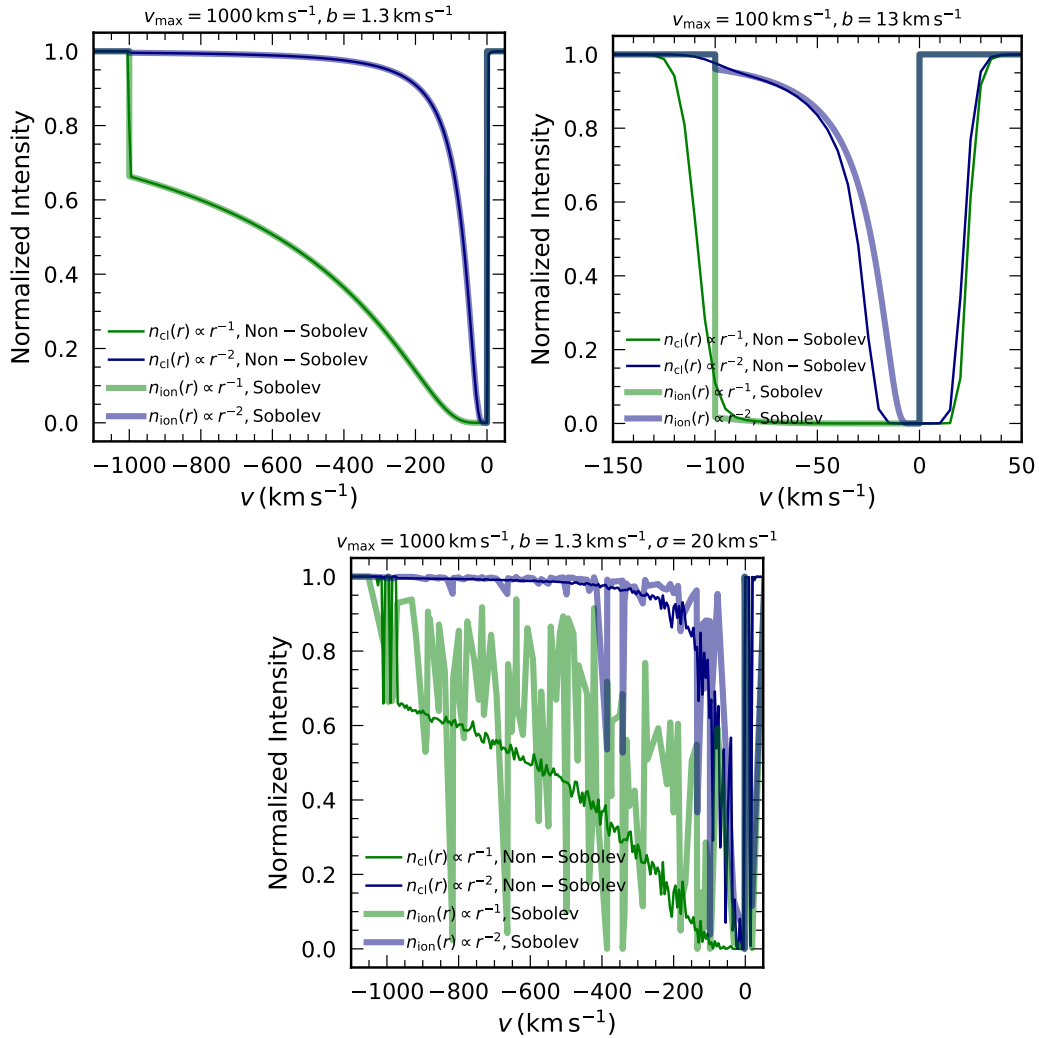


Figure 7.8: **Experiments designed to demonstrate the difference between the Sobolev and non-Sobolev modeling.** We consider a homogeneous medium vs. an extremely clumpy medium where the covering fraction $C_f(r) \simeq 1$ everywhere. *Left:* If the radial velocity gradient is large, the Sobolev models (thick curves) are consistent with the corresponding non-Sobolev models (thin curves), suggesting that the Sobolev approximation works in this regime. Two sets of models with two different number density profiles of the ions or clumps ($n(r) \propto r^{-1}$ and r^{-2}) are shown in green and blue, respectively. *Middle:* If the radial velocity gradient is small, the Sobolev models underpredict the amount of absorption on both the red and blue sides of the line center, suggesting that the Sobolev approximation starts to break down. *Right:* If the radial velocity gradient is large but there is a small random velocity ($\sigma = 20 \text{ km s}^{-1}$), the absorption line profiles predicted by the Sobolev approximation quickly become chaotic and noisy due to the stochasticity added to the velocity gradient, whereas the profiles predicted by non-Sobolev modeling remain basically unperturbed and stable.

7.7 Sobolev vs. Non-Sobolev

In this section, we explore the effect of the Sobolev approximation in the context of a clumpy galactic environment. The idea of the Sobolev approximation is that if the width of the absorption cross section in velocity space is much smaller than the change in the velocity of the absorbing gas within a short distance, the absorption at each velocity can be approximated as that absorption that only happens at the resonance point. Traditionally, the Sobolev approximation is usually applied to a continuous medium, such as a homogeneous wind (e.g., Prochaska et al. 2011a; Scarlata et al. 2015; Carr et al. 2022b). We hereby examine the use of the Sobolev approximation in a clumpy medium, and present a quantitative comparison between Sobolev and non-Sobolev modeling.

A Homogeneous Medium vs. An Extremely Clumpy Medium

In a homogeneous expanding wind, the Sobolev approximation gives the line optical depth at a given radius $\tau_S(r)$, which is solely determined by the gas number density and velocity gradient at that radius (Sobolev, 1960; Lamers et al., 1999):

$$\tau_S(r) = \frac{\pi e^2}{m_e c} f_{\text{line}} \lambda_{\text{line}} n_l(r) \left| \frac{dv}{dr} \right|_r^{-1} \quad (7.36)$$

where n_l is the number density of the relevant ion at the lower level of the transition. The essence of Eq. (7.36) is that it reduces the interaction between the photons and the ions to a *local* process, which simplifies the calculation of optical depth (which is generally an integral over distance) to an evaluation of the properties of the absorbing gas at a single point. The DTB absorption line profile can be calculated as:

$$I(v) = e^{-\tau_S(r(v))} \quad (7.37)$$

where $r(v)$ is the relation between velocity and radius that expresses the optical depth (and hence the line intensity) as a function of velocity.

We compare this solution obtained for a homogeneous medium with a hypothetical extremely clumpy model, where the halo is fully filled with clumps. We calculate the absorption of this model in a non-Sobolev way, meaning that the clumps are separated into a series of concentric shells (as we did in Section 7.2) that all contribute to the absorption at a particular observed velocity, regardless of whether the absorption is resonant. To ensure a direct comparison with the corresponding ho-

homogeneous model, we assign the following column densities to a particular shell whose midplane is located at r :

$$N_{\text{ion,cl}} = n_l(r)d_{\text{shell}} \quad (7.38)$$

where $n_l(r)$ is the corresponding ion number density in the homogeneous medium in Eq. (7.36). As in an extremely clumpy medium, $C_f(r) \simeq 1$ everywhere, the escape probability of a photon observed at velocity $-v$ is simply given by:

$$P_{\text{esc}}(-v) = \prod_{i=1}^{N_{\text{shell}}} e^{-\tau_{\text{ion}}(v-v_i)} \quad (7.39)$$

Eqs. (7.38) and (7.39) can be combined with Eqs. (7.4) – (7.7) to derive the normalized absorption line intensity as a function of velocity, $I(v)$, for an extremely clumpy medium.

To compare Sobolev modeling in a homogeneous medium with non-Sobolev modeling in an extremely clumpy medium more quantitatively, we have designed several numerical experiments. For the sake of simplicity, we assign both the ions in the homogeneous medium and the clumps in the clumpy medium a radial outflow velocity profile that increases linearly with r :

$$v_{\text{out}}(r) = \frac{r - r_{\text{min}}}{r_{\text{h}} - r_{\text{min}}} v_{\text{max}} \quad (7.40)$$

where v_{max} is the maximum outflow velocity achieved at r_{h} . In this case, the radial velocity gradient, $dv_{\text{out}}/dr = v_{\text{max}}/(r_{\text{h}} - r_{\text{min}})$ is constant. For the fiducial model, we assume $n_l(r) = n_{l,0}(r/r_{\text{min}})^{-\gamma}$ and $n_{l,0} = 10^{-7} \text{ cm}^{-3}$.

We present the results in Figure 7.8. In each panel, two sets of models with $\gamma = 1.0$ and 2.0 are shown. In the left panel, we set $v_{\text{max}} = 1000 \text{ km s}^{-1}$ and $b_{\text{D}} = 1.3 \text{ km s}^{-1}$. Such a choice satisfies the “large velocity gradient” criterion derived by Carr et al. (2022b):

$$\frac{\eta}{\gamma} \gg \frac{b_{\text{D}}}{v_{\text{out}}(r)} \quad (7.41)$$

where η is the power-law index in the velocity scaling with r : $v_{\text{out}} \propto r^\eta$. For an outflow velocity profile that increases linearly with r , we have $\eta = 1$. In this case, the Sobolev and non-Sobolev models are fully consistent with each other, suggesting that the Sobolev approximation is working well.

However, in the middle panel, we show the models with a decreased v_{\max} of 100 km s^{-1} and an increased b_D of 13 km s^{-1} , which corresponds to a low velocity gradient scenario that does not satisfy Eq. (7.41) anymore. In this case, the Sobolev models underpredict the amount of absorption on both the red and blue sides of the line center, suggesting that the Sobolev approximation is starting to break down.

In the right panel, we keep the large velocity gradient by setting $v_{\max} = 1000 \text{ km s}^{-1}$ and $b_D = 1.3 \text{ km s}^{-1}$ but add a small random velocity ($\sigma = 20 \text{ km s}^{-1}$) to the ions and clumps. In this case, the absorption line profiles predicted by the Sobolev approximation quickly become chaotic and noisy due to the stochasticity added to the velocity gradient dv/dr . In contrast, the profiles predicted by non-Sobolev modeling remain basically unperturbed and stable. In short, these experiments have demonstrated that in a homogeneous medium or an extremely clumpy medium, the Sobolev approximation only works where the velocity gradient is sufficiently large and the random motion of the gas is negligible.

A Not-So-Clumpy ($F_V \ll 1$) Medium

In a realistic CGM, the clumps are likely to be non-volume-filling and hence there will be many holes in the medium that the photons can pass through freely. In this case, the Sobolev optical depth given by Eq. (7.36) can no longer be used directly, as the absorption now depends on both the clump optical depth and the clump covering fraction. In fact, unlike the ion number density $n_l(r)$ or the velocity gradient dv/dr , the clump covering fraction $C_f(r)$ is not simply a function of the local properties of the clumps at r . In order to calculate $C_f(r)$, one needs to know the number of clumps that contribute to the geometric coverage of a sphere with radius r , which requires specifying and integrating over a finite width for such a sphere. This is why it is necessary to use a series of shells to properly calculate the absorption in ALPACA; one can also see from Eq. (7.3) that $C_f(r)$ not only depends on $n_{\text{cl}}(r)$ and $R_{\text{cl}}(r)$, but also the shell width d ¹⁵.

However, it is still possible to utilize the idea of the Sobolev approximation in a non-volume-filling clumpy medium. One can imagine that if the radial velocity gradient of the clumps is sufficiently large, the clumps that are moving at non-resonant

¹⁵Strictly speaking, one can derive a $C_f(r)$ profile that is merely a function of r and independent of the shell width d . For example, Dijkstra et al. (2012) set $d = 2R_{\text{cl}}(r)$ and derived $C_f(r) \simeq \frac{4}{3}\pi n_{\text{cl}}(r)R_{\text{cl}}^3(r)$, which is essentially accounting for all the clumps that can possibly intersect the sphere at r . In ALPACA, however, the shell width is always chosen to be smaller than $R_{\text{cl}}(r)$, so that each clump may intersect multiple shells. In this case, we need to use the shell-width-dependent version of $C_f(r)$ (given by Eq. 7.3) to avoid multiple-counting the contribution of the clumps.

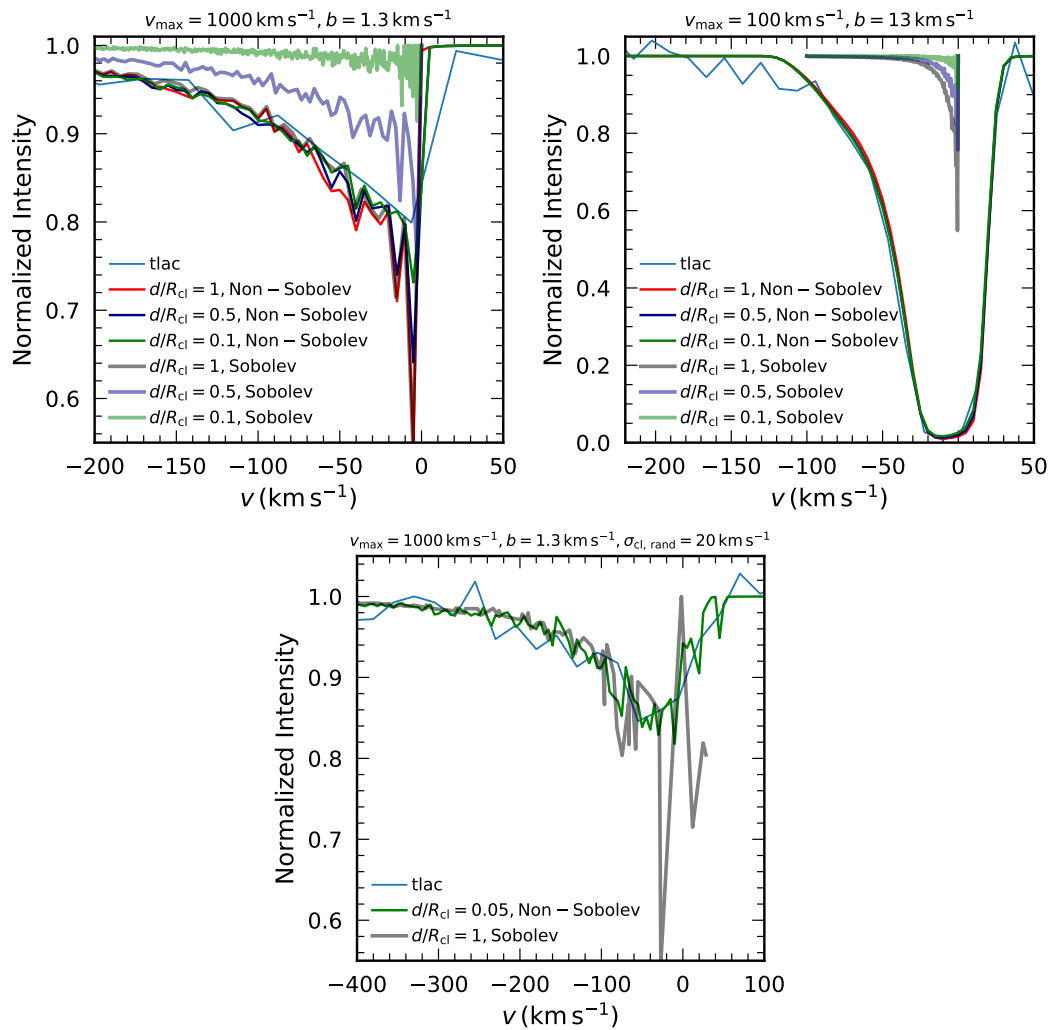


Figure 7.9: **Same as Figure 7.8, but for a non-volume-filling clumpy medium.** We consider a non-volume-filling clumpy medium that contains holes through which the photons can pass freely. *Left:* If the radial velocity gradient is large, the non-Sobolev models tend to converge to the Monte-Carlo simulations by t_{lac} as the number of shells increases (or equivalently, as d/R_{cl} decreases). However, the amount of absorption predicted by the Sobolev models (shown by thick curves) decreases as the number of clumps that produce resonant absorption at each velocity has decreased. Note that the $d/R_{\text{cl}} = 1$ Sobolev model is coincidentally consistent with the non-Sobolev models (see discussion in Section 7.7). *Middle:* If the radial velocity gradient is small, the Sobolev models always underestimate the amount of the absorption, regardless of the choice of the number of shells. *Right:* If the radial velocity gradient is large but there is a small random velocity ($\sigma_{\text{cl,rand}} = 20 \text{ km s}^{-1}$), the Sobolev model exhibits a significant deviation from the non-Sobolev model and the t_{lac} prediction, suggesting that the Sobolev approximation is breaking down.

velocities are shifted far away from resonance and will contribute negligibly to the absorption. In this case, we can possibly only account for resonant absorption and neglect all the non-resonant absorption, similar to how we applied the Sobolev approximation in a homogeneous medium. With regard to this, we similarly design several experiments to compare Sobolev and non-Sobolev modeling in such a non-volume-filling clumpy medium. In this regime, Monte-Carlo simulations from `tlac` can be conveniently performed at low computational costs to compare with the analytic models as an independent check.

We use the following set of parameters for the fiducial model: $F_V = 0.005$, $\log N_{\text{HI,cl}} = 14$, $\gamma = 2.0$, and $R_{\text{cl}} = 500 \text{ pc}$. We then assume the linearly increasing radial velocity profile as we do in Section 7.7. The non-Sobolev models are generated under the standard formalism of `ALPACA`, whereas the Sobolev models are generated with the same clump parameters, but we assume that the clumps only produce resonant absorption at one particular velocity. We present the results in Figure 7.9. In the left panel, we set $v_{\text{max}} = 1000 \text{ km s}^{-1}$ and $b_D = 1.3 \text{ km s}^{-1}$, i.e., a large velocity gradient for the clumps. We show that the model absorption line profiles predicted by `ALPACA` with an increasing number of shells (hence decreasing d/R_{cl} values) converge to the Monte-Carlo simulation result from `tlac`. This is because as the number of shells used in the model increases, the decrease of $C_f(r)$ in each shell is compensated for by the increase of the total number of shells. However, the amount of absorption predicted by the Sobolev approximation (shown by thick curves) decreases as the number of shells increases, which is simply because the number of clumps that provide resonant absorption at each velocity has decreased. In other words, the model will not converge under the Sobolev approximation. Interestingly, the Sobolev model with $d/R_{\text{cl}} = 1$ is actually consistent with the corresponding non-Sobolev model. We find that in this case, the velocity difference between two adjacent shells $\Delta v_{\text{cl}} = v_{\text{max}}/N_{\text{shell}}$ is about four times as large as the clump Doppler parameter b_D , which guarantees that at each observed velocity, only one shell can possibly contribute to the absorption and the other shells are all shifted far away from resonance. Therefore, in this case, whether or not using the Sobolev approximation gives the same absorption line profile.

Such a coincidental consistency between the Sobolev and non-Sobolev models is not always achievable. In the middle panel of Figure 7.9, we consider another scenario where $v_{\text{max}} = 100 \text{ km s}^{-1}$ and $b_D = 13 \text{ km s}^{-1}$, i.e., a low velocity gradient scenario. We find that in this case, the Sobolev models always underestimate the

amount of the absorption, regardless of the choice of the number of shells. This is because now Δv_{cl} cannot be much larger than b_{D} , so that at each observed velocity, there are always multiple shells that contribute to the absorption. Only accounting for resonant absorption and ignoring the other that happens near the line center will inevitably miss a significant portion of the absorption.

Lastly, in the right panel of Figure 7.9, we set $v_{\text{max}} = 1000 \text{ km s}^{-1}$ and $b_{\text{D}} = 1.3 \text{ km s}^{-1}$ while adding a small random motion to the clumps, $\sigma_{\text{cl,rand}} = 20 \text{ km s}^{-1}$. This time we only compare two models with the `tlac` simulation: a high-resolution non-Sobolev model with $d/R_{\text{cl}} = 0.05$ and a Sobolev model with $d/R_{\text{cl}} = 1$ – the one where the Sobolev approximation happens to predict the same line profile with the non-Sobolev models in the $\sigma_{\text{cl,rand}} = 0$ case. It can be seen that the non-Sobolev model is still consistent with the `tlac` simulations, but the Sobolev model exhibits a significant deviation from the other two models, suggesting that the Sobolev approximation is breaking down.

For the simple linear velocity profile given by Eq. (7.40), one can estimate the condition under which the Sobolev approximation may happen to predict the correct line profile in a non-volume-filling clumpy medium. The condition that is required for the Sobolev approximation to work is:

$$\Delta v_{\text{cl}} = v_{\text{max}}/N_{\text{shell}} \gg b_{\text{D}} \quad (7.42)$$

where N_{shell} is the number of shells used in the model. Note that the shell width cannot be chosen to be arbitrarily large; considering the clumps that can possibly contribute to the covering fraction of a shell at r should have their centers located within $r \pm R_{\text{cl}}$, $d/R_{\text{cl}} \lesssim 2$ should be satisfied. This condition translates to the following inequality:

$$N_{\text{shell}} \gtrsim \frac{r_{\text{h}} - r_{\text{min}}}{2R_{\text{cl}}} \quad (7.43)$$

Combining Eqs. (7.42) and (7.43), we have:

$$v_{\text{max}} \gg \frac{r_{\text{h}} - r_{\text{min}}}{2R_{\text{cl}}} b_{\text{D}} \quad (7.44)$$

We stress that in a realistic galactic environment (e.g., CGM), this requirement is especially difficult to satisfy, considering the following two constraints: (1) the clump

Doppler parameter b_D can be $10 \sim 20 \text{ km s}^{-1}$ due to moderate internal turbulence (e.g., Rudie et al. 2019; Qu et al. 2022), or even $\sim 100 \text{ km s}^{-1}$ if a “clump” is actually an ensemble of smaller droplets entrained by the hot medium (e.g., Gronke et al. 2022); (2) the clump size is often much smaller than the halo size (by two to three orders of magnitude, see, e.g., McCourt et al. 2018; Zahedy et al. 2019). Moreover, note that Eq. (7.44) is derived under the assumption that the clumps’ outflow velocity increases linearly with r . In reality, the clumps are usually accelerated to several hundred km s^{-1} at first, but the deceleration forces (e.g., due to gravity) start to dominate at large radii so that the velocity gradient of the clumps starts to decrease significantly. In addition, the velocity dispersion $\sigma_{\text{cl,rand}}$ of the clumps will effectively smooth out the clump velocity gradient. Therefore, the $\Delta v_{\text{cl}} \gg b$ condition is at best only satisfied within a narrow range of radii where the clumps are undergoing rapid acceleration and the Sobolev approximation may be applicable. In general, applying the Sobolev approximation to the entire halo will likely result in underestimating the amount of absorption significantly. When modeling the observed absorption line profiles, any attempt to only account for “local” absorption will generally overestimate the clump covering fraction, as the omission of non-resonant absorption needs to be compensated for by larger clump covering fractions at different radii.

7.8 Previous Work Modeling UV Absorption Lines

In this section, we briefly summarize previous work modeling UV absorption lines and compare it with ALPACA.

The Picket-Fence Model

One of the most widely used models for decoding UV absorption lines is the “picket-fence” model (e.g., Steidel et al., 2010; Heckman et al., 2011; Zackrisson et al., 2013; Jones et al., 2013; Borthakur et al., 2014; Alexandroff et al., 2015; Rivera-Thorsen et al., 2015; Erb, 2015; Vasei et al., 2016; Reddy et al., 2016; Rivera-Thorsen et al., 2017; Steidel et al., 2018; Gazagnes et al., 2018; Gazagnes et al., 2020), which assumes that the emitting source is partially covered by optically thick, clumpy gas material. Specifically, depending on whether dust is assumed to be present in the uncovered region (i.e., the “holes”), the normalized line intensity can be expressed as:

$$I_\lambda = 10^{-0.4k_\lambda E(B-V)} (C_f e^{-\tau_\lambda} + 1 - C_f) \quad (7.45)$$

with a uniform foreground dust screen, or:

$$I_\lambda = 10^{-0.4k_\lambda E(B-V)} C_f e^{-\tau_\lambda} + (1 - C_f) \quad (7.46)$$

if no dust is present in the uncovered region. In both cases, the observed photons escape either after being attenuated by the optically thick absorbing gas (the $C_f e^{-\tau_\lambda}$ term) or from the holes (the $1 - C_f$ term), and dust will provide additional attenuation to the spectrum.

The picket-fence model adopts a rather phenomenological prescription for the absorbing gas, as it parameterizes the effective absorption at each wavelength or velocity empirically with the gas covering fraction C_f and the effective optical depth τ_λ without considering the details of the interaction between the photons emitted at different frequencies and the atoms moving at different velocities. Depending on whether an individual line profile or a series of lines are fitted, the gas covering fraction C_f can be determined as either a function of velocity (e.g., Steidel et al. 2010; Jones et al. 2013; Rivera-Thorsen et al. 2015; Rivera-Thorsen et al. 2017) or as a wavelength-independent constant (e.g., Reddy et al. 2016; Steidel et al. 2018; Gazagnes et al. 2018; Gazagnes et al. 2020). In the former case, the Sobolev approximation (as explained in Section 7.8 below) is generally adopted, and some work has used empirical treatments to account for the internal differential velocity structure of the absorbing gas, e.g., Steidel et al. (2010) and Chisholm et al. (2016) both considered an accelerated radial outflow with slightly different analytic forms.

The Expanding Wind Model

Another major way of modeling the UV absorption lines is to assume a uniform, expanding wind of cool gas with radially varying densities and velocities (e.g., Prochaska et al., 2011a; Scarlata et al., 2015; Carr et al., 2018; Carr et al., 2021). This type of model accounts for the interaction between the emitted photons and moving atoms by using the Sobolev approximation (e.g., Sobolev 1960; Lamers et al. 1999), which assumes that the photons emitted at a given wavelength or velocity interact only with the outflowing gas at a single point of resonance in the reference frame of the gas. More specifically, the absorbing gas outflowing at v will only interact with the photons emitted at a frequency away from the line center by $\Delta\nu = -\frac{v}{c}\nu_0$. The outflowing gas will not have any effect on the photons that do not appear at resonance in the reference frame of the gas. Such an approximation holds when the radial velocity gradient of the clumps is much larger than the Doppler

parameter of the absorbing gas, but may not necessarily be valid otherwise (Carr et al., 2022b).

The expanding wind model can be used to predict absorption model spectra via either Monte Carlo RT simulations (e.g., Prochaska et al. 2011a) or semi-analytical calculations (e.g., Scarlata et al. 2015). The model can also be upgraded to account for more complex gas geometries, e.g., hemispherical or bi-conical (Prochaska et al., 2011a; Carr et al., 2018; Carr et al., 2021), as well as additional gas kinematics, e.g., inflows (Carr et al., 2022a). However, in general, the model assumes a homogeneous absorbing medium and does not account for the existence of holes or clumps in the outflow (Carr et al., 2022b).

Comparison Between ALPACA and Previous Models

We have identified the following differences between the results derived from modeling metal absorption lines using ALPACA and previous models:

- The gas covering fraction: in previous models, the gas covering fraction is either 1 (in a homogeneous medium, Scarlata et al. 2015), or constant (in a bi-conical medium, Carr et al. 2021), or a decreasing function with respect to r (in a clumpy medium, Steidel et al. 2010; Chisholm et al. 2016). The maximum gas covering fraction derived from these models is usually of order-of-unity. In non-Sobolev modeling, however, the derived clump covering fractions at different radii are generally much smaller than one. The halo is still “fully covered” by clumps to an external observer, in the sense that on average there are a few clumps along any sightline. However, the required number of clumps at a particular radius or moving at a particular velocity is much lower.
- The gas volume filling factor: previous models that assume a homogeneous, expanding wind correspond to a volume-filling gaseous medium. Whereas in ALPACA, the inferred clump volume filling factor is much smaller than 1. In this sense, the results predicted by ALPACA are more consistent with the most current physical picture of the cool gas in a galactic environment (e.g., McCourt et al. 2018; Gronke et al. 2018; Nelson et al. 2020; Fielding et al. 2022).
- The radial velocity of the absorbing gas: in previous models, the range of gas velocities strictly corresponds to the range of velocities where absorption is

seen. This means if the gas is purely outflowing, no redshifted absorption will be seen (Carr et al., 2022b). In ALPACA, however, we consider the superposition of clump outflow and clump velocity dispersion and account for all the non-resonant absorption, which makes it possible to have: (1) a maximum clump outflow velocity that is much smaller than the maximum absorption velocity (or the v_{90} parameter used by previous literature) by several hundred km s^{-1} ; (2) redshifted absorption without assuming the presence of external inflows. Moreover, in ALPACA, the clumps that contribute to the absorption observed at a particular velocity are not necessarily located all at the same radii; instead, they can be distributed at many different radial locations in the halo. In this sense, the gas absorption in ALPACA is more “democratic” than that in previous models.

7.9 Caveats and Outlook

In this section, we discuss several caveats that the readers should keep in mind when using ALPACA, as well as a number of possible applications of the model in the future.

Caveats

When we use ALPACA to predict DTB metal absorption line profiles, we only include the photons that travel radially and are not scattered by the clumps. Although along each sightline there are only a few clumps, the emergent absorption line profile represents the average frequency distribution of the photons that escape in all directions. In a real observation, the observed DTB absorption line profile represents the frequency distribution of the photons that emerge along the line of sight from a cylindrical region, whose radius is roughly the size of the ISM (i.e., a few kpc) and height is about the virial radius. One can estimate the number of clumps in such a cylindrical region:

$$N_{\text{cl,cyl}} \simeq \frac{F_{\text{V}} V_{\text{cyl}}}{V_{\text{cl}}} = \frac{F_{\text{V}} \pi r_{\text{cyl}}^2 r_{\text{h}}}{\frac{4}{3} \pi R_{\text{cl}}^3} \quad (7.47)$$

Taking $F_{\text{V}} = 10^{-3}$, $r_{\text{cyl}} = 2 - 3 \text{ kpc}$ ¹⁶, $r_{\text{h}} = 100 \text{ kpc}$ and $R_{\text{cl}} = 100 \text{ pc}$, we have $N_{\text{cl,cyl}} \simeq$

¹⁶Note that here we are considering the absorption against galaxies; for QSOs, r_{cyl} is much smaller and the number of clumps that contribute to the absorption along a sightline will be roughly $\sim f_{\text{c}}(b)$ (see Eq. 7.32), whose value is generally \sim a few in our model. Such a value is broadly consistent with recent observational measurements (e.g., Zahedy et al. 2019; Rudie et al. 2019; Churchill et al. 2020; Qu et al. 2022).

300 – 675. This is the estimated number of clumps that contribute to the absorption of the DTB spectrum of a galaxy. By comparing the model absorption line profiles predicted by ALPACA with the real DTB observations, we are essentially assuming the escape of photons is isotropic and the observed DTB profile is a representative sample of the frequency distribution of the escaped photons in all directions. Such an assumption may not be warranted if some of the galaxy’s properties are known to be angular asymmetric (e.g., if it exhibits a collimated outflow). We plan to account for such asymmetries in our future work.

In addition, in this work, we mainly explore an outflow-dominated kinematic profile for the clumps in the CGM of high- z star-forming galaxies with a highly simplistic semi-analytic model. For other types of galaxies (e.g., quiescent early-type galaxies), the CGM gas may be inflow-dominated due to cosmological accretion (e.g., Afruni et al. 2019). We stress that ALPACA is adaptable to various radial velocity profiles for the CGM gas and we will explore other possibilities in future works.

Lastly, our model does not account for any re-emission due to scattering via fluorescent channels. Our attempts to describe such fluorescent emission semi-analytically turn out to be unsuccessful, possibly because many photons are scattered multiple times and it is difficult to predict their behavior without running Monte-Carlo simulations. The infilling of fluorescent emission was considered to have a non-negligible effect on the absorption line profile of the resonant transition by previous work (e.g., Prochaska et al. 2011a; Scarlata et al. 2015), yet more recent work finds that the effect of infilling is generally insignificant (Mauerhofer et al. 2021; see also Wang et al. 2020 and Hayes et al. 2023). More work needs to be done on both the theoretical and observational sides to better quantify the importance of fluorescent emission in the future.

Outlook

The semi-analytic model that we present in this work, ALPACA, serves as a complementary tool to our $\text{Ly}\alpha$ radiative transfer model, `tlac`. As of now, these two models can be used to infer the properties of ISM and CGM via modeling the following types of observational data, including but not limited to:

1. spatially resolved $\text{Ly}\alpha$ profiles (Erb et al., 2023);
2. $\text{Ly}\alpha$ surface brightness vs. b ;
3. $\text{Ly}\alpha$ EW vs. b ;

4. DTB metal absorption line profiles;
5. metal absorption EW vs. b .

As we have already demonstrated in this work, the joint modeling of different datasets using ALPACA has the great potential of unveiling the intricate structure of galactic environments. Our joint modeling of the DTB absorption line profile and the EW vs. b profile stands as a successful proof-of-concept. Significant improvements can be achieved by incorporating additional data, such as more densely sampled, high-resolution line profiles observed at various impact parameters. When combined with Ly α modeling, crucial properties of the cool gas in the CGM (such as its kinematics, see Section 7.5) can be determined reasonably well. Such a new methodology even has several far-reaching benefits for other fields in addition to galaxy evolution. For example, constraining the structure of the ISM and CGM of high- z LyC emitters will help us understand how the ionizing photons propagate outwards and eventually contribute to cosmic reionization. In our next paper, we plan to apply our models on more statistically significant samples (e.g., KBSS and KLCS), with the aim of establishing a standard picture for the galactic environments of high- z galaxies. We believe these efforts will eventually shed light on the nature of the galactic environments and the many important physical processes they participate in that are crucial to galaxy evolution.

7.10 Conclusions

In this work, we present ALPACA, a new, fast semi-analytic model for UV absorption lines that emerge from a clumpy galactic outflow. The main conclusions of this work are:

1. We present a semi-analytic formalism for metal absorption lines, where the galactic halo is dissected into a series of concentric shells and the photons' escape probability is a function of the clump covering fraction and velocity in each shell. With ALPACA, we predict the DTB metal absorption line profiles and the EW of absorption at different impact parameters as a function of the properties of the clumps, including the clump kinematics, the clump volume filling factor, the clump number density profile and the clump ion column densities.
2. We compare the absorption line profiles predicted by ALPACA with the results obtained from a Ly α radiative transfer code, `tlac`. Our tests show

that the absorption line profiles predicted by `ALPACA` are consistent with the Monte-Carlo simulations performed by `tlac` over a wide range of parameters, suggesting the validity of the relatively simple formalism of `ALPACA`. We also present the effect of individual parameters of the clumps to the emergent absorption line profiles by varying each parameter individually.

3. We use `ALPACA` to jointly model the stacked DTB C II $\lambda 1334$ spectrum of a sample of $z \sim 3$ LBGs and the EW vs. b profile of a sample of $z \sim 2$ star-forming galaxy-galaxy pairs. The model successfully reproduced two datasets simultaneously, and the best-fit prefers a low volume filling factor ($\sim 3 \times 10^{-3}$) for the clumps. Moreover, the clumps' radial velocities are preferred to be a superposition of an outflow and a velocity dispersion; the outflow is rapidly accelerated to $v_{\text{cl, out}} \sim 400 \text{ km s}^{-1}$ and then gradually decelerated, whereas the velocity dispersion is $\sigma_{\text{cl, rand}} \sim 120 \text{ km s}^{-1}$. The best-fit clump number density decreases with radius as $n_{\text{cl}}(r) \propto r^{-1}$. As `ALPACA` accounts for clump random motion and non-resonant absorption, the best-fit model corresponds to a physical scenario where the absorption observed at a particular velocity is contributed by the clumps from a fairly broad range of radii, rather than from a single point of resonance.
4. We explore the usage of the commonly adopted Sobolev approximation in the context of a clumpy galactic environment. We find that in an extremely clumpy medium that resembles a homogeneous medium, the Sobolev approximation only works when the velocity gradient is sufficiently large and the random motion of the gas is negligible. Whereas in a realistic, non-volume-filling clumpy medium, the Sobolev approximation is at best only applicable within a narrow range of radii where the clumps are undergoing rapid acceleration and fails otherwise. Applying the Sobolev approximation to the entire halo of a galaxy has the risk of overestimating the clump covering fraction significantly.
5. We find that the clump radial velocity profile may not be fully constrained by the joint modeling of the DTB spectrum and the EW vs. b profile. The analysis of additional observational data, such as spatially resolved Ly α emission modeling, may help break the degeneracy and distinguish different clump radial velocity profiles.

Acknowledgements

We thank Phil Hopkins for providing computational resources. ZL acknowledges Cody Carr for the illuminating discussion. MG thanks the Max Planck Society for support through the Max Planck Research Group. CS and ZL have been supported in part by grant AST-2009278 from the U.S. National Science Foundation. Numerical calculations were run on the Caltech compute cluster “Wheeler”, allocations from XSEDE TG-AST130039 and PRAC NSF.1713353 supported by the NSF, and NASA HEC SMD-16-7592. We also acknowledge the use of the following software packages: Astropy (Astropy Collaboration et al., 2018), the SciPy and NumPy system (Virtanen et al., 2020; Harris et al., 2020).

7.11 Appendix

Model Convergence

In this section, we test how many shells are needed to achieve convergence for ALPACA. We choose the following set of parameters as our fiducial model: $F_V = 0.005$, $\mathcal{V} = 700 \text{ km s}^{-1}$, $\alpha = 2.0$, $\gamma = 0.0$, $\log N_{\text{HI,cl}} = 15$, $R_{\text{cl}} = 100 \text{ pc}$, $\sigma_{\text{cl,rand}} = 50 \text{ km s}^{-1}$, $b_D = 15 \text{ km s}^{-1}$. We find that changing any of the parameters does not visibly affect the condition for convergence, except for $\sigma_{\text{cl,rand}}$, which appears to have a moderate effect on the model spectra with different number of shells. Therefore, we test the model convergence by varying d/R_{cl} ($d = (r_{\text{h}} - r_{\text{min}})/N_{\text{shell}}$ is the spacing between the midplanes of two adjacent shells, where N_{shell} is the number of shells) with $\sigma_{\text{cl,rand}} = 50$ and 100 km s^{-1} . As shown in Figure 7.10, in both sets of models, the variation in the model spectra starts to become negligible at $d/R_{\text{cl}} \sim 0.1$, suggesting the convergence of the model has been achieved. We have also verified increasing N_{shell} even more no longer visibly changes the model absorption line profile.

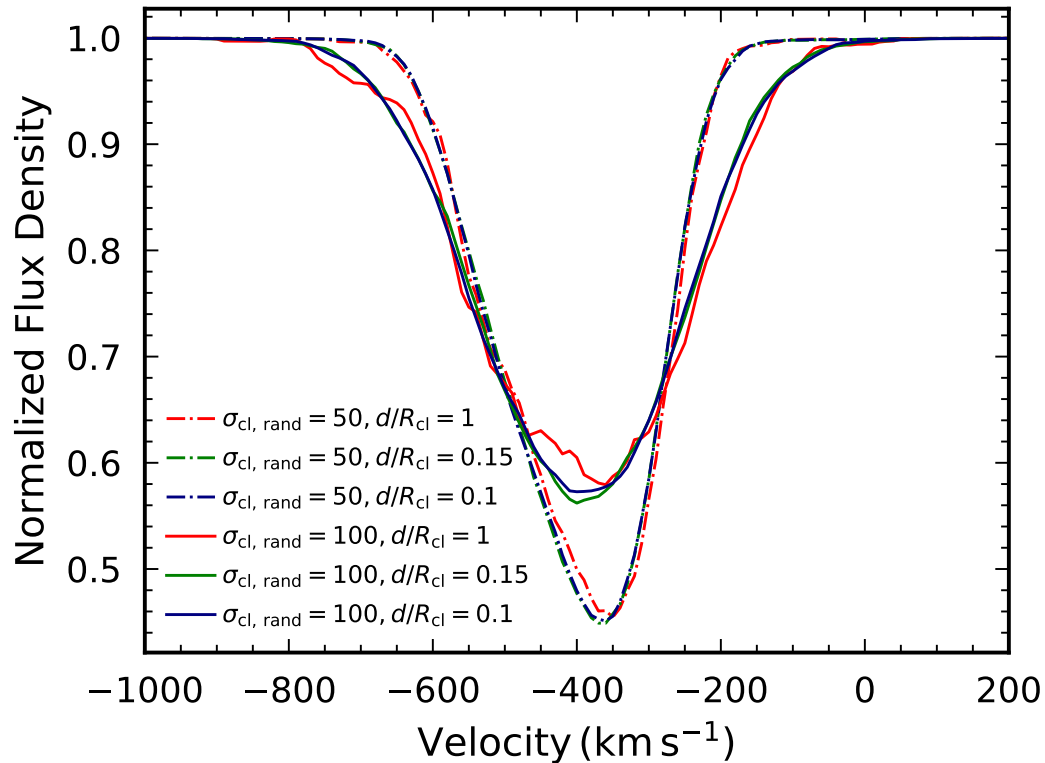


Figure 7.10: **Testing the convergence of ALPACA by varying d/R_{cl} .** The fiducial model parameters are given in the text, and two sets of models with $\sigma_{cl,rand} = 50$ and 100 km s^{-1} are calculated (shown in dash-dotted and solid lines, respectively). In each model set, the number of shells is varied (hence the d/R_{cl} values) and the model spectra are shown in different colors. For both sets of models, the convergence is achieved at $d/R_{cl} \sim 0.1$.

Chapter 8

SUMMARY AND OUTLOOK

A significant advantage of the two major new CGM models developed during my PhD, namely the multiphase, clumpy RT model and the ALPACA model, is their versatility. Not only can they be applied to a broad range of datasets of Ly α emission and metal absorption lines, but they can also be expanded to explore additional line transitions, such as the Mg II doublet. Equipped with these new tools, I am poised to better address pressing questions about the CGM: What is the physical and kinematic structure of the CGM? How do the properties of the CGM depend on those of its host galaxy? How do the properties of the CGM evolve with redshift?

The recent launch of the James Webb Space Telescope (JWST) has offered an unprecedented opportunity to unravel the enigmatic properties of the CGM at early cosmic epochs. Remarkably, JWST has detected spatially extended Ly α emission in the CGM of two galaxies at extremely high redshifts ($z = 7.8$ and 10.6 , respectively; Jung et al. 2023; Bunker et al. 2023), as well as LIS metal absorption lines from the CGM of galaxies at redshifts up to 6 (Bordoloi et al. 2023). However, extracting the physical properties of the CGM from these groundbreaking observational data remains a formidable challenge, achievable only through rigorous modeling with a physical CGM model. A comprehensive analysis of the newly obtained observational data using physically realistic CGM models such as the multiphase, clumpy model and the ALPACA model, is therefore urgent and holds profound scientific importance.

In light of the above, I envision that there are at least two compelling applications of the novel CGM models in the JWST era:

Constraining the CGM Properties and LyC Escape Fractions of Galaxies in the Reionization Era via Ly α Emission

Reionization is a pivotal and fascinating phase in the universe's history that marks its transition from obscurity to transparency. To date, it is commonly believed that star-forming galaxies within redshift $6 < z < 10$ are the main contributors to reionization. Nonetheless, our comprehension of this transformative process remains confined, primarily owing to our incomplete knowledge of the sources emitting

ionizing photons during the reionization epoch. Unfortunately, due to the rapidly increasing opacity of the neutral intergalactic medium (IGM) at $z \gtrsim 4$, even with the advent of JWST, a direct detection of ionizing photons in the reionization era remains unattainable.

One of the most promising work-arounds is to use Ly α photons to indirectly probe the escape of ionizing photons (also known as Lyman continuum photons; LyC). The advantage of using Ly α lies not only in its distinction as one of the most luminous emission lines, but also in its unique property of being resonantly scattered by neutral hydrogen and escaping afterwards, rather than being absorbed completely like LyC photons. This property enables Ly α to remain detectable throughout the entire reionization process. The emergent Ly α photons, originally produced via photo-ionization and recombination within stars, propagate outwards and interact with the ISM, the CGM, and ultimately the IGM. The physical properties of ISM, CGM, and IGM, including their spatial distributions, densities, and kinematics, are encoded in the emergent Ly α emission line profiles. These properties can be extracted via Ly α RT modeling and used to infer the escape of LyC photons and their contribution to reionization.

Since the launch of JWST, a large number of Ly α -emitting galaxies situated near or during the epoch of reionization have been observed. However, a systemic modeling of their Ly α profiles using a physically realistic model remains absent. Considering that many of these Ly α -emitting galaxies could be direct contributors to reionization, the immediate application of such a model to the recently obtained Ly α profiles, with the aim of determining the LyC escape fractions from these galaxies, stands as an urgent matter with profound scientific significance.

Therefore, I intend to leverage the newly acquired Ly α emission data of reionization-era galaxies through detailed modeling with the new CGM models that I have developed. I plan to model the Ly α data obtained by JWST from multiple large programs, including the JWST Advanced Deep Extragalactic Survey (JADES), the Cosmic Evolution Early Release Science Survey (CEERS), and the Grism Lens-Amplified Survey from Space (GLASS). Furthermore, I plan to use the newly commissioned IFU spectrograph, the Keck Cosmic Reionization Mapper (KCRM) on the Keck II telescope, which has the capability to obtain spatially resolved Ly α emission maps up to $z \simeq 7.5$.

It is worth noting that these Ly α profiles observed at $z \gtrsim 6$ must be modeled by accounting for the increased amount of attenuation from the neutral gas in the IGM.

Fortunately, recent studies (e.g., Byrohl et al. 2020) have shown that the incorporation of the IGM attenuation can be achieved by simply convolving the unattenuated Ly α spectra with the IGM transmission curves, thereby mitigating the necessity for an exhaustive RT calculation. This finding renders the application of my model to the Ly α profiles observed at $z \gtrsim 6$ a feasible endeavor.

I envision this project will include the following steps. Firstly, I will employ the multiphase, clumpy model to analyze the Ly α profiles of $z \gtrsim 6$ galaxies with a careful treatment of the physical structure of the ISM, CGM, and the IGM. Secondly, I will use the derived physical parameters to deduce the LyC escape fractions from these $z \gtrsim 6$ galaxies (e.g., Dijkstra et al. 2016). Thirdly, I will investigate the correlations between the LyC escape fractions and the properties of these galaxies, such as their stellar masses and star formation rates (SFR). Lastly, I will compare my findings with the results for galaxies at lower redshifts and explore the evolution of LyC escape fraction with redshift. This project will greatly enhance our understanding of the surrounding environments of galaxies that are directly responsible for reionization and the escape of ionizing photons from these galaxies.

Constraining the Redshift Evolution of CGM Properties Via a Synergistic Modeling of Ly α Emission and Metal Absorption

In addition to Ly α emission, an alternative way of probing the gas properties in the CGM involves the utilization of metal absorption lines observed in the spectra of high-redshift quasars. JWST has made it possible to observe these metal absorption lines at exceedingly high redshifts. Notably, the members of the JWST program EIGER¹ have recently reported the detection of Mg II absorption in the spectrum of a quasar at $z = 6.33$, J0100+2802 (Bordoloi et al. 2023). They also determined that the observed Mg II absorption originates from the CGM of 29 galaxies with redshifts up to 6 – a record-breaking high redshift for CGM observations.

Now with the ALPACA model, I am able to undertake the forward modeling of metal absorption lines from these $z \gtrsim 6$ galaxies in a more physically motivated manner. In contrast to the common practice of Voigt profile fitting and other empirical or phenomenological models, ALPACA is grounded in physical principles and properly accounts for the intricate interaction between the photons and the absorbing gas in the CGM. As of now, I have successfully used the pipeline to reproduce the Si II and C II absorption line profiles of a sample of star-forming galaxies at 2

¹EIGER is the acronym for “Emission-line galaxies and Intergalactic Gas in the Epoch of Reionization”.

$< z < 3$. At higher redshifts, a different line transition (such as Mg II) may become a more suitable choice for observations due to its longer wavelength compared to Si II and C II. Nevertheless, these transitions all trace the properties of the cool gas due to their similar ionization potentials, and their underlying physical mechanisms are fundamentally similar. Therefore, a simple replacement of the relevant line coefficients suffices to render ALPACA readily applicable for modeling the metal absorption lines observed at $z \gtrsim 6$.

In addition to analyzing the JWST observations, more importantly, I plan to construct a unique galaxy sample that has telescope coverage for both Ly α and metal absorption lines, so that I can perform simultaneous modeling with the multiphase, clumpy model and ALPACA. My research has revealed that the exclusive modeling of either Ly α emission or metal absorption lines frequently leads to significant parameter degeneracies in the CGM. The synergistic modeling of spatially resolved Ly α emission and metal absorption lines will therefore be a potent method to effectively break parameter degeneracies within a complex, high-dimensional CGM model and greatly enhance our ability to accurately determine the essential properties of the CGM.

At $z \sim 2 - 3$, such a galaxy sample is readily available from the Keck Baryonic Structure Survey (KBSS), with Ly α observations from the Keck Cosmic Web Imager (KCWI) and metal absorption observations from the Low Resolution Imaging Spectrometer (LRIS). At $z \sim 3 - 7$, the recent commissioning of the new IFU spectrograph, KCRM on the Keck II telescope, has provided an unprecedented opportunity to construct a galaxy sample with simultaneous coverage of Ly α and metal absorption lines, utilizing other Keck instruments like the deep imaging multi-object spectrograph (DEIMOS). Additionally, upcoming instruments on the Magellan telescopes, such as the large lenslet array Magellan spectrograph (LLAMAS) and the Magellan infrared multi-object spectrograph (MIRMOS), are also promising for achieving similar scientific goals.

With this regard, I envision the following steps for this project. Firstly, I will compile the observational data obtained from both JWST and the aforementioned instruments on the largest ground-based telescopes and pursue additional observing time if necessary. To properly analyze the observational data, I will build a large suite of RT models for Ly α and semi-analytic models for metal absorption lines to ensure exploration of a sufficiently broad parameter space. Secondly, I will model the Ly α emission and metal absorption lines of these high-redshift galaxies to con-

strain the properties of their CGM. I will also leverage complementary observations to determine the essential properties of these galaxies, such as their stellar masses and SFRs, and explore the correlations between the properties of these galaxies and the attributes of their CGM. Finally, I will investigate the redshift evolution of the CGM properties by comparing my findings with other CGM studies at lower redshifts. This project will extend the boundaries of our current comprehension of the CGM from $z \sim 2$ to $z \sim 7$, and provide crucial insights into the evolution of the CGM properties across cosmic times. The ultimate objective is not just to unveil the nature of the CGM of high-redshift galaxies, but also to unravel the underlying physical mechanisms that shape its distinct characteristics.

JWST has revolutionized our understanding of the universe and will undoubtedly continue to do so. Using the new CGM models I have developed, I will ensure the extraction of the maximum amount of physical information and accurate interpretation of Ly α emission and metal absorption lines obtained by both JWST and the new instruments on the world's largest ground-based telescopes. My modeling will establish the crucial framework needed to precisely translate these expanding observational endeavors into stringent constraints on galaxy evolution. My future research will push the frontiers of our current, albeit highly incomplete, understanding of the CGM from $z \sim 2$ all the way to $z \sim 10$, offering essential insights into the intricate nature of these "galactic atmospheres" at early cosmic epochs. Ultimately, this effort will significantly deepen our comprehension of the evolution of galaxies and their environments throughout cosmic history.

BIBLIOGRAPHY

- Abruzzo, Matthew W., Greg L. Bryan, and Drummond B. Fielding (Feb. 2022). “A Simple Model for Mixing and Cooling in Cloud-Wind Interactions”. In: *ApJ* 925.2, 199, p. 199. DOI: 10.3847/1538-4357/ac3c48. arXiv: 2101.10344 [astro-ph.GA].
- Abruzzo, Matthew W., Drummond B. Fielding, and Greg L. Bryan (May 2024). “Taming the TuRMoiL: The Temperature Dependence of Turbulence in Cloud-Wind Interactions”. In: *ApJ* 966.2, 181, p. 181. DOI: 10.3847/1538-4357/ad1e51. arXiv: 2210.15679 [astro-ph.GA].
- (July 2023). “TuRMoiL of Survival: A Unified Survival Criterion for Cloud-Wind Interactions”. In: *arXiv e-prints*, arXiv:2307.03228, arXiv:2307.03228. DOI: 10.48550/arXiv.2307.03228. arXiv: 2307.03228 [astro-ph.GA].
- Adams, Thomas F. (June 1972). “The Escape of Resonance-Line Radiation from Extremely Opaque Media”. In: *ApJ* 174, p. 439. DOI: 10.1086/151503.
- (Oct. 1975). “The Mean Photon Path Length in Extremely Opaque Media”. In: *ApJ* 201, pp. 350–351. DOI: 10.1086/153891.
- Adelberger, Kurt L., Charles C. Steidel, Max Pettini, et al. (Feb. 2005). “The Spatial Clustering of Star-forming Galaxies at Redshifts $1.4 < z < 3.5$ ”. In: *ApJ* 619.2, pp. 697–713. DOI: 10.1086/426580. arXiv: astro-ph/0410165 [astro-ph].
- Adelberger, Kurt L., Charles C. Steidel, Alice E. Shapley, et al. (Feb. 2003). “Galaxies and Intergalactic Matter at Redshift $z \sim 3$: Overview”. In: *ApJ* 584.1, pp. 45–75. DOI: 10.1086/345660. arXiv: astro-ph/0210314 [astro-ph].
- Afruni, Andrea, Filippo Fraternali, and Gabriele Pezzulli (May 2019). “Cool circumgalactic gas of passive galaxies from cosmological inflow”. In: *A&A* 625, A11, A11. DOI: 10.1051/0004-6361/201835002. arXiv: 1903.06182 [astro-ph.GA].
- Afruni, Andrea, Gabriele Pezzulli, and Filippo Fraternali (Feb. 2022). “Inflow of low-metallicity cool gas in the halo of the Andromeda galaxy”. In: *MNRAS* 509.4, pp. 4849–4864. DOI: 10.1093/mnras/stab3237. arXiv: 2111.05343 [astro-ph.GA].
- Ahn, Sang-Hyeon (Jan. 2004). “Singly Peaked Asymmetric Ly α from Starburst Galaxies”. In: *ApJ* 601.1, pp. L25–L28. DOI: 10.1086/381750. arXiv: astro-ph/0309594 [astro-ph].
- Ahn, Sang-Hyeon, Hee-Won Lee, and Hyung Mok Lee (Apr. 2003). “P Cygni type Ly α from starburst galaxies”. In: *MNRAS* 340.3, pp. 863–869. DOI: 10.1046/j.1365-8711.2003.06353.x. arXiv: astro-ph/0204004 [astro-ph].

- Ajiki, Masaru, Yoshiaki Taniguchi, Takashi Murayama, et al. (Sept. 2002). “A New High-Redshift Ly α Emitter: Possible Superwind Galaxy at $z=5.69$ ”. In: *ApJ* 576.1, pp. L25–L28. DOI: 10.1086/343026. arXiv: astro-ph/0207303 [astro-ph].
- Alexandroff, Rachael M., Timothy M. Heckman, Sanchayeeta Borthakur, et al. (Sept. 2015). “Indirect Evidence for Escaping Ionizing Photons in Local Lyman Break Galaxy Analogs”. In: *ApJ* 810.2, 104, p. 104. DOI: 10.1088/0004-637X/810/2/104. arXiv: 1504.02446 [astro-ph.GA].
- Ao, Y., Y. Matsuda, C. Henkel, et al. (Dec. 2017). “Deep Submillimeter and Radio Observations in the SSA22 Field. I. Powering Sources and the Ly α Escape Fraction of Ly α Blobs”. In: *ApJ* 850.2, 178, p. 178. DOI: 10.3847/1538-4357/aa960f. arXiv: 1704.05101 [astro-ph.GA].
- Ao, Yiping, Zheng Zheng, Christian Henkel, et al. (Mar. 2020). “Infalling gas in a Lyman- α blob”. In: *Nature Astronomy* 4, pp. 670–674. DOI: 10.1038/s41550-020-1033-3. arXiv: 2003.06099 [astro-ph.GA].
- Armillotta, L., F. Fraternali, J. K. Werk, et al. (Sept. 2017). “The survival of gas clouds in the circumgalactic medium of Milky Way-like galaxies”. In: *MNRAS* 470, pp. 114–125. DOI: 10.1093/mnras/stx1239. arXiv: 1608.05416 [astro-ph.GA].
- Arrigoni Battaia, Fabrizio, Joseph F. Hennawi, J. Xavier Prochaska, et al. (Aug. 2015). “Deep He II and C IV Spectroscopy of a Giant Ly α Nebula: Dense Compact Gas Clumps in the Circumgalactic Medium of a $z \sim 2$ Quasar”. In: *ApJ* 809.2, 163, p. 163. DOI: 10.1088/0004-637X/809/2/163. arXiv: 1504.03688 [astro-ph.GA].
- Astropy Collaboration, A. M. Price-Whelan, B. M. Sipőcz, et al. (Sept. 2018). “The Astropy Project: Building an Open-science Project and Status of the v2.0 Core Package”. In: *AJ* 156.3, 123, p. 123. DOI: 10.3847/1538-3881/aabc4f. arXiv: 1801.02634 [astro-ph.IM].
- Atek, H., D. Schaerer, and D. Kunth (Aug. 2009). “Origin of Ly α absorption in nearby starbursts and implications for other galaxies”. In: *A&A* 502.3, pp. 791–801. DOI: 10.1051/0004-6361/200911856. arXiv: 0905.1329 [astro-ph.CO].
- Bacon, R., M. Accardo, L. Adjali, et al. (July 2010). “The MUSE second-generation VLT instrument”. In: *Ground-based and Airborne Instrumentation for Astronomy III*. Ed. by Ian S. McLean, Suzanne K. Ramsay, and Hideki Takami. Vol. 7735. Society of Photo-Optical Instrumentation Engineers (SPIE) Conference Series, 773508, p. 773508. DOI: 10.1117/12.856027.
- Bacon, R., J. Vernet, E. Borisova, et al. (Sept. 2014). “MUSE Commissioning”. In: *The Messenger* 157, pp. 13–16.
- Balbus, S. A. and C. F. McKee (Jan. 1982). “The evaporation of spherical clouds in a hot gas. III - Suprathermal evaporation”. In: *ApJ* 252, pp. 529–552. DOI: 10.1086/159581.

- Baldwin, J. A., M. M. Phillips, and R. Terlevich (Feb. 1981). “Classification parameters for the emission-line spectra of extragalactic objects.” In: *PASP* 93, pp. 5–19. DOI: 10.1086/130766.
- Banda-Barragán, W. E., C. Federrath, R. M. Crocker, et al. (Jan. 2018). “Filament formation in wind-cloud interactions- II. Clouds with turbulent density, velocity, and magnetic fields”. In: *MNRAS* 473.3, pp. 3454–3489. DOI: 10.1093/mnras/stx2541. arXiv: 1706.06607 [astro-ph.GA].
- Banda-Barragán, W. E., E. R. Parkin, C. Federrath, et al. (Jan. 2016). “Filament formation in wind-cloud interactions - I. Spherical clouds in uniform magnetic fields”. In: *MNRAS* 455.2, pp. 1309–1333. DOI: 10.1093/mnras/stv2405. arXiv: 1510.05356 [astro-ph.GA].
- Banda-Barragán, W. E., F. J. Zertuche, C. Federrath, et al. (July 2019). “On the dynamics and survival of fractal clouds in galactic winds”. In: *MNRAS* 486.4, pp. 4526–4544. DOI: 10.1093/mnras/stz1040. arXiv: 1901.06924 [astro-ph.GA].
- Basu-Zych, Antara and Caleb Scharf (Nov. 2004). “X-Ray Detection of an Obscured Active Galactic Nucleus in a $z=3.09$ Radio-quiet $\text{Ly}\alpha$ Nebula”. In: *ApJ* 615.2, pp. L85–L88. DOI: 10.1086/426390. arXiv: astro-ph/0410311 [astro-ph].
- Beck, Melanie, Claudia Scarlata, Matthew Hayes, et al. (Feb. 2016). “Spectropolarimetry Confirms Central Powering in a $\text{Ly}\alpha$ Nebula at $z = 3.09$ ”. In: *ApJ* 818.2, 138, p. 138. DOI: 10.3847/0004-637X/818/2/138. arXiv: 1601.06786 [astro-ph.GA].
- Behrens, C., M. Dijkstra, and J. C. Niemeyer (Mar. 2014). “Beamed $\text{Ly}\alpha$ emission through outflow-driven cavities”. In: *A&A* 563, A77, A77. DOI: 10.1051/0004-6361/201322949. arXiv: 1401.4860 [astro-ph.GA].
- Behroozi, Peter S., Charlie Conroy, and Risa H. Wechsler (July 2010). “A Comprehensive Analysis of Uncertainties Affecting the Stellar Mass-Halo Mass Relation for $0 < z < 4$ ”. In: *ApJ* 717.1, pp. 379–403. DOI: 10.1088/0004-637X/717/1/379. arXiv: 1001.0015 [astro-ph.CO].
- Behroozi, Peter S., Risa H. Wechsler, and Charlie Conroy (June 2013). “The Average Star Formation Histories of Galaxies in Dark Matter Halos from $z = 0-8$ ”. In: *ApJ* 770.1, 57, p. 57. DOI: 10.1088/0004-637X/770/1/57. arXiv: 1207.6105 [astro-ph.CO].
- Bertin, E. and S. Arnouts (June 1996). “SExtractor: Software for source extraction.” In: *A&AS* 117, pp. 393–404. DOI: 10.1051/aas:1996164.
- Bordoloi, Rongmon, J. Xavier Prochaska, Jason Tumlinson, et al. (Sept. 2018). “On the CGM Fundamental Plane: The Halo Mass Dependency of Circumgalactic H I”. In: *ApJ* 864.2, 132, p. 132. DOI: 10.3847/1538-4357/aad8ac. arXiv: 1712.02348 [astro-ph.GA].

- Bordoloi, Rongmon, Robert A. Simcoe, Jorryt Matthee, et al. (July 2023). “EIGER IV: The cool 10^4K circumgalactic environment of high- z galaxies reveals remarkably efficient IGM enrichment”. In: *arXiv e-prints*, arXiv:2307.01273, arXiv:2307.01273. DOI: 10.48550/arXiv.2307.01273. arXiv: 2307.01273 [astro-ph.GA].
- Borisova, Elena, Sebastiano Cantalupo, Simon J. Lilly, et al. (Nov. 2016). “Ubiquitous Giant Ly α Nebulae around the Brightest Quasars at $z \sim 3.5$ Revealed with MUSE”. In: *ApJ* 831.1, 39, p. 39. DOI: 10.3847/0004-637X/831/1/39. arXiv: 1605.01422 [astro-ph.GA].
- Borthakur, Sanchayeeta, Timothy Heckman, Jason Tumlinson, et al. (Nov. 2015). “Connection between the Circumgalactic Medium and the Interstellar Medium of Galaxies: Results from the COS-GASS Survey”. In: *ApJ* 813.1, 46, p. 46. DOI: 10.1088/0004-637X/813/1/46. arXiv: 1504.01392 [astro-ph.GA].
- Borthakur, Sanchayeeta, Timothy M. Heckman, Claus Leitherer, et al. (Oct. 2014). “A local clue to the reionization of the universe”. In: *Science* 346.6206, pp. 216–219. DOI: 10.1126/science.1254214. arXiv: 1410.3511 [astro-ph.GA].
- Bouché, N., M. T. Murphy, G. G. Kacprzak, et al. (July 2013). “Signatures of Cool Gas Fueling a Star-Forming Galaxy at Redshift 2.3”. In: *Science* 341.6141, pp. 50–53. DOI: 10.1126/science.1234209. arXiv: 1306.0134 [astro-ph.CO].
- Bower, R. G., S. L. Morris, R. Bacon, et al. (June 2004). “Deep SAURON spectral imaging of the diffuse Lyman α halo LAB1 in SSA 22”. In: *MNRAS* 351.1, pp. 63–69. DOI: 10.1111/j.1365-2966.2004.07783.x. arXiv: astro-ph/0402456 [astro-ph].
- Braginskii, S. I. (Jan. 1965). “Transport Processes in a Plasma”. In: *Reviews of Plasma Physics* 1, p. 205.
- Brüggen, Marcus and Evan Scannapieco (May 2016). “The Launching of Cold Clouds by Galaxy Outflows. II. The Role of Thermal Conduction”. In: *ApJ* 822, 31, p. 31. DOI: 10.3847/0004-637X/822/1/31. arXiv: 1602.01843 [astro-ph.GA].
- Bunker, Andrew J., Aayush Saxena, Alex J. Cameron, et al. (Sept. 2023). “JADES NIRSpec Spectroscopy of GN-z11: Lyman- α emission and possible enhanced nitrogen abundance in a $z = 10.60$ luminous galaxy”. In: *A&A* 677, A88, A88. DOI: 10.1051/0004-6361/202346159. arXiv: 2302.07256 [astro-ph.GA].
- Byrohl, C. and M. Gronke (Oct. 2020). “Variations in shape among observed Lyman- α spectra due to intergalactic absorption”. In: *A&A* 642, L16, p. L16. DOI: 10.1051/0004-6361/202038685. arXiv: 2006.10041 [astro-ph.GA].
- Byrohl, Chris, Dylan Nelson, Christoph Behrens, et al. (July 2021). “The physical origins and dominant emission mechanisms of Lyman-alpha halos: results from the TNG50 simulation in comparison to MUSE observations”. In: *MNRAS*. DOI: 10.1093/mnras/stab1958. arXiv: 2009.07283 [astro-ph.GA].

- Cai, Zheng, Xiaohui Fan, Yujin Yang, et al. (Mar. 2017). “Discovery of an Enormous Ly α Nebula in a Massive Galaxy Overdensity at $z = 2.3$ ”. In: *ApJ* 837.1, 71, p. 71. DOI: 10.3847/1538-4357/aa5d14. arXiv: 1609.04021 [astro-ph.GA].
- Cantalupo, Sebastiano, Fabrizio Arrighi-Battaia, J. Xavier Prochaska, et al. (Feb. 2014). “A cosmic web filament revealed in Lyman- α emission around a luminous high-redshift quasar”. In: *Nature* 506.7486, pp. 63–66. DOI: 10.1038/nature12898. arXiv: 1401.4469 [astro-ph.CO].
- Cantalupo, Sebastiano, Simon J. Lilly, and Martin G. Haehnelt (Sept. 2012). “Detection of dark galaxies and circum-galactic filaments fluorescently illuminated by a quasar at $z = 2.4$ ”. In: *MNRAS* 425.3, pp. 1992–2014. DOI: 10.1111/j.1365-2966.2012.21529.x. arXiv: 1204.5753 [astro-ph.CO].
- Cantalupo, Sebastiano, Cristiano Porciani, Simon J. Lilly, et al. (July 2005). “Fluorescent Ly α Emission from the High-Redshift Intergalactic Medium”. In: *ApJ* 628.1, pp. 61–75. DOI: 10.1086/430758. arXiv: astro-ph/0504015 [astro-ph].
- Carr, C. and C. Scarlata (Nov. 2022a). “A Semianalytical Line Transfer Model. III. Galactic Inflows”. In: *ApJ* 939.1, 47, p. 47. DOI: 10.3847/1538-4357/ac93fa. arXiv: 2209.14485 [astro-ph.GA].
- Carr, Cody, Leo Michel-Dansac, Jeremy Blaizot, et al. (Sept. 2022b). “Testing SALT Approximations with Numerical Radiation Transfer Code Part 1: Validity and Applicability”. In: *arXiv e-prints*, arXiv:2209.14473, arXiv:2209.14473. arXiv: 2209.14473 [astro-ph.GA].
- Carr, Cody, Claudia Scarlata, Alaina Henry, et al. (Jan. 2021). “The Effects of Bi-conical Outflows on Ly α Escape from Green Peas”. In: *ApJ* 906.2, 104, p. 104. DOI: 10.3847/1538-4357/abc7c3. arXiv: 2011.02549 [astro-ph.GA].
- Carr, Cody, Claudia Scarlata, Nino Panagia, et al. (June 2018). “A Semi-analytical Line Transfer (SALT) Model. II: The Effects of a Bi-conical Geometry”. In: *ApJ* 860.2, 143, p. 143. DOI: 10.3847/1538-4357/aac48e. arXiv: 1805.05981 [astro-ph.GA].
- Cen, Renyue (June 2013). “Composition of Low-redshift Halo Gas”. In: *ApJ* 770, 139, p. 139. DOI: 10.1088/0004-637X/770/2/139. arXiv: 1304.3466 [astro-ph.CO].
- Chan, T. K., D. Kereš, P. F. Hopkins, et al. (Sept. 2019). “Cosmic ray feedback in the FIRE simulations: constraining cosmic ray propagation with GeV γ -ray emission”. In: *MNRAS* 488.3, pp. 3716–3744. DOI: 10.1093/mnras/stz1895. arXiv: 1812.10496 [astro-ph.GA].
- Chapman, S. C., G. F. Lewis, D. Scott, et al. (Feb. 2001). “Submillimeter Imaging of a Protocluster Region at $Z=3.09$ ”. In: *ApJ* 548.1, pp. L17–L21. DOI: 10.1086/318919. arXiv: astro-ph/0010101 [astro-ph].

- Chen, Hsiao-Wen, Kenneth M. Lanzetta, John K. Webb, et al. (May 1998). “The Gaseous Extent of Galaxies and the Origin of Ly α Absorption Systems. III. Hubble Space Telescope Imaging of Ly α -absorbing Galaxies at $z < 1$ ”. In: *ApJ* 498, pp. 77–94. DOI: 10.1086/305554. arXiv: astro-ph/9710310 [astro-ph].
- (Oct. 2001). “The Gaseous Extent of Galaxies and the Origin of Ly α Absorption Systems. V. Optical and Near-Infrared Photometry of Ly α -absorbing Galaxies at $z < 1$ ”. In: *ApJ* 559.2, pp. 654–674. DOI: 10.1086/322414. arXiv: astro-ph/0107137 [astro-ph].
- Chen, Yan-Mei, Christy A. Tremonti, Timothy M. Heckman, et al. (Aug. 2010). “Absorption-line Probes of the Prevalence and Properties of Outflows in Present-day Star-forming Galaxies”. In: *AJ* 140.2, pp. 445–461. DOI: 10.1088/0004-6256/140/2/445. arXiv: 1003.5425 [astro-ph.GA].
- Chen, Yuguang, Charles C. Steidel, Dawn K. Erb, et al. (Apr. 2021). “The KBSS-KCWI Survey: The connection between extended Ly α halos and galaxy azimuthal angle at $z \sim 2-3$ ”. In: *arXiv e-prints*, arXiv:2104.10173, arXiv:2104.10173. arXiv: 2104.10173 [astro-ph.GA].
- Chen, Yuguang, Charles C. Steidel, Cameron B. Hummels, et al. (Dec. 2020). “The Keck Baryonic Structure Survey: using foreground/background galaxy pairs to trace the structure and kinematics of circumgalactic neutral hydrogen at $z \sim 2$ ”. In: *MNRAS* 499.2, pp. 1721–1746. DOI: 10.1093/mnras/staa2808. arXiv: 2006.13236 [astro-ph.GA].
- Chevalier, R. A. and A. W. Clegg (Sept. 1985). “Wind from a starburst galaxy nucleus”. In: *Nature* 317.6032, pp. 44–45. DOI: 10.1038/317044a0.
- Child, Hillary L., Salman Habib, Katrin Heitmann, et al. (May 2018). “Halo Profiles and the Concentration-Mass Relation for a Λ CDM Universe”. In: *ApJ* 859.1, 55, p. 55. DOI: 10.3847/1538-4357/aabf95. arXiv: 1804.10199 [astro-ph.CO].
- Chisholm, J., S. Gazagnes, D. Schaerer, et al. (Aug. 2018). “Accurately predicting the escape fraction of ionizing photons using rest-frame ultraviolet absorption lines”. In: *A&A* 616, A30, A30. DOI: 10.1051/0004-6361/201832758. arXiv: 1803.03655 [astro-ph.GA].
- Chisholm, John, Christy A. Tremonti, Claus Leitherer, et al. (Oct. 2015). “Scaling Relations Between Warm Galactic Outflows and Their Host Galaxies”. In: *ApJ* 811.2, 149, p. 149. DOI: 10.1088/0004-637X/811/2/149. arXiv: 1412.2139 [astro-ph.GA].
- Chisholm, John, A. Tremonti Christy, Claus Leitherer, et al. (Nov. 2016). “A robust measurement of the mass outflow rate of the galactic outflow from NGC 6090”. In: *MNRAS* 463.1, pp. 541–556. DOI: 10.1093/mnras/stw1951. arXiv: 1605.05769 [astro-ph.GA].

- Chung, Andrew S., Mark Dijkstra, Benedetta Ciardi, et al. (Apr. 2019). “The circumgalactic medium in Lyman α : a new constraint on galactic outflow models”. In: *MNRAS* 484.2, pp. 2420–2432. DOI: 10.1093/mnras/stz149. arXiv: 1901.04015 [astro-ph.GA].
- Churchill, Christopher W., Jessica L. Evans, Bryson Stemock, et al. (Nov. 2020). “Mg II Absorbers in High-resolution Quasar Spectra. I. Voigt Profile Models”. In: *ApJ* 904.1, 28, p. 28. DOI: 10.3847/1538-4357/abbb34. arXiv: 2008.08487 [astro-ph.GA].
- Churchill, Christopher W., Charles C. Steidel, and Steven S. Vogt (Nov. 1996). “On the Spatial and Kinematic Distributions of Mg II Absorbing Gas in $\langle z \rangle$ approximately 0.7 Galaxies”. In: *ApJ* 471, p. 164. DOI: 10.1086/177960. arXiv: astro-ph/9605180 [astro-ph].
- Claeysens, A, J Richard, J Blaizot, et al. (2019). “Spectral variations of Lyman α emission within strongly lensed sources observed with MUSE”. In: *Monthly Notices of the Royal Astronomical Society* 489.4, pp. 5022–5029. DOI: 10.1093/mnras/stz2492.
- Colbert, James W., Harry Teplitz, Paul Francis, et al. (Feb. 2006). “Ultraviolet-bright, High-Redshift Ultraluminous Infrared Galaxies”. In: *ApJ* 637.2, pp. L89–L92. DOI: 10.1086/500647. arXiv: astro-ph/0512583 [astro-ph].
- Colbrook, M. J., X. Ma, P. F. Hopkins, et al. (May 2017). “Scaling laws of passive-scalar diffusion in the interstellar medium”. In: *MNRAS* 467, pp. 2421–2429. DOI: 10.1093/mnras/stx261. arXiv: 1610.06590.
- Conroy, Charlie, Alice E. Shapley, Jeremy L. Tinker, et al. (June 2008). “The Varied Fates of $z \sim 2$ Star-forming Galaxies”. In: *ApJ* 679.2, pp. 1192–1203. DOI: 10.1086/587834. arXiv: 0711.0001 [astro-ph].
- Cooke, J., E. V. Ryan-Weber, T. Garel, et al. (June 2014). “Lyman-continuum galaxies and the escape fraction of Lyman-break galaxies”. In: *MNRAS* 441.1, pp. 837–851. DOI: 10.1093/mnras/stu635. arXiv: 1404.0125 [astro-ph.GA].
- Cowie, L L and C F McKee (Jan. 1977). “The evaporation of spherical clouds in a hot gas. I - Classical and saturated mass loss rates”. In: *ApJ* 211, pp. 135–146. DOI: 10.1086/154911.
- Cox, Donald P. (Sept. 2005). “The Three-Phase Interstellar Medium Revisited”. In: *ARA&A* 43.1, pp. 337–385. DOI: 10.1146/annurev.astro.43.072103.150615.
- Crighton, Neil H. M., Joseph F. Hennawi, Robert A. Simcoe, et al. (Jan. 2015). “Metal-enriched, subkiloparsec gas clumps in the circumgalactic medium of a faint $z = 2.5$ galaxy”. In: *MNRAS* 446.1, pp. 18–37. DOI: 10.1093/mnras/stu2088. arXiv: 1406.4239 [astro-ph.GA].

- Daddi, E., F. Valentino, R. M. Rich, et al. (May 2021). “Three Lyman- α -emitting filaments converging to a massive galaxy group at $z = 2.91$: discussing the case for cold gas infall”. In: *A&A* 649, A78, A78. DOI: 10.1051/0004-6361/202038700. arXiv: 2006.11089 [astro-ph.GA].
- Davies, Richard, Alex Agudo Berbel, Erich Wiezorrek, et al. (2010). “KMOS data flow: reconstructing data cubes in one step”. In: *Proc. SPIE*. Vol. 7735. Society of Photo-Optical Instrumentation Engineers (SPIE) Conference Series, 77356V, p. 77356V. DOI: 10.1117/12.856380.
- Dawson, Steve, Hyron Spinrad, Daniel Stern, et al. (May 2002). “A Galactic Wind at $z=5.190$ ”. In: *ApJ* 570.1, pp. 92–99. DOI: 10.1086/339579. arXiv: astro-ph/0201194 [astro-ph].
- De Lucia, Gabriella and J r my Blaizot (Feb. 2007). “The hierarchical formation of the brightest cluster galaxies”. In: *MNRAS* 375.1, pp. 2–14. DOI: 10.1111/j.1365-2966.2006.11287.x. arXiv: astro-ph/0606519 [astro-ph].
- Dedner, A., F. Kemm, D. Kr ner, et al. (Jan. 2002). “Hyperbolic Divergence Cleaning for the MHD Equations”. In: *Journal of Computational Physics* 175.2, pp. 645–673. DOI: 10.1006/jcph.2001.6961.
- Dekel, Avishai and Yuval Birnboim (May 2006). “Galaxy bimodality due to cold flows and shock heating”. In: *MNRAS* 368.1, pp. 2–20. DOI: 10.1111/j.1365-2966.2006.10145.x. arXiv: astro-ph/0412300 [astro-ph].
- Dere, K. P., G. Del Zanna, P. R. Young, et al. (Apr. 2019). “CHIANTI—An Atomic Database for Emission Lines. XV. Version 9, Improvements for the X-Ray Satellite Lines”. In: *ApJS* 241.2, 22, p. 22. DOI: 10.3847/1538-4365/ab05cf. arXiv: 1902.05019 [astro-ph.SR].
- Dere, K. P., E. Landi, H. E. Mason, et al. (Oct. 1997). “CHIANTI - an atomic database for emission lines”. In: *A&AS* 125, pp. 149–173. DOI: 10.1051/aas:1997368.
- Dere, Ken (Aug. 2013). *ChiantiPy: Python package for the CHIANTI atomic database*. ascl: 1308.017.
- Dessauges-Zavadsky, M., S. D’Odorico, D. Schaerer, et al. (Feb. 2010). “Rest-frame ultraviolet spectrum of the gravitationally lensed galaxy “the 8 o’clock arc”: stellar and interstellar medium properties”. In: *A&A* 510, A26, A26. DOI: 10.1051/0004-6361/200913337. arXiv: 0912.4384 [astro-ph.CO].
- Dey, Arjun, Chao Bian, Baruch T. Soifer, et al. (Aug. 2005). “Discovery of a Large ~ 200 kpc Gaseous Nebula at $z \sim 2.7$ with the Spitzer Space Telescope”. In: *ApJ* 629.2, pp. 654–666. DOI: 10.1086/430775. arXiv: astro-ph/0503632 [astro-ph].
- Diemer, Benedikt and Michael Joyce (Feb. 2019). “An Accurate Physical Model for Halo Concentrations”. In: *ApJ* 871.2, 168, p. 168. DOI: 10.3847/1538-4357/aafad6. arXiv: 1809.07326 [astro-ph.CO].

- Diemer, Benedikt and Andrey V. Kravtsov (Jan. 2015). “A Universal Model for Halo Concentrations”. In: *ApJ* 799.1, 108, p. 108. DOI: 10.1088/0004-637X/799/1/108. arXiv: 1407.4730 [astro-ph.CO].
- Dijkstra, Mark (Oct. 2014). “Ly α Emitting Galaxies as a Probe of Reionisation”. In: *Publ. Astron. Soc. Australia* 31, e040, e040. DOI: 10.1017/pasa.2014.33. arXiv: 1406.7292 [astro-ph.CO].
- (Apr. 2017). “Saas-Fee Lecture Notes: Physics of Lyman Alpha Radiative Transfer”. In: *arXiv e-prints*, arXiv:1704.03416, arXiv:1704.03416. arXiv: 1704.03416 [astro-ph.GA].
- Dijkstra, Mark, Max Gronke, and Aparna Venkatesan (Sept. 2016). “The Ly α -LyC Connection: Evidence for an Enhanced Contribution of UV-faint Galaxies to Cosmic Reionization”. In: *ApJ* 828.2, 71, p. 71. DOI: 10.3847/0004-637X/828/2/71. arXiv: 1604.08208 [astro-ph.CO].
- Dijkstra, Mark, Zoltán Haiman, and Marco Spaans (Sept. 2006a). “Ly α Radiation from Collapsing Protogalaxies. I. Characteristics of the Emergent Spectrum”. In: *ApJ* 649.1, pp. 14–36. DOI: 10.1086/506243. arXiv: astro-ph/0510407 [astro-ph].
- (Sept. 2006b). “Ly α Radiation from Collapsing Protogalaxies. II. Observational Evidence for Gas Infall”. In: *ApJ* 649.1, pp. 37–47. DOI: 10.1086/506244. arXiv: astro-ph/0510409 [astro-ph].
- Dijkstra, Mark and Roban Kramer (Aug. 2012). “Line transfer through clumpy, large-scale outflows: Ly α absorption and haloes around star-forming galaxies”. In: *MNRAS* 424.3, pp. 1672–1693. DOI: 10.1111/j.1365-2966.2012.21131.x. arXiv: 1203.3803 [astro-ph.CO].
- Dijkstra, Mark, Adam Lidz, and J. Stuart B. Wyithe (May 2007). “The impact of The IGM on high-redshift Ly α emission lines”. In: *MNRAS* 377.3, pp. 1175–1186. DOI: 10.1111/j.1365-2966.2007.11666.x. arXiv: astro-ph/0701667 [astro-ph].
- Dijkstra, Mark and Abraham Loeb (Dec. 2009). “Ly α blobs as an observational signature of cold accretion streams into galaxies”. In: *MNRAS* 400.2, pp. 1109–1120. DOI: 10.1111/j.1365-2966.2009.15533.x. arXiv: 0902.2999 [astro-ph.CO].
- (May 2008). “The polarization of scattered Ly α radiation around high-redshift galaxies”. In: *MNRAS* 386.1, pp. 492–504. DOI: 10.1111/j.1365-2966.2008.13066.x. arXiv: 0711.2312 [astro-ph].
- Dopita, M. A. and R. S. Sutherland (2003). *Astrophysics of the diffuse universe*.
- Dorfi, E. A. and D. Breitschwerdt (Apr. 2012). “Time-dependent galactic winds. I. Structure and evolution of galactic outflows accompanied by cosmic ray acceleration”. In: *A&A* 540, A77, A77. DOI: 10.1051/0004-6361/201118082. arXiv: 1304.1311 [astro-ph.HE].

- Dursi, L. J. and C. Pfrommer (Apr. 2008). “Draping of Cluster Magnetic Fields over Bullets and Bubbles—Morphology and Dynamic Effects”. In: *ApJ* 677.2, pp. 993–1018. DOI: 10.1086/529371. arXiv: 0711.0213 [astro-ph].
- Dutton, Aaron A. and Andrea V. Macciò (July 2014). “Cold dark matter haloes in the Planck era: evolution of structural parameters for Einasto and NFW profiles”. In: *MNRAS* 441.4, pp. 3359–3374. DOI: 10.1093/mnras/stu742. arXiv: 1402.7073 [astro-ph.CO].
- Duval, F., D. Schaerer, G. Östlin, et al. (Feb. 2014). “Lyman α line and continuum radiative transfer in a clumpy interstellar medium”. In: *A&A* 562, A52, A52. DOI: 10.1051/0004-6361/201220455. arXiv: 1302.7042 [astro-ph.GA].
- Eide, Marius B., Max Gronke, Mark Dijkstra, et al. (Apr. 2018). “Unlocking the Full Potential of Extragalactic Ly α through Its Polarization Properties”. In: *ApJ* 856.2, 156, p. 156. DOI: 10.3847/1538-4357/aab5b7. arXiv: 1802.04280 [astro-ph.GA].
- Ellison, S. L., R. Ibata, M. Pettini, et al. (Jan. 2004). “The sizes and kinematic structure of absorption systems towards the lensed quasar APM08279+5255”. In: *A&A* 414, pp. 79–93. DOI: 10.1051/0004-6361:20034003. arXiv: astro-ph/0310221 [astro-ph].
- Erb, D. K., M. Pettini, C. C. Steidel, et al. (Oct. 2016). “A High Fraction of Ly α Emitters among Galaxies with Extreme Emission Line Ratios at $z \sim 2$ ”. In: *ApJ* 830, 52, p. 52. DOI: 10.3847/0004-637X/830/1/52. arXiv: 1605.04919.
- Erb, Dawn K. (July 2015). “Feedback in low-mass galaxies in the early Universe”. In: *Nature* 523.7559, pp. 169–176. DOI: 10.1038/nature14454. arXiv: 1507.02374 [astro-ph.GA].
- Erb, Dawn K., Milan Bogosavljević, and Charles C. Steidel (Oct. 2011). “Filamentary Large-scale Structure Traced by Six Ly α Blobs at $z = 2.3$ ”. In: *ApJ* 740.1, L31, p. L31. DOI: 10.1088/2041-8205/740/1/L31. arXiv: 1109.2167 [astro-ph.CO].
- Erb, Dawn K., Zhihui Li, Charles C. Steidel, et al. (Aug. 2023). “The Circumgalactic Medium of Extreme Emission Line Galaxies at $z \sim 2$: Resolved Spectroscopy and Radiative Transfer Modeling of Spatially Extended Ly α Emission in the KBSS-KCWI Survey”. In: *ApJ* 953.1, 118, p. 118. DOI: 10.3847/1538-4357/acd849. arXiv: 2210.02465 [astro-ph.GA].
- Erb, Dawn K., Charles C. Steidel, and Yuguang Chen (July 2018). “The Kinematics of Extended Ly α Emission in a Low-mass, Low-metallicity Galaxy at $z = 2.3$ ”. In: *ApJ* 862.1, L10, p. L10. DOI: 10.3847/2041-8213/aacff6. arXiv: 1807.00065 [astro-ph.GA].

- Erb, Dawn K., Charles C. Steidel, Alice E. Shapley, et al. (Aug. 2006). “H α Observations of a Large Sample of Galaxies at $z \sim 2$: Implications for Star Formation in High-Redshift Galaxies”. In: *ApJ* 647.1, pp. 128–139. DOI: 10.1086/505341. arXiv: astro-ph/0604388 [astro-ph].
- Erb, Dawn K., Charles C. Steidel, Ryan F. Trainor, et al. (Nov. 2014). “The Ly α Properties of Faint Galaxies at $z \sim 2-3$ with Systemic Redshifts and Velocity Dispersions from Keck-MOSFIRE”. In: *ApJ* 795.1, 33, p. 33. DOI: 10.1088/0004-637X/795/1/33. arXiv: 1408.3638 [astro-ph.GA].
- Everett, John E., Ellen G. Zweibel, Robert A. Benjamin, et al. (Feb. 2008). “The Milky Way’s Kiloparsec-Scale Wind: A Hybrid Cosmic-Ray and Thermally Driven Outflow”. In: *ApJ* 674.1, pp. 258–270. DOI: 10.1086/524766. arXiv: 0710.3712 [astro-ph].
- Farber, Ryan J. and Max Gronke (Feb. 2022). “The survival of multiphase dusty clouds in hot winds”. In: *MNRAS* 510.1, pp. 551–567. DOI: 10.1093/mnras/stab3412. arXiv: 2107.07991 [astro-ph.GA].
- Fardal, Mark A., Neal Katz, Jeffrey P. Gardner, et al. (Dec. 2001). “Cooling Radiation and the Ly α Luminosity of Forming Galaxies”. In: *ApJ* 562.2, pp. 605–617. DOI: 10.1086/323519. arXiv: astro-ph/0007205 [astro-ph].
- Faucher-Giguère, Claude-Andre and S. Peng Oh (Jan. 2023). “Key Physical Processes in the Circumgalactic Medium”. In: *arXiv e-prints*, arXiv:2301.10253, arXiv:2301.10253. DOI: 10.48550/arXiv.2301.10253. arXiv: 2301.10253 [astro-ph.GA].
- Faucher-Giguère, Claude-André, Philip F. Hopkins, Dušan Kereš, et al. (May 2015). “Neutral hydrogen in galaxy haloes at the peak of the cosmic star formation history”. In: *MNRAS* 449.1, pp. 987–1003. DOI: 10.1093/mnras/stv336. arXiv: 1409.1919 [astro-ph.GA].
- Faucher-Giguère, Claude-André, Dušan Kereš, Mark Dijkstra, et al. (Dec. 2010). “Ly α Cooling Emission from Galaxy Formation”. In: *ApJ* 725.1, pp. 633–657. DOI: 10.1088/0004-637X/725/1/633. arXiv: 1005.3041 [astro-ph.CO].
- Faucher-Giguère, Claude-André, Adam Lidz, Matias Zaldarriaga, et al. (Oct. 2009). “A New Calculation of the Ionizing Background Spectrum and the Effects of He II Reionization”. In: *ApJ* 703, pp. 1416–1443. DOI: 10.1088/0004-637X/703/2/1416. arXiv: 0901.4554 [astro-ph.CO].
- Federrath, Christoph and Supratik Banerjee (Apr. 2015). “The density structure and star formation rate of non-isothermal polytropic turbulence”. In: *MNRAS* 448.4, pp. 3297–3313. DOI: 10.1093/mnras/stv180. arXiv: 1412.2756 [astro-ph.GA].
- Ferland, G. J., K. T. Korista, D. A. Verner, et al. (July 1998). “CLOUDY 90: Numerical Simulation of Plasmas and Their Spectra”. In: *Publications of the Astronomical Society of the Pacific* 110, pp. 761–778. DOI: 10.1086/316190.

- Fielding, Drummond B. and Greg L. Bryan (Jan. 2022). “The Structure of Multiphase Galactic Winds”. In: *ApJ* 924.2, 82, p. 82. DOI: 10 . 3847 / 1538 – 4357/ac2f41. arXiv: 2108.05355 [astro-ph.GA].
- Fielding, Drummond B., Eve C. Ostriker, Greg L. Bryan, et al. (May 2020). “Multiphase Gas and the Fractal Nature of Radiative Turbulent Mixing Layers”. In: *ApJ* 894.2, L24, p. L24. DOI: 10 . 3847 / 2041 – 8213 / ab8d2c. arXiv: 2003.08390 [astro-ph.GA].
- Ford, Amanda Brady, Romeel Davé, Benjamin D. Oppenheimer, et al. (Oct. 2014). “Tracing inflows and outflows with absorption lines in circumgalactic gas”. In: *MNRAS* 444.2, pp. 1260–1281. DOI: 10 . 1093 / mnras / stu1418. arXiv: 1309.5951 [astro-ph.CO].
- Forero-Romero, Jaime E., Max Gronke, Maria Camila Remolina-Gutiérrez, et al. (Feb. 2018). “Modelling the gas kinematics of an atypical Ly α emitting compact dwarf galaxy”. In: *MNRAS* 474.1, pp. 12–19. DOI: 10 . 1093 / mnras / stx2699. arXiv: 1710.05534 [astro-ph.GA].
- Francis, Paul J., Bruce E. Woodgate, Stephen J. Warren, et al. (Feb. 1996). “A Group of Galaxies at Redshift 2.38”. In: *ApJ* 457, p. 490. DOI: 10 . 1086 / 176747. arXiv: astro-ph/9511040 [astro-ph].
- Fujita, Akimi, Crystal L. Martin, Mordecai-Mark Mac Low, et al. (June 2009). “The Origin and Kinematics of Cold Gas in Galactic Winds: Insight from Numerical Simulations”. In: *ApJ* 698.1, pp. 693–714. DOI: 10 . 1088 / 0004 – 637X / 698/1/693. arXiv: 0803.2892 [astro-ph].
- Furlanetto, Steven R., Joop Schaye, Volker Springel, et al. (Mar. 2005). “Ly α Emission from Structure Formation”. In: *ApJ* 622.1, pp. 7–27. DOI: 10 . 1086 / 426808. arXiv: astro-ph/0409736 [astro-ph].
- Fynbo, J. U., P. Møller, and S. J. Warren (May 1999). “Extended LY alpha emission from a damped LY alpha absorber at $z=1.93$, and the relation between damped LY alpha absorbers and Lyman-break galaxies”. In: *MNRAS* 305.4, pp. 849–858. DOI: 10 . 1046 / j . 1365 – 8711 . 1999 . 02520 . x. arXiv: astro-ph/9812434 [astro-ph].
- Gatkine, Pradip, Sylvain Veilleux, Daniel Perley, et al. (Feb. 2022). “The CGM-GRB Study. II. Outflow-Galaxy Connection at z 2-6”. In: *ApJ* 926.1, 63, p. 63. DOI: 10 . 3847 / 1538 – 4357 / ac408e. arXiv: 2010.10540 [astro-ph.GA].
- Gazagnes, S., J. Chisholm, D. Schaerer, et al. (Aug. 2018). “Neutral gas properties of Lyman continuum emitting galaxies: Column densities and covering fractions from UV absorption lines”. In: *A&A* 616, A29, A29. DOI: 10 . 1051 / 0004 – 6361 / 201832759. arXiv: 1802.06378 [astro-ph.GA].
- Gazagnes, S., J. Chisholm, D. Schaerer, et al. (July 2020). “The origin of the escape of Lyman α and ionizing photons in Lyman continuum emitters”. In: *A&A* 639, A85, A85. DOI: 10 . 1051 / 0004 – 6361 / 202038096. arXiv: 2005.07215 [astro-ph.GA].

- Gazagnes, Simon, Valentin Mauerhofer, Danielle A. Berg, et al. (May 2023). “Interpreting the Si II and C II line spectra from the COS Legacy Spectroscopic Survey using a virtual galaxy from a high-resolution radiation-hydrodynamic simulation”. In: *arXiv e-prints*, arXiv:2305.19177, arXiv:2305.19177. DOI: 10.48550/arXiv.2305.19177. arXiv: 2305.19177 [astro-ph.GA].
- Geach, J. E., D. M. Alexander, B. D. Lehmer, et al. (July 2009). “The Chandra Deep Procluster Survey: Ly α Blobs are Powered by Heating, Not Cooling”. In: *ApJ* 700.1, pp. 1–9. DOI: 10.1088/0004-637X/700/1/1. arXiv: 0904.0452 [astro-ph.CO].
- Geach, J. E., R. G. Bower, D. M. Alexander, et al. (Sept. 2014). “A Submillimeter Galaxy Illuminating its Circumgalactic Medium: Ly α Scattering in a Cold, Clumpy Outflow”. In: *ApJ* 793.1, 22, p. 22. DOI: 10.1088/0004-637X/793/1/22. arXiv: 1402.6335 [astro-ph.GA].
- Geach, J. E., Y. Matsuda, Ian Smail, et al. (Nov. 2005). “A submillimetre survey of Lyman α haloes in the SA22 protocluster at $z=3.1$ ”. In: *MNRAS* 363.4, pp. 1398–1408. DOI: 10.1111/j.1365-2966.2005.09538.x. arXiv: astro-ph/0508357 [astro-ph].
- Geach, J. E., D. Narayanan, Y. Matsuda, et al. (Nov. 2016). “ALMA Observations of Ly α Blob 1: Halo Substructure Illuminated from Within”. In: *ApJ* 832.1, 37, p. 37. DOI: 10.3847/0004-637X/832/1/37. arXiv: 1608.02941 [astro-ph.GA].
- Geach, J. E., Ian Smail, S. C. Chapman, et al. (Jan. 2007). “Spitzer Identifications and Classifications of Submillimeter Galaxies in Giant, High-Redshift, Ly α -Emission-Line Nebulae”. In: *ApJ* 655.1, pp. L9–L12. DOI: 10.1086/511676. arXiv: astro-ph/0612272 [astro-ph].
- Ginsburg, Adam and Jordan Mirocha (Sept. 2011). *PySpecKit: Python Spectroscopic Toolkit*. ascl: 1109.001.
- Girelli, G., L. Pozzetti, M. Bolzonella, et al. (Feb. 2020). “The stellar-to-halo mass relation over the past 12 Gyr. I. Standard Λ CDM model”. In: *A&A* 634, A135, A135. DOI: 10.1051/0004-6361/201936329. arXiv: 2001.02230 [astro-ph.CO].
- Goerdt, Tobias, A. Dekel, A. Sternberg, et al. (Sept. 2010). “Gravity-driven Ly α blobs from cold streams into galaxies”. In: *MNRAS* 407.1, pp. 613–631. DOI: 10.1111/j.1365-2966.2010.16941.x. arXiv: 0911.5566 [astro-ph.CO].
- Gordon, Karl D., Geoffrey C. Clayton, K. A. Misselt, et al. (Sept. 2003). “A Quantitative Comparison of the Small Magellanic Cloud, Large Magellanic Cloud, and Milky Way Ultraviolet to Near-Infrared Extinction Curves”. In: *ApJ* 594.1, pp. 279–293. DOI: 10.1086/376774. arXiv: astro-ph/0305257 [astro-ph].

- Gronke, M., P. Bull, and M. Dijkstra (Oct. 2015). “A Systematic Study of Lyman- α Transfer through Outflowing Shells: Model Parameter Estimation”. In: *ApJ* 812.2, 123, p. 123. DOI: 10.1088/0004-637X/812/2/123. arXiv: 1506.03836 [astro-ph.GA].
- Gronke, M. and M. Dijkstra (Oct. 2014). “Directional Ly α equivalent boosting - I. Spherically symmetric distributions of clumps”. In: *MNRAS* 444.2, pp. 1095–1103. DOI: 10.1093/mnras/stu1513. arXiv: 1406.6709 [astro-ph.GA].
- (July 2016a). “Lyman- α Spectra from Multiphase Outflows, and their Connection to Shell Models”. In: *ApJ* 826.1, 14, p. 14. DOI: 10.3847/0004-637X/826/1/14. arXiv: 1604.06805 [astro-ph.GA].
- Gronke, Max (Dec. 2017). “Modeling 237 Lyman- α spectra of the MUSE-Wide survey”. In: *A&A* 608, A139, A139. DOI: 10.1051/0004-6361/201731791. arXiv: 1709.07008 [astro-ph.GA].
- Gronke, Max, Mark Dijkstra, Michael McCourt, et al. (Dec. 2016b). “From Mirrors to Windows: Lyman-alpha Radiative Transfer in a Very Clumpy Medium”. In: *ApJ* 833.2, L26, p. L26. DOI: 10.3847/2041-8213/833/2/L26. arXiv: 1611.01161 [astro-ph.GA].
- Gronke, Max, Mark Dijkstra, Michael McCourt, et al. (Nov. 2017). “Resonant line transfer in a fog: using Lyman-alpha to probe tiny structures in atomic gas”. In: *A&A* 607, A71, A71. DOI: 10.1051/0004-6361/201731013. arXiv: 1704.06278 [astro-ph.GA].
- Gronke, Max and S. Peng Oh (Feb. 2020). “How cold gas continuously entrains mass and momentum from a hot wind”. In: *MNRAS* 492.2, pp. 1970–1990. DOI: 10.1093/mnras/stz3332. arXiv: 1907.04771 [astro-ph.GA].
- (Oct. 2018). “The growth and entrainment of cold gas in a hot wind”. In: *MNRAS* 480, pp. L111–L115. DOI: 10.1093/mnrasl/sly131. arXiv: 1806.02728 [astro-ph.GA].
- Gronke, Max, S. Peng Oh, Suoqing Ji, et al. (Mar. 2022). “Survival and mass growth of cold gas in a turbulent, multiphase medium”. In: *MNRAS* 511.1, pp. 859–876. DOI: 10.1093/mnras/stab3351. arXiv: 2107.13012 [astro-ph.GA].
- Grønnow, Asger, Thor Tepper-García, and Joss Bland -Hawthorn (Sept. 2018). “Magnetic Fields in the Galactic Halo Restrict Fountain-driven Recycling and Accretion”. In: *ApJ* 865.1, 64, p. 64. DOI: 10.3847/1538-4357/aada0e. arXiv: 1805.03903 [astro-ph.GA].
- Grønnow, Asger, Thor Tepper-García, Joss Bland -Hawthorn, et al. (Aug. 2017). “Magnetized High Velocity Clouds in the Galactic Halo: A New Distance Constraint”. In: *ApJ* 845.1, 69, p. 69. DOI: 10.3847/1538-4357/aa7ed2. arXiv: 1707.02697 [astro-ph.GA].

- Guo, Qi, Simon White, Michael Boylan-Kolchin, et al. (May 2011). “From dwarf spheroidals to cD galaxies: simulating the galaxy population in a Λ CDM cosmology”. In: *MNRAS* 413.1, pp. 101–131. DOI: 10.1111/j.1365-2966.2010.18114.x. arXiv: 1006.0106 [astro-ph.CO].
- Haiman, Zoltán and Martin J. Rees (July 2001). “Extended Ly α Emission around Young Quasars: A Constraint on Galaxy Formation”. In: *ApJ* 556.1, pp. 87–92. DOI: 10.1086/321567. arXiv: astro-ph/0101174 [astro-ph].
- Haiman, Zoltán, Marco Spaans, and Eliot Quataert (July 2000). “Ly α Cooling Radiation from High-Redshift Halos”. In: *ApJ* 537.1, pp. L5–L8. DOI: 10.1086/312754. arXiv: astro-ph/0003366 [astro-ph].
- Hansen, Matthew and S. Peng Oh (Apr. 2006). “Lyman α radiative transfer in a multiphase medium”. In: *MNRAS* 367.3, pp. 979–1002. DOI: 10.1111/j.1365-2966.2005.09870.x. arXiv: astro-ph/0507586 [astro-ph].
- Harrington, J. Patrick (Jan. 1973). “The scattering of resonance-line radiation in the limit of large optical depth”. In: *MNRAS* 162, p. 43. DOI: 10.1093/mnras/162.1.43.
- Harris, Charles R., K. Jarrod Millman, Stéfan J. van der Walt, et al. (Sept. 2020). “Array programming with NumPy”. In: *Nature* 585.7825, pp. 357–362. DOI: 10.1038/s41586-020-2649-2. arXiv: 2006.10256 [cs.MS].
- Hashimoto, Takuya, Anne Verhamme, Masami Ouchi, et al. (Oct. 2015). “A Close Comparison between Observed and Modeled Ly α Lines for $z \sim 2.2$ Ly α Emitters”. In: *ApJ* 812.2, 157, p. 157. DOI: 10.1088/0004-637X/812/2/157. arXiv: 1504.03693 [astro-ph.GA].
- Hayes, Matthew, Claudia Scarlata, and Brian Siana (Aug. 2011). “Central powering of the largest Lyman- α nebula is revealed by polarized radiation”. In: *Nature* 476.7360, pp. 304–307. DOI: 10.1038/nature10320. arXiv: 1108.3332 [astro-ph.CO].
- Hayes, Matthew J., Axel Runnholm, Max Gronke, et al. (Feb. 2021). “Spectral Shapes of the Ly α Emission from Galaxies. I. Blueshifted Emission and Intrinsic Invariance with Redshift”. In: *ApJ* 908.1, 36, p. 36. DOI: 10.3847/1538-4357/abd246. arXiv: 2006.03232 [astro-ph.GA].
- Hayes, Matthew J., Axel Runnholm, Claudia Scarlata, et al. (Apr. 2023). “Spectral shapes of the Ly α emission from galaxies - II. The influence of stellar properties and nebular conditions on the emergent Ly α profiles”. In: *MNRAS* 520.4, pp. 5903–5927. DOI: 10.1093/mnras/stad477. arXiv: 2302.04875 [astro-ph.GA].
- Heckman, Timothy M., Rachel M. Alexandroff, Sanchayeeta Borthakur, et al. (Aug. 2015). “The Systematic Properties of the Warm Phase of Starburst-Driven Galactic Winds”. In: *ApJ* 809.2, 147, p. 147. DOI: 10.1088/0004-637X/809/2/147. arXiv: 1507.05622 [astro-ph.GA].

- Heckman, Timothy M., Lee Armus, and George K. Miley (Dec. 1990). “On the Nature and Implications of Starburst-driven Galactic Superwinds”. In: *ApJS* 74, p. 833. DOI: 10.1086/191522.
- Heckman, Timothy M., Sanchayeeta Borthakur, Roderik Overzier, et al. (Mar. 2011). “Extreme Feedback and the Epoch of Reionization: Clues in the Local Universe”. In: *ApJ* 730.1, 5, p. 5. DOI: 10.1088/0004-637X/730/1/5. arXiv: 1101.4219 [astro-ph.CO].
- Hennawi, Joseph F. and J. Xavier Prochaska (Mar. 2013). “Quasars Probing Quasars. IV. Joint Constraints on the Circumgalactic Medium from Absorption and Emission”. In: *ApJ* 766.1, 58, p. 58. DOI: 10.1088/0004-637X/766/1/58. arXiv: 1303.2708 [astro-ph.CO].
- Hennawi, Joseph F., J. Xavier Prochaska, Sebastiano Cantalupo, et al. (May 2015). “Quasar quartet embedded in giant nebula reveals rare massive structure in distant universe”. In: *Science* 348.6236, pp. 779–783. DOI: 10.1126/science.aaa5397. arXiv: 1505.03786 [astro-ph.GA].
- Hennawi, Joseph F., J. Xavier Prochaska, Juna Kollmeier, et al. (Mar. 2009). “A $z = 3$ Ly α Blob Associated With a Damped Ly α System Proximate to Its Background Quasar”. In: *ApJ* 693.2, pp. L49–L55. DOI: 10.1088/0004-637X/693/2/L49. arXiv: 0807.2271 [astro-ph].
- Hennawi, Joseph F. and Jason X. Prochaska (Feb. 2007). “Quasars Probing Quasars. II. The Anisotropic Clustering of Optically Thick Absorbers around Quasars”. In: *ApJ* 655.2, pp. 735–748. DOI: 10.1086/509770. arXiv: astro-ph/0606084 [astro-ph].
- Hennawi, Joseph F., Jason X. Prochaska, Scott Burles, et al. (Nov. 2006). “Quasars Probing Quasars. I. Optically Thick Absorbers near Luminous Quasars”. In: *ApJ* 651.1, pp. 61–83. DOI: 10.1086/507069. arXiv: astro-ph/0603742 [astro-ph].
- Henry, Alaina, Claudia Scarlata, Crystal L. Martin, et al. (Aug. 2015). “Ly α Emission from Green Peas: The Role of Circumgalactic Gas Density, Covering, and Kinematics”. In: *ApJ* 809.1, 19, p. 19. DOI: 10.1088/0004-637X/809/1/19. arXiv: 1505.05149 [astro-ph.GA].
- Herenz, Edmund Christian, Matthew Hayes, and Claudia Scarlata (Jan. 2020). “Deciphering Lyman α blob 1 with deep MUSE observations”. In: *arXiv e-prints*, arXiv:2001.03699, arXiv:2001.03699. arXiv: 2001.03699 [astro-ph.GA].
- Herenz, Edmund Christian and Lutz Wisotzki (June 2017). “LSDCat: Detection and cataloguing of emission-line sources in integral-field spectroscopy datacubes”. In: *A&A* 602, A111, A111. DOI: 10.1051/0004-6361/201629507. arXiv: 1703.05166 [astro-ph.IM].

- Hine, N. K., J. E. Geach, D. M. Alexander, et al. (Jan. 2016a). “An enhanced merger fraction within the galaxy population of the SSA22 protocluster at $z = 3.1$ ”. In: *MNRAS* 455.3, pp. 2363–2370. DOI: 10.1093/mnras/stv2448. arXiv: 1506.05115 [astro-ph.GA].
- Hine, N. K., J. E. Geach, Y. Matsuda, et al. (Aug. 2016b). “The average submillimetre properties of Lyman α blobs at $z = 3$ ”. In: *MNRAS* 460.4, pp. 4075–4085. DOI: 10.1093/mnras/stw1185. arXiv: 1605.04912 [astro-ph.GA].
- Hopkins, Philip F. (Oct. 2016). “A constrained-gradient method to control divergence errors in numerical MHD”. In: *MNRAS* 462.1, pp. 576–587. DOI: 10.1093/mnras/stw1578. arXiv: 1509.07877 [astro-ph.IM].
- (June 2015). “A new class of accurate, mesh-free hydrodynamic simulation methods”. In: *MNRAS* 450, pp. 53–110. DOI: 10.1093/mnras/stv195. arXiv: 1409.7395 [astro-ph.CO].
- (Apr. 2017). “Anisotropic diffusion in mesh-free numerical magnetohydrodynamics”. In: *MNRAS* 466, pp. 3387–3405. DOI: 10.1093/mnras/stw3306. arXiv: 1602.07703 [astro-ph.IM].
- Hopkins, Philip F., T. K. Chan, Shea Garrison-Kimmel, et al. (May 2019). “But What About... Cosmic Rays, Magnetic Fields, Conduction, & Viscosity in Galaxy Formation”. In: *arXiv e-prints*, arXiv:1905.04321, arXiv:1905.04321. arXiv: 1905.04321 [astro-ph.GA].
- Hopkins, Philip F., Andrew Wetzel, Dušan Kereš, et al. (Oct. 2018). “FIRE-2 simulations: physics versus numerics in galaxy formation”. In: *MNRAS* 480, pp. 800–863. DOI: 10.1093/mnras/sty1690. arXiv: 1702.06148 [astro-ph.GA].
- Hummels, Cameron B., Britton D. Smith, Philip F. Hopkins, et al. (Sept. 2019). “The Impact of Enhanced Halo Resolution on the Simulated Circumgalactic Medium”. In: *ApJ* 882.2, 156, p. 156. DOI: 10.3847/1538-4357/ab378f. arXiv: 1811.12410 [astro-ph.GA].
- Inoue, Akio K., Ikkoh Shimizu, Ikuru Iwata, et al. (Aug. 2014). “An updated analytic model for attenuation by the intergalactic medium”. In: *MNRAS* 442.2, pp. 1805–1820. DOI: 10.1093/mnras/stu936. arXiv: 1402.0677 [astro-ph.CO].
- Izotov, Y I, G Worseck, D Schaerer, et al. (2018). “Low-redshift Lyman continuum leaking galaxies with high [O III]/[O II] ratios”. English. In: *Monthly Notices of the Royal Astronomical Society* 478.4, pp. 4851–4865. DOI: 10.1093/mnras/sty1378.
- Izotov, Y. I., G. Worseck, D. Schaerer, et al. (May 2021). “Lyman continuum leakage from low-mass galaxies with $M_{\star} < 10^8 M_{\odot}$ ”. In: *MNRAS* 503.2, pp. 1734–1752. DOI: 10.1093/mnras/stab612. arXiv: 2103.01514 [astro-ph.GA].

- Jacob, Svenja, Rüdiger Pakmor, Christine M. Simpson, et al. (Mar. 2018). “The dependence of cosmic ray-driven galactic winds on halo mass”. In: *MNRAS* 475.1, pp. 570–584. DOI: 10.1093/mnras/stx3221. arXiv: 1712.04947 [astro-ph.GA].
- Johnson, Sean D., Hsiao-Wen Chen, John S. Mulchaey, et al. (Nov. 2017). “The Extent of Chemically Enriched Gas around Star-forming Dwarf Galaxies”. In: *ApJ* 850, L10, p. L10. DOI: 10.3847/2041-8213/aa9370. arXiv: 1710.06441 [astro-ph.GA].
- Jones, T. W., Dongsu Ryu, and I. L. Tregillis (Dec. 1996). “The Magnetohydrodynamics of Supersonic Gas Clouds: MHD Cosmic Bullets and Wind-swept Clumps”. In: *ApJ* 473, p. 365. DOI: 10.1086/178151. arXiv: astro-ph/9606106 [astro-ph].
- Jones, Tucker A., Richard S. Ellis, Matthew A. Schenker, et al. (Dec. 2013). “Keck Spectroscopy of Gravitationally Lensed $z \sim 4$ Galaxies: Improved Constraints on the Escape Fraction of Ionizing Photons”. In: *ApJ* 779.1, 52, p. 52. DOI: 10.1088/0004-637X/779/1/52. arXiv: 1304.7015 [astro-ph.CO].
- Jung, Intae, Steven L. Finkelstein, Pablo Arrabal Haro, et al. (Apr. 2023). “CEERS: Diversity of Lyman-Alpha Emitters during the Epoch of Reionization”. In: *arXiv e-prints*, arXiv:2304.05385, arXiv:2304.05385. DOI: 10.48550/arXiv.2304.05385. arXiv: 2304.05385 [astro-ph.GA].
- Kacprzak, Glenn G., Crystal L. Martin, Nicolas Bouché, et al. (Sept. 2014). “New Perspective on Galaxy Outflows from the First Detection of Both Intrinsic and Traverse Metal-line Absorption”. In: *ApJ* 792.1, L12, p. L12. DOI: 10.1088/2041-8205/792/1/L12. arXiv: 1407.4126 [astro-ph.GA].
- Kakiichi, Koki and Max Gronke (Feb. 2021). “Radiation Hydrodynamics of Turbulent H II Regions in Molecular Clouds: A Physical Origin of LyC Leakage and the Associated Ly α Spectra”. In: *ApJ* 908.1, 30, p. 30. DOI: 10.3847/1538-4357/abc2d9.
- Kanjilal, Vijit, Alankar Dutta, and Prateek Sharma (Feb. 2021). “Growth and structure of multiphase gas in the cloud-crushing problem with cooling”. In: *MNRAS* 501.1, pp. 1143–1159. DOI: 10.1093/mnras/staa3610. arXiv: 2009.00525 [astro-ph.GA].
- Kawazura, Yohei, Michael Barnes, and Alexander A. Schekochihin (Jan. 2019). “Thermal disequilibrium of ions and electrons by collisionless plasma turbulence”. In: *Proceedings of the National Academy of Science* 116.3, pp. 771–776. DOI: 10.1073/pnas.1812491116. arXiv: 1807.07702 [physics.plasm-ph].
- Keel, William C., Seth H. Cohen, Rogier A. Windhorst, et al. (Dec. 1999). “Evidence for Large-Scale Structure at $z \sim 2.4$ from Ly α Imaging”. In: *AJ* 118.6, pp. 2547–2560. DOI: 10.1086/301139. arXiv: astro-ph/9908183 [astro-ph].

- Keeney, Brian A., John T. Stocke, Charles W. Danforth, et al. (May 2017). “Characterizing the Circumgalactic Medium of Nearby Galaxies with HST/COS and HST/STIS Absorption-line Spectroscopy. II. Methods and Models”. In: *ApJS* 230.1, 6, p. 6. DOI: 10.3847/1538-4365/aa6b59. arXiv: 1704.00235 [astro-ph.GA].
- Kennicutt Robert C., Jr., Peter Tamblyn, and Charles E. Congdon (Nov. 1994). “Past and Future Star Formation in Disk Galaxies”. In: *ApJ* 435, p. 22. DOI: 10.1086/174790.
- Kereš, Dušan and Lars Hernquist (July 2009). “Seeding the Formation of Cold Gaseous Clouds in Milky Way-Size Halos”. In: *ApJ* 700, pp. L1–L5. DOI: 10.1088/0004-637X/700/1/L1. arXiv: 0905.2186 [astro-ph.CO].
- Kereš, Dušan, Neal Katz, David H. Weinberg, et al. (Oct. 2005). “How do galaxies get their gas?” In: *MNRAS* 363.1, pp. 2–28. DOI: 10.1111/j.1365-2966.2005.09451.x. arXiv: astro-ph/0407095 [astro-ph].
- Kim, Eunchong, Yujin Yang, Ann Zabludoff, et al. (May 2020). “What Makes Ly α Nebulae Glow? Mapping the Polarization of LABd05”. In: *ApJ* 894.1, 33, p. 33. DOI: 10.3847/1538-4357/ab837f. arXiv: 2003.13915 [astro-ph.GA].
- Kimm, Taysun, Jérémy Blaizot, Thibault Garel, et al. (June 2019). “Understanding the escape of LyC and Ly α photons from turbulent clouds”. In: *MNRAS* 486.2, pp. 2215–2237. DOI: 10.1093/mnras/stz989. arXiv: 1901.05990 [astro-ph.GA].
- Kimm, Taysun, Adrienne Slyz, Julien Devriendt, et al. (May 2011). “Are cold flows detectable with metal absorption lines?” In: *MNRAS* 413.1, pp. L51–L55. DOI: 10.1111/j.1745-3933.2011.01031.x. arXiv: 1012.0059 [astro-ph.CO].
- Klein, Richard I., Christopher F. McKee, and Philip Colella (Jan. 1994). “On the Hydrodynamic Interaction of Shock Waves with Interstellar Clouds. I. Nonradiative Shocks in Small Clouds”. In: *ApJ* 420, p. 213. DOI: 10.1086/173554.
- Kollmeier, Juna A., Zheng Zheng, Romeel Davé, et al. (Jan. 2010). “Ly α Emission from Cosmic Structure. I. Fluorescence”. In: *ApJ* 708.2, pp. 1048–1075. DOI: 10.1088/0004-637X/708/2/1048. arXiv: 0907.0704 [astro-ph.CO].
- Komarov, S. V., E. M. Churazov, M. W. Kunz, et al. (July 2016). “Thermal conduction in a mirror-unstable plasma”. In: *MNRAS* 460, pp. 467–477. DOI: 10.1093/mnras/stw963. arXiv: 1603.00524 [astro-ph.HE].
- Kornei, Katherine A., Alice E. Shapley, Dawn K. Erb, et al. (Mar. 2010). “The Relationship between Stellar Populations and Ly α Emission in Lyman Break Galaxies”. In: *ApJ* 711.2, pp. 693–710. DOI: 10.1088/0004-637X/711/2/693. arXiv: 0911.2000 [astro-ph.CO].

- Körtgen, Bastian, Christoph Federrath, and Robi Banerjee (Feb. 2019). “On the shape and completeness of the column density probability distribution function of molecular clouds”. In: *MNRAS* 482.4, pp. 5233–5240. DOI: 10.1093/mnras/sty3071. arXiv: 1811.02864 [astro-ph.GA].
- Kravtsov, A. V., A. A. Vikhlinin, and A. V. Meshcheryakov (Jan. 2018). “Stellar Mass—Halo Mass Relation and Star Formation Efficiency in High-Mass Halos”. In: *Astronomy Letters* 44.1, pp. 8–34. DOI: 10.1134/S1063773717120015. arXiv: 1401.7329 [astro-ph.CO].
- Krogager, Jens-Kristian, Johan P. U. Fynbo, Cédric Ledoux, et al. (Aug. 2013). “Comprehensive study of a $z = 2.35$ DLA Galaxy: mass, metallicity, age, morphology and SFR from HST and VLT”. In: *MNRAS* 433.4, pp. 3091–3102. DOI: 10.1093/mnras/stt955. arXiv: 1304.4231 [astro-ph.CO].
- Krumholz, Mark R. and Nickolay Y. Gnedin (Mar. 2011). “A Comparison of Methods for Determining the Molecular Content of Model Galaxies”. In: *ApJ* 729, 36, p. 36. DOI: 10.1088/0004-637X/729/1/36. arXiv: 1011.4065 [astro-ph.CO].
- Kubo, M., T. Yamada, T. Ichikawa, et al. (Jan. 2016). “An extremely dense group of massive galaxies at the centre of the protocluster at $z = 3.09$ in the SSA22 field”. In: *MNRAS* 455.3, pp. 3333–3344. DOI: 10.1093/mnras/stv2392. arXiv: 1510.04816 [astro-ph.GA].
- Kubo, Mariko, Toru Yamada, Takashi Ichikawa, et al. (Jan. 2015). “NIR Spectroscopic Observation of Massive Galaxies in the Protocluster at $z = 3.09$ ”. In: *ApJ* 799.1, 38, p. 38. DOI: 10.1088/0004-637X/799/1/38. arXiv: 1411.2663 [astro-ph.GA].
- Kuhlen, M. and C.-A. Faucher-Giguère (June 2012). “Concordance models of reionization: implications for faint galaxies and escape fraction evolution”. In: *MNRAS* 423, pp. 862–876. DOI: 10.1111/j.1365-2966.2012.20924.x. arXiv: 1201.0757 [astro-ph.CO].
- Kulas, Kristin R., Alice E. Shapley, Juna A. Kollmeier, et al. (Jan. 2012). “The Kinematics of Multiple-peaked $\text{Ly}\alpha$ Emission in Star-forming Galaxies at $z \sim 2-3$ ”. In: *ApJ* 745.1, 33, p. 33. DOI: 10.1088/0004-637X/745/1/33. arXiv: 1107.4367 [astro-ph.CO].
- Kulkarni, Varsha P., Frances H. Cashman, Sebastian Lopez, et al. (Dec. 2019). “Probing Structure in Cold Gas at $z \lesssim 1$ with Gravitationally Lensed Quasar Sight Lines”. In: *ApJ* 886.2, 83, p. 83. DOI: 10.3847/1538-4357/ab4c2e. arXiv: 1910.10759 [astro-ph.GA].
- Kulsrud, R M (1983). “MHD description of plasma”. In: *Handbook of Plasma Physics*. Ed. by R N Sagdeev and M N Rosenbluth. Princeton University.
- Kunz, Matthew W, Alexander A Schekochihin, and James M Stone (May 2014). “Firehose and Mirror Instabilities in a Collisionless Shearing Plasma”. In: *Phys. Rev. Lett.* 112.2, p. 205003. DOI: 10.1103/physrevlett.112.205003.

- Kusakabe, Haruka, Kazuhiro Shimasaku, Rieko Momose, et al. (June 2019). “The dominant origin of diffuse Ly α halos around Ly α emitters explored by spectral energy distribution fitting and clustering analysis”. In: *PASJ* 71.3, 55, p. 55. DOI: 10.1093/pasj/psz029. arXiv: 1803.10265 [astro-ph.GA].
- Lake, Ethan, Zheng Zheng, Renyue Cen, et al. (June 2015). “On the Diffuse Ly α Halo around Ly α Emitting Galaxies”. In: *ApJ* 806.1, 46, p. 46. DOI: 10.1088/0004-637X/806/1/46. arXiv: 1502.01349 [astro-ph.CO].
- Lamers, Henny J. G. L. M. and Joseph P. Cassinelli (1999). *Introduction to Stellar Winds*.
- Lao, Bing-Xin and Aaron Smith (Sept. 2020). “Resonant-line radiative transfer within power-law density profiles”. In: *MNRAS* 497.3, pp. 3925–3942. DOI: 10.1093/mnras/staa2198. arXiv: 2005.09692 [astro-ph.GA].
- Laursen, Peter, Florent Duval, and Göran Östlin (Apr. 2013). “On the (Non-)Enhancement of the Ly α Equivalent Width by a Multiphase Interstellar Medium”. In: *ApJ* 766.2, 124, p. 124. DOI: 10.1088/0004-637X/766/2/124. arXiv: 1211.2833 [astro-ph.CO].
- Laursen, Peter and Jesper Sommer-Larsen (Mar. 2007). “Ly α Resonant Scattering in Young Galaxies: Predictions from Cosmological Simulations”. In: *ApJ* 657.2, pp. L69–L72. DOI: 10.1086/513191. arXiv: astro-ph/0610761 [astro-ph].
- Laursen, Peter, Jesper Sommer-Larsen, and Alexei O. Razoumov (Feb. 2011). “Intergalactic Transmission and Its Impact on the Ly α Line”. In: *ApJ* 728.1, 52, p. 52. DOI: 10.1088/0004-637X/728/1/52. arXiv: 1009.1384 [astro-ph.CO].
- Leclercq, Floriane, Roland Bacon, Anne Verhamme, et al. (Mar. 2020). “The MUSE Hubble Ultra Deep Field Survey. XIII. Spatially resolved spectral properties of Lyman α haloes around star-forming galaxies at $z > 3$ ”. In: *A&A* 635, A82, A82. DOI: 10.1051/0004-6361/201937339. arXiv: 2002.05731 [astro-ph.GA].
- Leclercq, Floriane, Roland Bacon, Lutz Wisotzki, et al. (Dec. 2017). “The MUSE Hubble Ultra Deep Field Survey. VIII. Extended Lyman- α haloes around high- z star-forming galaxies”. In: *A&A* 608, A8, A8. DOI: 10.1051/0004-6361/201731480. arXiv: 1710.10271 [astro-ph.GA].
- Lehmer, B. D., D. M. Alexander, S. C. Chapman, et al. (Nov. 2009a). “The Chandra Deep Protocluster Survey: point-source catalogues for a 400-ks observation of the $z = 3.09$ protocluster in SSA22”. In: *MNRAS* 400.1, pp. 299–316. DOI: 10.1111/j.1365-2966.2009.15449.x. arXiv: 0907.4369 [astro-ph.CO].

- Lehmer, B. D., D. M. Alexander, J. E. Geach, et al. (Jan. 2009b). “The Chandra Deep Protocluster Survey: Evidence for an Enhancement of AGN Activity in the SSA22 Protocluster at $z = 3.09$ ”. In: *ApJ* 691.1, pp. 687–695. DOI: 10.1088/0004-637X/691/1/687. arXiv: 0809.5058 [astro-ph].
- Leitherer, Claus, Rupali Chandar, Christy A. Tremonti, et al. (Aug. 2013). “Far-ultraviolet Observations of Outflows from Infrared-luminous Galaxies”. In: *ApJ* 772.2, 120, p. 120. DOI: 10.1088/0004-637X/772/2/120. arXiv: 1306.0419 [astro-ph.CO].
- Li, Shule, Adam Frank, and Eric G. Blackman (Sept. 2013). “Magnetohydrodynamic Shock-Clump Evolution with Self-contained Magnetic Fields”. In: *ApJ* 774.2, 133, p. 133. DOI: 10.1088/0004-637X/774/2/133. arXiv: 1307.3316 [astro-ph.SR].
- (Nov. 2014). “Triggered star formation and its consequences”. In: *MNRAS* 444.3, pp. 2884–2892. DOI: 10.1093/mnras/stu1571. arXiv: 1404.5924 [astro-ph.SR].
- Li, Zhihui and Max Gronke (July 2022a). “Deciphering the Lyman- α emission line: towards the understanding of galactic properties extracted from Ly α spectra via radiative transfer modelling”. In: *MNRAS* 513.4, pp. 5034–5051. DOI: 10.1093/mnras/stac1207. arXiv: 2111.03671 [astro-ph.GA].
- Li, Zhihui, Philip F. Hopkins, Jonathan Squire, et al. (Feb. 2020). “On the survival of cool clouds in the circumgalactic medium”. In: *MNRAS* 492.2, pp. 1841–1854. DOI: 10.1093/mnras/stz3567. arXiv: 1909.02632 [astro-ph.GA].
- Li, Zhihui, Charles C. Steidel, Max Gronke, et al. (Apr. 2021). “Revisiting the gas kinematics in SSA22 Lyman- α Blob 1 with radiative transfer modelling in a multiphase, clumpy medium”. In: *MNRAS* 502.2, pp. 2389–2408. DOI: 10.1093/mnras/staa3951. arXiv: 2008.09130 [astro-ph.GA].
- Li, Zhihui, Charles C. Steidel, Max Gronke, et al. (July 2022b). “Where outflows meet inflows: gas kinematics in SSA22 Ly α blob 2 decoded by advanced radiative transfer modelling”. In: *MNRAS* 513.3, pp. 3414–3428. DOI: 10.1093/mnras/stac958. arXiv: 2104.10682 [astro-ph.GA].
- Liang, Cameron J. and Hsiao-Wen Chen (Dec. 2014). “Mining circumgalactic baryons in the low-redshift universe”. In: *MNRAS* 445.2, pp. 2061–2081. DOI: 10.1093/mnras/stu1901. arXiv: 1402.3602 [astro-ph.CO].
- Liang, Cameron J., Andrey V. Kravtsov, and Oscar Agertz (May 2016). “Column density profiles of multiphase gaseous haloes”. In: *MNRAS* 458, pp. 1164–1187. DOI: 10.1093/mnras/stw375. arXiv: 1507.07002 [astro-ph.GA].
- Liang, Cameron J. and Ian Remming (Feb. 2020). “On the model of the circumgalactic mist: the implications of cloud sizes in galactic winds and haloes”. In: *MNRAS* 491.4, pp. 5056–5072. DOI: 10.1093/mnras/stz3403. arXiv: 1806.10688 [astro-ph.GA].

- Liang, Cameron J. and Ian S. Remming (June 2018). “On the model of the circumgalactic mist: the implications of cloud sizes in galactic winds and halos”. In: *arXiv e-prints*, arXiv:1806.10688, arXiv:1806.10688. arXiv: 1806.10688 [astro-ph.GA].
- Loeb, Abraham and George B. Rybicki (Oct. 1999). “Scattered Ly α Radiation around Sources before Cosmological Reionization”. In: *ApJ* 524.2, pp. 527–535. DOI: 10.1086/307844. arXiv: astro-ph/9902180 [astro-ph].
- Ludlow, Aaron D., Julio F. Navarro, Raúl E. Angulo, et al. (June 2014). “The mass-concentration-redshift relation of cold dark matter haloes”. In: *MNRAS* 441.1, pp. 378–388. DOI: 10.1093/mnras/stu483. arXiv: 1312.0945 [astro-ph.CO].
- Luridiana, V., C. Morisset, and R. A. Shaw (Jan. 2015). “PyNeb: a new tool for analyzing emission lines. I. Code description and validation of results”. In: *A&A* 573, A42, A42. DOI: 10.1051/0004-6361/201323152. arXiv: 1410.6662 [astro-ph.IM].
- Mac Low, Mordecai-Mark, Christopher F. McKee, Richard I. Klein, et al. (Oct. 1994). “Shock Interactions with Magnetized Interstellar Clouds. I. Steady Shocks Hitting Nonradiative Clouds”. In: *ApJ* 433, p. 757. DOI: 10.1086/174685.
- Madau, Piero, Lucia Pozzetti, and Mark Dickinson (May 1998). “The Star Formation History of Field Galaxies”. In: *ApJ* 498.1, pp. 106–116. DOI: 10.1086/305523. arXiv: astro-ph/9708220 [astro-ph].
- Mao, S. Alwin and Eve C. Ostriker (Feb. 2018). “Galactic Disk Winds Driven by Cosmic Ray Pressure”. In: *ApJ* 854.2, 89, p. 89. DOI: 10.3847/1538-4357/aaa88e. arXiv: 1801.06544 [astro-ph.GA].
- Markevitch, Maxim and Alexey Vikhlinin (May 2007). “Shocks and cold fronts in galaxy clusters”. In: *Phys. Rep.* 443, pp. 1–53. DOI: 10.1016/j.physrep.2007.01.001. arXiv: astro-ph/0701821 [astro-ph].
- Martin, Chris, Anna Moore, Patrick Morrissey, et al. (July 2010). “The Keck Cosmic Web Imager”. In: *Ground-based and Airborne Instrumentation for Astronomy III*. Ed. by Ian S. McLean, Suzanne K. Ramsay, and Hideki Takami. Vol. 7735. Society of Photo-Optical Instrumentation Engineers (SPIE) Conference Series, 77350M, p. 77350M. DOI: 10.1117/12.858227.
- Martin, Crystal L. (Mar. 2005). “Mapping Large-Scale Gaseous Outflows in Ultraluminous Galaxies with Keck II ESI Spectra: Variations in Outflow Velocity with Galactic Mass”. In: *ApJ* 621.1, pp. 227–245. DOI: 10.1086/427277. arXiv: astro-ph/0410247 [astro-ph].
- Martin, Crystal L. and Nicolas Bouché (Oct. 2009). “Physical Conditions in the Low-ionization Component of Starburst Outflows: The Shape of Near-Ultraviolet and Optical Absorption-line Troughs in Keck Spectra of ULIRGs”. In: *ApJ* 703.2, pp. 1394–1415. DOI: 10.1088/0004-637X/703/2/1394. arXiv: 0908.4271 [astro-ph.CO].

- Martin, Crystal L., Mark Dijkstra, Alaina Henry, et al. (Apr. 2015). “The Ly α Line Profiles of Ultraluminous Infrared Galaxies: Fast Winds and Lyman Continuum Leakage”. In: *ApJ* 803.1, 6, p. 6. DOI: 10.1088/0004-637X/803/1/6. arXiv: 1501.05946 [astro-ph.GA].
- Martin, Crystal L., Alice E. Shapley, Alison L. Coil, et al. (Dec. 2012). “Demographics and Physical Properties of Gas Outflows/Inflows at $0.4 < z < 1.4$ ”. In: *ApJ* 760.2, 127, p. 127. DOI: 10.1088/0004-637X/760/2/127. arXiv: 1206.5552 [astro-ph.CO].
- Martin, D. Christopher, Daphne Chang, Matt Matuszewski, et al. (May 2014). “Intergalactic Medium Emission Observations with the Cosmic Web Imager. II. Discovery of Extended, Kinematically Linked Emission around SSA22 Ly α Blob 2”. In: *ApJ* 786.2, 107, p. 107. DOI: 10.1088/0004-637X/786/2/107. arXiv: 1402.4809 [astro-ph.GA].
- Martin-Alvarez, Sergio, Julien Devriendt, Adrienne Slyz, et al. (Sept. 2018). “A three-phase amplification of the cosmic magnetic field in galaxies”. In: *Monthly Notices of the Royal Astronomical Society* 479.3, pp. 3343–3365. DOI: 10.1093/mnras/sty1623. arXiv: 1806.06866 [astro-ph.GA].
- Mas-Ribas, Lluís and Mark Dijkstra (May 2016). “On the Contribution of Fluorescence to Ly α Halos around Star-Forming Galaxies”. In: *ApJ* 822.2, 84, p. 84. DOI: 10.3847/0004-637X/822/2/84. arXiv: 1603.04840 [astro-ph.GA].
- Mas-Ribas, Lluís, Mark Dijkstra, Joseph F. Hennawi, et al. (May 2017). “Small-scale Intensity Mapping: Extended Ly α , H α , and Continuum Emission as a Probe of Halo Star Formation in High-redshift Galaxies”. In: *ApJ* 841.1, 19, p. 19. DOI: 10.3847/1538-4357/aa704e. arXiv: 1703.02593 [astro-ph.GA].
- Matsuda, Y., D. Iono, K. Ohta, et al. (Oct. 2007). “High-Resolution Submillimeter Imaging of the Ly α Blob 1 in SSA 22”. In: *ApJ* 667.2, pp. 667–672. DOI: 10.1086/521076. arXiv: 0707.0525 [astro-ph].
- Matsuda, Y., T. Yamada, T. Hayashino, et al. (Jan. 2011). “The Subaru Ly α blob survey: a sample of 100-kpc Ly α blobs at $z = 3$ ”. In: *MNRAS* 410.1, pp. L13–L17. DOI: 10.1111/j.1745-3933.2010.00969.x. arXiv: 1010.2877 [astro-ph.CO].
- Matsuda, Yuichi, Toru Yamada, Tomoki Hayashino, et al. (Aug. 2004). “A Subaru Search for Ly α Blobs in and around the Protocluster Region At Redshift $z = 3.1$ ”. In: *AJ* 128.2, pp. 569–584. DOI: 10.1086/422020. arXiv: astro-ph/0405221 [astro-ph].
- Matthee, Jorryt, David Sobral, Matthew Hayes, et al. (July 2021). “The X-SHOOTER Lyman α survey at $z = 2$ (XLS-z2) I: what makes a galaxy a Lyman α emitter?” In: *MNRAS* 505.1, pp. 1382–1412. DOI: 10.1093/mnras/stab1304. arXiv: 2102.07779 [astro-ph.GA].

- Mauerhofer, V., A. Verhamme, J. Blaizot, et al. (Feb. 2021). “UV absorption lines and their potential for tracing the Lyman continuum escape fraction”. In: *A&A* 646, A80, A80. DOI: 10.1051/0004-6361/202039449. arXiv: 2012.03984 [astro-ph.GA].
- McCourt, Michael, Ryan M. O’Leary, Ann-Marie Madigan, et al. (May 2015). “Magnetized gas clouds can survive acceleration by a hot wind”. In: *MNRAS* 449.1, pp. 2–7. DOI: 10.1093/mnras/stv355. arXiv: 1409.6719 [astro-ph.GA].
- McCourt, Michael, S. Peng Oh, Ryan O’Leary, et al. (Feb. 2018). “A characteristic scale for cold gas”. In: *MNRAS* 473.4, pp. 5407–5431. DOI: 10.1093/mnras/stx2687. arXiv: 1610.01164 [astro-ph.GA].
- McKee, C. F. and L. L. Cowie (July 1977). “The evaporation of spherical clouds in a hot gas. II. Effects of radiation.” In: *ApJ* 215, pp. 213–225. DOI: 10.1086/155350.
- (Feb. 1975). “The interaction between the blast wave of a supernova remnant and interstellar clouds.” In: *ApJ* 195, pp. 715–725. DOI: 10.1086/153373.
- McLean, Ian S., Charles C. Steidel, Harland Epps, et al. (July 2010). “Design and development of MOSFIRE: the multi-object spectrometer for infrared exploration at the Keck Observatory”. In: *Proc. SPIE*. Vol. 7735. Society of Photo-Optical Instrumentation Engineers (SPIE) Conference Series, 77351E, 77351E. DOI: 10.1117/12.856715.
- McLean, Ian S., Charles C. Steidel, Harland W. Epps, et al. (Sept. 2012). “MOSFIRE, the multi-object spectrometer for infra-red exploration at the Keck Observatory”. In: *Proc. SPIE*. Vol. 8446. Society of Photo-Optical Instrumentation Engineers (SPIE) Conference Series, 84460J, 84460J. DOI: 10.1117/12.924794.
- McLinden, Emily M., Steven L. Finkelstein, James E. Rhoads, et al. (Apr. 2011). “First Spectroscopic Measurements of [O III] Emission from Ly α Selected Field Galaxies at $z \sim 3.1$ ”. In: *ApJ* 730.2, 136, p. 136. DOI: 10.1088/0004-637X/730/2/136. arXiv: 1006.1895 [astro-ph.CO].
- McLinden, Emily M., Sangeeta Malhotra, James E. Rhoads, et al. (Apr. 2013). “[O III] Emission and Gas Kinematics in a Lyman-alpha Blob at $z \sim 3.1$ ”. In: *ApJ* 767.1, 48, p. 48. DOI: 10.1088/0004-637X/767/1/48. arXiv: 1301.0622 [astro-ph.CO].
- McQuinn, Matthew (Sept. 2016). “The Evolution of the Intergalactic Medium”. In: *ARA&A* 54, pp. 313–362. DOI: 10.1146/annurev-astro-082214-122355. arXiv: 1512.00086 [astro-ph.CO].
- Méndez-Hernández, H., P. Cassata, E. Ibar, et al. (Oct. 2022). “Metal content of the circumgalactic medium around star-forming galaxies at $z \sim 2.6$ as revealed by the VIMOS Ultra-Deep Survey”. In: *A&A* 666, A56, A56. DOI: 10.1051/0004-6361/202142553. arXiv: 2206.08923 [astro-ph.GA].

- Miniati, Francesco, T. W. Jones, and Dongsu Ryu (May 1999). “On the Exchange of Kinetic and Magnetic Energy between Clouds and the Interstellar Medium”. In: *ApJ* 517, pp. 242–255. DOI: 10.1086/307162. arXiv: astro-ph/9901048 [astro-ph].
- Mitchell, Peter D., Jérémy Blaizot, Corentin Cadiou, et al. (Mar. 2021). “Tracing the simulated high-redshift circumgalactic medium with Lyman α emission”. In: *MNRAS* 501.4, pp. 5757–5775. DOI: 10.1093/mnras/stab035. arXiv: 2008.12790 [astro-ph.GA].
- Momose, Rieko, Masami Ouchi, Kimihiko Nakajima, et al. (2014). “Diffuse Ly α haloes around galaxies at $z = 2.2$ – 6.6 : implications for galaxy formation and cosmic reionization”. English. In: *Monthly Notices of the Royal Astronomical Society* 442.1, pp. 110–120. DOI: 10.1093/mnras/stu825.
- (2016). “Statistical properties of diffuse Ly α haloes around star-forming galaxies at $z \sim 2$ ”. English. In: *Monthly Notices of the Royal Astronomical Society* 457.3, pp. 2318–2330. DOI: 10.1093/mnras/stw021.
- Mori, Masao, Masayuki Umemura, and Andrea Ferrara (Oct. 2004). “The Nature of Ly α Blobs: Supernova-dominated Primordial Galaxies”. In: *ApJ* 613.2, pp. L97–L100. DOI: 10.1086/425255. arXiv: astro-ph/0408410 [astro-ph].
- Morrissey, Patrick, Mateusz Matuszewski, Chris Martin, et al. (Sept. 2012). “The Keck Cosmic Web Imager: a capable new integral field spectrograph for the W. M. Keck Observatory”. In: *Ground-based and Airborne Instrumentation for Astronomy IV*. Ed. by Ian S. McLean, Suzanne K. Ramsay, and Hideki Takami. Vol. 8446. Society of Photo-Optical Instrumentation Engineers (SPIE) Conference Series, 844613, p. 844613. DOI: 10.1117/12.924729.
- Morrissey, Patrick, Mateusz Matuszewski, D. Christopher Martin, et al. (Sept. 2018). “The Keck Cosmic Web Imager Integral Field Spectrograph”. In: *ApJ* 864.1, 93, p. 93. DOI: 10.3847/1538-4357/aad597. arXiv: 1807.10356 [astro-ph.IM].
- Moster, Benjamin P., Thorsten Naab, and Simon D. M. White (Feb. 2013). “Galactic star formation and accretion histories from matching galaxies to dark matter haloes”. In: *MNRAS* 428.4, pp. 3121–3138. DOI: 10.1093/mnras/sts261. arXiv: 1205.5807 [astro-ph.CO].
- Moster, Benjamin P., Rachel S. Somerville, Christian Maulbetsch, et al. (Feb. 2010). “Constraints on the Relationship between Stellar Mass and Halo Mass at Low and High Redshift”. In: *ApJ* 710.2, pp. 903–923. DOI: 10.1088/0004-637X/710/2/903. arXiv: 0903.4682 [astro-ph.CO].
- Mouschovias, T. C. (July 1976a). “Nonhomologous contraction observations of the equilibria of self-gravitating, magnetic interstellar clouds embedded in an intercloud medium: star formation. II. Results.” In: *ApJ* 207, pp. 141–158. DOI: 10.1086/154478.

- Mouschovias, T. Ch. (June 1976b). “Nonhomologous contraction and equilibria of self-gravitating, magnetic interstellar clouds embedded in an intercloud medium: star formation. I. Formulation of the problem and method of solution.” In: *ApJ* 206, pp. 753–767. DOI: 10.1086/154436.
- Murray, Norman, Eliot Quataert, and Todd A. Thompson (Jan. 2005). “On the Maximum Luminosity of Galaxies and Their Central Black Holes: Feedback from Momentum-driven Winds”. In: *ApJ* 618.2, pp. 569–585. DOI: 10.1086/426067. arXiv: astro-ph/0406070 [astro-ph].
- Naidu, Rohan P., Jorryt Matthee, Pascal A. Oesch, et al. (Mar. 2022). “The synchrony of production and escape: half the bright Ly α emitters at $z \approx 2$ have Lyman continuum escape fractions ≈ 50 per cent”. In: *MNRAS* 510.3, pp. 4582–4607. DOI: 10.1093/mnras/stab3601. arXiv: 2110.11961 [astro-ph.GA].
- National Academies of Sciences, Engineering and Medicine (2021). *Pathways to Discovery in Astronomy and Astrophysics for the 2020s*. DOI: 10.17226/26141.
- Navarro, Julio F., Carlos S. Frenk, and Simon D. M. White (Aug. 1995). “Simulations of X-ray clusters”. In: *MNRAS* 275.3, pp. 720–740. DOI: 10.1093/mnras/275.3.720. arXiv: astro-ph/9408069 [astro-ph].
- Nelson, Dylan, Prateek Sharma, Annalisa Pillepich, et al. (Oct. 2020). “Resolving small-scale cold circumgalactic gas in TNG50”. In: *MNRAS* 498.2, pp. 2391–2414. DOI: 10.1093/mnras/staa2419. arXiv: 2005.09654 [astro-ph.GA].
- Nestor, Daniel B., Alice E. Shapley, Katherine A. Kornei, et al. (Mar. 2013). “A Refined Estimate of the Ionizing Emissivity from Galaxies at $z \sim 3$: Spectroscopic Follow-up in the SSA22a Field”. In: *ApJ* 765.1, 47, p. 47. DOI: 10.1088/0004-637X/765/1/47. arXiv: 1210.2393 [astro-ph.CO].
- Nestor, Daniel B., Alice E. Shapley, Charles C. Steidel, et al. (July 2011). “Narrowband Imaging of Escaping Lyman-continuum Emission in the SSA22 Field”. In: *ApJ* 736.1, 18, p. 18. DOI: 10.1088/0004-637X/736/1/18. arXiv: 1102.0286 [astro-ph.CO].
- Neufeld, David A. (Apr. 1991). “The Escape of Lyman-Alpha Radiation from a Multiphase Interstellar Medium”. In: *ApJ* 370, p. L85. DOI: 10.1086/185983.
- (Feb. 1990). “The Transfer of Resonance-Line Radiation in Static Astrophysical Media”. In: *ApJ* 350, p. 216. DOI: 10.1086/168375.
- Nilsson, K. K., J. P. U. Fynbo, P. Møller, et al. (June 2006). “A Lyman- α blob in the GOODS South field: evidence for cold accretion onto a dark matter halo”. In: *A&A* 452.3, pp. L23–L26. DOI: 10.1051/0004-6361:200600025. arXiv: astro-ph/0512396 [astro-ph].

- Ohyama, Youichi, Yoshiaki Taniguchi, Koji S. Kawabata, et al. (July 2003). “On the Origin of Ly α Blobs at High Redshift: Kinematic Evidence of a Hyperwind Galaxy at $z = 3.1$ ”. In: *ApJ* 591.1, pp. L9–L12. DOI: 10.1086/376959. arXiv: astro-ph/0305028 [astro-ph].
- Orlitová, I., A. Verhamme, A. Henry, et al. (Aug. 2018). “Puzzling Lyman-alpha line profiles in green pea galaxies”. In: *A&A* 616, A60, A60. DOI: 10.1051/0004-6361/201732478. arXiv: 1806.01027 [astro-ph.GA].
- Orr, Matthew E., Christopher C. Hayward, Philip F. Hopkins, et al. (Aug. 2018). “What FIREs up star formation: the emergence of the Kennicutt-Schmidt law from feedback”. In: *MNRAS* 478, pp. 3653–3673. DOI: 10.1093/mnras/sty1241. arXiv: 1701.01788 [astro-ph.GA].
- Ott, Thomas (Oct. 2012). *QFitsView: FITS file viewer*. ascl: 1210.019.
- Ouchi, Masami, Yoshiaki Ono, Eiichi Egami, et al. (May 2009). “Discovery of a Giant Ly α Emitter Near the Reionization Epoch”. In: *ApJ* 696.2, pp. 1164–1175. DOI: 10.1088/0004-637X/696/2/1164. arXiv: 0807.4174 [astro-ph].
- Ouchi, Masami, Yoshiaki Ono, and Takatoshi Shibuya (Aug. 2020). “Observations of the Lyman- α Universe”. In: *ARA&A* 58, pp. 617–659. DOI: 10.1146/annurev-astro-032620-021859. arXiv: 2012.07960 [astro-ph.GA].
- Pahl, Anthony J., Alice Shapley, Charles C. Steidel, et al. (Oct. 2022). “The connection between the escape of ionizing radiation and galaxy properties at $z \sim 3$ in the Keck Lyman Continuum Spectroscopic Survey”. In: *arXiv e-prints*, arXiv:2210.16697, arXiv:2210.16697. arXiv: 2210.16697 [astro-ph.GA].
- Patrício, Vera, Johan Richard, Anne Verhamme, et al. (Mar. 2016). “A young star-forming galaxy at $z = 3.5$ with an extended Lyman α halo seen with MUSE”. In: *MNRAS* 456.4, pp. 4191–4208. DOI: 10.1093/mnras/stv2859. arXiv: 1512.01212 [astro-ph.GA].
- Planck Collaboration, N. Aghanim, Y. Akrami, et al. (Sept. 2020). “Planck 2018 results. VI. Cosmological parameters”. In: *A&A* 641, A6, A6. DOI: 10.1051/0004-6361/201833910. arXiv: 1807.06209 [astro-ph.CO].
- Prada, Francisco, Anatoly A. Klypin, Antonio J. Cuesta, et al. (July 2012). “Halo concentrations in the standard Λ cold dark matter cosmology”. In: *MNRAS* 423.4, pp. 3018–3030. DOI: 10.1111/j.1365-2966.2012.21007.x. arXiv: 1104.5130 [astro-ph.CO].
- Prescott, Moire K. M., Arjun Dey, and Buell T. Jannuzi (Apr. 2012). “A Successful Broadband Survey for Giant Ly α Nebulae. I. Survey Design and Candidate Selection”. In: *ApJ* 748.2, 125, p. 125. DOI: 10.1088/0004-637X/748/2/125. arXiv: 1111.2603 [astro-ph.CO].

- Prescott, Moire K. M., Arjun Dey, and Buell T. Jannuzi (Sept. 2009). “The Discovery of a Large Ly α +He II Nebula at $z \approx 1.67$: A Candidate Low Metallicity Region?” In: *ApJ* 702.1, pp. 554–566. DOI: 10.1088/0004-637X/702/1/554. arXiv: 0906.4785 [astro-ph.CO].
- Prescott, Moire K. M., Nobunari Kashikawa, Arjun Dey, et al. (May 2008). “The Overdense Environment of a Large Ly α Nebula at $z \approx 2.7$ ”. In: *ApJ* 678.2, p. L77. DOI: 10.1086/588606. arXiv: 0803.4230 [astro-ph].
- Price, D. J. and J. J. Monaghan (Feb. 2007). “An energy-conserving formalism for adaptive gravitational force softening in smoothed particle hydrodynamics and N-body codes”. In: *MNRAS* 374, pp. 1347–1358. DOI: 10.1111/j.1365-2966.2006.11241.x. arXiv: astro-ph/0610872 [astro-ph].
- Prochaska, J. Xavier and Joseph F. Hennawi (Jan. 2009). “Quasars Probing Quasars. III. New Clues to Feedback, Quenching, and the Physics of Massive Galaxy Formation”. In: *ApJ* 690.2, pp. 1558–1584. DOI: 10.1088/0004-637X/690/2/1558. arXiv: 0806.0862 [astro-ph].
- Prochaska, J. Xavier, Joseph F. Hennawi, Khee-Gan Lee, et al. (Oct. 2013). “Quasars Probing Quasars. VI. Excess H I Absorption within One Proper Mpc of $z \sim 2$ Quasars”. In: *ApJ* 776.2, 136, p. 136. DOI: 10.1088/0004-637X/776/2/136. arXiv: 1308.6222 [astro-ph.CO].
- Prochaska, J. Xavier, Daniel Kasen, and Kate Rubin (June 2011a). “Simple Models of Metal-line Absorption and Emission from Cool Gas Outflows”. In: *ApJ* 734.1, 24, p. 24. DOI: 10.1088/0004-637X/734/1/24. arXiv: 1102.3444 [astro-ph.GA].
- Prochaska, J. Xavier, Marie Wingyee Lau, and Joseph F. Hennawi (Dec. 2014). “Quasars Probing Quasars. VII. The Pinnacle of the Cool Circumgalactic Medium Surrounds Massive $z \sim 2$ Galaxies”. In: *ApJ* 796, 140, p. 140. DOI: 10.1088/0004-637X/796/2/140. arXiv: 1409.6344 [astro-ph.GA].
- Prochaska, J. Xavier, Jean-Pierre Macquart, Matthew McQuinn, et al. (Oct. 2019). “The low density and magnetization of a massive galaxy halo exposed by a fast radio burst”. In: *Science* 366.6462, pp. 231–234. DOI: 10.1126/science.aay0073. arXiv: 1909.11681 [astro-ph.GA].
- Prochaska, J. Xavier, B. Weiner, H. -W. Chen, et al. (Oct. 2011b). “Probing the Intergalactic Medium/Galaxy Connection. V. On the Origin of Ly α and O VI Absorption at $z < 0.2$ ”. In: *ApJ* 740.2, 91, p. 91. DOI: 10.1088/0004-637X/740/2/91. arXiv: 1103.1891 [astro-ph.CO].
- Qu, Zhijie, Hsiao-Wen Chen, Gwen C. Rudie, et al. (Nov. 2022). “The Cosmic Ultraviolet Baryon Survey (CUBS) V: on the thermodynamic properties of the cool circumgalactic medium at $z \lesssim 1$ ”. In: *MNRAS* 516.4, pp. 4882–4897. DOI: 10.1093/mnras/stac2528. arXiv: 2209.01228 [astro-ph.GA].

- Quataert, Eliot, Yan-Fei Jiang, and Todd A. Thompson (Feb. 2022a). “The physics of galactic winds driven by cosmic rays - II. Isothermal streaming solutions”. In: *MNRAS* 510.1, pp. 920–945. DOI: 10.1093/mnras/stab3274. arXiv: 2106.08404 [astro-ph.GA].
- Quataert, Eliot, Todd A. Thompson, and Yan-Fei Jiang (Feb. 2022b). “The physics of galactic winds driven by cosmic rays I: Diffusion”. In: *MNRAS* 510.1, pp. 1184–1203. DOI: 10.1093/mnras/stab3273. arXiv: 2102.05696 [astro-ph.GA].
- Rahmati, Alireza, Andreas H. Pawlik, Milan Raičević, et al. (Apr. 2013). “On the evolution of the H I column density distribution in cosmological simulations”. In: *MNRAS* 430, pp. 2427–2445. DOI: 10.1093/mnras/stt066. arXiv: 1210.7808 [astro-ph.CO].
- Rathjen, Tim-Eric, Thorsten Naab, Stefanie Walch, et al. (June 2023). “SILCC - VII. Gas kinematics and multiphase outflows of the simulated ISM at high gas surface densities”. In: *MNRAS* 522.2, pp. 1843–1862. DOI: 10.1093/mnras/stad1104. arXiv: 2211.15419 [astro-ph.GA].
- Rauch, Michael, Wallace L. W. Sargent, and Thomas A. Barlow (June 2001a). “Small-Scale Structure at High Redshift. II. Physical Properties of the C IV Absorbing Clouds”. In: *ApJ* 554.2, pp. 823–840. DOI: 10.1086/321402. arXiv: astro-ph/0104216 [astro-ph].
- Rauch, Michael, Wallace L. W. Sargent, Thomas A. Barlow, et al. (Nov. 2001b). “Small-Scale Structure at High Redshift. III. The Clumpiness of the Intergalactic Medium on Subkiloparsec Scales”. In: *ApJ* 562.1, pp. 76–87. DOI: 10.1086/323523. arXiv: astro-ph/0107516 [astro-ph].
- Rauch, Michael, Wallace L. W. Sargent, Thomas A. Barlow, et al. (Sept. 2002). “Small-Scale Structure at High Redshift. IV. Low-Ionization Gas Intersecting Three Lines of Sight to Q2237+0305”. In: *ApJ* 576.1, pp. 45–60. DOI: 10.1086/341267. arXiv: astro-ph/0204461 [astro-ph].
- Rauch, Michael, Wallace L. W. Sargent, and Tom A. Barlow (Apr. 1999). “Small-Scale Structure at High Redshift. I. Glimpses of the Interstellar Medium at Redshift ~ 3.5 ”. In: *ApJ* 515.2, pp. 500–505. DOI: 10.1086/307060.
- Recchia, S., P. Blasi, and G. Morlino (Nov. 2016). “Cosmic ray driven Galactic winds”. In: *MNRAS* 462.4, pp. 4227–4239. DOI: 10.1093/mnras/stw1966. arXiv: 1603.06746 [astro-ph.HE].
- Reddy, Naveen A., Max Pettini, Charles C. Steidel, et al. (July 2012). “The Characteristic Star Formation Histories of Galaxies at Redshifts $z \sim 2-7$ ”. In: *ApJ* 754.1, 25, p. 25. DOI: 10.1088/0004-637X/754/1/25. arXiv: 1205.0555 [astro-ph.CO].
- Reddy, Naveen A. and Charles C. Steidel (Feb. 2009). “A Steep Faint-End Slope of the UV Luminosity Function at $z \sim 2-3$: Implications for the Global Stellar Mass Density and Star Formation in Low-Mass Halos”. In: *ApJ* 692.1, pp. 778–

803. DOI: 10 . 1088 / 0004 - 637X / 692 / 1 / 778. arXiv: 0810 . 2788 [astro-ph].
- Reddy, Naveen A., Charles C. Steidel, Max Pettini, et al. (Sept. 2016). “The Connection Between Reddening, Gas Covering Fraction, and the Escape of Ionizing Radiation at High Redshift”. In: *ApJ* 828.2, 108, p. 108. DOI: 10 . 3847/0004-637X/828/2/108. arXiv: 1606.03452 [astro-ph.GA].
- Richling, S. (Sept. 2003). “Resonance line transfer in clumpy media”. In: *MNRAS* 344.2, pp. 553–561. DOI: 10 . 1046/j.1365-8711.2003.06849.x.
- Richter, P., F. B. S. Paerels, and J. S. Kaastra (Feb. 2008). “FUV and X-Ray Absorption in the Warm-Hot Intergalactic Medium”. In: *Space Sci. Rev.* 134, pp. 25–49. DOI: 10 . 1007/s11214-008-9325-4. arXiv: 0801.0975 [astro-ph].
- Rivera-Thorsen, T. E., H. Dahle, M. Gronke, et al. (Nov. 2017). “The Sunburst Arc: Direct Lyman α escape observed in the brightest known lensed galaxy”. In: *A&A* 608, L4, p. L4. DOI: 10 . 1051/0004-6361/201732173. arXiv: 1710.09482 [astro-ph.GA].
- Rivera-Thorsen, T. Emil, Håkon Dahle, John Chisholm, et al. (Nov. 2019). “Gravitational lensing reveals ionizing ultraviolet photons escaping from a distant galaxy”. In: *Science* 366.6466, pp. 738–741. DOI: 10 . 1126/science.aaw0978. arXiv: 1904.08186 [astro-ph.GA].
- Rivera-Thorsen, Thøger E., Matthew Hayes, Göran Östlin, et al. (May 2015). “The Lyman Alpha Reference Sample. V. The Impact of Neutral ISM Kinematics and Geometry on Ly α Escape”. In: *ApJ* 805.1, 14, p. 14. DOI: 10 . 1088/0004-637X/805/1/14. arXiv: 1503.01157 [astro-ph.GA].
- Robertson, B. E., R. S. Ellis, S. R. Furlanetto, et al. (Apr. 2015). “Cosmic Reionization and Early Star-forming Galaxies: A Joint Analysis of New Constraints from Planck and the Hubble Space Telescope”. In: *ApJ* 802, L19, p. L19. DOI: 10 . 1088/2041-8205/802/2/L19. arXiv: 1502.02024.
- Robertson, Brant E. and Andrey V. Kravtsov (June 2008). “Molecular Hydrogen and Global Star Formation Relations in Galaxies”. In: *ApJ* 680, pp. 1083–1111. DOI: 10 . 1086/587796. arXiv: 0710.2102 [astro-ph].
- Rodríguez-Puebla, Aldo, Vladimir Avila-Reese, Xiaohu Yang, et al. (Feb. 2015). “The Stellar-to-Halo Mass Relation of Local Galaxies Segregated by Color”. In: *ApJ* 799.2, 130, p. 130. DOI: 10 . 1088/0004-637X/799/2/130. arXiv: 1408.5407 [astro-ph.GA].
- Rodríguez-Puebla, Aldo, Joel R. Primack, Vladimir Avila-Reese, et al. (Sept. 2017). “Constraining the galaxy-halo connection over the last 13.3 Gyr: star formation histories, galaxy mergers and structural properties”. In: *MNRAS* 470.1, pp. 651–687. DOI: 10 . 1093/mnras/stx1172. arXiv: 1703.04542 [astro-ph.GA].

- Rogerson, J. A. and P. B. Hall (Apr. 2012). “Investigating Mg II absorption in paired quasar sight-lines”. In: *MNRAS* 421.2, pp. 971–982. DOI: 10.1111/j.1365-2966.2011.20317.x. arXiv: 1112.1729 [astro-ph.CO].
- Rosdahl, J. and J. Blaizot (June 2012). “Extended Ly α emission from cold accretion streams”. In: *MNRAS* 423.1, pp. 344–366. DOI: 10.1111/j.1365-2966.2012.20883.x. arXiv: 1112.4408 [astro-ph.CO].
- Rubin, Kate H. R., Aleksandar M. Diamond-Stanic, Alison L. Coil, et al. (Dec. 2018). “Galaxies Probing Galaxies in PRIMUS. II. The Coherence Scale of the Cool Circumgalactic Medium”. In: *ApJ* 868.2, 142, p. 142. DOI: 10.3847/1538-4357/aad566. arXiv: 1806.08801 [astro-ph.GA].
- Rubin, Kate H. R., J. Xavier Prochaska, David C. Koo, et al. (Oct. 2014). “Evidence for Ubiquitous Collimated Galactic-scale Outflows along the Star-forming Sequence at $z \sim 0.5$ ”. In: *ApJ* 794.2, 156, p. 156. DOI: 10.1088/0004-637X/794/2/156. arXiv: 1307.1476 [astro-ph.CO].
- Rubin, Kate H. R., J. Xavier Prochaska, David C. Koo, et al. (Mar. 2012). “The Direct Detection of Cool, Metal-enriched Gas Accretion onto Galaxies at $z \sim 0.5$ ”. In: *ApJ* 747.2, L26, p. L26. DOI: 10.1088/2041-8205/747/2/L26. arXiv: 1110.0837 [astro-ph.CO].
- Rubin, Kate H. R., Benjamin J. Weiner, David C. Koo, et al. (Aug. 2010). “The Persistence of Cool Galactic Winds in High Stellar Mass Galaxies between $z \sim 1.4$ and ~ 1 ”. In: *ApJ* 719.2, pp. 1503–1525. DOI: 10.1088/0004-637X/719/2/1503. arXiv: 0912.2343 [astro-ph.CO].
- Rudie, Gwen C., Charles C. Steidel, Max Pettini, et al. (Nov. 2019). “Column Density, Kinematics, and Thermal State of Metal-bearing Gas within the Virial Radius of $z \sim 2$ Star-forming Galaxies in the Keck Baryonic Structure Survey”. In: *ApJ* 885.1, 61, p. 61. DOI: 10.3847/1538-4357/ab4255. arXiv: 1903.00004 [astro-ph.GA].
- Rudie, Gwen C., Charles C. Steidel, Alice E. Shapley, et al. (June 2013). “The Column Density Distribution and Continuum Opacity of the Intergalactic and Circumgalactic Medium at Redshift $z = 2.4$ ”. In: *ApJ* 769.2, 146, p. 146. DOI: 10.1088/0004-637X/769/2/146. arXiv: 1304.6719 [astro-ph.CO].
- Rudie, Gwen C., Charles C. Steidel, Ryan F. Trainor, et al. (May 2012). “The Gaseous Environment of High- z Galaxies: Precision Measurements of Neutral Hydrogen in the Circumgalactic Medium of $z \sim 2-3$ Galaxies in the Keck Baryonic Structure Survey”. In: *ApJ* 750.1, 67, p. 67. DOI: 10.1088/0004-637X/750/1/67. arXiv: 1202.6055 [astro-ph.CO].
- Runholm, Axel, Max Gronke, and Matthew Hayes (Mar. 2021). “The Lyman Alpha Spectral Database (LASD)”. In: *PASP* 133.1021, 034507, p. 034507. DOI: 10.1088/1538-3873/abe3ca. arXiv: 2010.02927 [astro-ph.GA].

- Rupke, David S., Sylvain Veilleux, and D. B. Sanders (Sept. 2005). “Outflows in Infrared-Luminous Starbursts at $z < 0.5$. II. Analysis and Discussion”. In: *ApJS* 160.1, pp. 115–148. DOI: 10.1086/432889. arXiv: astro-ph/0506611 [astro-ph].
- Saito, Tomoki, Kazuhiro Shimasaku, Sadanori Okamura, et al. (Mar. 2008). “Deep Spectroscopy of Systematically Surveyed Extended Ly α Sources at $z \sim 3-5$ ”. In: *ApJ* 675.2, pp. 1076–1094. DOI: 10.1086/527282. arXiv: 0705.1494 [astro-ph].
- Saito, Tomoki, Kazuhiro Shimasaku, Sadanori Okamura, et al. (Sept. 2006). “Systematic Survey of Extended Ly α Sources over $z \sim 3-5$ ”. In: *ApJ* 648.1, pp. 54–66. DOI: 10.1086/505678. arXiv: astro-ph/0605360 [astro-ph].
- Sarazin, Craig L. (1988). *X-ray emission from clusters of galaxies*.
- Savage, B. D., N. Lehner, and A. Narayanan (Dec. 2011). “COS Observations of Metal Line and Broad Lyman- α Absorption in the Multi-phase O VI and Ne VIII System at $z = 0.20701$ toward HE 0226-4110”. In: *ApJ* 743, 180, p. 180. DOI: 10.1088/0004-637X/743/2/180. arXiv: 1111.1697 [astro-ph.CO].
- Scannapieco, Evan and Marcus Brüggen (June 2015). “The Launching of Cold Clouds by Galaxy Outflows. I. Hydrodynamic Interactions with Radiative Cooling”. In: *ApJ* 805, 158, p. 158. DOI: 10.1088/0004-637X/805/2/158. arXiv: 1503.06800 [astro-ph.GA].
- Scarlata, C., J. Colbert, H. I. Teplitz, et al. (Dec. 2009). “He II Emission in Ly α Nebulae: Active Galactic Nucleus or Cooling Radiation?” In: *ApJ* 706.2, pp. 1241–1252. DOI: 10.1088/0004-637X/706/2/1241. arXiv: 0910.4998 [astro-ph.CO].
- Scarlata, C. and N. Panagia (Mar. 2015). “A Semi-analytical Line Transfer Model to Interpret the Spectra of Galaxy Outflows”. In: *ApJ* 801.1, 43, p. 43. DOI: 10.1088/0004-637X/801/1/43. arXiv: 1501.07282 [astro-ph.GA].
- Schaerer, D. and A. Verhamme (Mar. 2008). “3D Ly α radiation transfer. II. Fitting the Lyman break galaxy MS 1512-cB58 and implications for Ly α emission in high- z starbursts”. In: *A&A* 480.2, pp. 369–377. DOI: 10.1051/0004-6361:20078913. arXiv: 0801.1187 [astro-ph].
- Schaye, Joop, Robert F. Carswell, and Tae-Sun Kim (Aug. 2007). “A large population of metal-rich, compact, intergalactic CIV absorbers - evidence for poor small-scale metal mixing”. In: *MNRAS* 379.3, pp. 1169–1194. DOI: 10.1111/j.1365-2966.2007.12005.x. arXiv: astro-ph/0701761 [astro-ph].
- Schneider, Evan E., Eve C. Ostriker, Brant E. Robertson, et al. (May 2020). “The Physical Nature of Starburst-driven Galactic Outflows”. In: *ApJ* 895.1, 43, p. 43. DOI: 10.3847/1538-4357/ab8ae8. arXiv: 2002.10468 [astro-ph.GA].

- Schneider, Evan E. and Brant E. Robertson (Apr. 2015). “CHOLLA: A New Massively Parallel Hydrodynamics Code for Astrophysical Simulation”. In: *ApJS* 217.2, 24, p. 24. DOI: 10.1088/0067-0049/217/2/24. arXiv: 1410.4194 [astro-ph.IM].
- Shapley, Alice E., Charles C. Steidel, Max Pettini, et al. (May 2003). “Rest-Frame Ultraviolet Spectra of $z \sim 3$ Lyman Break Galaxies”. In: *ApJ* 588.1, pp. 65–89. DOI: 10.1086/373922. arXiv: astro-ph/0301230 [astro-ph].
- Sharma, Mahavir and Biman B. Nath (May 2012). “The Roles of Radiation and Ram Pressure in Driving Galactic Winds”. In: *ApJ* 750.1, 55, p. 55. DOI: 10.1088/0004-637X/750/1/55. arXiv: 1112.3447 [astro-ph.CO].
- Shin, Min-Su, James M. Stone, and Gregory F. Snyder (June 2008). “The Magnetohydrodynamics of Shock-Cloud Interaction in Three Dimensions”. In: *ApJ* 680, pp. 336–348. DOI: 10.1086/587775. arXiv: 0802.2708 [astro-ph].
- Skilling, John (Nov. 2004). “Nested Sampling”. In: *American Institute of Physics Conference Series*. Ed. by Rainer Fischer, Roland Preuss, and Udo Von Toussaint. Vol. 735. American Institute of Physics Conference Series, pp. 395–405. DOI: 10.1063/1.1835238.
- (Dec. 2006). “Nested sampling for general Bayesian computation”. In: *Bayesian Anal.* 1.4, pp. 833–859. DOI: 10.1214/06-BA127. URL: <https://doi.org/10.1214/06-BA127>.
- Smith, Aaron, Rahul Kannan, Sandro Tacchella, et al. (Nov. 2021). “The physics of Lyman-alpha escape from disc-like galaxies”. In: *arXiv e-prints*, arXiv:2111.13721, arXiv:2111.13721. arXiv: 2111.13721 [astro-ph.GA].
- Smith, Aaron, Xiangcheng Ma, Volker Bromm, et al. (Mar. 2019). “The physics of Lyman α escape from high-redshift galaxies”. In: *MNRAS* 484.1, pp. 39–59. DOI: 10.1093/mnras/sty3483. arXiv: 1810.08185 [astro-ph.GA].
- Smith, Daniel J. B. and Matt J. Jarvis (June 2007). “Evidence for cold accretion onto a massive galaxy at high redshift?” In: *MNRAS* 378.1, pp. L49–L53. DOI: 10.1111/j.1745-3933.2007.00318.x. arXiv: astro-ph/0703522 [astro-ph].
- Smith, Daniel J. B., Matt J. Jarvis, Mark Lacy, et al. (Sept. 2008). “Infrared and millimetre-wavelength evidence for cold accretion within a $z = 2.83$ Lyman α blob”. In: *MNRAS* 389.2, pp. 799–805. DOI: 10.1111/j.1365-2966.2008.13580.x. arXiv: 0806.4384 [astro-ph].
- Sobolev, V. V. (1960). *Moving Envelopes of Stars*. DOI: 10.4159/harvard.9780674864658.
- Socrates, Aristotle, Shane W. Davis, and Enrico Ramirez-Ruiz (Nov. 2008). “The Eddington Limit in Cosmic Rays: An Explanation for the Observed Faintness of Starbursting Galaxies”. In: *ApJ* 687.1, pp. 202–215. DOI: 10.1086/590046. arXiv: astro-ph/0609796 [astro-ph].

- Solimano, Manuel, Jorge González-López, Manuel Aravena, et al. (June 2022). “Revealing the nature of a Lyman- α halo in a strongly-lensed interacting system at $z = 2.92$ ”. In: *arXiv e-prints*, arXiv:2206.02949, arXiv:2206.02949. arXiv: 2206.02949 [astro-ph.GA].
- Song, Hyunmi, Kwang-Il Seon, and Ho Seong Hwang (Sept. 2020). “Ly α Radiative Transfer: Modeling Spectrum and Surface Brightness Profiles of Ly α -emitting Galaxies at $Z = 3-6$ ”. In: *ApJ* 901.1, 41, p. 41. DOI: 10.3847/1538-4357/abac02. arXiv: 2007.08172 [astro-ph.GA].
- Sparre, Martin, Christoph Pfrommer, and Kristian Ehlert (Dec. 2020). “Interaction of a cold cloud with a hot wind: the regimes of cloud growth and destruction and the impact of magnetic fields”. In: *MNRAS* 499.3, pp. 4261–4281. DOI: 10.1093/mnras/staa3177. arXiv: 2008.09118 [astro-ph.GA].
- Sparre, Martin, Christoph Pfrommer, and Mark Vogelsberger (Feb. 2019). “The physics of multiphase gas flows: fragmentation of a radiatively cooling gas cloud in a hot wind”. In: *MNRAS* 482.4, pp. 5401–5421. DOI: 10.1093/mnras/sty3063. arXiv: 1807.07971 [astro-ph.GA].
- Speagle, Joshua S. (Apr. 2020). “DYNESTY: a dynamic nested sampling package for estimating Bayesian posteriors and evidences”. In: *MNRAS* 493.3, pp. 3132–3158. DOI: 10.1093/mnras/staa278. arXiv: 1904.02180 [astro-ph.IM].
- Spitzer, Lyman and Richard Härm (Mar. 1953). “Transport Phenomena in a Completely Ionized Gas”. In: *Physical Review* 89, pp. 977–981. DOI: 10.1103/PhysRev.89.977.
- Springel, Volker (Dec. 2005). “The cosmological simulation code GADGET-2”. In: *MNRAS* 364, pp. 1105–1134. DOI: 10.1111/j.1365-2966.2005.09655.x. arXiv: astro-ph/0505010 [astro-ph].
- Squire, J., A. A. Schekochihin, E. Quataert, et al. (2019). “Magneto-immutable turbulence in weakly collisional plasmas”. In: *J. Plasma. Phys.* 85.1, p. 905850114. DOI: 10.1017/S0022377819000114.
- Stanway, E. R. and J. J. Eldridge (Sept. 2018). “Re-evaluating old stellar populations”. In: *MNRAS* 479.1, pp. 75–93. DOI: 10.1093/mnras/sty1353. arXiv: 1805.08784 [astro-ph.GA].
- Stark, Daniel P., Richard S. Ellis, Stéphane Charlot, et al. (Jan. 2017). “Ly α and C III] emission in $z = 7-9$ Galaxies: accelerated reionization around luminous star-forming systems?” In: *MNRAS* 464.1, pp. 469–479. DOI: 10.1093/mnras/stw2233. arXiv: 1606.01304 [astro-ph.GA].
- Steidel, Charles C., Kurt L. Adelberger, Mark Dickinson, et al. (Jan. 1998). “A Large Structure of Galaxies at Redshift Z approximately 3 and Its Cosmological Implications”. In: *ApJ* 492.2, pp. 428–438. DOI: 10.1086/305073. arXiv: astro-ph/9708125 [astro-ph].

- Steidel, Charles C., Kurt L. Adelberger, Alice E. Shapley, et al. (Mar. 2000). “Ly α Imaging of a Proto-Cluster Region at $\langle z \rangle = 3.09$ ”. In: *ApJ* 532.1, pp. 170–182. DOI: 10.1086/308568. arXiv: astro-ph/9910144 [astro-ph].
- (Aug. 2003). “Lyman Break Galaxies at Redshift $z \sim 3$: Survey Description and Full Data Set”. In: *ApJ* 592.2, pp. 728–754. DOI: 10.1086/375772. arXiv: astro-ph/0305378 [astro-ph].
- Steidel, Charles C., Milan Bogosavljević, Alice E. Shapley, et al. (Aug. 2011). “Diffuse Ly α Emitting Halos: A Generic Property of High-redshift Star-forming Galaxies”. In: *ApJ* 736.2, 160, p. 160. DOI: 10.1088/0004-637X/736/2/160. arXiv: 1101.2204 [astro-ph.CO].
- Steidel, Charles C., Milan Bogosavljević, Alice E. Shapley, et al. (Dec. 2018). “The Keck Lyman Continuum Spectroscopic Survey (KLCS): The Emergent Ionizing Spectrum of Galaxies at $z \sim 3$ ”. In: *ApJ* 869.2, 123, p. 123. DOI: 10.3847/1538-4357/aaed28. arXiv: 1805.06071 [astro-ph.GA].
- Steidel, Charles C., Dawn K. Erb, Alice E. Shapley, et al. (July 2010). “The Structure and Kinematics of the Circumgalactic Medium from Far-ultraviolet Spectra of $z \sim 2-3$ Galaxies”. In: *ApJ* 717.1, pp. 289–322. DOI: 10.1088/0004-637X/717/1/289. arXiv: 1003.0679 [astro-ph.CO].
- Steidel, Charles C., Gwen C. Rudie, Allison L. Strom, et al. (Nov. 2014). “Strong Nebular Line Ratios in the Spectra of $z \sim 2-3$ Star Forming Galaxies: First Results from KBSS-MOSFIRE”. In: *ApJ* 795.2, 165, p. 165. DOI: 10.1088/0004-637X/795/2/165. arXiv: 1405.5473 [astro-ph.GA].
- Steinwandel, Ulrich P., Klaus Dolag, Harald Lesch, et al. (Jan. 2022a). “Driving Galactic Outflows with Magnetic Fields at Low and High Redshift”. In: *ApJ* 924.1, 26, p. 26. DOI: 10.3847/1538-4357/ac2ffd.
- Steinwandel, Ulrich P., Chang-Goo Kim, Greg L. Bryan, et al. (Dec. 2022b). “The structure and composition of multiphase galactic winds in a Large Magellanic Cloud mass simulated galaxy”. In: *arXiv e-prints*, arXiv:2212.03898, arXiv:2212.03898. DOI: 10.48550/arXiv.2212.03898. arXiv: 2212.03898 [astro-ph.GA].
- Stocke, John T., Brian A. Keeney, Charles W. Danforth, et al. (Feb. 2013). “Characterizing the Circumgalactic Medium of Nearby Galaxies with HST/COS and HST/STIS Absorption-line Spectroscopy”. In: *ApJ* 763.2, 148, p. 148. DOI: 10.1088/0004-637X/763/2/148. arXiv: 1212.5658 [astro-ph.CO].
- Stocke, John T., Steven V. Penton, Charles W. Danforth, et al. (Apr. 2006). “The Galaxy Environment of O VI Absorption Systems”. In: *ApJ* 641, pp. 217–228. DOI: 10.1086/500386. arXiv: astro-ph/0509822 [astro-ph].
- Strom, Allison L., Charles C. Steidel, Gwen C. Rudie, et al. (Feb. 2017). “Nebular Emission Line Ratios in $z = 2-3$ Star-forming Galaxies with KBSS-MOSFIRE: Exploring the Impact of Ionization, Excitation, and Nitrogen-to-Oxygen Ratio”. In: *ApJ* 836.2, 164, p. 164. DOI: 10.3847/1538-4357/836/2/164. arXiv: 1608.02587 [astro-ph.GA].

- Su, Kung-Yi, Philip F. Hopkins, Christopher C. Hayward, et al. (Oct. 2017). “Feed-back first: the surprisingly weak effects of magnetic fields, viscosity, conduction and metal diffusion on sub- L^* galaxy formation”. In: *MNRAS* 471, pp. 144–166. DOI: 10.1093/mnras/stx1463. arXiv: 1607.05274 [astro-ph.GA].
- Tacconi, Linda J., Reinhard Genzel, and Amiel Sternberg (Aug. 2020). “The Evolution of the Star-Forming Interstellar Medium Across Cosmic Time”. In: *ARA&A* 58, pp. 157–203. DOI: 10.1146/annurev-astro-082812-141034. arXiv: 2003.06245 [astro-ph.GA].
- Tang, Mengtao, Daniel P. Stark, Jacopo Chevallard, et al. (Oct. 2019). “MMT/MMIRS spectroscopy of $z = 1.3 - 2.4$ extreme [O III] emitters: implications for galaxies in the reionization era”. In: *MNRAS* 489.2, pp. 2572–2594. DOI: 10.1093/mnras/stz2236. arXiv: 1809.09637 [astro-ph.GA].
- Taniguchi, Yoshiaki and Yasuhiro Shioya (Mar. 2000). “Superwind Model of Extended $\text{Ly}\alpha$ Emitters at High Redshift”. In: *ApJ* 532.1, pp. L13–L16. DOI: 10.1086/312557. arXiv: astro-ph/0001522 [astro-ph].
- Taniguchi, Yoshiaki, Yasuhiro Shioya, and Yuko Kakazu (Nov. 2001). “On the Origin of $\text{Ly}\alpha$ Blobs at High Redshift: Submillimetric Evidence for a Hyperwind Galaxy at $z = 3.1$ ”. In: *ApJ* 562.1, pp. L15–L17. DOI: 10.1086/338101. arXiv: astro-ph/0110355 [astro-ph].
- Tasitsiomi, Argyro (July 2006). “ $\text{Ly}\alpha$ Radiative Transfer in Cosmological Simulations and Application to a $z \sim 8$ $\text{Ly}\alpha$ Emitter”. In: *ApJ* 645.2, pp. 792–813. DOI: 10.1086/504460. arXiv: astro-ph/0510347 [astro-ph].
- Tasitsiomi, Argyro, Andrey V. Kravtsov, Risa H. Wechsler, et al. (Oct. 2004). “Modeling Galaxy-Mass Correlations in Dissipationless Simulations”. In: *ApJ* 614.2, pp. 533–546. DOI: 10.1086/423784. arXiv: astro-ph/0404168 [astro-ph].
- Theios, Rachel L., Charles C. Steidel, Allison L. Strom, et al. (Jan. 2019). “Dust Attenuation, Star Formation, and Metallicity in $z \sim 2-3$ Galaxies from KBSS-MOSFIRE”. In: *ApJ* 871.1, 128, p. 128. DOI: 10.3847/1538-4357/aaf386. arXiv: 1805.00016 [astro-ph.GA].
- Thompson, Todd A., Eliot Quataert, and Norman Murray (Sept. 2005). “Radiation Pressure-supported Starburst Disks and Active Galactic Nucleus Fueling”. In: *ApJ* 630.1, pp. 167–185. DOI: 10.1086/431923. arXiv: astro-ph/0503027 [astro-ph].
- Thompson, Todd A., Eliot Quataert, Dong Zhang, et al. (Jan. 2016). “An origin for multiphase gas in galactic winds and haloes”. In: *MNRAS* 455.2, pp. 1830–1844. DOI: 10.1093/mnras/stv2428. arXiv: 1507.04362 [astro-ph.GA].
- Trainor, Ryan F. and Charles C. Steidel (June 2012). “The Halo Masses and Galaxy Environments of Hyperluminous QSOs at $z \sim 2.7$ in the Keck Baryonic Structure Survey”. In: *ApJ* 752.1, 39, p. 39. DOI: 10.1088/0004-637X/752/1/39. arXiv: 1204.3636 [astro-ph.CO].

- Trainor, Ryan F., Charles C. Steidel, Allison L. Strom, et al. (Aug. 2015). “The Spectroscopic Properties of Ly α -Emitters at $z \sim 2.7$: Escaping Gas and Photons from Faint Galaxies”. In: *ApJ* 809.1, 89, p. 89. DOI: 10.1088/0004-637X/809/1/89. arXiv: 1506.08205 [astro-ph.GA].
- Trainor, Ryan F., Allison L. Strom, Charles C. Steidel, et al. (Dec. 2016). “The Rest-frame Optical Spectroscopic Properties of Ly α -emitters at $Z \sim 2.5$: The Physical Origins of Strong Ly α Emission”. In: *ApJ* 832.2, 171, p. 171. DOI: 10.3847/0004-637X/832/2/171. arXiv: 1608.07280 [astro-ph.GA].
- Trebitsch, Maxime, Anne Verhamme, J  r  my Blaizot, et al. (Oct. 2016). “Lyman- α blobs: polarization arising from cold accretion”. In: *A&A* 593, A122, A122. DOI: 10.1051/0004-6361/201527024. arXiv: 1604.02066 [astro-ph.GA].
- Tumlinson, Jason, Molly S. Peeples, and Jessica K. Werk (Aug. 2017). “The Circumgalactic Medium”. In: *ARA&A* 55.1, pp. 389–432. DOI: 10.1146/annurev-astro-091916-055240. arXiv: 1709.09180 [astro-ph.GA].
- Tumlinson, Jason, Christopher Thom, Jessica K. Werk, et al. (Nov. 2013). “The COS-Halos Survey: Rationale, Design, and a Census of Circumgalactic Neutral Hydrogen”. In: *ApJ* 777.1, 59, p. 59. DOI: 10.1088/0004-637X/777/1/59. arXiv: 1309.6317 [astro-ph.CO].
- Uchimoto, Yuka K., Toru Yamada, Masaru Kajisawa, et al. (May 2012). “Assembly of Massive Galaxies in a High- z Protocluster”. In: *ApJ* 750.2, 116, p. 116. DOI: 10.1088/0004-637X/750/2/116. arXiv: 1203.0814 [astro-ph.CO].
- Uchimoto, Yuka Katsuno, Ryuji Suzuki, Chihiro Tokoku, et al. (Aug. 2008). “Subaru/MOIRCS Near-Infrared Imaging in the Proto-Cluster Region at $z = 3.1$ ”. In: *PASJ* 60, p. 683. DOI: 10.1093/pasj/60.4.683. arXiv: 0802.3958 [astro-ph].
- Umehata, H., M. Fumagalli, I. Smail, et al. (2019). “Gas filaments of the cosmic web located around active galaxies in a protocluster”. In: *Science* 366.6461, pp. 97–100. ISSN: 0036-8075. DOI: 10.1126/science.aaw5949. eprint: 1910.01324.
- Umehata, Hideki, Yuichi Matsuda, Yoichi Tamura, et al. (Jan. 2017). “ALMA Reveals Strong [C II] Emission in a Galaxy Embedded in a Giant Ly α Blob at $z = 3.1$ ”. In: *ApJ* 834.2, L16, p. L16. DOI: 10.3847/2041-8213/834/2/L16. arXiv: 1701.00043 [astro-ph.GA].
- Vanzella, E., A. Grazian, M. Hayes, et al. (Apr. 2010). “The unusual N IV] -emitter galaxy GDS J033218.92-275302.7: star formation or AGN-driven winds from a massive galaxy at $z = 5.56$ ”. In: *A&A* 513, A20, A20. DOI: 10.1051/0004-6361/200913042. arXiv: 0912.3007 [astro-ph.CO].
- Vasei, Kaveh, Brian Siana, Alice E. Shapley, et al. (Nov. 2016). “The Lyman Continuum Escape Fraction of the Cosmic Horseshoe: A Test of Indirect Estimates”. In: *ApJ* 831.1, 38, p. 38. DOI: 10.3847/0004-637X/831/1/38. arXiv: 1603.02309 [astro-ph.GA].

- Veilleux, Sylvain, Gerald Cecil, and Joss Bland-Hawthorn (Sept. 2005). “Galactic Winds”. In: *ARA&A* 43.1, pp. 769–826. DOI: 10.1146/annurev.astro.43.072103.150610. arXiv: astro-ph/0504435 [astro-ph].
- Veilleux, Sylvain, Roberto Maiolino, Alberto D. Bolatto, et al. (Apr. 2020). “Cool outflows in galaxies and their implications”. In: *A&ARv* 28.1, 2, p. 2. DOI: 10.1007/s00159-019-0121-9. arXiv: 2002.07765 [astro-ph.GA].
- Verhamme, A., Y. Dubois, J. Blaizot, et al. (Oct. 2012). “Lyman- α emission properties of simulated galaxies: interstellar medium structure and inclination effects”. In: *A&A* 546, A111, A111. DOI: 10.1051/0004-6361/201218783. arXiv: 1208.4781 [astro-ph.CO].
- Verhamme, A., I. Orlitová, D. Schaerer, et al. (Jan. 2017). “Lyman- α spectral properties of five newly discovered Lyman continuum emitters”. In: *A&A* 597, A13, A13. DOI: 10.1051/0004-6361/201629264. arXiv: 1609.03477 [astro-ph.GA].
- Verhamme, A., D. Schaerer, H. Atek, et al. (Nov. 2008). “3D Ly α radiation transfer. III. Constraints on gas and stellar properties of $z \sim 3$ Lyman break galaxies (LBG) and implications for high- z LBGs and Ly α emitters”. In: *A&A* 491.1, pp. 89–111. DOI: 10.1051/0004-6361:200809648. arXiv: 0805.3601 [astro-ph].
- Verhamme, A., D. Schaerer, and A. Maselli (Dec. 2006). “3D Ly α radiation transfer. I. Understanding Ly α line profile morphologies”. In: *A&A* 460.2, pp. 397–413. DOI: 10.1051/0004-6361:20065554. arXiv: astro-ph/0608075 [astro-ph].
- Verhamme, Anne, Ivana Orlitová, Daniel Schaerer, et al. (June 2015). “Using Lyman- α to detect galaxies that leak Lyman continuum”. In: *A&A* 578, A7, A7. DOI: 10.1051/0004-6361/201423978. arXiv: 1404.2958 [astro-ph.GA].
- Virtanen, Pauli, Ralf Gommers, Travis E. Oliphant, et al. (Feb. 2020). “SciPy 1.0: fundamental algorithms for scientific computing in Python”. In: *Nature Methods* 17, pp. 261–272. DOI: 10.1038/s41592-019-0686-2. arXiv: 1907.10121 [cs.MS].
- Wang, Bingjie, Timothy M. Heckman, Guangtun Zhu, et al. (May 2020). “A Systematic Study of Galactic Outflows via Fluorescence Emission: Implications for Their Size and Structure”. In: *ApJ* 894.2, 149, p. 149. DOI: 10.3847/1538-4357/ab88b4. arXiv: 2004.06105 [astro-ph.GA].
- Waskom, Michael L. (2021). “seaborn: statistical data visualization”. In: *Journal of Open Source Software* 6.60, p. 3021. DOI: 10.21105/joss.03021. URL: <https://doi.org/10.21105/joss.03021>.
- Webb, T. M. A., T. Yamada, J. -S. Huang, et al. (Feb. 2009). “Spitzer Observations of Extended Lyman- α Clouds in the SSA22 Field”. In: *ApJ* 692.2, pp. 1561–1570. DOI: 10.1088/0004-637X/692/2/1561. arXiv: 0812.0991 [astro-ph].

- Wechsler, Risa H., James S. Bullock, Joel R. Primack, et al. (Mar. 2002). “Concentrations of Dark Halos from Their Assembly Histories”. In: *ApJ* 568.1, pp. 52–70. DOI: 10.1086/338765. arXiv: astro-ph/0108151 [astro-ph].
- Weijmans, Anne-Marie, Richard G. Bower, James E. Geach, et al. (Mar. 2010). “Dissecting the Lyman α emission halo of LAB1”. In: *MNRAS* 402.4, pp. 2245–2252. DOI: 10.1111/j.1365-2966.2009.16055.x. arXiv: 0911.3667 [astro-ph.CO].
- Weiner, Benjamin J., Alison L. Coil, Jason X. Prochaska, et al. (Feb. 2009). “Ubiquitous Outflows in DEEP2 Spectra of Star-Forming Galaxies at $z = 1.4$ ”. In: *ApJ* 692.1, pp. 187–211. DOI: 10.1088/0004-637X/692/1/187. arXiv: 0804.4686 [astro-ph].
- Weldon, Andrew, Naveen A. Reddy, Michael W. Topping, et al. (May 2023). “The MOSDEF-LRIS Survey: Detection of Inflowing Gas Towards Three Star-forming Galaxies at $z \sim 2$ ”. In: *arXiv e-prints*, arXiv:2305.16394, arXiv:2305.16394. DOI: 10.48550/arXiv.2305.16394. arXiv: 2305.16394 [astro-ph.GA].
- Werk, Jessica K., J. Xavier Prochaska, Sebastiano Cantalupo, et al. (Dec. 2016). “The COS-Halos Survey: Origins of the Highly Ionized Circumgalactic Medium of Star-Forming Galaxies”. In: *ApJ* 833, 54, p. 54. DOI: 10.3847/1538-4357/833/1/54. arXiv: 1609.00012 [astro-ph.GA].
- Werk, Jessica K., J. Xavier Prochaska, Christopher Thom, et al. (Feb. 2013). “The COS-Halos Survey: An Empirical Description of Metal-line Absorption in the Low-redshift Circumgalactic Medium”. In: *ApJS* 204.2, 17, p. 17. DOI: 10.1088/0067-0049/204/2/17. arXiv: 1212.0558 [astro-ph.CO].
- Werk, Jessica K., J. Xavier Prochaska, Jason Tumlinson, et al. (Sept. 2014). “The COS-Halos Survey: Physical Conditions and Baryonic Mass in the Low-redshift Circumgalactic Medium”. In: *ApJ* 792, 8, p. 8. DOI: 10.1088/0004-637X/792/1/8. arXiv: 1403.0947 [astro-ph.CO].
- Whitaker, Katherine E., Marijn Franx, Joel Leja, et al. (Nov. 2014). “Constraining the Low-mass Slope of the Star Formation Sequence at $0.5 < z < 2.5$ ”. In: *ApJ* 795.2, 104, p. 104. DOI: 10.1088/0004-637X/795/2/104. arXiv: 1407.1843 [astro-ph.GA].
- Wilman, R. J., J. Gerssen, R. G. Bower, et al. (July 2005). “The discovery of a galaxy-wide superwind from a young massive galaxy at redshift $z \sim 3$ ”. In: *Nature* 436.7048, pp. 227–229. DOI: 10.1038/nature03718. arXiv: astro-ph/0507315 [astro-ph].
- Wisotzki, L., R. Bacon, J. Blaizot, et al. (Mar. 2016). “Extended Lyman α haloes around individual high-redshift galaxies revealed by MUSE”. In: *A&A* 587, A98, A98. DOI: 10.1051/0004-6361/201527384. arXiv: 1509.05143 [astro-ph.GA].

- Wisotzki, L., R. Bacon, J. Brinchmann, et al. (Oct. 2018). “Nearly all the sky is covered by Lyman- α emission around high-redshift galaxies”. In: *Nature* 562.7726, pp. 229–232. DOI: 10.1038/s41586-018-0564-6. arXiv: 1810.00843 [astro-ph.GA].
- Xu, Xinfeng, Timothy Heckman, Alaina Henry, et al. (July 2022). “CLASSY III. The Properties of Starburst-driven Warm Ionized Outflows”. In: *ApJ* 933.2, 222, p. 222. DOI: 10.3847/1538-4357/ac6d56. arXiv: 2204.09181 [astro-ph.GA].
- Xue, Rui, Kyoung-Soo Lee, Arjun Dey, et al. (Mar. 2017). “The Diversity of Diffuse Ly α Nebulae around Star-forming Galaxies at High Redshift”. In: *ApJ* 837.2, 172, p. 172. DOI: 10.3847/1538-4357/837/2/172. arXiv: 1611.03510 [astro-ph.GA].
- Yang, Huan, Sangeeta Malhotra, Max Gronke, et al. (Apr. 2016). “Green Pea Galaxies Reveal Secrets of Ly α Escape”. In: *ApJ* 820.2, 130, p. 130. DOI: 10.3847/0004-637X/820/2/130. arXiv: 1506.02885 [astro-ph.GA].
- Yang, Huan, Sangeeta Malhotra, Max Gronke, et al. (Aug. 2017). “Ly α Profile, Dust, and Prediction of Ly α Escape Fraction in Green Pea Galaxies”. In: *ApJ* 844.2, 171, p. 171. DOI: 10.3847/1538-4357/aa7d4d. arXiv: 1701.01857 [astro-ph.GA].
- Yang, Yujin, Ann Zabludoff, Daniel Eisenstein, et al. (Aug. 2010). “Strong Field-to-field Variation of Ly α Nebulae Populations at $z \approx 2.3$ ”. In: *ApJ* 719.2, pp. 1654–1671. DOI: 10.1088/0004-637X/719/2/1654. arXiv: 1008.2776 [astro-ph.CO].
- Yang, Yujin, Ann Zabludoff, Christy Tremonti, et al. (Mar. 2009). “Extended Ly α Nebulae at $z = 2.3$: An Extremely Rare and Strongly Clustered Population?” In: *ApJ* 693.2, pp. 1579–1587. DOI: 10.1088/0004-637X/693/2/1579. arXiv: 0811.3446 [astro-ph].
- Yao, Y., Q. D. Wang, S. V. Penton, et al. (June 2010). “The Dearth of Chemically Enriched Warm-Hot Circumgalactic Gas”. In: *ApJ* 716, pp. 1514–1521. DOI: 10.1088/0004-637X/716/2/1514. arXiv: 1005.0923 [astro-ph.CO].
- Zabl, Johannes, Nicolas F. Bouché, Ilane Schroetter, et al. (May 2019). “MusE GAS FLOW and Wind (MEGAFLOW) II. A study of gas accretion around $z \approx 1$ star-forming galaxies with background quasars”. In: *MNRAS* 485.2, pp. 1961–1980. DOI: 10.1093/mnras/stz392. arXiv: 1901.11416 [astro-ph.GA].
- Zackrisson, Erik, Akio K. Inoue, and Hannes Jensen (Nov. 2013). “The Spectral Evolution of the First Galaxies. II. Spectral Signatures of Lyman Continuum Leakage from Galaxies in the Reionization Epoch”. In: *ApJ* 777.1, 39, p. 39. DOI: 10.1088/0004-637X/777/1/39. arXiv: 1304.6404 [astro-ph.CO].

- Zahedy, Fakhri S., Hsiao-Wen Chen, Thomas M. Cooper, et al. (Sept. 2021). “The Cosmic Ultraviolet Baryon Survey (CUBS) - III. Physical properties and elemental abundances of Lyman-limit systems at $z < 1$ ”. In: *MNRAS* 506.1, pp. 877–902. DOI: 10.1093/mnras/stab1661. arXiv: 2106.04608 [astro-ph.GA].
- Zahedy, Fakhri S., Hsiao-Wen Chen, Sean D. Johnson, et al. (Apr. 2019). “Characterizing circumgalactic gas around massive ellipticals at $z \sim 0.4$ - II. Physical properties and elemental abundances”. In: *MNRAS* 484.2, pp. 2257–2280. DOI: 10.1093/mnras/sty3482. arXiv: 1809.05115 [astro-ph.GA].
- Zhang, Dong (Nov. 2018). “A Review of the Theory of Galactic Winds Driven by Stellar Feedback”. In: *Galaxies* 6.4, p. 114. DOI: 10.3390/galaxies6040114. arXiv: 1811.00558 [astro-ph.GA].
- Zheng, Zheng, Renyue Cen, David Weinberg, et al. (Oct. 2011). “Extended Ly α Emission around Star-forming Galaxies”. In: *ApJ* 739.2, 62, p. 62. DOI: 10.1088/0004-637X/739/2/62. arXiv: 1010.3017 [astro-ph.CO].
- Zheng, Zheng and Jordi Miralda-Escudé (Oct. 2002). “Monte Carlo Simulation of Ly α Scattering and Application to Damped Ly α Systems”. In: *ApJ* 578.1, pp. 33–42. DOI: 10.1086/342400. arXiv: astro-ph/0203287 [astro-ph].
- Zheng, Zheng and Joshua Wallace (Oct. 2014). “Anisotropic Lyman-alpha Emission”. In: *ApJ* 794.2, 116, p. 116. DOI: 10.1088/0004-637X/794/2/116. arXiv: 1308.1405 [astro-ph.CO].
- Zweibel, Ellen G. (May 2017). “The basis for cosmic ray feedback: Written on the wind”. In: *Physics of Plasmas* 24.5, 055402, p. 055402. DOI: 10.1063/1.4984017.